Modelling woody debris dam form to function to location for flood purposes

David Furnues

Hydro-environmental Research Centre

School of Engineering, Cardiff University, Cardiff CF24 3AA, U.K.

A thesis submitted to Cardiff University

In candidature for the degree of

Doctor of Philosophy

October 2023

Abstract

With traditional flood defences seen as costly and no longer able to mitigate the effects of climate change, Natural Flood Management (NFM) has become the new paradigm, to complement hard engineered flood defences in a less expensive and more environmentally sustainable way. Unlike hard engineered flood defences which speeds the flow through communities, NFM slows the flow through upper catchments and reduces the flood peak. NFM could involve planting riparian and floodplain woodland, installing water storage ponds, re-meandering water courses and installing engineered woody debris dams (WDDs). However, the evidence base of NFM is relatively new and many gaps remain, especially about its effectiveness in large flood events. To give confidence in the implementation of NFM, a robust scientific evidence base is needed and to this end the United Kingdom (UK) governments have invested in NFM projects for research.

Engineered WDDs are installed in upper catchments as part of nature-based solutions to reduce fluvial flood risk. They are designed to slow the flow through the catchment, enhance channel floodplain connectivity and increase temporary water storage, so attenuating the flow. As the effect of an individual WDD in slowing the flow is small, a large number is required at the catchment scale. Hydro-environmental modelling has become increasingly popular to predict the effectiveness of multiple WDDs in attenuating the flow at the larger scale. However, with no standardised tool to simulate them and a lack of quantifiable empirical data to validate results, uncertainty remains in representing WDDs in the modelling domain.

This research investigates the efficacy of a network of WDDs, in attenuating peak flow. To address this aim, this thesis examines the effectiveness of WDD structural design, on sediment transport dynamics, to inform the development of a suitable hydraulic unit for use in a hydro-environmental model. As local scour is fundamental for investigating WDD design, providing insight into the hydraulics at WDDs, flume experiments with an erodible bed, were conducted to investigate bathymetric changes in respect to structural design. Structures were composed of three horizontal wooden key members stacked vertically one above the other, representative of WDDs installed at Wilderhope Brook, Shropshire, UK. WDD design criteria plays an important role in establishing the extent of scour and deposition with key member heights above the bed and gaps between key members altering flow hydraulics. To verify

experiments conducted in the flume, the flume was simulated in Flood Modeller v6.1. using 1D, 1D-2D linked and 2D models. Hydro-environmental modelling was used to ascertain, bed / boundary shear stress distributions, velocity profiles and flow depths whereby statistical analysis was performed to examine the accuracy of the hydraulic unit that was used to represent WDDs.

To further examine WDD induced morphological effects in the real-world, a field survey at Wilderhope Brook (2019) was conducted which involved examining channel planform adjustment by comparing the surveyed water course to historical maps. To examine how effective the WDDs are at attenuating peak flow in the real-world, catchment descriptors obtained through the field survey enabled 1D hydro-environmental modelling of the catchment. WDD effectiveness in attenuating peak flow was simulated for two storm events with results verified using field data.

This thesis helps to inform optimal WDD design criteria for the desired function in this specific location, while offering a hydraulic structural representation which can be manipulated to account for seasonal changes. Additionally, this thesis, in part, showcases the optimum WDD design for the desired function and provides a hydraulic structural representation unit which addresses the research gap into how best to simulate WDDs in the modelling domain enabling improved understanding of the potential efficiency of installed WDDs at other real-world upper catchments.

Acknowledgements

Table of Contents

List of Figures

List of Tables

List of Appendices

Acronyms

1D	One dimensional
2D	Two dimensional
3D	Three dimensional
ADI	Alternating Direction Implicit
ADV	Acoustic Doppler Velocimeter
AoI	Area of Interest
API	Application Processing Interface
ATM	Airborne Thematic Mapper
BAJ	Bar Apex Jam
BGS	British Geological Survey
BTJ	Bar Top Jam
CEH	UK Centre of Ecology and Hydrology
CSAI	Cranfield Soil and AgriFood Institute
DDF	Depth, Duration, Frequency
DEFRA	Department for Environment Food and Rural Affairs – UK
DEM	Digital Elevation Model
DGPS	Differential Global Positioning System
DN	Digital Number
DSM	Digital Surface Model
DTM	Digital Terrain Model
EA	Environment Agency
ESRI	Environmental Systems Research Institute

FCRM	Flood and Coastal Risk Management
FEH	Flood Estimation Handbook
FM	Flood Modeller v6.1.
FoV	Field of Vision (m)
GCD	Geometric Change Detection
GIS	Global Information Systems
GloVis	Global Visualization viewer
GNSS	Global Navigation Satellite System
GPS	Global Positioning Systems
GVF	Gradually Varied Flow
HOST	Hydrology Of Soil Type
IDW	Inverse Distance Weighted
IPCC	International Panel on Climate Change
IR	Infra-Red (Hz)
LandIS	Cranfield Soil and Agrifood Institute: Soilscape
LIDAR	Light Detection and Ranging techniques
MDPE	Medium Density Polyethylene
MJ	Meander Jam
NBS	Nature-based Solutions
NCDBDY	Normal / Critical Depth Boundary
NDVI	Normalized Difference Vegetation Index
NFM	Natural Flood Management
NIR	Near Infra-Red
NSRI	National Soil Resources Institute

OLI	Operational Land Imager
OS	Ordnance Survey
POM	Particulate Organic Matter
PVC	Polyvinyl Chloride
QHBDY	Flow-Head Boundary
QTBDY	Flow-Time Boundary
RAF	Runoff Attenuation Feature
ReFH	Revitalised Flood Hydrograph
RGB	Red, Green, Blue
RMSE	Root-Mean-Square Deviation
SuDS	Sustainable Drainage Systems
SWIR	Short Wave Infra-Red
TIFF	Tag Image File Format
TIN	Triangular Irregular Network
TIRS	Thermal Infra-Red Sensor
TVD	Total Variation Diminishing
UK	United Kingdom
USGS	United States Geological Survey
WDD	Woody Debris Dam
WwNP	Working With Natural Processes

Nomenclatures

Symbol	Unit	Description
$\overline{d_{se}}$	m	Mean scour depth at equilibrium
$\overline{h_{fc}}$	m/s	Average flow depth in the flow contraction
$\hat{z}_i$	---	Expected vertical values
$A_{d_{50}}$	mm^2	Frontal area of the particle
W	m^2	Wetted area
A_{dim}	mm^3	Predicted scour depth and volume
A_p	m^2	Structural blockage area
B	mm or m	Main channel width
$\overline{B}$	Mm or m	Average main channel width
b	m	Weir width
Δm_s	m	computational grid size
Δt	s	Simulated unit of time
B_A	%	Total in-channel attenuation as a percentage of total flow volume
B_A+B_p	%	Catchment attenuation percentage
B_f	m	Flume width
B_{fp}	m	Width of flood plain
b_l	set value: 7.5cm	Kinect base length
B_p	%	Total floodplain attenuation as a percentage of total flow volume
B_r	---	Blockage ratio
B_{sw}	m	Bankfull stage width
C	$m^{\frac{1}{2}}/s$	Chezy constant

c... (Sub prefix x, y)	px	Axis direction of Principle point
C_D	---	Drag coefficient
C_d	---	Weir coefficient derived from spill coefficient
C_f	---	Calibration factor
C_L	---	Lift coefficient
C_p	---	Number of correctly classified pixels in each category
C_s	---	Chi-squared
C_T	---	Column Total
d	---	Difference per paired value
d_f	---	Sediment stored at the dam face
Di_c	mm	Key member diameter
Di_p	mm	Pier diameter
d_r	mm	Representative sediment grain size
d_s	mm	Local scour depth from established datum prior to flow conditions
d_{se}	mm	Local scour depth at equilibrium
d_{smax}	mm	Maximum scour depth
e	mm	Depth of the bottom of the structure to the bed
E	mm	Kinect depth accuracy error
E_1	J/Kg	Specific energy upstream of the WDD
E_2	J/Kg	Specific energy downstream of the WDD
E_n	J	Energy
E_{nt}	---	Channel entrenchment
F	N	Force
f	---	Friction factor coefficient
f... (Sub prefix x, y)	px	Axis focal length

F_D	---	Drag force
F_L	Pa	Lift force
Fr	---	Froude number
Fr_c	---	Contracted flow Froude number
f_v	---	Vortex shedding frequency for subcritical regions given in Schlichting (1979)
g	9.81 m/s^2	Gravity
G	mm	Vertical spacing between two key members or aperture size
G_w	mm	Disturbed wetted depth from bottom of structure to bed
H	mm	Effective weir head
h	mm	Flow depth
h_1	mm	Upstream flow depth
h_1-h_2	mm or m	Afflux
h_2	mm	Downstream flow depth
h_a	mm	Mean velocity Increment height
h_c	mm	Critical depth
h_{fp}	m	Height of flood plain
h_{max}	mm	Maximum height of exit dune
h_{mc}	m	Height of main channel
h_n	mm	Normal flow depth
h_s	m	Bankfull stage
h_t	mm	Maximum height of structure above bed
I	kg/yr	Inflow of Total Suspended Sediment
I_{QR}	---	Inter quartile range

K	px	Digital measured distance from Kinect to principal point, Z direction
k	---	Matlab established radial distortion coefficients
k… (sub-prefix 1, 2, 3)	---	Radial distortion coefficients
K_0	m^3/s	Conveyance
K_c	---	kappa coefficient
KE	J	Kinetic energy
K_m	px	Kinect digital measured distance
K_s	---	Particle roughness
K_w	px	Kinect measured width, x direction
L	mm	Longitudinal direction / distance
L_a	---	Boundary layer separation zone
L_{cmax}	m	Centre line of the channel between the determined start and end point
L_o	m	Horizontal distance between the determined start and end point
m	Kg/m^3	Mass of water
m_p	---	Kinect parameter of a linear normalisation as found in Khoshelham and Elberink (2012).
n	$s/m^{\frac{1}{3}}$	Manning's n roughness coefficient
n_m	---	Rank of the observed occurrences when arranged in descending order
n_u	---	Number of samples
n_y	---	Number of recorded years
O	kg/yr	Outflow of Total Suspended Sediment
O_l	---	Outliers
O_r	---	Output raster

p… (Sub prefix 1, 2)	---	Tangential distortion coefficients
P_c	---	Pearson's correlation coefficient
P_D	N/m^2	Average stream pressure on the debris due to the flow
px	px	Pixel
Q	l/s or m^3/s	Discharge
$q(z_{bs})$	mm	Kinect Quantization size / Depth resolution
Q… (super-prefix 1,2,3)	m^3/s	Discharge incrementally increasing
Q_2	m^3/s	Downstream discharge
Q_{bf}	m^3/s	Bankfull discharge
Q_c	---	Discharge coefficient
R	m	Hydraulic radius
r… (super-prefix 2,4,6)	---	The square root of the sum of x… (super-prefix 2,4,6) or y… (super-prefix 2,4,6)
Re*	---	Particle Reynolds number
Re_h	---	Hydraulic Radius Reynolds number
R_T	---	Row Total
S… (sub-prefix 1,2,3)	---	Subset features (sub-prefix denotes individual features)
S_0	m/m	Channel slope angle / gradient
S_e	m/m	Energy gradient
S_f	m/m	Surface slope / Hydraulic gradient
S_i	---	Sinuosity Index
Ss	---	Specific gravity of sediment divided by Specific gravity of water
St	---	Strouhal number

S_w	mm	Kinect sensor width, RGB = 3.58 mm, IR = 6.66 mm
t	hrs	Time
T_A	m^3	In-channel total attenuation
$T_A + T_p$	m^3	Catchment attenuation
T_{cpd}	---	Total number of classified pixels (diagonal total), based on confusion matrix
T_{cpr}	---	Total number of classified pixels in that category (row total), based on confusion matrix
T_{cs}	---	Total corrected samples
T_d	m	Actual true real-world measured distance
t_e	hrs	Time to develop equilibrium scour depth
T_p	m^3	Total floodplain attenuation
T_{rpc}	---	Total number of reference pixels in that category (column total), based on confusion matrix
T_{rpd}	---	Total number of Reference pixels (diagonal), based on confusion matrix
T_s	---	Total sampled
U	m/s	Localised velocity
U^*	m/s	Shear velocity
U_0	m/s	Mean velocity
U_2	m/s	Downstream localised velocity
U_{co}	m/s	Contracted flow velocity
U_d	m/s	Critical deposition velocity
U_{max}	m/s	Maximum velocity (at free surface)
U_r	m/s	Velocity reference
U_t	m/s	Velocity at top of particle
v	1×10^{-6} m^2/s	Kinematic viscosity

V_{ol}	m^3	Volume
W_{fpa}	m	Width of the flood prone area
W_h	m	Weir head elevation
W_n	---	WDD number
w_p	m^2	Wetted area blocked by the structure
w_u	m^2	Wetted area unobstructed by the structure
x	---	Horizontal axis (graphical x-direction) also being the horizontal direction along the channel in x-direction
$\bar{x}$	---	Mean of the values of the x-variable
x_d	---	Depth corresponding distortion point (x direction)
x_i	---	Values of the x-variable in a sample
y	---	Vertical axis (graphical y-direction)
$\bar{y}$	---	Mean of the values of the y-variable
y_d	---	Depth corresponding distortion point (y direction)
y_i	---	Values of the y-variable in a sample
y_k	---	Pier coefficient
z	---	Depth (graphical z-direction)
z_a	m	Depth average velocity height
Z_{bs}	m	Real measured distance, Kinect sensor to target
Z_i	---	Observed vertical values
γ	$9.81N/m^3$	Specific weight of water
ε	---	Relative roughness
θ	°	Angle
θ_s	°	Separation angle

μ	kg/m/s	Coefficient of dynamic viscosity
ρ	1000kg/m³	Relative submerged specific density
P_e	m	Wetted perimeter
σ	---	Standard deviation
τ*	---	Shields parameter, nondimensionalized by dividing submerged specific weight and the mean sediment size
$τ_c$	---	Critical tractive force required to initiate motion
$τ_b$	---	Bed / Boundary shear stress
$τ_e$	---	Excess shear stress

1

Introduction

1.1. Context

Fluvial floods are one of the most common natural hazards across the world, leading to loss of life, destruction of property and ecological damage (Dadson et al., 2017). The International Panel of Climate Change (IPCC, 2013) predicts that due to climate change, Europe is at high risk of experiencing heavy rainfall events with a 10% annual rainfall rise by 2100 compared to between 1985-2005, with it predicted that by the end of the century, both rainfall severity and frequency will increase. Intense precipitation over a short duration raises the risk of flash flood events. A study conducted by the Met Office Hadley Centre, points out there is growing evidence heavy rainfall events in the UK are becoming more frequent, citing climate change as a potential cause (Christidis et al., 2021). Using IPCC cumulative, high emission scenario CO_2 emissions, this would create a predicted warming of 3.5 - 4.8°C by 2080 which would expose a further 250,000 - 400,000 Europeans to river flood risk (IPCC, 2014).

Developing countries are especially vulnerable to the harmful effects of floods as they lack the socio-economic and governmental support to cope, resulting in a high number of fatalities due to the relatively low levels of flood protection (Tanoue et al., 2016). In developed countries fatalities are less prominent, however, capital destruction and economic loss can be higher. Since the mid-twentieth century there has been a major increase in socio-economic loss caused by flooding mainly due to population growth, increased economic activities on floodplains and greater exposure and vulnerability to flood risk (Jongman, et al., 2012; Winsemius et al., 2016).

People most vulnerable to floods generally live on floodplains, lack warning systems and have poor awareness of the flood hazard. Even though floodplains face increased flood risk, a large

proportion of the global population choose to live on them. Historically, floodplains attracted settlements due to their flat lands, fertile soils, and closeness to water supplies (Diehl et al., 2021), with the Ancient Egyptians noted to have settled on the Nile floodplains to aid their trade and economic development, defensive capabilities and access to fertile farmlands (Postel, 1999).

In England, ≈ 325,000 properties are located in areas with a 1:100 year return period (Flood Zone 3). Without action, this number is expected to increase to ≈ 555,000 by 2055 (National Infrastructure Commission, 2022). Building developments with impermeable surfaces on floodplains can exacerbate runoff, reduce lag-time and cause rivers to burst their banks (Evans et al, 2004).

Hard engineered flood defences are expensive to build and maintain, provide only localised solutions to flooding and can compound flood risk further downstream which, with continued development on the floodplains and climate change increasing flood risk, puts pressure on these structures, with a shift towards soft engineering as a complementary approach. Natural Flood Management, intended to reduce flood risk by natural sustainable techniques, has grown in popularity, focusing on a more holistic and integrated form of flood management (Werritty, 2006).

Related terms, often used interchangeably with NFM, include Working with Natural Processes (WwNP), a broad term used for any work that restores and protects natural processes, and Nature-based Solutions (NBS), a subset of WwNP that restore the natural processes by addressing societal challenges and adaptively providing human well-being (Hollis, 2021). This whole catchment approach uses adaptative techniques rather than mitigation, which enables communities to become involved in the ecological environment and embrace land use changes, that work with nature, as a non-climatic driver (Wilby et al., 2008). Since the end of the 20th century, Green Infrastructure policies and Sustainable Drainage Systems (SuDS) have globally gained impetus in environmental policy (EEA, 2015; Defra, 2019), making space for water, and helping urban communities become more flood resilient (Everett et al., 2015). To address the challenges of urban sustainability, several nature-based solutions and ecosystem strategies have been developed across the world that use natural processes to restore the hydrologic function of the urban environment. This paradigm of NFM using sacrificial land is

nothing new, given the Vikings used their 'Ings' or flood meadows to store excess water in the UK.

1.1.1.   A Natural Flood Management approach

Governments across the world are adopting nature-based approaches (Hankin et al., 2020). However, unlike large scale hard engineering defences, which have an accepted evidence base, NFM lacks a robust, scientific evidence-based approach, needed to enhance confidence in implementing future NFM strategies (Ellis et al., 2021).

In the 2007 UK summer floods, 50% of hard engineering flood defences became overtopped (Pitt, 2008). These events, alongside increases in flood risk due to climate change (Evans et al., 2004) and floodplain development, have thrown doubt on whether conventional approaches to flood management alone are sufficient. As discussed, with flood variability and severity likely to increase as a result of climate change, problems associated with traditional hard engineering approaches arise such as levee breaches, with the levee preventing overspill re-entering into the channel. With an estimated 2.4 million properties at risk of river and coastal flooding in England and Wales (Environment Agency, 2009) engineered flood defences which protect localised areas would not be cost effective to build and maintain everywhere in the catchment (SEPA, 2015). Such Hard engineering requires continual maintenance with associated costs and can cause environmental disturbance (Dyer, 2004).

Technical Flood Management uses hard engineering techniques to provide space for additional discharge (Q) during a flood event within the river channel. This is achieved by increasing the water course depth using flood walls, raised embankments and levees to re-direct peak discharge downstream, thus protecting high valued areas. Hard engineering may use artificially straightened channels to lower flow resistance, increasing localised velocity and thus the rate excess water is conveyed away from the local area (von Lany and Palmer, 2007). Although, this approach of re-directing flow lessens the local risk it can increase flood risk of downstream communities (Fleming, 2002). This increased risk is due to decreases in downstream velocity associated with the channel change from the anthropogenically managed channelised water course to the natural channel. In natural channels, local velocity

decreases due to increased flow resistance. During heavy rainfall and slowed velocity in natural channels, the wetted area (W) increases as calculated using Equation 1.1. Therefore, high discharge can increase flood risk, unless velocity increases. Increased flood risk is caused by the flow depth increasing as channel geometry remains relatively constant.

$$Q = U.W \hspace{4cm} (1.1)$$

Continuity Equation 1.1, calculates discharge (Q) using localised velocity (U) and wetted area (W).

Flood policy has been driven by a need for flood mitigation that is not only cost-effective but can manage flooding in the wider catchment (Fleming, 2002). NFM is intended to address flooding as a whole catchment approach, hopefully enabling people to live with water in light of climate change.

> *'NFM aims to reduce flood risk by protecting, restoring and emulating the natural hydrological and morphological processes, features and characteristics of catchments using environmentally sensitive and beneficial techniques to manage sources and flow pathways of flood waters'* (Environment Agency, 2010; SEPA, 2015).

There has become a movement away from flood defence to flood management. As shown in Figure 1.1, the Flood and Coastal Risk Management (FCRM) strategy shows a long-term interest in nature-based solutions in reducing flood risk using a 'catchment-based approach' to manage the flow of water from source to sink (Environment Agency, 2022a). For example, New Forest Conservationists have announced a 10-year project to re-meander previously straightened channels and in the 2016 budget the UK Government pledged £15 million for a 25 Year Environment Plan to use NFM (Future Climate Info., 2022). In this way, nature-based solutions and engineered flood and coastal defences can complement each other to manage flood risk to communities.
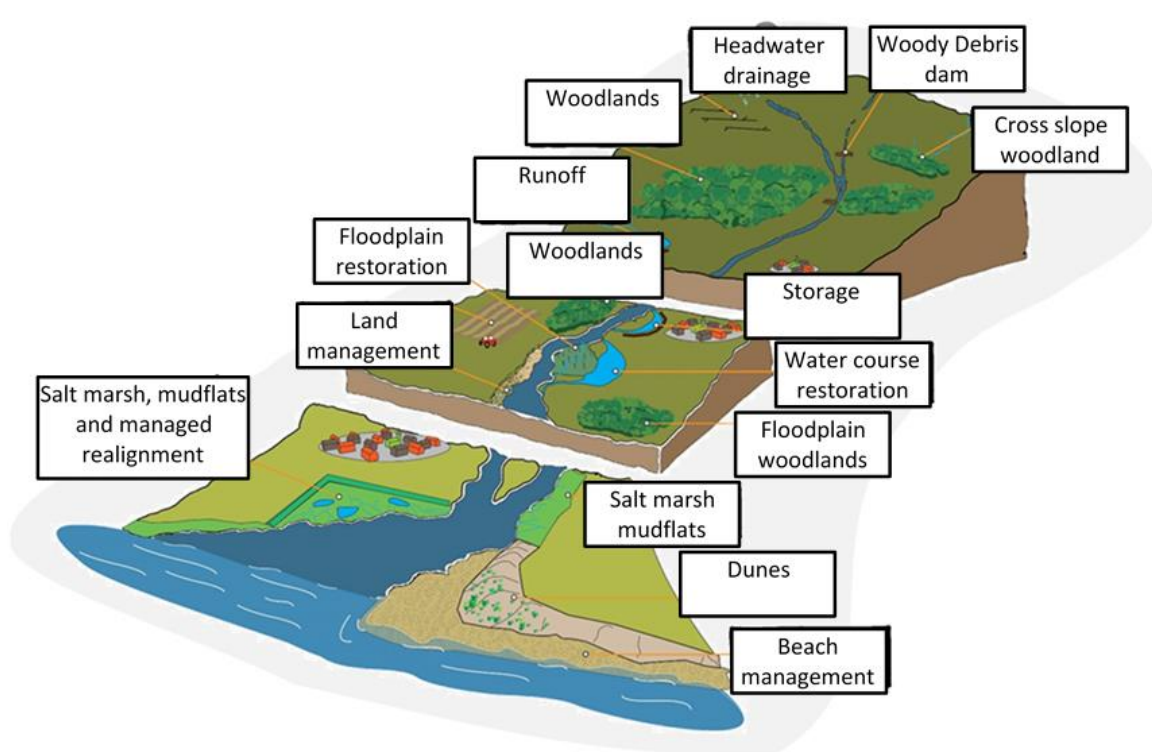
Figure 1.1: Working with Natural Processes (WwNP) from source to sink with WDDs displayed in the upper catchment (adapted from Burgess-Gamble et al., 2018).

Where there is space, NFM techniques store and slow the flow from upstream in response to high discharge, to help reduce flood levels to downstream communities. In the UK, the Environment Agency (EA) invests in green infrastructure in urban areas and complements traditional hard engineering defences with NFM or WwNP to reduce flood risk (Ngai et al., 2017). NFM involves tree planting or silvicultural activities, reconnecting rivers to their floodplains, temporarily storing water on open land and installing small-scale Runoff Attenuation Features (RAFs) such as WDDs, designed to slow the flow and create temporary storage of water during periods of high flow (DEFRA, 2019). The technique of building engineered WDDs can also reduce soil erosion, trap sediments and protect water courses (DEFRA, 2019). This study is motivated to investigate through modelling and empirical data how the installation of multiple WDDs in a small, first-order upland stream, can impact the flood risk to downstream communities.

1.1.2.   Woody debris dams within natural flood management

Installing engineered WDDs in the upper catchment can reduce flood magnitude by lowering the peak discharge and hence reducing the risk of breaches in downstream flood defences. WDDs can form naturally when trees fall into water courses, are built by beavers or constructed anthropogenically, constricting and confining the flow. They create backwaters, new ponding sites and infill existing storage areas, enabling greater time for infiltration and percolation so slowing the flow (Figure 1.2) (Ngai et al., 2017). Over time debris (for example leaves) can accumulate around key members with the dam reducing through-flow and soil erosion but also enhancing trapping efficiency, providing habitats for ecosystems and protecting the water course from erosion (DEFRA, 2019). By desynchronising peak discharges from tributaries, slowing one tributary compared to another, downstream peak discharge can be reduced (Ferguson and Fenner, 2020). Desynchronisation is dependent upon duration, timing and location of inundation, which is critical as to how NFM impacts upon drainage functionality.
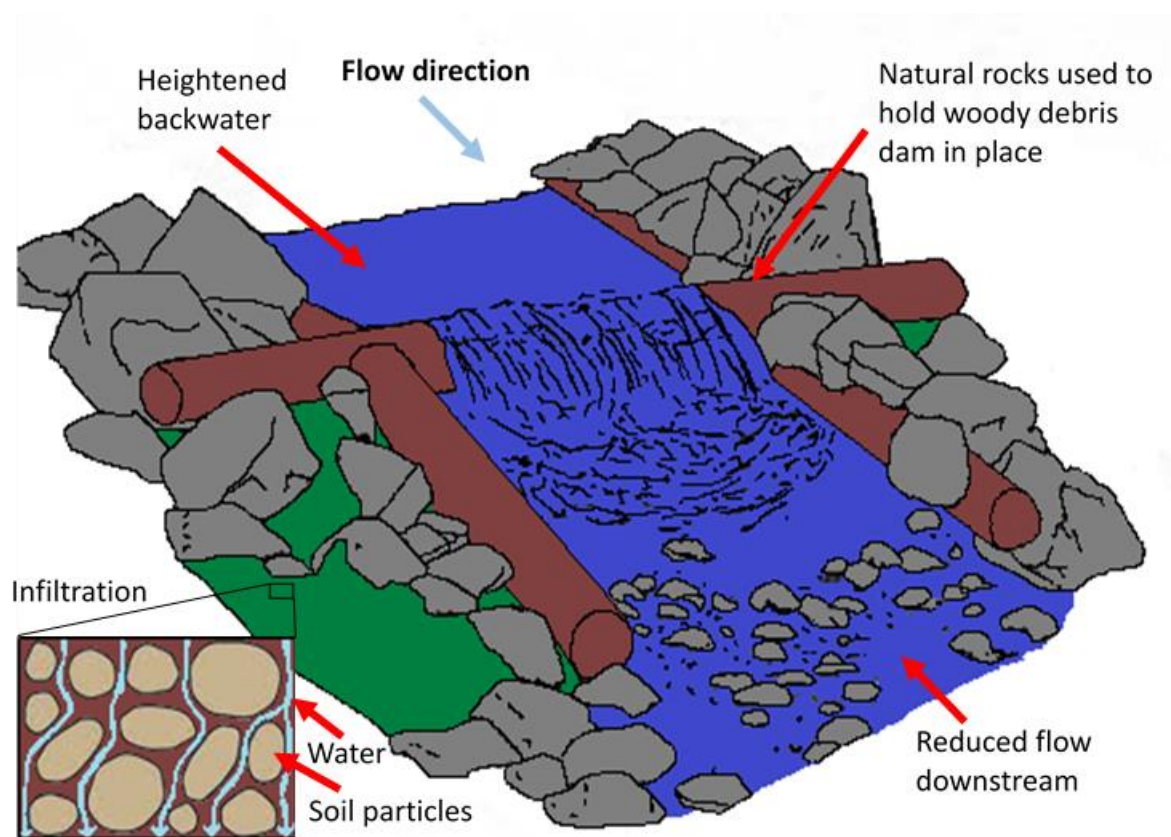
Figure 1.2: Diagram of a complete WDD with heightened backwater as a result of the key member held in place by naturally placed rocks and debris surrounding.

With the shift towards NFM, there has been an increase in the literature regarding the impact of WDDs at a local scale. However, the effectiveness of WDDs in larger catchments remains ambivalent. Though the uptake of WDDs remains uncertain (Waylen et al, 2017) due to the evidence gap surrounding their effectiveness at the catchment scale, SEPA (2016) highlights the importance of NFM as a sustainable flood risk technique to manage flooding at its source rather than relying on traditional hard methods further down the catchment. Today, in the UK, there are conflicting views as to whether the use of WDDs can effectively attenuate flow.

Difficulties involved in using engineered WDDs is understanding their effects on sediment supply and transfer, erosion and deposition, morphological changes and water storage in varying locations within catchments (Beechie et al., 2010). Furthermore, the behaviour of individual WDDs and their impact in different localities remains generally unknown. A common method to understand the overall effects of multiple WDDs within the catchment is through hydraulic modelling however as WDDs are complex in structure and can temporally change in design with varying blockage (Manners, 2007), without greater research into WDDs at a local scale, inserting them into numerical hydraulic models is uncertain (Leakey et al., 2020).

There remains uncertainty as to whether a network of multiple WDDs can mitigate flooding (Dadson et al., 2017). This research sets out to capture the complex hydraulics at different WDD designs and to validate a hydraulic model to assess the efficacy of WDDs. The latest long-term investment plan published by Benn et al. (2019), notes NFM alone is not sufficient to manage flood risk. It is suggested that NFM should be used in a complementary capacity, alongside conventional FCRM (Benn et al., 2019). Benn et al. (2019) outlines significant uncertainties surrounding NFM, noting most NFM projects cover small catchments and there is lack of scientific evidence about the effectiveness of WDDs in large catchments to manage floods. As aforementioned, the UK Government invested £15 million for NFM projects with part of this being for research on WDDs. However, the indicative proportion of investment in different FCRM activities, dependent on national variation, reveals that 7% was invested in NFM and 84% invested in conventional FCRM (Benn et al., 2019).

<div style="text-align: right; font-size: 3em; font-weight: bold;">2</div>

Literature review

2.1. Introduction

Flooding is a socio-economic and environmental problem which, with climate change, is predicted to increase in line with increasing precipitation Depth, Duration and Frequency (DDF) (Alfieri et al., 2016; Pitt, 2008). Since records began in 1766, annual mean precipitation in the UK has remained much the same however, seasonal mean precipitation has become highly variable. Since the 1960s, with event frequency and changes in seasonality, the magnitude of extreme rainfall has doubled over parts of the UK, and intensities previously experienced, on average every 25 years, now occur at 6-year intervals (Fowler and Kilsby, 2003). These climate changes have socio-economic implications in terms of flooding with multi-day intense rainfall events, defined as extreme precipitation on consecutive days, being an important cause of recent severe flooding in the UK, and any change in the magnitude of these events can have severe impacts on urban flood defences (Du et al., 2022). It is extremely difficult to mitigate flooding as it is a result of complex and intricate interrelationships between weather and catchment characteristics (size, shape, slope angle / gradient, storage capacity) (Ellis et al., 2021). For instance, research into slope has found steeper catchments can influence runoff transit time with water transported more quickly to the outlet (Tetzlaff et al., 2009), vegetation has been found to decrease quick runoff as it increases surface roughness and soil infiltration capacity (Lull and Reinhart, 1972), However, the complex, interrelationships between catchment characteristics make it difficult to quantify the relationship between one single catchment characteristic responsible for generating flooding. For example, Pitlick (1994) found that flood magnitude did not vary with catchment slope in their particular study region. To tackle the source of the problem, NFM a catchment-based

approach has been implemented, to slow and store flood water in the upper catchment which can influence downstream flooding. This reduces the reliance on engineered flood defences which are built in and around the downstream high valued areas prone to flood risk (SEPA, 2015). Fluvial flood management is undergoing a paradigm shift from engineered hard flood defences with concrete walls and raised embankments, to NFM, which use green infrastructures, to emulate natural hydrological and morphological processes to store water and reduce flow through the landscape. NFM is more economical and environmentally sustainable than relying on hard engineered flood defences alone (Cook et al., 2016). NFM is used in areas where the cost benefit ratio is not high enough to warrant hard engineered defences (SEPA, 2015). This nature-based approach to flood risk management has gained impetus in the UK, Europe and further afield (Wesselink et al., 2015; Ellis et al., 2021). However, NFM lacks certainty associated with the limited scientific research on its efficacy to cope with extreme floods and large catchments (Metcalfe et al., 2017; Wilkinson et al., 2019).

Literature asserts that hydrological processes are impacted by climate change and land change which has increased flood frequency (O'Connell et al., 2007; IPCC, 2013). Increased building and Infrastructures such as roads have decreased storage capacity and reduced runoff time so increasing flood peaks Historic changes in land use practices have had effect on the speed of flood propagation during heavy precipitation which can cause downstream flooding (Newcastle University, Environment Agency, 2011). Since the Second World War, there has been a radical change in land use management practices in the UK, in the demand for self-sufficiency in food production which has entailed the loss of forests and hedgerows, channelised streams with no riparian zones and new cultivation practices leading to increased surface runoff into water courses (O'Connell et al., 2007). Historically, woody debris which naturally fell into water courses became regarded as a navigation problem and a cause of flooding and so was routinely removed (Montgomery et al., 2003; Wohl, 2014; Roni et al., 2014). Floods that affected the UK during 2000 and 2001 reinforced growing concern that changed agricultural practices were responsible for increased flood risk (Wheater, 2006). It has been suggested that agricultural intensification in Northern Europe has also caused increased water course flood peaks from excess runoff yields (Pinter et al., 2006). Pitt (2008) recognised water management as being inextricably linked to land management and proposed that appropriate land management interventions should be adopted to reduce

downstream flood risk and used as a cost effective, complementary natural solution to hard engineering flood defences. There has become growing evidence that natural processes in the uplands control the catchment water balance, and that water interception has enhanced surface runoff at the local scale (O'Connell et al., 2007).

The runoff ratio depends on the soil moisture content, with the fraction of precipitation that appears as runoff entering the water course as discharge (Fryirs and Brierley, 2013). Infiltration flows through soil pores as throughflow depending on soil type and channel slope angle / gradient. Open passageways in the soil, caused for example by decaying roots or field drains, allow water to infiltrate and percolate deeper into the sub-surface. Once the soil can no longer absorb the water fast enough, then infiltration-excess overland flow occurs. If the subsurface soil becomes saturated, the water table rises and water flows across the surface into the channel. When surface runoff exceeds the upland channel network conveyance capacity this can lead to high valued areas becoming inundated downstream particularly where the timings of flood peaks of tributaries combine within the high stream order channel. The challenge is to understand not only the consequences of local nature-based processes but their mechanisms, how they work together and the interrelation between the local and catchment effects so NFM can be anthropogenically restored at the catchment scale (O'Connell et al., 2007).

With climate change projected to increase precipitation DDF and hence flood risk, the UK government is investing in NFM as a complementary technique to conventional hard engineered flood defences (Wingfield et al., 2019; Environment Agency, 2019). It is believed that hard engineering flood defences alone could not offset the more extreme scenarios of climate change to manage major floods and that building bigger defences is not the answer (Environment Agency, 2019). Extreme events are, by their nature, unpredictable as to when they will occur and where their greatest impact will be felt. Nature-based solutions attenuate the flow in the upper catchment and by slowly releasing it, reduce flood heights downstream so alleviating the pressure on conventional downstream defences. In this way, NFM supports conventional flood defences during high discharge (Environment Agency, 2021a). While hard engineered flood defences are designed to direct flow away from high risk areas using concrete and sheet-piled structure defence walls, raised embankments, weirs and culverts, NFM emulates natural processes to manage flow pathways using land management

techniques such as contour ploughing to slow surface runoff, turning offline measures such as ponds online to store excess water during high discharge and in-channel structures such as WDDs to delay and retain water in upper catchments.

2.2. Engineered woody debris dam design

Engineered WDDs are Runoff Attenuation Features (RAFs) situated in the upland agricultural catchments. A RAF is an anthropogenically engineered landscape intervention designed to intercept and attenuate a hydrological flow pathway for managing floods. Flow pathways are defined as routes including fluvial channels that convey the flow regime from source to sink (Hall et al., 2003). The idea is to locate a network of small RAFs throughout the upper rural landscape so they can slow, store and filter runoff. One type of RAF, used as a flood mitigation solution, is the WDD (Quinn et al., 2013a). They are generally built of wood and branches placed across streams to create backwaters, provide sediment trapping and increase channel roughness. The chief purpose of an engineered WDD is to temporarily store water in upper catchments during storm events, delaying peak discharge downstream (Grabowski et al., 2019). They are designed to intercept and attenuate rapid runoff during storms and create temporary storage areas, whilst enhancing channel-floodplain connectivity (Thomas and Nisbet, 2012; Grabowski et al., 2019; Barnsley et al., 2021).

There is no standard way to design an engineered WDD for its intended function. Though they mimic natural WDDs in the water course, there is currently a vast array of different designs of engineered WDDs mainly due to the lack of effective design criteria (Leakey et al., 2020; Hankin et al., 2020). Variation in design could also be due to the inadequate understanding of the effects of WDDs on channel hydraulics. Research providing greater insight into the hydraulics at WDDs could help inform design criteria (Bennett et al., 2015).

There is a lack of standardised terms used to differentiate between WDDs (Water Friendly Farming, 2020). This can lead to some confusion in literature which uses several terms for WDDs including leaky barriers (Leakey et al., 2020), leaky woody dams (Bradshaw, 2017), debris dams (Smock et al., 1989) large woody debris (Thompson et al., 2017), engineered log dams (Norbury et al., 2018), wood placements and flow restrictors (Ngai et al., 2017). These

disparate terms are often used interchangeably, though in the search for design effectiveness in attenuating the flow there has become more distinction (Water Friendly Farmer, 2020). In literature, terms continue to be interchangeable and with new designs other terms have come into use such as the horse jump type (Bradshaw, 2017), the Board Dam, the Living Dam and the Wedged Log Jam (Thames21, 2021), used as descriptors. The term leaky barrier has been introduced, though this type of instream restriction refers to the general functioning of natural and engineered wood structures as well as other instream structures such as boulder placements (Ngai et al., 2017). Leaky barriers and WDDs (Figure 2.1) were given distinct differences in their characteristics and functions (Water Friendly Farmer, 2020). Engineered leaky barriers have their bottom key member located > 30 cm above the winter base flow and are designed to attenuate high discharge while some engineered WDD designs can impede all flows, create varied flow with local erosion and pools upstream of them for instream habitats (Water Friendly Farmer, 2020).

Leaky Barrier	Woody Debris Dams (WDDs)
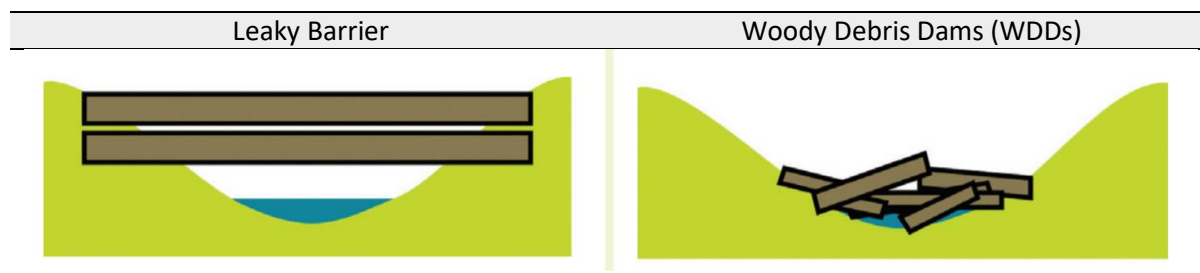
Figure 2.1: Leaky barriers attenuate peak discharge and are built to remain stable over their lifetime. WDDs attenuate all flows and create channel diversification, varied flow conditions and diverse stream habitats however WDDs can become unstable with channel erosion and degrade quicker than leaky barriers. Images taken from Water Friendly Farming (2020).

WDDs are designed with varying levels of complexity, from two or three pieces of wood across a channel to multiple stacked logs with accumulated detritus (SEPA., 2015). They are complex, porous structures which change over time, caused naturally by the build-up of various wood pieces and leaf material. Initially, they comprise of basic key members, which are large pieces of immobile wood housed in the channel, and by acting as a trapping device for smaller debris floating in the water course, they develop into intricate matrices of sediment build-up, snagged twigs, leaves and other materials lodged against one another (Manners, 2006; Dixon, 2013). These smaller pieces of wood which snag and trap against the key members are called racked members. The key members are usually longer and half the bankfull stage width of the channel which gives them stability and they are generally wide branching or multiple stemmed so that racked members easily snag on them (Dixon, 2013). It is suggested that woody material in stream channels have a diameter > 0.1 m and a length > 1 m (Keller and Swanson 1979; Linstead and Gurnell, 1999). Some key members have attached root wads which give them added stability in the water course with some remaining partially anchored through their root to the bankside to maintain firmness in their location. Additionally, root wads give key members greater complexity of shape (Dixon, 2013). To become hydraulically efficient, small debris accumulates and clings to the key members to act as a sieve to the fine debris and sediment (Wallerstein and Thorne, 1995). Engineered WDDs mimic the composition of the naturally formed dams and are a common tool in NFM and restoration projects. Some engineered WDDs have key members with root wads and stacked members which are slightly smaller linking pieces of wood which reinforce the structural integrity of the WDD. Racked members, which are the smallest and most variable in size, are sometimes the only members

visible after construction, giving a dense and disordered appearance to the WDD (Abbe et al., 2003).

The complex hydraulic effects of different WDD designs are associated with different functions (Dixon, 2015). WDDs have been classified in several ways but the most notable is probably that of active, partial and complete (Gregory et al., 1985) (Figure 2.2) as defined as:

> **Active**: which transverse the entire main channel width, inducing a step in the surface slope / hydraulic gradient at all flows. These dams are hydraulically effective and block the entire main channel width. Active dams pool water upstream during normal flow conditions and create a step in the hydraulic gradient (Sear et al., 2010). Relative to reaches without WDDs, during high discharge, active dams can cause overbank flow leading to flooding on the floodplain (Sear et al., 2010).

> **Complete**: which transverse the main channel width but are leaky and have little impact on the hydraulic gradient at low flows (Figure 2.1 and Figure 2.3) (Linstead and Gurnell, 1999).

> **Partial**: do not completely transverse the entire main channel width, occupying ≈ 75%.
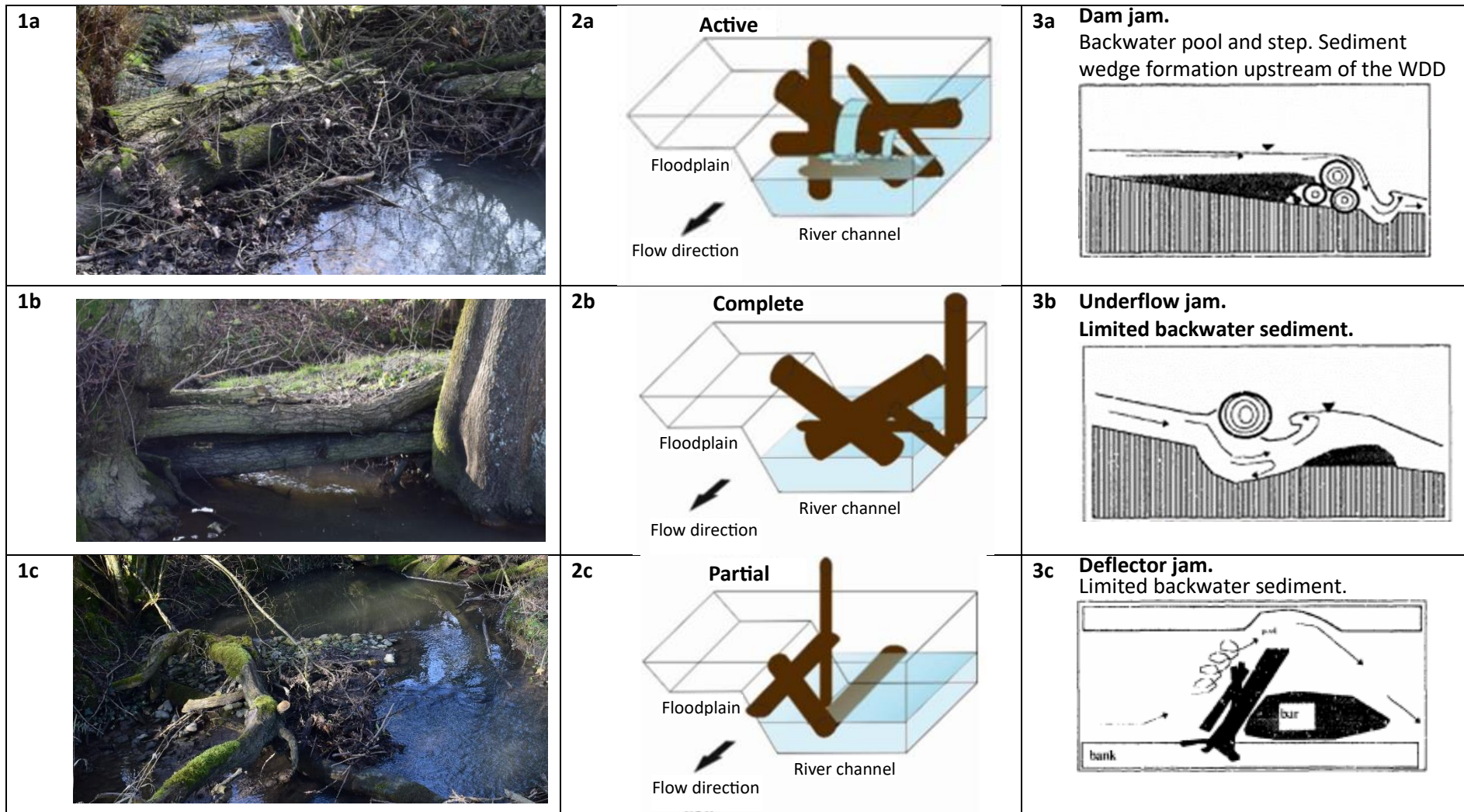
Figure 2.2: The photographs on the left were taken at the Wilderhope, Shropshire field site (Oct, 2018), depicting an active (1a), complete (1b) and partial (1c) dam The representations in the centre column by Dixon (2013) (2a, 2b, 2c) shows the three types of WDD recognised by Gregory et al. (1985) as active, complete and partial which are comparable to the field site photographs and later classification shown on the right (3a, 3b, 3c) as dam jam, underflow jam and deflector jam (Wallerstein and Thorne, 1997). The active and dam jam (1a, 2a, 3a) can be considered alike in that they display a complete barrier across the width of the channel and a step with a backwater pool. The complete dam and underflow jam (1b, 2b, 3b) are comparable as they demonstrate a complete barrier across the width of the channel but no definite step and no impact upon the water surface profile during low flows. The partial and deflector jam (1c, 2c, 3c) are similar as they extend across part of the main channel width and are therefore incomplete.
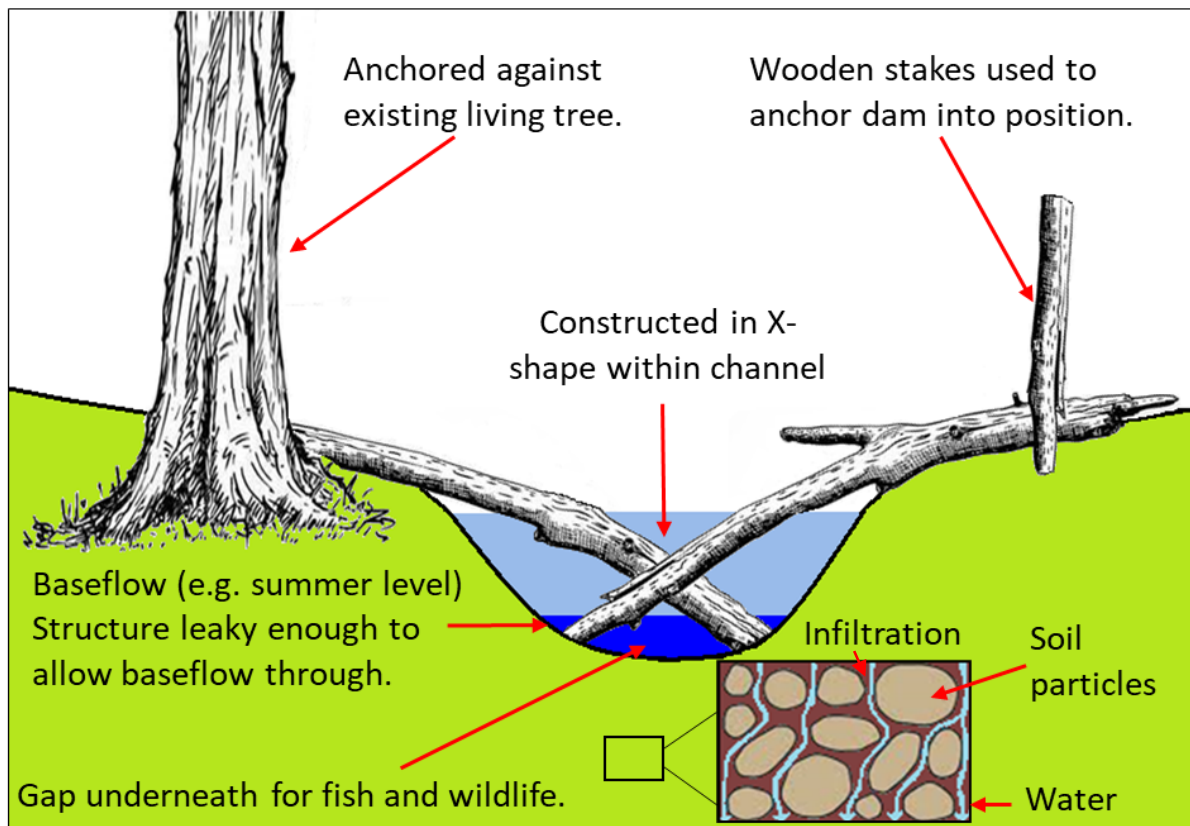
Figure 2.3: A simplified diagrammatic representation of a complete WDD. This WDD is held in position to ensure it is sufficiently robust and does not pose a safety risk to downstream communities should it become loose.

This classification of WDDs by Gregory et al. (1985) has been built upon with them named parallel, deflector, underflow and dam log jams (Wallerstein and Thorne, 1997). Active, Partial and Complete WDDs, as initially described by Gregory et al. (1985), have been diagrammatically represented (Dixon, 2013) and can be shown to be comparable to the subsequent classification by Wallerstein and Thorne (1997) (Figure 2.2). WDDs have subsequently been classified as bartop jams (BTJs), where the WDDs are unstable and chaotic, bar apex jams (BAJs) and meander jams (MJs). This was then reclassified into 10 WDDs based on key members and their orientation within the water course (Abbe et al., 2003). The simple classification of WDDs in headwater streams which is based on hydraulic impact continues to be used: active, complete and partial dams.

Active WDDs compared to complete WDDs are less porous in structural design and it is this that creates a hydraulic jump in the flow regime (Dixon, 2013). As leaf litter is seasonal in areas with deciduous trees and prevalent in the autumn months between October to December, it

is reasonable to presume that as the material biodegrades and is mobilised, then active and complete dams can become synonymous in structure and that WDDs can change temporally (Gregory et al., 1985; Sear et al., 2010; Thomas and Nisbet, 2012). As the composition of WDDs is complex and changeable, differing in porosity between dams and within the dam itself over time, its hydraulic nature is in a constant state of change (Manners, 2006).

WDDs vary in size and structure and the distance they extend into the channel with each generating a different hydraulic effect and producing different geomorphologic influences (Dixon, 2015). Within the same classification, two active WDDs may have different blockage ratios with one filling the entire cross-sectional area of the channel, having a less porous structure with a dense accumulation of debris compared to the other, so having different hydraulic effects and different functions (Dixon 2015).

There is uncertainty in the use of WDD forms for specific functions at different locations (Grabowski et al., 2019; Hankin et al., 2020). Questions arise as to which design is best suited in a specific location for the intended purpose and would particular designs be needed for locations in a network (Grabowski et al., 2019). By strategically positioning WDDs, this can have the desired effect of deflecting flows onto floodplains during storms, increasing water storage and lag time. It is suggested WDDs should be sited where there is room for water to be stored and spread, with runoff pathways where water courses and floodplains can interact or where there is high surface connectivity (Nicholson et al., 2012; Hankin et al., 2020).

2.3. Attenuating the Flow

The main purpose of an engineered WDD is to act as an in-stream intervention to slow the flow and create storage areas during high discharge (Grabowski et al., 2019; Wilkinson et al., 2019; Leakey et al., 2020). As WDDs are porous this enables temporary storage of runoff while allowing movement of water through and under them so reducing localised velocity and delaying the flood peak (Metcalfe et al., 2017). The attenuation effect of one WDD is small which suggests a network of WDDs would be needed to have the desired effect on high discharge at the larger scale (Bokhove et al., 2018). The purpose of multiple WDDs across upland catchments is to reduce peak discharge and increase lag-time, so altering the

downstream hydrograph. NFM does not propose to reduce the cumulative discharge during a storm event but rather to change the shape of the hydrograph to reduce the peak discharge by spreading it over a longer duration. The theory is to transfer discharge from the peak of the hydrograph to the falling limb (Thomas and Nisbet, 2017). Flood modelling is now typically used to quantify flow attenuation at WDDs by modelling changes to the stream hydrograph (McParland, 2019).

By adding engineered WDDs into an upland stream, high discharge runs slower through and around them producing longer lag times, the principle being to reduce flood magnitude to downstream communities (Figure 2.4). During a flood event where precipitation falls throughout the catchment, peak discharges are delivered to the lower water course from separate tributaries. If the peak discharge from one of the sub catchments can be delayed, arriving at the lower water course after the flood peak, the main flood peak will reduce. However, interventions slowing the flow in one sub-catchment could be counterproductive, as it could combine into the lower water course, synchronising with other tributaries which were previously asynchronous, only to worsen the situation (Environment Agency, 2017). Synchronisation could prove problematic as if peaks coincide from different sub-catchments, this could potentially exacerbate flooding downstream. The delay of upstream peak discharge caused by WDD networks on one sub-catchment must be carefully timed to ensure it is desynchronised to other sub-catchments to reduce flood magnitude (Pattison et al, 2014). It is therefore essential within a catchment scale approach to spatially evaluate where best to install WDD interventions to ensure the lag-time does not coincide with the flood peak arrival time from other tributaries into the lower water course (Dixon et al., 2016; Dadson et al., 2017).

This was demonstrated in a simulation study of flood hydrographs on the River Ouse (Yorkshire) whereby it was found that timings of flood hydrographs from sub-catchments had impact on peak discharge and flow depth (h) and therefore flooding downstream (Odoni and Lane, 2010a). Due to the potentiality for coincident flood waves, the location of a WDD intervention can increase, decrease or have no impact on downstream flood magnitude as measured by the flood peak reduction (Odoni and Lane, 2010a). Further complexity is added, as rainfall has no specific spatial property within catchments which means there is no homogeneity across the catchment and uncertainty therefore arises in flow attenuation of a

sub-catchment in a combination of tributaries (I-Hsien Porter, 2011). Odoni and Lane (2010a) found the installation of 100 leaky barriers reduced the magnitude of a flood event by 7.5%, from 29.5 m^3/s to 27.3 m^3/s. Odoni and Lane (2010a) showed by modelling riparian planting and leaky barriers the magnitude of the reduction increased for larger events. However, early modelling research based on a site in the New Forest, Hampshire, UK using observed hydrograph travel times, found that over a 4.028 km reach, travel time was increased by over 100 mins where there were WDDs for a discharge of 0.1 m^3/s, but this decreased to 10 mins at a higher discharge of 1 m^3/s (Gregory et al., 1985). Gregory et al. (1985) findings suggest, like Odoni and Lane (2010a), that WDDs located in upland streams prove to be more effective in increasing lag time during low discharge rather than at high discharge however their findings slightly differ. This could be a result of the difference in catchment setting or modelling approaches to represent WDDs.
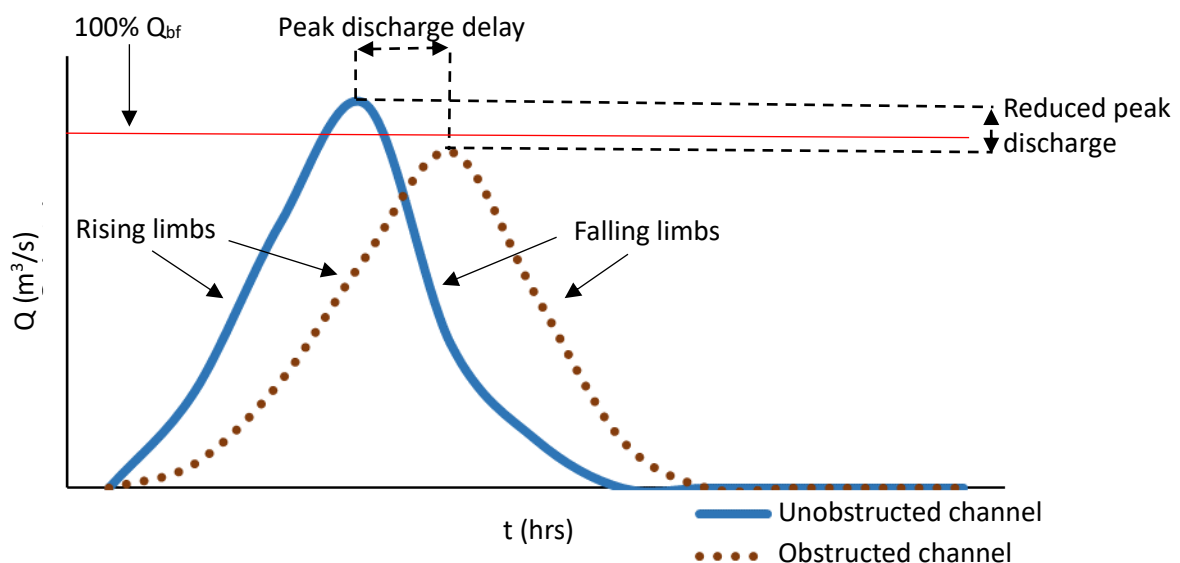
Figure 2.4: Hydrograph displaying discharge (Q) against time (t). The horizontal red line shows 100% bankfull (100% Q_{bf}) at which point flooding may occur once discharge surpasses this value. WDDs can increase lag time and reduce peak discharge causing the curve to flatten, whereby downstream discharge can become <100% Q_{bf}. By introducing WDDs in upper catchments the flow can be slowed.

There is a lack of confidence in the efficacy of networks of WDDs being able to alter the downstream hydrograph and whether findings from one catchment would be transferrable to another (Dadson et al., 2017; Waylen et al., 2017; Wingfield et al., 2019). There is uncertainty

that multiple WDDs would be sufficiently effective in combining to mitigate major flooding at the catchment scale (Dadson et al., 2017; Metcalfe et al., 2017; Environment Agency, 2019; Grabowski et al., 2019; Wingfield et al., 2019). The main reason for the limited adoption of WDD networks as RAFs is the lack of conclusive evidence of their effectiveness in delaying and attenuating flow during a storm event (Wingfield et al., 2019). This uncertainty is explained as a lack of unequivocable scientific evidence testing the effectiveness of a network of WDDs in holding back floodwater at the larger scale (Dadson et al., 2017). The problem is that this cumulative effect is highly uncertain because there remains limited understanding of the effects of an individual WDD on flow (Metcalfe et al., 2017). Scaling from plot to catchment is a major problem. Though WDDs may be more effective during low discharge at the local scale, there is a low level of confidence that they will mitigate flooding at the catchment scale during larger floods (Ngai et al., 2017; Bokhove et al., 2018). Furthermore, the geomorphic structure and hydrologic response in one catchment differs from another (Rodriguez-Iturbe and Valdes, 1979). With hydrodynamic dispersion, precipitation which falls in the same location at the same time in the same catchment can reach the outlet at different times due to flow resistance and storage attenuation (Pattison et al., 2014). The movement of a storm across a catchment can impact on discharge responses and the flood hydrograph depending on the catchment descriptors (size, channel slope angle / gradient, geology, land use and altitude) (Nikolopoulos et al., 2014). This is compounded by attempting to transfer findings between catchments with unique descriptors which control runoff generation and transmission across the landscape. Additionally, each storm event is denoted by its individual intensity and controlled by the catchment structure such as how hillslope and tributary flows combine (Pattison and Lane, 2012). Interplay between catchment spatio-temporal mechanisms can alter extreme flood events as they are dependent on antecedent soil moisture conditions and rainfall intensity. This means that the same rainfall depth, when averaged over a period of time can lead to a different peak discharge. Land management is another important factor in runoff with differences in land use within the sub-catchment and between catchments. The complexities of translating findings between catchments are made more difficult by the intermittent frequency of storms, with each flood characterised by several variables. The difficulty lies in that flood hazards are stochastic, with uncertainty and randomness, whereas flood modelling is deterministic, assuming variables are known and can be accurately measured, which does not account for the complexity and unpredictability. It is suggested that gathering sufficient

data to make robust scientific conclusions at catchment scales could take an inordinate amount of time (Pattison and Lane, 2012).

2.4. Flood modelling

Research has turned to up-scaling WDDs through hydro-environmental modelling, (hydro-environmental modelling referring here to the dynamic parameters i.e. water levels and velocities, and environmental in the context of the catchment parameters) however, the challenge is to find an appropriate method to model their complex forms and porosity. Much of the literature uses modelling rather than field-based observations to overcome problems with the lack of study sites, the need for data over long periods and challenges in overcoming the plot to catchment scaling problem. However, there is some scepticism in modelling NFM (DEFRA, 2020).

Hydraulic models can be used to simulate flow regimes by using fluid motion equations to simulate flow depth, velocity, and flood extent (Teng et al., 2017; Hosseiny et al., 2020). One-dimensional (1D) flood modelling assumes water moves in the longitudinal direction of the river and represents the channel by generating a series of cross-sections at regular intervals, which delineates the topography of the channel and its immediate, adjacent floodplain (Thomas and Nisbet, 2012; Babister at al., 2012) (Figure 2.5). As 1D models describe the water course and floodplain by cross-sections, they require topographical data (Betsholtz and Nordlöf, 2017). Additionally, methods for presenting structures such as bridges, weirs and culverts are well developed in 1D modelling, and are included in 1D standard empirical equations (Crowder, 2009; Babister et al., 2012). As a rule, 1D hydraulic models are used to simulate fluvial flood events (Betsholtz and Nordlöf, 2017) since they have accurate flow depth calculations where there is unidirectional flow, have a range of hydraulic structure options available and can simulate backwater effects (Environment Agency, 2021b). Limitations in 1D-hydraulic modelling, include only being able to simulate flood wave on the unidirectional longitudinal plane, localised velocity being perpendicular to cross-sections and the topography being used as cross-sections rather than as a continuous surface (Dasallas et al., 2019).
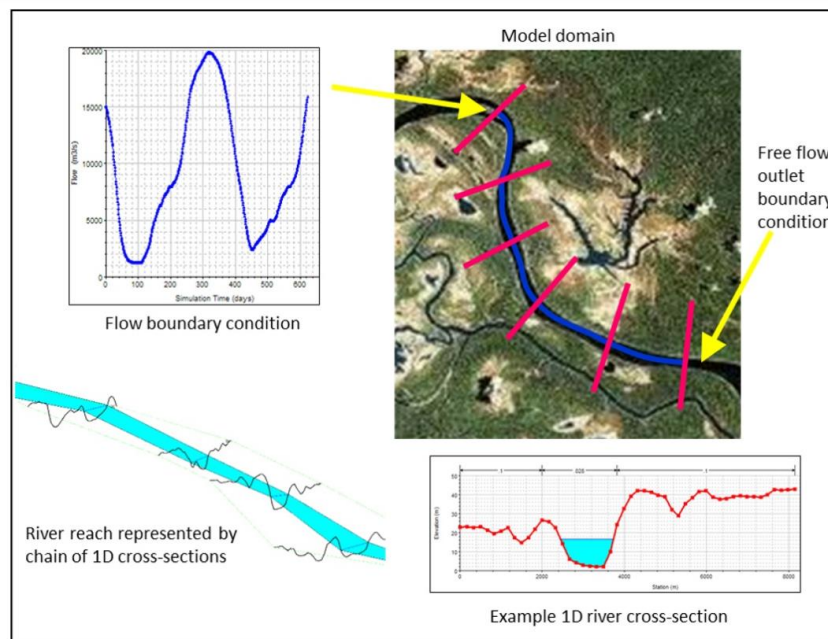
Figure 2.5: Basic 1D fluvial model of a river, showing a river reach with 1D cross-sections, boundary conditions and associated graphical images of 1D cross-section and flow boundary conditions. Taken from Trigg (2016).

Two dimensional (2D) models assume discharge moves multidirectionally, in both the longitudinal and lateral direction, using a continuous mesh or a raster grid to define the water course (Dasallas et al., 2019) (Figure 2.6). 2D is more detailed and can capture complex flow patterns. However, it is data intensive, requiring a high level of catchment detail and tends to have long run-times.
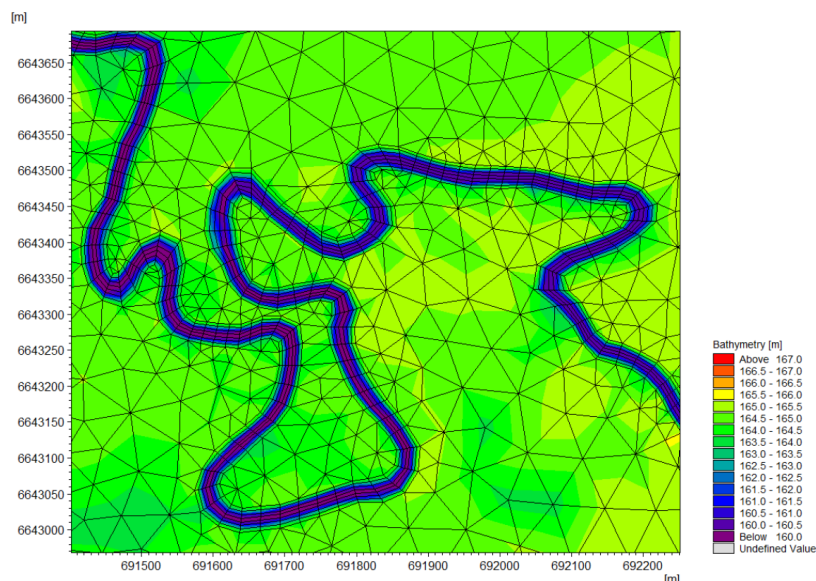
Figure 2.6: Triangulated Irregular Network (TIN) displaying topographical features of the Lower Namoi Valley. Taken from Mackay et al. (2015).

As the 1D modelling approach is the most appropriate for modelling in-channel flows and 2D modelling for modelling floodplain flows, a linked 1D-2D model has the advantage of both approaches (Néelz and Pender, 2009; Pender and Néelz, 2011). 1D-2D models, represent the water course by 1D flow between cross-sections, and the floodplain by a 2D mesh. The drawback of using a linked 1D-2D approach is that more time is spent understanding and setting up the models compared to single model approaches. Furthermore, exchanges between in-channel flows and floodplains can be represented in different ways which suggests the predictive capacity of the modelling approaches could vary (Vojinovic and Tutulic, 2009).

3D hydraulic models, are used on a longitudinal, lateral and vertical plane (Liu and Merwade, 2018) (Figure 2.7). They can predict flow depth and localised velocity fields (Xing et al., 2018). However, 3D analysis is generally avoided as it needs a high level of computational power and extensive data requirements which can be costly, complex and time consuming to run, in contrast to 1D and 2D models (Crowder, 2009).
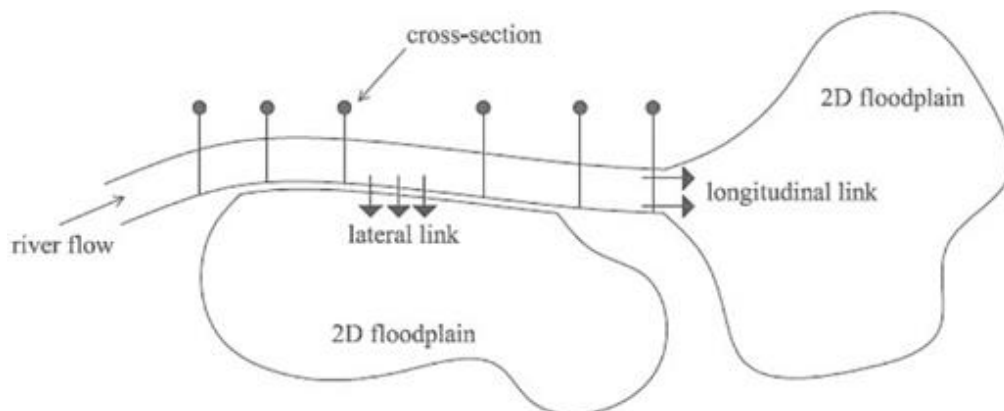
Figure 2.7: Schematic representing lateral and longitudinal linked 1D-2D model. Taken from Kvocka (2017).

1D-hydraulic modelling is increasingly deployed as a conceptual mathematical tool to analyse the effects of multiple, in-channel WDDs. By inputting data into the model to generate a numerical representation of the real-world, a wide range of fluvial processes such as backwater effects and flood inundation can be simulated (Paiva et al., 2011; Environment Agency, 2021c). A system of 1D cross-sectionally-averaged Saint-Venant equations denote flooding in terms of flood flow depth, peak discharge and localised velocity which represent

the principles of conservation of mass (Equation 1.1. as shown in section 1.1.1.) and momentum (Abdullah, 2012). As flow travels downstream with associated changes in discharge and flow depth, equations have been designed to solve the numerical terms which govern the flow pathway from one point to another (Nkwunonwo et al., 2020). Flood modelling software is constantly developing, and its application has grown with greater computational capacity and easier access to DEMs available using Light Detection and Ranging techniques (LIDAR) (Ali et al., 2015). LIDAR offers vast information content to parameterize topography which can be used in hydraulic modelling (Abdullah, 2012). Due to the advancement of LIDAR, high-resolutions DEMs have become more available.

Hydraulic modelling increases the understanding of the effectiveness of engineered WDDs for flood risk management. However, there is a lack of studies testing the flood risk performance of NFM, particularly during high discharge at large catchment scales (Wingfield et al., 2019). With difficulties in transferring results between different catchments and the low frequency of flood events, there is some scepticism whether sufficient empirical data can be gathered to produce statistically robust conclusions at the catchment scale (Pattison and Lane, 2012). Flood models enable the holistic means to examine the efficacy of engineered WDDs at the catchment scale using catchment descriptors including topography and precipitation. Models offer innumerable, replicable experiments to conceptually analyse predictive theories regarding flow (Norbury et al., 2021). However, although there has been great advancement in flood modelling techniques, there remains uncertainty surrounding their use in accurately capturing WDDs hydraulics. Hydraulic and hydrological modelling of WDDs is challenging, mainly due to difficulties in representing a network of WDDs as realistically as possible. The research gap remains as to how best to simulate the hydraulic, hydrological and morphological complexities caused by WDDs within hydro-environmental modelling (Addy and Wilkinson, 2019).

WDD effects on turbulent flow and fluid forces operating on and around their complex, natural geometries remain uncertain (Bennett et al., 2015). WDDs temporarily store water during high discharge with water leaking from the storage area, with the amount of leakage dependent upon WDD porosity. WDD effectiveness in attenuating flow is a function of several parameters including the storm event precipitation DDF in respect to WDD storage volume, size, porosity and design (Senior et al., 2022). These parameters differ in the natural world and across sites

and the precise WDD porosity / leakiness difficult to determine. There remains the need for greater understanding of the hydraulic functioning of WDDs and their hydrological and sedimentological effects, particularly due to their unique differences in size and porosity. This can be achieved by using a combination of controlled laboratory experiments and numerical experiments alongside field observations (Quinn et al., 2022). Catchment descriptors which differ in the natural world and across sites, along with the unique geometry of individual WDDs leading to there being no standard approach of representing them in hydraulic models (Liu et al., 2004; Addy and Wilkinson, 2019). As a result, WDDs are represented in different ways including adjustments to geometry by creating perturbations in the DEM to represent the WDDs, altering channel roughness by creating isolated areas of increased Manning's n roughness coefficients (n) where WDDs are located or by creating a hydraulic structure unit to represent their complex characteristics (Addy and Wilkinson, 2019) (Figure 2.8). Additionally, modelling WDD efficiency in mitigating downstream flooding is inhibited by the dearth of empirical data to validate results which suggests observed / field data could improve modelling accuracy rather than relying on Flood Estimation Handbook (FEH) designer flood events (Senior et al., 2022; Lavers et al., 2022).
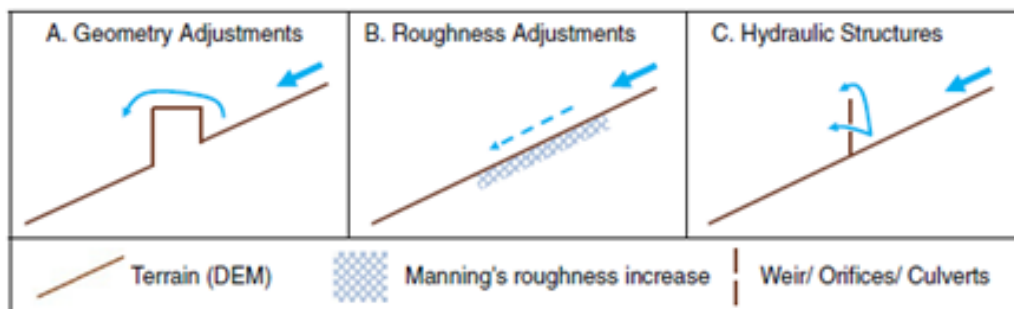
Figure 2.8: A representation of three techniques used to represent WDDs in hydraulic models to overcome there being no standardised method of representing WDDs in hydraulic models. These techniques were first proposed by Addy and Wilkinson (2019). Taken from Senior et al. (2022).

2.4.1. 1D and 2D modelling within the context of WDD design and analysis

Researchers have turned to modelling to quantify and predict the behaviour of WDDs to investigate their effects on flood hydrographs (Thomas and Nisbet, 2012) or floodplain connectivity (Kitts, 2010; Keys et al., 2018). Despite progress in modelling WDDs, there remains uncertainty in the suitability of models and approaches to represent them in hydraulic and hydrological models, mainly due to their complex nature. Typically, WDDs are represented by adjusting the channel geometry, increasing channel roughness (or both), or as a hydraulic structure by using weir or sluice gate units, frequently using models such as HEC-RAS (Keys et al., 2018), Hydro2de (Kitts 2010), Infoworks (Thomas and Nisbet, 2012) and Flood Modeller (Pinto et al., 2019). 1D modelling simulates linear domains, such as stream / river channels and uses cross-sections to examine flow depths, velocity or discharge. 2D models are useful in simulating the spread of flow over a 2D horizontal domain represented using a DEM and are often used to replicate complex overland flow and flooding processes which allows for analysis of, for example, WDD / floodplain inundation and channel-floodplain connectivity (Hill et al., 2023). The choice of model employed needs to lend itself to how the modeller conceptualises the NFM features which have complex characteristics and no standard way of modelling them. The challenge for the modeller is that there are many methods for conceptualising WDD representations and many different models.

WDDs can be modelled using the hydraulic structure representation approach, by comparing them to well-understood hydraulic structures such as weirs or culverts. The engineering equations, representing the features, are often inbuilt into hydraulic modelling packages such as Flood Modeller and HEC-RAS. Mathematical models of existing control structures are popular methods to calculate the effects of WWDs. Keys et al. (2018) used a weir function at each WDD location using HEC-RAS 2D simulations, to show increased channel-floodplain connectivity.

One physically based way to model is using a hydraulic structural representation to simulate WDDs by altering the channel geometry. Thomas and Nisbet (2012) used Infoworks in a 1D hydrodynamic model, to apply a 70% blockage ratio and varied roughness coefficients to represent the WDD in the channel. This is an attractive method since it captures the expected

flow profile of hydraulic structures in natural channels which are irregular in shape and accounts for the WDD blockage capacity by modelling the hydraulic flow upstream and downstream of the structures. Their findings showed that modelling a 9.2km^2 catchment at the River Fenni, South Wales, using field data, resulted in a 2 to 3 minute delay per WDD. However, a minimum effect upon the height of the flood peak was noted. The main problem is that this conceptualisation of WDDs, where the wetted area is reduced, assumes structures are impermeable generally resulting in an overestimated impact. Unless a sluice gate or a culvert is added, WDD structures appear solid (McPartlin, 2021). Metcalfe et al. (2017) combined TOPMODEL using 1D modelling with hydraulic equations for trash screen structures and sluice gates to model WDD, and represented the channel with a trapezoidal shape. By using a simplified trapezoidal shaped channel, this simplifies the hydraulic complexities at the WDDs.

Their model demonstrated that using 59 WDDs at a 29-km^2 catchment in North Yorkshire, had an 11% reduction in peak discharge. These researchers concluded that although WDDs reduced flooding during moderate rainfall events their effectiveness, during successive storm events, would be reduced due to backwater storage retainment. Pinto et al., (2019) used Flood Modeller (Jacobs 2018) 1D and represented WDDs as blockage ratios, calculated using the length of WDDs relative to channel width, with 37.7–74.1% of the channel blocked. Like Thomas and Nisbet (2021), Manning's n values were also manipulated at cross-sections and analysis focused on the 1D modelling component to assess the impact of WDDs on stage comparison. They found afflux increased gradually as blockage ratio increased, with a marked increase in afflux at the 95% blockage ratio.

Currently, the most utilised method to represent WDDs in models is achieved by changing the channel roughness coefficient, whereby increasing the roughness at the location of a WDD simulates the increased flow resistance. Kitts (2010) used a 2D simulation, in Hydro2de, to validate increasing the Manning's n roughness coefficient at the scale of a single, naturally occurring, dense WDD and showed that predictions of inundation, matched visual observations. Hydro2de is a 2D grid-based floodplain flow model (Beffa and Connell, 2001) which can model patterns of inundation in stream woodlands as they are not unidirectional. WDD roughness values were added to assess their influence on flood inundation extent. It was reasoned that by deploying the Manning's n value at the WDD location, proved better

than using geometry adjustment. However, changing the Manning's n to represent WDDs has drawbacks given its impact on high and low flows and having little effect on steep slopes (Leakey et al., 2020). Manning's n is also dependent on flow stage, as once WDDs are surcharged, they can be drowned out (Dixon, 2013). It is a widely held view that a physically based approach in modelling, which can be validated using field data, is likely to give a better representation of the functioning of WDDs in comparison to other methods (Metcalfe et al., 2017).

2.5. Flow resistance

Many modellers overcome the problem of having no standardised unit to represent a WDD by not modelling the WDD itself but instead using their measured hydraulic effects such as roughness coefficients or channel confinement (Metcalfe et al., 2018; Addy and Wilkinson, 2019; Leakey, 2020; Haunton, personal communication, August 2023). As there is no specific method to simulate a WDD in modelling, a common means to represent a WDD is to use an increased Manning's n roughness coefficient at their location (Addy and Wilkinson, 2019). Hydraulically, WDDs create roughness within the channel which results in a higher Manning's n, with varied flow, reducing localised velocity and discharge which can delay and reduce downstream flood risk (Gippel, 1995; Linstead and Gurnell, 1999). The different classifications (active, complete and partial) refer to WDDs that are hydraulically effective with different associated Manning's n roughness coefficients (Table 2.1). Such findings suggest that Manning's n roughness coefficients are lower at high discharge (Sear et al., 2010). To quantify the hydraulic effect of WDDs to flow resistance, Manning's n expresses roughness or friction applied to the flow regime by the channel. Experiments have shown that a reach with an active WDD can cause an increased flow resistance, however, as discharge increases Manning's n decreases. Whereby, research by Gregory et al. (1995) found as discharge increases, WDD Manning's n roughness reduced from $1.02 s/m^{\frac{1}{3}}$ to $0.31 s/m^{\frac{1}{3}}$ (Gregory et al., 1985). The hydraulic resistance of debris varies as a function of discharge; as discharge increases, the WDD becomes submerged, and its Manning's n roughness reduces. Once WDDs become submerged their effectiveness in reducing flood risk diminishes. There is, therefore, a need for strategic placement of multiple WDDs placed one after the other in succession, otherwise

they can drown upstream WDDs out, so reducing their attenuation effectiveness (Nicholson et al., 2012). However, though Manning's n roughness decreases with discharge, roughness increases upon bank overtopping (Jarrett, 1985).

Table 2.1: Literature review table of calculated WDD Manning's n from different studies. Adapted from Addy and Wilkinson (2019).

Study	WDD type	Catchment area (km^2)	Channel slope angle / gradient (m/m)	Channel type	Mean n $\left(s/m^{\frac{1}{3}}\right)$	WDD No.	Q (m^3/s)
Sear et al. (2010)	Active	25.23	0.0092	Meandering with braiding, Clay and Sand	1.42	90	Different flows
	Partial				0.32		
	Complete				0.25		
Dixon (2013)	Active	< 15	0.004	Meandering, Coarse gravel bed	0.24	8	High (> 0.8 m^2/s)
	Partial		0.012-0.013		0.083	16	
Kitts (2010)	Active (Overflow)	11.2	0.0057	Meandering, Coarse gravel bed	1.4	4	Low (< 0.2 m^2/s)
	Active (Underflow)				0.27	9	
	Partial (Deflector)				0.32	12	
Curran and Wohl (2003)	Active	9.6	0.06-0.18	Gravel / cobble bed	0.6	20	Low (< Q$_{bf}$)
Linstead and Gurnell (1999)	Active and Complete	-	-	-	0.677	8	
	Partial				0.348	6	
Shields and Gippel (1995)	Partial	927	0.0005-0.0008	Straight, sand bed	0.058	9	Different flows
	Partial				0.075	3	< Q$_{bf}$
Gregory et al. (1985)	Active	< 15	-	-	0.224	1	-

2.6. Morphological change

Literature documents the influence WDDs have on the morphology of upland streams for biological purposes (Keller and Swanson, 1979; Gregory et al., 1985; Gurnell and Sweet, 1998; Linstead and Gurnell, 1999; Montgomery et al., 2003). However, there is limited literature on the geomorphological benefits of WDDs for flood risk management (Grabowski et al., 2019). It is important to account for WDDs morphological effects, so their benefits in flood management can be utilised (Barlow et al., 2014). Morphological changes occur relatively quickly particularly during high discharge (Gurnell and Grabowski, 2016; Tomsett, 2021). However, to initiate diverse and geomorphic complexity, WDDs must be strategically located to obtain the desired effects. SEPA (2015) advises to assess the best placement options for WDDs for their required functions prior to installing them. Generally, their presence has been found to increase channel stability, though, if they are located inappropriately, they could prove detrimental to flood risk further downstream (Grabowski et al., 2019). To attain channel stability for flood risk purposes, this requires understanding of the relationship between the WDD structure, their resultant hydraulic processes in the location they are to be placed and the potential geomorphologic changes (Manners, 2006).

The hydraulic effect of WDDs causes geomorphological adjustments which increases water storage within the channel and on the floodplain (Linstead and Gurnell, 1999). Morphological features induced by active WDDs include backwater pools, plunge pools and lateral scour pools (Keller and Tally, 1979). During high discharge, the upstream pools can overtop at 100% bankfull (Q_{bf}) and flow onto the floodplain (Linstead and Gurnell, 1999). Floodplain connectivity enhances storage and increases ground infiltration which slows the surface flow, reducing downstream flooding. High rates of sedimentation in upstream pools can elevate the bed and the flow regime which promotes bank overtopping. Vegetation growth can, over time, colonise the stored sediment, introducing further roughness and slowing the flow (Robinwood and Forestry Commission Wales, 2008). The result of this is to raise the flow depth and reconnect the channel to its floodplain (Figure 2.9). During high discharge, WDDs increase bank overtopping resulting in deposition of sediment and Particulate Organic Matter (POM) or bring about accelerated bank erosion with scour of the floodplain. By increasing flow depth and reconnecting channels to their floodplains, WDDs can restore riparian wetland habitats and improve water quality as well as slowing the flow (Montgomery and Abbe, 2006).

Figure 2.9: Temporal development of WDDs over a period of 15 months, showing the effect on sedimentation build-up. The sequence of photographs shows evidence of a WDD generating out-of-bank flow with sediment build-up as the floodplain is inundated. The WDD has widened the channel which was previously incised. There is evidence of sediment build-up and vegetation growth adding to roughness upstream of the WDD. Images taken from Robinwood and Forestry Commission Wales (2008).

Floodplains are important because they have a high biological diversity with many ecosystems. They are sometimes described as 'mobile mosaics' in that as floods destroy one area another area regenerates (Hughes 2003). Additionally, floodplains store water and sediment and dissipate energy at high discharge (Hughes, 2003; National Geographic, 2019). Water stored on the floodplain is released slowly after the flood peak has passed so reducing peak discharge and increasing the lag time. Lag times are greater on forested floodplains with higher interception rates, increasing hydraulic roughness, reducing flood magnitude and allowing downstream communities longer to prepare (National Geographic, 2019).

Generally, the presence of WDDs has been found to increase channel stability (Gurnell et al., 2002). Plunge pools tend to form downstream of active WDDs as water surcharges the structure. The backwater pooling effect increases the hydraulic radius (R) and with the creation of pools, the localised velocity is decreased with reduced energy and τ_b which induces deposition (Wallerstein and Thorne, 1997; Manners et al., 2007). Channel obstructions such as WDDs, control sediment transport and local hydraulics causing turbulent flow conditions and flow convergence which induces local scour and deposition (Montgomery et al., 1995). By generating pool-riffle sequences, this enhances bed heterogeneity, and slows the flow through the undulating bed. This action can create channel bends and greater sinuosity, increasing the flow pathway and decreasing the channel slope angle / gradient, thereby increasing lag time (Sholtes and Doyle, 2011; Toledo, 2020).

2.6.1. Pool-Riffle Units

Pool-riffle sequences are ubiquitous in alluvial channels with gradients exceeding 0.02 m/m (Madej, 1999; Maxwell and Papanicolaou, 2001; Thompson, 2013). They exist as the deep and shallow parts of the channel and create an undulating bedform with pools as the topographic lows, and riffles as the topographic highs (Montgomery and Buffington, 1997). Free-formed pools result from the fluvial hydraulics of the water course and patterns of meander development (Madej, 1999). Pools and riffles form in both straight and meandering channels, creating a repetitive, alternating pattern of $\approx 5B_{sw}$ to $7B_{sw}$ in length (Leopold et al., 1964) where bankfull stage width is given as B_{sw}. Forced pools also occur where obstructions such as a boulder or large wood creates scour and deposition (Montgomery et al., 1995) and these forced pool-riffle sequences have been found to have closer spacing than those which are free-formed (Montgomery et al., 1995) or often

have no regular spacing because of the irregular distribution of forcing elements (Madej, 1999). Straight pool-riffle sequences are often the precursors to meander development, though meanders can take many years to form (Thompson, 1986; DEFRA, 2009). In meandering water courses, pools form on the outer edges of the meander where it is deep and undercut and riffles form between the meander loops in the shallow, straight and wide sections (Thompson, 1986). Pools and riffles offer variation in flow depth and localised velocity (U) (Thomas and Nisbet, 2012; Thompson, 2013).

At low discharge, pools may generate laminar flow providing relatively deep, still water while riffles are generally associated with faster flowing turbulence indicated by the presence of white water with high dissolved oxygen concentration (Clifford and Richards, 1992). Riffles are shallow areas, often comprised of exposed, larger bed material and sloping alternately, first in the direction towards one bank and then towards the opposite bank. Riffles run diagonally across the channel length and at low discharge, water travels along the lowest points of the riffle taking the easiest route and dissipating the least energy.

The theory of minimum rate of energy dissipation states that a water course is in a state of equilibrium when its energy dissipation remains at a minimum (Yang et al., 1981). However, when the water course is not at equilibrium it will gain / lose energy until it returns to its original state of equilibrium (Yang et al., 1981). One of the main functions of the pool-riffle sequence is thought to be to maintain the equilibrium of the water course by minimising potential energy expenditure per unit mass of water (Yang, 1971). In essence, a natural water course takes the path of least resistance to minimise energy expenditure and constantly responds to constraints to regain equilibrium. Pools and riffles, which deviate from a uniform longitudinal bed, are important in determining sediment transport and energy required to initiate sediment motion (Stall and Yang, 1972). This is illustrated by the longitudinal bed profile having undulating deeps of pools and shallows of riffles which is regulated by shear stress. During low discharge, riffles behave as hydraulic controls from the upstream pools (Richards, 1978) and at high discharge, riffles can become submerged increasing bed roughness and potentially enhancing turbulence (Caamano et al., 2012). In this way, pool-riffle sequences are shown to be important stabilisation mechanisms by minimising energy expenditure. Stable water courses transport sediment supplied by the watershed, otherwise instability can occur when scouring causes channel degradation or excessive deposition causing aggradation. Sediment load and grain size can be determined through the

critical tractive force method with entrained particles proportional to relative gravity (g), relative submerged specific density, channel slope angle / gradient and hydraulic radius in relation to discharge. Change in just one parameter can cause adjustment in the channel. During low discharge, potential energy is dominant in the pool with a larger hydraulic radius, sediment is dropped out of motion causing infilling. While at the riffle, kinetic energy is more dominant with a restricted hydraulic radius creating higher flow intensities and enhancing scouring. Therefore, pool and riffle sequences establish a dynamic equilibrium which in turn interrelates with other parameters such as sediment load, channel slope angle / gradient or bed configuration, which if altered can lead to the morphological readjustment of the water course (Leopold et al., 1964).

Although there are specific criteria to identify pools and riffles which includes the hydraulic gradient and sediment grain size (from clays: very fine 0.0005 mm up to boulders: very large 4.026 m size) (Julien, 1998), where pools are characterised by a hydraulic gradient near zero and riffles with a relatively steep hydraulic gradient (Yang, 1971) the identification of pools and riffles can be quite subjective particularly at 100% Q_{bf}. In hydraulics, the Froude number (Fr) (Equation 2.1) has become recognised as a method for characterising pools and riffles (Jowett, 1993) where for pools: Fr < 0.18 and riffles: Fr > 0.41 (Jowett, 1993., Hilldale and Mooney, 2007).

$$Fr = \sqrt{\frac{U_0{}^2}{gh}} \qquad \text{Where: } \begin{cases} Fr < 1 \text{ is Sub} - \text{critical flow} \\ Fr > 1 \text{ is Supercitical flow} \end{cases} \qquad (2.1)$$

Equation 2.1 calculated Froude number (Fr) using localised velocity (U), gravity (g) and flow depth (*h*).

Mean velocity quantifies gravitational forces, whilst combining gravity and flow depth provides a measure of inertial forces. Inertia is a measure of an object's resistance to a change in motion. The combination of gravity and flow depth gives the relative submerged specific density (ρ), its inertia. As high flow depth has greater inertia and exerts increased pressure compared to low flow depth, with a constant discharge the Fr can provide a means of classifying flow conditions based on whether the discharge along the channel has deep flow depth and slow localised velocity, or shallow flow depth and fast localised velocity. This is because with high flow depth, slow local velocity, inertial forces dominate the flow whereas with fast flow, gravity dominates the flow conditions. In this way, the Fr gives an indication of the pools and riffles in the water course.

2.6.2. Natural and Forced Pools

There are two mechanisms that govern pool formation: one is a forced pool associated with a physical perturbation blocking the flow regime such as a boulder or a WDD and the other is a free-formed pool (Montgomery et al., 1995; Thompson and McCarrick, 2010). Pool-riffle maintenance is described as the areal sorting of channel bed material into relatively fine material in pools and larger, coarser material forming riffles through fluvial sedimentation. At baseflow, riffles have been observed to have higher localised velocities and steeper hydraulic gradients than pools (Wohl, 2007). Fine sediment tends to accumulate in the lower localised velocity zone of the pool, however, despite this, the pool is permanently present and persists as a topographic low in the channel bed (Wohl, 2007). This assumes that scouring of bed substrate, during a given discharge, maintains pools, otherwise pools would infill (Wohl, 2007). To explain this phenomenon, the velocity reversal hypothesis was developed to investigate the mechanism of pool-riffle self-maintenance and areal sorting of bed materials in alluvial streams (Seddon, 1900; Gilbert, 1914; Keller, 1971).

The tractive-force reversal theory attempts to explain the areal sorting of bed material with finer material in pools and coarser, relatively larger bed material forming riffles. During low discharge and low velocity, riffles exhibit τ_b > critical tractive force required to initiate motion (τ_c) and so scouring occurs with pools creating an area of deposition; however, at high discharge and high velocity, pools exhibit τ_b > τ_c and so larger particles are transported from the pools onto the surface layer of the riffle (Keller, 1971). Near-bed velocity, affected by bathymetry and discharge, is a major influence on traction which is responsible for transport and sorting of bed material. It has been hypothesised that velocity reversal provides a mechanism for maintaining the pool-riffle sequences and that reversal of near-bed velocity with corresponding reversal of the τ_b causes scouring and sediment removal from the pool and deposition on the downstream riffle (Caamaño et al., 2009; Jackson et al., 2015). It is known that the shear velocity (U^*) is related to the τ_b being responsible for transport and sorting of bed material, and that channel slope angle / gradient and discharge exercise influence (Gilbert, 1914; Keller, 1971). Velocity reversal was originally based on the observation that during low discharge, deposition occurs in pools while riffles are aggraded, however during high discharge, the opposite process occurs (Keller, 1971). This hypothesis states that at low discharge, the shear velocity in the pool is less than its adjacent riffle but with increasing discharge increases at a faster rate until at relatively high discharge the pool near-bed velocity exceeds that of the riffle which enhances localised pool scouring (Figure 2.10).
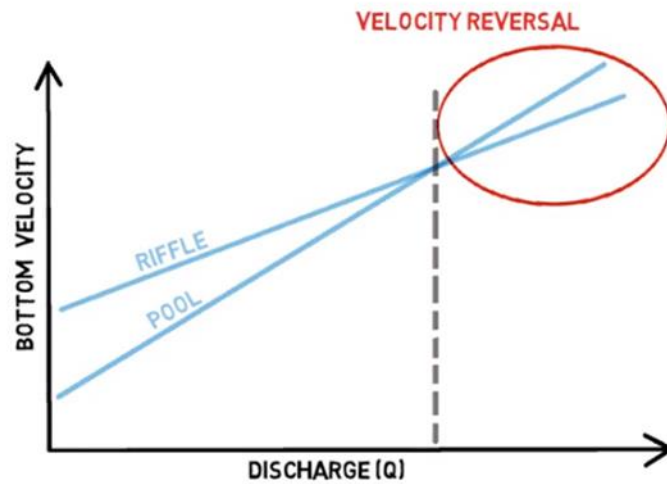
Pool-Riffle maintenance

Figure 2.10: Pool-Riffle Maintenance taken from Martin (2017). As discharge increases, the average near-bed velocity in the pool starts to increase faster than in the riffle, until it approaches 100% Q_{bf} (represented by the vertical broken line), when the near-bed velocity of the pool then exceeds that of the riffle.

Another theory is that the presence of boulders, bedrock outcrops and WDDs immediately upstream of a pool create flow constrictions and can create turbulence resulting in localised elevated τ_b (Thompson et al., 1996). Figure 2.11 shows formation of a recirculating eddy that may lead to elevated τ_b behind a constriction with an increased hydraulic gradient at the entrance of the pool (Thompson et al., 1998; Milan et al., 2002). The recirculating eddy produced by a constriction at the entrance of the pool generates a jet of higher localised velocity in the centre of the pool enhancing scouring and preventing deposition (Thompson et al., 1996; Thompson et al., 1999).
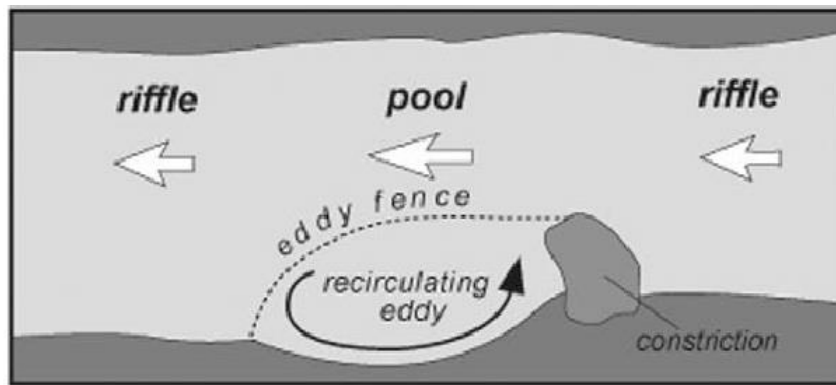
Figure 2.11: Diagram showing the effect of a water course constriction. The recirculating eddy has transported water in the upstream direction and effectively reduces the cross-sectional area of the downstream flow, scouring the bed downstream of the constriction. Taken from Thompson (2010).

Pool-riffle sequences are generally obstacle-related in small upland streams (Smith et al., 1993). WDDs influence local hydraulics which has effect on sediment entrainment and transportation and can form backwater pools and plunge pools (Wohl and Scott, 2017) and local scour associated with WDD hydraulics can generate pools. Geomorphic change can be brought about in water courses by WDDs enhancing local hydraulics and sediment routing, creating the formation of forced pools and riffles accounting for the heterogeneous complexities of the channel bed (Montgomery et al., 2003). The mechanisms by which pools and riffles are formed at WDDs differ from natural pool riffle maintenance in which case sediment transport in small, forested upland gravel streams will be dissimilar to other water courses in different environments (Smith et al., 1993).

Literature suggests pool-riffles are initiated at instream perturbations such as WDDs with roller eddies upstream and downstream of the WDD (Clifford, 1993). Over time, the local scouring deepens and extends at the obstacle. The localised scour process of a single pool at the obstacle creates deposition downstream which then generates the next-downstream pool-riffle. The pool-riffle sequence is autogenically formed as a unit of pool-riffles and is maintained by local near-bed turbulence that starts downstream of the obstacle.

It has been argued that current concepts hinge on flow convergence to explain the erosion or deposition of contiguous pools and riffles constituting a self-maintenance mechanism and sediment-size sorting process (Keller and Florsheim, 1993; Thompson et al., 1996; Wohl, 2007; Thompson and Wohl, 2009). The concept of obstacle induced flow convergence complements some of the original observations of the velocity reversal or tractive force reversal, in that flow

convergence at higher discharge creates a narrow jet of water which increases localised velocity and τ_b than those in adjacent riffles. It has been suggested that flow convergence is the governing factor on pool formation in forced pools, but that multiple mechanisms may be responsible for pool-riffle maintenance (MacWilliams et al., 2006; Thompson and Wohl, 2009). There are many conflicting ideas regarding the sediment routing and associated hydraulics which make it difficult to determine conclusively how pool-riffle units are maintained. Yet as pools ubiquitously continue to persist as topographic lows and riffles as topographic highs on the channel bed then there must be a self-maintenance preferential scouring mechanism to explain this phenomenon.

To help inform WDD design criteria, literature places importance on experimental research into investigating the hydraulics at WDDs which generate local scour pools. Beschta (1983) conducted early flume experimentation into the scour mechanisms using in-channel horizontal wood, revealing discharge, diameter relative to flow depth, depth of the base of the structure to the bed and localised velocity affected scour depth and areal extent. Beschta (1983) found turbulence at the horizontal wood, downward advection of flow at the WDD and in its wake was responsible for local scour with increased discharge rather than increased shear stress, which calls into question whether pools are formed by the shear stress (tractive force) reversal mechanism at WDDs (Smith et al., 1993). Cherry and Beschta (1989) conducted flume experimentation on single logs oriented at different positions to analyse the hydraulic effects on the patterns of scour and deposition. However, these studies using single logs oversimplify the physical characteristics of many WDDs.

Turbulent energy dissipation has been found downstream of an obstacle, such as WDDs, in water courses. As water passes by the obstacle it is subjected to drag because of pressure gradients and surface friction. Frictional drag occurs surrounding the obstacle resulting in decreased localised velocity (Equation 2.2). For each object shape, there is a defined relationship between the drag coefficient (C_D) and the Cylinder Reynolds number because localised velocity must be determined over the entire surface of the object which has an uneven roughness. The pattern of flow therefore varies depending on the Re_c.

$$F_D = \frac{1}{2}\rho C_D A_p U^2 \tag{2.2}$$

Equation 2.2 calculated Drag force (F_D) using the drag coefficient (C_D), relative submerged specific density (ρ), localised velocity (U) and structural area blocking flow (A_p) (Manners, 2006).

As shown in Figure 2.12a the Re_c is low and the pattern at the upstream/downstream and below/above the object is symmetrical but as shown in Figure 2.12b as the Re_c increases, the symmetry between upstream/downstream of the obstacle differs and the flow downstream of the obstacle widens with vortices in this widened gap; the upper vortices running clockwise and the lower vortices running anticlockwise. Figure 2.12c reveals that when $Re_c \geq 60$ the downstream flow becomes unstable oscillating up and down and then expanding before dissipating and leaving the cylinder. As shown in Figure 2.12d, when $Re_c > 1000$ a turbulent state forms in the wake of the cylinder with the vortices becoming mixed together. Distant from the wake a steady state of flow is maintained with smooth laminar flow. There is decreased localised velocity in the wake of the cylinder due to the large-scale eddies and turbulence increase. Therefore, there is a high rate of energy dissipation, resulting in decreased downstream pressure.
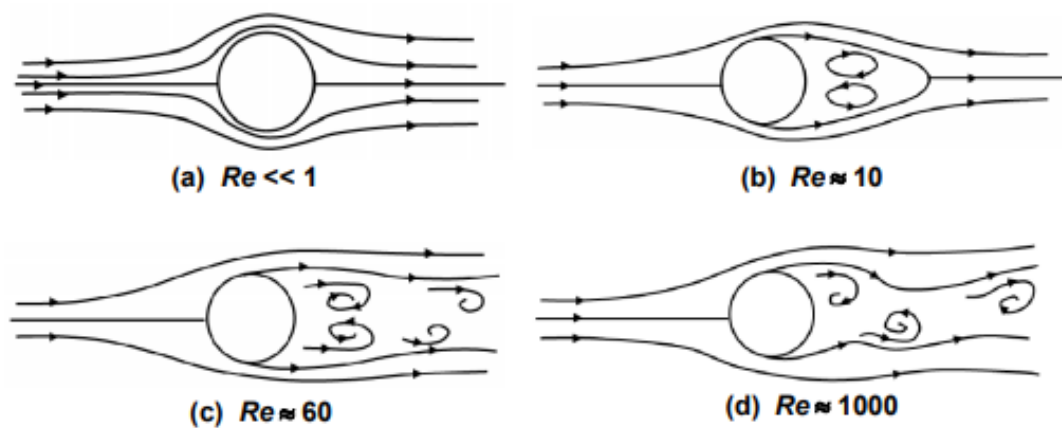
Figure 2.12: Streamlines showing flow pattern generated round a circular object dependent on Reynolds number. Taken from Sato and Kobayashi (2012).

While WDDs can be treated as single, solid cylindrical structures they have complex hydraulic influences due to their porosity and matrix. Porous WDDs with throughflow significantly impact on localised velocity, turbulence, debris transport and storage, kinetic energy and wake length (Xu and Liu, 2017). WDDs are complex, irregular structures which change temporally and can alter from relatively solid barriers to porous obstacles or obstacles with interlocking wood. Compact leaves and other organic materials can accumulate and become stored between the snags, moulding themselves to the WDD matrix and altering their characteristics to become less porous. With abscission during the autumn months, deciduous tree leaves can enter the water course and

become snagged on WDDs (Benfield, 1996). Alternatively, active dams can become more porous as leaves bio-degrade and are washed downstream. Due to their unique configurations, with some WDDs being relatively more porous than others, their flow fields can significantly differ. For instance, low porosity can lead to backwater effects (Papanicolaou et al., 2018a). Single cylinder flume experimentation investigating WDD hydraulics, conducted by Beschta (1983), highlights how under certain conditions the intricate complexities of WDDs can affect drag force (F_D) and entrain sediment and organic matter. For example, it is suggested that the roughness of wooden cylinders can increase lift and that blockage capacity across the entire main channel width and surcharge level can affect lift and F_D whilst in other conditions the increased complexities of WDDs can reduce the C_D (Shields and Alonso, 2012). It is therefore difficult to determine the hydraulic effects of complex porous structures that can differ in design and temporally alter (Xu and Liu 2017) or quantify their behaviour in field conditions due to the many variables which are difficult to identify and control.

2.7. Sediment Storage

Channel morphological form is controlled mainly by discharge, sediment transportation and deposition, and local boundary conditions such as catchment descriptors (Fryirs and Brierley, 2013). The boundary conditions and forcing factors such as change in sediment supply through farming management or climate change, affect the geomorphological, hydrodynamic and sedimentological balance of the river system (Wang et al., 2006; Owens et al., 2010). Channel geomorphology adjusts according to discharge and localised velocity with most sediment transport taking place during high discharge. Most of the sediment is transported during flash floods and storm runoff periods with greater erosion taking place (Guy, 1964). To maintain dynamic equilibrium, as discharge increases, the water course increases sediment capacity by incising the channel. However, with decreased discharge, sediment load decreases and aggradation occurs with sediment fining according to size (Lane, 1954). Deviation from the balanced sediment regime can lead to sediment deficiency with the water course having more than necessary capacity to carry sediment with the potential outcome being the erosion of the channel boundary which could lead to channel instability through bed incision (Wohl, 2015). Channel stability is described as the ability of the water course to transport sediment so that the water course maintains its dimension,

pattern and profile without either aggrading or degrading so maintaining equilibrium. Conversely, over time if there is degradation or aggradation this would lead to instability (Rosgen, 1996).

Alluvial river channels morphologically change over time, adjust their channel geometry (main channel width, flow depth and localised velocity) and therefore their capacity to contain flood water over time according to the discharge and upstream sediment yield (Slater, 2016). During heavy precipitation, fast-moving runoff across rural land can lead to excess sediment transfer into upland streams (Nietch et al., 2005). This excess sediment can lead to loss of discharge carrying capacity and have the potential to increase flood risk. One of the main drivers of excess sediment is agricultural intensification which is impacted further by livestock puddling at the channel banks and furrowed tracks from farm vehicles (Henshaw et al, 2013). In a study by Heathwaite et al (1989) it was found that 53% of rainfall was converted to runoff on grazed land while this decreased to 7% in ungrazed fields. Furthermore, infiltration reduced by 80% on grazed areas compared to land with no grazing (Heathwaite et al., 1990). Studies conclude land cover change from forestry to agriculture increases erosion and sediment production (Clarke, 1995). Pastoral fields are common in upper catchments and are susceptible to soil degradation and erosion (Pattison and Lane, 2012). The problem is that wash-material load as a driver of geomorphological change is under-researched in the field of catchment-based sedimentology (Dangerfield, 2013). While there is a sizable amount of literature on the effects of water related risks to flood management, there is far less research regarding sediment related risks (Thorne, 2011). A large gap exists regarding research into the link between sediment, morphology and flood risk. There remains a lack of understanding of the consequences of excess sediment run off from source to sink, how alterations in channel geomorphology and conveyance capacity can increase flood risk and how WDDs can provide sediment storage which regulates sediment transport through the fluvial system. By providing sediment storage, WDDs create buffer zones which regulate sediment transport through the fluvial system (Gurnell et al., 2002; Ngai et al., 2017).

WDDs can bring about changes in sediment routing and storage and over time can generate channel geomorphic effects (Montgomery et al, 2003). One of the main functions of WDDs is to facilitate deposition and storage of sediment, that would otherwise remain in transit in the water course. WDDs operate as flow obstructions, disrupting the continuity of the flow regimes resulting in backwater areas that capture sediment and over time in live bed conditions can become completely submerged with deposition (Keller and Swanson, 1979). Scour and deposition depend

on factors such as wood orientation, bed substrate and WDD characteristics (Montgomery et al., 1995). At an active dam, traversing the main channel width (B), sediment can be stored upstream of the WDD in a rectangular area covering a maximum length of 2B (Davidson, 2016). The side view of the deposited sediment forms a triangular wedge shape (Figure 2.13). Due to the hydraulic resistance of the vegetation, the residence time of sediment around WDDs is greater than that trapped against boulders and rocks though this depends on the size, composition and orientation of the WDD (Fisher et al. 2010). It has been estimated that potentially the sum of the storage area and pool areas within a reach with WDDs can be greater than the entire bed area of the reach (Davidson, 2016).
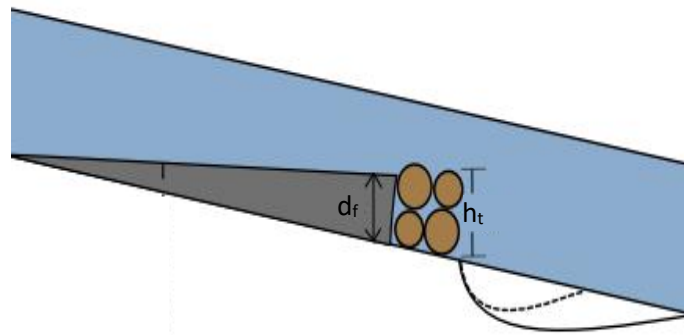
Figure 2.13: This modified schematic (Davidson, 2016) shows the effect an active dam, spanning the entire main channel width, can have on sediment storage. A side view of sediment accumulated upstream of the WDD as a triangular wedge shape and pool scour downstream. This is conceptually consistent to findings which state that WDDs reduce pool spacings and increase pool surface area in the reach (Montgomery et al., 1995) though this is dependent on bed substrate, wood orientation and composition of the dam (Thompson, 2012). The sediment stored at the dam face (d_f) is shown by wedge shape and maximum height of structure above bed (h_t).

WDDs play a major role in sediment storage capacity, modulating its transport through the channel and reducing energy expenditure (Keller et al., 1995). During high discharge, WDDs protect the integrity of the downstream channel by preventing excessive pulses of sediment (Cordone and Kelley, 1961). Although during a short duration high discharge event, there can be a significant sediment output, WDDs have the trapping efficiency to control sediment transport from source to sink, increasing lag time. The lag time operates until the sediment capacity fills behind the WDD, at which point a higher budget of sediment will be transported through the channel with increased sediment capacity (Davidson, 2016).

The effects of WDDs on erosion, deposition, transport and storage of sediment primarily depends on discharge intensity (Manners et al., 2007). Active dams store high rates of sediment upstream with reduced kinetic energy and downstream with increased kinetic energy scour occurs creating pools, with a pressure gradient from sub-critical (Fr < 1) more towards super-critical (Fr > 1) flow conditions at the pool (Wang and Zhang, 2012). Energy is dissipated further downstream with flow reverting back to sub-critical. The energy gain after the WDD, is often referred to as hungry waters, because the excess energy is typically expended on erosion of the channel bed, resulting in incision and coarsening of the bed material until equilibrium is reached and the material can no longer be entrained by the flow (Kondolf, 1997).

Partial dams connected to one bank (Deflector dam) (Figure 2.14a) trap sediment on their lee side in bar deposits and flow scours one or both banks. However, complete dams (underflow dam) (Figure 2.14b) do not greatly affect the flow continuity and consequently do not have high scour and deposition rates. Likewise, the partial dam centred (flow parallel debris dam) (Figure 2.14c) blocks the flow to a lesser extent reducing scour and deposition (Wallerstein and Thorne, 2004). This means that peaks in storage and scour predominantly occur at active and partial dams connected to one bank (deflector jams).
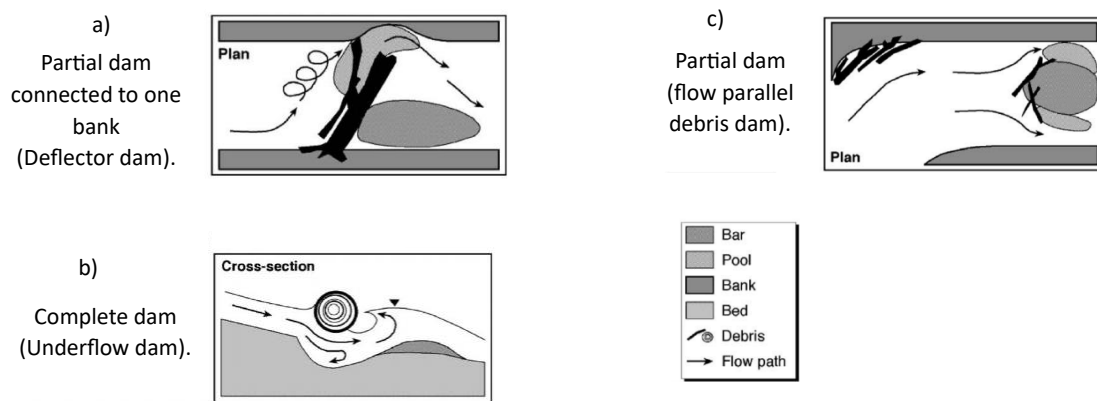
Figure 2.14: Wallerstein and Thorne (2004) modified from Wallerstein et al. (1997). a) deflector jam, b) underflow jam, c) flow parallel/ bar head jam. Diagrammatic form showing the classification of WDDs, their trapping efficiency and scour similarities and differences.

Following this rationale some WDDs could help maintain channel stability while others could potentially reduce it depending whether the net sediment budget at a given WDDs is positive or negative. Opinion is divided as to whether WDDs help maintain channel stability: either they create channel stability by storing sediment and scouring with a positive net sediment budget

(Thompson, 1995) or WDDs create turbulence, mobilising sediment downstream with a negative net sediment budget (Smith et al., 1993). However, in degraded channels with bank instability, WDDs can be helpful in a negative feedback mechanism in that they cause energy flow dissipation and potentially store sediment more than scouring thus accelerating channel evolution recovery (Wallerstein and Thorne, 2004). It is suggested that the sediment net budget at the majority of WDDs is positive and that in degraded systems they benefit the geomorphology with a higher trapping efficiency than sediment being mobilised through the WDDs, accelerating recovery of a stable longitudinal profile following channel incision. WDDs cause scour of the bed and banks through partial flow deflection and sediment storage through active dams traversing the main channel width due to blockage and energy dissipation (Wallerstein and Thorne, 2004).

Depending upon their design and location, WDDs have varying effects on channel morphology. For example, while all WDDs can tentatively be said to improve channel stability, partial deflector dams tend to have greater impact in increasing bank erosion and active dam and partial deflector dams are the most efficient in storing sediment (Wallerstein and Thorne, 2004). Hydraulic forces of WDDs are heavily reliant on C_D which changes depending on diameter and surcharge, blockage ratio, depth of the base of the structure to the bed and orientation along with particle Reynolds number (Re*) and Fr (Gippel et al., 1992; Penna et al., 2020a). They comprise of complex matrices of wood with spacings in between the wood pieces creating greater complexity in degradation, aggradation and sediment storage (Manners et al., 2007) which impacts on their trapping efficiency and net sediment budget.

2.8. Research gaps

Research gaps were identified from the literature review as outlined in chapter 2.

- Though engineered WDDs are purposefully built to temporarily store water in the upper catchments during high discharge events so delaying downstream flow (Grabowski et al., 2019) there is little guidance on how to design them from an NFM perspective (Burgess-Gamble, 2018). Literature indicates that designs of engineered WDDs vary widely mainly due to the lack of design criteria (Gregory et al, 1985; Wallerstein and Thorne, 2004; Leakey et al., 2020; Hankin et al., 2020) and their complicated effects on hydraulics and turbulent flows that are not well understood (Bennett et al., 2015; Huang et al., 2022). Some flume studies use a single solid key member to examine the hydraulic effects of the structures on local scour (Beschta, 1985; Cherry and Beschta, 1989; Svoboda and Russell, 2011) but this oversimplifies the complexity of the physical characteristics of WDDs, ignoring their porosity and multiple key members. Given the popularity in WDD use in NFM, this knowledge gap prevents complete understanding of their hydraulic and geomorphic impact for flood purposes. Anthropogenic WDDs are designed with varying levels of complexity, from two or three wood pieces across the water course to multiple stacked logs (SEPA., 2015). Literature continues to use the design criteria laid out by Gregory et al. (1985) of active, complete and partial dams, which reflect their hydraulic impact (Linstead and Gurnell, 1999; Osei et al 2015; Parker et al., 2017; Pinto et al., 2019; Addy and Wilkinson, 2019) for some standardisation. This thesis intends to add to the understanding of the effectiveness of structure design and condition on sediment transport dynamics as recommended by Ngai et al. (2017, Gap 2.4.8.5.).

- There are numerous studies that take a biological perspective towards the impact of wood in water courses and its importance in aquatic habitats (Gurnell et al., 1995; Gurnell et al., 2002; Gregory et al., 2003; Wohl et al., 2016), however there is far less evidence concerning the geomorphological role of WDDs in relation to flood risk (SEPA and Forestry Commission Scotland, 2012; Environment Agency, 2014; Ngai et al., 2017). There is especially little attention paid to the potential morphological impacts of WDDs in the field as WDDs are subject to variable parameters unique to their individual catchment such as landcover, geology, channel entrenchment. This thesis intends to determine the scale and location of

effective WDDs and collect site-specific catchment data to develop a methodology for predicting how WDDs reduce flow using empirical data.

- There is currently a great deal of interest shown in hydraulic modelling to overcome upscaling from plot to catchment, but currently there is a lack of study sites and the need for data over long periods (Thomas and Nisbet, 2012; Xu and Liu, 2017; Metcalfe et al., 2017; Leakey et al, 2020). However, despite the progress made in the field of hydraulic modelling, the challenge remains to find an appropriate method to model the complex forms and porosity of WDDs which temporally changes. There is currently no standardised modelling hydraulic unit to represent WDDs in the modelling domain and this has led to uncertainty in modelling and potentially unrealistic predictions (Ngai et al, 2017; Metcalfe et al., 2018; Addy and Wilkinson, 2019). Many studies tend to adjust the Manning's n at the location of the WDD to simulate flow resistance (Kitts, 2010). However, this method has limitations as Manning's n increases, the localised velocity decreases and, as cross-sectional-area increases so does the localised velocity which does not give a realistic representation of WDDs. This research will examine a structural hydraulic representation unit to simulate the impounding effect of a network of WDDs.

2.9. Thesis aim and objectives

The aim of this research is to develop a modelling methodology within Flood Modeller which was subsequently validated empirically, in assessing the effectiveness of WDDs in slowing peak storm flows. The aim of this research will be explored by the following four objectives.

1. To empirically assess the impact of different WDD structures on bathymetric evolution in a controlled laboratory water flume, in order to analyse WDD design effects and make comparisons to current modelling capabilities;

2. To thoroughly map the scale and location of pre-existing WDDs using on ground and LIDAR techniques, to act as input terms to the developed 2D model to be used in conjunction with collected real world empirical storm data;

3. To develop and validate an empirically derived hydraulic modelling unit for NFM prediction methodology;

4. Using the developed modelling approach assess the effectiveness of WDDs in attenuating storm events in the study catchment.

2.10. Novelty and Contribution

The novelty and contributions of this research will concentrate on the following aspects, linked to the main chapters, and described in the sub-sections below.

2.10.1. Woody debris dam induced bathymetric evolution

Flume experiments investigating local scour at WDDs will be performed and modelled, with FM used to validate results. A computational flume will be generated with and without an obstacle which will calibrate flow depths and velocity distributions. Within FM, a broad crested weir unit will be used to mimic the hydraulic effects of the structure inserted in the flume study.

In the flume experimentation, a Kinect v1.0 camera, initially developed by Microsoft for the Xbox 360, will be used to derive point clouds and generate DEMs of channel bathymetry. There is potential for the Kinect as a non-intrusive method to map channel bathymetry with an erodible bed. A Kinect will capture downstream bed evolution to enable visualisation of local scour and deposition at a WDD.

2.10.2. The effects of woody debris dams on upland stream geomorphology

A comparative assessment between historic and contemporary maps of Wilderhope will determine channel realignment. This will be achieved using both site surveying and Global Information Systems (GIS) to assess channel evolution and how WDDs have altered the flow regime. Areas of channel overtopping will be spatially identified with the formation of new channels, chutes and pool development. This novel approach links geomorphology to flow attenuation by examining catchment descriptors in respect to WDD induced channel change.

2.10.3. Modelling hydraulic and hydrological impacts of woody debris dams

In the modelled study, pier-loss bridge units will simulate a network of WDDs with different structural designs unique to location. Empirical field data at Wilderhope will be imported as boundary conditions within FM. Results will be calibrated using on-site automated monitoring equipment whereby two real storm events at different times of the year will be simulated. Within hydro-environmental literature, there is a lack of field data, with most studies using Revitalised Flood Hydrograph (ReFH) datasets to obtain catchment descriptors and boundary conditions.

2.11. Thesis Structure

Chapter 1 introduces the background to the research.

Chapter 2 reviews the literature, focusing particularly on initiation of motion, complex structures of WDDs and their impacts on channel hydraulics, flood modelling, sediment dynamics and morphology, whilst identifying the research gaps, thesis aims and objectives.

Chapters 3, 5 and 6 address one or more of the research objectives. Inclusive to each of these three chapters is a method, results, discussion and conclusions, relevant to its research question.

Chapter 3 uses flume experimentation, to analyse how the structural design of a WDD creates geomorphological changes, in scour depth and deposition and their extent and patterns. Chapter 3 results informed the accuracy / limitations of the modelling unit employed in representing the WDDs in chapter 5.

Chapter 4 discusses the site characteristics including study site and field equipment and outlines the reason this particular study site was chosen to investigate the impact of WDDs on flooding.

Chapter 5 analyses catchment and reach variables controlling stream geomorphology. Variable data analyses highlight how WDDs have affected the stream since their installation. This enables greater understanding of the network of engineered WDDs at the catchment scale.

Chapter 6 uses a hydraulic structure representation approach to represent WDDs in FM. Simulations of two real storm events are run on a network of WDDs. To account for the physical properties of WDDs, blockage and gap areas were investigated using photography in the field.

Chapter 7 presents the overall conclusions of the thesis and potential future research.

3

Woody debris dam induced bathymetric evolution

3.1. Introduction

With extreme weather events projected to increase in frequency and severity due to climate change, there has been growing realisation that Natural Flood Management (NFM), along with soft engineering techniques, should form an important part in future flood risk management planning. After the 2007 floods, when many parts of the UK suffered flash floods with rivers bursting their banks, which had a devastating impact on homes and infrastructure, there was a demand for something to be done, so in 2008 the Government commissioned the Pitt Review. The Pitt Review (2008) proposed that flood risk could no longer be managed by building increasingly larger hard engineered flood defences but should be complemented by natural approaches. This nature-based approach was to be catchment based, aimed at slowing the flow and storing water on rural floodplains. It was recommended that there should be site specific assessment and demonstrative evidence that flood risk would be mitigated by this scheme.

Since the Pitt Review (2008), an alternative method, other than reliance on conventional, hard engineered flood defences, has gained credence in UK policy (Environment Agency, 2022b). However, there is uncertainty as to how a nature-based approach, including planting of trees in the uplands, installing instream WDDs, and creating ponds to store excess water, would work on a large scale (McIntyre and Thorne, 2013). Consequently, the Government has invested £15 million to learn more about NFM through 60 pilot schemes across England, one of which is Shropshire Slow the Flow – Seven Tributaries, with £626,000 allocated to research on how to reduce flood risk to homes (Environment Agency, 2022b). Shropshire is historically highly susceptible to floods, with the EA identifying properties inclusive of homes and businesses located on the River Corve catchment prone to flooding. The Shropshire NFM project aims to use WDDs to reduce downstream flood magnitude, decreasing flood peaks and increasing lag or travel times.

This study examines how WDDs slow the flow, as part of the Shropshire Slow the Flow Project by representing the structures at the field site in controlled conditions. WDDs alter channel hydraulics which divert flows, vary velocities, shear stresses and turbulence and generates increased flow resistance (Grabowski et al., 2019). Interactions between discharge (Q) and the WDD causes complex eddies and wakes to form. WDDs alter local hydraulics and sediment routing, which can rapidly induce morphological channel adjustment (Beschta, 1983; Elosegi et al, 2016; Gurnell and Grabowski, 2016; Spreitzer et al., 2021). By facilitating fine sediment deposition on the channel bed (Faustini and Jones, 2003), promoting sediment storage areas (Wohl and Scott, 2017; Welling, 2019) and creating vertical variations in the channel bed, such as through forced pool-riffle sequencing with fast and slow flowing areas (Linstead and Gurnell, 1999; Montgomery et al., 2003, Elosegi et al., 2016), WDDs contribute to greater morphological sinuosity and channel heterogeneity which lengthens the flow pathway and creates temporary water storage areas so reducing downstream peak discharge (Grabowski et al., 2019; Barnsley et al., 2021).

Although there have been many flume studies investigating flow around cylindrical bridge piers etc., fewer investigations focus on scouring at horizontal key members spanning the channel width. This is relevant because engineered WDDs are installed perpendicular to the flow direction either positioned on the bed, or suspended at varied elevations creating complex local flows and scour mechanisms. The hydraulics associated with WDDs are complex by their unique designs and varied porosity. They alter the flow dynamics based on their structure (Lisle, 1986), with their composition defined as the number and size of wood pieces which varies the blockage capacity and hence porosity (Manners, 2006). This study intends to enhance the understanding of WDD design on channel hydraulics which alters channel bathymetry.

Early experimentation conducted by Beschta (1983) using a single horizontal cylinder positioned at different elevations, identified that at higher discharge, key members positioned on and above the bed displayed different amounts of scour and found the principal cause of scouring was extremely high turbulence at the bottom of the pool. Cherry and Beschta (1989) found the position, orientation and size of a single cylinder affected the scour depth. More recently, Penna et al. (2020b) investigated local turbulence generated by a single, horizontal cylinder at different elevations above the bed whereby during steady state conditions, deeper scour formed at the cylinder positioned on the bed rather than those elevated above the bed. The submarine piggyback pipeline, used for oil and gas transport, runs along the seabed and has two pipelines,

with the small pipeline located directly above the larger diameter one. Submarine piggyback pipeline experimentation, gives indication of the interaction of complex vortices between the bottom pipe and the bed and the space between the two pipes which in some respects is comparable to the present study. Zhao et al. (2018), investigating the influence of piggyback pipelines on scour, found that higher localised velocity (U) created deeper and wider scour pool and that a smaller gap ratio could induce a larger maximum scour depth. So far, only a few laboratory experiments have investigated the effect of WDD models consisting of multiple horizontal cylinder arrangements, on scour for NFM purposes. For instance, Müller et al. (2021) conducted laboratory flume experiments on multiple horizontal structures to investigate how current physical designs of leaky barriers impact on fish movement. Muhawenimana et al. (2021) attempts to address the backwater effects of leaky barrier designs to determine the extent of flood attenuation in laboratory experimentation which uses a non-erodible bed which affects results. While many studies conduct experimentation on a single key member and some have started flume experimentation to capture the complexities of WDD designs, this flume experimentation focuses on flow with an erodible bed and structures with three horizontal key members, which is typical of engineered WDDs (Figure 3.1a). This gives greater realism and understanding of the hydraulic complexities at WDDs which are strongly dependent on the design and porosity (Figure 3.1b). The present study explores the hydraulic effects of WDD designs on local scour.
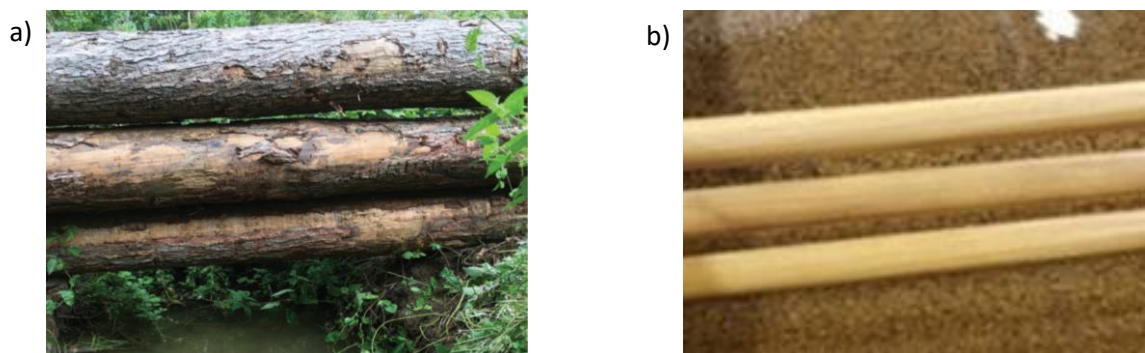
Figure 3.1: a) An engineered WDD in the field, commonly composed of 3 key members laid one above the other, spanning the width of the channel with varying gaps between woods and a gap between the base log and the channel bed. The wood is usually locally sourced. Taken from Water Friendly Farming (2020). b) Structure, representative of an engineered WDD, used in this laboratory flume experiment. Depth of the base of the structure to the bed (e) and vertical spacing between two key members (G) are shown on the image.

The complex flow conditions, and mechanisms of local scour dependent upon WDD design is still not sufficiently understood (Bennet et al., 2015; Leakey et al., 2020). Engineered WDDs can be installed without consideration of their morphological effect on the channel however their morphological impacts are important as they can generate benefits to NFM but can also have adverse impact on flood attenuation (Pearson, 2020). The purpose of this study is to model the impact of WDDs on channel bathymetry and flow regimes to inform design criteria. It is important to know how morphology changes in respect to WDD design to help select the optimal design for the desired function. The objective is to empirically assess the impact of different WDDs on bathymetric evolution to analyse WDD design effects. This experimentation took place in a laboratory flume, using simplified horizontal structures, each composed of three wooden key members with differing gaps at the bed and vertical spacings between subsequent key members above, whilst maintaining the same overall blockage area. This study addresses the knowledge gap identified by the WwNP (Burgess-Gamble et al., 2018) which targets the need for better understanding of the effectiveness of structure design and condition on sediment transport dynamics (Ngai et al., 2017, Gap, 2.4.8.5.).

3.2. Methodology

3.2.1. Flume experimentation

3.2.1.1. Experimental set-up

Experiments were conducted in a straight, tilting, unidirectional and recirculating, plexiglass-sided laboratory flume of length 10 m, width 1.2 m and depth 0.3 m, in the School of Engineering, at Cardiff University. Two PVC sections each measuring 10 m x 0.3 m x 0.225 m were adhered to the flume bed and sides to form two waterproof boxes which acted as floodplains, narrowing the main channel width (B) to 0.6 m, which allowed 100% bankfull (Q_{bf}) (series A) and 80% Q_{bf} (series B) flow conditions. An erodible sediment bed height of 75 mm with a representative sediment grain size of 1 mm (as determined in section 3.2.1.1.2.), was placed on the channel base (Figure 3.2). Prior to each run the bed was manually levelled with a gradient of 0.001 m/m.
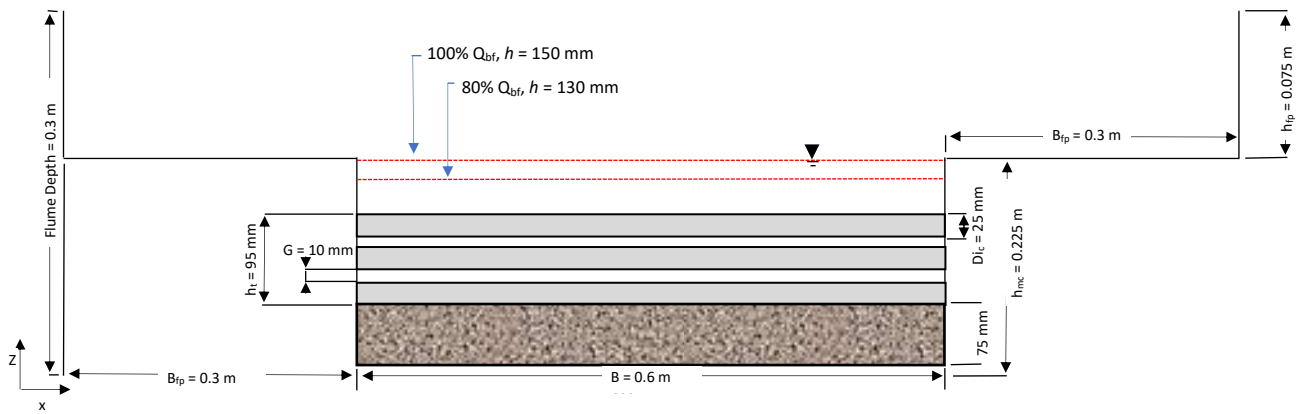
Figure 3.2: Schematic diagram of series 1A and 1B experimental set-up. Series 1 structure comprises 3 horizontal wooden dowels, each with a diameter (Di_c) of 25 mm, sediment height of 75 mm, depth of the base of the structure to the bed (e) of 0 mm, vertical spacing between two cylinders (G) of 10 mm and maximum height of structure above bed (h_t) of 95 mm. The main channel has a height (h_{mc}) of 0.225 m and main channel width (B) of 0.6 m which allows for 100% bankfull (Q_{bf}) flow depth (h) of 150 mm and 80% Q_{bf} (h = 130 mm). The flume width (B_f) of 1.2 m with two floodplains of width (B_{fp}) 0.3 m x 2 at each side of the main channel to allow for bank overtopping.

The discharge was controlled by altering the power provided to the pump via the control box. The water, having passed along the flume, falls into a settling tank and is then recirculated, guaranteeing a constant flow rate throughout the experiment (Falconer, no date).

Prior to the structure being inserted, uniform flow conditions were established at two discharges (series A: 0.022 m³/s; series B: 0.018 m³/s), using a tailgate to control flow depth. A Nixon Tecfluid Ultrasonic Flowmeter, Model: CU100 measured instantaneous and cumulative discharge. To validate localised velocity readings, a Nortek Vectrino Acoustic Doppler Velocimetry (ADV) (velocity accuracy: ±1 mm/s) (Poindexter et al., 2011) was attached to an instrument carriage mounted on a track which was located on top of the flume at a distance of 0.5 m downstream of the structure. The ADV was set to a height above the bed of 60 mm (series A) and 52 mm (series B), as calculated using the one-seventh power law (Equation 3.1). The one-seventh power law of velocity distribution states that the velocity at any point in the cross-section will be proportional to the one-seventh power of the distance from the walls. This value enabled positioning of the ADV at the mean velocity (U_0) profile. A separate instrument carriage carried a Vernier point gauge (accuracy: ±0.1 mm) (Sankar, 2015) and Kinect v1.0, to measure bathymetric channel change for different structural designs.

$$\left(\frac{h_a}{h}\right)^{\frac{1}{7}} . U_{max} = 0.875 U_{max}$$

$$h_a = h(0.875)^7 = 0.4h$$

$$\therefore U_0 = 0.875 U_{max} \text{ occuring at } 0.4h \tag{3.1}$$

The seventh power law velocity distribution, with derivations, shown in Equation 3.1 determined the appropriate height to set the ADV at the mean velocity profile. Variable for calculation include mean velocity (U_0), mean velocity increment height (h_a), maximum velocity (at free surface) (U_{max}) and flow depth (*h*).

A number of parameters were maintained: structure location (5 m upstream of the tailgate), the sediment bed including the sediment grain size and sediment height, blockage ratio (B_r) in respect to the two set discharges (series A: B_r = 0.5; series B: B_r = 0.58), while structure characteristics such as depth of the base of the structure to the bed (e) and vertical spacing between two cylinders (G) varied in size.

Between runs, uniform flow conditions were maintained for each series (Appendix A). For optimum gate height, to ensure uniform flow conditions, results were determined by finding the slope which gave a parallel surface slope / hydraulic gradient (S_f) to channel slope angle / gradient (S_0) (Figure 3.3). Uniform flow conditions are defined as when the wetted area (W) and velocity remain relatively constant along the channel. Maintaining a longitudinal velocity was checked by examining if the flow depth and the hydraulic radius remained constant along the flume.
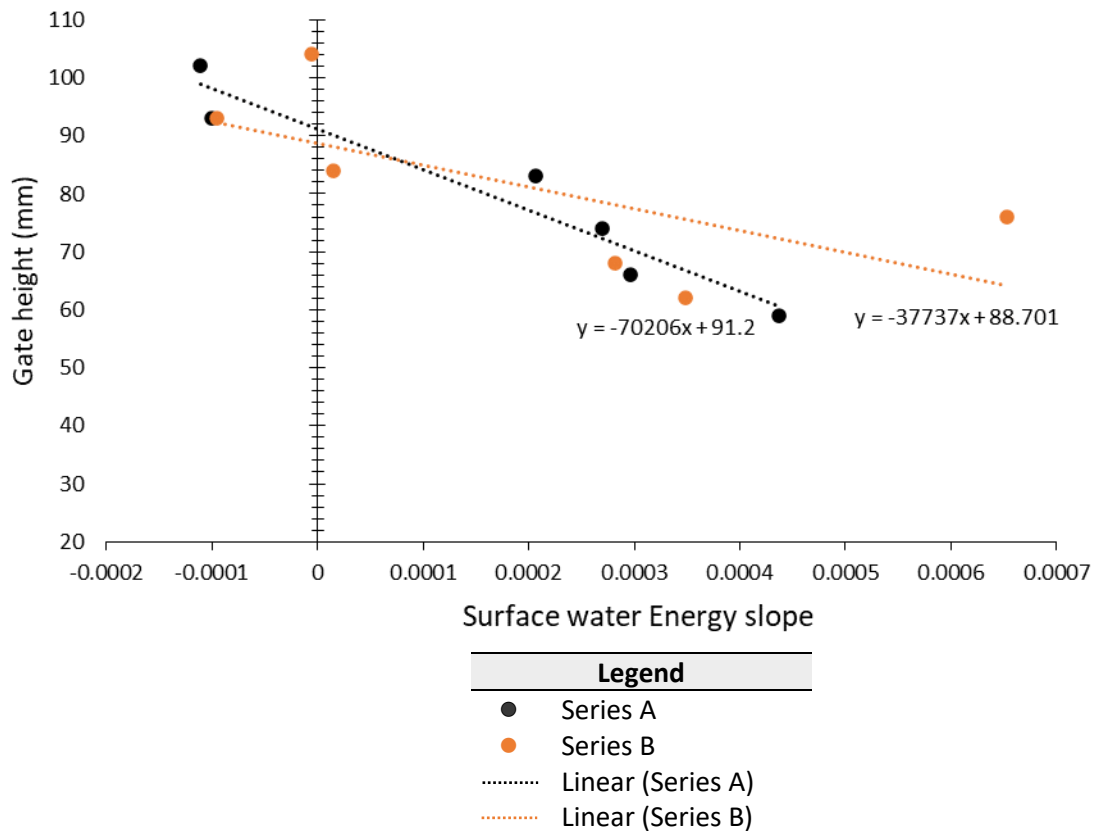
Figure 3.3: To calculate uniform flow conditions, the graph establishes tail gate height for series A and series B. The functions (series A: y = 70206x + 91.2 and series B: y = -37737x + 88.7) end values give height of tail gate (series A: 91.2 mm and series B: 88.7 mm).

3.2.1.1.1. Woody debris dam designs

Four simplified structures (1,2,3 and 4) to represent WDDs were constructed to assess the influence of their designs on the local scour. The dimensions and arrangements of the four structures are as set out in Figure 3.4. Each structure was made of three wooden cylinders with a key member diameter (Di_c) of 25 mm, vertically stacked and with differing spacings between them. From this point forwards, wooden cylinders will be referred to as key members, which are the main pieces of large wood that form a WDD (Manners, 2006). Three key members were chosen for designs, from observations in the field (two photograph datasets, dated Aug. 2019; Sept. 2020, and a survey of WDD physical characteristics conducted between 11-15th Feb. 2019). Using a three-log stack has been suggested as an indicative design proposed by the Rural Payments Agency (2020). Each structure transversed the width of the flume and was aligned perpendicular to the flow regime. e and G size varied dependent upon WDD design (Figure 3.4).

Series 1A: 100% Q_{bf} Series 1B: 80% Q_{bf}	Series 2A: 100% Q_{bf} Series 2B: 80% Q_{bf}	Series 3A: 100% Q_{bf} Series 3B: 80% Q_{bf}	Series 4A: 100% Q_{bf} Series 4B: 80% Q_{bf}
Single-column vertical stack WDD design with G = 10 mm or G = 0.4Di_c and e = 0.	Single-column vertical stack WDD design with G = 10 mm or G = 0.4Di_c and e = 35 mm or e = 1.4Di_c.	Single-column vertical stack WDD design with G = 20 mm or G = 0.8Di_c and e = 0.	Single-column vertical stack WDD design with G = 20 mm or G = 0.8Di_c and e = 15 mm or e = 0.6Di_c.

Figure 3.4: Series composition: Schematic representation of the horizontal structure designs and the geometrical conditions of the experimental series and runs. The Z axis denotes depth while y axis represents longitudinal direction along the flume. Series A is 100% Q_{bf} and series B is 80% Q_{bf} and structures are numbered 1-4.

The gap ratio between the base of the structure to the bed is referred to as (e/Di_c) and the spacing ratio between two key members is referred to as (G/Di_c) (Yang et al., 2019). Structures 1 and 3 had e = 0, structure 2 had e = 35 mm (1.4Di_c), and structure 4 had e = 15 mm (0.6Di_c). G was set to 10 mm (0.4Di_c) (structures 1 and 2) and 20 mm (0.8Di_c) (structures 3 and 4). Structural blockage area (A_p) was maintained at 0.045 m^2, by fully submerging all structures for all tests. Each structure was tested at 100% Q_{bf} and 80% Q_{bf} to analyse scour at the two discharges.

3.2.1.1.2. Sediment characteristics and flow conditions

To determine the required representative sediment grain size (d_r) for the experimentation under clear water conditions, the Critical Tractive Force method was used. Clear water conditions are defined as a case when the bed is in equilibrium, whereby sediment is stable in the flow regime (Tammela et al., 2010). By calculating a Shields parameter (τ^*) of 0.061 using Equation 3.2 and particle Reynolds number (Re^*) of 31.32 (series A) and 29.83 (series B) using Equation 3.3. Once the variables were derived, the selected sediment grain size of $\approx$ 1 mm was plotted on the Shields diagram (1936) (Figure 3.5) to establish if the sediment size was appropriate for this study. The Critical Tractive Force method established the point at which threshold of motion was reached where bed / boundary shear stress equals critical tractive fore required to initiate motion ($\tau_b = \tau_c$) (Grass, 1970; Southard, 2006). When $\tau_b > \tau_c$, excess shear stress (τ_e) is displayed, causing the bed to erode (Habibi, 1994). Many different parameters are considered by the Critical Tractive Force method, and it is therefore viewed as an established approach to determine threshold of motion.

$$\tau^* = \frac{\tau_c}{\rho g (S_S - 1) d_r} \tag{3.2}$$

Equation 3.2 calculated the Shields parameter non dimensionalized (τ^*) using critical tractive force required to initiate motion (τ_c), relative submerged specific density (ρ), gravity (g), specific gravity of sediment divided by specific gravity of water (S_s), representative sediment grain size (d_r). If the τ^* is greater than the τ^*critical value, then the bed is in motion.

$$Re^* = \frac{U^*(d_r)}{v} \qquad \text{Where: } U^* = \sqrt{gRS_0} \tag{3.3}$$

Equation 3.3 calculated the particle Reynolds number (Re^*) using shear velocity (U^*) and kinematic viscosity (v) and representative sediment grain size (d_r), hydraulic radius (series A: R = 0.09 m and series B: R = 0.078 m) and channel slope angle / gradient ($S_0 = 0.001$ m/m).
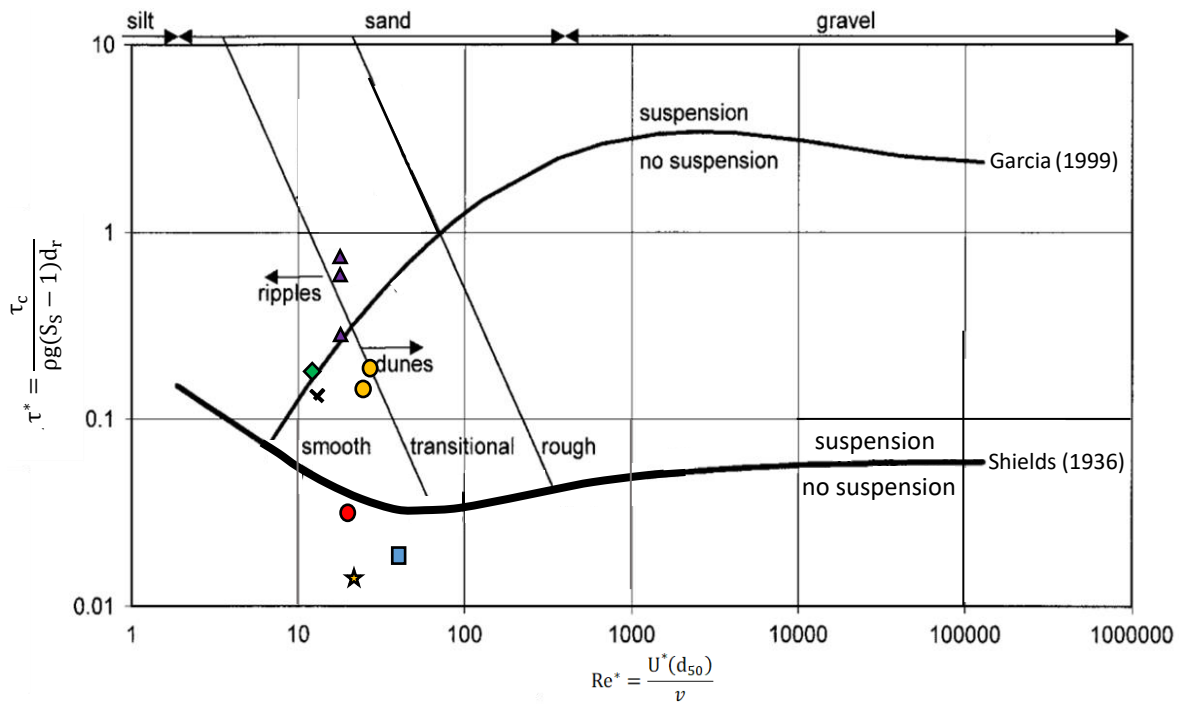
Figure 3.5: Shields Diagram showing Re* (x-axis) compared to τ* (y-axis). Shields, through a series of flume experiments under uniform flow conditions, established initiation of motion. Comparative flume experiments are displayed for comparison to the present study.

For the flume experimentation, representative sediment grain size (d_r) and flow regime conditions were set just below the threshold of motion so that the bed was stable on the verge of being entrained before the structure was inserted. Sediment is initiated into motion at the structure, with $\tau_b > \tau_c$ with a decrease in the hydraulic radius value caused by the structure blockage ratio. At the structure, sediment is initially scoured at a higher Shields parameter non dimensionalised (τ^*) of 0.13 for series A and 0.118 for series B before decreasing until the local scour depth at equilibrium is reached at which point the bed re-stabilises. Typically, τ^* values are found to range from 0.025-0.8 depending on sediment size (Berenbrock and Trammer, 2008). For the flume experimentation, τ^* values are shown with the red dot just below the threshold of motion and the yellow dots indicating τ_b at the structure for both series (Figure 3.5).

Present study parameters were compared to similar experimental literature. Penna et al. (2020b), Dey and Singh (2008) and the present study are just below the threshold of motion, due to having a lower τ^* with a larger sediment size of $\approx$ 1.53 mm, 1.86 mm and 1 mm respectively, compared to Lee et al. (2018), Gao et al. (2006) and Beebe (2000) with $\approx$ 0.52 mm, 0.44 mm and 0.38 mm respectively (Figure 3.5 with further details provided in Appendix B). Dey and Singh (2008) have a larger hydraulic radius than the present study and Penna et al. (2020b) which results in a higher Re^*. Lee et al. (2018), Gao et al. (2006) and Beebe (2000) more closely follow the Garcia curve (1999), an extended version of the Shields diagram, due to their smaller sediment grain size in comparison to the other studies (Simoes, 2014).

A sieve analysis (Figure 3.6) assessed sediment grain size distribution and compared this to the supplier grain size specifications (Table 3.1). A random sample of sediment weighing: 450 g was put through a sieving process for 10 minutes using an Electro-mechanical sieve shaker. The sieving process consisted of using three separate sieves of sizes: 1 mm, 1.18 mm and 2 mm. Experiments were carried out using grain size 1-2 mm, though slight variance occurred (Table 3.1).

Figure 3.6: Electro-mechanical sieve shaker. Sediment was put through the sieve process for 10 minutes, with progressively smaller graded sieve mesh to obtain the average particle size and range. When the sediment distribution was obtained this was checked against the particle standards to ascertain the correct grade of sediment. Sediment range displayed in Table 3.1.

Table 3.1: Sediment distribution was obtained by weighing the trays before and after the sieving process for the percentage captured by each sieve and the percentage able to pass through. Majority of sample: 52% ranged from 1-1.18 mm.

Sieve size:	Supplier specifications (% passing):	Sieving process (% passing):
2.00	95 – 100	95
1.18	5 – 30	60
1.00	0 – 5	12
Tray	0 – 1	0

3.2.1.2. Measurements

3.2.1.2.1. Equilibrium scour depth

In literature the concept of local scour depth at equilibrium remains subjective, which has implications for precision. Some argue that equilibrium cannot be quantified towards the end of clear-water experiments as the local scour depth from the established datum prior to flow conditions is asymptotic over time (t) and is so small that it is almost imperceptible and therefore difficult to accurately measure (Oliveto and Hager, 2005). During the early stage, the scour depth sharply increases, then during the later stages, the scouring process gradually decreases until finally the scour rate becomes stable and approaches the point of equilibrium with a very small scour rate. This study used a graphical solution to construct nonparametric regression functions for estimating local scour depth at equilibrium according to discharge. Local scour depth at equilibrium (d_{se}) was reached when the bed re-stabilises (Papanicolaou et al., 2018b). Therefore, the time to develop equilibrium scour depth (t_e) was determined as the point of initiation of the plateau, with the point of plateau defined as when the reduction of the scour rate is < 0.05 of the key member diameter (Di_c) within 24 hrs. Key members are the main supporting logs of the WDD. A consistent time of 96 hrs for shutting down the experiments was set to examine the differences in the bed morphological changes, ensuring precision and adequate time for local scour depth at equilibrium to be reached. To obtain the appropriate time to equilibrium an absolute plot was constructed for all series with time (x-axis) and scour depth (y-axis).

To ensure precision, verification of plateauing and easy identification of outliers a non-dimensional log-log plot was additionally constructed for series 1A, 1B and 2A with t/t_e (x-axis) and d_s/d_{se} (y-axis). The parameters influencing curve construction are blockage ratio in respect

to discharge. Parameters to be used are series A: Q = 0.022 m^3/s; B$_r$ = 0.5 and for series B: Q = 0.018 m^3/s; B$_r$ = 0.58. Discharges and blocking ratios are found in section 3.2.1.1. (Experimental set-up). Logarithmic values were used for local scour depth at equilibrium finite time, according to asymptotic functions that exist within the quasi-equilibrium period (Liang et al., 2020).

3.2.1.2.2. Bed profiling and measurement of scour

A Kinect v1.0 input device, designed for the Microsoft Xbox 360 video-games system was used in this study as a short-range 3D infrared-imaging system with the capability of producing bed elevation data with relatively good accuracy, being non-intrusive to the flow regime (Khoshelham and Elberink, 2012; Chourasiya et al., 2017). The Kinect can detect movement towards and away from it by using an infrared (IR) depth-sensing emitter and receiver (Figure 3.7). Data collection and basic data analysis using the Kinect, proves useful as an observational tool in stream bathymetry and sedimentological topographic mapping in this type of flume experimentation (Mankoff and Russo, 2013; Chourasiya et al., 2017).
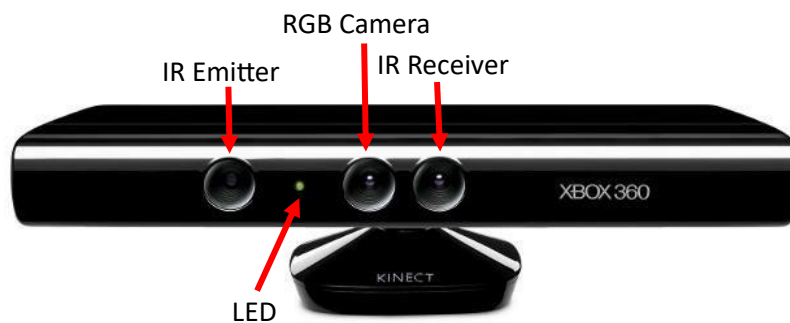
Figure 3.7: Kinect v1.0 depicting camera and sensors. Diagram showing IR emitter and IR receiver; RGB camera and LED locations. Image adapted from Andrews (2010).

3.2.1.2.3. Calibration of Kinect

Prior to the experiments, the Kinect was calibrated to minimise any measurement uncertainty and obtain reliable results. The calibration of the Kinect refers to the mapping from raw digital number (DN) coordinates to real-world, x, y, z points (Mankoff and Russo, 2013). Poor

calibration of the Kinect can create inaccuracies, errors and imperfections in the captured point cloud imagery. Appropriate calibration for robust applications is essential to generate greater accuracy, to prevent systematic imprecisions in measurements and irregularities in geometric distortion (Khoshelham and Elberink, 2012; Basso et al., 2018). The calibration of the Kinect, including spatial resolution, depth accuracy, depth resolution and precision, and geometric calibration are described in the following sections below.

3.2.1.2.3.1. Spatial resolution of the Kinect

To obtain real-world values spatial resolution was examined. An external calibration procedure was used to convert the spatial resolution (K_m), defined as the number of pixels utilised in construction of the point cloud (Spring et al., 2020), into real measured distance (T_d) using a calibration factor. To obtain the Kinect horizontal and vertical resolutions (x and y directions), the Kinect was positioned at a true measured distance (Z_{bs}) of 1.025 m perpendicular from a planar surface. In this case the planar surface was a flat wall with homogeneity of colour and reflectivity spanning the full Field of Vision (FoV) (Khoshelham and Elberink, 2012; Yang et al, 2015; Pohlmann et al., 2016). IR camera points were marked in the x and y directions at the maximum Kinect FoV, with T_d between points measured using a tape measure (accuracy: ±0.3 mm) (Tape Store, 2020). The calibration factor or x and y spatial resolution was quantified using Equation 3.4. For the present study, the Kinect needed a FoV of the entire main channel width (0.6 m) and as much of the longitudinal distance (L = 10 m) as possible, while achieving a high spatial resolution with reduced pixel blocking. A distance x and y spatial resolution analysis was required to quantify the appropriate Z_{bs}. Two Z_{bs} were conducted, the calibration factor / x and y spatial resolution at Z_{bs} = 1.025 m was 1.6 x 1.67 mm compared to Z_{bs} = 0.8 m at 1.32 x 1.35 mm. This is verified by Szasz et al. (2011) that at Z_{bs} = 0.8 m, the spatial resolution was just over 1.3 mm per pixel. The Kinect has an optimal recommended working distance of 0.8-4.0 m (Pagliari and Pinto, 2015; Al-Naji, 2017; Ouma, 2019). It can be noted that at a closer distance the resolution improves, however, it was decided to use Z_{bs} = 1.025 m as deposition caused the Kinect to black out within the minimum threshold working distance (Z_{bs} = 0.8 m) (Chourasiya et al., 2017). Once appropriate spatial resolution was obtained, future point clouds K_m in the x and y directions were converted into T_d by multiplying K_m by the calibration factor (C_f).

$$C_f = \frac{T_d}{K_m} \hspace{6cm} (3.4)$$

Equation 3.4 calculated the Calibration factor (C_f) (x and y-direction). The calibration factor was quantified at a true measured distance (Z_{bs}) of 1.025 m with real measured distance (T_d) measured at 1.024 m (x-direction) and 0.802 m (y-direction). At Z_{bs} = 0.8 m, T_d was measured at 0.845 m (x-direction) and 0.648 m (y-direction). The Kinect resolution was set at K_m = 640 px (x-direction) and K_m = 480 px (y-direction).

3.2.1.2.3.2. Depth accuracy of the Kinect

Tests were carried out to validate the depth accuracy. Kinect depth accuracy is the difference between the digital measured distance from Kinect to the principal point (K), as compared to the true measured distance (Z_{bs}) (Mankoff and Russo, 2013; Mallick et al., 2014; Wasenműller and Stricker, 2017). As Z_{bs} increases, the depth accuracy measured by the Kinect decreases quadratically (Khoshelham and Elberink, 2012; Mallick et al., 2014). Depth accuracy was obtained by measuring the Z_{bs} to the K, directly in front of the Kinect. A point cloud of the planar surface provided DNs that acted as the K variable. At Z_{bs} = 1.025 m, the Kinect reading was K = 1024. Depth accuracy error (E) from K to Z_{bs} was calculated at 0.1% or E = 1.03 mm at this distance (Equation 3.5). This value is substantiated by Pohlmann et al. (2016) whose equation calculated that at Z_{bs} = 1.2 m, the Kinect had a E < 2 mm, while Mankoff and Russo (2013) stated at Z_{bs} = 1 m, E = 2 mm and at Z_{bs} = 4 m, E = 47 mm. A similar method to converting K_m into T_d, was used to convert K into Z_{bs} through multiplication of the calibration factor (C_f) (Equation 3.6) by the K variable to determine point cloud depth accuracy.

$$E = \frac{(Z_{bs} - K)}{Z_{bs}} \hspace{5cm} (3.5)$$

Equation 3.5 calculated Kinect depth accuracy percentage error (E) using the true measured distance (Z_{bs}) and conveyance (K_0) (Mankoff and Russo, 2013).

$$C_f = \frac{Z_{bs}}{K_0} \tag{3.6}$$

Equation 3.6 calculated the Calibration factor (C_f) used for depth accuracy in Z-direction at a set Z_{bs} of 1.025 m. This equation was used to convert the digital measured distance from the Kinect to the principal point to the true measured distance.

To check results, a book of known dimensions (width = 89 mm; depth = 40 mm; length = 245 mm) (Figure 3.8) (Khoshelham and Elberink, 2012; Pohlmann et al., 2016) was placed on the flume bed. The obtained calibration factor was applied to point cloud values to quantify Kinect depth accuracy and establish spatial resolution. Once the calibration factor was verified, it was applied to all bed morphological point clouds.
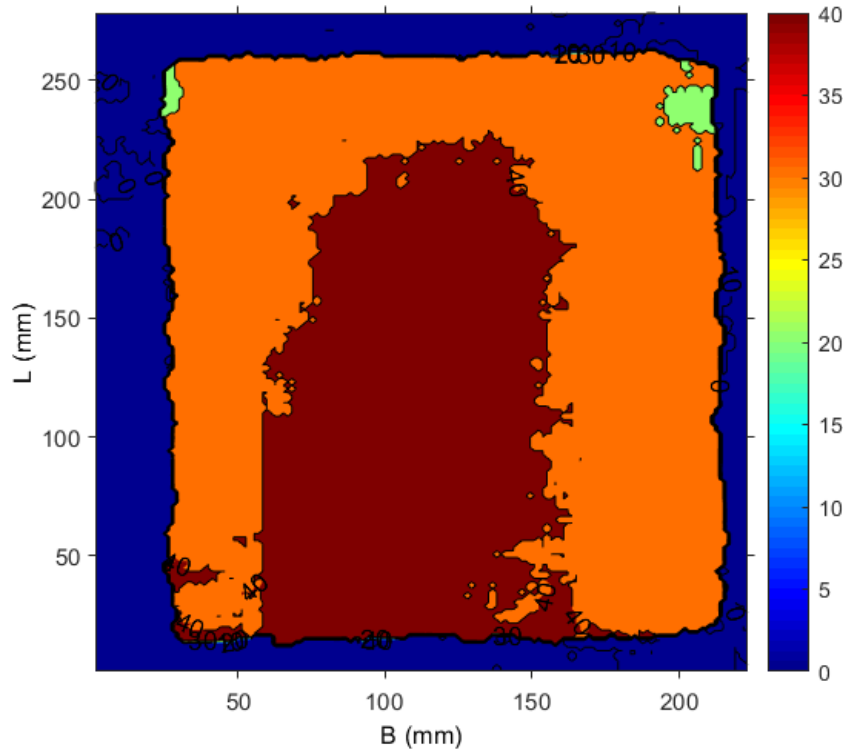
Figure 3.8: Calibration of sensor from a known object (in this case a book was used) at Z_{bs} = 1.025 m. The width, length and depth of a book was used (width = 89 mm; depth = 40 mm; length = 245 mm). Point cloud values were converted into real-world distances using Equation 3.4 and Equation 3.6.

3.2.1.2.3.3. Depth resolution and precision of the Kinect

Depth resolution is the step sized deviation from the depth accuracy and is the smallest measured distance between points that is repeatable under unchanged conditions (Smisek et

al., 2011; Mankoff and Russo, 2013; Mallick et al., 2014; Smisek, personal communication, May 2020). Precision is defined as the spread of measurements around the mean and is also repeatable under unchanged conditions (Mankoff and Russo, 2013; Wasenmüller and Stricker, 2017; Mankoff, personal communication, May 2020). The smaller the distance difference detectable, the better the depth resolution and the spatial density achieved (Spring et al., 2020). Depth resolution is determined by the number of DNs used with the Kinect consisting of 11-bit integers providing 2,048 levels of sensitivity (Khoshelham and Elberink, 2012).

The Kinect sensor measures depth values by triangulation with the IR emitter projecting a fixed speckled pattern onto the object and the IR receiver capturing the reflected pattern and correlating it against the stored reference pattern of the original surface. This pattern analysis method of depth measurement is known as a structured light approach (Mallick et al, 2014; Sarbolandi et al., 2015). Depending on the Z_{bs}, the reflected speckled pattern shifts in the direction of the Kinect baseline between the IR emitter and the IR receiver which is 75 mm apart (Sarbolandi et al., 2015; Pagliari and Pinto, 2015).

In image acquisition this speckled pattern technique may miss a DN and this value is replaced with a similar value from a nearby pixel creating the appearance of steps based on the reference pattern (Sarbolandi et al., 2015; Wasenmüller and Stricker, 2017). The Kinect internally makes the best match to the disparity value to achieve sub-pixel depth accuracy using a Gaussian distribution (Stommel et al., 2013; Landau et al., 2016). Each depth image on the Kinect contains a fixed 640 x 480px, however, as the Z_{bs} increases the point density decreases and steps appear further apart with lower depth resolution found at greater distances (An et al., 2016) (Appendix C). To analyse this, trials were carried out at two distances of Z_{bs} = 1.025 m and Z_{bs} = 0.8 m (Figure 3.9). Using Equation 3.7 (Khoshelham and Elberink, 2012) the maximum depth resolution for the present study is ≈ 2.7 mm at Z_{bs} = 1.025 m. This is also verified by Equation 3.8 at ≈ 3 mm (Smisek et al., 2011; Smisek, personal communication, May 2020) and Appendix C at ≈ 3 mm (Mankoff and Russo, 2013; Mankoff, personal communication, May 2020). Khoshelham and Elberink (2012), Smisek et al. (2011) and Mankoff and Russo (2013) determined step size by positioning a Kinect at different Z_{bs} from a planar target and constructing a normalised depth disparity curve, Z_{bs} versus DN. The constructed graphs allow formulation of equations which enables depth values to be calculated from the normalised disparities and quantization (q) steps at chosen Z_{bs}. Kinect

depth accuracy was cross-referenced to the point gauge and for the present study a mean precision of 1.5 mm was verified.

$$q(z_{bs}) = \left(\frac{m_p}{fb_l}\right) z_{bs}{}^2 \qquad (3.7)$$

Equation 3.7 determined the quantization step size ($q(Z_{bs})$) defined as being the depth difference corresponding to two successive levels of disparity. This involved using the Khoshelham and Elberink (2012) equation where $\left(\frac{m_p}{fb_l}\right)$ was pre-determined as being 2.85Exp-5.
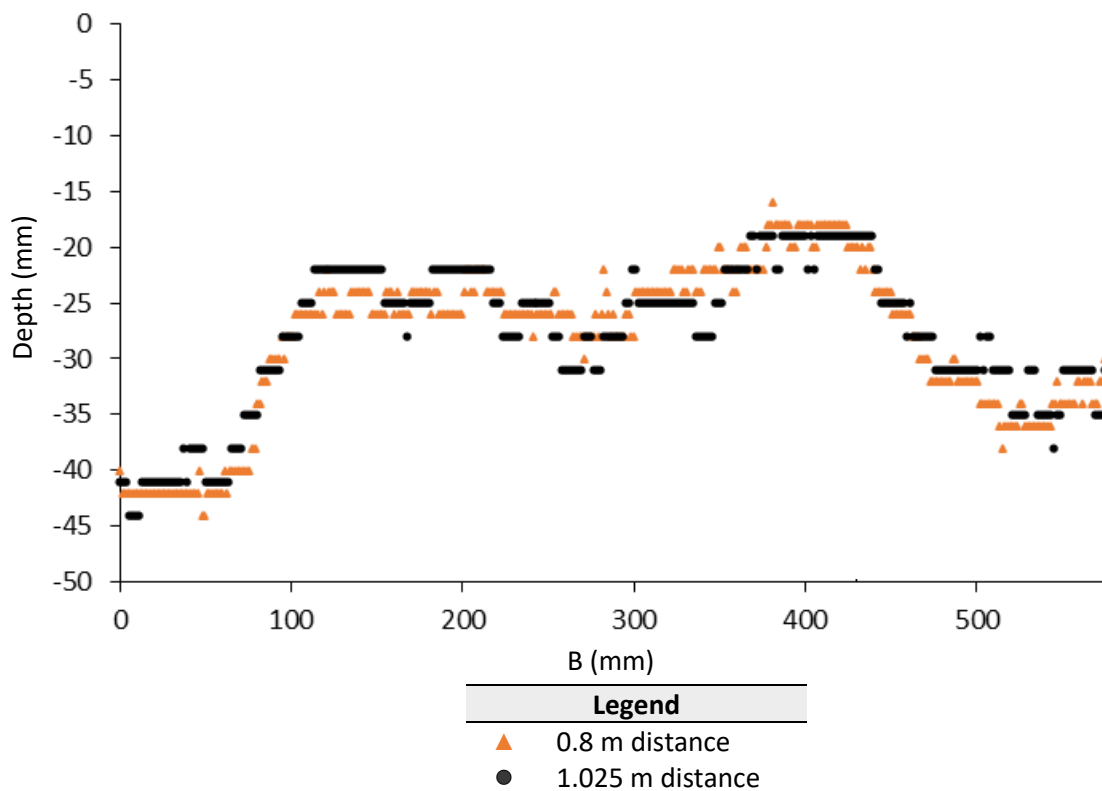
Figure 3.9: Two Z_{bs} trialled in flume experiments to analyse the effects of per patch error (Z_{bs} = 1.025 m and 0.8 m). When moving the Kinect closer to the bed the 1.025 m image was captured however the exact location to align images is lost due to moving the location of the Kinect and re-focusing. Transects formed from point clouds taken 10 mm downstream of the structure after flow (series 2B, run 2). It is noted step size increases from 1.8 mm to 2.7 mm using Equation 3.7.

$$q(z_{bs}) = 2.73 z_{bs}{}^2 + 0.74 z_{bs} - 0.58 \qquad (3.8)$$

Equation 3.8 determined the depth resolution as a function of distance (Smisek et al. 2011) with true measured distance (Z_{bs}) required.

3.2.1.2.3.4. Geometric calibration of the Kinect

To calibrate common correspondence and identify lens distortion and de-centring, it was important to calculate correlation parameters, such as radial and tangential lens distortion. The visible effect of radial distortion causes the image to bow slightly inwards at the edges. Tangential distortion occurs when the lens and the image plane are not quite parallel (Matlab, 2020a).

Depth calibration consists of deformation analysis to reduce point cloud curvature. When obtaining the calibration factor, geometric calibration was also undertaken to reduce depth disparity and improve Kinect spatial resolution of point clouds (Andersen et al. 2012). Amplitude and range were examined for variations relative to the neighbouring pixels. The point clouds initially exhibited a quadratic increase in curvature at the corners (Figure 3.10). To reduce the radial distortion around the point cloud edges, the model proposed by Brown (2002) for camera distortion correction using least-squares adjustment was applied (Equation 3.9) through a computer processing and camera calibrator app using Matlab. For polynomial radial distortion two coefficients were calculated by firstly preparing and then examining distortion from 15 images of a known sized checkerboard (checkerboard sized square: 20 mm). By adding and removing imagery, reprojection errors were decreased with a mean calibration accuracy of 0.14, camera parameters were exported so bed morphological point clouds could have the distortion removed (Figure 3.11). Image standard error corresponding to each actual value of a given parameter (focal length, principal point and distortion coefficient) was then analysed to calculate confidence intervals within a 95% standard deviation (Matlab, 2020b). If the reprojection or estimation error was within the 95% confidence threshold, the calibration accuracy was considered acceptable. However, those images outside this threshold were either excluded or redefined. The camera parameters were compared to published literature to examine distortion coefficients and ensure that a reduction in any error was sufficient (Appendix D).
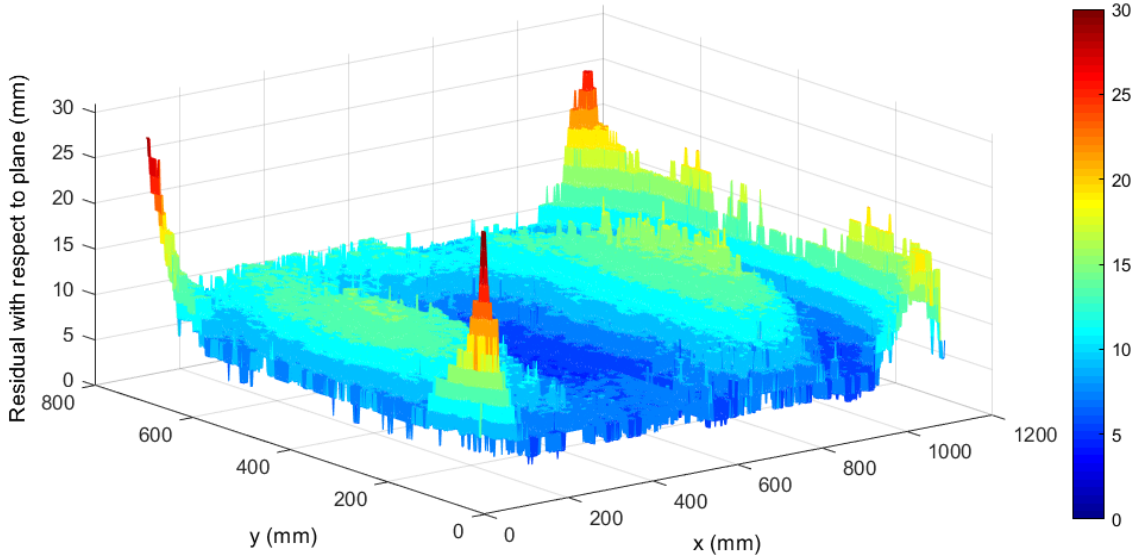
Figure 3.10: Radial IR distortion with respect to the plane at Z_{bs} = 1.025 m. The DNs were computed and represented as a point cloud, in which a surface plot was interpolated using Matlab. Kinect IR distortion shows that the further from the Kinect to the principal point, the greater the size of the pixel displacements where the edges are heightened and curved (Smisek et al. 2011). Radial effects increase with the distance between Kinect and target (Mallick et al., 2014). The residuals can reach approximately 1cm to tens of centimetres at the corners at maximum usable ranges (Lachat et al., 2015).

$$x_d = x(1 + k_1 r^2 + k_2 r^4 + k_3 r^6) \qquad \text{Where: } r = \sqrt{x^2 + y^2} \qquad (3.9a)$$

$$y_d = y(1 + k_1 r^2 + k_2 r^4 + k_3 r^6) \qquad\qquad\qquad (3.9b)$$

Equation 3.9a and b determined calibration to remove distortion (Li, 2018). For Equation 3.9a this involved letting x be the ideal coordinates on the image plane, x_d being the corresponding real observed coordinates and 0, 0 denoted the principal point, free of any distortion and k_1, k_2, k_3 denotes the radial distortion coefficients. While for Equation 3.9b, distortion is removed in the y plane. Zhang and Zhang (2011) claims the first two terms in these equations are sufficient to adequately undistort images in most cases. r is the square root of the sum of x and y which was used to obtain the undistorted image.
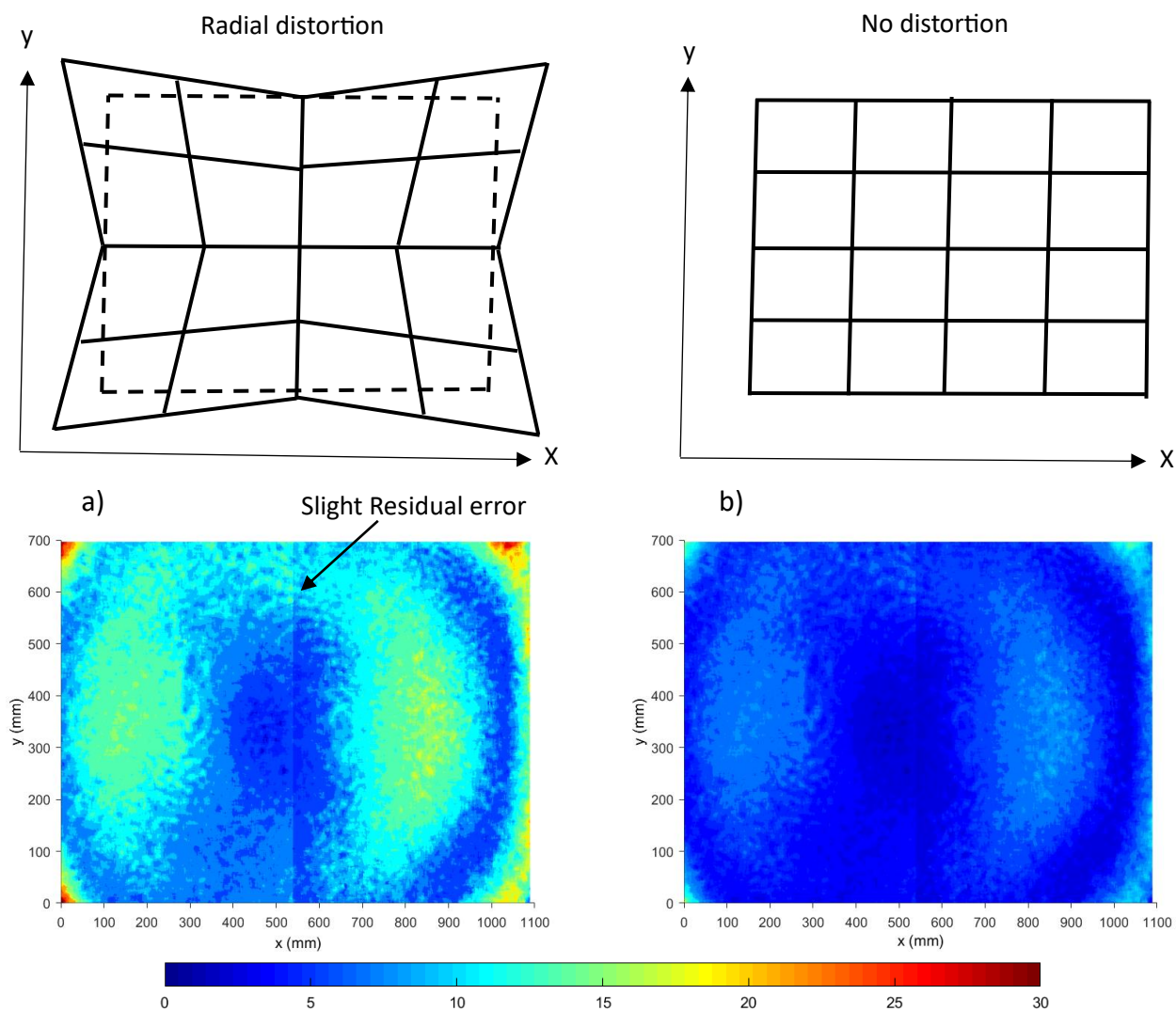
Figure 3.11: Schematic of radial distortion removal (top row) (adapted from Li, 2018) compared to point cloud deviations between radial distorted images and corrected images (bottom row). Colour representation of the residuals with respect to a fitted plane (Z_{bs} = 1.025 m), a) before correction and b) after correction. A slight residual vertical error line can be seen at the point cloud centre line. After calibration there remains a slight residual error due to the limitations of the Kinect cameras.

3.2.1.3. Scientific procedure

The experiment was started by establishing uniform flow conditions and a constant flow depth in the flume. Uniform flow is achieved when there is no change in the flow depth along the length of the water body. The tailgate heights for series A and B were calculated, as mentioned earlier in the setup section (3.2.1.1.), and were fixed depending on the discharge value (series A and B). Flow conditions were controlled by using the tailgate at the downstream end of the flume. A Vernier point gauge was used to measure the centre line flow depth (h) and water surface profile before each structure was inserted. In each run, the structure was fully

submerged (series A: h = 150 mm and series B: h = 130 mm). With the insertion of the structure the flow conditions changed, with the water surface profile generating gradually varied flow (GVF) conditions. The flow depth was measured using a Vernier point gauge, and discharge was instantaneously and cumulatively monitored by the flow meter. Initially, scour increased rapidly over time before slowing, with sediment transport rates tending towards zero and plateauing. Experiments were run for 96 hours until a maximum depth of scour at equilibrium was achieved. Upon completion of each experiment, the pumps were gradually shut down and the water slowly drained from the flume to preserve the integrity of the channel morphologic details. The Vernier point gauge measured the centreline measurements at the end of the runs. The centre line is displayed in Figure 3.12. Images were acquired using a Kinect mounted above the bed on the carriageway (Z_{bs} = 1.025 m). Point clouds captured the dry bed to increase accuracy and reduce errors from water reflection and refraction, as well as prevent potential interference of the ADV aggregate on the image.
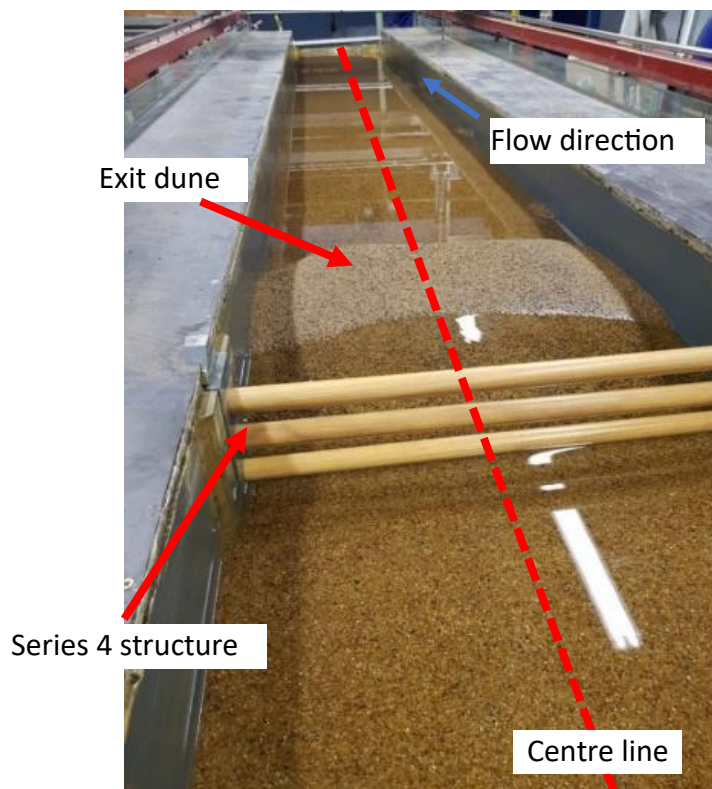
Figure 3.12: A Vernier point gauge measured the centre line flow depth before and after the structure was inserted.

The Kinect, in conjunction with Matlab Image Acquisition toolbox, was used to create and measure Digital Elevation Models (DEMs) of scour and deposition to generate accurate

representations of the channel bathymetry. The Image Acquisition toolbox allowed interactive detection and configuration of Kinect properties from the Kinect triggering to point cloud acquisition. The Image Acquisition toolbox provided image processing, visualisation and algorithm development to display and analyse the data from the flume by generating Matlab script for graph construction or scripts, which were exported to excel for numerical analysis.

DEM accuracy was validated using point gauge measurements along the centreline at 0.05 m spacings, 1.4 m downstream of the structure, to make comparisons to point cloud accuracy representing the channel bathymetry. Bed profiles were measured from a predefined datum above the flume using the point-gauge. Three cross-sections at notable elevations were measured in the lateral direction at 0.05 m intervals, within 1.4 m distance downstream of the structure. Both cross-sections and longitudinal profiles were compared to the DEM to check Kinect depth accuracy and confirm the calibration factor was precise on the applied DEMs. Identified outliers were repeated. Lateral averages down the longitudinal profile were extracted from the DEM to analyse spatial distribution of scour and deposition.

3.2.2. Hydro-environmental modelling

Hydro-environmental modelling relates to the hydraulic parameters, water levels and velocities, and environmental refers to the site characteristics as included in Flood Modeller v6.1. (FM), detailed in this thesis. To obtain non-intrusive estimates of local velocity, verify water surface profiles and examine τ_b spatial distributions, FM was chosen as it enabled attenuation modelling through numerical solvers and the ability to simulate the impact of hydraulic structures on the flow regime (Jacobs Flood Modeller, 2023a). 1D modelling enables hydraulic simulations of in-channel flow, while 2D modelling can explore spatial variations in τ_b (McParland et al., personal communication, February 2023).

3.2.2.1. 1D model scheme (schematization)

3.2.2.1.1. Cross-section construction

To delineate the channel centre line, a 5 m polyline was drawn using the standard format polyline shapefile. Upon acquiring the channel centre line, 100 cross-sections were generated with distances between cross-sections set at 0.05 m along the polyline. A global Manning's n roughness coefficient of $0.03 \, \text{s/m}^{\frac{1}{3}}$ was set as recommended by the Engineering Toolbox (2001). The first node name was defined as 'X_sect1' and subsequent node names having the numerical number incrementally increase by 1 for every 0.05 m, with an extra cross-section added at the end of the polyline. Upon inserting variables, new cross-sections were displayed on the network section. Cross-sections were individually selected, and the channel geometry was constructed to replicate the flume channel (Figure 3.2). To improve channel conveyance so the model could run with reduced errors, panel markers were added.

3.2.2.1.2. Boundary conditions

To replicate flume study flow conditions, boundary conditions were inserted into a Flow-Time boundary (QTBDY) node, positioned at the top of the network, which enabled construction of a discharge hydrograph. This unit specified the flow entering the system, whereby over a 24 hr period discharge (series A: 0.022 m³/s; series B: 0.018 m³/s) was maintained. At the bottom of the network, a Normal / Critical Depth Boundary (NCDBDY) was inserted which enabled flow to leave the system. This boundary generated a flow-head relationship based on cross-section data (Jacobs Flood Modeller, 2023b). A Flow-Head boundary (QHBDY) was not selected as discharge remained constant throughout simulations and therefore a rating curve could not be constructed. Upon set-up of both the cross-sections and boundary conditions, this acted as the unobstructed channel which was saved as a 1D River Network.

3.2.2.1.3. Simulations

Steady state simulations provided initial conditions (Flow and Stage). Errors in simulations were checked using the '1D model health check'. Additionally, fatal error codes were checked in the FM technical reference online manual. These diagnostic messages provided information regarding three types of messages: fatal errors which caused the termination of simulations, warning messages stating certain elements in the model should be checked and notes which could assist in interpreting the results (Jacobs Flood Modeller: Online Manual, 2022a). Simulation severity was provided with a code from 1-5 where 1 represents a fatal error and 5 represents a note.

Steady state simulations had the 'Direct Method Transcritical Solver' option applied, so comparisons could be made between the unobstructed and obstructed channel. When simulating structures in the obstructed channel, the nonlinear 1D Saint-Venant equations, which represent mass and momentum conservation, were applied with the numerical scheme reversing the upstream and downstream flow direction in superficial parts of the network. The 'Transcritical solver' enables supercritical flow to be modelled by negating the $\partial A/\partial y$ part of the advective acceleration term in the momentum Equation 3.10 when the Fr exceeds a specifically designated term. Within FM these terms were set to the default values of 0.75 (lower Fr) and 0.9 (upper Fr). A limitation involved within the 'Transcritical solver' is that as it solves the momentum equation in the differential form, solutions for the hydraulic jump can be inaccurate (Jacobs Flood Modeller: Online Manual, 2022b). Hydraulic jumps and bores can be complicated to represent in hydro-environmental models due to the flow's highly turbulent nature downstream of a structure or perturbation (Wang et al., 2017). Instead of the hydraulic jump being noted as gradually increasing, a sharp change in the surface water profile can occur.

$$\underbrace{\frac{\partial U}{\partial t}}_{Acceleration} + \underbrace{\frac{\partial A}{\partial y}\left(\frac{Q^2}{W}\right)}_{\substack{Conservation \\ acceleration}} + \underbrace{g\frac{\partial h}{\partial y}}_{\substack{Pressure \\ force}} - \underbrace{g(S_0 - S_f)}_{\substack{gravity\ multiplied\ by \\ Bed\ friction}} = 0 \tag{3.10}$$

Momentum Equation 3.10 denoted equilibrium as calculated using localised velocity (U), time (t), wetted area (W), longitudinal direction along the flume in y-direction (y), discharge (Q), gravity (g), flow depth (h), channel slope angle / gradient (S_0) and surface slope / hydraulic gradient (S_f) adapted from Jacobs Flood Modeller: Online Manual (2022c).

3.2.2.1.4. Obstructed channel

To convert the unobstructed channel into an obstructed channel, firstly, the unobstructed 1D River Network was saved and copied before editing could begin. To best replicate structure 1 within FM, a broad crested weir unit with the same size blockage area was inserted. As experiments were run using a constant discharge with structural surcharging, a weir unit was well suited, when discharge varies structures with leakiness are required so low discharge is not attenuated. WDDs resemble open sluice gates as they are both vertical structures, partly blocking the channel and are largely open to the air (McParland, 2021). However, sluice gates only allow flow to pass up to a depth equal to the height of the soffit because they are solid at the top (Gribbin, 2013), while WDDs are porous and do not have a definite soffit. However, WDDs can be surcharged and in this way behave more like a broad crested weir whereby the water passes above the flat crest that covers most of the channel (Benn et al., 2004) and so broad crested weir formulae are used to model flow that overtops the structure.

FM has a built-in capacity for sediment transport modelling and channel changes, but 1D simulations are unable to account for the sediment transport caused by structures (McParland et al., personal communication, February 2023). Therefore, as structure 1 has e = 0, a broad crested weir unit was well suited to represent structural induced hydraulics without the structure being undermined. Within the copied network, this unit was inserted 2 m downstream of the QTBDY and 3 m upstream of the NCDBDY. Insertion of the structure between two cross-sections was achieved by firstly placing a replicate unit, to enhance model stability, before placing the broad crested weir (Figure 3.13).
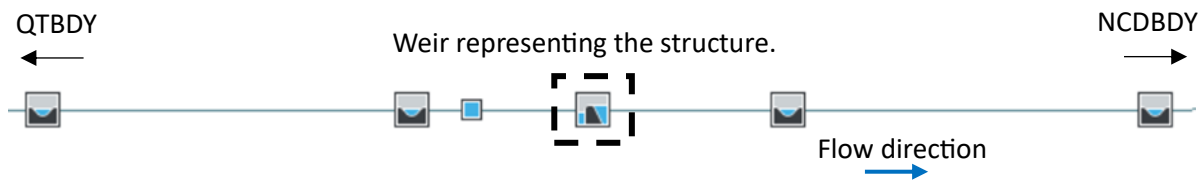
Figure 3.13: Schematic displaying the structure represented by a broad crested weir. To simulate flow entering the system a QTBDY was located at the top of the network while to simulate flow leaving the system a NCDBDY was located at the bottom of the network.

To replicate the design of structure 1 within FM, the weir geometry was altered. Elevation of the crest was set to 0.15 m to account for the sediment height, with the breadth of the crest being set to 0.6 m in order to transverse the main channel width and weir length in the longitudinal direction / distance (L) was set to 0.25 m to replicate the key member diameter (Di_c) (Figure 3.14).
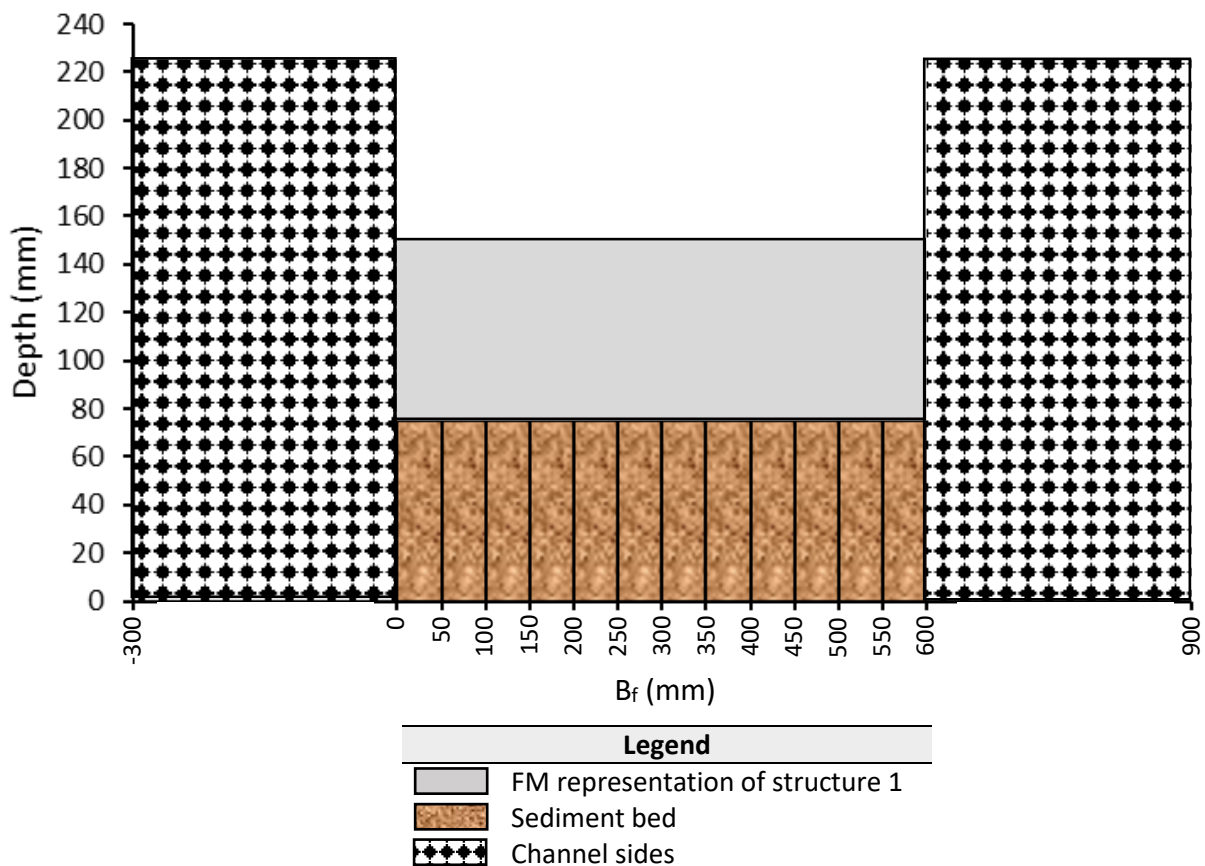
Figure 3.14: Displays how design of structure 1 was represented in FM using a broad crested weir. Structure 1 variables were replicated in FM to mimic the effects of the structure using a hydraulic structure representation approach.

To replicate the downstream tailgate to match the flume experiments within FM, a sharp crested weir was inserted at the bottom of the network (Figure 3.15). The weir plate height above the bed was set to the same height as used within the flume experiments as shown in Figure 3.4.
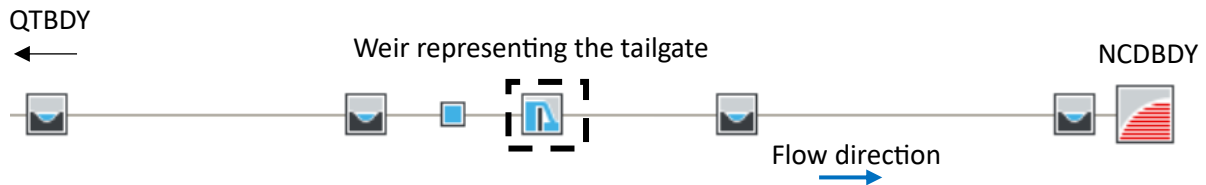
Figure 3.15: Schematic displaying the tailgate represented by a sharp crested weir. To simulate flow entering the system a QTBDY was located at the top of the network, while to simulate flow leaving the system a NCDBDY was located at the bottom of the network.

The effects of the flow contraction and backwater rise posed by the sharp crested weir were expressed using a discharge coefficient (Q_c) (Equation 3.11). Early experimentation work of Rehbock (1929) found that $Q_c = 0.611$. Equation 3.11 assumes that the flow does not contract as it overtops the weir (Henderson, 1974).

$$Q = \frac{2}{3} Q_c \sqrt{2gH^{\frac{3}{2}}}$$

(3.11)

Discharge (Q) in respect to a sharp crested weir was calculated using Equation 3.11 with variables including the discharge coefficient (Q_c), gravity (g) and effective weir head (H).

3.2.2.1.5. 1D-2D linked model

In the 1D simulation, in-channel flood mapping was constructed. To create this, a 'triangulate selected file' was selected within FM Toolbox. This enabled representation of the surface morphology (ArcMap, 2021a) by converting the flow depth points to a hydraulic gradient. The maximum flow depth was displayed using a Triangular Irregular Network (TIN) with data extracted from the 1D network located in the layer panel. A flood depth grid, which illustrates the flood depth, was constructed using the '1D flood map calculator'. Flood depth grids are useful in that they provide information regarding spatial variations in flood severity (Federal

Emergency Management Agency, 2019), whereby in FM flood depth grids were used to illustrate the backwater caused by the structure.

3.2.2.2. 2D model

3.2.2.2.1. DEM construction of the computational flume

To run 2D simulations, an active area with ground elevation details was required (Jacobs Flood Modeller: Online Manual, 2022d). In FM, two DEMs were created displaying the unobstructed (Figure 3.16a) and the obstructed channels (Figure 3.16b). Point clouds were created using Microsoft Excel 365 which produced a matrix displaying 6 columns: Cross-section ID, X, Y, Z, Manning's n roughness and representative sediment grain size. Typically for a broad scale model, FM uses a 2D grid cell size of 25 m x 25 m (rural) and for a detailed model 10 m x 10 m (urban) (Crowder, 2009). However, as the model was representing a flume, a smaller 2D grid cell size of 0.05 m was used, with DEMs showing 800 mm upstream and 1400 mm downstream of the structure. Upon creating the matrix, it was then imported into ArcGIS Pro 2.9.0. This involved saving the output feature class as a shapefile and setting the coordinate system to British national grid. The shapefile was converted into a DEM using the 3D analyst tool, with the output cell size being set to 0.05 m and imported into FM.
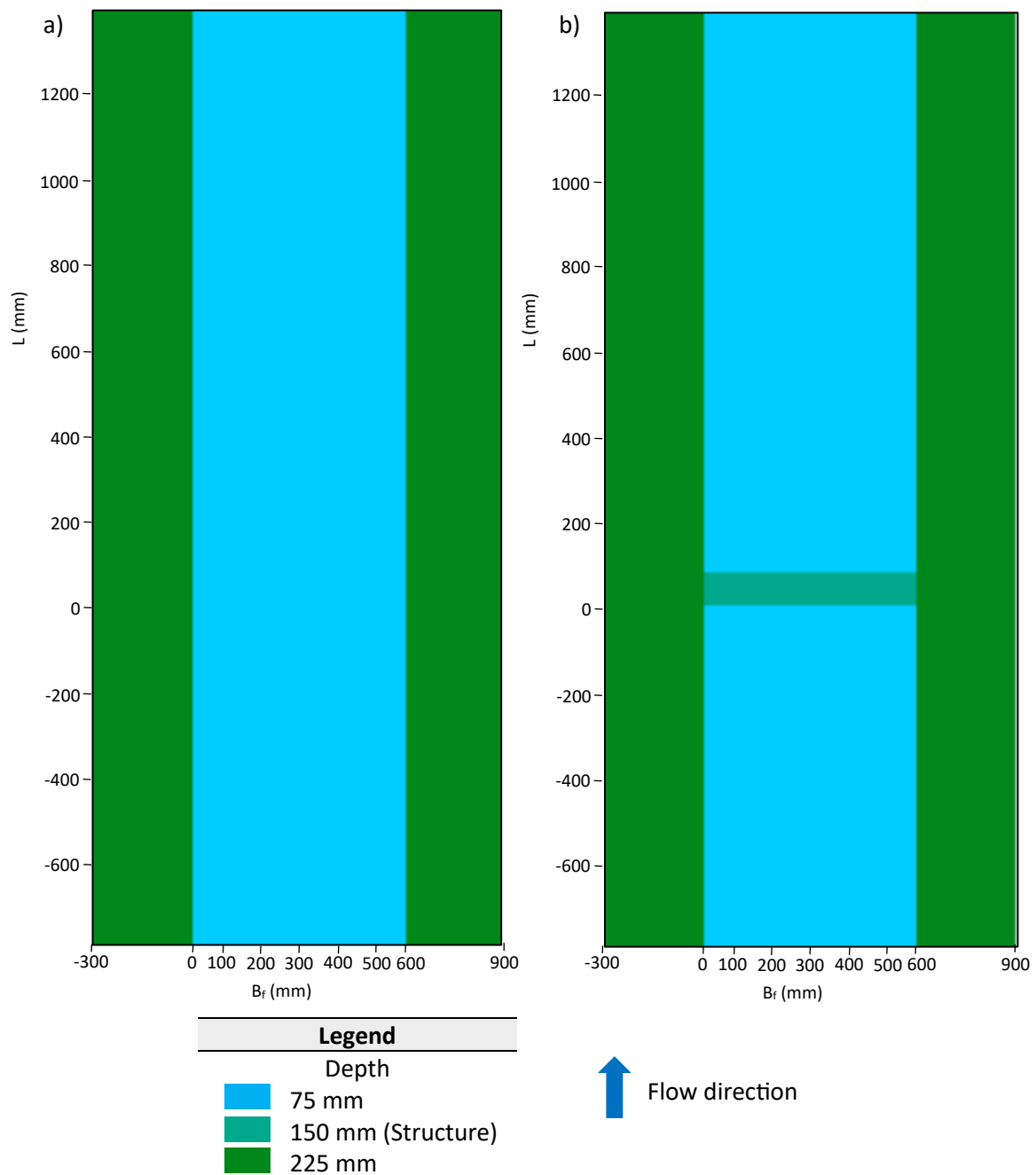
Figure 3.16: Digital Elevation Model (DEM) displaying a) unobstructed channel with banks, b) Obstructed channel with banks. A broad crested weir with an elevated bed represented series 1 within the flume experimentation. Flume width (B_f) is displayed on the x-axis and Longitudinal direction / distance (L) on the y-axis.

3.2.2.2.2. 2D simulation processing

A computational area was drawn around the Area of Interest (AoI) and calculations were restricted to this area. The computational area was drawn smaller than the DEM so Flood

Modeller could conduct calculations and so the model could be more efficient by only simulating flow in the AoI (Jacobs Flood Modeller: Online Manual, 2022e).

The channel inflow and outflow of the model were defined along with the channel and floodplain. Spatially varying roughness values with different roughness values between the channel and the floodplain were added. Manning's n roughness coefficients were inserted whereby the channel was set to $0.03 \, s/m^{\frac{1}{3}}$ and the floodplain set to $0.011 \, s/m^{\frac{1}{3}}$ as recommended by the Engineering Toolbox (2001).

For the obstructed channel, to maintain uniformity, the same computational area, active area, boundary line inflow and outflow were kept the same as the unobstructed channel. However, to give the structure a different roughness to that of the channel, a new roughness polygon was drawn around the structure with a Manning's n roughness coefficient of $0.056 s/m^{\frac{1}{3}}$. This value was selected as a study by Shields and Gippel (1995) who concluded that WDDs in a straight and sand bed channel had a Manning's n roughness coefficient of $0.056 \, s/m^{\frac{1}{3}}$ (Table 2.1 as shown in section 2.5.).

A new 2D simulation was constructed with the 'Run Timing' option, start time set to 0 hrs and finish time set to 24 hrs. Within the subdomain details tab, the preconstructed unobstructed channel layer was inserted into the topography field while the drawn active area was inserted into the active area field. Within a different simulation, the obstructed channel layer was inserted into the topography field. Within the ADI 2D solver it is recommended that the time step should be half the grid size (Jacobs Flood Modeller: Online Manual, 2022f), which in this case was set to 0.025 secs as the grid size was 0.05 m. The roughness polygon was added so the Manning's n roughness coefficient previously inserted could be used within the simulation.

The inflow boundary line was inserted and the boundary condition was set to 'inflow', with a 'constant inflow' set to 0.022 m³/s (series A) and 0.018 m³/s (series B) in respect to simulation. This process was repeated for the outflow boundary line, with the boundary condition set to 'normal depth' and the channel slope angle / gradient set to 0.001 m/s to replicate the flume experimentation.

To investigate the full shallow water equations (i.e., mass and momentum conservation), the Alternating Direction Implicit (ADI) finite difference solution procedure was applied, as it is typically used for flat floodplains, while the Total Variation Diminishing (TVD) algorithm was added when abrupt changes occur in the velocity. Output parameters were set to depth, elevation, discharge, velocity and τ_b. 'Shear stress setting' was inserted as having a representative sediment grain size of 1 mm, average sediment density as 1602 kg/m^3, relative submerged specific density (ρ) as 1000 kg/m^3 and the dimensionless critical stress was set to the default value of 0.047, as recommended by FM user manual. Simulations were run, with time-series results being displayed.

3.3. Results

3.3.1. Flume experimentation

3.3.1.1. Time to equilibrium

All series A runs with higher discharge of 0.022 m^3/s, mean velocity of 0.244 m/s and greater wetted area of 0.09 m^2 resulted in a deeper maximum scour depth compared to series B where discharge was 0.018 m^3/s, mean velocity was 0.222 m/s and wetted area was 0.078 m^2 (Figure 3.17). For example: series 1A run 3 had a maximum scour depth of 61 mm compared to series 1B, run 3 at 40.1 mm (Appendix A). Experimentation showed with increased mean velocity (U_0), local scour depth from established datum prior to flow conditions (d_s) takes longer to reach equilibrium, whereby series A reached equilibrium at 72 hrs and series B reached equilibrium at 48 hrs. Therefore, time to develop equilibrium scour depth (t_e) for series A continued for 24 hrs longer than series B.

Figure 3.17 shows local scour depth at equilibrium (d_{se}) is dependent on the depth of the bottom of the structure to the bed (e) and vertical spacing between two key members or aperture size (G) values. At 100% Q_{bf}, the structures with the greatest d_{se} are those with smaller G values (series 1A and 2A with G = 0.4Di_c) and between these, the structure with the greatest d_{se} is series 1A, with e = 0. Structures with larger G have reduced d_{se} (series 3A and 4A with G = 0.8Di_c) and between these, the structure with the lowest d_{se} is series 4A, with e = 0.

Series A had a greater maximum scour depth variance (13.9 mm) between the largest (series 1A, run 3) and smallest values (series 4A, run 1) depending upon the structural design. In comparison series B had a lower maximum scour depth variance (13 mm) between the largest (series 3B, run 2) and smallest values (series 4B, run 1), also dependent upon the structural design. Additionally, series A showed a higher maximum scour depth standard deviation (σ) of 5.82 compared to series B at 4.12 (Equation 3.12). This suggests that the structural design in respect of discharge governs the maximum scour depth.
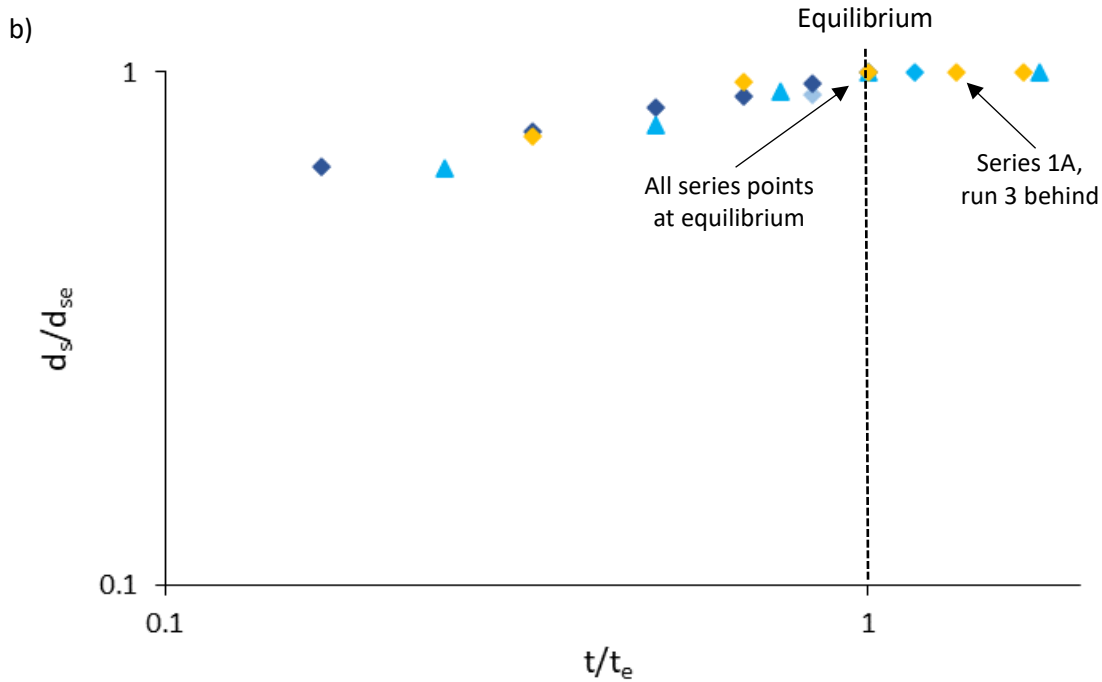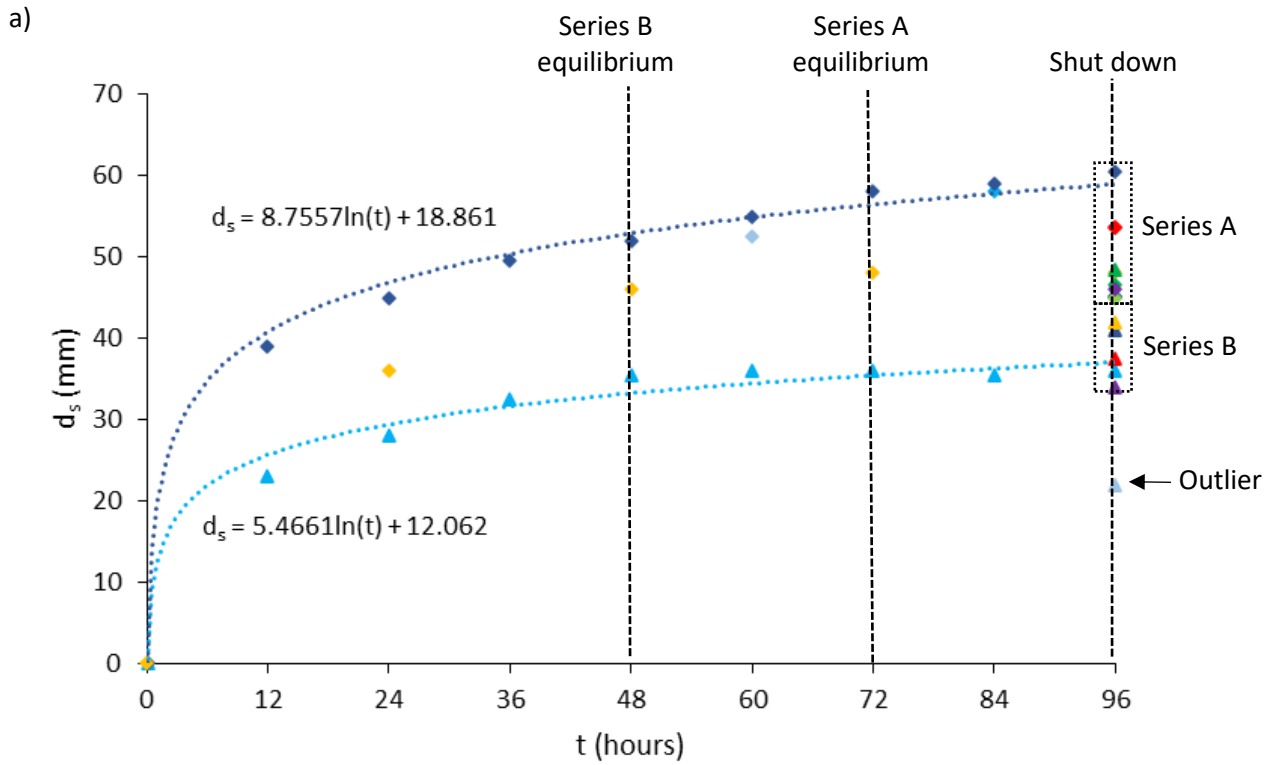
Figure 3.17: a) Linear scale graph showing local scour depth from established datum prior to flow conditions to bed (d_s) as a function of time (t). b) Non-dimensional log-log plot for predicting the time variation of maximum scour depth. Local scour depth from established datum prior to flow conditions (d_s) in clear-water conditions is asymptotic and so threshold criteria is when scour development in time has reduced to negligible change. The threshold criteria used is at the time the scour rate reaches the initiation of plateau which gives consistency of scour development for all series.

$$\sigma = \sqrt{\frac{\sum\left(d_{se} - \overline{d_{se}}\right)^2}{n_u}} \qquad (3.12)$$

Equation 3.12 calculated standard deviation (σ) using local scour depth at equilibrium (d_{se}), mean scour depth at equilibrium ($\overline{d_{se}}$) and number of samples (n_u).

3.3.1.2. Structural design affecting channel bathymetry

3.3.1.2.1. Temporal development of scour and depositional features

This section describes bathymetric evolution caused by a WDD, with channel evolution dependent upon discharge and the structural design in clear-water conditions. All series were run for 96 hrs, though local scour depth at equilibrium was reached at 72 hrs (series A) and 48 hrs (series B). However, bathymetric evolution continues past time to develop equilibrium scour depth, as seen with the exit dune extending further downstream. Scour starts at the front of the structure ($\approx$ 30 mm) and progressively develops through submerged erosion beneath the structure, with some upstream sediment removed from the bottom key member before equilibrium is reached. Figure 3.18 shows that the maximum scour depth continues to deepen from 51.7 mm to 58 mm to 61 mm over 36 hrs (series 1A, Run 1 / 2 / 3 respectively) (Appendix A) and progressively moves downstream after reaching equilibrium. This was also seen with the maximum height of the exit dune (h_{max}) extending downstream over time (L = 526 mm, h_{max} = 47.1 mm to L = 830 mm, h_{max} = 52.7 mm to L = 947 mm, h_{max} = 55.1 mm) (Appendix A) but as the exit dune lengthens and flattens, elongating further downstream, the angle of repose decreases (Figure 3.19).

Local scour depth is strongly dependent on time according to discharge. Within the first 60 hrs, the local scour depth increased rapidly to 51.7 mm, while within an additional 36 hrs, the local scour depth value deepened by 9.3 mm. This is also shown with the maximum height of the exit dune, whereby within the first 60 hrs, the maximum height of the exit dune increased rapidly before slowly increasing in the following 36 hrs. However, within the final 36 hrs the channel bathymetry considerably changed with the length of the exit dune extending 421 mm downstream (Figure 3.18).
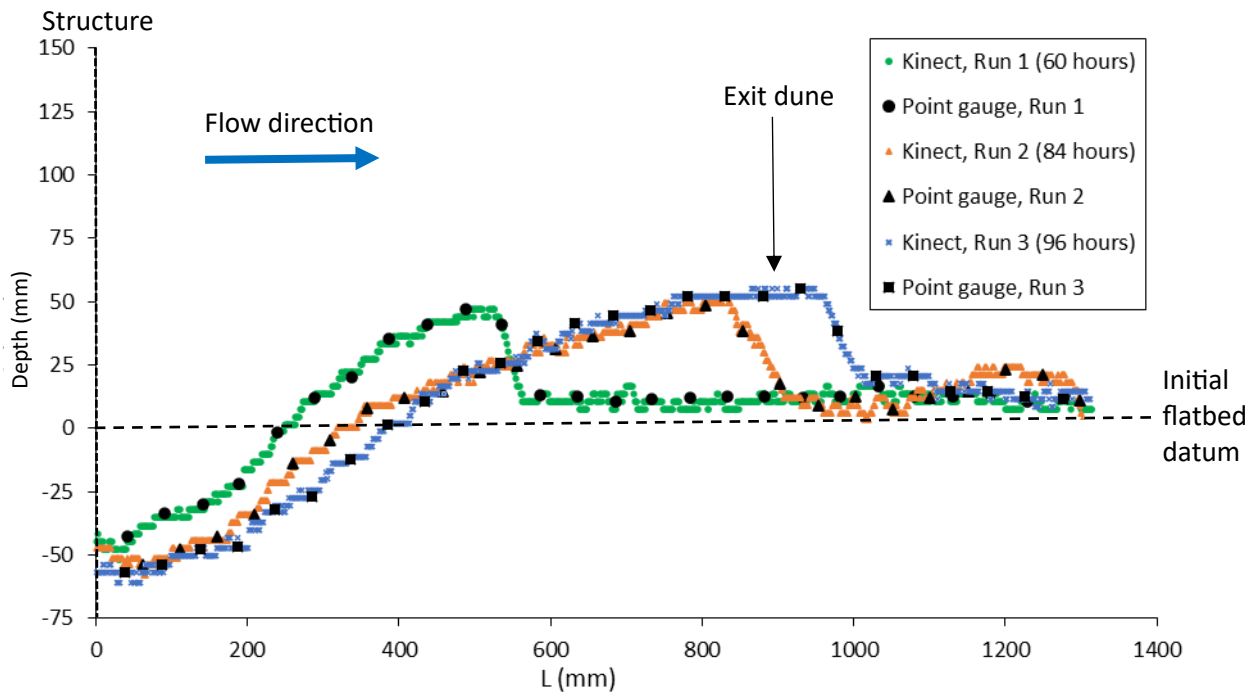
Figure 3.18: Centreline longitudinal scour profiles around a horizontal structure with e = 0 and G = 0.4Di$_c$ showing temporal development of evolution. Three separate runs for series 1A were completed over different times (60 hrs, 84 hrs and 96 hrs). The structure was placed at 0 mm (x-axis) on the graph. The Kinect measurements for each run were verified by the point gauge for accuracy.

As depicted in Figure 3.19, the scour hole and exit dune are not evenly distributed across the width. To examine spatial distribution of scour and deposition across the main channel width, lateral averages were plotted. Lateral averages offer a realistic over-view of scour and deposition across the main channel width as opposed to a narrow band at the centreline. It was noted all centrelines exhibited a taller maximum height of the exit dune and deeper maximum scour depth than lateral averages showed.

Series 1A, Run 1 shows that the exit dune forms a 'tongue' pattern perpendicular to the crest which is distinguishable in Figure 3.19 but is not distinguishable on the centreline (Figure 3.18). Similarly, in series 1A, Run 2, there is a crescent-shaped crest which is bowed downstream and in series 1A, Run 3, there is a bow shaped indent towards the centreline, where one side of the exit dune is shallower than the other.
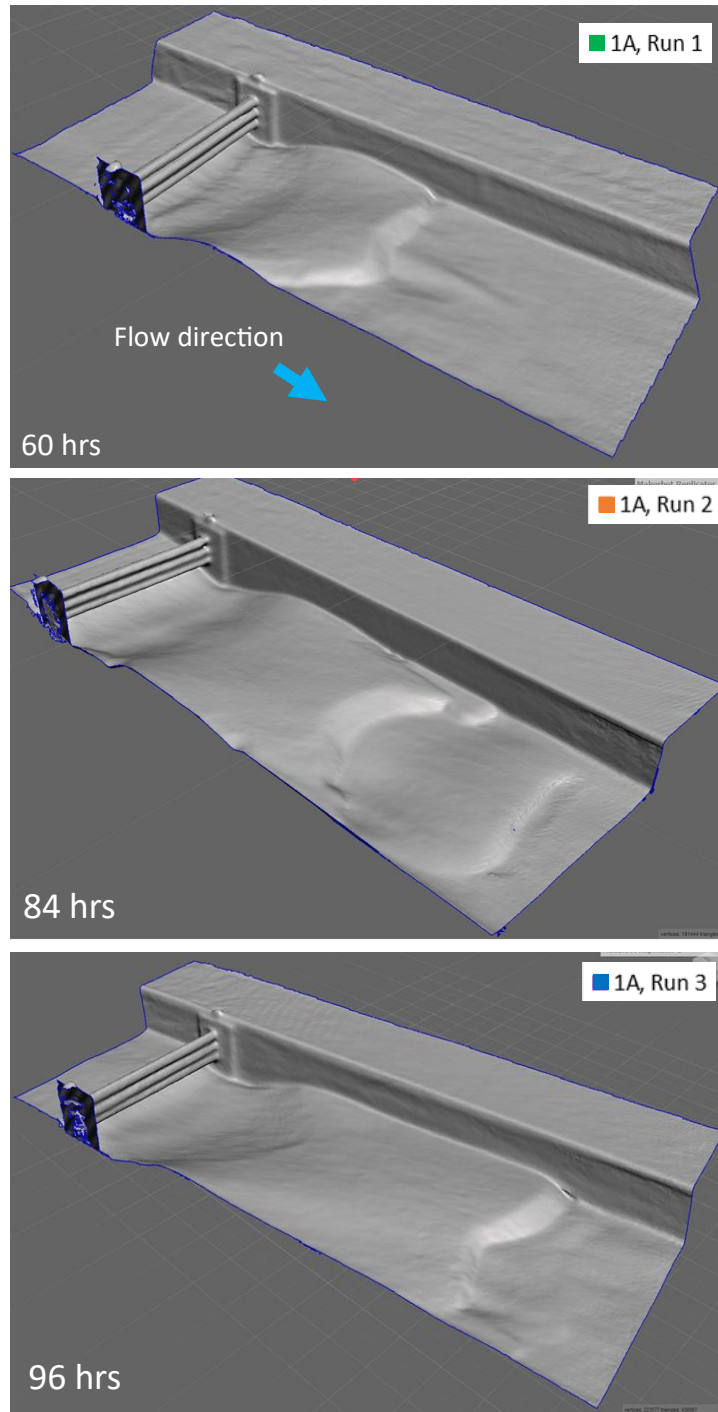
Figure 3.19: A 3D point cloud mesh showing the temporal development of the scour hole and exit dune with evolutionary changes in bed morphology. Series 1A, Run 1 has yet to reach equilibrium (72 hrs). Series 1A; Run 1 continued for 60 hrs, Run 2: 84 hrs and Run 3: 96 hrs. It can be noted local scour depth continues to deepen from 60 hrs to 84 hrs with the exit dune extending further downstream past the time to develop equilibrium scour depth. Though series 1A, Run 2 has approached time to equilibrium with slight change over 12 hrs, this is shown with Run 2 having a maximum scour depth of 58 mm compared to Run 3 at 61 mm. Therefore, the exit dune continued to develop along the channel.

3.3.1.2.2. Scour depth with variation in discharge

Figure 3.20 displays centreline longitudinal profiles with comparisons for different discharge values. It can be noted there are changes in the scour hole and exit dune size according to discharge, with series A displaying deeper scour holes and taller exit dunes upon reaching time to equilibrium. Series A exit dunes developed further downstream than series B exit dunes. It is evident that structure-related scour is sensitive to variations in discharge. For example, series 1A, Run 3 had a maximum scour depth of 61 mm compared to series 1B, Run 3 at 40.1 mm (Appendix A).

a) Series 1A, Run 3 and series 1B, Run 2.

b) Series 2A, Run 2 and series 2B, Run 1.

c) Series 3A, Run 1 and series 3B, Run 1.

d) Series 4A, Run 1 and series 4B, Run 1.

Flow direction

Legend	
●	100% Q_{bf}
▲	80% Q_{bf}
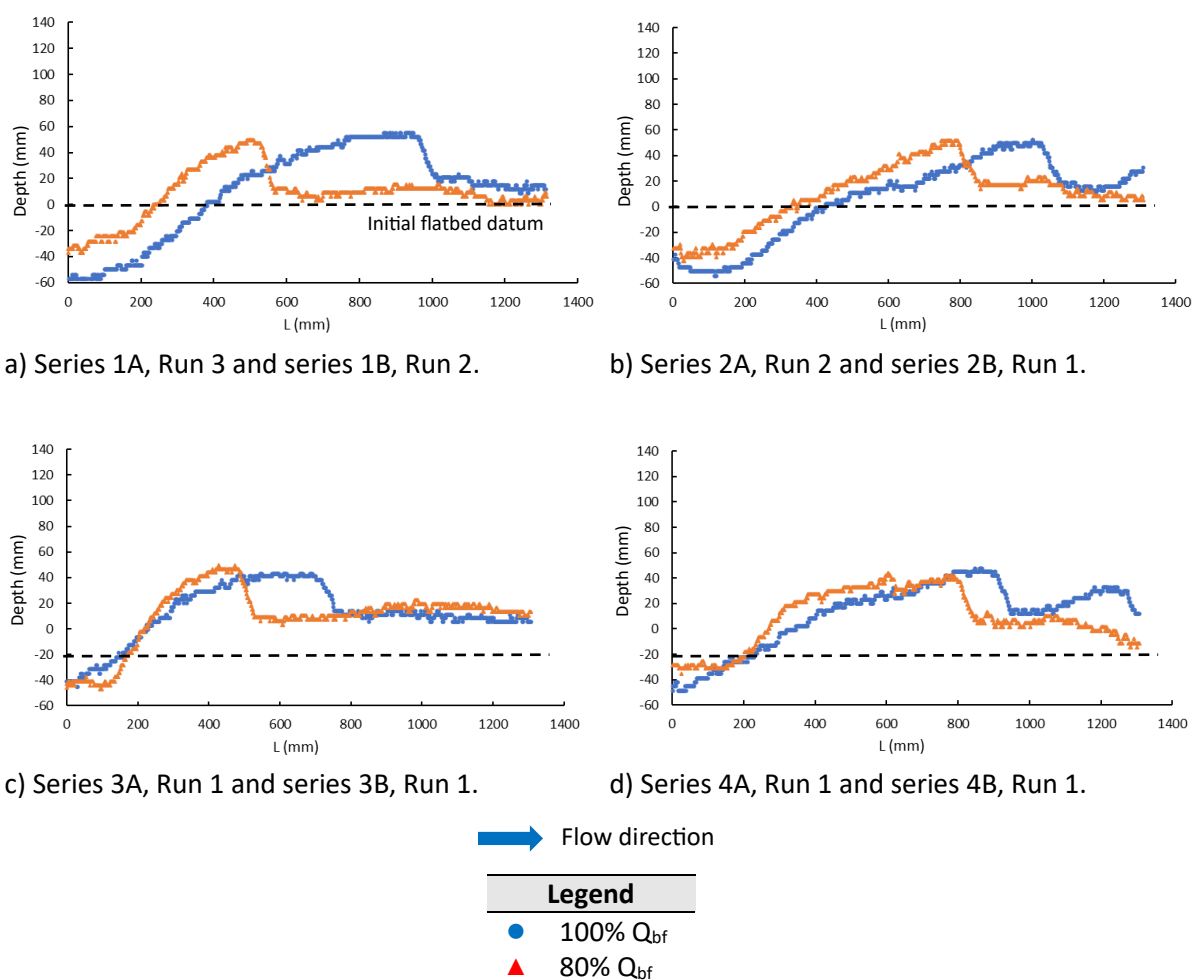
Figure 3.20: Diagrams display Kinect acquired point cloud longitudinal centrelines including initial flatbed datum. Channel bathymetric evolution, using 100% Q_{bf} and 80% Q_{bf} flow conditions, for the four structural designs: a) series 1, b) series 2, c) series 3 and d) series 4 are displayed.

Depth of the bottom of the structure to the bed influences bathymetric evolution which is particularly notable for series 1A and 1B (Figure 3.20a). At 100% Q_{bf}, series 1A had the largest scour hole with a gentle and extended angle of repose, plateauing at the crest of the exit dune. Series 1A and 1B (Figure 3.20a) and series 3A and 3B (Figure 3.20c) had similar scour hole and exit dune spatial patterns, although the size of the hole and height of the exit dune varied between the structural designs. For instance, series 1A had a deeper d_{se} and a larger maximum height of the exit dune with steeper angles of repose, compared to series 3A.

Series 2A and 2B and 4A and 4B with e > 0 display similar bathymetric patterns (Figure 3.20b and Figure 3.20d) with positioning of scour holes and exit dunes. However, size differs with series 2A having a gentler angle of repose and the exit dune having a short plateau compared to series 4A. Therefore, structures with e = 0 had steeper angles of repose compared to when e > 0.

Discharge and the depth of the bottom of the structure to the bed are the main drivers of varied scour, but these are not the only drivers. At 100% Q_{bf}, e interacts with G to increase the local scour depth. Structures with $G = 0.4Di_c$ had deeper d_{se} compared to structures with $G = 0.8Di_c$. For instance, Series 1A (e = 0; $G = 0.4Di_c$) and series 2A (e = $1.4Di_c$; $G = 0.4Di_c$) had deeper d_{se} compared to series 3A (e = 0; $G = 0.8Di_c$) and series 4A (e = 0.6; $G = 0.8Di_c$) (Appendix A). This shows that, as well as bathymetric change being dependent upon e/Di_c, it is also dependent upon G/Di_c and blocking capacity. This suggests, to attain deeper d_{se} during high discharge, structures should have e = 0 and a small G.

3.3.1.2.3. Digital Elevation Models

The larger the depth of the bottom of the structure to the bed (e), the further downstream the scour pool and exit dune initiates. Series 2A and 2B (e = $1.4Di_c$) had the maximum scour depth moved further downstream from beneath the structure (Figure 3.21) with large areal extent. Series 1B and 2B show a different spatial pattern compared to series 1A and 2A as they reveal a blunter scour boundary which does not extend as far downstream. Series B exit dunes are smaller in extent and closer to the scour hole with steeper angle of repose towards the exit dunes.
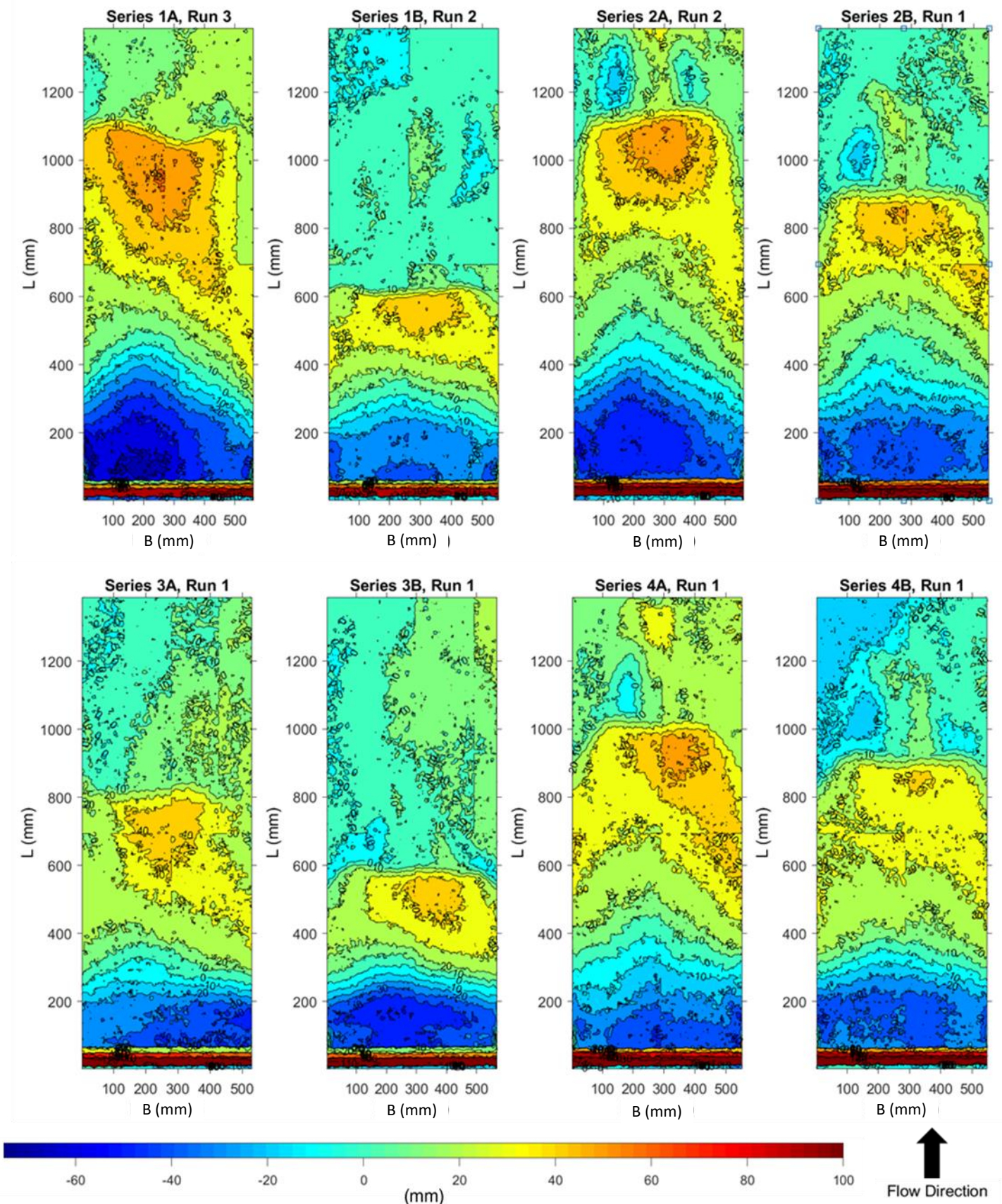
Figure 3.21: DEMs displaying series 1 - 4 (100% and 80% Q_{bf}) showing spatial distribution of scour and deposition using clear-water conditions. Bed topographical contours placed at 10 mm height elevations. 0 mm refers to a fixed datum established prior to water flow. All locality and scour patterns are shown from the structure to 1.35 m downstream. Longitudinal direction / distance (L) is displayed on the x-axis and main channel width (B) on the y-axis.

3.3.1.2.4. Downstream turbulence

As shown in Figure 3.22, turbulence was visually observed downstream of the structures creating scour with vortices. Structures with a smaller vertical spacings between two key members (G) generated greater downstream vortices, which enhanced turbulence and sediment transport. Vortices were particularly noted at series 1A. These observations confirmed that turbulence was important in the entrainment and scouring process. As depicted (Figure 3.4), series 1A allows vortices to surcharge the structure and form between key members (G = 0.4Di$_c$), when e = 0. This creates turbulence in the wake of the structure capable of entraining sediment. Series 2A with G = 0.4Di$_c$ and e = 1.4Di$_c$ which enabled a 20 mm structural surcharge, had less turbulence occurring downstream of the structure which accounted for the reduced d$_{se}$.
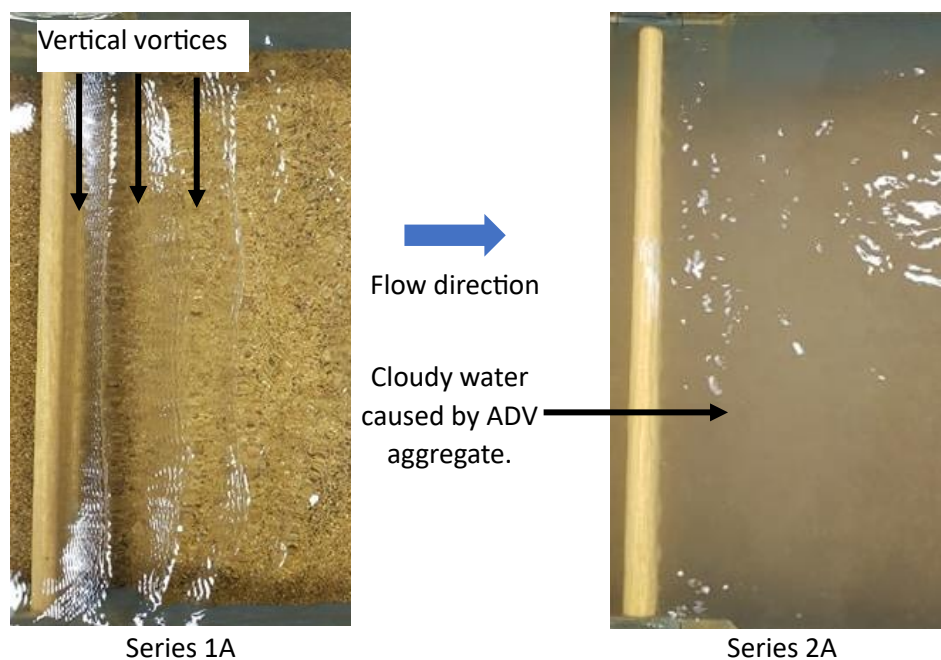
Series 1A   Series 2A

Figure 3.22: Turbulence observed in the wake of the structure. Series 1A depicted with e = 0, G = 0.4Di$_c$. As shown here at 100% Q$_{bf}$ the structural surcharge is 55 mm which is the maximum of all four design structures. For comparison, series 2A is shown with e = 1.4Di$_c$, G = 0.4Di$_c$ and structural surcharge of 20 mm. ADV aggregate has clouded the water at series 2A.

To obtain the pressure loss caused by the structure, relative roughness (ε) and Reynolds number for the hydraulic radius (Re$_h$) were required for calculation of the friction factor coefficient (f). It was noted that for a uniform boundary sediment, particle roughness (k$_s$) ≈ representative sediment grain size which in this study was 1 mm (Nikuradse, 1933; Kironoto

and Graf, 1994). The ε value for the normal flow depth (h_n) was calculated as 0.01 (series A) and 0.0111 (series B) (Equation 3.13). To examine turbulent logarithmic flow, Re_h was calculated at 24060 to 24534 (series A) and 20021 to 20866 (series B) in respect to 0.5 m upstream and downstream of the structure (Equation 3.14). ε was calculated at 0.0097 to 0.0101 (series A) and 0.01 to 0.011 (series B). In determining the velocity flow distribution and f values, both ε and Re_h were plotted on the Moody diagram (Appendix E). To verify the moody diagram, the empirical Colebrook-White Equation 3.15 was used to calculate the friction factor coefficient. The friction factor coefficient was calculated to be 0.03987 to 0.04029 (series A) and 0.04064 to 0.04167 (series B). Along the longitudinal profile, all flow conditions remained in the transitional zone, with smooth turbulence flow and roughness elements lying within or just outside of the laminar sub-layer. Transition turbulent flow was calculated at 0.378 (Equation 3.16).

$$\varepsilon = \frac{k_s}{R} \tag{3.13}$$

Equation 3.13 calculated Relative roughness (ε) in an open channel using particle roughness (k_s) and hydraulic radius (R) (Fenton, 2010).

$$Re_h = \frac{U.R}{v} \tag{3.14}$$

Equation 3.14 calculated Reynolds number of the hydraulic radius (Re_h) using localised velocity (U), hydraulic radius (R) and kinematic viscosity (v).

$$\frac{1}{\sqrt{f}} = -2\log\left(\frac{\varepsilon}{3.7R} + \frac{2.51}{Re_h\sqrt{f}}\right) \tag{3.15}$$

The Colebrook-White Equation 3.15 for open channel flow calculated the friction factor coefficient (f) using relative roughness (ε), hydraulic radius (R) and Reynolds number of the hydraulic radius (Re_h). (EngineerExcel, 2023).

$$U_o = U^* \left(2.5 \log_e \left(\frac{z_a U^*}{v} \right) + 5.56 \right)$$

$$U_o = \frac{U^*}{h} \int_0^h \left(2.5 \log_e \left(\frac{z_a U^*}{v} \right) + 5.56 \right) dz_a = \frac{U^*}{h} \left(2.5 z_a \log_e \left(\frac{z U^*}{v} \right) - 2.5 z_a + 5.56 z_a \right) \Big|_0^h$$

$$\therefore U_o = \frac{U^*}{h} \left(2.5h \log_e \left(\frac{h U^*}{v} \right) + 3.06h \right) = U^* \left(2.5h \log_e \left(\frac{h U^*}{v} \right) + 3.06h \right)$$

$$\therefore \text{ For } z_a \text{ when velocity} = U_0$$

$$U_o = U^* \left(2.5h \log_e \left(\frac{z_a U^*}{v} \right) + 5.56 \right) = U^* \left(2.5h \log_e \left(\frac{h U^*}{v} \right) + 3.06h \right)$$

$$\therefore 2.5 \left(\log_e \left(\frac{z_a U^*}{v} \right) - \log_e \left(\frac{h U^*}{v} \right) \right) = 3.06 - 5.56$$

$$\text{or } 2.5 \log_e \left(\frac{z_a U^*}{h U^*} \right) = -2.5$$

$$e^{-1} = \frac{z_a}{h} = 0.368 \qquad\qquad (3.16)$$

Equation 3.16 determined the transitional turbulent flow, with derivations shown, using mean velocity (U_0) and height of depth average velocity (z_a) which can be calculated using Shear velocity (U^*), kinematic viscosity (v) and flow depth (h).

3.3.1.2.5. Insertion of the structure altering hydrodynamics

The flume study was initially run under uniform flow conditions with a sediment grain size selected at the threshold of motion ($\tau_c = \tau_b$). Upon inserting the structure for a localised $\tau_b > \tau_c$, this caused scouring and non-uniform flow conditions. Within the critical tractive force method, insertion of the structure only changed the hydraulic radius value (Equation 3.2) and therefore scouring occurred until equilibrium or the threshold of motion was re-established. As all series were run at the threshold of motion, after the structure was inserted and at time to equilibrium, the same size hydraulic radius occurred along the channel with slight variances in d_{se}, caused by key member friction, vortices placement, localised velocity and slope angle ' gradient increased upstream of the structure. Initially when the structure was inserted, a hydraulic gradient of 0.032 m/m occurred over the structure, however when equilibrium was re-established a decrease of ≈ 44% occurred in the friction slope, giving a hydraulic gradient of 0.018 m/m (Figure 3.23).
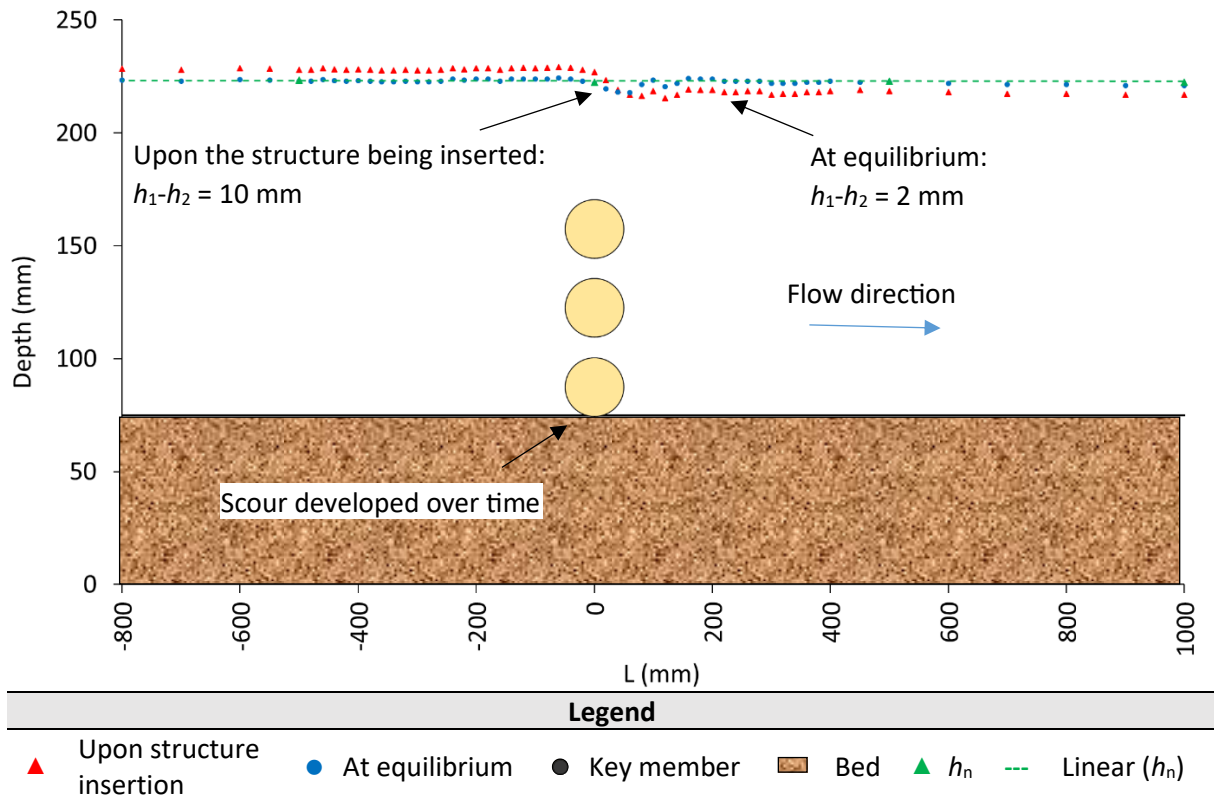
Figure 3.23: Surface water profile of series 1A, Run 2. A point gauge measured flow depth every 0.02 m for 0.5 m upstream and downstream of the structure followed by distances of 0.05 m for 0.1 m and 0.1 m for an additional 0.4 m. Larger h_1-h_2 was measured when the structure was first inserted however when equilibrium was re-established, h_1-h_2 decreased. The normal flow depth (h_n) is displayed to show how the structure altered the surface water profile.

Within this study the hydraulic gradient value was calculated over a 0.28 m distance to negate turbulence. Upon insertion of the structure, the GVF increased the upstream flow depth by ≈ 5 mm above datum, set at the normal flow depth. However, upon reaching equilibrium, the upstream flow depth decreased by ≈ 4.5 mm. In comparison when examining the downstream flow depth, upon insertion of the structure, the downstream flow depth reduced by ≈ 5 mm and upon reaching the time to develop equilibrium scour depth, this increased by ≈ 3.5 mm, to more closely follow the normal flow depth, though to a lesser extent.

3.3.2. Hydro-environmental modelling

3.3.2.1. 1D modelling

Both flume and FM results showed that when the structure was inserted, GVF conditions were displayed with an increased afflux (h_1-h_2). h_1-h_2 is defined as the increase in flow depth upstream of a perturbation that was created as a result of an obstruction to the flow regime

(Lamb et al., 2006a). Statistical analysis quantified significance between datasets with series A having a very strong positive relationship with a Pearson's correlation coefficient of 0.911 and series B having a strong positive relationship of 0.871 (Equation 3.17).

To examine how the flow varied between the obstructed and unobstructed channel, the statistical t-test Paired Two Sample of Means (Equation 3.18) was undertaken. The t-test could not be used to verify the Pearson's correlation coefficient (P_c) in examining the variation between the flume experimentation and FM as both datasets required the same number of data points. At 100% Q_{bf} within FM, the absolute value of the t-statistic (-8.087) was less than the critical t value for both datasets (Obstructed: 1.657 and Unobstructed: 1.979). As the P-values (Obstructed: 2.459Exp-13 and Unobstructed: 4.918Exp-13) were greater than the value of alpha (0.05) the null hypothesis was accepted and therefore the mean of both datasets are equal (Figure 3.24a). A similar pattern followed at 80% Q_{bf} where the absolute value of the t-statistic was -8.005 which was less than the critical value for both datasets (Obstructed: 1.657 and Unobstructed: 1.979). Additionally, as the P-values (Obstructed: 3.808Exp-13 and Unobstructed: 7.615Exp-13) were greater than the alpha (0.05), the null hypothesis was accepted with the means between samples being equal (Figure 3.24b). Statistical analysis suggests that the flow depth varied once the structure was inserted, though not significantly. Additionally, statistical analysis showed that within FM, the sharp crested weir was a suitable unit to represent the flume experimentation tailgate with both the flume experimentation and FM displaying similar downstream flow depths (Figure 3.24a and b).

$$P_c = \frac{\sum(x_i - \bar{x})(y_i - \bar{y})}{\sqrt{\sum(x_i - \bar{x})^2 \sum(y_2 - \bar{y})^2}}$$

(3.17)

Equation 3.17 calculated the Pearson's correlation coefficient (P_c) using x-values in a sample (x_i), mean of the x-values ($\bar{x}$), y-values in a sample (y_i) and mean of the y-values ($\bar{y}$).

$$T = \frac{\sum d}{\sqrt{\frac{n_u(\sum d^2) - (\sum d)^2}{n_u - 1}}}$$

(3.18)

Equation 3.18 displays the T-Test for Paired Two Sample for Means (T). Variables required for this equation include the number of samples (n_u) which in FM was number of cross-sections (120). The difference per paired value (d) was also required.

Figure 3.24: a) Series A surface water profile displayed with a 0.05 m spatial resolution. Comparison is made between the obstructed channel (solid line) versus the unobstructed channel (dotted line). sediment bed height is shown without erosion as readings were taken at the beginning of the experiment.
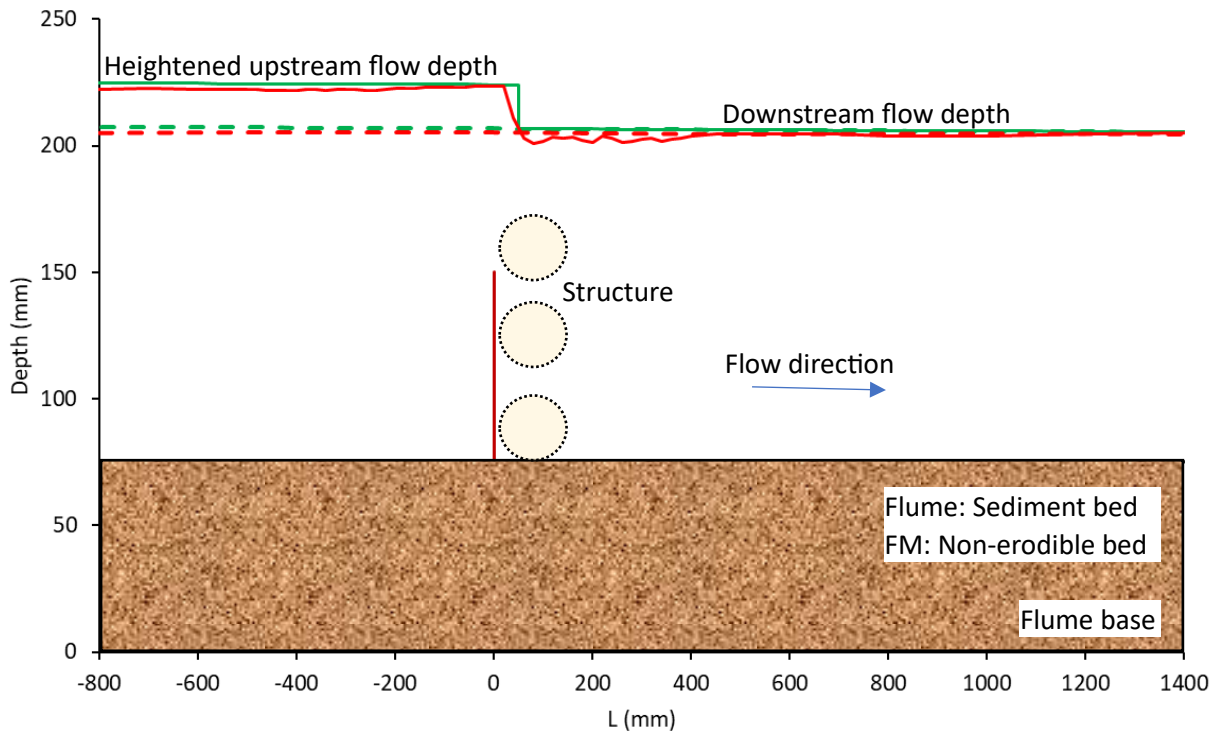
Legend				
		FM		Point gauge
Bed		— Obstructed channel		— Obstructed channel
I FM structure		- - - Unobstructed channel		- - - Unobstructed channel
Flume individual key member				

Series A statistics	Obstructed channel		Unobstructed channel	
	FM	Point gauge	FM	Point gauge
Standard Error (mm)	4.66	5.78	1.59	2.94
Standard deviation (σ)	5.21	5	1.77	1.02
Sample Variance	2.71	2.5	0.312	0.104
Kurtosis	-1.505	-1.9	-1.199	0.102
Skewness	0.599	-0.149	-0.0298	1.043
Flow depth minimum (mm)	220	218	220	222
Flow depth maximum including outliers (mm)	233	232	226	224
Confidence Level (95.0%)	0.922	1.15	0.314	0.647

t-Test: Paired Two Sample for Means	
	FM: Obstructed vs unobstructed channel
Hypothesised mean difference	0
Degree of Freedom	120
t- statistic	-8.087
P (T ≤ t) one-tail (Obstructed channel)	2.459Exp-13
t Critical one-tail (Obstructed channel)	1.657
P (T ≤ t) two-tail (Unobstructed channel)	4.918Exp-13
t Critical two-tail (Unobstructed channel)	1.979

Figure 3.24: b) Series B surface water profile displayed with a 0.05 m spatial resolution. Comparison is made between the obstructed channel (solid line) versus the unobstructed channel (dotted line). sediment bed height is shown without erosion as readings were taken at the beginning of the experiment.

| | Obstructed channel | | Unobstructed channel | |
Series B statistics	FM	Point gauge	FM	Point gauge
Standard Error (mm)	8.59	1.1	1.58	1.9
Standard deviation (σ)	9.61	9.57	1.76	0.67
Sample Variance	92.3	92	3.1	4.5
Kurtosis	-1.523	-1.994	-1.198	0.924
Skewness	0.672	-0.0658	-0.0336	-0.8009
Flow depth minimum (mm)	203	202	203	204
Flow depth maximum including outliers (mm)	226	224	209	206
Confidence Level (95.0%)	1.7	2.2	0.313	0.443

| t-Test: Paired Two Sample for Means | |
FM: Obstructed vs unobstructed channel	
Hypothesised mean difference	0
Degree of Freedom	120
t- statistic	-8.005
P (T ≤ t) one-tail (Obstructed channel)	3.808Exp-13
t Critical one-tail (Obstructed channel)	1.657
P (T ≤ t) two-tail (Unobstructed channel)	7.615Exp-13
t Critical two-tail (Unobstructed channel)	1.979

When comparing the flume experimental results to the FM results, the findings showed a similar pattern, whereby for GVF conditions, a backwater pool was created which increased the upstream flow depth. However, though they follow similar patterns, the h_1-h_2 extent differed noticeably. For series A, the h_1-h_2 value was found to be 11 mm for the flume experiments and 8 mm for FM, while for series B the results were larger giving h_1-h_2 of 20 mm for the flume experiments and 17 mm for FM. This variance was caused by series A having slight bank overtopping, which reduced h_1-h_2, while for series B the flow was confined to the channel.

FM has been designed to simulate small to large river reaches, typically > 3 m wide with distances between cross-sections of 50-200 m (McParland et al., personal communication, February 2023). Therefore, as FM simulated relatively shallow flow in the flume, a hydraulic jump was not observed. Instead, a sharp change in the surface water profile occurred. This finding supports other small-scale studies such as Ambiental (2019), which used FM to predict backwater rise upstream of a culvert.

Within the flume experiments increased turbulence was noted downstream of the structure. In contrast FM did not display turbulence as this can constantly fluctuate in time and space. Modelling turbulence at this scale would require advanced and evolving numerical simulations, typically based on direct numerical simulations which are very demanding in terms of computational time and storage (Wang et al., 2017). Turbulence was accounted for by representations of channel conveyance derived from the steady state simulations (Jacobs Flood Modeller: Online Manual, 2022b). However, as turbulence alters temporally and spatially it is not displayed in Figure 3.24a and b.

FM results showed that τ_b increased immediately downstream of the structure between the two cross-sections. This finding is supported by other hydro-environmental modelling packages such as HEC-RAS. Both FM and HEC-RAS use linear interpolation to obtain conveyance as the rate of energy loss is usually not linear (Brunner et al., 2021; Jacobs Flood Modeller: Online Manual, 2022b). To improve model accuracy at the AoI, it is recommended to use more user defined cross-sections. If cross-sections are placed too far apart, a representative energy loss will not be determined. However, if cross-sections are placed too close together with significantly varied cross-sectional size and shape this could lead to inaccuracies in the representation of the nonlinear conveyance function unless a large eddy

simulation turbulence model (or similar) is included (Jacobs Flood Modeller: Online Manual, 2022b).

FM results showed that τ_b increased significantly at the structure site by 0.573 (Series A) and 0.431 (series B) caused by channel confinement (Figure 3.25a and b). The closer the τ_b is to 0 the less likely the channel is to erode. Both series A and series B showed that upstream of the structure in the obstructed channel, τ_b was closer to 0 compared to the unobstructed channel. This meant deposition was more likely to occur upstream of the structure while scouring initiated at the structure. Downstream of the structure, after the sudden increase in τ_b, the downstream value of τ_b in the obstructed channel equalled that of the unobstructed channel.

To account for the larger discharge and hence larger d_{se} in series A ,compared to series B, an '8-period moving average' was plotted for series A and a '5-period moving average' was plotted for series B. Variation in period size was determined to replicate the scour longitudinal distance displayed in the flume experiments, whereby the period size was set to the point where the longitudinal distance had d_{se} set to datum (i.e., d_{se} = 0 m).

Figure 3.25: Diagrams focusing on structural induced τ_b at varied L along the centre line at a) 100% Q_{bf} and b) 80% Q_{bf} flow conditions.

3.3.2.2. 1D-2D modelling

Similar to the 1D hydraulic model, the 1D-2D linked flood depth grids showed that at 100% Q_{bf} and 80% Q_{bf}, the structure increased the upstream flow depth whilst decreasing the downstream flow depth (Figure 3.26a and b), which showed that the structure was creating in-channel attenuation. When constructing the flood depth grids, flow depth points were grouped together and an average calculated. Averages were represented using a single colour. Therefore, the flood depth grids displayed banding with the upstream flow depth being greater than the downstream flow depth ($h_1 > h_2$).
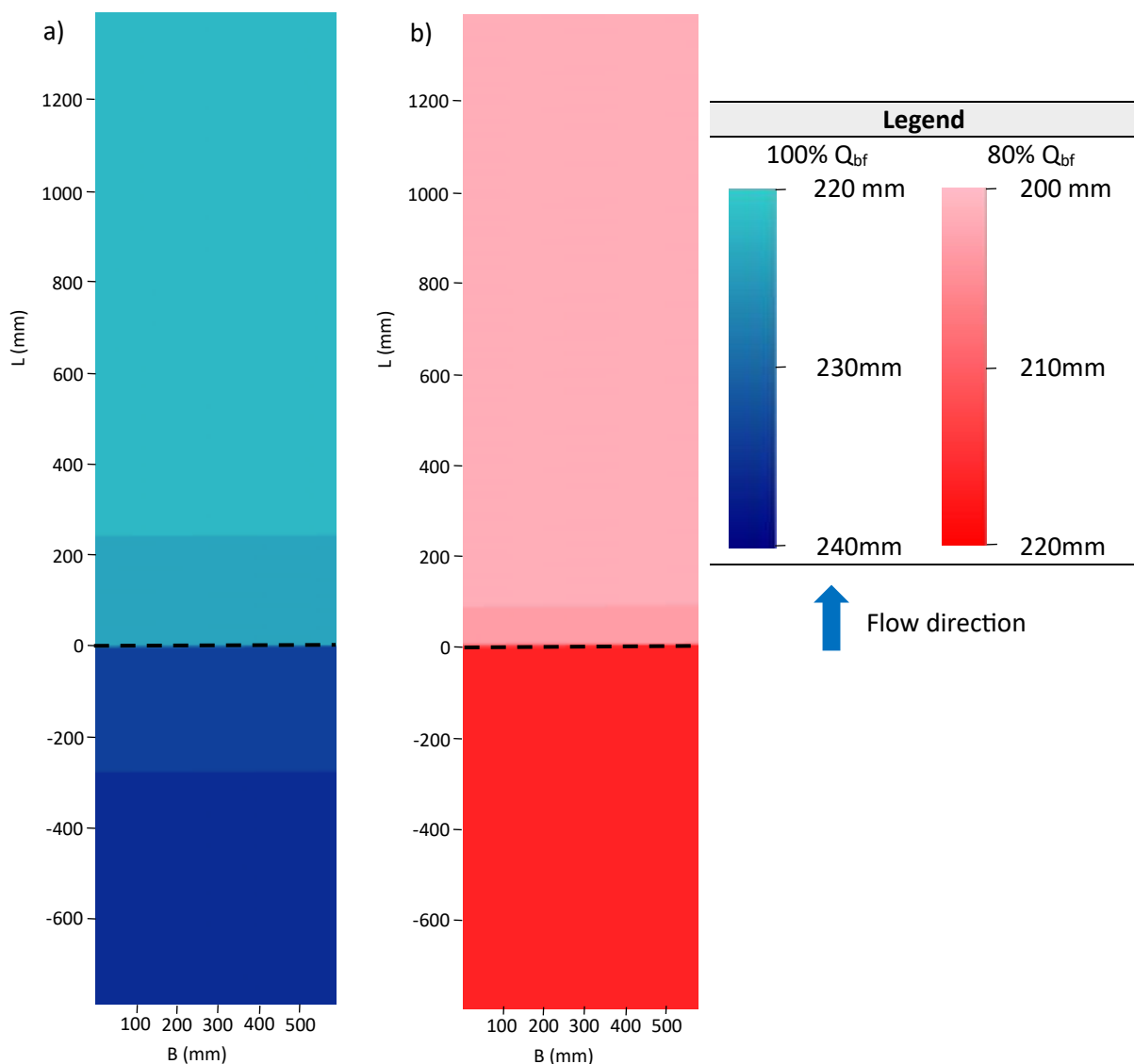
Figure 3.26: Flood depth grid displaying flow depth spatial variations including sediment height. The structure has been marked with a black dashed line. Flow conditions were simulated at a) 100% Q_{bf} and b) 80% Q_{bf}.

3.3.2.3. 2D modelling

The 2D hydro-environmental modelling showed for larger the discharge, the greater the τ_b. This was particularly noticeable at the structure, whereby series A displayed a greater τ_b effect compared to series B. A similar pattern could be seen downstream of the structure between 400-600 mm, whereby for series A the effect of τ_b was larger. Additionally, series A showed at 200 mm downstream of the structure that an area of higher τ_b occurred at the left bank. Modelling of the distribution of τ_b showed that at a higher discharge more downstream scouring occurred, as also noted in the flume experiments.

Within FM, using the ADI solver, velocity vectors are calculated at cell edges which enables the model to determine flow fields (Jacobs Flood Modeller, 2023c). Velocity vectors and streamlines show flow is structured as it approaches the structure (Figure 3.27). However, in series A just before the structure localised velocity slowed (Figure 3.28) and became less structured towards the bank sides (Figure 3.27). The streamline direction change was caused by the structure heightening the upstream flow depth, which was more prominent for high values of discharge. Downstream of the structure both series A and B, streamlines began to re-establish more structured flow with localised velocity quickening (Figure 3.28).

Legend:

100% Q_{bf}	80% Q_{bf}	τ_b
		0 − 0.05
		0.05 − 0.1
		0.1 − 0.15
		0.15 − 0.2
		0.2 − 0.25
		0.25 − 0.3
		0.3 − 0.35
		0.35 − 0.4
		0.4 − 0.45
		0.45 − 0.5
		0.5 − 0.55
		0.55 − 0.6
		0.6 − 0.65
		0.65 − 0.7
		0.7 − 0.75
		0.75 − 0.8
		0.8 − 0.85
		0.85 − 0.9
		0.9 − 0.95
		0.95 − 1
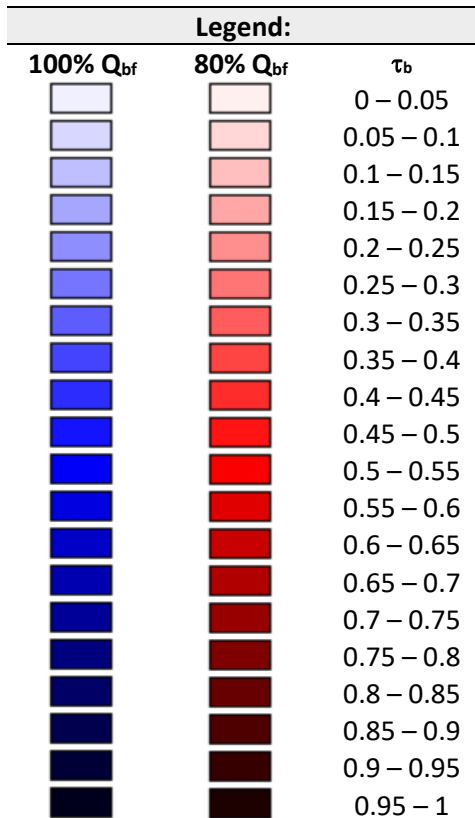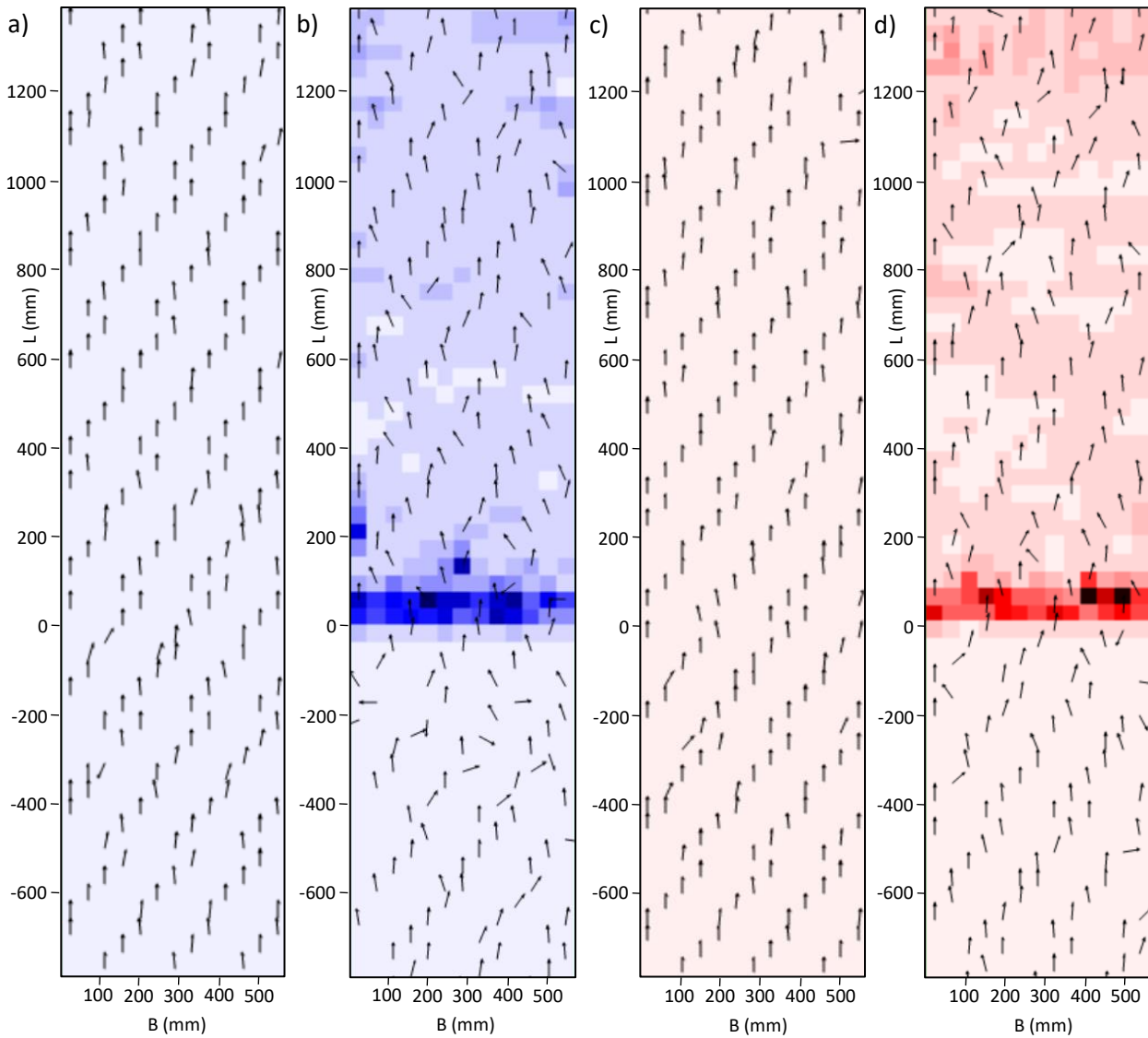
Flow direction

Figure 3.27: Diagrams displaying τ_b spatial distribution with velocity vectors. 100% Q_{bf} flow conditions are shown in the obstructed channel (a) and the unobstructed channel (b). 80% Q_{bf} flow conditions are shown in the unobstructed channel (c) and obstructed channel (d).
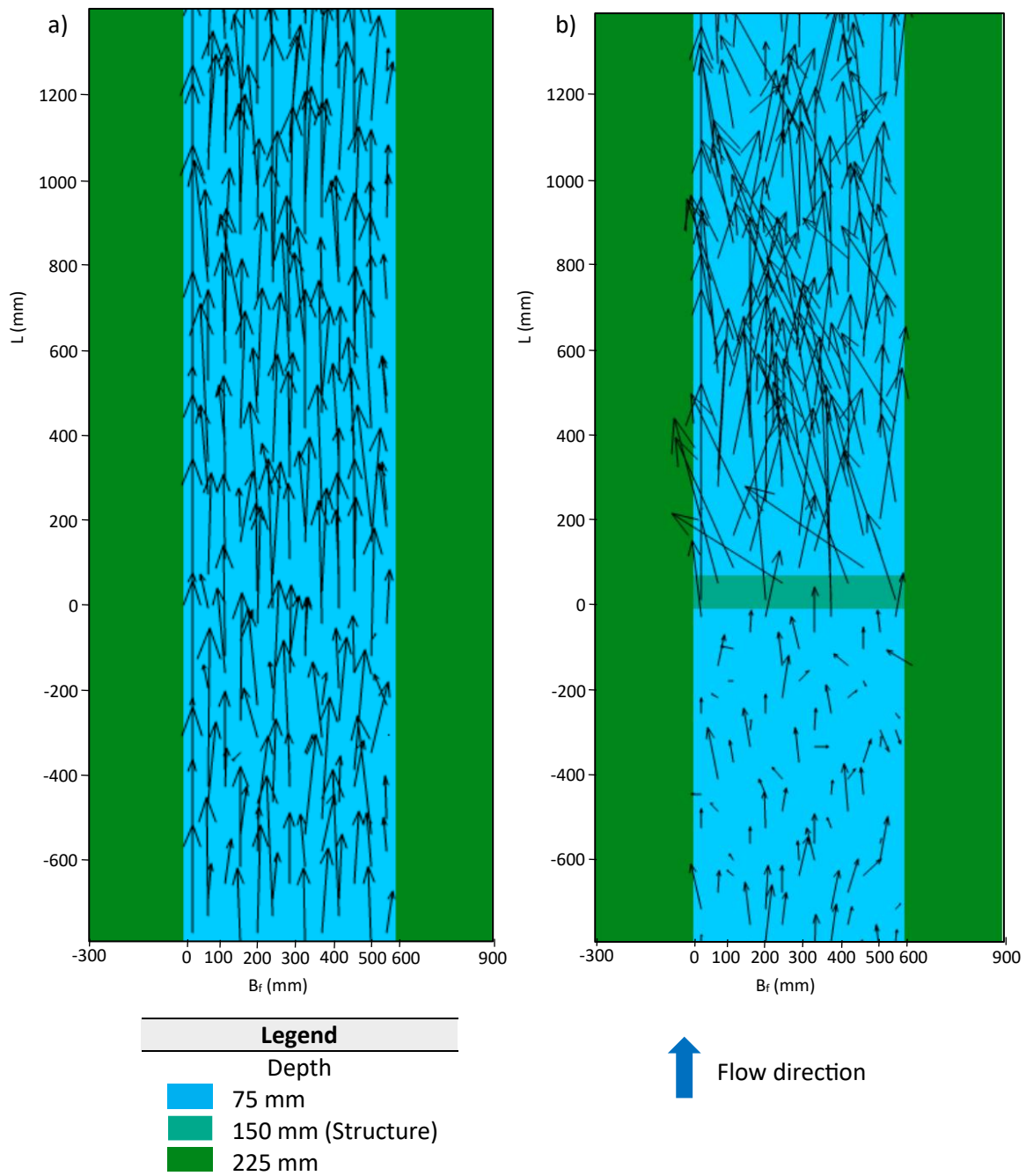
Figure 3.28: Diagrams displaying velocity vectors at 100% Q_{bf} in the (a) unobstructed channel and (b) obstructed channel. Flume width (B_f) is displayed on the x-axis and Longitudinal direction / distance (L) on the y-axis.
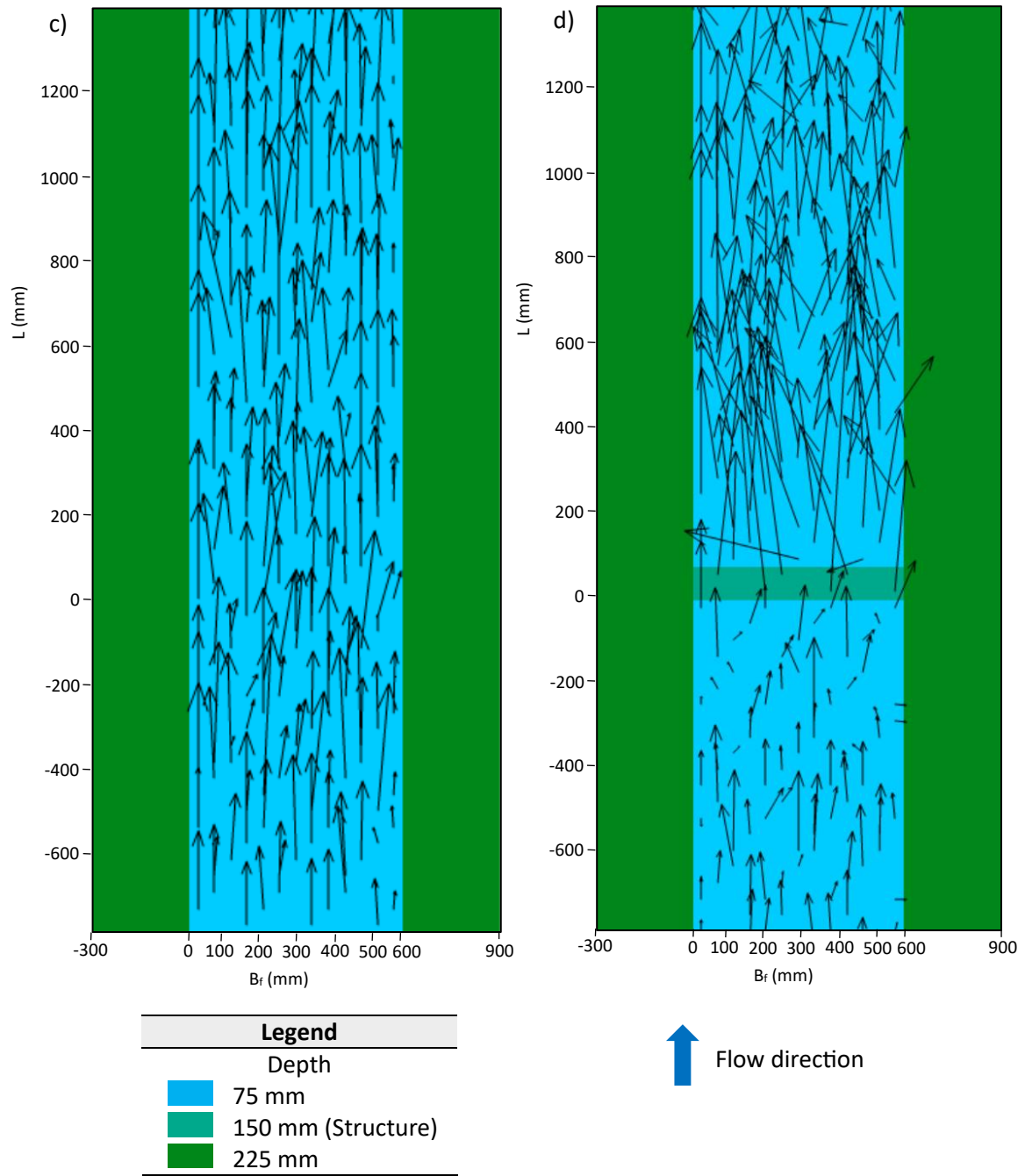
Figure 3.28: Diagrams displaying velocity vectors at 80% Q_{bf} in the unobstructed channel (c) and obstructed channel (d). Flume width (B_f) is displayed on the x-axis and Longitudinal direction / distance (L) on the y-axis.

3.4. Discussion

To date, there is a lack of effective design criteria for engineered WDDs (Burgess-Gamble, 2018), potentially due to their complex hydraulic effects not being well understood (Bennett et al., 2015; Huang et al., 2022). This leads to major drawbacks on their effective installation in the field and can lead to unrealistic results in hydraulic modelling. Numerous types of WDD representations are being used in hydrodynamic and hydro-environmental modelling which to a large extent is due to there being no standardised design for engineered WDDs and no specific tool to represent them in the modelling domain (Addy and Wilkinson, 2019). This study provides a greater understanding of the hydraulic impacts of WDDs on the channel bathymetry and offers, in part, a way into optimising their design.

3.4.1. Discharge and structural design

Results suggest a correlation between the local scour depth and discharge. Figure 3.17 indicates that at 100% Q_{bf} (Series A), it took longer to reach equilibrium compared to 80% Q_{bf} (Series B). At high discharge, τ_b is greater than at low discharge, as verified through hydro-environmental modelling (Figure 3.24 and Figure 3.27), therefore 100% Q_{bf} took longer to re-establish the threshold of motion compared to 80% Q_{bf}. With flow continuity being disrupted by the structure, decreasing the hydraulic radius and increasing velocity, with d_{se} taking longer to be reached. Localised velocity over the scour hole controls τ_b and therefore the extent of scour. Tammela et al. (2010) highlighted that with the structure restricting the hydraulic radius, scouring continues until critical velocity exceeds the local velocity. Increased localised velocity values take longer to decrease to critical velocity under the structure and with an increase in the local scour depth, the scour rate therefore decreases taking longer to re-establish equilibrium.

Key member ratios, the gap ratio between the base of the structure to the bed (e/Di_c) , and the spacing ratio between two key members (G/Di_c) were investigated under clear-water conditions to analyse design effects. An interpretation of the findings in Figure 3.17 revealed a correlation between the structural design and discharge with local scour depth. Findings indicate that e/Di_c, along with G/Di_c have a strong influence on scour, whereby the rate of

scour decreased with an increase in the local scour depth. Series 1A, with e = 0 and the smallest G (i.e., $0.4Di_c$) takes the longest time to reach equilibrium, as compared to series 4A with a larger e ($0.6Di_c$) and G ($0.8Di_c$) and which reaches equilibrium quicker with the least scour. This indicates that structures with the smallest e and G create the deepest local scour depth. Moreover, series 3A (e = 0 and G = $0.8Di_c$) had less scour than series 1A (e = 0 and G = $0.4Di_c$), even though both had e = 0, because series 1A had a smaller G value. Likewise, series 2A (e = $1.4Di_c$ and G = $0.4Di_c$) created deeper scour holes than series 4A (e = $0.6Di_c$ and G = $0.8Di_c$) as series 2A had a smaller G value. This finding supports the findings of Zhao et al. (2018) who experimented on a piggyback pipeline (e = 0) and found time to develop equilibrium scour depth increased when the G/Di_c decreased, with small G/Di_c, creating a larger maximum scour depth.

When e = 0, as in series 1A, the approaching flow becomes confined by the structure, causing the shear velocity to increase and a pressure difference to form, thereby forcing the flow underneath the structure, known as a seepage flow (Fredsøe, 2016). This erodes the sediment downstream of the structure and starts to initiate scour, which is followed by tunnel erosion with a jet flow drawn violently under the structure (Lee et al., 2018). The increased localised velocity beneath the base key member causes erosion to occur. In this way the scour hole rapidly deepens, increasing the flow intensity under the structure. Eventually the bottom localised velocity at the deepest point of the scour hole decreases with the scour depth increasing. This mechanism takes longer for the scour rate to reach d_{se} for structures with e = 0 in comparison to a structure with e> 0 (Figure 3.17). Consequently, at structures with decreased e/Di_c, once the scour hole increased, local scour depth slows scouring and the bed takes longer to reach equilibrium (Cheng et al., 2014).

The scouring mechanism is most pronounced at structures with e = 0 and small G/Di_c. Series 1A generates large downstream vortices with strong interaction between the shed vortices from e and G. Increased turbulence was especially noted downstream in series 1A with G = $0.4Di_c$ (Figure 3.22). However, at structures with increased G/Di_c and e/Di_c, higher throughflows and lower localised velocity values occurred under the structure (Zhao et al., 2018) with the intensity of the mutual interactions between vortices becoming weaker. This interaction was weaker for series B than series A (Appendix F).

During high discharge, structures with e = 0 and small G will, in effect, become elevated above the bed by scouring beneath them, which can have major implications for the design of engineered WDDs. In turn, this would decrease the WDD effectivity in attenuating peak discharge and could compromise structural stability and integrity. Burgess-Gamble (2018) puts forward that WDDs should be inspected after a high discharge event to check for wood accumulation, which could create destabilisation and cause channel blockage. Furthermore, it was found that series 1A, with increased scouring during high discharge as mentioned, will lose its effectiveness in attenuating peak discharge by ≈ 44% upon reaching equilibrium (Figure 3.23). Therefore, flume experimentation into examining WDD effectiveness in attenuating the peak discharge, conducted on a non-erodible bed, will produce unrealistically high attenuation predictions.

3.4.2. Computational model of the flume experiment

FM 1D and 2D simulations were able to replicate τ_b at the structure in the flume experiments with τ_b increasing immediately downstream of the structure along the centreline. This finding supports the flume experiment whereby the deepest maximum scour depth value occurred immediately downstream of the structure. The computational model of the flume in FM showed that when the structure was inserted, the flow regime changed. Upstream of the structure, between -800 mm to -500 mm, streamlines were set on a structured trajectory but once the flow got closer to the structure, backwater effects were induced at -500 mm, and the streamline began to deviate off the structured course. The streamline direction changes were caused by the structurally induced backwater effects, which created an upstream buffer zone, reducing the localised velocity values as illustrated with shorter velocity vectors (Figure 3.28).

Both the 2D model and series 1A DEM showed increased τ_b and a scour hole, which developed close to the left bank (0 mm). This pattern, which was notably seen at 100% Q_{bf}, was potentially caused by the structure changing channel flow dynamics, whereby as the flow surcharged the structure, velocity vectors pointed towards the left bank. This finding is caused by computational models having difficulty in representing flow discontinuity at structures, representing what the model assumes as mixing, as grid scale oscillation (Falconer, 1986). This

explains why a deep scour hole existed close to the left bank, as displayed in the 2D simulation (Figure 3.27). This velocity vector pattern was also observed at 80% Q_{bf} but to a lesser extent.

3.4.3. Strength and limitation in hydro-environmental modelling

Unfortunately, it was not possible to empirically measure velocities across and along the flume during experimentation, due to covid-19 preventing access to the laboratory flume after the flow depth and scour comparisons had been recorded. However, in order that the required values of local velocity and local τ_b could be obtained, a computational flume was constructed in FM. These values were generated using imported channel characteristics from the flume experiments.

A strength in 1D modelling was that it was able to replicate the surface water profile at the start of the flume experiments, with a very strong and positive relationship being established having a Pearson's correlation coefficient of 0.911 (series A) and 0.871 (series B). A statistical analysis showed that FM was able to computationally replicate the start of the flume experiments before the bathymetric channel changes occurred, with both datasets displaying similar h_1-h_2 values and degrees of flow attenuation.

A limitation associated with the FM 1D and 2D simulations is that it could not simulate an erodible surface with structures and therefore could not model the scour and deposition evolution shown in the flume experiments. However, FM could solve changes in τ_b and τ^* to infer how sediment transport might change (McParland et al., personal communication, February 2023) but only for discrete temporal locations. If simulations could be run with an erodible bed, then this would most likely produce a similar scour and deposition pattern. However, to accurately replicate the real-world bathymetry this would require a high level of computational power with full channel details being included in the model (Dasallas et al., 2019) which could not be practically achievable.

A computational modelling limitation is that there is no standardised unit to replicate WDDs and therefore a weir unit was assessed to replicate the structural blockage. In the flume experiment as the structure was constructed with three key members there would have been flow separation around the key members whilst FM does not have a unit to replicate spacings

between horizontal key members. Different structural designs mean velocity vectors and τ_b spatially varied in the water column between the flume experiment and FM with higher local velocity values occurring at different locations. This means that the scour and deposition extent would vary between the real-world experiments and computationally modelled results.

3.5. Conclusion

Higher discharge values took longer to reach equilibrium, with series A reaching equilibrium at 72 hrs and series B at 48 hrs. After time to develop equilibrium scour depth was reached, the channel continued to evolve, as shown with the series 1A exit dune extending further downstream from 526 mm – 830 mm – 947 mm. This illustrated that sufficient time was required to enable the channel bathymetric changes to fully develop. Hence all experimental runs were left for 96 hrs before completion.

The flume experiments showed, that the higher the discharge value the more scour and deposition occurred. This finding was supported by the FM 2D simulation, whereby when discharge increased so did the τ_b. Additionally, the higher the discharge value, the greater the structural design maximum scour depth standard deviation. This showed that the higher the discharge value, the greater the bathymetric changes between the structural designs.

Structural design played an important role in establishing the extent of scour and deposition. When e = 0, the greatest d_{se} values occurred and when e > 0, d_{se} decreased. As well as e controlling d_{se}, G influenced the extent of scour. Structures with a small G value show a stronger interaction with vortices, which creates a greater d_{se} than structures with a large G value. Series 1A, Run 3 (G = $0.4Di_c$) showed observable higher levels of turbulence downstream and a larger maximum scour depth at 61 mm, compared to series 3A, Run 1 (G = $0.8Di_c$) at 49 mm.

As the scour hole developed and sediment was entrained, the flow undercuts the structure. This means that, over time, the flow bypassed the structure thereby reducing the effectiveness of WDDs in attenuating the in-channel flow. Within the present study h_1-h_2 was shown to decrease by ≈ 44% upon reaching the time to develop equilibrium scour depth.

The FM 1D simulations replicated the surface water profile accurately at the start of the flume experiments, with a very strong and positive relationship having a Pearson's correlation coefficient of 0.911 (series A) and 0.871 (series B). The 1D and 2D simulations were also able to replicate the τ_b and τ^* values at the start of the flume experiments where scour started to occur.

<div align="right">

4

</div>

Site characteristics and field equipment

4.1. Site description of Wilderhope Brook

The UK government invested £15 million to develop knowledge in promoting practical solutions for implementing NFM. This thesis is part of one of the pilot schemes in examining the effectiveness of WDDs in reducing downstream flooding at the River Corve, Shropshire, UK. Within the River Corve catchment, flood risk is projected to increase with climate creating more flash flood events. Data acquired from the Environment Agency (EA) was used to construct Figure 4.1 which identifies 11 zone 3 hotspots with 50 rural properties at high risk of flooding with a recurrence interval of 1:100-year flood event (Committee on Climate Change, 2018). The main hotspot on the River Corve catchment is Ludlow with 167 properties located in flood zone 3, 16 km downstream of Wilderhope Brook.

At Wilderhope Brook, an upland tributary of the River Corve, from 1999 to 2013 precipitation Depth, Duration and Frequency (DDF) has increased, coupled with shorter return periods (Equation 4.1) (Critchley et al., 1991) as seen in Figure 4.3. Return periods show the likelihood of flood frequency, for instance a 1:100 return period has a 1% chance of being exceeded in any given year. Examining 1:500 return period is difficult due to low occurrence. However, at Wilderhope Brook catchment rainfall intensity has increased while rainfall duration has shortened, creating more flash flood events and the chance of 1:500 return period storm events more probable. As precipitation DDF has increased this provided the reason as to why WDDs have been installed at Wilderhope in order to prevent downstream flooding to communities such as Ludlow.

$$\text{Return Period} = \frac{n_y + 1}{n_m} \qquad (6.1)$$

Equation 4.1 calculates Return Period using number of recorded years (n_y) and observed occurrence rank when arranged in descending order (n_m) (Rajneesh and Anil, 2015).
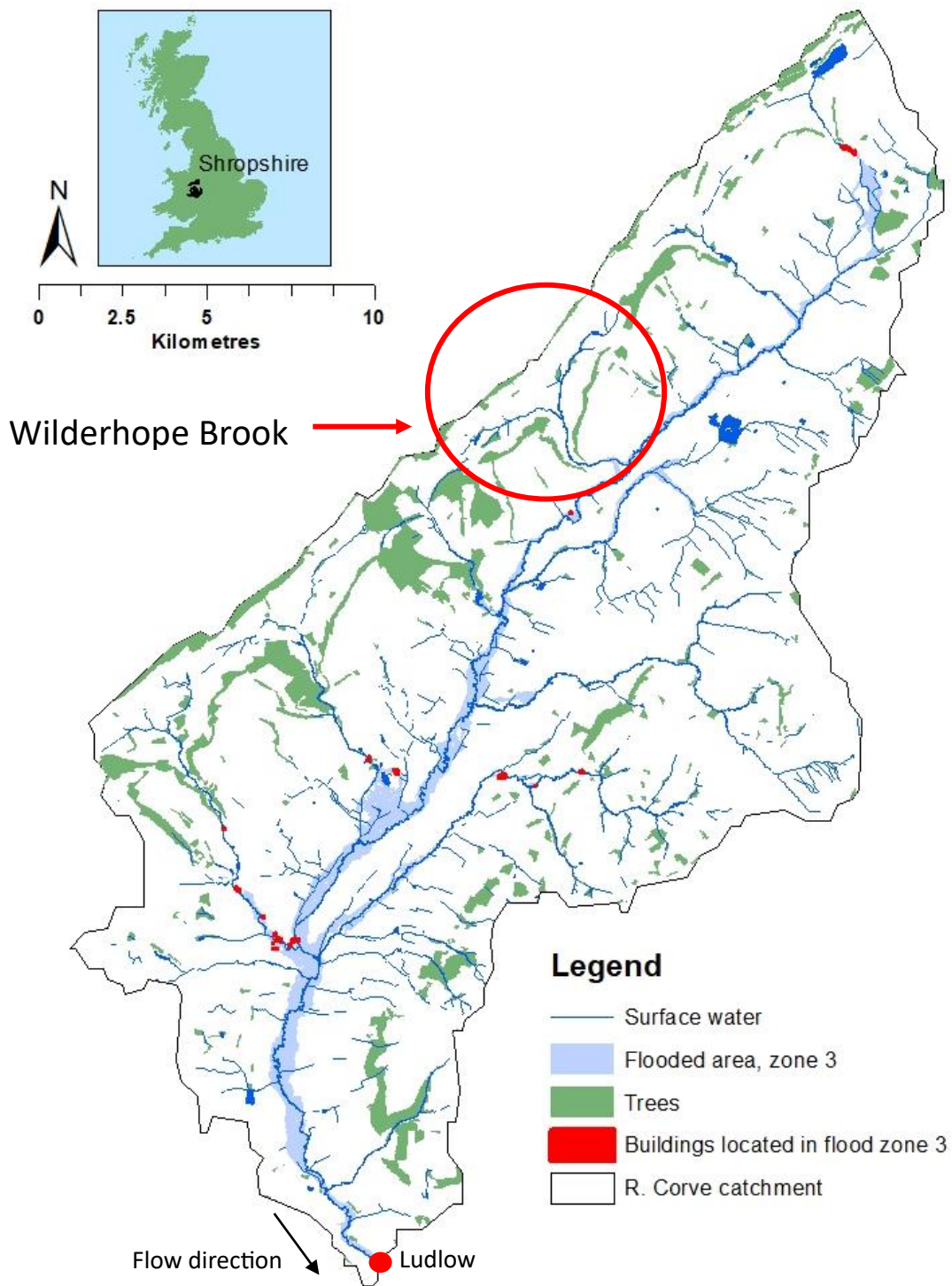
Figure 4.1: Geographic Information Systems (GIS) map of the River Corve catchment displaying property located in the Environment Agency flood zone 3 risk area. The map shows the extent a 100-year flood event with 2017 flood adaption methods put in place. The River Corve is 30.98 km from source to the River Teme confluence.
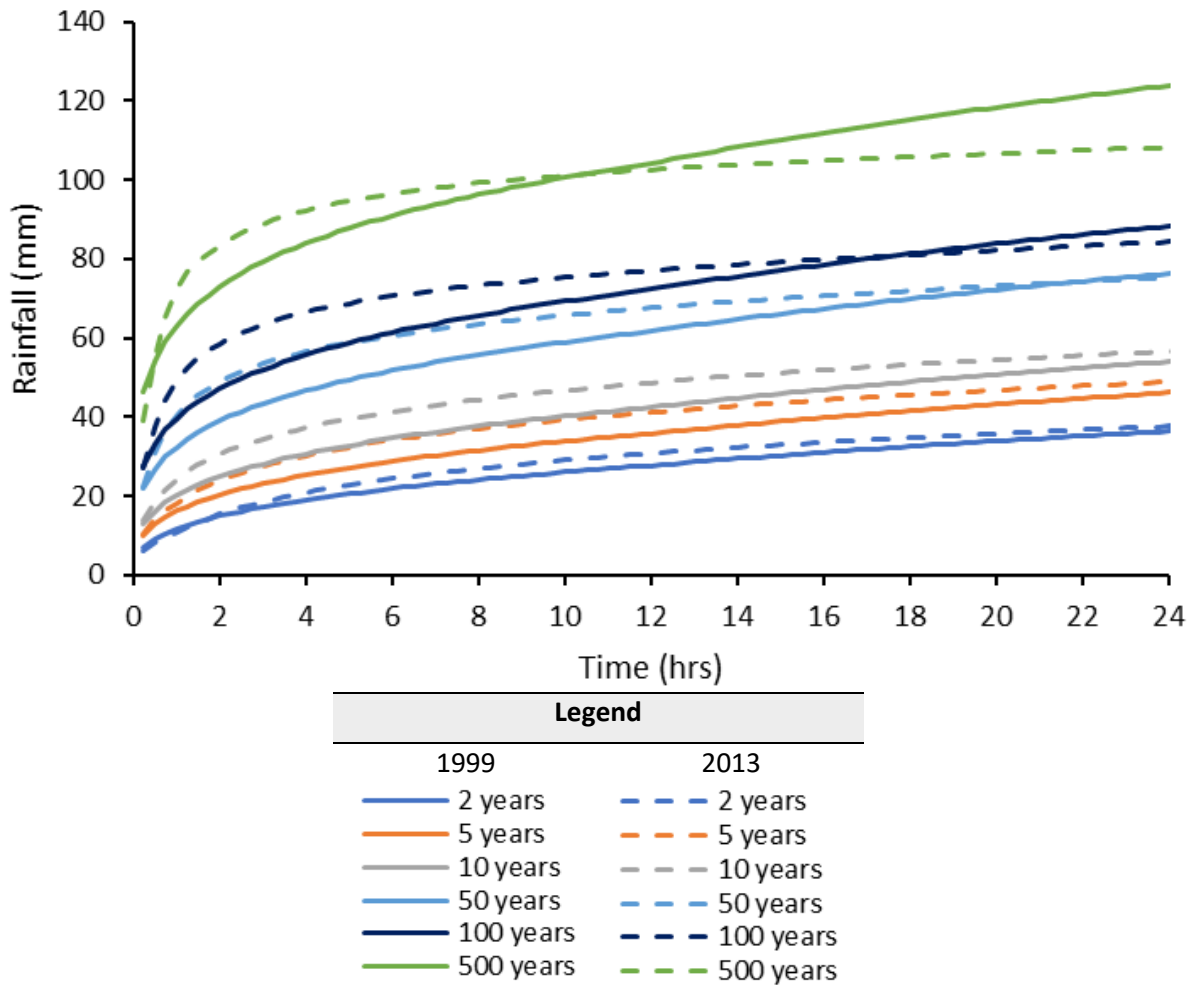
Figure 4.2: Graph displaying precipitation DDF at Wilderhope Brook catchment with return periods displayed indicating climate change has increased rainfall intensity while rainfall duration has shortened. Data obtained from the Centre of Ecology and Hydrology (CEH, 2022).

To alleviate downstream flooding, 105 engineered WDDs were installed (2017) on Wilderhope Brook. Each WDD was geotagged and numbered from 1 to 105 (Figure 4.3), starting where Wilderhope Brook enters the River Corve (523290.59E, 5817990.09N) and ending at the source of Wilderhope Brook (522554.59E, 5820344.6N). WDDs have been grouped into three sections depending upon location: lower, mid and upper reaches, with landowner cooperation (Figure 4.3). The purpose of engineered WDDs is to mimic the effects of natural wood by slowing the flow and attempting to reduce flood magnitude (Addy and Wilkinson, 2019).
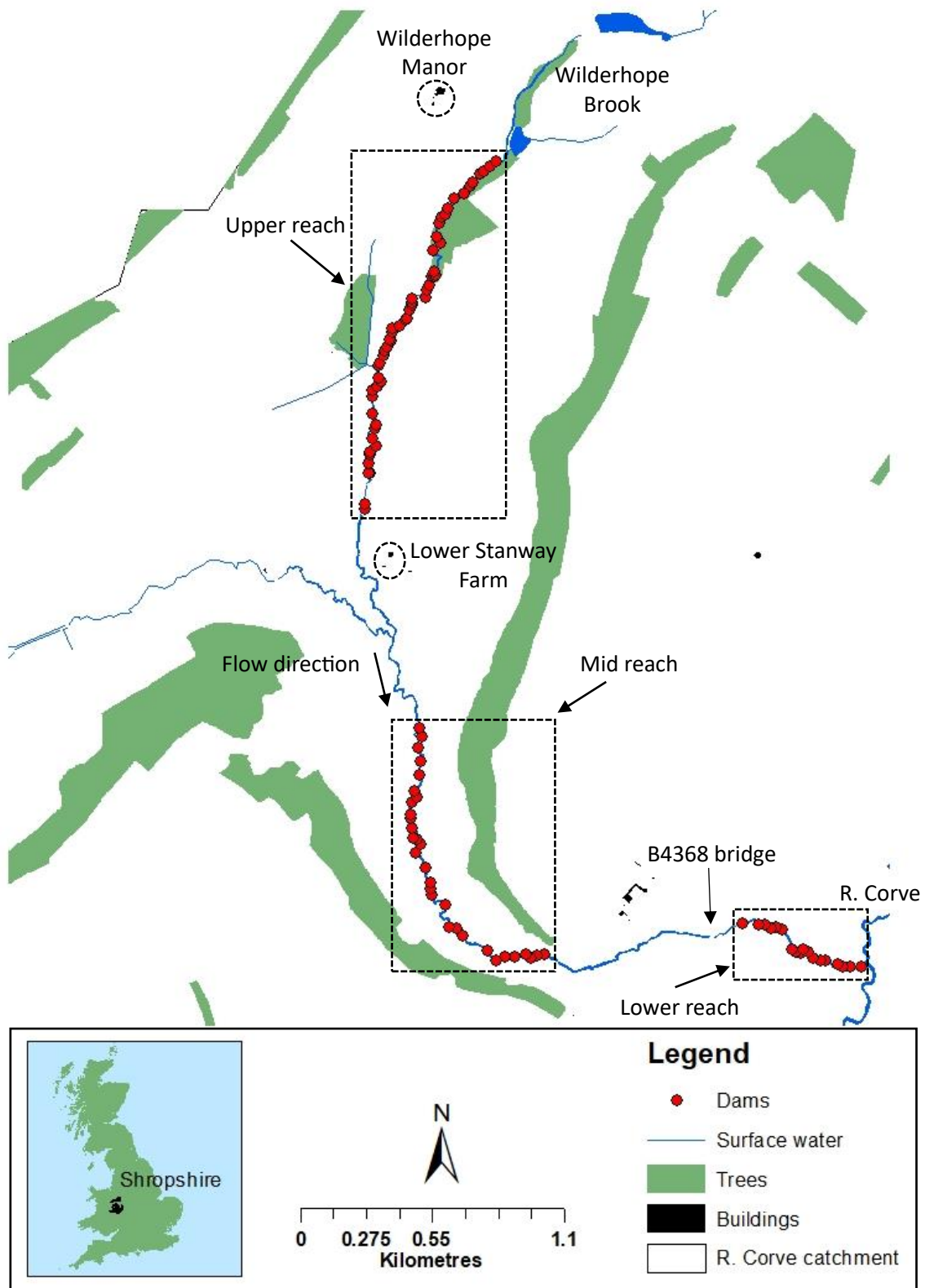
Figure 4.3: Map displaying 105 geo-positioned WDD locations along Wilderhope Brook water course. WDDs in Wilderhope Brook have been grouped into three sections: lower, mid and upper reaches as displayed in the figure.

Wilderhope Brook has a catchment size of ≈ 5.6 km^2, and a total channel length of ≈ 3.98 km, initiated by runoff at Wenlock Edge in the upper Shropshire hills. It is located in a V-shaped valley bordered by Rickhouse Coppice to the west and Stanway Coppice to the east (Figure 4.3).

River corridor enhancement, such as planting alder, plays an important role in preventing livestock from puddling the channel banks, providing bank stability and intercepting sediment surface runoff, so slowing the flow (Parkyn, 2004). Forest thinning and coppicing provides more growth capability for the remaining trees and can aid in future vegetation development (FISRWG, 1998). The Wilderhope Brook riparian buffer strip consists of alder, hawthorn, holm oak, ash, beech, holly and hazel. In the lower reach, forestry is sparse with sporadic trees, while further up the longitudinal profile towards the source, vegetation becomes denser.

WDD maintenance can alter dam design (Beschta, 1979) while channel restoration can create rapid geomorphological changes (Kail et al., 2007). Therefore, studies were conducted prior to WDD maintenance and riparian tree felling. Long-term loss of riparian vegetation can result in increased bank erosion and channel widening (Hartman et al., 1987; Oliver and Hinckley, 1987; Shields et al., 1994). Riparian vegetation removal has been shown to increase peak discharge (FISRWG, 1998). River restoration objectives tend to rank geomorphology and sediment transport as a low priority compared to supporting diverse biodiversity and creating areas of flood attenuation / sacrificial land (Mant and Soar, 2009). Readings were examined from the 2nd April 2019 until 2nd April 2020 after which time tree felling, WDD maintenance (Appendix K) and channel restoration occurred, in light of phytophthora disease and the climate crisis respectively. In line with common practice, the affected alder trees were removed or coppiced to protect the riparian woodland from further disease (Webber et al., 2004). By anthropogenically altering the water course through catchment maintenance this meant monitoring natural geomorphic change could not be achieved after 2nd April 2020, without recategorizing the WDDs and by re-surveying and re-examining spatial change caused by anthropogenic influence.

4.2. Field equipment

To monitor the effectiveness of the WDDs in the field appropriate equipment that addressed the study research objectives was chosen. This was achieved by acquiring through contractors the necessary field equipment with advantages and disadvantages identified (Appendix J). Field data enabled catchment specific boundary conditions that could be applied to hydro-environmental models.

The chosen field equipment is as follows:

4.2.1. Tipping bucket rain gauge

A Lambrecht 4cm^3 Tipping Bucket Rain Gauge (precision: 0.2 mm) supporting a Hobo Pendant Event Logger (Appendix L) was installed at Stanway Farm to the Northwest of Wilderhope Brook catchment (352113E, 289342N). The tipping bucket rain gauge collected precipitation DDF from the 2nd April 2019 until the 2nd April 2020.

4.2.2. Flow logger

At the B4368 bridge located to the west of the lower reach (355147E, 290683N) (Figure 4.3), open channel flow was monitored by a Hach FL900 Flow Logger supporting an AV9000 Area Velocity Sensor. The sensor module was bolted to a stainless-steel plate which was secured using a stainless steel Unistrut channel, downstream of a secondary bridge and rectangular culvert (Figure 4.4). The sensor module with a threshold working depth of 0 to 3 m, measured flow depth, localised velocity, discharge and temperature every 15 mins while the automated flow logger recorded readings. Project contractors collected flow logger recorded readings.
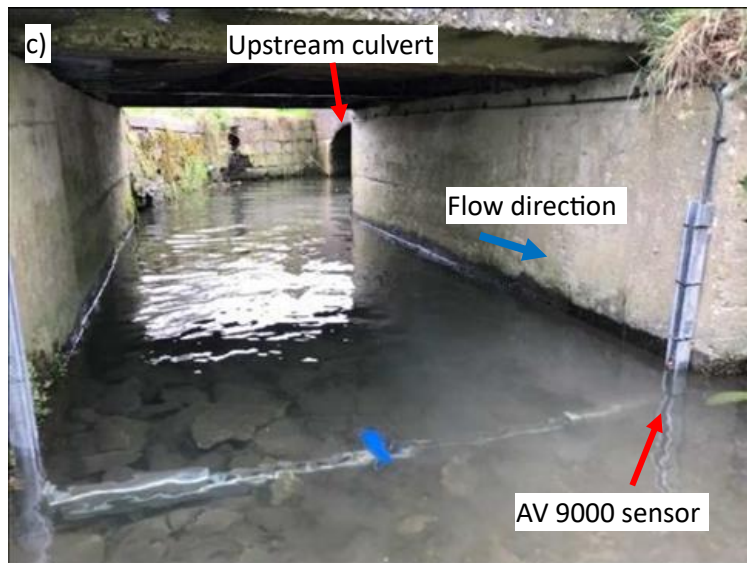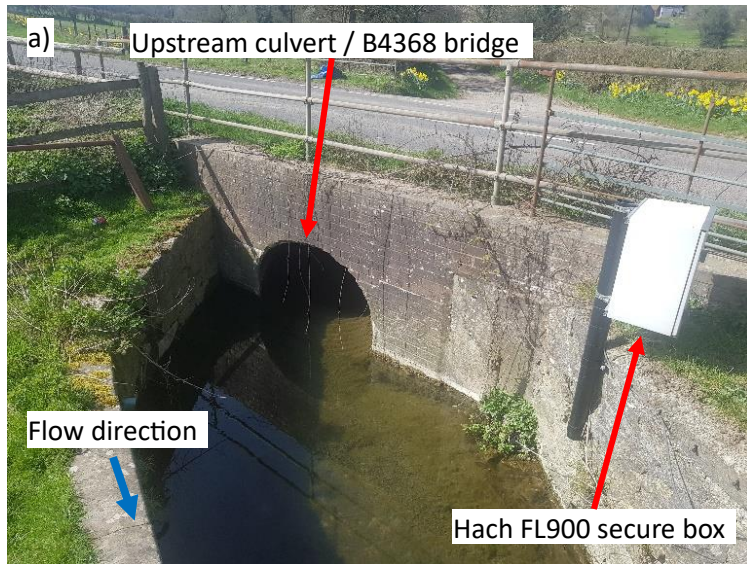
Figure 4.4: Photographs displaying: a) flow logger, housed in a secure box, placed next to the B4368 bridge. b) Flow logger outside of the secure box. c) The velocimeter placed downstream of second bridge culvert.

4.2.3. Pressure level sensors

Two Orpheus Mini, pressure level sensors were installed upstream and downstream of a chosen WDD located in the lower reach. Pressure level sensors were installed to monitor the upstream and downstream flow depths so as to examine structural attenuation. Pressure level sensors were located in positions to avoid pronounced meanders or boulder outcroppings with the levels submerged under base flow conditions. Pressure level sensors have a threshold working depth of 0 to 4 m with readings recorded every 15 mins. The upstream pressure level sensor was installed in a MDPE stilling tube on the left bank, 3.8 m upstream of the WDD face and a second pressure level sensor located on the right bank, 3.9 m from the WDD downstream face. Pressure level sensors were positioned above the bankfull stage close to the stilling wells.

Pressure level sensors were geo-positioned and geo-referenced using a Differential Global Positioning System (DGPS) and set to a 160 m datum in order to quantify flow depth. A pin was placed at the top of the left bank between the two pressure level sensors which acted as a backup reference point to verify flow depths if the stilling wells became dislodged. The pin could be used to manually check flow depths on the pressure level sensors during site visits.

5

The effects of Woody Debris Dams on upland stream geomorphology to reduce flood risk

5.1. Introduction

Streams play an important role in transporting sediment from upland sources to downstream sinks. As they travel through and over various landforms, streams dissipate their excess energy by incising the valley, transporting sediment, and creating turbulence (Kondolf, 1997). This process of transporting and depositing sediment is recognised as governing the upland catchment geomorphology (Hassan et al., 2005; Joyce et al., 2020). Changes in the flow regime, and upstream sediment supply, trigger channel adjustments and act as local drivers of morphological change, shaping the environment within the catchment (Todd-Burley et al., 2021). Water courses constantly evolve in response to influences such as instream perturbations (rocks and wood), climate and anthropogenic activities (farming and urbanisation). The water course alters through hydrodynamic processes attempting to re-establish equilibrium by creating features such as deeper and wider channels, meanders and backwaters (Winterbottom, 1995; Joyce et al., 2020).

Wood is one of the natural instream perturbations in upland streams which has profound impact on fluvial geomorphological processes. It has been suggested that instream wood causes more channel changes than any other natural means (Bevan, 1948). Engineered WDDs are now commonly installed into upland water courses as part of nature-based solutions to reduce flood risk, due to their hydraulic effects whereby they impound the flow regime and add channel resistance (Grabowski et al., 2019; Lo et al., 2021) By decreasing velocity fields and increasing flow depth, flow can be diverted onto the flood plain which provides temporary storage, enhances infiltration and gives additional time for evaporation. These effects have

been found to increase flow complexity and water retention which attenuates peak discharge and increases lag time (Gregory et al., 1985; Thomas and Nisbet, 2012; Wuang et al., 2022).

Large wood is also a dominant control in forcing morphologic features (Todd-Burley et al., 2021) such as pool riffle sequences (Keller and Swanson, 1979), bank scour which can widen the channel and cause a change in channel direction (Gurnell and Sweet, 1998) and storing sediment (Montgomery et al., 2003). However, from a flood risk perspective, the impact of WDDs on geomorphology is viewed with less certainty (Pearson, 2020). If used appropriately, these geomorphological features, induced by WDDs, can have beneficial effects which can be harnessed to deliver nature-based solutions for managing flood risk (Grabowski et al., 2019). Their geomorphological impacts can be used to the benefit of nature-based solutions for flood risk management, but can induce, negative effects from a flood risk perspective. WDDs can induce scour which can cause structural instability resulting in increased flood risk. Though there is research into WDD hydrodynamic impact, there is less focus on geomorphological evidence to reduce flooding (Pearson, 2020).

Wohl et al. (2016) highlight the geomorphological benefits of wood, but state WDDs can alter sediment dynamics, resulting in lateral channel movement across the floodplain or local sour or aggradation (Wohl, 2011; Collins et al., 2012), each of which can cause flooding. Lo et al. (2021) proposed Natural Flood Management (NFM) structures have a primary effect on flood risk and a secondary effect, contributing to bed heterogeneity which provides for aquatic organisms and ecological benefits. To fill this knowledge gap, it is essential to confirm whether these secondary benefits have additional advantages that can be used in flood management (Barlow et al., 2014). The present study proposes that WDD geomorphologic effects are intermeshed with hydrological effects. As such when designing and placing WDDs for flood risk purposes, care must be taken of their geomorphological impacts as well as their flood attenuation effects. WDD effects on channel morphology is site specific depending upon catchment variables such as landcover, geology and valley bottom width (Black et al., 2021). As variable parameters are unique to NFM catchment sites and can prevent standardisation of empirical data on peak flow attenuation and flow attenuated by WDDs (Salazar et al., 2012; Senior et al., 2022), to elucidate WDD effectiveness, with any degree of confidence, catchment variables at Wilderhope were considered. WDDs were researched within the study site on a

unique catchment basis with a view to gathering information on geomorphological benefits for flood management details of which may be transferrable to other sites.

The aim of this study is to address the research gap – the effectiveness of WDDs as a NFM technique in reducing peak discharge at the catchment scale (Ngai et al., 2017, Gap: 2.4.8.2.). The objective is to understand the scale and location of effective WDDs and collect site-specific catchment data. It is intended to investigate whether the engineered WDDs at the field site effectively enhanced geomorphological changes for NFM purposes and investigated where best to locate WDDs for the desired effect (SEPA, 2015). Catchment variables which influence water course change in respect to WDD placement are an important consideration explored in this study.

5.2. Methodology

In this study, a temporal series of georeferenced data was implemented using a combination of topographic historical maps, field survey data, OS mapping (2017) and a Digital Terrain Model (DTM) (2017) using ArcMap 10.5.1. Topography and river discharge govern channel hydraulics and ultimately spatial patterns of erosion and deposition and therefore channel change. Literature supports the use of OS maps, Light Detection and Ranging techniques (LIDAR) data, flood zones, land use and topography and GIS to investigate historic geomorphological changes in the channel and best practice in design and construction of engineered WDDs to improve their effectiveness.

5.2.1. Site reconnaissance

A mid-reach survey site was selected to elucidate temporal geomorphological changes that have occurred in Wilderhope Brook. This study reach, being lined with alder, holm oak, ash and hazel did not obstruct the Field of Vision (FoV) of field equipment and allowed easy access unlike the lower and upper courses which were lined with seasonal vegetation of hawthorn, brambles and nettles. The chosen surveying location was based around three WDDs in the mid-reach, with the mid-reach shown in Figure 4.3 (section 4.1.). The chosen WDDs satisfied

the three classifications proposed by Gregory et al. (1985) that was defined in section 2.2.2. These designs are representative of the engineered WDD forms at Wilderhope Brook.

5.2.2. Sampling

To enable measurement of geomorphic change within the study reach, a field survey of the mid-reach was conducted, with the construction of 14 cross-sections, a planform and a longitudinal profile (Figure 5.1). A reach is defined as being geomorphologically homogeneous (Eyquem, 2007). To encapsulate the morphologic diversity within the reach, a length of stream with similar channel gradient, form and bed and bank composition was chosen. It is suggested that reaches should extend to a length equivalent to 30 times bankfull stage width (Simon and Castro, 2003). Field survey morphology of the area (2019) was compared to historical mapping (1935, 1995 and 2017) to examine if and how channel sinuosity has changed. In-channel WDDs have the potential to trigger changes in channel planform by deflecting flows and eroding opposite banks, encouraging increased channel sinuosity. Without meanders the stream length is shortened, and the gradient steepened, which can lead to higher water velocities and potentially greater downstream flooding (Ellis-Sugai and Godwin, 2002). Examining channel change in historical maps acted as a control for determining how installed WDDs have affected channel morphology. A combination of ground-based survey, historical mapping and remote survey technologies were adopted having the advantage of providing data of the entire study area and over a relatively long study duration.

a) Cross-section

Bankfull width

A_l | A_r

Maximum depth

Centre depth

Cross-section area

$$\frac{Area}{Width} = Mean\ depth$$

$$\frac{A_l}{A_r} = Asymmetry$$

$$\frac{Width}{Mean\ depth} = Width{:}depth\ ratio$$

b) Planform

Floodplain width

Meander belt width

Valley width

Valley length

c) Long profile

Riffles

Water surface
High discharge
Low discharge

Pools
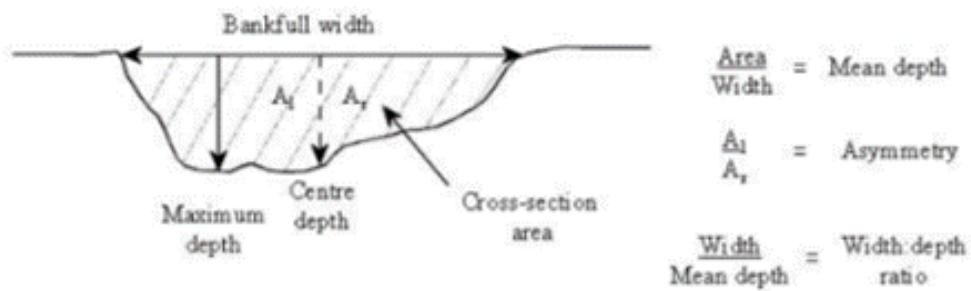
Figure 5.1: Three dimensions (3D) of the river channel: a) the cross-section, b) planform and c) long-profile. These dimensions relate to the discharge and sediment transport. In the field bankfull refers to the break of slope between the riverbanks and the adjacent farmland. Pools and riffles are fundamental features of stream morphology affecting the shape, location and direction of the channel temporally. (Sear et al., 2004).

Several studies have researched channel planform changes such as width, migration and sinuosity based on topographic maps using aerial photographs, field surveys and from satellite imagery (Yao et al., 2013; Magliulo, 2016). Though research has examined topographical channel changes through a combination of recent field surveying, historical maps and DTM merging to home in on morphologic changes in the bedform, fewer studies have investigated older evolutionary topographical changes to gain greater understanding of recent evolutionary changes caused by WDDs. Details of methodologies and protocols followed are given in studies such as: Wallerstein and Thorne (1997). Literature synopsis (Appendix G) gives indication of similar methodologies employed.

5.2.3. Surveying

A field survey was conducted over 1 week between 11-15th February 2019 focusing on the mid-reach study area. The control point was geo-positioned and geo-referenced using a Zenith25 Pro4 Series GNSS receiver supporting GPS of static horizontal accuracy of 3 mm and a static vertical accuracy of 5 mm. The tripod head was levelled before attaching the Trimble M3 Manual Total station (distance accuracy: ±0.001 m; angle accuracy: 0.2 mg - 0.5 mg). To ensure accuracy of surveyed readings, the total station was precisely aligned over the control point using an optical plummet. Upon setting up the total station, the geo-referenced control point was input into the total station internal memory. Finally, the total station was focused upon a distant object close to the target area of the channel to sharpen the image and reduce parallax error.

A second team member was designated the task of walking along the centreline (length: 187.08 m) holding the reflector. The reflector was positioned at 120 points down the longitudinal profile. Fourteen transects, were established using stakes perpendicular to the channel. Transects were positioned <20B from each other to improve longitudinal resolution, precision and further enhance geomorphic analysis (Samuels, 1990). To enhance precision the reflector was placed at 5 stratified intervals across the wet width, distance depending upon channel size, then 2 x 1 m, 4 x 5 m and 3 x 10 m intervals up the bank sides and across the flood plain (Figure 5.2).
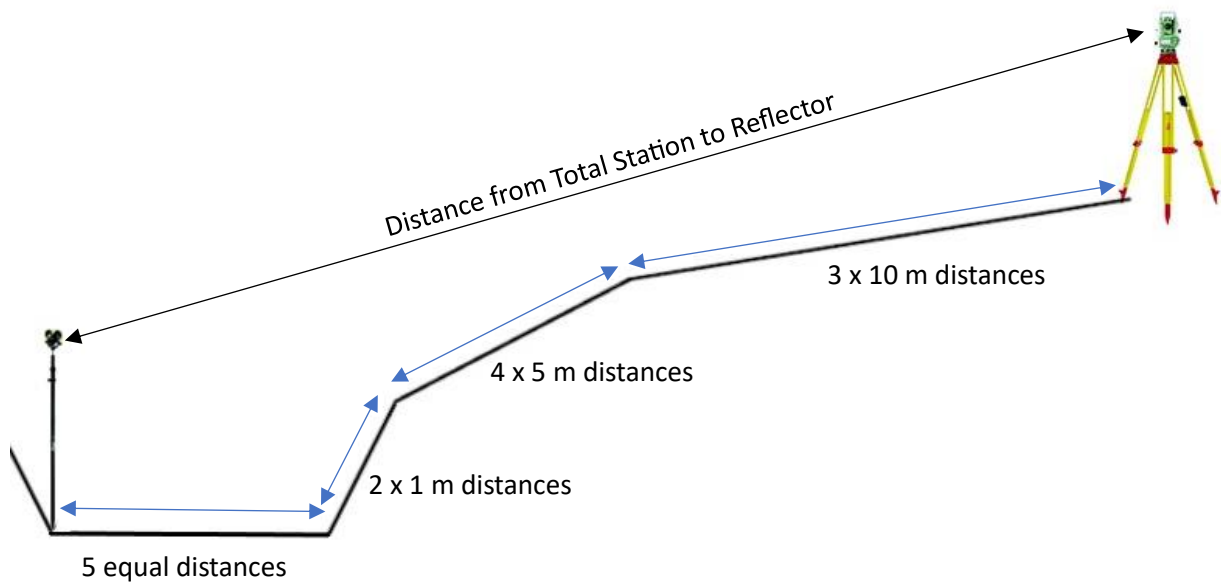
Figure 5.2: Schema showing positions of reflector in a channel without obstacles obstructing total station view to the reflector.

5.2.4. Global information systems

5.2.4.1. Online acquisition and processing of data

Environmental Systems Research Institute (ESRI), ArcGIS, ArcMap 10.5.1 allowed digital interface geoprocessing to analyse patterns, identify relationships and outliers and allowed conceptualisation of collected data. This geo-processing tool enabled comparison between different historical maps and collected field data, between DTMs and collected field data and construction of a catchment geological map along with a contour map. Additionally, ArcGIS online provided a cloud-based mapping platform that enabled 3D analysis to identify catchment characteristics and extent, which was then imported into ArcMap.

EDINA, Digimap allowed an interface to browse and acquire historical, contemporary OS, geological base maps along with contour datasets. The EDINA online portal provided a simple search feature to enable navigation to the Area of Interest (AoI) (Wilderhope, Shropshire), data acquisition and download facility for GIS processing.

DEFRA data service platform is an 'application processing interface (API) which offered a method of accessing and downloading openly available data. This platform was used to acquire an EA LIDAR composite digital surface model (DSM) (2017).

To enable remote sensing classification of landcover to depict spatial variances in sediment yields, United States Geological Survey (USGS) datasets were acquired. The data service platform, USGS global visualization viewer (GloVis) allowed a dataset library search, application of search criteria and download facilities for acquisition of remote sensing data.

5.2.4.2. Historical

To analyse spatio-temporal change in the lower course, two high definition (1:2500) maps were chosen: a 2nd revision County Series (1935) and 1st edition National Grid (1995), providing detailed historical base maps whereby key features and points of interest could be extracted. To make comparison to the historical maps, a high definition (1:1000) OS mastermap (2017) was additionally selected. Within historic geomorphological studies, map sourcing tends to be restricted to ≈ 100 years before present as although earlier maps exist there is reduced precision which generally entails a larger resolution (James et al., 2012). In the lower section, all required base maps including a (1:2500) 2nd revision Country series (1935), a (1:2500) 1st edition National Grid (1995) and a (1:1000) OS mastermap (2017) were compared.

5.2.4.3. Topographical change

To construct a precise DSM of Wilderhope Brook catchment a LIDAR technique, which uses a time of flight laser (500 Mhz) to measure distance between the camera to the target was used (UK Government, 2021a). This laser cannot easily penetrate surface water meaning water covered channel bathymetry may not generate a precise real-world comparison (Betsholtz and Nordlöf, 2017). To account for this, a DSM was acquired during a dry period with low discharge in the channel. LIDAR acquisition of DSM data provides a higher level of detail compared to traditional methods of constructing DSMs (Marston, 1982; EDINA, 2021). LIDAR

precision is dependent on camera resolution and time of flight distance and for the present study, the selected DSM displayed a 2 m spatial resolution with a z accuracy of ±0.15 m RMSE (Equation 5.1) (UK Government, 2021a).

$$RMSE = \sqrt{\sum_{i=1}^{n_u} \frac{(\hat{z}_i - \hat{z}_i)^2}{n_u}} \qquad (5.1)$$

Equation 5.1 calculated the Root Mean Square Errors (RMSE) for vertical (z) direction. This equation requires the Number of samples (n_u), expected vertical values ($\hat{z}_i$) and observed vertical values (Z_i).

Algorithms and manual editing of data enabled conversion of DSMs into DTMs (Environment Agency, 2022a). Algorithms are applied to remove unwanted surface objects easily and quickly and prevent the need for manual removal of single trees. However, algorithms such as Ground proofing have been shown to reduce average correctness by 9% (Mousa et al., 2021). As Wilderhope Brook mid reach passes through arable land, there is sparse tree cover outside the riparian corridor. Within the riparian corridor, vegetation becomes denser and therefore, algorithms were not applied to the whole catchment but instead manual editing was used.

The mapping and spatial analysis software, ArcGIS Pro 2.9.0. was used to derive the DTM from the DSM (Figure 5.3). To identify unwanted vegetation located in Wilderhope Brook buffer strip, different coloured shaded reliefs were applied to the raster image. To reclassify pixels, regions and objects, the Pixel Editor tool enabled editing of elevation data to remove the unwanted vegetation and create a bare earth elevation surface (ESRI, 2021b). These prominent height change features were selected and compared to bare ground pixels in the vicinity. To achieve the bare earth elevation surface, a polygon was drawn around the identified features. The 'Interpolate from vertices', linear tinning method was applied with a blend mix set at 2 pixels (ESRI, 2021a). This manual method converted the DSM into a DTM before being imported into ArcMap. Linear tinning involved converting the centre points of each cell obtained from an array of triangular structures which join to represent a surface. This surface was interpolated into a DTM (ArcMap, 2021b).
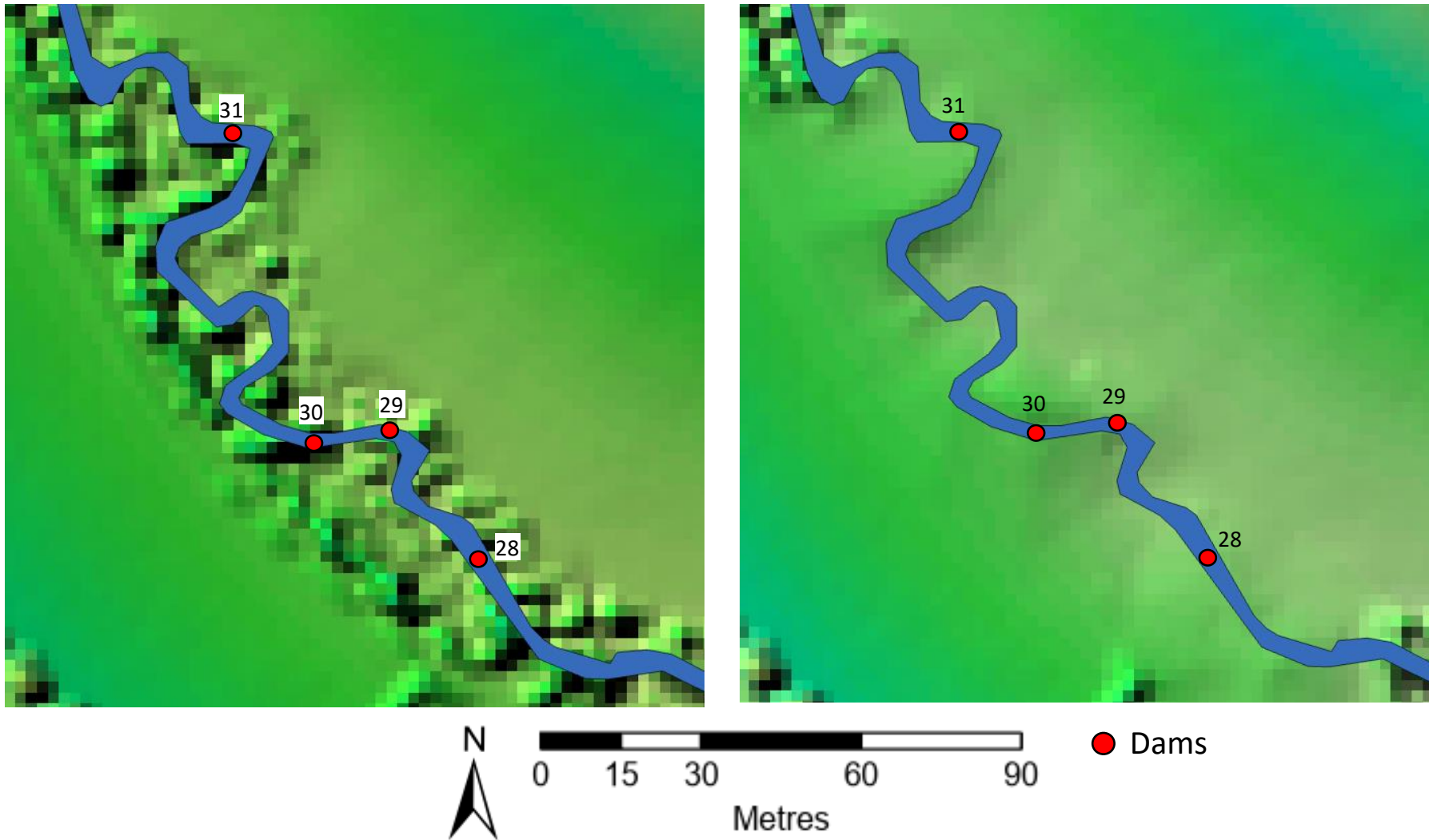
Figure 5.3: 3D representations of the surface shaded relief at Wilderhope Brook mid reach, with (left) and without trees (right) bordering the channel. Water course has been highlighted in blue. WDDs 28-31 are displayed. Constructed using ArcGIS Pro 2.9.0. by manual editing tree removal.

To further analyse topographical spatial change, the EDINA, Digimap acquired 5 m vertical interval contour (2020) dataset was overlayed upon the OS (2017) Wilderhope Brook water course. This constructed map, captured during a period of dry weather, provides visualisation of ground elevation, overview of catchment landforms and was used to depict valley incision.

5.2.4.4. Soils, geology and drainage

To understand local drainage (groundwater flows, throughflow, infiltration and surface runoff) for geomorphological evolution within the catchment, analysis between soil type, bedrock geology and drainage variations was undertaken. As aforementioned in section 5.1. understanding catchment descriptors in respect to WDD location is important in understanding the role of WDDs in the catchment. To achieve the aim, Cranfield Soil and AgriFood Institute (CSAI) datasets incorporating the National Soil Resources Institute (NSRI), Hydrology of soil type (HOST) and a British Geological Survey (BGS) datasets from ArcGIS online were obtained. The AoI was chosen, downloaded in ESRI shapefile format and processed using ArcMap. Separate soil types, geology and drainage areas were selected before being extracted and clipped to Wilderhope Brook catchment. By using the 'identify' icon, information regarding different soil types, geology and drainages could by examined.

5.2.4.5. Remote sensing of sedimentological water course input

To examine spatial variances in sediment yields at different points of Wilderhope Brook, a remote sensing supervised classification map showing vegetation distribution was constructed. To achieve this, initially, the AoI was located using Easting and Northing (522554.59E and 5820344.6N), before selecting which datasets were most applicable. LANDSAT8 (TH654) was used due to having full FoV of the entire study site and a 16-day repeated cycle to allow comparison between datasets to obtain best results (Table 5.1). Meta-data filters removed unwanted datasets where cloud-cover was restricted to < 20% (Selected at: 11.46%) and only datasets from the months June to August were displayed to show greater variance in Normalized Difference Vegetation Index (NDVI) without the interference of

weather events such as snow affecting feedback, or the shadow effect caused by the sun's low angle of incidence predominantly found in winter months.

Appropriate datasets were imported into ARCGIS Pro. so that ground cover vegetation could be examined. Bands were stacked using the composite bands geo-processing tool to form a single multi-spectral composite image which enabled merging of selected bands in raster format. Short wave infra-red (SWIR, band: 6), near infra-red (NIR, band: 5) and visible red (band: 4) were selected to symbolise the multi-band composite image for vegetation analysis (Table 5.1). Oniemayin et al., (2016) highlighted electromagnetic spectrum close to the Near Mid Infra-Red provides strong information for separating vegetation land cover.

Table 5.1: Displaying information regarding LANDSAT8 imagery of Wilderhope Brook.

Data set: Acquisition date: Return period: Processing: Pixel Size, depth and Resolution:	Landsat 8 Operational Land Imager (OLI) and Thermal Infra-red Sensor (TIRS) 28th April 2019 16 days Level 1T - Terrain Corrected • Size: OLI Multispectral bands and TIRS Thermal bands resolution: 30 m^2 • Depth: 32 Bit		
		Mean (pixel)	St. dev (pixel)
Chosen Band wavelength:	Band 4- Visible red	5330	4171
	Band 5- Near infra-red (NIR)	9280	8174
	Band 6- Short wave infra-red 1 (SWIR)	6431	5235
Total Cloud cover:	11.46%		
Sun angle:	45.98°		

The image classification toolbar enabled the multi-band raster image to be manually classified using training samples to group the spectral signatures. Training samples were defined by drawing and merging polygons on the raster image of pre-determined landcovers. Determination of landcover was achieved by examining: a false colour image of the AoI, using Google maps, NDVI along with a field reconnaissance. Distinct training samples were created using a process of trial and error whereby low accuracy training samples were reassigned prior to re-processing to construct the output raster (O_r). The O_r was classified by the deep learning object-based approach grouping neighbouring pixels together based on how similar the spectral signatures are in a process known as segmentation. Segmentation considers colour and the shape characteristics when deciding pixel groupings. This approach is achieved by

averaging electromagnetic pixel spectral signatures while accounting for geographic information and therefore, the groupings created from segmentation more closely resemble real-world features like fields compared to a pixel-based approach.

To assess the accuracy of the classification, user accuracy (Equation 5.2), producer accuracy (Equation 5.3), kappa coefficient (Equation 5.4) and overall accuracy (Equation 5.5) were calculated by comparing the classified raster to a reference dataset that of a ground truth taken at the time (28th Aug. 2019). The accuracy assessment was constructed using a set of random points which compared the classified raster to the ground truth as displayed in a confusion matrix.

$$\text{User Accuracy} = \frac{C_p}{T_{cpr}} \times 100 \tag{5.2}$$

Equation 5.2 calculated the supervised classification raster user accuracy using Number of correctly classified pixels in each category (C_p) and Total number of classified pixels in that category (The row total) (T_{cpr}).

$$\text{Producer Accuracy} = \frac{C_p}{T_{rpc}} \times 100 \tag{5.3}$$

Equation 5.3 calculated the supervised classification raster producer accuracy using Number of correctly classified pixels in each category (C_p) and Total number of reference pixels in that category (The column total) (T_{rpc}).

$$K_c = \frac{(T_s \times T_{cs}) - \sum(C_T \times R_T)}{T_s{}^2 - \sum(C_T - R_T)} \times 100 \qquad (5.4)$$

Equation 5.4 Calculated the supervised classification raster kappa coefficient (K_c) using the Total sampled (T_s), Total corrected samples (T_{cs}), Column Total (C_T), and Row Total (R_T).

$$\text{Overall Accuracy} = \frac{T_{cpd}}{T_{rpd}} \qquad (5.5)$$

Equation 5.5 calculated the supervised classification raster overall accuracy using the Total number of classified pixels (The diagonal total) (T_{cpd}) and Total number of Reference pixels (Diagonal) (T_{rpd}).

5.2.5. Processing

To identify and navigate to the AoI (Wilderhope catchment), the search toolbar within ArcGIS online was used. The perform analysis tool selected the 'watershed' and enabled creation of a polygon representing Wilderhope catchment. This polygon was imported into ArcMap along with the historical maps (1935, 1995 and 2017). All historical maps were then clipped to the polygon shapefile.

For the base maps, to obtain river outlines and wanted key features, the raster data extraction tools were applied by firstly, identifying the water course. The geoprocessing tool helped remove noisy unwanted data, allowing the creation of a spatial subset. To extract the wanted layers in an O_r format, the Arc toolbox, spatial analyst, extract by attribute, allowed query building from selected subset features and table records (Equation 5.6). To examine these spatio-temporal changes all O_rs were overlayed and aligned by defining the projection using the data management projection and transformation tool. To maintain uniformity and help alignment, all layers were set the coordinate system of 'British National Grid'. The raster data was vectorised and converted to a polygon feature. The editor toolbar was then used which enabled correction of finite errors in alignment.

$$O_r = S_1 + S_2 + S_3 \tag{5.6}$$

Equation 5.6 was used to extract the wanted layers using the query building function. This created an Output raster (O_r) using subset features (S: sub-prefix 1,2,3…).

Total station geopositioned centreline longitudinal profile (120 intervals) and 14 transects in tabular format were input into ArcMap as event layers with the transformation coordinate system set as 'British National Grid'. The x, y and z coordinates (Eastings, Northings and Elevations) were displayed as points. Erroneous points that were incorrectly geo-positioned were identified and corrected in excel before re-importing the longitudinal profile and transects as both points and lines. The longitudinal profile and transects were overlayed on the historic maps to note spatio-temporal change in the mid-reach.

5.2.6. Processing and analysing transects

Two methods were used to construct transects. Firstly, transect points been imported into ArcMap and coordinate system set, including scale properties and measurement tool enabled planar distance measurements to be made between the transect points in a 2D cartesian domain. The second method involved using excel to calculate the distance between following transect points using the Geo-positions (Eastings and Northings) established by the total station. For both methods, excel accounted for the channel slope angle / gradient between transect points using the Pythagoras theorem. Excel enabled distance between points to be plotted with elevations.

5.2.7. Sinuosity index

When a water course becomes sinuous, the channel length extends and the channel slope angle / gradient decreases which slows local velocity (Ellis-Sugai and Godwin, 2002). Water courses temporally adjust to WDDs and can alter channel sinuosity (Taylor and Clarke, 2021). To conceptualise channel meanders caused by the installed WDDs the Brice sinuosity index (S_i) was applied to the two study reaches. The Brice index can be defined as the ratio between the length of the channel bed (L_{cmax}) to the length of the axis of the meanders (L_0) as shown in Equation 5.7.

$$S_i = \frac{L_{cmax}}{L_o} \qquad (5.7)$$

Equation 5.7 calculated the sinuosity index (S_i) using the Brice formula (modified by Friend and Sinha, 1993). Variables within this equation include Centre line of the channel between the determined start and end point (L_{cmax}) and the horizontal distance between the determined start and end point (L_o).

A straight water course, $S_i = 1$ is the length of the valley, indicating the more the water course meanders the greater the ratio would be > 1 (Gordon et al., 2005). There is general consensus that channels with a $S_i < 1.5$ are referred to as sinuous while channels with $S_i \geq 1.5$ are referred to as meandering (Leopold and Wolman, 1957; Brice, 1984; Alvarez, 2005; Singh, 2005; Ozturk and Sesli, 2015). Schumm (1963) recommends five classifications: straight (≤ 1.1) transitional (1.3), regular (1.7), irregular (1.8) and tortuous (≥ 2.3). There are numerous methods to calculate the sinuosity index with advantages and disadvantages as outlined in Appendix H.

5.2.8. Channel incision

When channels become straighter, this causes their length to become shorter, steeper and create faster flowing water, which in turn can lead to enhanced local erosion and incision (Ellis-Sugai and Godwin, 2002). Like a confined valley, an entrenched water course is unable to access its floodplain during high discharge. The Rosgen channel entrenchment (E_{nt}) ratio is a

field measurement of channel incision and is estimated by using the ratio of the width of the flood prone area (W_{fpa}) to bankfull stage width (B_{sw}) (Equation 5.8). In a non-entrenched channel, the bankfull stage or 100% Q_{bf} is the elevation of the floodplain adjacent to the active channel. If the stream is entrenched, the h_s is identified as a scour line or viewed as the point of vegetation change (Figure 5.4).

$$E_{nt} = \frac{W_{fpa}}{B_{sw}} \qquad (5.8)$$

Equation 5.8 calculated channel entrenchment (E_{nt}) using width of the flood prone area (W_{fpa}) and bankfull stage width (B_{sw}) (Rosgen, 1994).
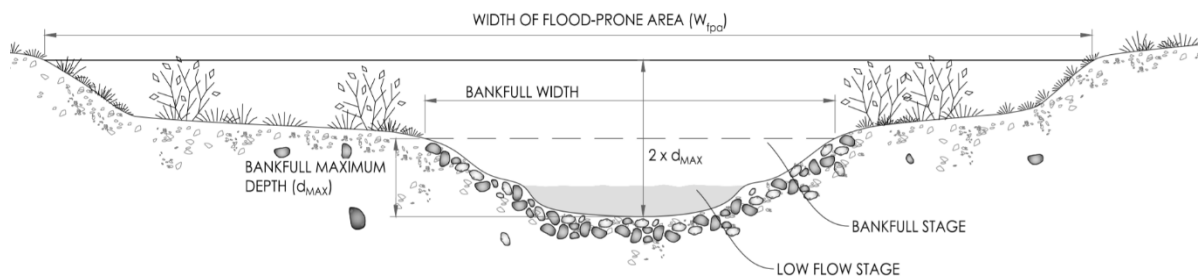
Figure 5.4: Schematic showing variations in channel entrenchment from the bankfull stage (Stantec, 2018). Maximum depth of scour (d_{smax}), width of the flood prone area (W_{fpa}) and bankfull stage width (B_{sw}) are displayed.

The flood-prone width is the cross-sectional measurement at the elevation corresponding to twice the maximum depth of the bankfull stage. The channel entrenchment ratio defines the vertical containment of the channel with the ratios of 1: 1.4, entrenched; 1.41: 2.2, moderately entrenched and >2.2 slightly entrenched (Rosgen, 1994). While Hall et al. (2007) classifies entrenched channels as having a ratio ≤3.8, unconfined and > 3.8, confined based on field experimentation lateral channel migration.

5.2.9. Valley bottom width

The shape and size of the valley bottom, comprised of the water course and low-lying land, dictates the form and function of the water course (Brierley and Fryirs, 2013) as well as its

potential to adjust (Philips, 2010). Consequently, it is essential to accurately measure the valley bottom width to consider WDD impact on the extent of possible change in the water course and the extent of the floodplain in areas of bank overtopping. ArcGIS online, 'scene' was used to determine the valley bottom width. The study site was located using the search toolbar where Wilderhope Brook catchment was highlighted through adding the pre-constructed 'watershed' layer. Basemap imagery enabled visualisation and analysis of valley features so distance measurement could be acquired using the point to measure analyse tool.

5.2.10. Accuracy and Precision

Temporal geospatial analysis of Wilderhope Brook channel evolution was quantified by using empirical data where Ground-based topographical field survey was compared to historical maps. The accuracy of the historical mapping is the extent to which the measurements comply to measurements in reality conforming to data layers that indicate any outliers or untrue values. Precision is defined as the extent to which measurements are limited by the source data instrumental and spatial resolution. Uncertainty therefore accounts for location and position of data (horizontal and vertical differences with conversion of scale being important), coverage inconsistencies with omissions needing to be checked and discrepancies between temporal source material. A historical DTM (2017) was constructed in GIS, which acted as a control prior to WDD insertion and elucidating historical mapping where geomorphic change had taken place. Geospatial analysis using historical 2D and 3D cartography and contemporary survey uses length, width (x and y) and elevation (z) over time (Langran, 1992). The location of change is dependent on the reliability of historical mapping data whereas precisely when and why changes occurred were examined through inference known as geometric change detection (GCD). Historic changes in the geomorphology of Wilderhope Brook were made by making quantitative comparison between time-discrete elevation surfaces at different times. The DTM generated in GIS enabled static data layers to identify locations of geomorphic variation, approximate rates of change, when the water course demonstrates stability or dynamic behaviour, periods of anthropogenic forcing, and past trends.

The main limitation of using historic maps for reconstructing channel change is the level of data accuracy. Field survey is also key to providing data for geomorphology. Global positioning

systems (GPS) and increases accuracy in marking locations and increases mapping and surveys as baseline data sources.

5.3. Results

5.3.1. Sediment input areas

Anthropogenic modification of land usage comprises grassland typically composed of sheep farming and agricultural farmland. Arable land is located primarily to the west of Wilderhope Brook catchment while in the east improved grassland is the dominant landcover (Figure 5.5). The western perennial water course has a high sediment yield in the winter months with sediment runoff from the fallow fields. WDDs located downstream of the perennial water course receive a higher sediment yield during winter months while this increased sediment yield dissipates during the summer months. The eastern landcover has a lower sediment input into the water course due to the improved grassland creating a protective layer to the bare ground. However, with much of this grassland used for sheep and cattle grazing, there is much sediment input into the water course due to animals poaching the ground down to the channel banks. There are small pockets of agricultural land in the western area. The distant valley edges are tree-lined with the wider area of forestland to the west, and riparian trees at the streambank particularly in the lower part of the upper course. The presence of riparian trees in the upper course helps reduce erosion with tree roots reinforcing the bank (Hubble et al., 2010). Riparian vegetation has also been found to slow runoff and retain sediment acting as a buffer from the adjacent agricultural fields (Krzeminska et al., 2019). However, the riparian forest at Wilderhope Brook, is generally in poor condition, with Phytophthora disease of alder trees requiring them to be felled which contributes to sediment runoff. The loss of alder trees, a natural choice for use in flood-mitigation schemes and for coppicing, creates bank instability and erosion (Forest Research, 2021).
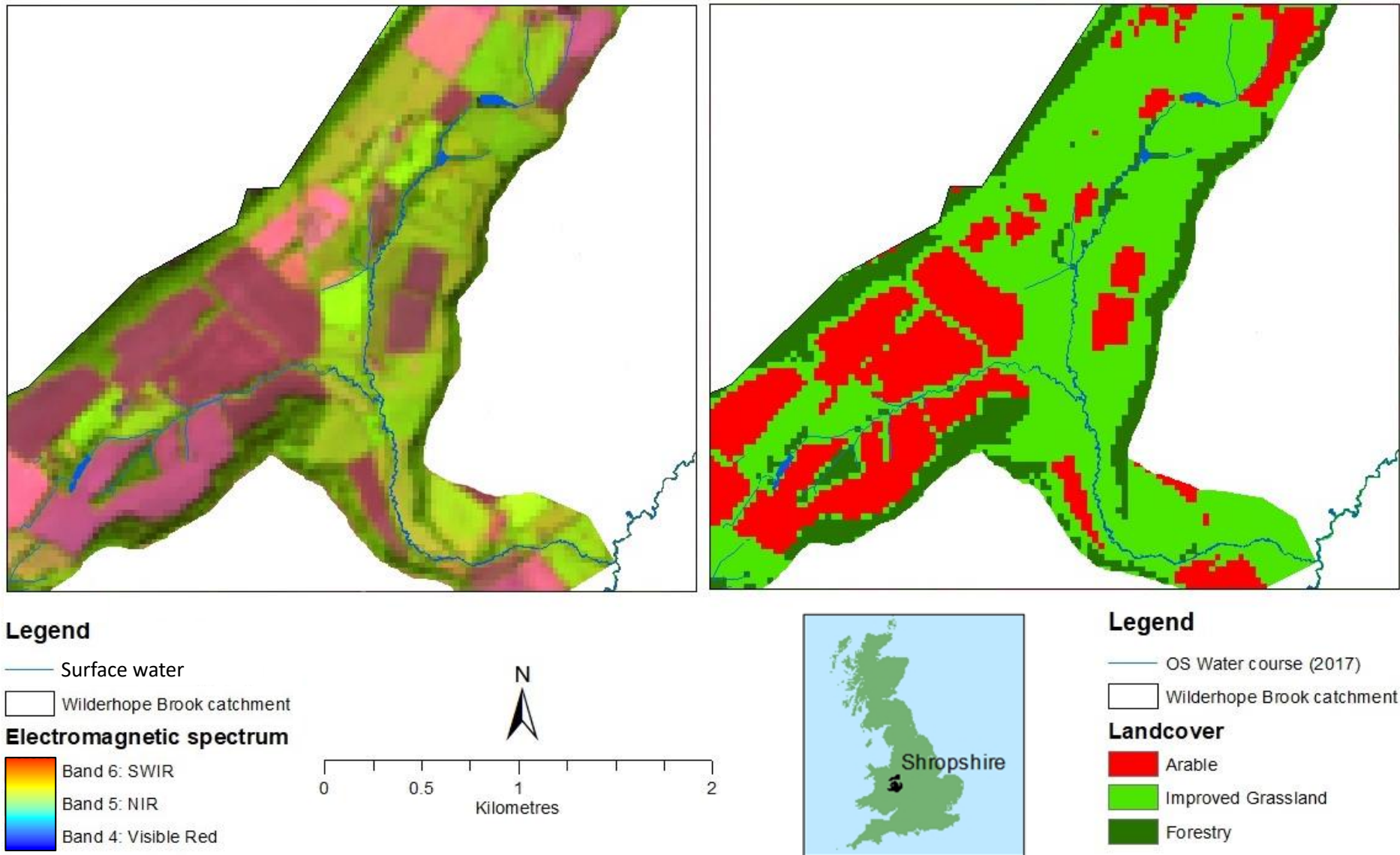
Figure 5.5: Airborne Thematic Mapper (ATM) with NDVI (Left) and Multi-band supervised classification image (Right). Three landcover classifications have been assigned so spatial NDVI variations can easily be depicted. Dataset captured on 28th August 2019 using LANDSAT8.

5.3.2. Model assessment

To assess the accuracy of the supervised classification map, a confusion matrix was constructed. The overall accuracy was calculated at 95% (Table 5.2) while the Kappa coefficient shows a 94% interrater agreement.

Table 5.2: Confusion matrix displaying the user accuracy, producer accuracy and overall accuracy for supervised classification.

	Improved Grassland	Arable	Forestry	Row total	User Accuracy
Improved Grassland	22	2	1	25	91%
Arable	1	24	0	25	96%
Forestry	0	0	25	25	100%
Column total	23	26	26	75	
Producer Accuracy	96%	92%	96%		Overall accuracy: 95%

5.3.3. Soils, geology and drainage

A soils map (Figure 5.6) with information (Appendix I) was constructed to examine areas prone to surface runoff, infiltration and percolation. The map shows that clayey soil to stoneless fine silty are common in the upper course of Wilderhope Brook catchment. This soil type, with a sediment grain size of 0.004 - 0.016 mm (Julien, 1998), requires low τ_c and therefore is easily transported particularly during high discharge. This suggests WDDs located in the upper course trap fine sediment and are more prone to scouring during high discharge. In Wilderhope Brook lower course, larger particles ($\approx$ 0.062 mm) are located without the presence of coarse clayey soils (Julien, 1998). Enlarged particles reduce transportation as more energy is required to initiate these particles into motion. Spatial variations in soil suggest in the upper course with fine sediment, WDD induced backwater pools can become infilled with fine sediment. While in the lower course the content of backwater pools alters with larger particles.
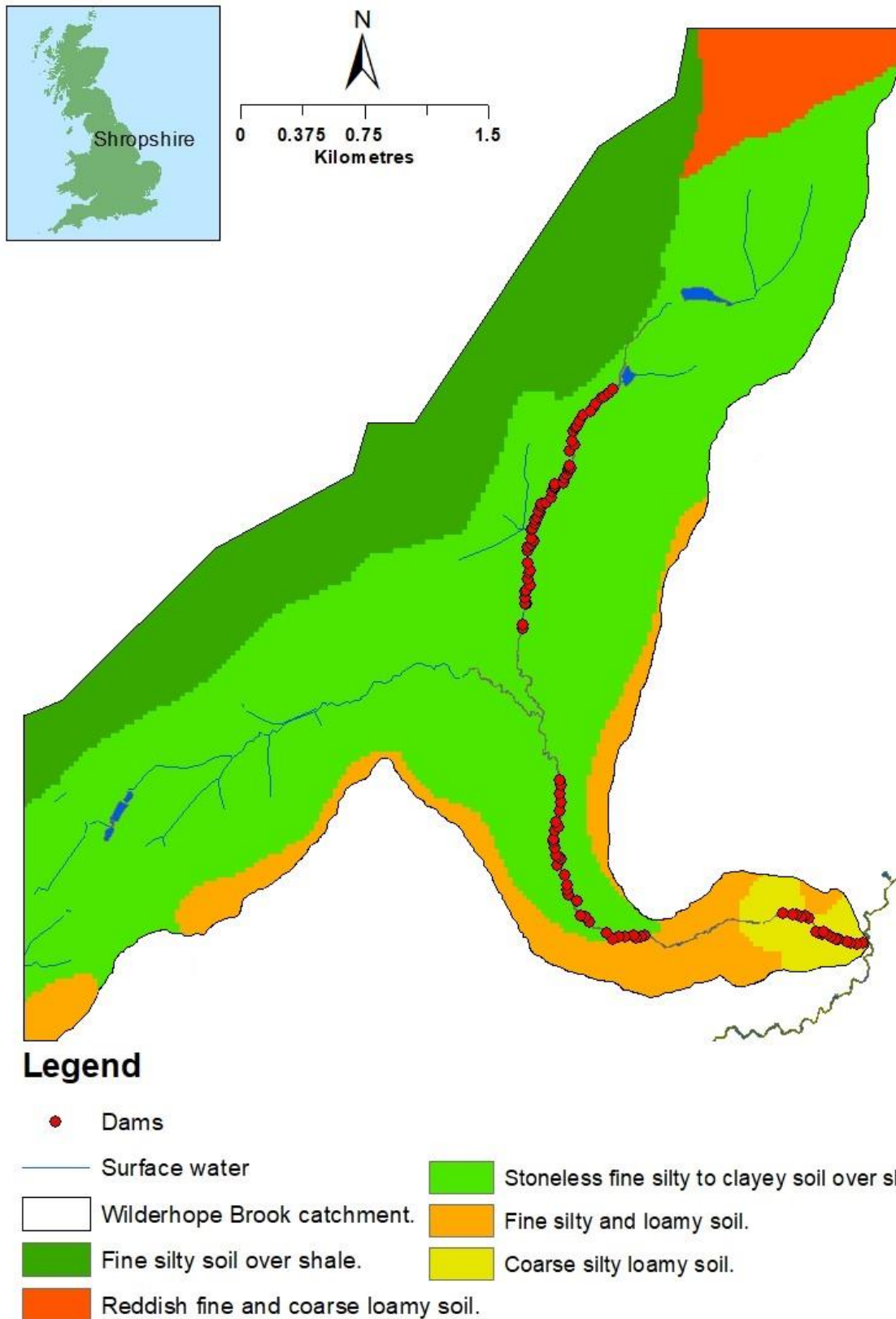
Figure 5.6: Soil map displaying Wilderhope Brook catchment with the water course (2017). Further details on soil catchment characteristics are given in Appendix I.

Wilderhope Brook catchment bedrock geology consists largely of mudstone, siltstone and sandstone stratifications although there are outcrops of limestones and underlying shale located in the north and centre of Wilderhope Brook catchment (Figure 5.7). Outcrop sedimentary rock formations occur over different periods and epochs and have remained generally unchanged since their formation. Rock erodibility varies with rock type. Sandstone is highly resistant to weathering compared to other sedimentary rocks such as mudstone and siltstone which governs sediment entrainment rates. Limestone is prone to chemical weathering and therefore solution is the primary mode of initiation of transportation in these areas (lower to mid reach) and is less likely to add to the accumulations behind WDDs compared to mudstone, siltstone and sandstone. Therefore, understanding spatial variations in geology in respect to WDD location is important to ascertain rate of backwater pool infilling.

Superficial bedrock in the mid to lower reaches are fluvial in origin with sedimentary depositions consisting of sorted to semi-sorted detrital coarse to fine-grain sediment. To the north of Lower Stanway Farm, in the upper reach, superficial bedrock is predominantly glaciogenic in origin formed during the Quaternary period (British Geological Survey, 2021). To verify NSRI, HOST and BGS datasets, a borehole survey was conducted from the 26th Sept. 2012 until the 1st Oct. 2012, located in an intermittent stream 454 m to the west of Wilderhope upper reach (521948.45E and 5819461.97N) (Figure 5.7). Surveyed results showed: brown clay and gravel at a depth of 0-3.5 m, Grey / brown mudstone 3.5-12 m and Medium / hard grey mudstone (limestone) 12-46 m, with 0 m datum denoting the surface. From Sept. to Oct. 2012 the bore hole survey showed groundwater was struck at 3 m, 10 m and 16 m intervals (Woolcock, 2012).

Geology and soils in the mid-upper reaches tend to be seasonally waterlogged and particularly during winter months, these areas have a slow permeability, allowing for faster surface runoff into the river system during storm events (Figure 5.8). 85 WDDs are located in the mid-upper reaches, on these seasonally waterlogged soils, with the WDDs contributing to the heightened water table by holding water in situ and enabling prolonged infiltration. Seasonal variations creating surface runoff can create increased soil erosion and sediment supply to river systems with bare ground stripped of nutrients and sediment (Han et al., 2018). WDDs therefore exhibit a seasonal variation in sediment supply and diurnal sediment rates.
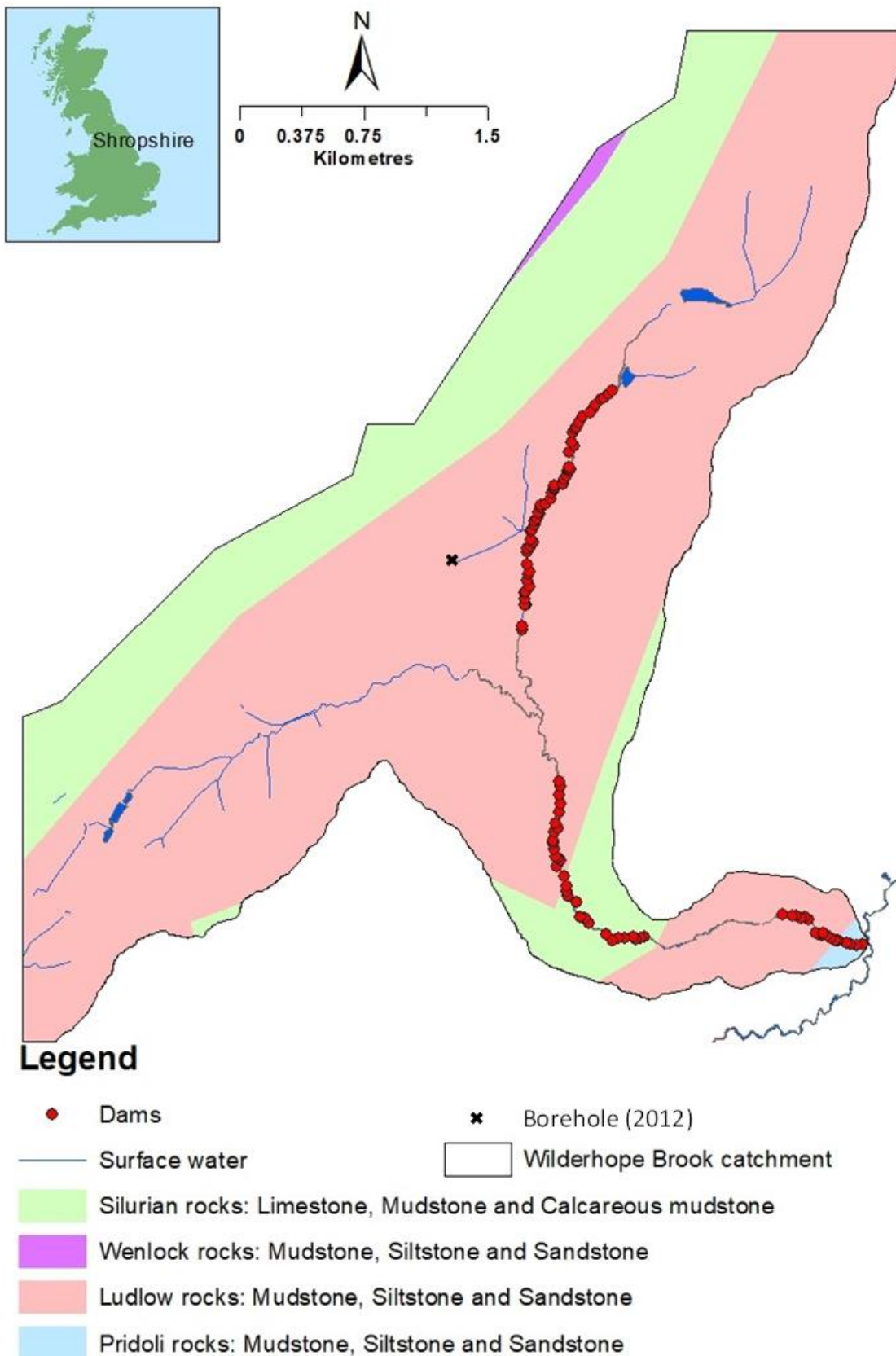
Figure 5.7: Bedrock geology map displaying Wilderhope Brook catchment with the water course (2017). BGS data was acquired through EDINA showing bedrock formation of periods and epochs along with bedrock type. The geology map gives bedrock location and indication of types of bedrock eroded and transported into the river system.
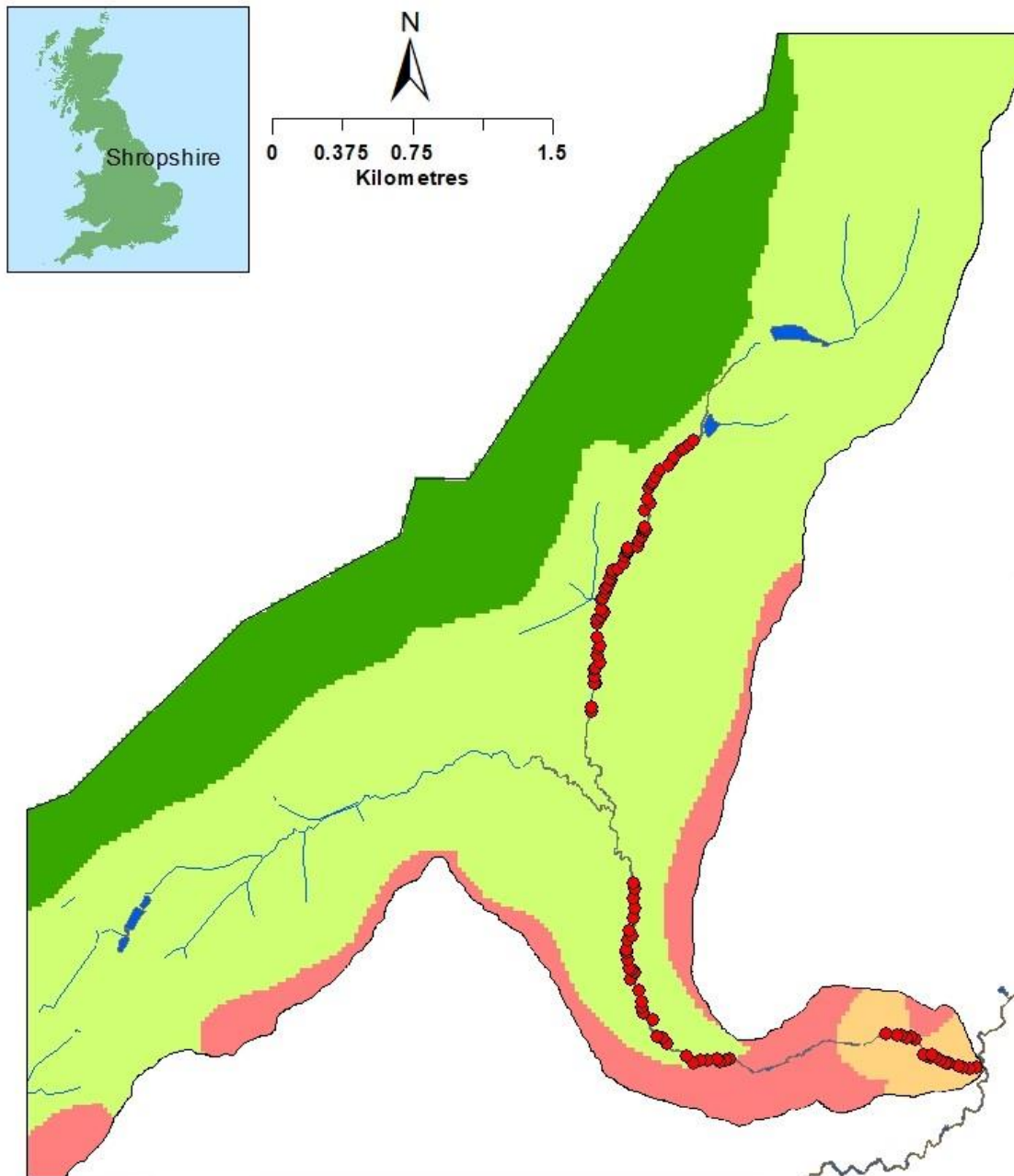
Figure 5.8: Drainage map displaying Wilderhope Brook catchment with the water course (2017). This map displays seasonal spatial variations in drainage.

5.3.4. Mid-reach study site

5.3.4.1. Digital terrain model and Centre line

When comparing the surveyed centre line (2019) to the OS water profile (2017), the presence of WDDs has started to enhance channel sinuosity in the mid reach of Wilderhope Brook. Wallerstein and Thorne (1997), who investigated sediment routing and the impact of WDDs on bedform morphology, confirm that WDDs alter channel morphology temporally.

Figure 5.9, shows that upstream of dam 30, there is evidence of channel chute-offs at two meanders creating channelisation. At this point in the reach, there are no WDDs located; vertical erosion is more dominant than lateral erosion, whereby gravitational forces exceed resisting friction forces, of interlocking and cohesion (Lawler et al., 1997; Henshaw et al., 2013). The original meanders are progressively cutoff with the flow regime changing course as evidenced by the centreline.

As the flow approaches the partial dam (30) meander at ≈ 80°, energy is dissipated by the partial dam blocking the flow regime, which in turn reduces expected erosion of the outer bank and sedimentation occurring on the inner bank due to the dam blocking helicoidal flow from transporting sediment (Figure 5.10a). With the WDD reducing erosion of the outer bank, meander enlargement is slowing whilst preventing a chute.

Figure 5.9 shows that the flow regime is deflected towards the active dam (29). It can be noted that historically at this meander a large siltation bar has formed on the inner bank, whereby sediment eroded from the meander is transported to the inner bank. However, due to the active dam, backwater has increased which reduces velocity and force. During low discharge, sediment is deposited in the backwater creating a sediment infilled pool rather than sediment being deposited on the bar (Wildman and MacBroom, 2005). With the formation of the pool, the water course has grown more laterally and hence the centre line has shifted from its historic course, towards the outer bank. Dam 29 is stable and fixed between two mature coppice trees, just upstream of the meander. On the outside bank of the meander the tree is reducing bank erosion, however there is vertical erosion with the formation of a steep plunge pool directly downstream of the WDD (Figure 5.10b).
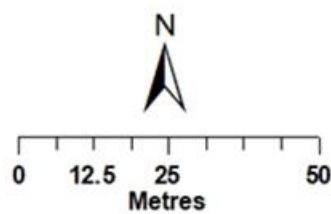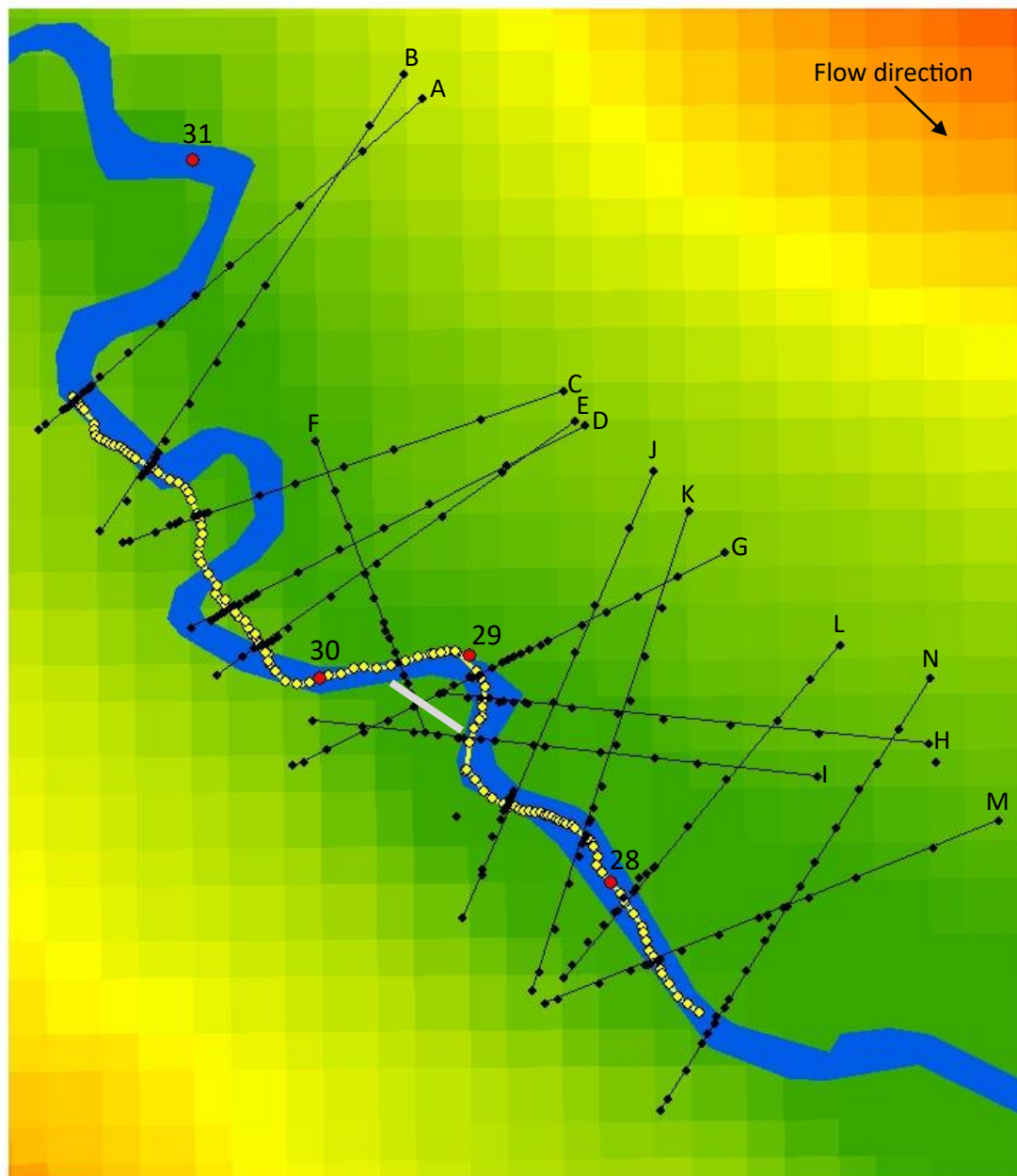
Figure 5.9: GIS comparing surveyed centre line data (2019) to an OS extracted surface water profile (2017). Additional comparison was also made from surveyed bank geomorphology (2019) to the historic DTM (2017). Total station was set-up on the east bank.
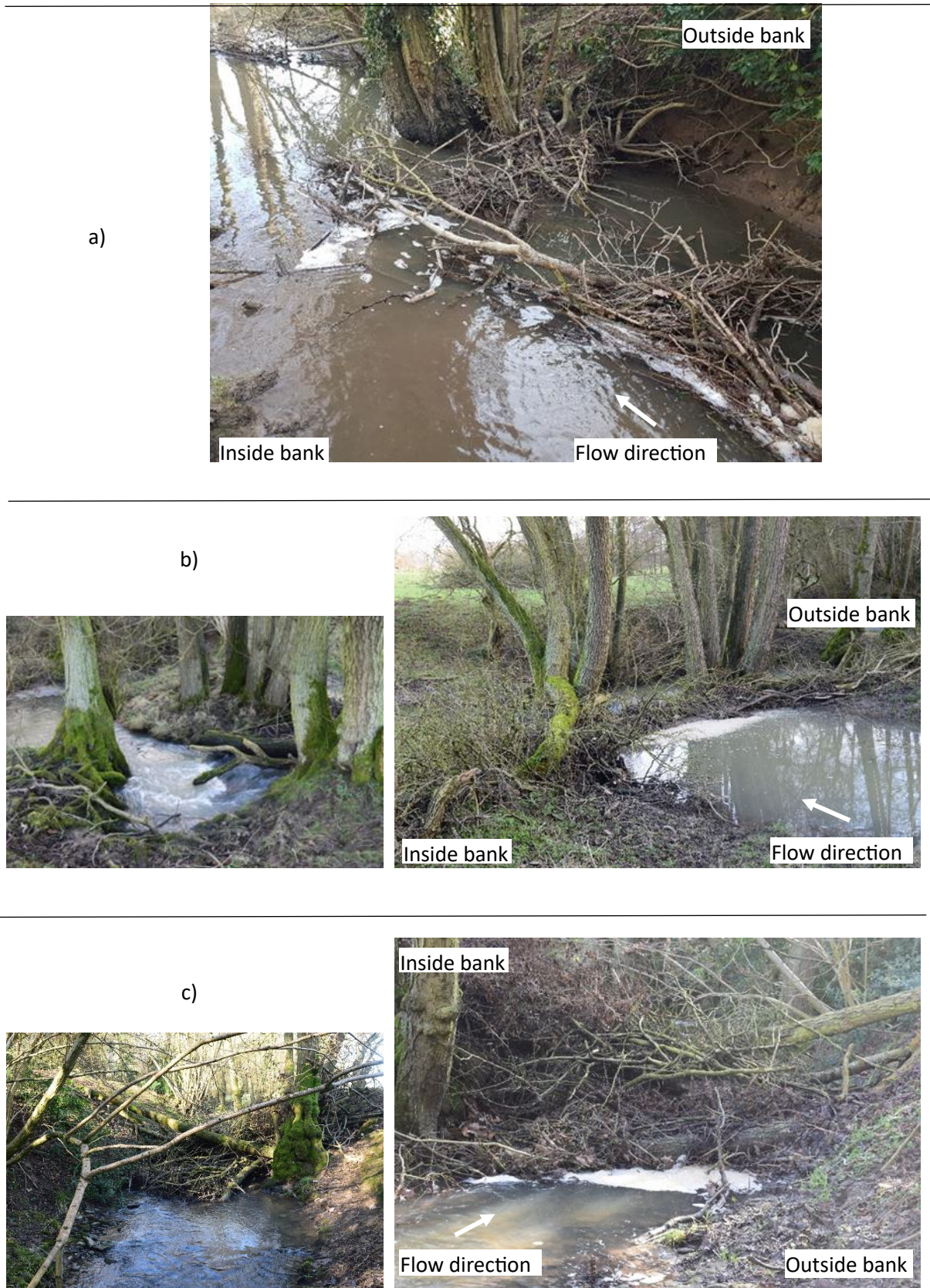
Figure 5.10: Photographs taken on the 15th February 2019 displaying: a) Partial dam (30) located on meander with highly erodible silty clay. b) Active dam (29) located prior to a meander on hard rock creating fast flow conditions just downstream. c) Complete dam (28) located in a straight channel on pebbly ground.

Complete dam 28 is located on a gradually sloping straight channel section with varied flow conditions. During high discharge, backwater build-up occurs. Similar to dam 29, downstream pool-riffle sequencing can be noted but to a lesser extent with smaller pools and riffles (Figure 5.10c).

As shown in Figure 5.11 the contour map of Wilderhope Brook catchment, the mid reach has a narrower valley bottom indicating the channel is more topographically confined within the valley in this location having less space to laterally adjust. In the upper reach there is greater space for channel adjustment with the tributary broadening the valley bottom width. Spatial variations in valley confinement mean WDDs located in the mid reach are more prone to flash flood events. Topographic mapping Figure 5.9 and Figure 5.11 shows where the concentrations of colour gradient and contouring change respectively, from dark to light or sparse to dense indicating sloping within the catchment and channel confinement.
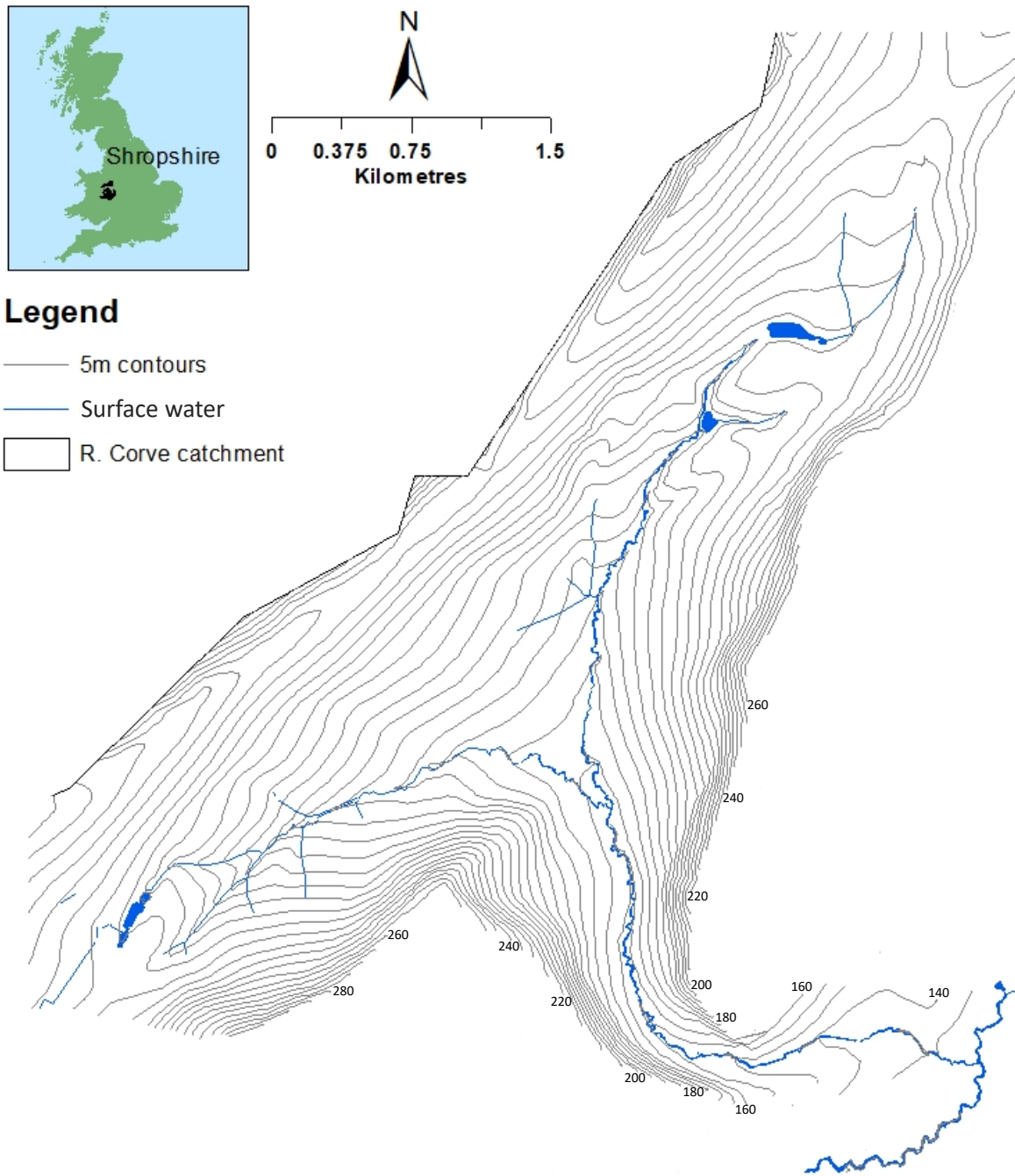
Figure 5.11: GIS displaying 5 m contouring at Wilderhope Brook catchment. Gradual rounding of the valley bottom can be seen which creates high gradient towards the distal edges of the valley.

5.3.4.2. Transects

In the mid study reach the channel is confined between two distal edge slopes of 0.41 m/m to the west and 0.36 m/m to the east. Smallest bottom main channel width can be noted at this point as 126 m (Figure 5.12).
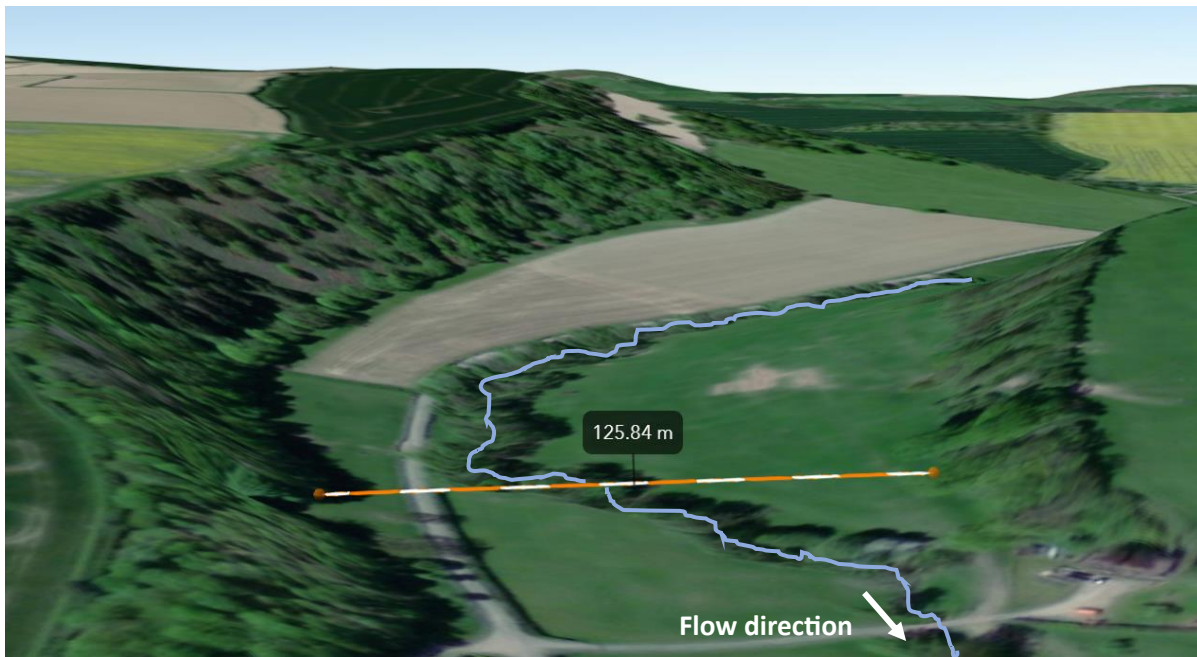
Figure 5.12: A 3D view of Wilderhope catchment mid reach with a valley bottom width (126 m). Wilderhope Brook water course is outlined in blue.

The gradually sloping valley bottom width and high slope to the distal edges of the valley topographically confine the channel. At the mid study reach, all transects displayed a V-shape channel with generally steep channel gradient and a relatively narrow channel base, typical of an upland stream. This valley confinement allows less space for the channel to laterally adjust within the steep sided valley (Nagel et al., 2014). Temporally all transects, except A and F, displayed evidence of channel incision with the historical channel (2017) lying above the surveyed channel (2019) (Figure 5.13).

Figure 5.13C displays topographic evolution, at transect C, whereby historically the water course used the eastern deeper channel, as displayed in Figure 5.9. However, by 2019 the historical eastern channel had infilled (0.28 m) and a new cutoff channel has formed, to the

west. Over time the eastern channel has infilled which has cutoff the historic meander. The surveyed transect also shows the right bank has a steeper gradient of 0.56 m/m compared to the left bank at 0.22 m/m.

Figure 5.13F displaying transect F located 12.35 m upstream of dam 29. Transect F shows that lateral erosion is more dominant with both channel banks gradually sloped (left: 0.08 m/m, right: 0.17 m/m), a wide pool channel base with a bankfull stage width of 5.88 m and maximum scour depth of 0.89 m (datum taken from the bankfull stage denoted by edge of georeferenced vegetation cover) (Table 5.3). Historically, a pool, 0.14 m deeper than the surveyed (2019) transect existed which has infilled since the installation of active dam 29. Transect F, has a slight entrenchment of 1.97 while transect G, located downstream of dam 29 is moderately entrenched at 2.21. This indicates the channel is incising, supplying sediment to the downstream channel network. Figure 5.13G shows lateral erosion has transitioned to more dominant vertical erosion with a steeper V-shaped valley having a left bank gradient of 0.28 m/m and right bank gradient of 0.14 m/m and the formation of a deeper V-shaped pool with a maximum scour depth of 1.5 m.

Historically (2017), transect I was geomorphologically shaped as a trapezoidal channel. However, since WDD 29 was installed, the channel has morphologically incised and changed in shape to become V-shaped with an increased maximum scour depth of 0.94 m (Figure 5.13I).

Historically (2017/19), transect N displays a higher bank elevation and when surveyed in 2019 this elevation has flattened potentially caused by surface runoff. A hollow located 50 m from the total station has infilled with the depth decreasing by 0.3 m.

153
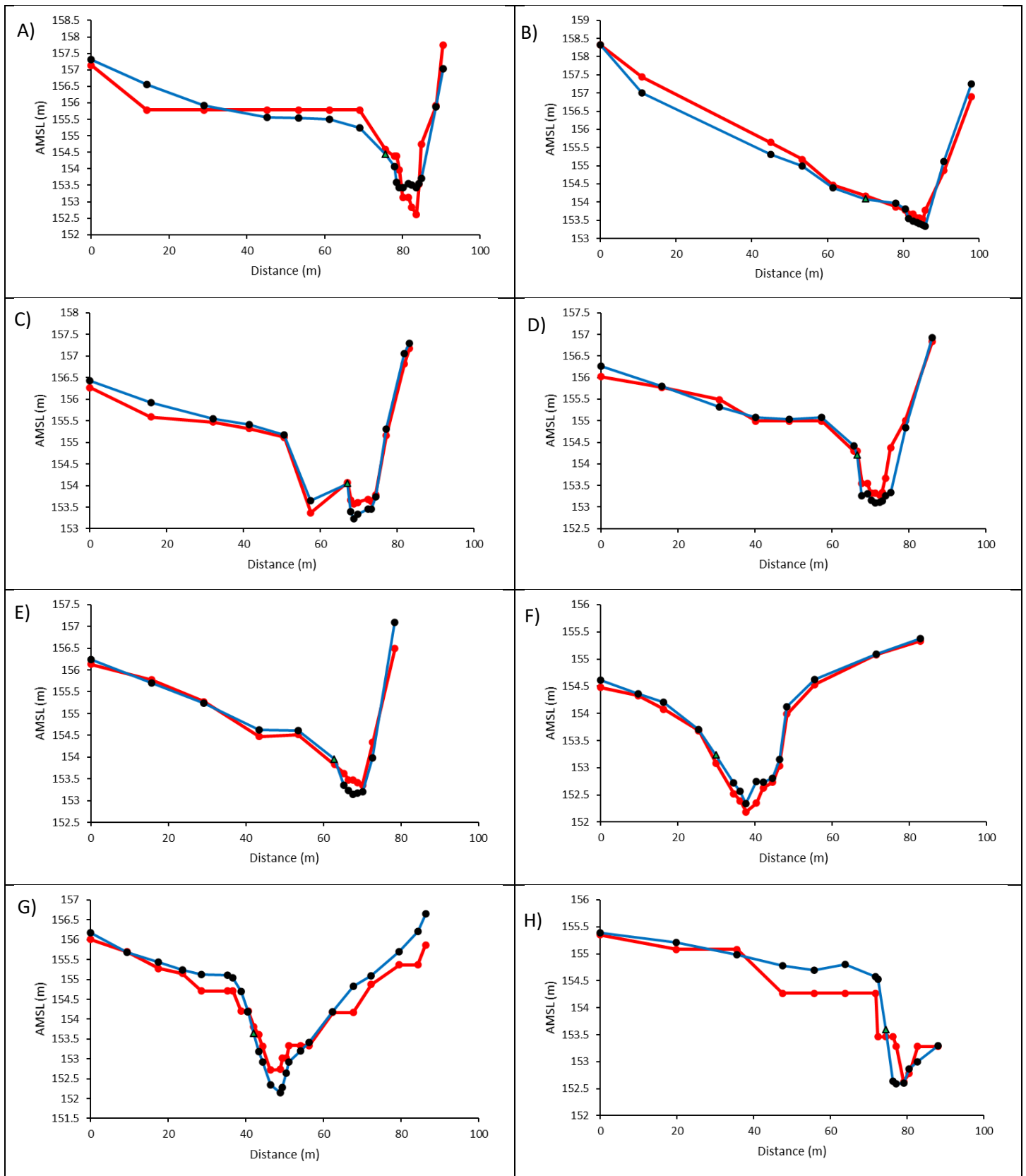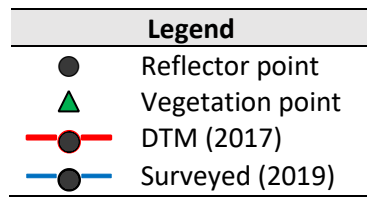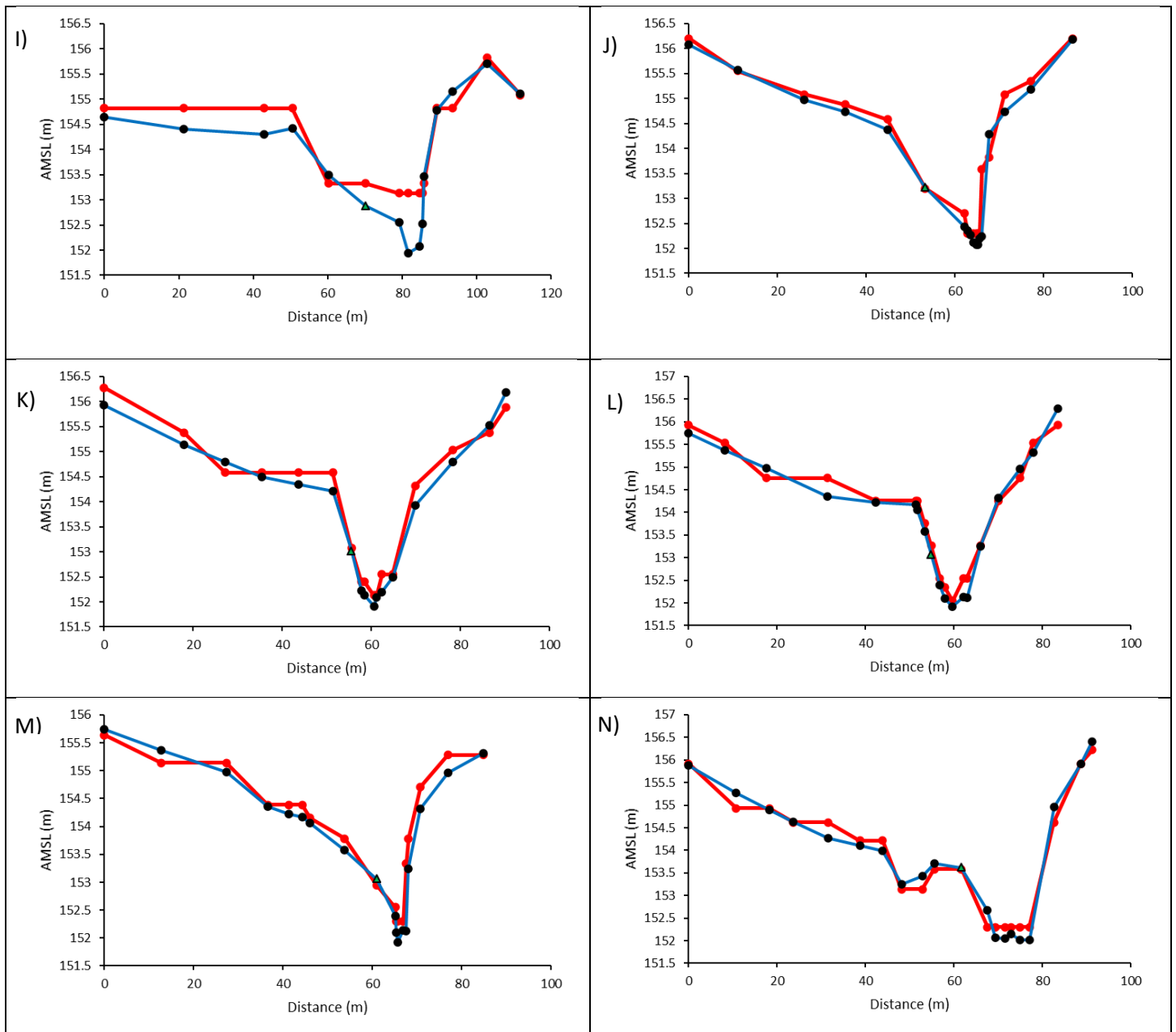
Figure 5.13: Surveyed transects taken in February 2019. First transect point taken on left bank at 0 m distance. Heights given are measured from Average Height above Sea Level (AMSL). Vegetation point is displayed on left bank, which enables quantification of bankfull stage width (B_{sw}).

Table 5.3: Transect information displaying bank gradient, maximum scour depth, Bankfull stage width, width of flood prone area and channel entrenchment.

Transects	A	B	C	D	E	F	G	H	I	J	K	L	M	N
Left bank gradient (m/m)	0.11	0.05	0.09	0.14	0.14	0.08	0.28	0.4	0.08	0.11	0.25	0.27	0.11	0.12
Right bank gradient (m/m)	0.35	0.32	0.17	0.26	0.37	0.17	0.14	-	0.37	0.92	0.22	0.23	0.47	0.38
Maximum scour depth (m)	1.01	0.73	0.81	1.11	0.81	0.89	1.5	1.01	0.94	1.14	1.11	1.14	1.14	1.58
Bankfull stage width (m)	10.4	17.4	17	11.4	9.68	16.5	16	-	15.8	13.8	11.4	10.6	6.04	18.2
Width of flood prone area (m)	25	34	24	22.6	21	32.5	35.4	-	28.5	22.9	20.7	18.4	28.8	72
Channel entrenchment	2.4	1.95	1.41	1.98	2.17	1.97	2.21	-	1.8	1.66	1.81	1.73	4.77	3.96

Channel evolution from 2017-2019 was examined by comparing the DTM (2017) to the surveyed longitudinal profile elevations (2019). When comparing the centre line longitudinal profiles from the DTM to the survey, a Pearson's correlation coefficient of 0.9366 was calculated (Equation 3.17 as shown in section 3.3.2.1.) (Figure 5.15). When comparing the transects from the DTM to the survey, a Pearson's correlation coefficient of 0.9569 was calculated. Therefore, though the centre line longitudinal profile showed a weaker relationship than the transects, this correlation difference was not statistically significant with both datasets having a strong relationship. This correlation difference could be a result of total station calibration distortions, LANDSAT8 image resolution or acquisition errors (satellite angle of incidence or sparse vegetation removal) or geomorphic evolutionary change between 2017-2019 (Roland and Balzter, 2007; de Musso et al., 2020). Wilderhope catchments valley sides lacked dense vegetation unlike landcover surrounding the channel and therefore when calibrating to remove the unwanted vegetation from the DTM, this potentially was the main cause of a weaker Pearson's correlation between the DTM and surveyed centre line compared to the transects.

When quantifying the depth (graphical z-direction) z value accuracy the surveyed (observed, $\hat{z}_i$) and DTM (predicted, observed vertical values [z_i]) centre line profiles had the greatest z value accuracy of 0.13 m RMSE compared to both the projected LIDAR z value accuracy of 0.15 m RMSE (UK Government, 2021a) and calculated surveyed ($\hat{z}_i$) and DTM (z_i) transect z value accuracy of 0.16 m RMSE (Equation 5.1).

To examine the accuracy of the DTM in relation to the survey and whether topographical evolution occurred, statistical significance was quantified for both centre line and DTM through the t-Test Paired Two Sample for Means method (Equation 3.18 as shown in section 3.3.2.1.). This method ascertained whether the null hypothesis (means of two datasets are equal) can be accepted or rejected. This method was applied as it is typically used to test temporal datasets of the same type (Frontline Solvers, 2021). Between the DTM and longitudinal centre line the probability of the absolute value of the t-Statistic (14.504) being observed was higher in absolute value than the Critical t value for both datasets (Surveyed: 1.6579 and DTM: 1.9803). Since the centre line P-values (Surveyed: 2.7Exp-28 and DTM: 5.4Exp-28) were less than the alpha (0.05) the null hypothesis was rejected with no significant difference in the means of each dataset (Figure 5.14). The same result was observed when comparing the DTM to surveyed transects with an absolute value of the t-Statistic (8.827) and Critical t value for both datasets (Surveyed: 1.6511 and DTM: 1.9697). Similar to the centre line the transects P-values (Surveyed: 5.8Exp-15 and DTM: 1.2Exp-14) were less than the alpha (0.05) so the null hypothesis was again rejected (Figure 5.15). Rejection of the null hypotheses indicates evolutionary change.

A)
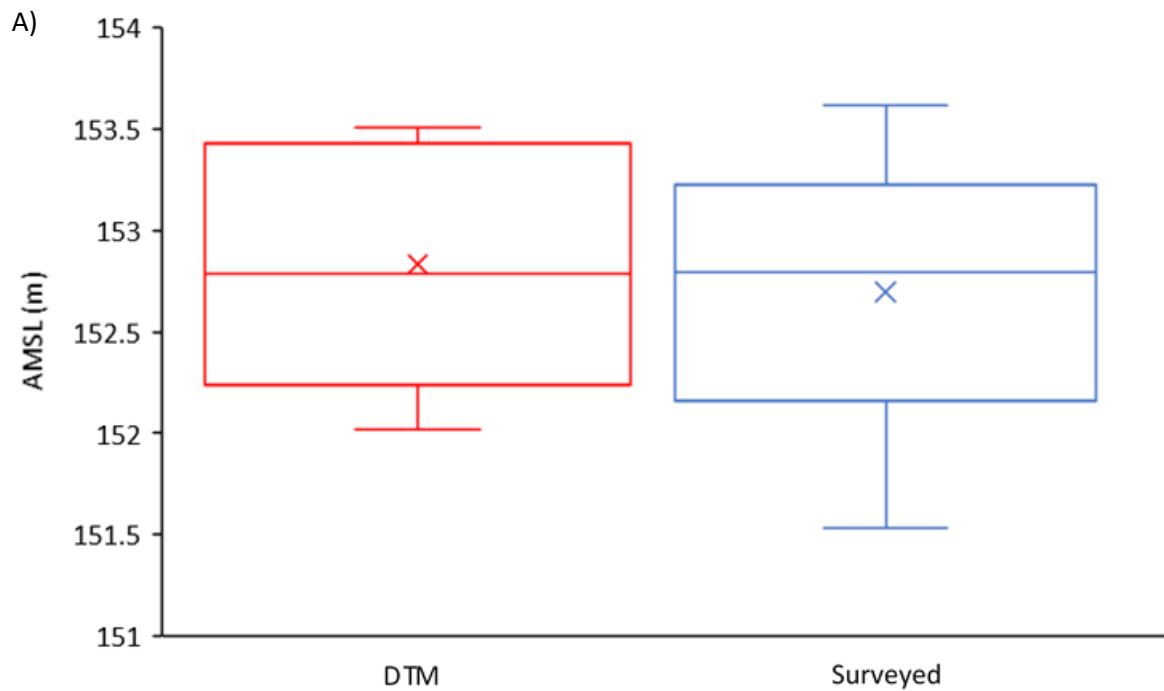
	DTM (AMSL, m)	Surveyed longitudinal (AMSL, m)
Mean	152.833	152.699
Standard Error	4.99Exp-2	5.3Exp-2
Standard deviation	0.544	0.578
Sample Variance	0.296	0.335
Kurtosis	-1.68	-1.308
Skewness	-0.122	-0.188
Range	1.49	2.09
Minimum	152.02	151.531
Maximum	153.51	153.621
Lower quartile	152.24	152.16
Upper quartile	153.43	153.23
Confidence Level (95.0%)	9.88Exp-2	0.105
t-Test: Paired Two Sample for Means		
Hypothesised mean difference	0.135	
Degree of Freedom	118	
T statistic	-14.504	
P (T ≤ t) one-tail (Surveyed)	2.7Exp-28	
t Critical one-tail (Surveyed)	1.658	
P (T ≤ t) two-tail (DTM)	5.4Exp-28	
t Critical two-tail (DTM)	1.98	

Figure 5.14: Box and whiskers diagram showing a 0.003 m median variance between the DTM and the surveyed longitudinal centre line. The X on the box and whiskers shows the position of the mean.
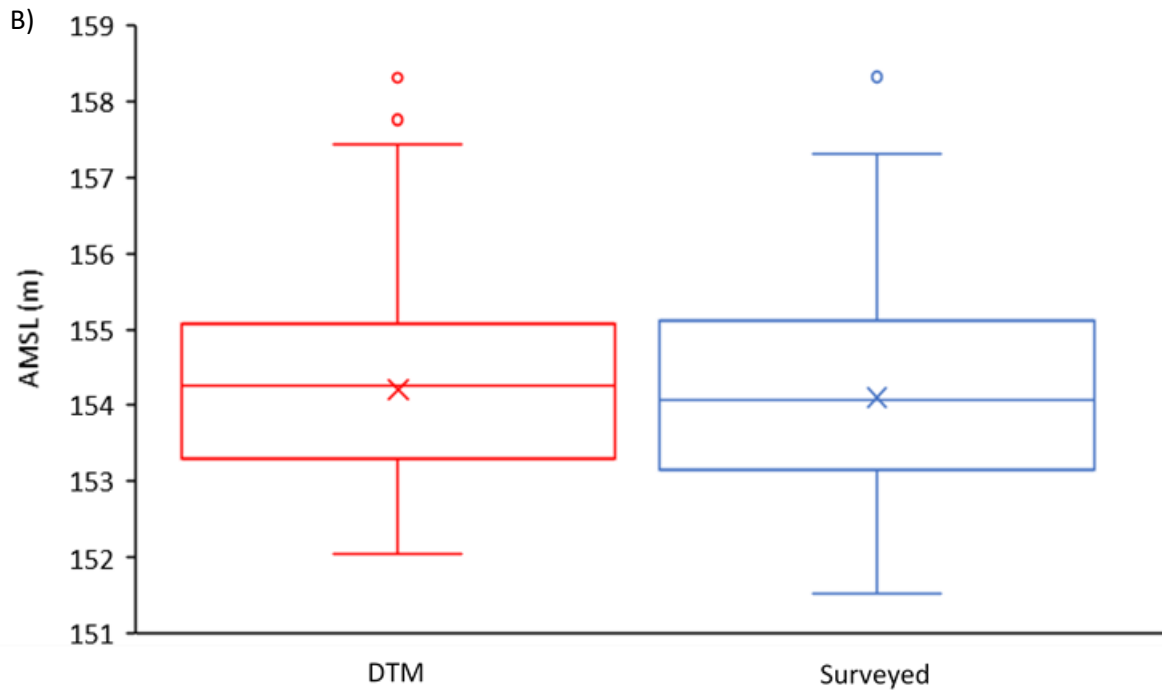
	DTM (AMSL, m)	Surveyed transects (AMSL, m)
Mean	154.213	154.107
Standard Error	8Exp-2	8.8Exp-2
Standard deviation	1.256	1.372
Sample Variance	1.579	1.883
Kurtosis	-0.267	-0.483
Skewness	0.358	0.304
Range	6.27	6.808
Minimum	152.05	151.521
Maximum	158.32	158.328
Lower quartile	153.295	153.15
Upper quartile	155.08	155.11
Confidence Level (95.0%)	0.158	0.173
t-Test: Paired Two Sample for Means		
Hypothesised mean difference	0.106	
Degree of Freedom	244	
T statistic	8.827	
P (T ≤ t) one-tail (Surveyed)	5.8Exp-15	
t Critical one-tail (Surveyed)	1.651	
P (T ≤ t) two-tail (DTM)	1.2Exp-14	
t Critical two-tail (DTM)	1.97	

Figure 5.15: Box and whiskers diagram showing a 0.182 m median variance between the DTM and the surveyed transects. The X on the box and whiskers shows the position of the mean.

5.3.4.3. Longitudinal profile

Wilderhope Brook is a headwater stream, located at the upper stage of the River Severn concave profile. Figure 5.16 shows the 187.08 m mid-reach surveyed intersection of Wilderhope Brook with pool-riffle sequencing. Since partial dam 30 was installed (2017) a V-shaped pool (depth: 0.67 m; length: 18.91 m) has formed initiating 8.34 m upstream of the dam at the meander apex (Figure 5.9). Active dam 29, due to attenuating and slowing the flow, has created infilling of the pool located 0-18 m upstream. Downstream of active dam 29 vertical erosion has taken place with the formation of a deep pool (depth: 0.62 m; length: 10.91 m). Scour initiates at dam 29 rather than upstream as at partial dam 30 with a secondary pool having developed 23.83 m downstream. Dam 28 is located on a straight channel section with a shallow U-shaped pool (depth: 0.19 m) initiating 3.51 m upstream of the dam centre causing undercutting. A second deeper pool (depth: 0.44 m) has initiated 10.41 m downstream of dam 28 (Figure 5.16).
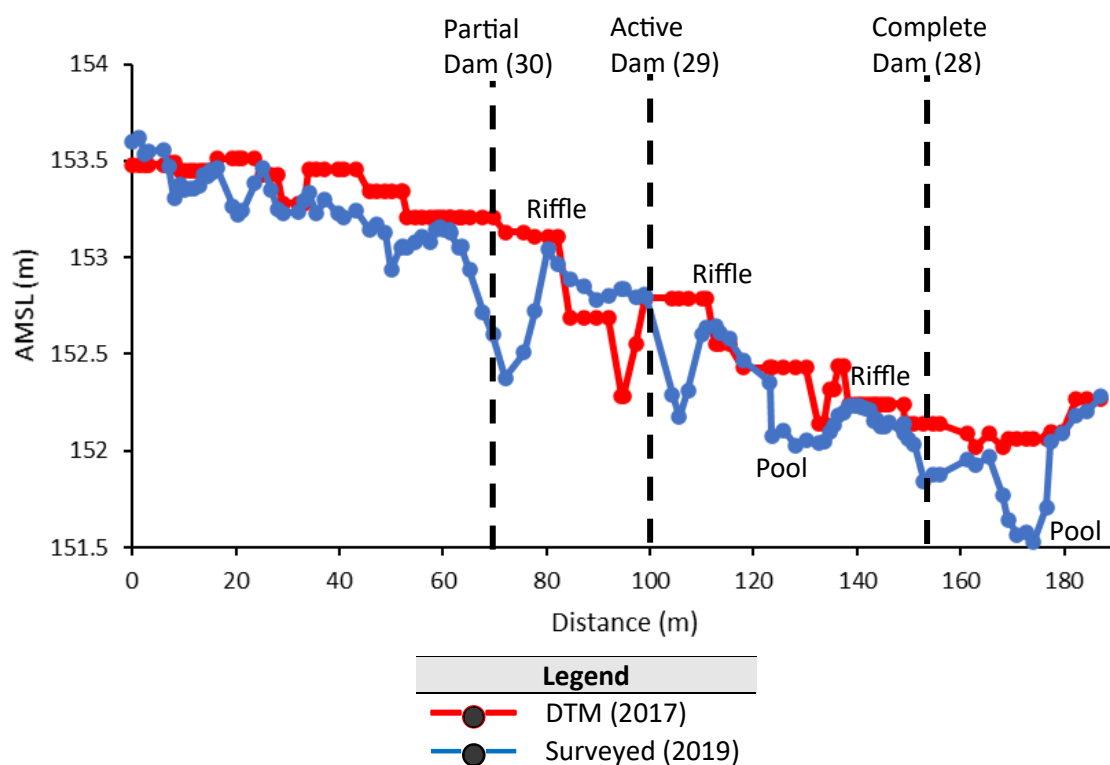
Figure 5.16: Longitudinal profile downstream at sampling points measured from Average Height above Sea Level (AMSL).

Comparative analysis between the DTM (2017) to the surveyed longitudinal profile (2019) shows spatio-temporal change has occurred since dam installation. As forementioned in section 5.2.4.3. comparison can be made between the surveyed section and the DTM as the DTM was acquired during a period of dry weather at low discharge. This meant the LIDAR could capture a precise bathymetric point cloud.

Geomorphological variability has increased which previously was relatively morphologically homogenous with less height variability. The natural pools were historically associated with bends (e.g. distance: 83-100 m). With WDDs causing river forcings there is greater diversity of hydraulic conditions resulting in a greater quantity of pools and riffles and larger areal extent. WDD presence has resulted in rapid local morphological changes over 2-4 years (2017-19).

5.3.5. Lower reach study site

In the lower course Wilderhope Brook joins the River Corve and therefore the valley bottom width runs parallel to the River Corve's longitudinal profile. The channel remains relatively straight with slight changes becoming more sinuous with a sinuosity index (S_i) calculated at 1.221 (1935) and 1.233 (1995) before stabilising at 1.23 in 2017 (Figure 5.17). Particularly notable between active dams 16 and 17 a 40.91 m meander has developed over a period of 60 years (1935-95). The remains of the historic channel 21.47 m long remain active in 1995. By 2017 the historic channel has infilled which is still notable in 2020 (Figure 5.18). By 2017 the bar has become submerged. Flow depth is dependent upon season and therefore in winter months the water course can resemble the 2017 planform. Active dam 16 (Figure 5.17, photograph), located at the meander exit, has formed a seasonally varied backwater pool.

Between the confluence of the River Corve and Wilderhope Brook to complete dam 2 there is evidence that the average main channel width ($\overline{B}$) narrowed from 1935 to 1995 (1935: $\overline{B}$ = 2.6 m, 1995: $\overline{B}$ = 1.26 m) before widening between 1995 to 2017 (2017: $\overline{B}$ = 2.13 m). It can also be noted that the channel becomes increasingly straight between the confluence and dam 2 (1935: S_i = 1.17, 1995: S_i = 1.045, 2017: S_i = 1.038) (Figure 5.17).
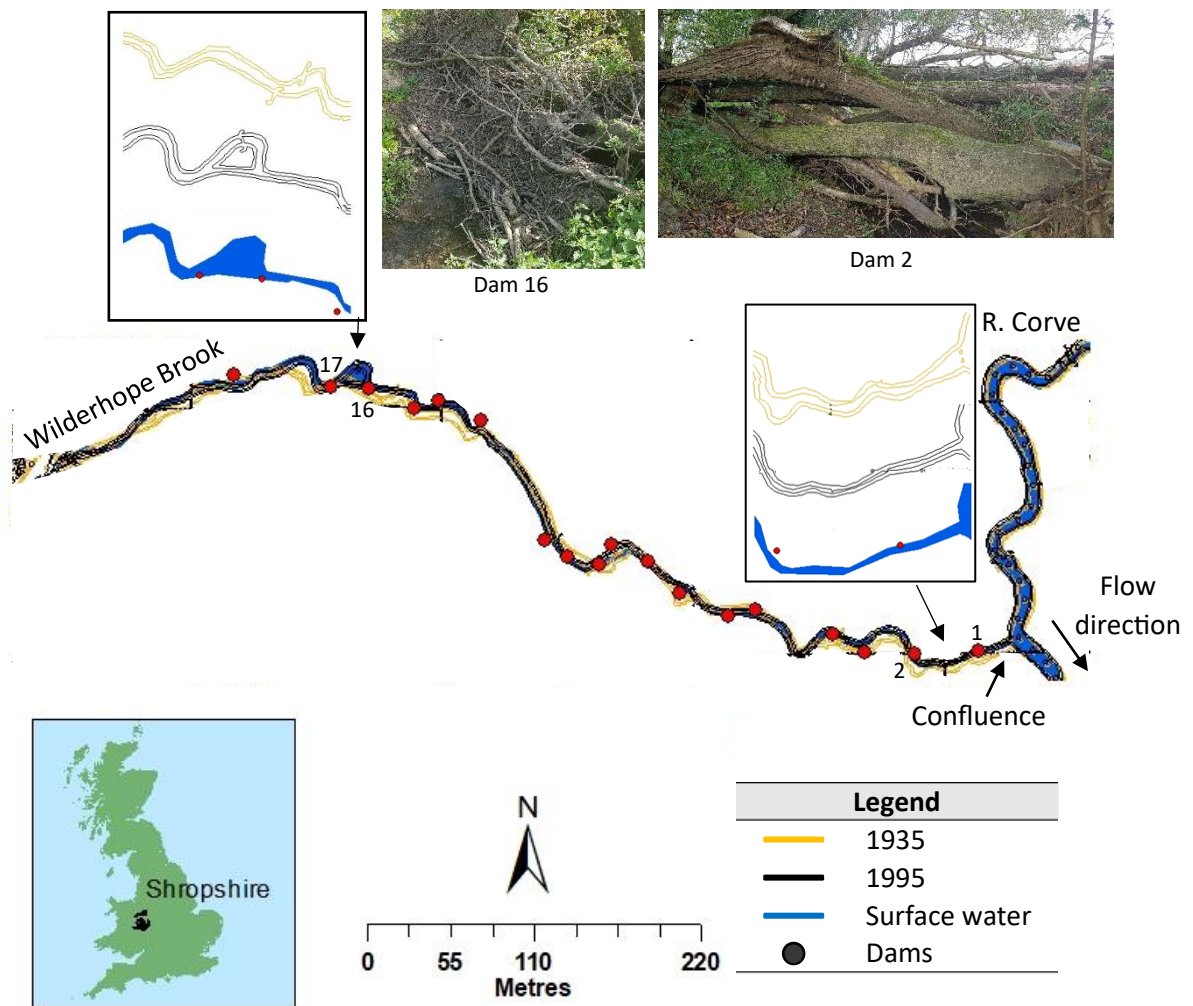
Figure 5.17: A GIS map making comparison between 1935, 1995 and Surface water (2017). Two sections are extracted to show greater variance between dates. Between dam 16 and 17 the channel has developed into a small meander prior to infilling. Dam 16 photograph displays an active dam that can successfully lead to bar overtopping particularly during high discharge. Between the confluence and dam 2 the channel has become narrower and straighter. Dam 2, a complete dam, is located at the start of the straight and narrow channel.
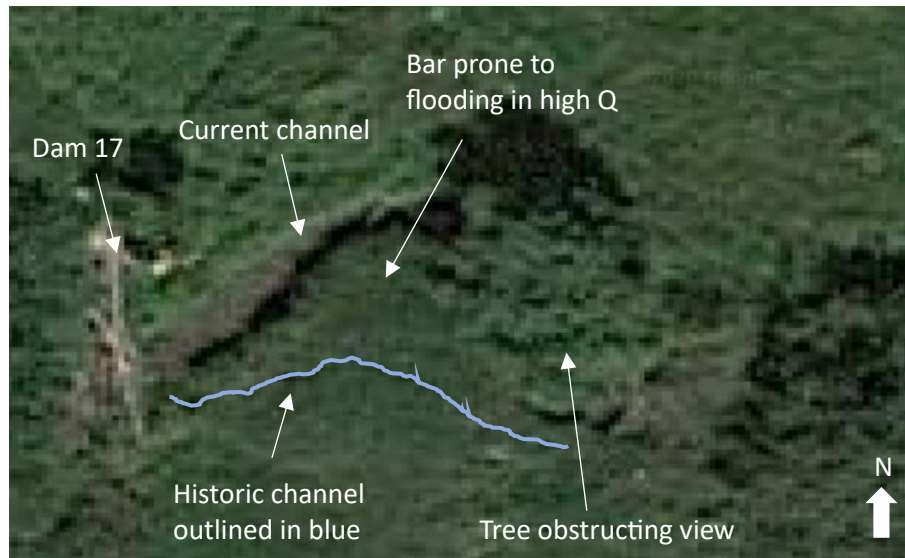
Figure 5.18: An annotated google maps satellite image (2020) showing Wilderhope Brook lower reach with the historic channel (outlined in blue) and 2021 channel displayed on image. Dam 17 is displayed to the west of the image. Image has a 0.15 m spatial resolution.

5.3.6. Sinuosity index

Overall, within the study reaches, there has been negligible change. Channels with a sinuosity index less than 1 are referred to as straight and between 1 - 1.5 are referred to as sinuous (Gordon et al., 2005). This indicates Wilderhope Brook is relatively straight with slight sinuosity curvatures depending upon location. In the mid study reach the channel has changed from transitional to relatively straight and in the lower study reach, channel sinuosity has changed negligibly (Table 5.4).

Table 5.4: Study reach channel sinuosity.

Study Reach sections	Sources	Route length (m)	Direct length (m)	S_i	Change
Mid	OS map, 2017	207.93	156.71	1.327	Decrease 10%
	Surveyed, 2019	187.08	156.71	1.194	
Lower	County series, 1935	776.71	636.11	1.221	Increase 0.98% Relatively stable
	National Grid, 1995	784.08	636.11	1.233	
	OS map, 2017	782.15	636.11	1.23	

5.4. Discussion

5.4.1. Planform adjustment within the catchment

Valley bottom width is a good indication of whether water courses are confined or unconfined as it shows if there is available space for lateral migration (O'Brien et al., 2019; Joyce et al., 2020). Wilderhope Brook, has a relatively large valley bottom width ranging from 126 m – 847 m mid reach to upper course (Figure 5.11 and Figure 5.12) which by itself presents as topographically unconfined. However, the mid reach is relatively narrow compared to the upper course. The gradually sloping valley bottom width and high slope to the distal edges of the valley, topographically confine the channel. Valley confinement allows less space for the channel to laterally adjust. In the mid study reach, the channel varies from slight to moderately entrenched. In upper catchments, low order streams are reported to often have entrenched channels and are generally topographically confined within narrow valleys (Montgomery and Buffington, 1993) proving resistant to planform adjustment (Fuller et al., 2019).

5.4.2. Pool-riffle and meander formation

Between 1935-95, a meander formed in the lower study reach. Figure 5.17 shows in 1935 (S_i = 1.221) the channel was relatively straight however by 1995 (S_i = 1.233) a meander had developed. During high discharge the water course can flow faster, with least resistance, taking the most direct course across the old channel. By 2017, it is evident that dam 17 at the meander entrance can overtop during high discharge. Dam 16 at the meander exit, with a low throughput attenuates flow, which effectively slows the flow.

WDDs in the mid study reach initiated forced pool-riffle sequences. Transect G has a bankfull stage width (B_{sw}) of 16 m and from riffle to riffle before and after dam 29 is 32.37 m giving a spacing of ≈ 2.02B_{sw} which indicates significant morphological channel adjustment has taken place caused by forced pool-riffle sequencing. The findings of the present study corroborate those of Montgomery et al. (1995) who found that forced pool-riffle sequences typically have pool spacing of < 2B_{sw}. It has been suggested pool-to-pool or riffle-to-riffle spacing normally occurs ≈ 5B_{sw} to 7B_{sw} (Leopold et al., 1964) or ≈ 3B_{sw} to 10B_{sw} with an average of 6B_{sw} (Hey

and Thorne, 1986). Pool erosion and deposition under and downstream of horizontal perturbations depend on structural design: wood height above the bed, key member diameter, key member spacings and wood type but also depend upon discharge and angle of attack (Beschta 1983; Cherry and Beschta 1989). Those WDDs placed perpendicular to the flow regime, above the bed, advect flow downwards towards the bed creating deep scour initiating under the dam (Robison and Beschta, 1990). The mid reach longitudinal profile indicates that the pools have become deep and varied in their depth as demonstrated at dams 28, 29 and 30 (Figure 5.16). This finding is supported by Abbe and Montgomery (1996) who state WDD induced pools demonstrate larger and more variable depth than other types of pools. Since engineered WDD were installed (2017), the planform morphology of pool-riffle sequencing in the mid study reach has changed with increased wetted perimeter and water contact with the channel bed, slowing the flow (Figure 5.16).

5.4.3. Chute Cutoffs

Between the winter of 2017, when the engineered WDDs were installed and 2019 when the field survey was undertaken in the mid study reach, a chute realignment at two meanders had evolved between transects B and F (Figure 5.9). A chute realignment is illustrated in Figure 5.19. Chute cutoffs at meanders are characteristic in water courses of low sinuosity (Van Dijk et al., 2012) such as Wilderhope Brook. A chute cutoff is defined as the formation of a new channel across an inner bend enclosed by a meander loop, which results in the gradual closure of the meander by sedimentation. The abandoned channel is referred to as the cutoff channel and the new channel is referred to as the chute channel (Eekhout and Hoitink, 2015).

Straightening / realignment
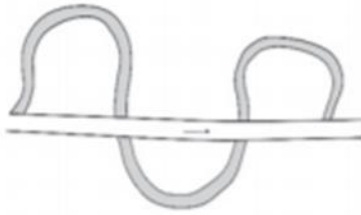
Surveyed mid reach realignment, yellow circles denought sampling points taken (2017-2019)
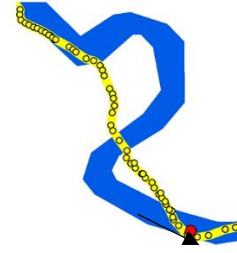
Before adjustment		After adjustment		2017	● Dams	○	Centre line

Figure 5.19: Boundary adjustment. Width adjustments can occur at the channel. Lateral contraction of the channel occurs when the channel decreases its main channel width.

Active dam 29 contributed to the formation of a chute (Figure 5.20), with both chute and cutoff remaining simultaneously active. This WDD has a high trapping efficiency which has infilled the backwater pool, 18 m long. From 2017 to 2019, the pool had infilled by 0.14 m. Dependent upon blocking capacity, dam 29 can restrict the wetted area creating unsteady flow conditions which can enhance shear velocity and downstream erosion.
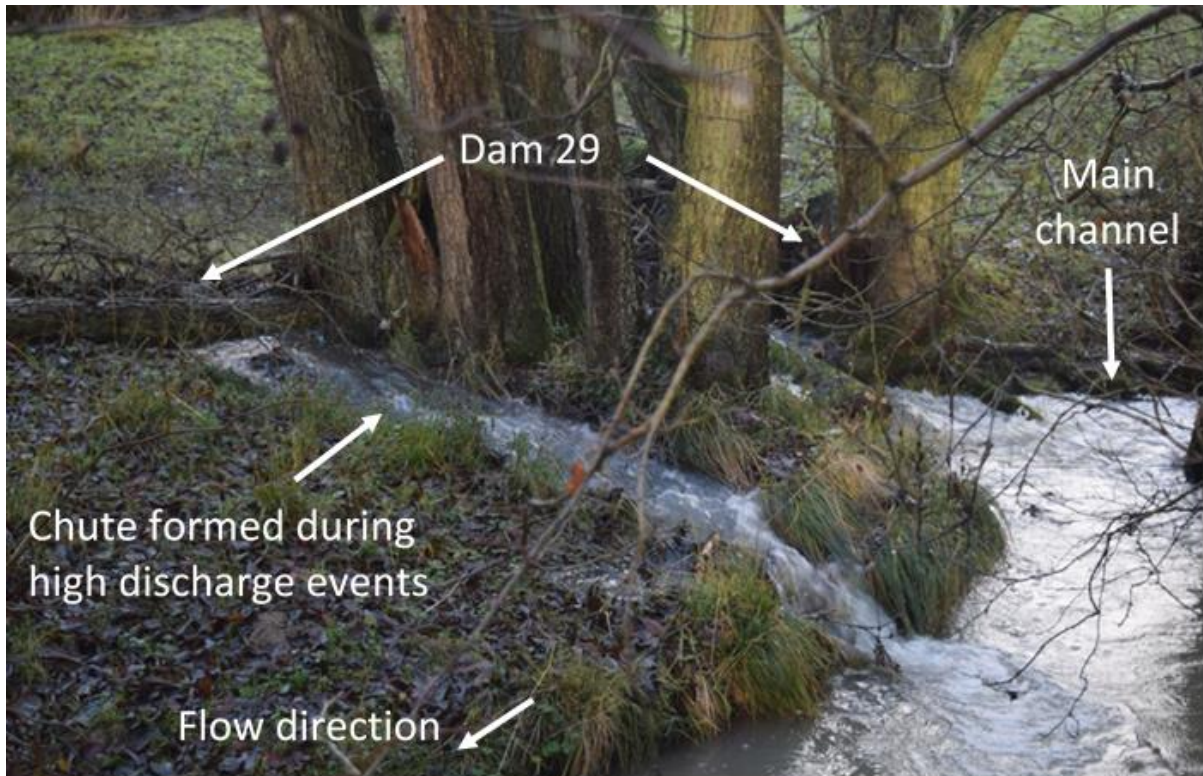
Figure 5.20: Shows a chute and meander remaining simultaneously active. During high discharge, dam 29 has caused the flow to overtop the channel bank and form a chute across the meander neck. This process of channel blockage caused by a WDD is corroborated by Keller and Swanson (1979). The chute diversion can reduce the main channel capacity with enhanced shoaling until eventually the chute becomes the sole flow route (Pinter et al., 2004). However, Grenfell et al. (2012) report partitioned meanders and chutes can continue to co-exist for decades. Photograph by Neden (21 December 2018).

The chute at dam 29 formed across a meander neck during high discharge where the flow regime could no longer be confined to the channel and bank overtopping occurred. Chute formation can develop over several high discharge events (Iwasaki et al., 2016). During high discharge, the new chute breaches the meander entrance limb and takes a short-cut downstream across the meander neck (Constantine et al., 2010). This is caused by a perturbation (dam 29) at the meander entrance where a zone of decreased shear velocity leads to deposition with a build-up of sediment upstream of the WDD. During high discharge, this leads to avulsion whereby the flow overtops the bank, runs across the land and re-enters the main water course. The chute then erodes a new channel back across the meander neck. Meander chute cutoffs reconnect with the main water course through shorter and steeper pathways which increases velocity, thus exacerbating flood risk downstream. The partitioned channel, at dam 29, with the chute and cutoff remaining in action, accelerates discharge.

As chutes form, the water course shortens with a steeper bed and hydraulic gradient which transports more sediment downstream due to increased shear velocity and particle Reynolds number. The channel bed is mobilised by increased τ_b. The ratio of τ_b to τ_c is known as the shear stress ratio (τ_b / τ_c) whereby when τ_b / τ_c exceeds unity or the 'excess shear stress (τ_e)' $\tau_b - \tau_c > 0$ the bed material becomes mobilised. The formation of chute cutoff mechanisms trigger rapid sediment transport into the water course, at much higher rates than bends produce (Zinger et al., 2011). This sediment can be deposited immediately downstream, leading to changes in channel geomorphology. Over time the chute became deeper and wider.

Chute cutoff mechanisms, like dam 29, are related to floods as they require high discharge and high sediment yields (Van Dijk et al., 2014). As WDDs create backwaters and sediment storage areas behind them, when positioned at the meander, they can serve as a location of flow avulsion during high discharge, enhancing chute formation. However, in moderately entrenched / confined channels, vertical change in the bed due to deposition behind WDDs must be higher than in unconfined channels as there is little space for lateral movement around the WDD (Buffington, 2003). Wilderhope Brook, which is a relatively confined channel, will be in this position but in other locations such as dam 29 in the mid reach there is space for lateral migration with a large pool.

5.4.4. Woody debris dams as stabilising and destabilising influences on channel morphology

WDDs at Wilderhope Brook, depending upon design and location, have both stabilising and destabilising influences either promoting or preventing erosion, entrainment and deposition. Destabilisation can occur when the WDD is initially installed, causing $\tau_b > \tau_c$, enabling sediment entrainment. Dependent upon design, a WDD can alter the fluvial hydraulic processes and trigger changes in channel morphology (Keller and Swanson, 1979). Channel stabilisation changes with varying discharge. During high discharge, instability will increase with a higher τ_b. In comparison during low discharge with $\tau_b < \tau_c$ the water course lacks the ability to scour.

WDDs in the mid study reach have the potential to exhibit increased or decreased channel and bank stability, dependent upon their form and location, which can have adverse morphological impact on flood risk. Partial dam 30 in the mid study reach acts as bank protection, stabilising the outer bank while deflecting the flow towards the inner bank causing destabilisation through erosion. Bank erosion can potentially enhance flood risk through channel capacity reduction (Slater et al. 2015) or generate morphological effects further upstream due to varying sediment yields. Due to the position of dam 30, located at the bend apex and exit, the partial dam blocks helicoidal flow and in turn reduces lateral erosion on the outside bank. The high localised velocity core is instead forced downwards increasing bed erosion (Figure 5.21). The partial dam also restricts the hydraulic radius which increases shear velocity and τ_b causing further erosion. Since partial dam 30 was installed (2017) a pool (depth: 0.67 m; length: 18.91 m) was formed by 2019. During high discharge this equilibrium imbalance becomes more prominent with the 'channel corridor' / area adjusting to entrain more sediment (Lane, 1955) though this will stabilise in time with conditions remaining constant. WDD design can spatially vary stability and instability. This finding is supported by Smith (1992), Wallerstein and Thorne (1997) and Rowntree and Dollar (1999) who determined that WDDs can either act as natural flood protection devices or can exacerbate instability by deflecting flow towards a bank.
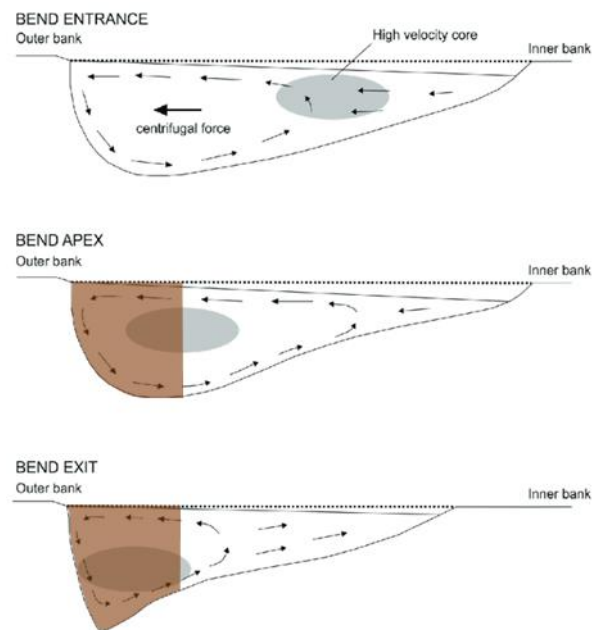
Figure 5.21: A schematic displaying helicoidal flow around a meander bend. The three cross-sections represent different parts of the bend: upstream, middle, and downstream. The grey ellipse represents the high localised velocity core and the brown shaded area represents the wetted area blocked by the partial dam 30. The arrows illustrate the direction of the secondary flow. It can be noted that the partial dam blocks part of the high localised velocity core and therefore will influence the localised velocity core position. Adapted from Kasvi et al. (2017).

Active dam 29, located at the meander apex creates spatial stability by slowing the flow, dissipating energy and enabling deposition in the backwater pool (Rolauffs, 1999). Additionally, dam 29 creates instability by degradation of the bed with the formation of a downstream plunge pool (depth: 0.62 m; length: 10.91 m) caused by the theory of 'hungry water' (Kondolf, 1997). This plunge pool was not present prior to dam 29 installation. The increase in energy downstream of the WDD creates pools with increased scouring, with a pressure gradient from sub-critical ($Fr < 1$) towards super-critical ($Fr > 1$) flow conditions (Kocaman et al., 2020). Energy is dissipated further downstream with flow reverting to sub-critical (Keller and Swanson, 1979). The energy gain after the dam, is often referred to as hungry water, because the excess energy is typically expended on erosion of the channel bed, resulting in incision, Energy (E_n) of the bed, armouring and coarsening of the bed material until equilibrium is reached and the material can no longer be entrained by the flow (Kondolf, 1997; Federal Interagency Stream Restoration Working Group, 2001).

The bed surface is said to be armoured when it is coarser than the sub-surface. The armouring of the bed surface is a result of the flow developing shear stresses being insufficient to move large particles but able to entrain fine particles, winnowing them from the bed surface. This creates a protective coarse layer above the fine particles reducing vertical erosion (Heede, 1981). Increased flow resistance prevents the water course from accelerating downstream. The armoured bed causes turbulence which dissipates flow energy. When flow energy is converted into turbulent eddies, vortices are generated eventually decreasing into smaller vortices with energy being dissipated by viscous forces (Nezu and Nakagawa, 1993). High discharge can break up armoured layers, where larger particles can be entrained at higher τ_b, which can result in channel incision (Curran and Tan, 2010).

Sediment capture behind active WDDs can have a profound impact on the geomorphology of the water course downstream. For instance, in high discharge, if WDDs are located on a meander bend, as dam 29, overbank flow can lead to local avulsion and / or chute formation. There are several examples of armouring and coarsening of the bed downstream of WDDs at Wilderhope Brook whereby during low discharge the cobbles can be seen (Figure 5.22).

Figure 5.22: Downstream of dam 28 in the mid reach illustrating armouring of the bed. The presence of an armoured layer on the bed surface is quite a common phenomenon which increases the roughness of the bed surface downstream of the WDD. Photograph taken: 19th Sept. 2020.

To maintain the required sinuosity over a prolonged time, while continuing to incise, upland streams use meander chute cutoffs to decrease sinuosity (Van Dijk et al., 2012). However, in streams such as Wilderhope Brook, with a low sinuosity, chutes are not effective in balancing lateral erosion to find their steady state (Van Dijk et al., 2012). For example, by adjusting the meander curvature, migration rate and erosional and depositional patterns can alter (Knighton, 1998). A chute forms across a meander neck when the threshold is reached where the channel planform can no longer be maintained, where flow energy and sediment supply is reduced (Environment Agency, 2007). If a channel has a high sinuosity index and a high curvature radius, there is greater potential for geomorphological adjustment. In upland streams such as Wilderhope Brook, with a low sinuosity the ratio of chute to bend curvature is small compared to channels with high sinuosity.

Partial avulsion with divided active channels joining at a confluence further downstream can be seen at dam 29 during high discharge. As a result of avulsion, two channels co-exist: the established or parent channel whose flow has been diverted and the newly formed channel which creates a new route. Full avulsions transfer the flow into the new channel abandoning the original route, whereas this partial avulsion transfers only part of the flow with the two channels co-existing. Backwater can slow the flow downstream during low discharge creating areas of storage but can speed the flow during high discharge, adding additional pre-stored water (Quinn et al., 2007). Meanders and chutes can co-exist, dependent on discharge and sediment transport. With reduced discharge, the sediment transport capacity in the original channel decreases. If the sediment transport capacity remains greater than the supply, both the original channel and the chute can stay active (Grenfell et al., 2012) (Figure 5.20). Otherwise, a sediment plug bar can cause the original channel to close (Van Dijk *et al*., 2012; Van Dijk et al., 2014) which is gradually infilled with fine sediment.

5.4.5. Woody debris dam trapping efficiency

Figure 5.23 (dam 42) illustrates sediment accumulation which can exert changes to the morphology, with the WDD creating a sediment storage zone which acts as a barrier in the sediment routing system (Bilby, 1980). WDDs can cause channel geomorphological change by restricting the wetted area and reducing channel capacity which can generate bank

overtopping and connectivity to the floodplain. Temporally, WDDs within streams can enable sediment storage by reducing sediment transport which creates steeper channel gradients than similar channels without WDDs. By storing sediment, WDDs can create steps in the hydraulic gradient and variability in the bed gradient (Faustini and Jones, 2003). Steps and variability created in the water course dissipate energy that otherwise is available for sediment transport (Keller and Swanson 1979).
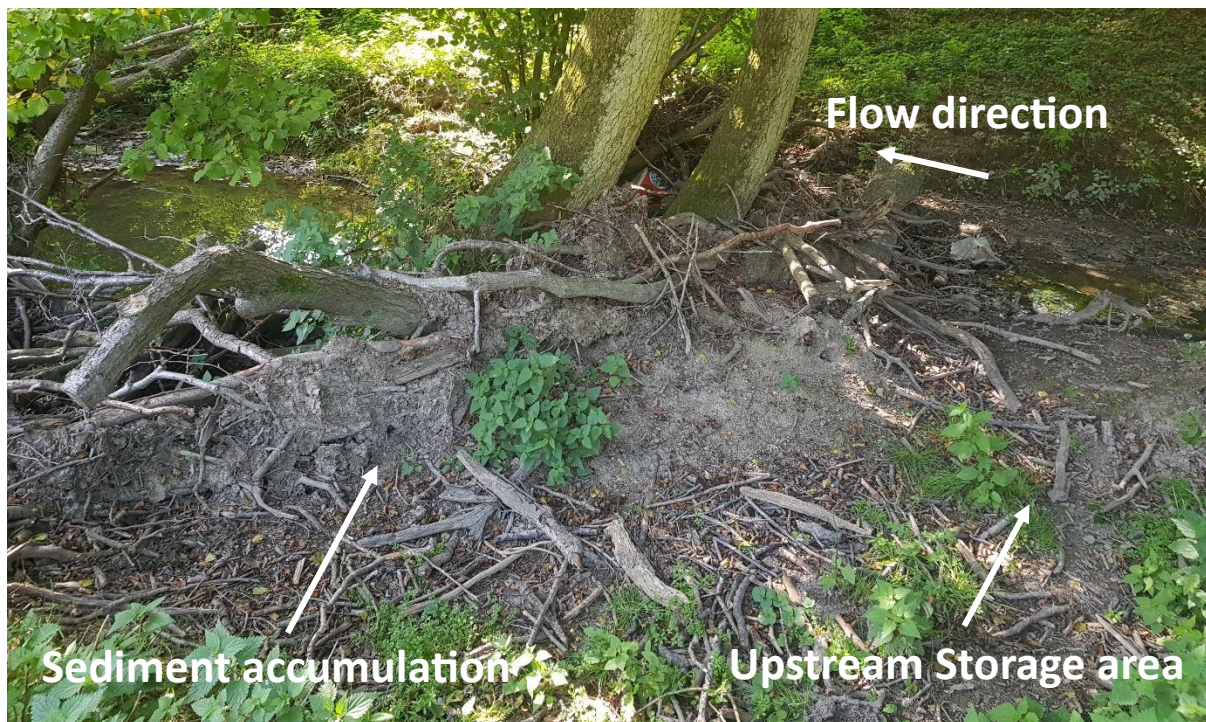
Figure 5.23: Dam 42 upstream sediment accrued behind the dam which could lead to avulsion in high discharge and / or flow avulsing around the WDD. Photograph taken: 19th Sept. 2020.

5.4.6. Morphological response to increased sediment

Fine sediment originates from agricultural land runoff (Palmer, 2012) which proves problematic at Wilderhope Brook with large areas of the catchment being arable and pastureland (Figure 5.5), farmed to the channel banks. The riparian forest which is in generally poor condition along with poaching of land by sheep and heavy farm machinery both contribute to sediment runoff. Pastureland dominates the sloped areas to the east of the catchment, while arable land dominates the west of the catchment (Figure 5.5). After

harvesting, this bare ground can lead to increased surface runoff and reduced lag-time with the west perennial tributary having greater sediment supply compared to the east tributary. WDDs located downstream of the confluence can accumulate more sediment depending upon season compared to WDDs located on the east tributary, upstream of the confluence. Improved grassland holds the soil structure together, reduces soil erosion and reduces sediment transport rates. A study conducted by Dong et al. (2015) found grass cover reduced soil erosion by 63.9 – 92.75% and sediment transport rate by 80.59 - 96.17% under different valley slope angles / gradients and rainfall intensities. It was also found that bare ground showed significantly higher soil erosion and transportation compared to grass-covered land. Randall et al. (2015) found that agriculture land accounts for ≈ 76% of sediment input into UK rivers which restricts channel capacity and can lead to flooding. Wilderhope Brook, spatial variability of erosion can be determined by comparing the remote sensing image (Figure 5.5) to the soil, geology and drainage maps (Figure 5.6, Figure 5.7 and Figure 5.8 respectively).

Increased precipitation Depth, Duration and Frequency (DDF) has made areas such as Ludlow, Shropshire more susceptible to severe flooding. With sediment bed aggradation input increased and narrowing of the channel, the River Corve discharge would exceed channel capacity and flooding can occur (Collier et al., 1996). When the River Corve discharge exceeds channel capacity, flooding can be caused by increased precipitation DDF and/or decreased channel capacity. Increases in the flood hazard frequency amplify both hydrologic and geomorphic effects. Slater (2016) validates that the effect of alteration in channel capacity on flooding can prove hazardous. Excess sediment transferred from the upland tributaries can affect the channel capacity of the River Corve by increasing the flood hazard through increased roughness, scour and deposition and the main channel width (Slater et al., 2015., Dadson et al., 2017). Figure 5.24 shows high levels of sediment exiting the Severn Estuary, the River Severn originating from its source tributaries including Wilderhope Brook.
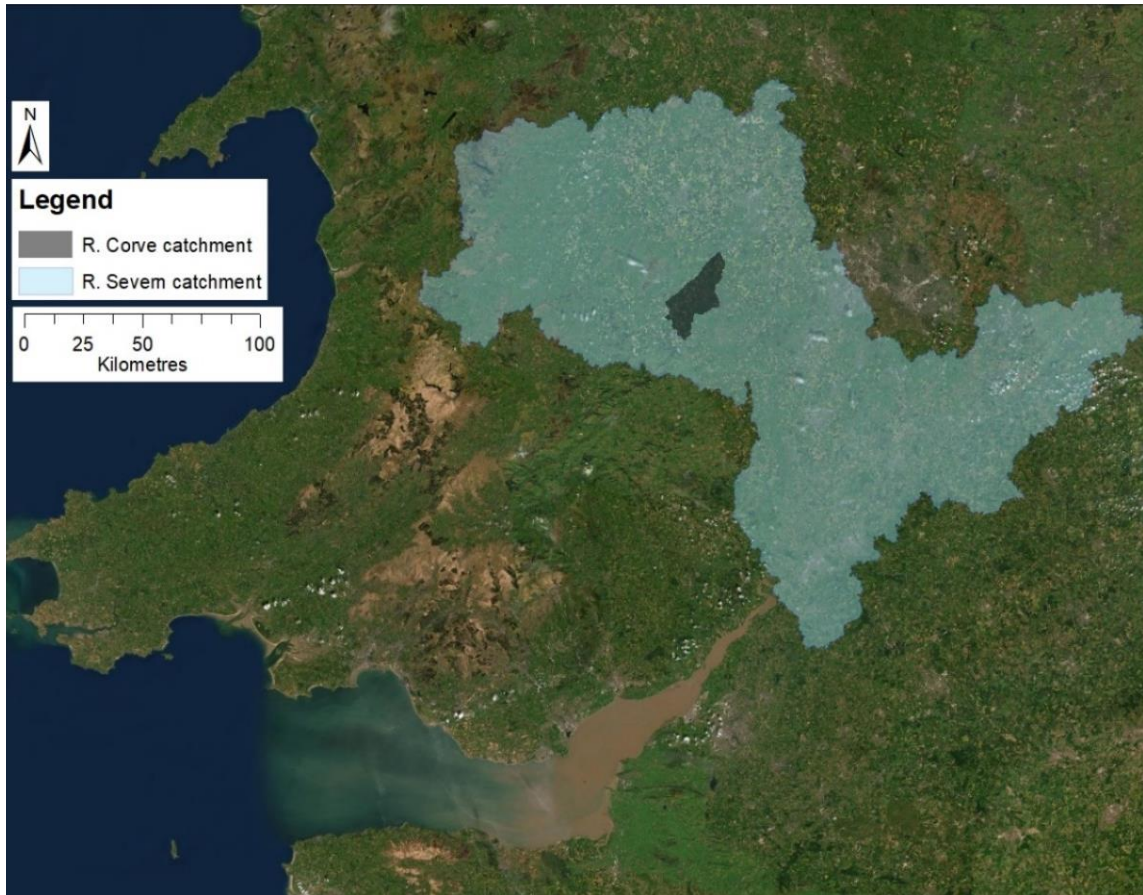
Figure 5.24: Ground truth Terracolor satellite imagery (2020) displaying sediment leaving the River Severn estuary with the River Severn and River Corve catchments also shown. Image resolution ranges from 0.3 m to 0.03 m (down to ≈ 1:280 m in select communities). Base map source credit: Esri, Maxar, GeoEye, Earthstar Geographics, CNES/Airbus DS, USDA, USGS, AeroGRID, IGN, and the GIS User Community.

In low discharge, ponding behind an active dam increases the upstream flow depth whilst decreasing upstream localised velocity. However, during high discharge, with the additional antecedent ponding, the flow depth further increases submerging the WDD until it has little effect on attenuating the flow regime (Wilkinson et al., 2019). Therefore, the effect of active dams on slowing the flow is minimised during high discharge but during low discharge, the lag time increases creating more flood preparation time.

The present study found that to prevent chute cutoff development active dams should be positioned on straight sections with sacrificial land available rather than on meanders, however, constant monitoring and maintenance is required to prevent erosion undermining the structure (Figure 5.25) and becoming unstable during peak discharge. A study in Knyszyńska, Poland, found that if dams were not maintained, within 3-5 years, they lost ≈ 50%
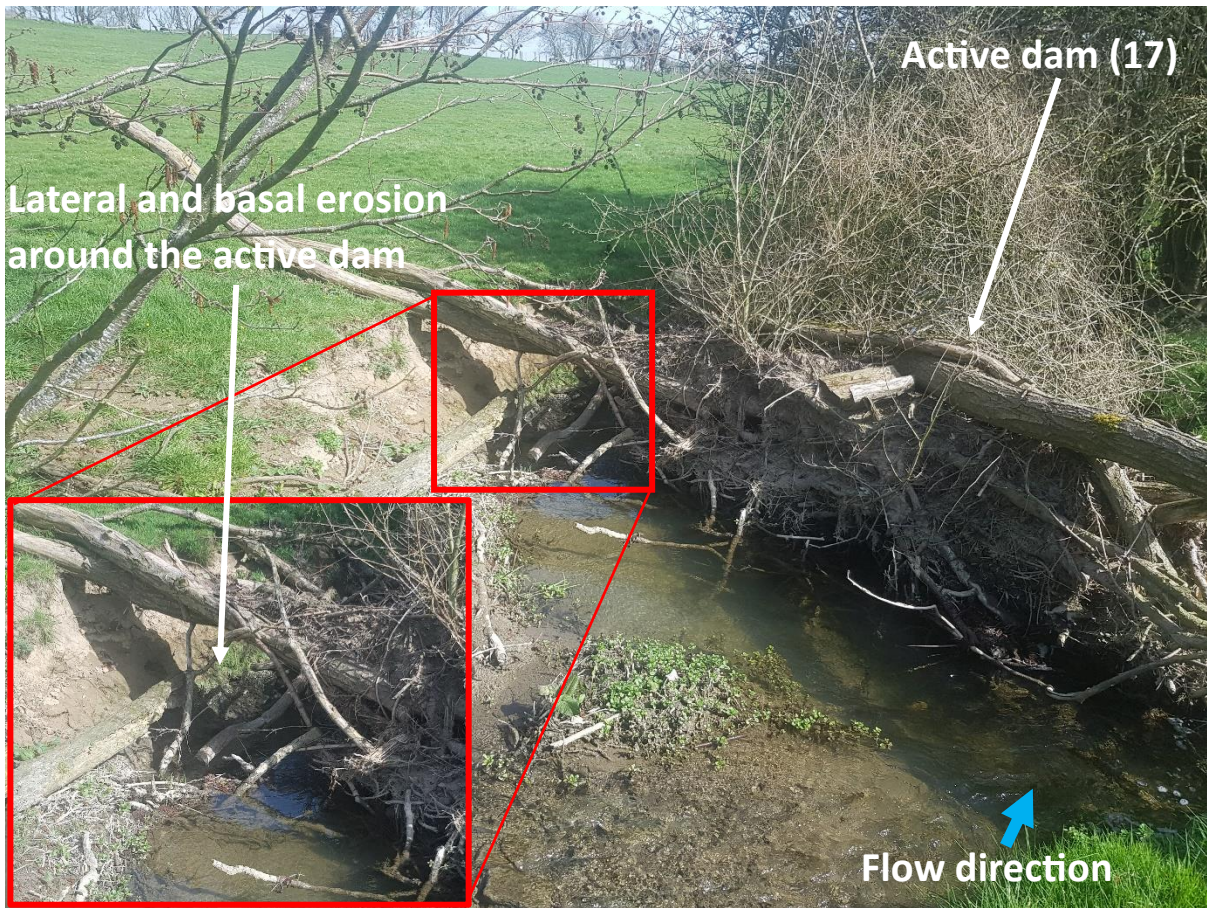
Figure 5.25: Image taken 31 March 2021, over three years after dam installation. This image shows the necessity of maintaining a WDD for maximum hydraulic and sedimentological retention.

In natural riparian woodland streams WDDs typically occur every 7 times bankfull stage width (B_{sw}) to $10B_{sw}$ (Linstead and Gurnell, 1999). Having large spaces between WDDs means that one dam will not affect the next. For instance, dam 29 is located $4.4B_{sw}$ from dam 30 and therefore the backwater generated at dam 29 is submerging portions of dam 30 reducing its effectiveness in preventing outer bank erosion and attenuating the flow. This backwater effect exhibits greater prominence during high discharge where the backwater may completely submerge the upstream dam depending upon location, design and flow depth. The Countryside Stewardship Grant, that pays UK landowners to install WDDs on water courses requires spaces between WDDs to be between $5B_{sw}$ to $7B_{sw}$ (Rural Payments Agency and Natural England, 2020).

5.5. Conclusion

Wilderhope Brook has over the past 84 years remained a single thread first order stream of low sinuosity. The mid study reach channel is largely confined with limited ability to meander. The DTM demonstrates the steep slope angles either side of the channel provide limited scope for lateral migration. Cross-sections in the mid study reach indicate slight / moderate channel Energy (E_n). From 2017-19, since WDD installation, the channel has straightened with chute cutoffs being prevalent at channel bends. The input of engineered WDDs for NFM purposes at Wilderhope Brook has had demonstrable geomorphological NFM effects upon the water course. As geomorphological effects are common to all WDDs, it is crucial to design and strategically place them for the desired hydro-morphologic NFM purposes.

WDDs influence channel morphological processes by inducing pool-riffle sequences as demonstrated in the mid-study reach longitudinal profile (2019). Pools and riffles increase bed roughness, bed heterogeneity, flow variations and turbulence, dissipating energy and so slowing the flow. Partial dam 30, creates bank stability by protecting the outer bank from erosion while deflecting the flow towards the inner bank and downstream enhancing meander development. Concomitantly, dam 30 creates bank instability on the inner bank with increased localised shear velocity to hydraulic radius restriction promoting bank erosion, though this will stabilise in time providing conditions remain constant.

Active dam 29, with low porosity, traversing the main channel width causes a step in the hydraulic gradient. This dam creates instability with deposition in the backwater pool, while downstream of dam 29, degradation occurs with the formation of a plunge pool incising the channel. Heightened backwater caused by trapped sediment results in accelerated overbank avulsion during high discharge and at this location a chute cutoff across the meander neck is developing. Dependent on design and location, WDDs can induce chute development which accelerates the flow downstream by reducing channel sinuosity, shortening the flow pathway and increasing channel gradient. This is an example of an adverse geomorphological effect of WDDs for NFM purposes.

To reduce downstream flood magnitude, design and location of WDDs are important. During high discharge, flow rapidly overtops WDDs. Complete dam (28) designed with large key members positioned just below the bankfull stage, restricts flow during high discharge,

however, during low discharge, flow can pass underneath with no resistance. Therefore, complete WDDs can change their functionality during high discharge.

Flows at stream bends generate hydraulic complexities with point bars on the inner bank and pools on the outer bank positioned on the meander bend apex and riffles located upstream and downstream of the bend. The meander creates heterogeneous spatial depths and velocities, shaping bedform topography. This study indicates it is best to avoid locating active dams on channel bends, as bends already have hydraulic complexities displaying active erosional and depositional processes. If an active dam is installed on the bend there is the potential for sediment and backwater build-up, with the possibility of chute cutoffs straightening the channel which would lead to greater sediment transport, thus limiting channel capacity downstream, which could cause flooding. Dams should be located in areas that enable bank overtopping onto sacrificial land during high discharge. Dams located in entrenched V-shaped valleys have little storage capacity with less likelihood of bank overtopping.

All three designs (active, partial and complete) were found to be effective in the mid-study reach in creating a heterogenous bed morphology of pools and riffles. The three dam designs described by Gregory et al. (1985) all behave differently and have varying hydraulic effects depending upon locality and discharge. Appraisal of WDD effectiveness within the catchment is necessary to ensure their design and location have the desired morphological function to attenuate flow.

The present study focuses on one catchment with its unique characteristics. Future research should extend this work to other catchments to analyse whether these findings are transferrable and consider how to best locate WDDs to utilise their geomorphological benefits for NFM purposes.

6

Modelling hydraulic and hydrological impacts of woody debris dams in an upland stream at Wilderhope Brook, Shropshire, UK

6.1. Introduction

Since the mid-20th century, there have been major changes in agricultural practices and land use in the UK, in response to government policy and technological development, chiefly prompted by demand for self-sufficiency for food production (Wheater et al., 2008; Zayed and Loft, 2019). To make farming more efficient, farmers were encouraged to increase field size by removing hedgerows allowing larger, more powerful machinery (Robinson and Sutherland, 2002). This led to channelised streams with no riparian buffers, changes in land drainage connecting hill slopes to stream channels, heavy machinery ploughing to the stream banks and cultivation practises resulting in soil compaction, reduced infiltration and greater surface runoff to the water courses (O'Connell et al., 2007; Wheater et al., 2008). Changes in land use practices have therefore inadvertently led to a decrease in the capacity for many catchments to retain storm runoff (Wheater et al., 2008). Heavy precipitation and runoff, generated at a local scale, have been found to propagate at the catchment scale combining to impact on increased downstream flood risk (Welton and Quinn, 2011). At 2°C climate change scenario, there is medium confidence that heavy precipitation and associated flooding is projected to intensify and become more frequent across Europe (IPCC, 2021).

One Natural Flood Management (NFM) approach is to use Runoff Attenuation Features (RAFs) in agricultural catchments. A WDD is an in-channel RAF, designed as a small-scale intervention structure to slow flow and store water during high discharge (Q), so reducing downstream flooding. The natural characteristics of WDDs are complex, with porous accumulations of wood and other organic material difficult to represent in experimentation because their

hydrological and geomorphological function varies dependent on their individual physical form and location (Hankin et al., 2020). WDD designs range from basic structures, composed of a single key member in the stream, to channel spanning tree trunk with accumulated wood pieces composed of twigs and leaves (Manners et al., 2007). Furthermore, their hydraulic effects are sensitive to discharge (Beschta, 1983) and are poorly understood (Bennett et al., 2015).

Empirical field-based research has inbuilt logistical challenges, hence more recently, numerical models of the efficacy of WDDs have become a favoured approach to parametrise variations within individual catchments (Leakey et al., 2020). Flood modelling has the advantage of investigating the effectiveness of multiple engineered WDDs at the catchment scale to quantify flow attenuation during peak discharges (Metcalfe et al., 2017). However, there are uncertainties in using WDDs in models due to the inherent difficulty of realistically representing their hydrological and hydraulic complexities (Dixon, 2015). There is no absolute agreed approach in representing WDDs to capture their hydraulic effects in flood modelling which results in variation between studies (Ngai et al., 2017). Scientific knowledge gaps remain; in particular, how best to represent WDDs in hydraulic and hydrological flood modelling as there are currently no bespoke tools (Nisbet et al., 2011; Ngai et al., 2017; Addy and Wilkinson, 2019; Leakey et al., 2020).

To date the most established approach to representing WDDs in models is altering the channel roughness at the WDD location, which simulates observed flow resistances empirically derived from field investigations (Addy and Wilkinson, 2019). The impact of WDDs on in-channel roughness has been investigated by numerous researchers (Kitts, 2010; Dixon et al., 2016; Rasche et al., 2019). However, the use of Manning's n roughness coefficient (n) in modelling has drawbacks, being different between catchments. Moreover, Manning's n roughness is dependent upon flow stage, as once WDDs are surcharged, they can be drowned out (Dixon, 2013). Also, WDD characteristics change seasonally, gathering organic detritus during the autumn months thus changing from complete to active dams impacting their relative drag and roughness (Manners et al., 2007). Another approach is to use geometry adjustment whereby the channel bed is raised to create WDDs (Xu and Liu, 2017; Bair et al., 2019). However, the limitation with this approach is that WDDs are represented as solid objects rather the porous structures they are in reality.

The hydraulic structure representation approach is used to conceptually simulate the effects of WDDs analogous to weirs or culverts (Tammela et al., 2010; Pearson, 2020). For all the above reasons there is currently no specified unit to replicate the effects of WDDs (Ngai et al., 2017; Leakey et al., 2020). Metcalfe et al. (2017) proposed the use of Dynamic TOPMODEL to represent simplified flow restrictors, though no validation was undertaken to predict the complexities of WDD hydraulic effects. Other modellers have used orifices to replicate WDD hydraulic effects (Keys et al., 2018). For instance, Keys et al. (2018) modelled weir embankments using randomly placed orifices. Nonetheless, WDDs contain many of the basic elements of simplified shapes which are used in experimentation to gain understanding of their influence on bed morphology (Thompson and McCarrick, 2010).

There is a call to research into strengthening the reliability of modelling WDDs using the hydraulic structural approach (Addy and Wilkinson, 2019). As the hydraulic effects of WDDs are not static, research which models their temporal dynamics in size and geometry to capture their range of effects is required. The aim of this study is therefore to address the research gap in accurately representing WDDs in a modelling domain (Ngai et al., 2017; Gap: 2.4.8.4.). The objective of this study is to develop an empirically derived hydraulic modelling unit for NFM prediction methodology towards assessing the efficacy of WDDs in attenuating storm events.

6.2. Methodology

To process field data, enable hydrological analysis and quantify the effectiveness of WDDs in flood attenuation, a modelling component was required as modelling provides the ability to conceptualise and replicate flow conditions and build predictive theories (Norbury et al., 2021). Flood Modeller 6.1. (FM) was selected as a suitable software platform providing a wide range of hydrological models, methods and tools capable of modelling Wilderhope Brook. FM has previously been benchmarked against other recognised software packages such as ESTRY, HEC-RAS, InfoWorks ICM and MIKE FLOOD (Environment Agency, 2021c). To benchmark software packages, 5 criteria were used including numerical accuracy, capability, reproducibility, adaptability and form and function (Crowder et al., 2004). Criteria were tested by comparing to real-world situations which are used to standardise flood modelling software

packages, enabling the adoption of consistent principles at each step of the process (SEPA, 2015).

A 1D model was created of Wilderhope Brook within FM, as typically used to simulate in-channel flow conditions which are predominantly confined, as in upland water courses (Ervine and MacLeod, 1999; Garcia-Navarro et al., 1999; Werner, 2001; Collell et al., 2019). 1D modelling primarily focuses upon in-channel flows, including the effects of in-channel structures, while 2D modelling cannot accurately represent structures or in-channel flow especially narrow channels (SEPA, 2016) such as Wilderhope Brook. In the 1D model, floodplain storage was accounted for using a reservoir unit to quantify bank overtopping volume and duration but did not account for floodplain shape and overland flow pathways. To simulate the floodplain at Wilderhope, one reservoir unit was used due to the catchment being small in size with a relatively flat geomorphology that is homogeneous in nature. However, on larger catchments with variable floodplains, separate reservoir units are required.

FM does not include an inbuilt unit specifically designed for modelling WDDs. To represent WDDs, pier-loss bridge units were used to restrict flow and alter roughness. This unit was chosen as opposed to a weir unit, used in chapter 3, because pier-loss bridge units are leaky by design, allowing throughflow during all discharge. This unit was used in accordance with Environment Agency (2021d) guidelines when no specific WDD unit is available within a hydro-environmental model. For modelling purposes, a structure with a ratio of its downstream width to height of less than 5 can be classified as a bridge (Environment Agency, 2021b). Therefore, WDDs within this study were deemed eligible to be modelled as bridges. In agreement with past studies, this unit provides similar hydraulic effects to WDDs (Lisle, 1986). However, it is noted that 1D modelling poses the disadvantage of spatial resolution, whereby model precision is dependent upon user-defined node distances within the river network.

To represent Wilderhope Brook flow conditions within the model, hydrological monitoring was undertaken using field site equipment as discussed in section 4.2.

Due to their porous nature, engineered WDDs allow flow through and over them and are designed with spacings between key members (Water Friendly Farming, 2020). During high discharge, depending upon blockage capacity, WDDs can become surcharged. This can result in bank overtopping, resulting in temporary out of channel water storage areas. This enhances

ground infiltration, slows the flow and reduces discharge by extending the lag time and hence reduces flood magnitude. As previously discussed, during the autumn, natural accumulation of leaf detritus and sediment, by WDDs, seasonally change their design making them less porous and altering their hydraulic effects and attenuation rates. Photography provided a means of documenting WDD structural changes between the winter and summer. These photographs taken at the study site (Wilderhope Brook) were used to create a benchmark for modelling the pier-loss bridge units to more realistically represent WDD blockage capacity.

6.2.1. Model scheme (schematisation)

6.2.1.1. Field surveying using leveller and photography applications

A surveying study at both the Mid (15 m upstream and 3 m downstream of WDD 23) and the lower reaches was conducted at Wilderhope Brook on the 1st Aug. 2019. This study enabled acquisition of detailed cross-sections which are essential for hydraulic modelling as the river bathymetry controls flow characteristics (Betsholtz and Nordlöf, 2017). Before conducting the survey, weather conditions were monitored for a one-week dry period. This dry period ensured reduced discharge allowing for a mostly dry bed to be observed.

Using a similar technique as outlined in section 5.2.3. a standard aluminium tripod was set up but this time a leveller was finely positioned directly above the control point using the optical plummet. Upon leveller set-up, a chain was stretched perpendicular to the water course, from the closest tripod leg to the channel, across the main channel width to a vertical geo-referenced post placed on the adjacent bank (Figure 6.1). Additionally, a taut 30 m PVC tape (resolution: ±0.001 m) was stretched between the tripod leg and the adjacent post. The chain and PVC tape helped guide a second person holding a DeWalt DE0734, 5 m Aluminium Construction Grade Rod. The person holding the rod placed it on the bed in a vertical upright position with readings taken at distances every 0.25 m. The person at the leveller focused the telescopic sights on the rod and read where the stadial cross hairs met with readings taken to the nearest centimetre.
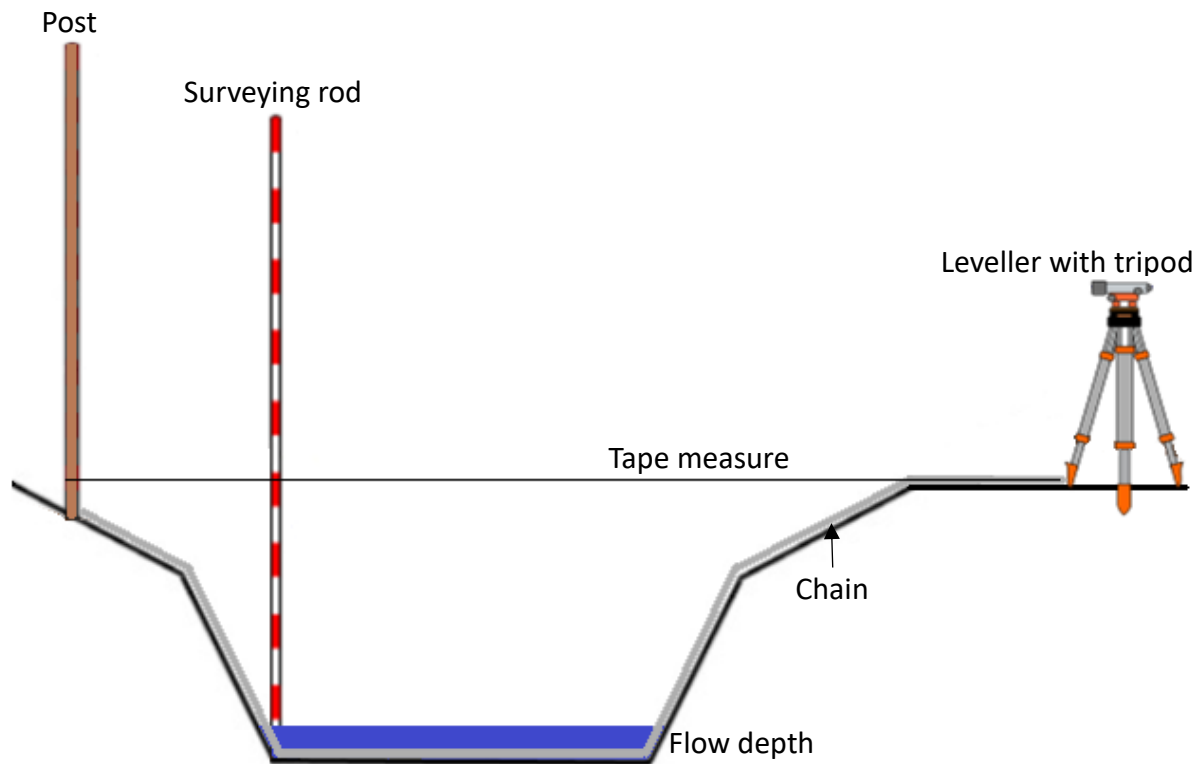
Figure 6.1: Schematic showing set-up of levelling equipment.

The photography application (app) method was undertaken and compared to the leveller survey to ascertain surveying precision and enable calibration. 'ImageMeter pro' app was identified as a suitable tool to aid analysis. The pro version of the 'ImageMeter' app allowed unlimited measurements that were needed to construct cross-sections (ImageMeter, 2021). The app was specifically chosen for its capability of measuring distances from photographs without the need for in-person physical measurements. To ascertain measurements and distances, calibration of photographs was required. Within the app, the 'perspective references' tool was used to measure a physical object of a known size which acted as a benchmark referencing point to measure distances. Use of the 'perspective references' tool enabled geometric computational distortion correction (ImageMeter, 2021).

In addition, a 'Level Camera' app was used enabling orientation of photographs by providing a horizon line with inclination angle upon photograph acquisition. This was achieved using a spirit level with acoustic feedback within the app. As per recommendations, magnets and electric fields of nearby objects were avoided as they potentially influence sensor feedback and distort the orientation.

Upon completion of the leveller survey, the leveller was removed and replaced with a box of a known size (width: 0.305 m, height: 0.235 m). This box acted as the 'perspective reference' for the 'Imagemeter' app. To increase accuracy, the chosen reference was as large as practicable (ImageMeter, 2021). Photographs were taken using the 'Level camera' app in the water course perpendicular to the chain spanning across the main channel width (B). The box, post and chain were positioned in a single plane within the camera FoV. Vegetation cover was carefully removed to ensure FoV could be maintained. Images were imported into the 'Imagemeter' app and distances calculated using the app. Both the leveller and photography app methods of surveying were applied upstream and downstream of WDD 23, as displayed in Figure 4.3 (section 4.1.) which is located in the mid-reach. Once the photography app method was verified, it was used to survey the 0.2 km section located in the lower reach.

6.2.1.2. Digital terrain model construction

Flood modelling software tools are constantly developing and their application has grown with greater computational capacity and easier access to DTMs and Light Detection and Ranging techniques (LIDAR) (Ali et al., 2015).

An online portal (Bluesky mapshop) provided an interface to browse and acquire a Digital Surface Model (DSM) dataset. A DSM is an elevation model that contains height values of the surface terrain including above-ground features such as buildings and vegetation. In comparison, a DTM is derived by removing above-ground features to expose the bare-ground (ESRI, 2021a). Firstly, a DSM of the study area (Wilderhope) was acquired by navigating to the Area of Interest (AoI) through the BlueSky mapshop search toolbox. The 'draw box' icon allowed fine tuning of the selected area within the viewport. After selecting the AoI, a Photogrammetric DSM (Resolution: 0.25 m, horizontal accuracy: ±1 m RMSE, vertical accuracy: ±1.5 m RMSE) was downloaded as an ARC ASCII 9 km x 9 km Mosaic Grid file (date of acquisition: 23rd April 2021).

The DSM was acquired through LIDAR using an Optech Galaxy with integrated Optech LW640 Thermal Camera mounted to a surveying aircraft (Figure 6.2) (BlueSky, 2021). Generally, aerial LIDAR is the best DTM for flood modelling (SEPA, 2020).

Figure 6.2: Photograph displaying an Optech Galaxy with integrated Optech LW640 Thermal Camera mounted to a surveying aircraft (BlueSky, 2021).

A similar method to convert the DSM into a DTM, as described in section 5.2.5.3., manual editing removed unwanted above-ground features (Figure 6.3 and Figure 6.4). Once the DTM was constructed, it was imported into FM.
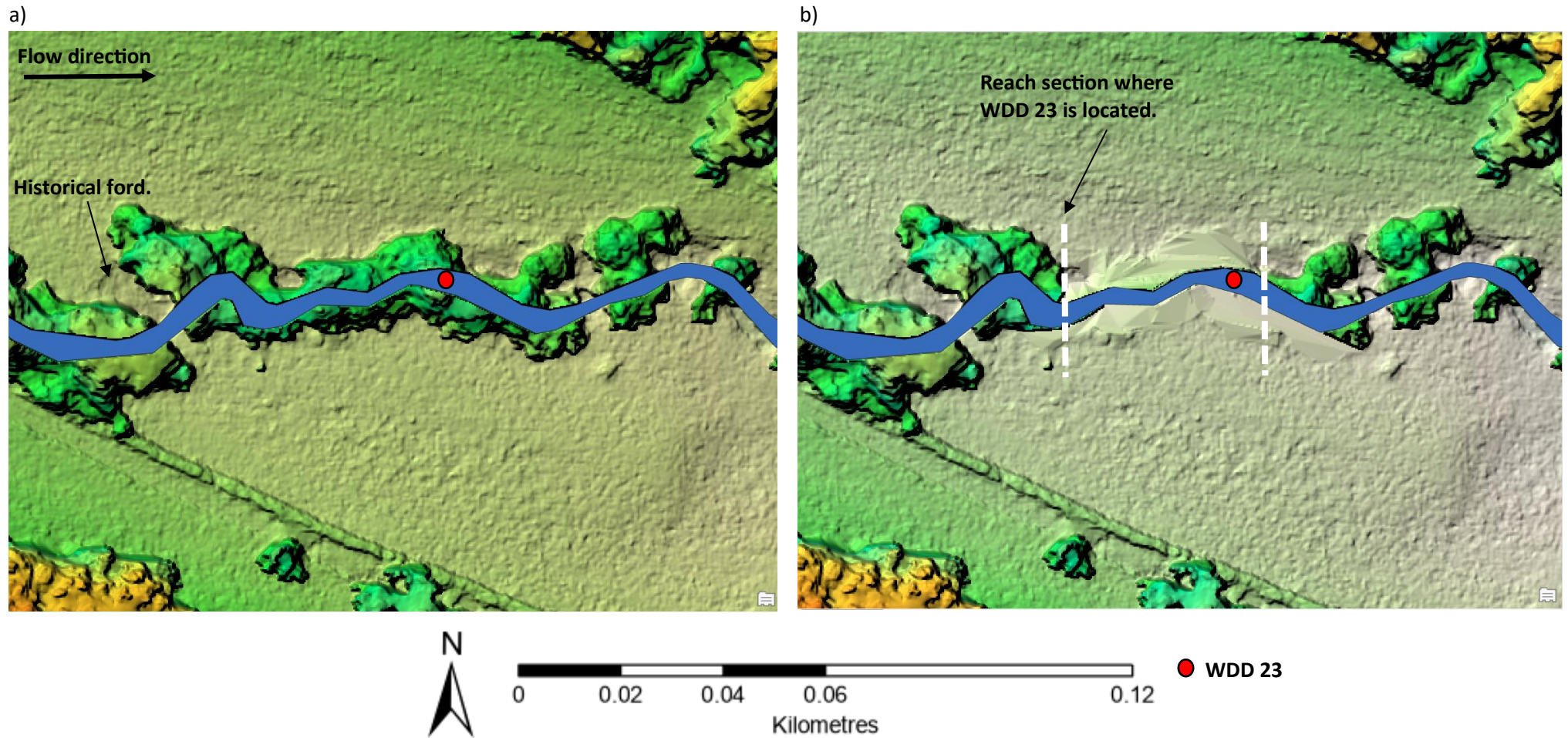
Figure 6.3: 3D representations of the surface shaded relief at Wilderhope Brook mid reach, a) with trees and b) without trees on the floodplain and bordering the channel. The water course has been highlighted in navy and WDD 23 is represented by a geo-positioned red dot. The beginning and end of the study reach marked with white dashed lines. 3D representations were constructed using ArcGIS Pro 2.9.0. by manual editing tree removal.
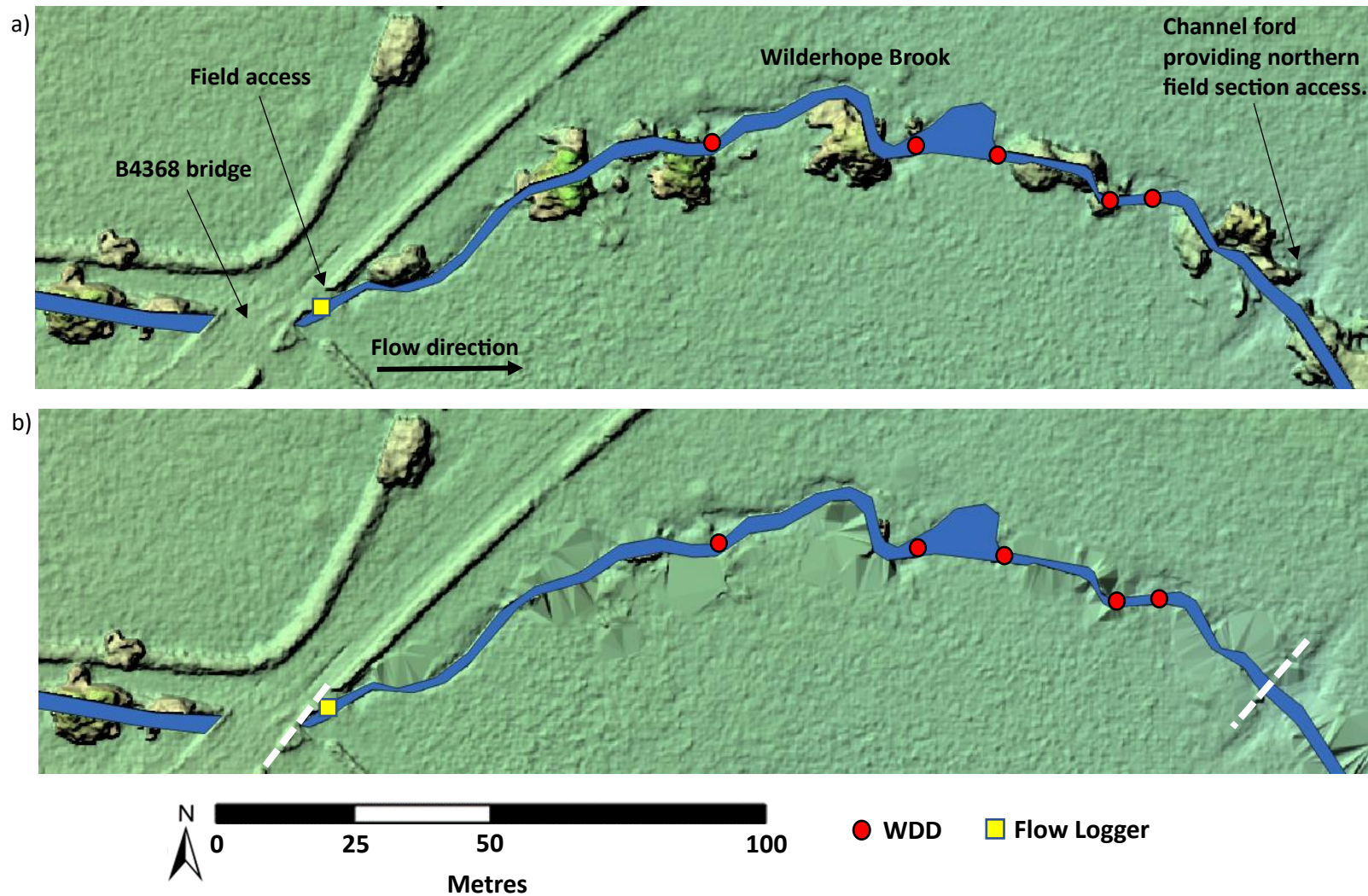
Figure 6.4: 3D representations of the surface shaded relief at Wilderhope Brook lower reach, a) with trees and b) without trees on the floodplain and bordering the channel. The water course has been highlighted in blue and the beginning and end of the study reach marked with white dashed lines. 3D representations were constructed using ArcGIS Pro 2.9.0. by manual editing tree removal.

6.2.1.3. Surface water acquisition

To highlight the water course, EDINA Digimap allowed an interface to browse and acquire an OS mastermap (2017) which was downloaded and imported into ArcMap 10.5.1. This mastermap acted as a base map which provided an outline of the water course with the project and transformation coordinate system set to 'British National Grid'. The water course was identified within the geoprocessing tool to enable the creation of a spatial subset and remove noisy, unwanted data, external to the water course. The water course was extracted in an original 'raster' format using the Arc toolbox > spatial analyst > extract by attribute, which allowed query-building from selected subset features and table records (Equation 5.6 as shown in section 5.2.5.). Once the water course (2017) polygon had been extracted it was imported into FM.

6.2.2. Model calibration

Model calibration is defined as 'The procedure of adjustment of parameter values of a model to reproduce the response of reality within the range of accuracy specified in the performance criteria' (Refsgaard and Henriksen, 2004). Statistically, this requires adjusting the parameter values of the data-set input of the model, to ensure the output data closely matches the empirical data. Many studies that represent WDDs have not calibrated results using on-site field data (Leakey et al., 2020).

To calibrate the model to field data, WDD 23 located in the mid reach (Figure 5.1) was chosen as pressure level sensors were placed upstream and downstream of this WDD as discussed in section 4.2.3.

6.2.2.1. Constructing cross-sections

Upon ascertaining both the DTM and water surface profile layers, these layers were imported into FM. The DTM layer provided initial vertical elevation data (z-values) for the construction of new cross-sections and enabled geo-referencing of data to set viewport boundaries. The water surface profile highlighted the water course location within the DTM. A water course centre line was drawn as a standard format polyline shapefile, using the FM shapefile editing

tools starting 15 m upstream of WDD 23 and ending 3 m downstream (Figure 6.3). As Wilderhope Brook is a single thread stream, a single polyline was required.

The cross-section generator enabled the creation of cross-sections along the water course centre line. Cross-sections were set at fixed distances of 12.5 m along the centre line longitudinal profile with a global Manning's n roughness coefficient of $0.022 \text{ s/m}^{\frac{1}{3}}$. An appropriate channel roughness value was categorised as 'Earth channel – clean' (Chow, 1959) due to the bed being constructed of coarse silty loamy soils (Figure 6.5:). Points per each cross-section were set at 12 for left / right bank length: 3 m. The first node name was defined as 'Wilderhope_1', with subsequent node names incrementally increased by 1 every 12.5 m with an extra cross-section added to the end of the polyline. Upon inserting variables, new cross-sections were created and displayed on the Network section and loaded into the viewport.

The edit tool enabled node cross-section segment extension with the number of points per click set at 10, minimum distance between points set at 0.25 m and Manning's n was set to $0.03 \text{ s/m}^{\frac{1}{3}}$ to represent the floodplain (Chow, 1959). Both banks were extended perpendicular to the flow regime. To assign z-values to points on the node cross-section, the set missing z function in the layer editor allowed extraction of ground elevation data from the DTM. To reduce and remove error and enhance precision, regular review of node cross-sections was undertaken by selecting and checking each of them.

To verify the DTM, photography app method of the surveyed cross-section was compared to the DTM z-values within the channel. Points per each cross-section were compared at 0.25 m distances with number of points depending upon the size of main channel width at the chosen location.
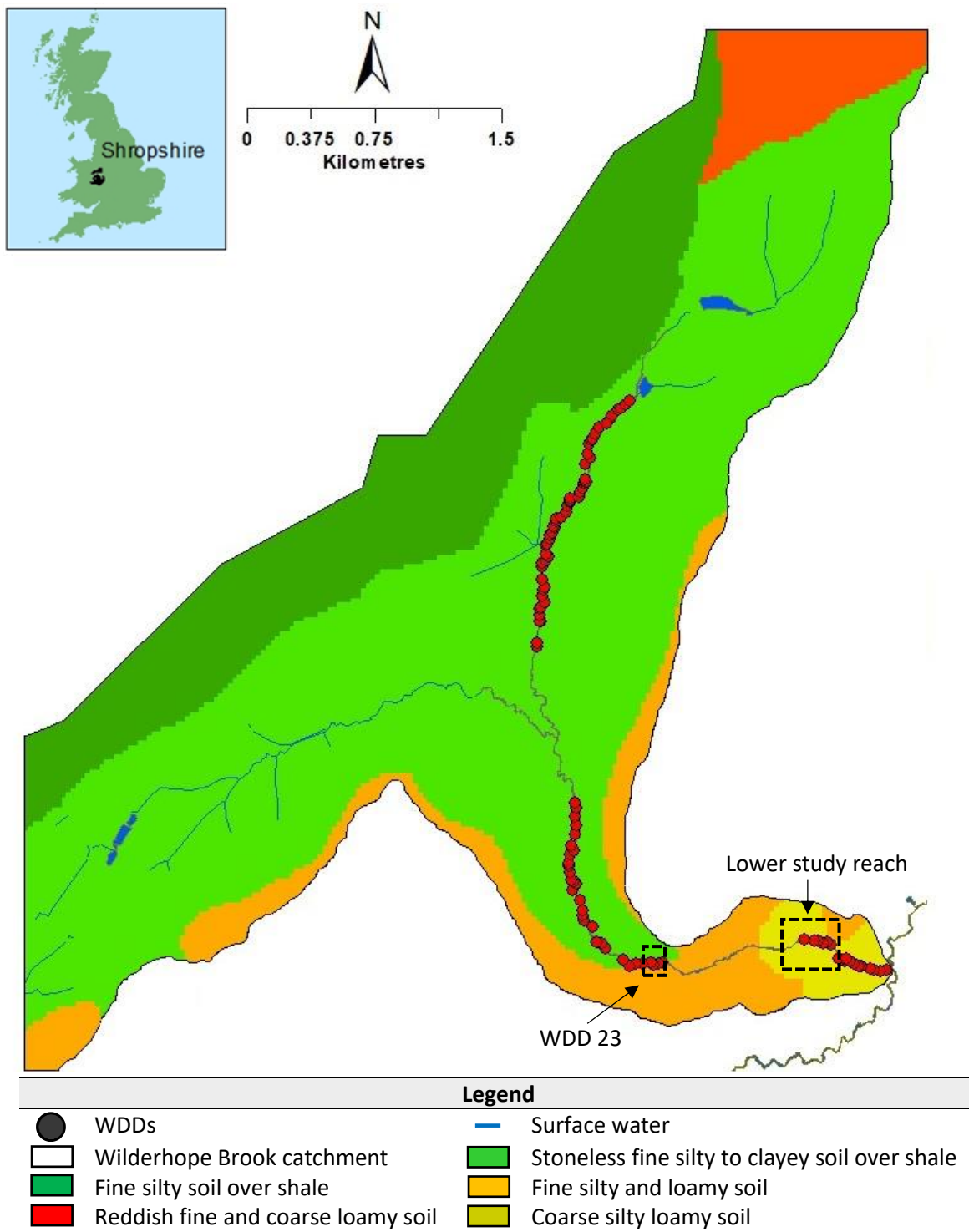
Figure 6.5: Soil map displaying Wilderhope Brook catchment with the water course (2017). WDD 23 and the lower study reach have been labelled to the south of the catchment.

6.2.2.2. Boundary and flow conditions

The 1D build, flow-time boundary (QTBDY), enabled construction and modelling of a discharge hydrograph (Figure 6.6b). The QTBDY was selected and inserted at the upstream end of the network ('Wilderhope_1'). To ascertain appropriate QTBDY conditions, a notable 100-year return rate summer storm event (10th – 12th June 2019) and a 50-year return rate winter storm event (15th – 17th Feb 2020) (Figure 4.2 as shown in section 4.1.) was identified using the tipping bucket rain gauge and verified in Microsoft excel using discharge data provided by the flow logger. As per the Meteorological Seasons, summer months were defined as June, July and August while winter months were defined as December, January and February. There is limited empirical evidence of the influences WDDs have on storm events due to their stochastic nature and the difficulty in capturing long term storm data (Keys et al. 2018; Wingfield et al., 2019).
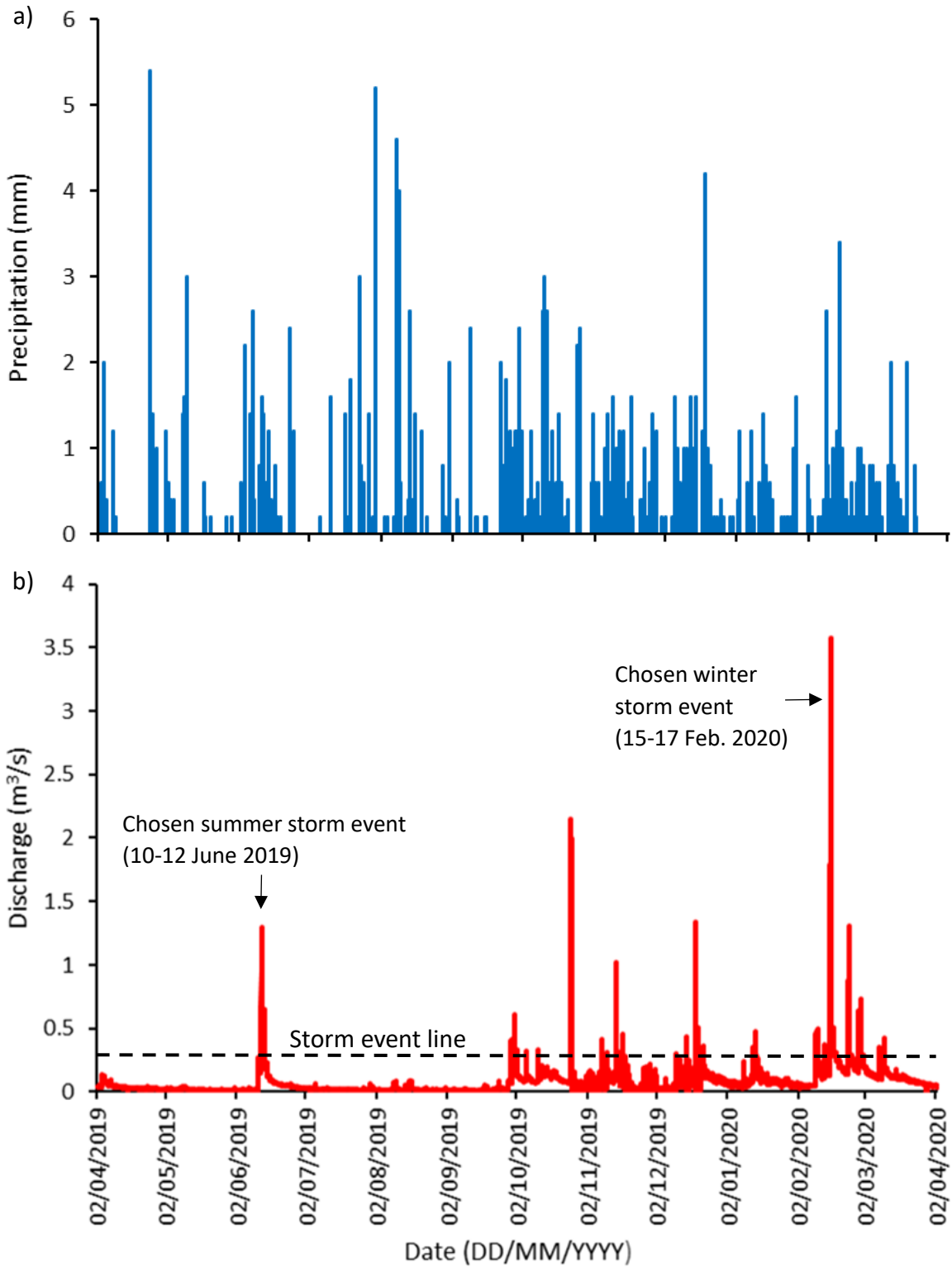
Figure 6.6: a) Hyetograph displaying rainfall intensity as measured using the tipping bucket rain gauge. b) Hydrograph displaying discharge variability as measured using the flow logger. Storm events are identified with discharge more than 0.2 m³/s.

The hydrograph (Figure 6.6b) displays 10 notable storm events that occurred between the 2nd April 2019 and the 2nd July 2020. For the present study both summer and winter storm events were selected providing a maximum discharge of 1.3 m^3/s and 3.57 m^3/s respectively. Storm event data was extracted and input as a boundary condition within FM. A summer event was chosen as previous rainfall would not affect modelling and therefore WDD efficiency was explored with minimal interference from past events. A winter storm event with increased blockage capacity, representative of additional detritus material, was also selected to make comparison to the summer storm event, where it would be assumed the WDD would be more porous and the catchment more permeable (La Torre Torres et al., 2011).

Dry and wet periods were identified from Figure 6.6 with predominantly dry periods occurring during the summer months (2nd April 2019 until the 27th Sept. 2019) and wet periods predominately occurring during winter months (27th Sept. 2019 until the 10th March 2020). During the summer storm event the dry and warm weather was interrupted by sporadic thunderstorms with heavy depth, short duration rainfall with reports of localised flash flooding (Smith, 2019). The soil type in the mid-upper reach consists of stoneless fine silty to clayey soil over shale, while in the lower reach coarse silty loamy soil is dominant. During the prolonged dry spell, the clayey soil dries and shrinks which causes desiccation cracks to form in the mid-upper reach (Tanner, 1978). This compacted hardened ground would have resulted in increased surface runoff, by sheeting water, into the channel though these areas are sparse with most of the land cover consisting of vegetation. Vegetation breaks the surface soil, enhancing infiltration with the summer providing a low water table which slows the flow (Umholtz, 2020).

During the winter storm event the sub-surface layer was prior saturated by Storm Ciara, which it is perceived would have decreased infiltration, enhanced surface-runoff and increased channel flow depth (Met Office, 2020). On 16th February 2020, Ludlow recorded the worst flooding in more than a decade with 50 properties flooded in lower Ludlow. Ludlow is situated at the confluence of the River Teme and the River Corve. Wilderhope Brook is an upstream tributary of the River Corve. The worst affected areas were Lower Corve and Temeside where it has been stated the flood walls, which protect the town should be raised (Kibbler, 2021).

For the present study, storm events were determined as being outliers (O_I) which exceeded normal flow. Equation 6.1 calculated O_I with variables including the upper quartile (Q_3) and Interquartile range (I_{QR}). Upon calculation of O_I, discharge exceeding 0.2 m^3/s were determined as storm events.

$$O_I = Q_3 + 1.5 \times I_{QR} \tag{6.1}$$

Equation 6.1 calculated storm events as defined as being outliers (O_I) to the normal flow depth. To calculate O_I, the upper quartile (Q_3) and an Interquartile range (I_{QR}) are required.

To examine whether high discharge events were directly caused by high intensity rainfall events, data from Wilderhope tipping bucket rain gauge was compared to Wilderhope flow logger readings and catchment descriptors marked with a Flood Estimation Handbook Rainfall Runoff Method Boundary (FEHBDY). For validation of results, flow logger data was cross referenced to the tipping bucket rain gauge as aforementioned in section 4.2. Data was additionally cross referenced to Met Office historic rain station data located at Shawbury (355200E, 322100N), ≈ 48.3 km north of Wilderhope to compare rainfall variability across the catchment and further afield within the county. This Met Office rain station was chosen as it is the closest to Wilderhope in which historical data is available (Met Office, 2023). Upon validating results, discharge data was extracted and imported as a boundary condition along with storm event time duration (Table 6.1).

Table 6.1: 24-hour discharge and precipitation readings taken over the peak of both summer and winter storm events (10-12 June 2019 and 15–17 Feb 2020). Peak discharge row is highlighted in blue with 11 hours before and 12 hours after peak storm event. Data extracted from the Wilderhope flow logger was imported as the QTBDY along with tipping bucket rain gauge data.

Time (Hours)	Summer storm event		Winter storm event	
	Rainfall (mm/hr)	Discharge (m³/s)	Rainfall (mm/hr)	Discharge (m³/s)
0	0	0.259	2.8	0.46
1	0.4	0.239	8.2	0.54
2	0.2	0.212	8.4	0.61
3	0	0.2	4	0.69
4	0.2	0.182	1	0.65
5	0.8	0.161	0.8	0.67
6	0.4	0.167	0.6	1.48
7	0.4	0.161	1	1.6
8	1.2	0.189	2.4	1.44
9	2.6	0.18	0	1.45
10	3.4	0.385	1.8	0.79
11	4.4	0.984	2.8	1.22
12	1.4	1.297	1.6	3.57
13	0.8	1.083	0.2	3
14	1.6	0.955	1	3.06
15	0	0.92	0.4	2.94
16	0.4	0.798	0	2.76
17	0.2	0.756	0	2.87
18	0.2	0.663	0	1.77
19	0.2	0.599	0	1.95
20	0	0.542	0	1.86
21	0.2	0.501	0.2	1.76
22	0	0.456	0.2	1.72
23	0	0.416	0	1.61
24	0	0.259	0	1.59
Sum	19	-	37.4	-

A Normal / Critical Depth boundary (NCDBDY) was inserted at the bottom of the network located 3 m downstream of WDD 23 (Figure 6.7). The NCDBDY generated a flow-head relationship based on the inserted data. Rating curves for the summer and winter storm events were created using the last cross-sectional node for comparison between steady and unsteady simulations. Boundary condition was located ≈3 m downstream of WDD 23 so that model inaccuracies, caused by unobserved geomorphic features such as downstream plunge pools, did not affect results. Bathymetry immediately downstream of a WDD could not be precisely acquired due to plunge pool formations. LIDAR is unable to precisely penetrate

turbulent flow and pools are water storage areas making bathymetry data capture difficult (Betsholtz and Nordlöf, 2017). A sensitivity test was performed for structure coefficients especially in areas of high uncertainty (SEPA, 2020).

Legend	
Symbol	**Units**
	QTBDY
	Cross-section unit
	NCDBDY

Figure 6.7: Schematic displaying model boundary nodes without WDD 23 installed. This schematic shows model set-up with three cross-sections, QTBDY and NCDBDY. Distances between cross-sections were set in the river section tab.
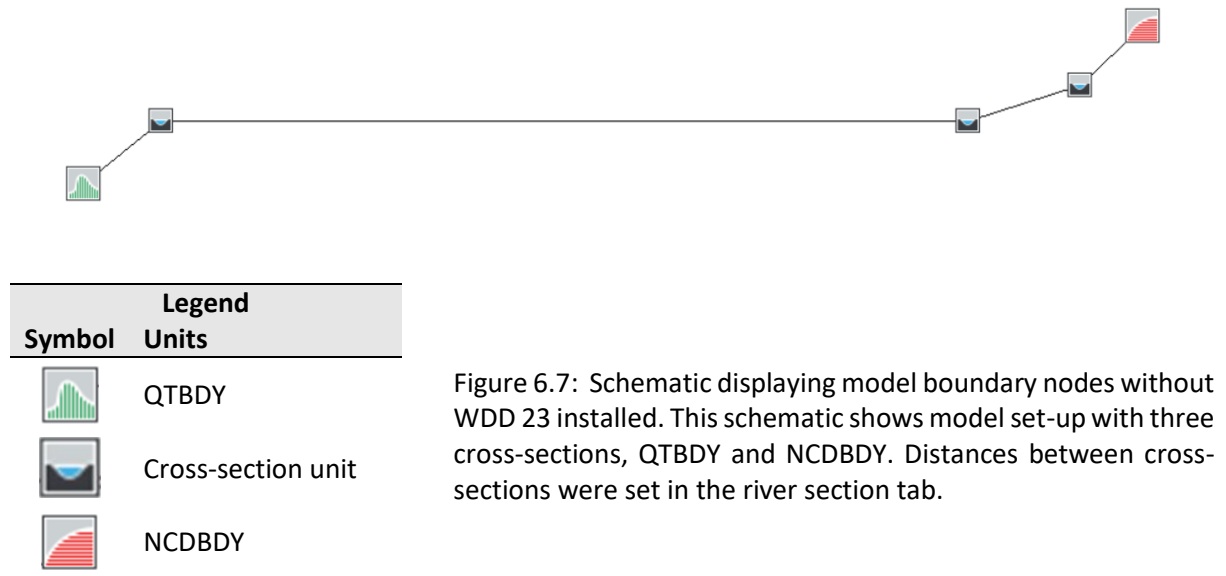
6.2.2.3. Trial steady state simulation

Steady state simulations enabled initial conditions (Flow and Stage) to be obtained. A trial simulation ensured that every model node was inter-connected and appropriate discharge was selected. Failed simulations were assessed using the online FM 1D diagnostic database with errors in code located and rectified. An inbuilt '1D model health check' enabled analysis of the network and listing any potential problems that could generate instabilities during future simulations. This health check carried out consistency checks on model boundaries however it did not examine data validity, model style or physical representations used (Jacobs Flood Modeller: Online Manual, 2021h). Poor conveyance is another cause of instability. Each cross-section was examined, with panel markers added to relevant points respective to poor conveyance areas.

6.2.2.4. Woody debris dam representation

As discussed previously, as per the recommendations of Addy and Wilkinson (2019), the hydraulic structure representation approach was used in this study, with pier-loss bridge units selected to represent WDDs within FM. These units are particularly useful in modelling low discharge conditions where the dominant cause of energy loss is bridge pier friction (Jacobs Flood Modeller: Online Manual, 2021a). The pier-loss bridge unit was chosen rather than using the traditional method of representing hydraulic structures by manipulating the Manning's n roughness because they enable structure porosity and throughflow during low discharge. Raised key members positioned out of water would not attenuate or affect flow, however, when discharge increases these key members can become active.

To model attenuation or h_1-h_2 caused by pier-loss bridge units the Equation 6.2 was used. Equation 6.2 shows that the term h_1-h_2 is dependent upon the shape of pier coefficient (Y_k), ratio of the wetted area blocked by the structure (W_p) to the wetted area unobstructed by the structure (W_u), along with the downstream localised velocity (U_2) and flow depth to calculate h_1-h_2 (Benn et al., 2004).

$$h_1 - h_2 = 2Y_k\left(Y_k + 10\frac{\left(\frac{U_2^2}{2g}\right)}{h_2} - 0.6\right)\left(\frac{w_p}{w_u} + 15\frac{w_p^4}{w_u}\right)\frac{U_2^2}{2g} \tag{6.2}$$

Yarnell Equation 6.2 was used to calculate afflux (h_1-h_2). Variables within this equation include shape of pier coefficient (Y_k), downstream localised velocity (U_2), gravity (g), wetted area blocked by the structure (w_p) and wetted area unobstructed by the structure (w_u).

The WDD blockage capacity and aperture size were based on the w_p (Figure 6.8) and a downstream bridge/WDD length of 0.3 m was selected to represent WDD 23. The pier-loss bridge unit with a flat soffit was positioned in the same location as the geo-tagged and geo-referenced WDD 23 in the mid reach (Figure 4.3 given in section 4.1.).
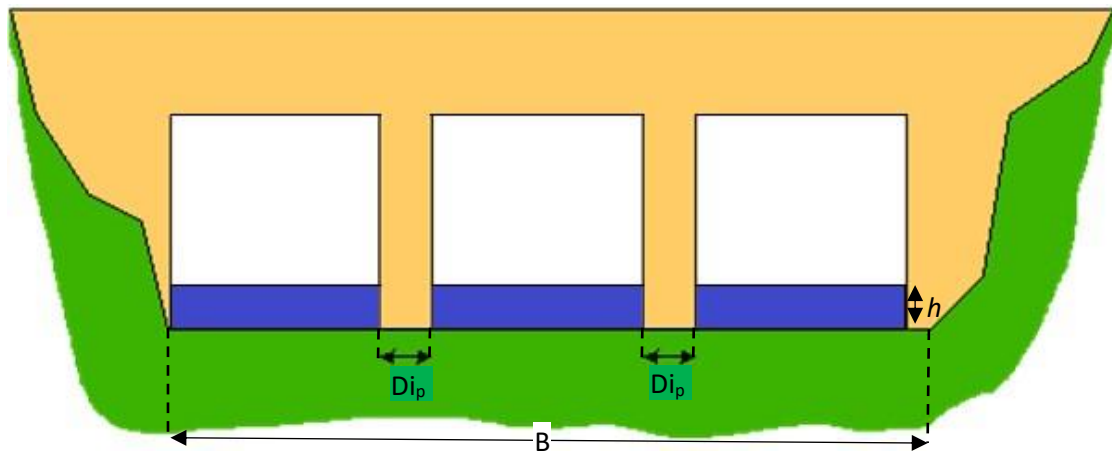
Figure 6.8: A pier-loss bridge unit schema with flat soffit representing WDDs with pier diameter (Di_p), main channel width (B) and flow depth (*h*) displayed (adapted from Jacobs Flood Modeller: Online Manual, 2021g).

Monitoring of the WDDs took place approximately every 6 months between the 2nd April 2019 until the 31st March 2021 with long term seasonal photography documenting WDD evolution and change. The WDDs were categorised using Gregory et al. (1985) definitions that were discussed in section 2.2. Photography from the relevant period (August 2019 and February 2020) quantified blockage capacity whereby gaps between key members and WDD porosity were examined (Figure 6.9). As would be expected the WDD porosity varied seasonally with organic matter, leaf retention and overgrowth, particularly noted during the autumn / winter months with leaf litter accumulation being at its highest so decreasing the effective WDD porosity (Thomas and Nisbet, 2012). Therefore, for this study, both summer and winter storm events were modelled accounting for seasonal variations in porosity (Manners and Doyle, 2008). Modelling two storm events from different seasons enabled comparisons on how hydraulic restrictions influence flow attenuation. To ascertain WDD characteristics a survey was conducted between the 11th – 15th February 2019 examining key member positions, number of stems and WDD design (Appendix M). To simulate changes in blockage capacity, pier diameter (Di_p) was altered to restrict the flow. The legs of the pier-loss bridge unit can be altered in size changing the orifice coefficient to better replicate the blockage of the WDD, prior to structural surcharging, which makes the unit more realistic. To calibrate FM to the pressure level sensors for the summer and winter storm events, h_1-h_2 across the WDD was represented by tuning the pier diameter value until the pressure level sensors agreed with the field data. Similar studies representing WDDs using modelling data are listed in the literature synopsis Appendix N.

a) Summer (August 2019)

b) Bankfull stage conditions (January 2020)

c) Winter (February 2020)

Figure 6.9: Photography documenting WDD 23 evolution and WDD change. Figure shows three photograph datasets taken in a) August (2019) displaying lower blockage capacity with less build-up of detritus, b) January (2020), during bankfull stage conditions with the WDD surcharged and submerged, c) February (2020) with cumulative build-up of detritus which increased structural density and decreased porosity.

As a model calibration, WDD 23 was represented in FM. Dependent upon blockage capacity and discharge, backwater can result in bankfull conditions (Figure 6.9c), finally resulting in bank overtopping, which creates a hydraulic gradient change and generates model instability.

Bank overtopping was examined by inserting a quasi-2D reservoir unit. To construct the reservoir unit a polygon shapefile was drawn around the flood prone area, located to the south of Wilderhope Brook. The 'Run Reservoir Generator' enabled z-value extraction from the DTM. Upon calculation of level and depth values these were then imported into the Reservoir units. To check the plan area, reservoir topographical geometry / reservoir storage capacity was plotted (Figure 6.10). This reservoir unit was typical of many other UK flood storage reservoirs in being relatively shallow and large in area (Environment Agency, 2016). The reservoir unit was positioned south of the water course due to the low-lying floodplain. Spill units were inserted using the 'Run Spill Generator' where Wilderhope Brook mid reach polyline was selected as the spill unit shape file and z-values were extracted from the DTM. The 'spill unit details' tab enabled input of cross-sectional sizes that are prone to bank overtopping along with a weir coefficient set at 1.2 and a modular limit set at 0.9. Spill units connected each cross-sectional node to the reservoir unit (Figure 6.11).
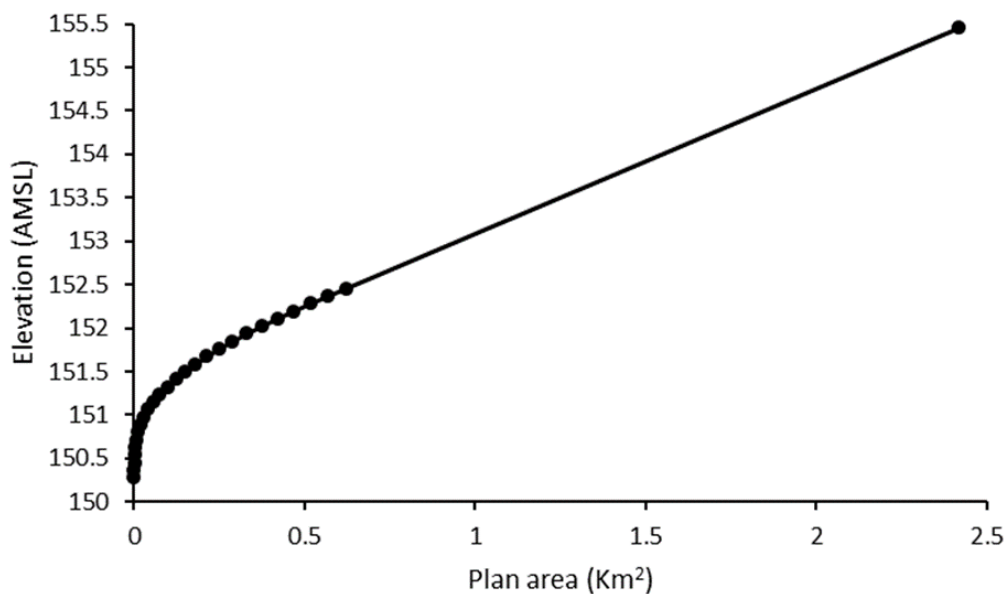
Figure 6.10: Graph displaying Plan area (x-axis) to Elevation (y-axis). It can be seen that the larger the elevation, the greater the Reservoir storage capacity. The reservoir unit was positioned on the floodplain located south of Wilderhope Brook mid reach.

WDD represented by pier-loss bridge unit and a spill unit

Bank overtopping represented by a reservoir and two spill units
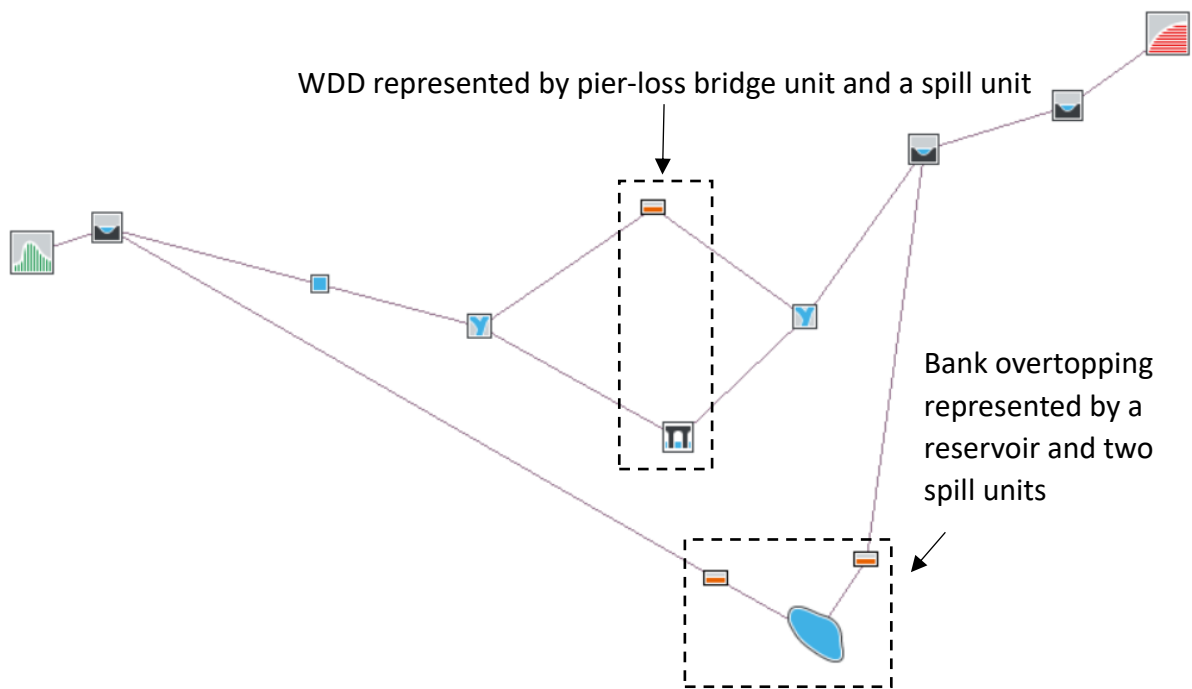
Legend	
Symbol	**Units**
	QTBDY
	Cross-section unit
	Replicate unit
	Pier-loss bridge unit
	Spill unit
	Reservoir unit
	NCDBDY

Figure 6.11: Schematic displaying WDD 23 as modelled with a pier-loss bridge unit in parallel to a spill unit. To simulate flow entering into the system a QTBDY was located at the top of the network while to simulate flow leaving the system a NCDBDY was located at the bottom of the network.

To make a smooth transition from upstream to downstream of the pier-loss bridge unit timestep/iteration size could be reduced to improve model sensitivity and accuracy (Brunner, 2016). A limitation of using the pier-loss bridge unit is that the bankfull stage should be below the bridge soffit to prevent surcharging (Jacobs Flood Modeller: Online Manual, 2021a). Upon surcharge occurring the pier-loss bridge unit transitions to an orifice unit at a given depth, defined as the unit form. Therefore, when the pier-loss bridge is surcharged, an orifice equation is applied along with the weir equation, as it is better represented as a rectangular orifice type flow through the defined bridge openings. The spill unit calculates surcharge using the rectangular weir equation presented in Equation 6.3 (Hamill, 1995). Both the spill and pier-

loss bridge units were connected using an 'open junction' (Figure 6.11) with the upstream open junction connected to a replicate unit. The replicate unit 'drop in bed level from the previous section' was set at 0.087 m/m which was obtained by increasing and decreasing the channel slope angle / gradient until the bed jump was removed.

$$Q_2 = \frac{2}{3}B(2g)^{\frac{1}{2}}h_1^{\frac{3}{2}}$$ (6.3)

Rectangular weir Equation 6.3 calculates the downstream discharge (Q_2) using main channel width (B) assuming spill / rectangular weir crest transverses the B, gravity (g) and upstream flow depth (h_1) (Hamill, 1995).

6.2.2.5. Steady / unsteady simulations

After insertion of the pier-loss bridge and spill units, a steady state simulation was run which enabled initial conditions (flow and stage) to be obtained for the storm events. Steady state simulations provided model validation so errors could then be identified and corrected. Steady state simulations were required to apply a single flow rate at the QTBDY in the mid and lower reaches along with the ReFH in the lower reach. As volume is not represented within the steady state model, it is not a suitable model to use for investigating significant attenuation or storage (UK Government, 2021b; Environment Agency, 2021c). Within FM two methods of determining steady state could be applied to optimise run-time and enhance model stability (Jacobs Flood Modeller: Online Manual, 2021b). The Pseudo-timestepping method using a Preissmann 4-point scheme requires input of initial flow and stage conditions. This method can become unstable creating errors depending upon model size (Jacobs Flood Modeller: Online Manual, 2021c). In comparison, the direct method is more commonly used due to its efficiency and high accuracy. This method reduces convergence errors by using automated distance step size control options during computation which informs users whether extra interpolated sections are required within the model. The direct method provides an optional 'transcritical solver', capable of modelling hydraulic jumps, subcritical and supercritical flow conditions (Jacobs Flood modeller: Online Manual, 2021d). As the 'transitional solver' cannot be used to simulate unsteady, steady 'timestepping' or flood route models, the direct method transitional solver was not applied (Jacobs Flood Modeller: Online Manual, 2022g). The direct method was particularly well suited for modelling WDDs using

bridges as the piers create variations in the hydraulic gradient. Therefore, for this study the direct step method was applied to steady state simulations. Steady state simulations could be checked in the viewport at individual cross-sections or along the longitudinal profile.

The completed steady state simulation results acted as an initial condition for future unsteady simulations. Unsteady flows provide a more concise view of flooding in comparison to steady flows, however, unsteady simulations rely on peak discharge and discharge accuracy, which is problematic as discharge is temporally varying. To quantify varied flow conditions using numerical models, the model would need to run several simulations with different discharges which can create inaccuracies. Unsteady simulations are generally used in flood mapping projects to map flood extent and are used if flood extent or attenuation are significant (UK Government, 2021b; Environment Agency, 2021c). Unsteady simulations were set at a computational time step of 20s enabling respective hydraulic model calculations which was determined using the Courant number formula based on transient simulations (Equation 6.4). The Courant number indicates how much information travels across the computational grid size (Δm_s) in a simulated unit of time (Δt) (Domino, 2023). Upon completing an unsteady simulation, the graphical display showed 2-6 iterations performed per time step, convergence information and model inflows and outflows. For comparison, the obstructed channel (with bridge piers), steady and unsteady state simulation results were plotted on the longitudinal profile alongside an unsteady state simulation displaying an unobstructed channel (without bridge piers).

$$C_o = \frac{U\Delta t}{\Delta m_s} \qquad (6.4)$$

Equation 6.4 calculates the Courant number (C_0) using localised velocity (U), simulated unit of time (Δt) and computational grid size (Δm_s).

6.2.3. Lower reach

This study used a 1D model to examine the effectiveness of WDDs in attenuating flow by focusing on a 0.2 km long section containing 5 engineered WDDs in Wilderhope Brook lower reach (Figure 6.12).
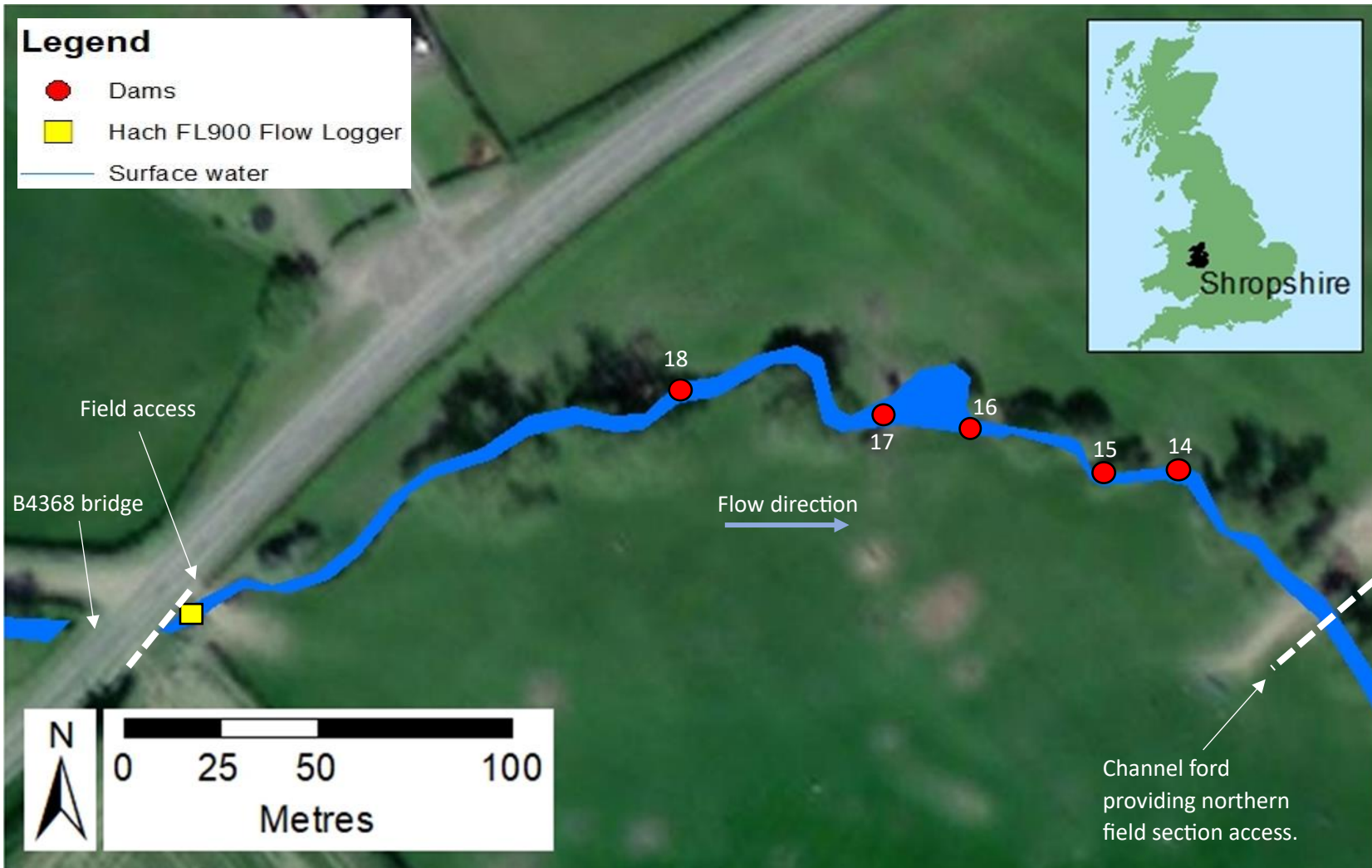
Figure 6.12: ArcMap 10.5.1. constructed map with the Surface water (2017) extracted from a 1:1000 OS master map (2017) and overlayed upon an aerial view base map (2020) with WDDs (14-18) and the flow logger (Figure 6.5). White dashed line (upstream and downstream) shows lower reach study area extent. Source: Esri, Maker, GeoEye, Earthstar Geographies, CNES/Airbus DS, USDA, USGS, AeroGRID, IGN, and the GIS user community.

Within the lower reach study section, a network of 5 WDDs were constructed using the same modelling procedure as used to represent WDD 23 in the mid reach. To model the 5 WDDs, a polyline shapefile was drawn starting at the B4368 bridge / flow logger (355147E, 290683N) and ending downstream at Wilderhope Brook lower reach ford (355321E, 290686N). Cross-sections were set at fixed distances of 12.5 m along the 0.2 km longitudinal profile. However, though distance between cross-sections was set to 12.5 m, 1D modelling assumes that the channel geometry remains constant between cross-sections, which impacts on the accuracy of prediction (Ambient Environmental Assessment, 2022).

Engineered WDDs installed in Wilderhope lower reach have been documented on a 6-month basis from the 2nd April 2019 until the 31st March 2021. WDDs were categorised using Gregory et al. (1985) definitions with 3 active and 2 partial dams in place. However, as has been discussed in detail earlier, temporal foliage, leaf retention and organic debris can create seasonal variations between dam designs. Quantification of seasonal blockage capacity are set out in Appendix T.

The lower reach channel is unconfined with relatively low channel entrenchment and is therefore prone to bank overtopping. An unconfined channel is defined as consisting of an undefined valley which displays gradual slopes where in wide flat reaches of the channel, bank overtopping can occur onto the floodplain (Lindroth et al., 2020). In comparison, a confined channel consists of a narrow valley where higher banks prevent bank overtopping. Confinement limits the lateral extent of the valley floor and the water course floodplain (Imran et al., 2004; Nagel et al., 2014; Credit Valley Conservation, 2015). As used in the mid reach a reservoir unit was inserted to simulate bank overtopping with site specific reservoir geometry plotted (Figure 6.13). A comparison was made between the bank overtopping by using a reservoir unit and a confined channel by using glass walls (dflood) set to 10 m. This was achieved to examine the effects of WDDs with and without a floodplain and to explore the effects of WDDs placed in entrenched channels.
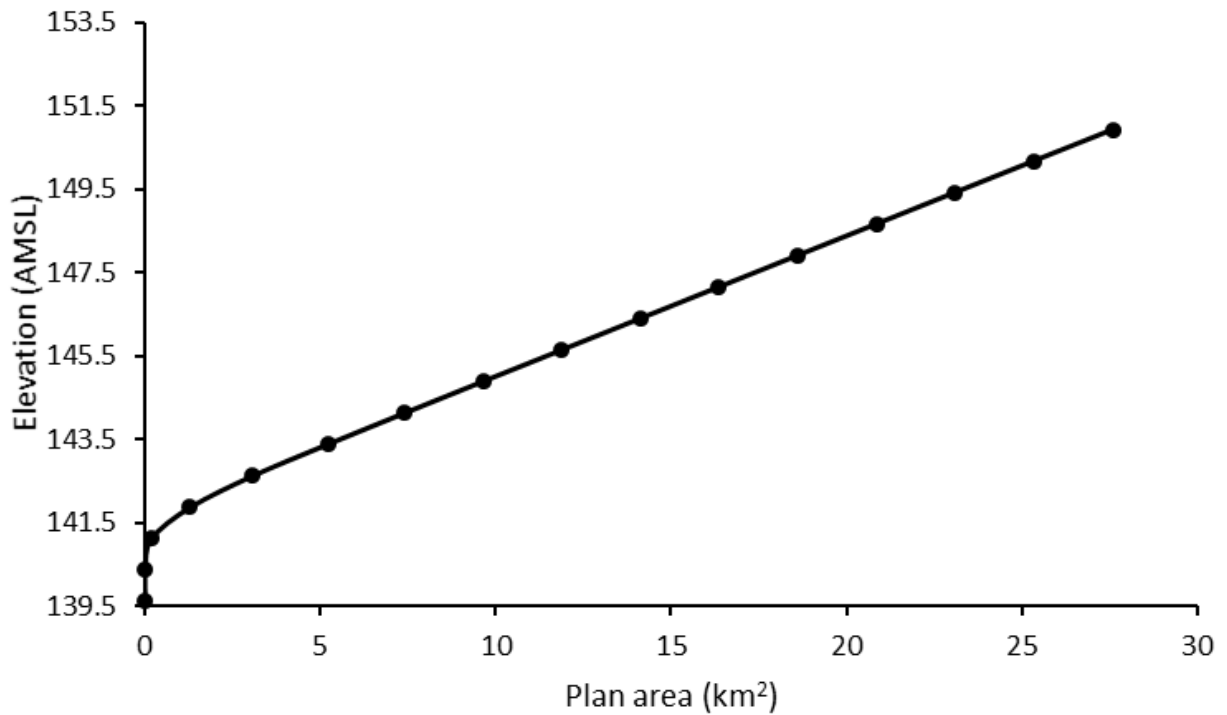
Figure 6.13: Graph displaying Plan area (x-axis) to Elevation (y-axis). Reservoir unit positioned on the floodplain located south of Wilderhope Brook lower reach.

6.2.3.1. Revitalised Flood Hydrograph boundary conditions

To represent surface runoff in the channel downstream of the flow logger, hydraulic models require a description of the study area (Collell et al., 2019). To simulate surface runoff a ReFH boundary condition was added at one location in the lower reach in conjunction with a Lateral Inflow unit (Figure 6.14). ReFH boundary is a rainfall runoff model that enables surface runoff to be taken into account, by inserting localised catchment descriptions. Localised data of catchment descriptors and precipitation DDF supporting derivation of runoff rates and quantity were obtained from the UK Centre for Ecology and Hydrology (2022), FEH Web Service. Obtained UK Centre for Ecology and Hydrology (CEH) catchment descriptors were verified using analysis of catchment descriptors aforementioned in chapter 5.

The search tool was used to locate the AoI in the lower reach. Two appropriate catchment boundary intervals with a ±1 m accuracy were imported as a ReFH unit at the B4368 bridge and at the ford. To obtain localised catchment descriptors and surface runoff from the field, the ReFH unit at the B4268 bridge was subtracted from the ReFH unit at the ford. This calculated ReFH unit was then imported into FM (Table 6.2).

ReFH unit including lateral inflow

Reservoir unit including spills
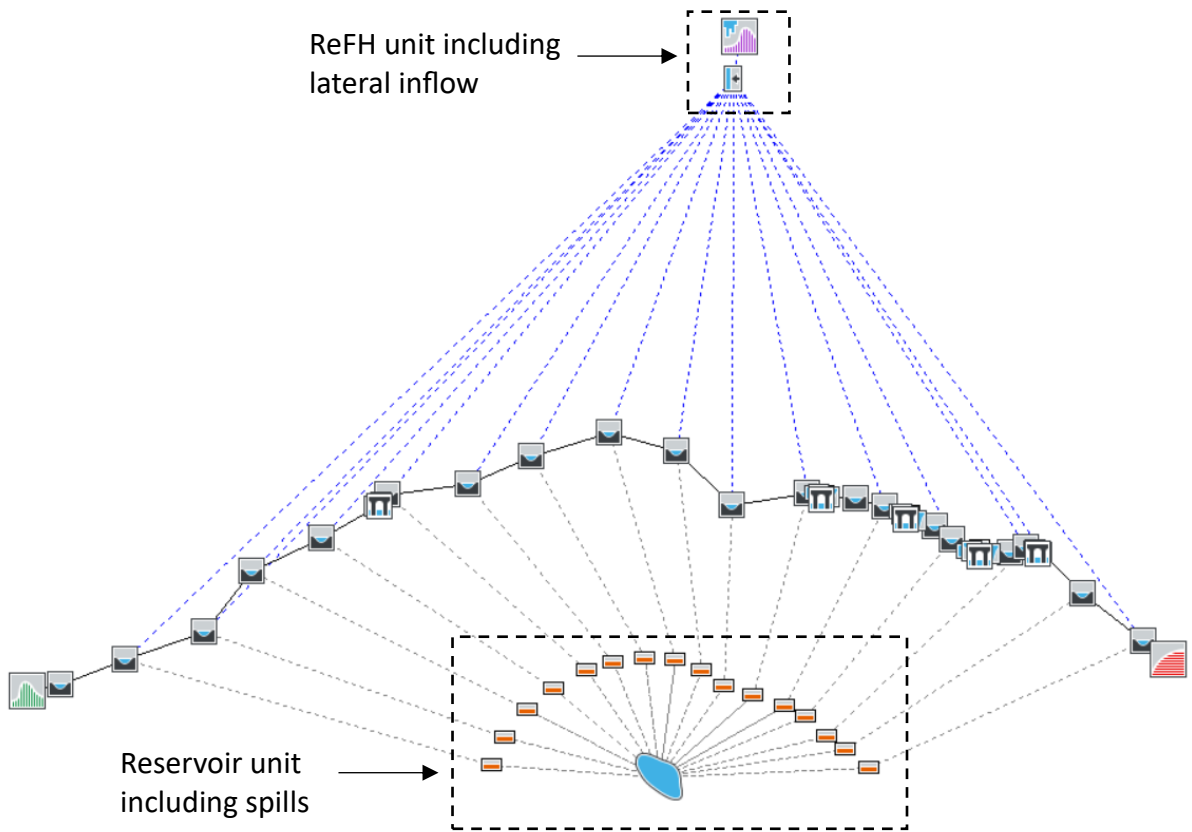
Legend	
Symbol	**Units**
	QTBDY
	ReFH boundary condition
	Cross-section unit
	Replicate unit
	Lateral inflow unit
	Pier-loss bridge unit
	Spill unit
	Reservoir unit
	NCDBDY

Figure 6.14: Wilderhope Brook network with 5 WDDs. ReFH boundary condition (located to the north of Wilderhope Brook) and the Reservoir unit (located to the south of Wilderhope Brook).

Table 6.2: Displaying FEH catchment descriptors. The used FEH catchment descriptors were obtained by subtracting the B4368 bridge from the Ford (adapted from the Institute of Hydrology, 1999).

Name	Descriptor	FEH values		
		B4368 bridge	Ford	Used catchment descriptors
ALTBAR	Mean catchment altitude (AMSL), derived from the DTM.	214	213	213
ASPBAR	Catchment slope gradient (°).	140	139	139
ASPVAR	Invariability in catchment slope gradient (°).	0.23	0.25	0.25
AREA	Catchment drainage area (km^2), derived from the DTM.	5.2725	5.4725	0.2
BFIHOST	Base flow index is a measure of catchment responsiveness derived using the 29-class Hydrology Of Soil Types (HOST) classification.	0.518	0.521	0.521
c	Precipitation DDF model parameter c.	-0.02496	-0.02496	-0.02496
d1	Precipitation DDF model parameter d1.	0.33843	0.33866	0.33866
d2	Precipitation DDF model parameter d2.	0.39424	0.39425	0.39425
d3	Precipitation DDF model parameter d3.	0.29623	0.29629	0.29629
DPLBAR	Mean distance between DTM nodes and the catchment outlet (km). Used to characterise catchment size and configuration.	2.79	2.98	0.19
DPSBAR	Mean drainage path slope obtained from a DTM.	116.4	115.6	115.6
e	Catchment descriptor – Precipitation DDF model parameter e.	0.28863	0.28865	0.28865
f	Catchment descriptor – Precipitation DDF model parameter f.	2.42573	2.4256	2.4256
FARL	The Flood Attenuation by Reservoirs and Lakes (FARL) index.	1	1	1
FPDBAR	Mean water depth on floodplains in a 1:100-year event.	0.187	0.212	0.212
FPEXT	Defined floodplain extent as a fraction of the catchment that is estimated to be inundated by a 1:100-year event.	0.0208	0.0233	0.0025
FPLOC	Location of floodplains within the catchment.	0.712	0.658	0.658
LDP	Longest drainage path (km), from a catchment node to the defined outlet.	4.92	5.2	0.28
PROPWET	FEH (1999) index of proportion of time that soil is wet.	0.36	0.36	0.36
SAAR	Average annual rainfall (mm) from 1961-1990.	772	772	772
SPRHOST	Standard runoff (%) associated with each HOST soil class.	29.66	29.51	29.51
URBEXT	Urban and suburban land cover index expressed as a fraction.	0	0	0

6.3. Results

6.3.1. Determining storm events

A cumulative precipitation graph (Figure 6.15) enabled identification of storm events with vertical inclines showing periods of high precipitation and horizontal movement showing dry periods. Wilderhope tipping bucket rain gauge recorded a total of 1172 mm between the 2nd April 2019 and the 2nd April 2020. Therefore, extrapolated throughout the ≈ 5.4725 km^2 catchment to the mid lower course (Ford) provided a total of 6,412,675.5 m^2, assuming rainfall fell equally throughout the catchment.
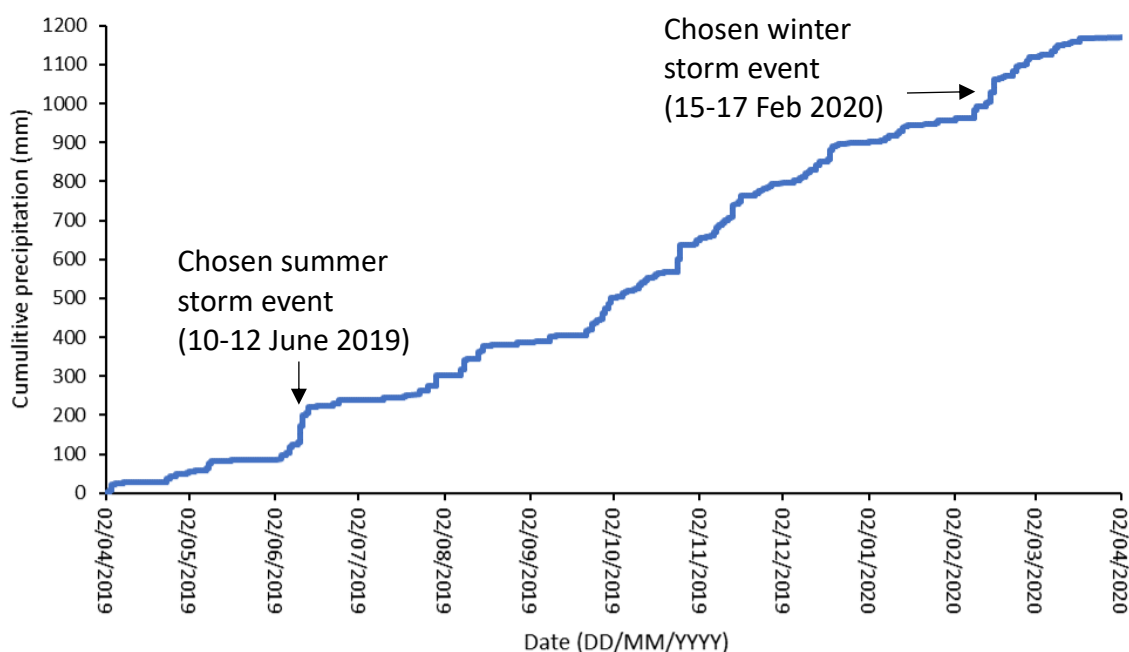
Figure 6.15: Wilderhope cumulative rainfall from the 2nd April 2019 until the 2nd April 2020. Vertical increase shows periods of rainfall with intensity depending upon incline. Horizontal movement shows periods of no rainfall with duration depending upon horizontal length. Maximum annual rainfall from the 2nd April 2019 until the 2nd April 2020 recorded at 1171.8 mm. Chosen storm event 10-12 June 2019 is labelled.

Two storm events were determined, a summer storm event (10-12 June 2019) and a winter storm event (15-17 Feb 2020). During the summer storm event, Wilderhope tipping bucket rain gauge recorded 76 mm of rainfall falling in 48 hrs compared to 57 mm falling during the winter storm event. Though more precipitation was recorded during the summer storm event, precipitation was of a lower intensity for a longer duration compared to the winter storm event with a greater intensity for a shorter duration. Therefore, the summer storm event hyetograph is more bowed while the winter storm event is more pointed (Figure 6.16).
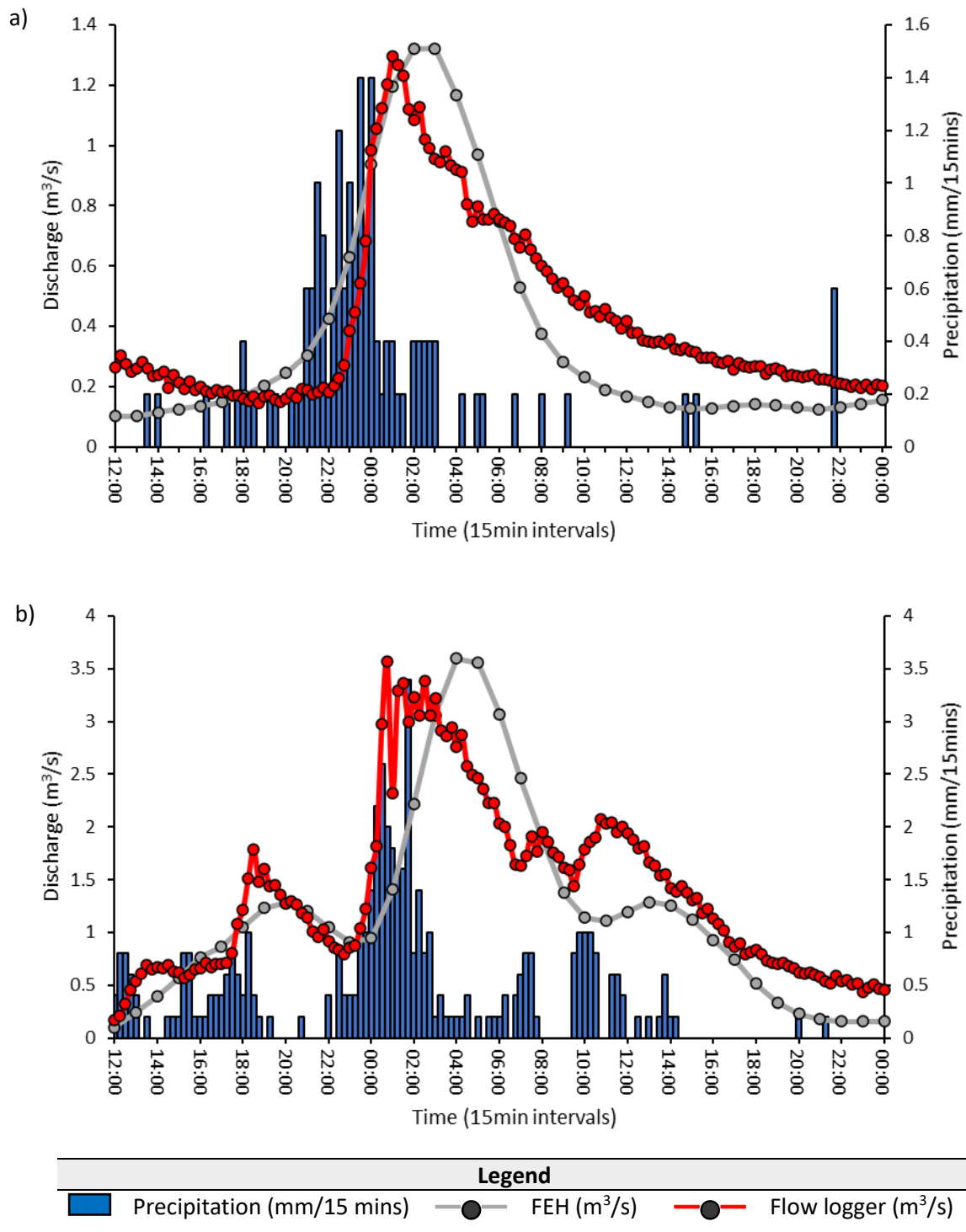
Figure 6.16: a) Wilderhope summer storm hydrograph / hyetograph displaying discharge and precipitation in 15 min intervals between the 12-14 June 2019. Increased lag time is labelled and measured at 86 mins. b) Wilderhope winter storm hydrograph / hyetograph displaying discharge and precipitation in 15 min intervals between the 15-17 Feb 2020 (Storm Dennis). Increased lag time is labelled and measured at 9 mins.

When making direct comparison between Figure 6.16 a) and b), Figure 6.16a) has a smaller y-axis scale. This scale has been chosen to display small changes.

Examining the time of peak rainfall intensity to time of peak discharge enabled quantification of lag time. Lag time is dependent upon rainfall intensity and spatial location within the catchment (Black et al., 2021). For the summer storm event, peak rainfall occurred at 23:36 (11th June 2019) and peak discharge occurred at 01:00 (12th June 2019) as measured with the flow logger. Therefore, Wilderhope catchment lag time for the summer storm event, was calculated as being 84 mins (Figure 6.16a). In comparison using FEH catchment descriptors, peak discharge occurred at 02:00 (12th June 2019) with a catchment lag time of 144 mins. Wilderhope tipping bucket rain gauge for the winter storm event recorded peak rainfall occurred at 00:36 (16th Feb. 2020) and the flow logger recorded peak discharge occurred at 00:45. Therefore, the winter storm event lag time was calculated as being 9 mins (Figure 6.16b). In comparison, the FEH catchment descriptors showed peak discharge occurred at 04:00 with a catchment lag time of 204 mins. The flow logger recorded shorter lag times compared to the FEH catchment descriptors, suggesting both storm events were localised in the catchment with peak precipitation / runoff occurring closer to the B4368 bridge. FEH catchment descriptors do not always accurately reflect catchment spatial variations with a single numeric value assigned to represent a particular descriptor within the catchment (UK Government, 2021c). Catchment homogeneity, not accounting for precipitation spatial variations, can lead to differences between the real measured lag time to the FEH modelled lag time.

Runoff tends to be smaller during dry periods and greater during wet periods (La Torre Torres et al., 2011; Rahman and Ennos, 2016). During the winter storm event low lying land, particularly noted at Ludlow, was described as being completely saturated due to the high intensity rainfall over a short duration (Smith, 2020). To account for a heightened water table caused by past storm events (Storm Ciara) and reduced infiltration during the winter storm event, percentage runoff was set at 54.66%. This value is comparable to studies such as Moore et al. (2015) who used a rural percentage runoff of 55%. Therefore, for the present study, of the total volume of net rainfall that fell (286,017 m^3), 160,910.4 m^3 entered the channel as runoff. In comparison, during the summer storm event, to account for a lower water table enabling infiltration, percentage runoff was set at 29.66%. The total volume of net rainfall that fell during the summer storm event was 155,200.6 m^3 and 46,730.9 m^3 entered Wilderhope Brook as runoff.

To validate Wilderhope tipping bucket rain gauge precipitation readings, results were compared to Shawbury rain gauge installed ≈ 48.3 km north of Wilderhope (355200E,

322100N at 72 m AMSL) (Figure 6.17). Results indicated a Pearson's correlation coefficient of 0.8717 showing a strong positive relationship between both rain gauges and therefore validating results (Equation 3.17 as shown in section 3.3.2.1.).
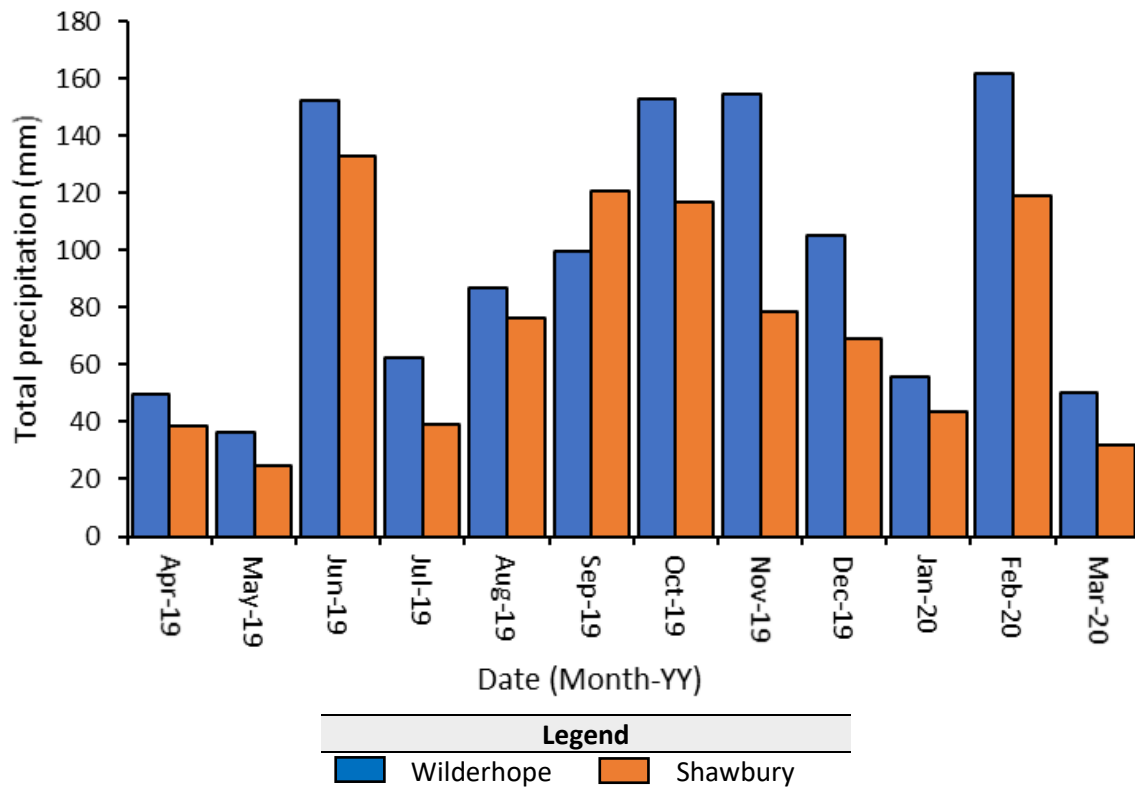
	Wilderhope rain gauge	Shawbury rain gauge
Mean	97.367	74.3
Standard Error	13.707	11.414
Standard deviation	47.484	39.541
Sample Variance	2254.733	1563.487
Kurtosis	-1.722	-1.629
Skewness	0.243	0.269
Range including outliers	125.2	108.6
Minimum	36.6	24.6
Maximum including outliers	161.8	133.2
Confidence Level (95.0%)	30.17	25.123
t-Test: Paired Two Sample for Means		
Hypothesised mean difference	23.067	
Degree of Freedom	11	
t- statistic	-4.9Exp-6	
P (T ≤ t) one-tail (Wilderhope)	0.5	
t Critical one-tail (Wilderhope)	1.796	
P (T ≤ t) two-tail (Shawbury)	1	
t Critical two-tail (Shawbury)	2.201	

Figure 6.17: Comparison between Wilderhope and Shawbury rain gauges. Wilderhope tipping bucket rain gauge was installed at Stanway Farm to the Northwest of Wilderhope Brook catchment (352113E, 289342N). Shawbury rain gauge was installed (355200E, 322100N at 72 m AMSL) at distance of ≈ 48.3 km north of Wilderhope tipping bucket rain gauge. Accompanying table displays information regarding differences between both Wilderhope and Shawbury rain gauges.

To determine whether the null hypothesis (means of two datasets are equal) could be accepted or rejected, the t-test Paired Two Sample for Means method (Equation 3.18 as shown in section 3.3.2.1.) was applied. This method quantified statistical significance between Wilderhope and Shawbury rain gauges. The absolute value of the t-statistic (4.9×10^{-06}) was less than the critical t value for both rain gauge datasets (Wilderhope: 1.796 and Shawbury: 2.201). Since the rain gauge P-values (Wilderhope: 0.5 and Shawbury: 1) were greater than the alpha (0.05) the null hypothesis was accepted and therefore the mean of both rain gauges datasets are equal (Figure 6.17).

To further verify the chosen storm events, Met office reports were cross referenced with Wilderhope tipping bucket rain gauge data. The Met office recorded ≈ 75-100 mm of rainfall from 10-12 June 2019 (Appendix O), while Wilderhope tipping bucket rain gauge recorded 76 mm of rainfall, 1 mm above the minimum Met office value. In comparison from 15-16 Feb 2020, the Met office recorded ≈ 50-75 mm of rainfall (Appendix P) while Wilderhope tipping bucket rain gauge recorded 57 mm.

6.3.2. Mid-reach calibration

6.3.2.1. Conveyance

Conveyance (K_0) was examined and adjusted to improve model stability. K_0 provides a measure of the discharge carrying capacity which is calculated using Equation 6.5. Channel characteristics influencing K_0 are channel geometry, wetted area (W) and flow resistance variability calculated through the Manning's n roughness coefficient (Equation 6.6) (Collell et al., 2019). Though channel K_0 provides convenience in grouping channel properties into a single term, K_0 is independent of channel slope angle / gradient (S_0). K_0 provides a useful mechanism when simulating overbank flows in stream cross-sections and can be used to determine velocity distribution coefficients (Minnesota Department of Transportation, 2000). The K_0 variable shows the channel ability to convey water has a direct influence on flow depth, which can affect flooding.

$$Q = K_0 . S_0^{\frac{1}{2}}$$
<div align="right">(6.5)</div>

Conveyance Equation 6.5 calculates discharge (Q) as a means of conveyance (K_0), channel slope angle / gradient (S_0) (Vasilyev, 2015).

$$Q = \frac{1}{n} \frac{W^{\frac{5}{3}}}{P_e^{\frac{2}{3}}} S_0^{\frac{1}{2}} \qquad \text{or} \qquad Q = \frac{1}{n} WR^{\frac{2}{3}} S_e^{\frac{1}{2}}$$
<div align="right">(6.6)</div>

Equation 6.6 calculates the discharge (Q) using Manning's n roughness coefficient (n), wetted perimeter (P_e) and channel slope angle / gradient (S_0) or wetted area (W), Hydraulic radius (R), energy gradient (S_e) (Collell et al., 2019).

Cross-section K_0 was kept to a minimum to improve model stability (Jacobs Flood modeller: Online Manual, 2021f). The K_0 plotting tool provided a reference to check that K_0 increased smoothly with stage (Appendix Q). Panel markers were added to areas of varying K_0 where the flow depth was likely to overtop the banks. The upstream cross-section had a lower K_0 with increased stage until 151.57 m in comparison to the downstream cross-section. When the stage became > 151.57 m, the downstream cross-section K_0 increased more rapidly by 55 m^3/s in 0.54 m compared to the upstream cross-section with 55 m^3/s in 0.62 m.

6.3.2.2. Structural design

WDD 23 was modelled using both summer and winter wetted area blocked by the structure (w_p), with the summer w_p calculated at 0.525 m^2 (Figure 6.18a) and the winter w_p calculated at 0.538 m^2 (Figure 6.18b). To replicate increased debris accumulation during the winter, the left pier diameter was extended by 0.05 m accounting for 0.013 m^2 of extra accumulated material. The steady state simulations showed during the winter storm event at 12 hrs, h_1-h_2 was calculated as being 0.083 m compared to 0.043 m during the summer storm event. This showed with greater discharge, greater h_1-h_2 was exhibited (Table 6.3) with negligible bank overtopping. The unsteady state simulation also showed a lower h_1-h_2 during the summer storm event (0.06 m) compared to the winter storm event (0.079 m) with a lower upstream flow depth during the summer storm event (0.757 m) compared to the winter storm event (1.251 m). Therefore, from the dry to wet periods the upstream flow depth increased.

When comparing the steady to the unsteady simulations, during the summer storm event, the upstream flow depth was modelled at 0.359 m for the steady state simulation and 0.494 m for the unsteady state simulation. Additionally, a greater h_1-h_2 value was measured for the unsteady compared to steady state simulations (Table 6.3). These findings corroborate why the unsteady simulation was better suited to model discharge and attenuation, showing the WDD attenuated more with variations in flow rate (Environment Agency, 2021c).

Downstream of WDD 23 for both summer and winter storm events the downstream flow depth reverted to the normal flow depth as simulated in the unobstructed channel (Figure 6.19). Therefore, the WDD did not decrease the downstream flow depth from the normal flow depth but rather the WDD created an area of attenuation upstream with increased upstream flow depth. During the summer storm event the WDD attenuated ≈ 1.8 m^3 compared to the unobstructed channel assuming the cross-sectional area did not change within 15 m upstream of the WDD. In comparison, during the winter storm event the WDD attenuated ≈ 3.83 m^3 compared to the unobstructed channel. This attenuation decrease indicates that WDD 23 has more impact in increasing upstream flow depth during high discharge than compared to low discharge.
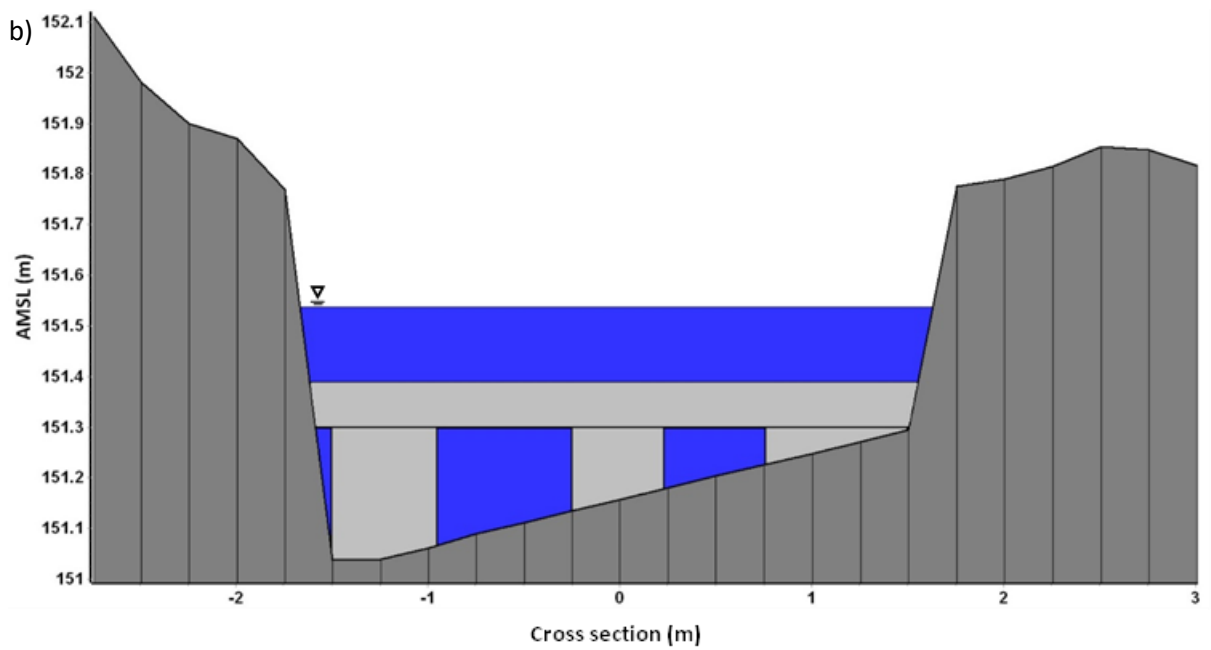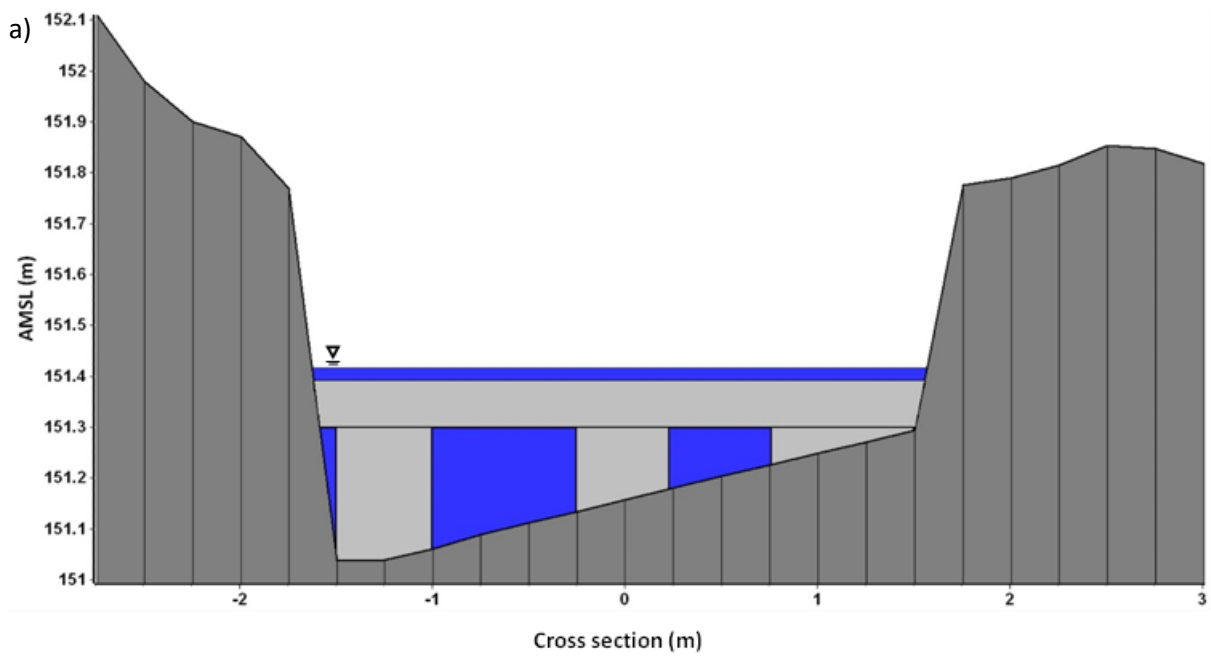
Figure 6.18: Diagrams displaying WDD 23 design for the a) summer storm event and b) winter storm event. Flow depth shown at 10 hrs. In the winter storm event, the left pier leg, pier diameter (Di_p) has been extended by 0.5 m to replicate 0.01195 m^2 of extra material that accumulated during the winter.

Table 6.3: Displaying flow height change upstream and downstream of WDD 23.

	Summer			Winter		
	Upstream flow depth (m)	Downstream flow depth (m)	h_1-h_2 (m)	Upstream flow depth (m)	Downstream flow depth (m)	h_1-h_2 (m)
Obstructed- steady	0.359	0.316	0.043	0.494	0.411	0.083
Obstructed- unsteady	0.757	0.697	0.06	1.251	1.172	0.079
Unobstructed- unsteady	0.697	0.697	0	1.172	1.172	0

Legend

▨ Bed elevation (m)	
Summer	Winter
—— Obstructed channel- steady	—— Obstructed channel- steady
- - - Obstructed channel- unsteady	- - - Obstructed channel- unsteady
········ Unobstructed channel- unsteady	········ Unobstructed channel- unsteady
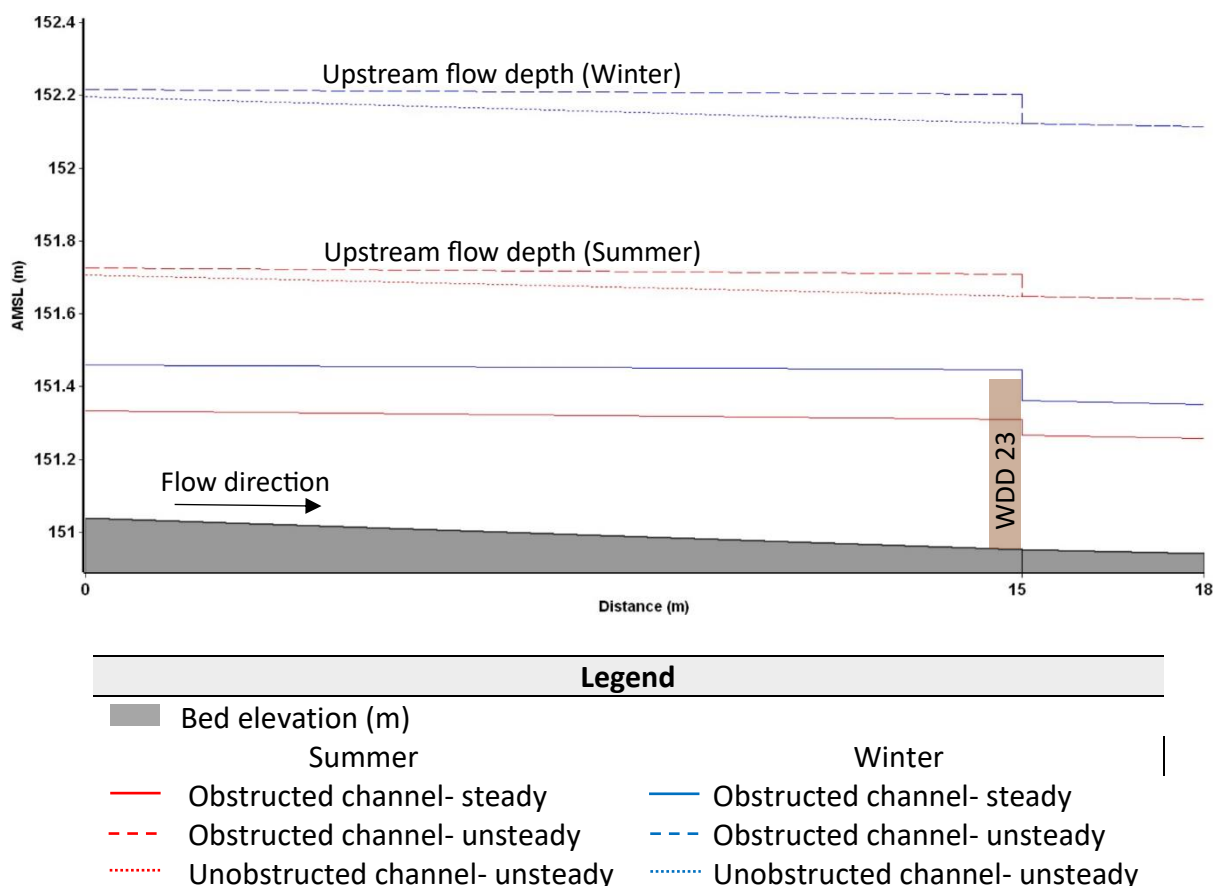
Figure 6.19: Diagram displaying h_1-h_2 caused by WDD 23. Steady, unsteady and unobstructed channel shown for both summer and winter storm events. Flow depth values are presented in Table 6.3.

Figure 6.20 shows bank overtopping at WDD 23 during the winter storm event. Discharge exceeding 0 m³/s shows bank overtopping while discharge below 0 m³/s shows water re-entering the channel. During peak discharge at 12 hrs bank overtopping was simulated with WDD 23 causing 0.655 m³/s compared to an unobstructed channel at 0.544 m³/s. The WDD caused bank overtopping to occur for a shorter duration from 11 hrs 25 mins until 12 hrs 35 mins, 5 mins less than the unobstructed channel with bank overtopping occurring until 12 hrs 40 mins. Though the unobstructed channel caused bank overtopping to occur for a longer

duration the flow depth value was lower (Figure 6.20). In total WDD 23 created 0.44 m^3 of bank overtopping during the 24 hrs, while the unobstructed channel created 0.36 m^3. In the unobstructed channel, less bank overtopping occurred with less water re-entering the channel compared to the obstructed channel. During the summer storm event, no bank overtopping occurred and is therefore not displayed on Figure 6.20.

| Legend |
| Winter |
| - - - Obstructed channel- unsteady |
| ·········· Unobstructed channel- unsteady |
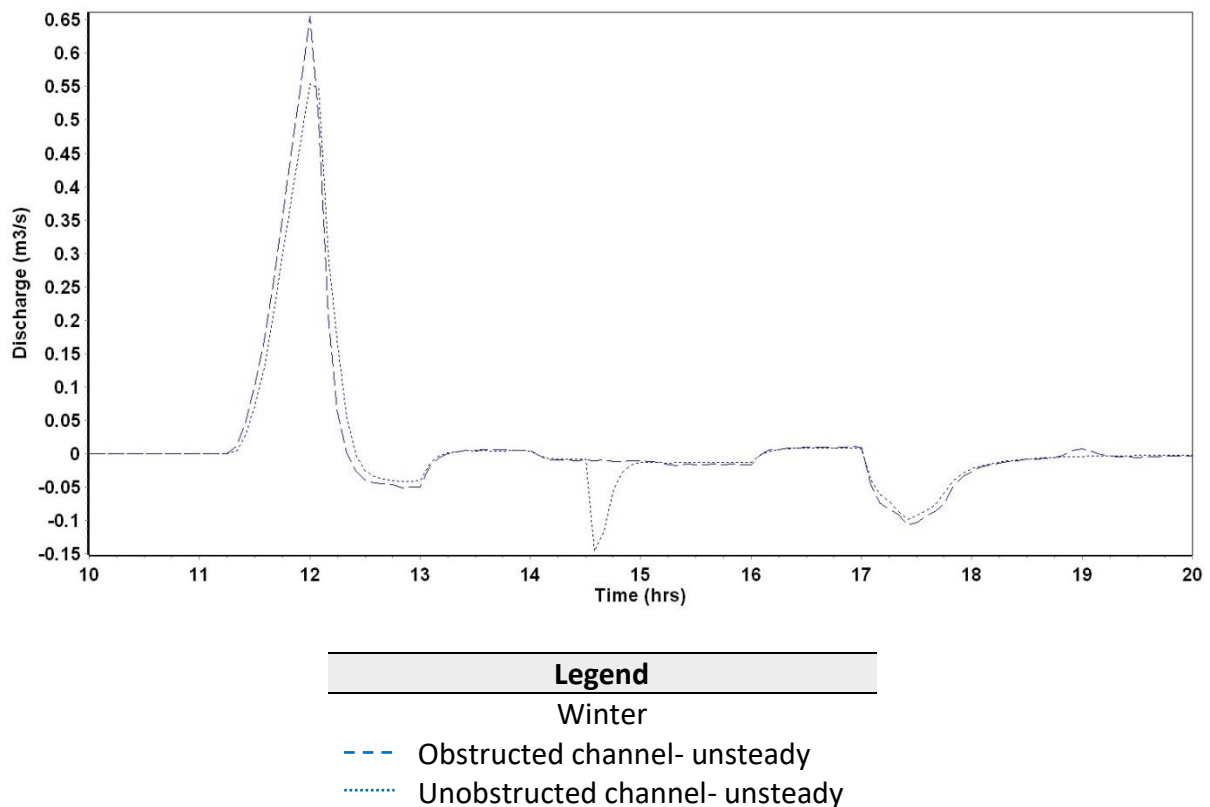
Figure 6.20: Time-series graph displaying winter storm event bank overtopping 15 m upstream of WDD 23 and comparative bank overtopping in an unobstructed channel. Discharge exceeding 0 m^3/s shows bank overtopping while discharge below 0 m^3/s shows water re-entering the channel.

WDD size did not increase proportionately to discharge and therefore with increased discharge the blockage ratio decreased. A blockage ratio (B$_r$) of 0.34 was observed during the summer storm event compared to 0.26 during the winter storm event (Equation 6.7). A lower contracted flow velocity (U$_{co}$) through the structure, blockage capacity and lower Froude number (Fr$_c$) was observed during the summer storm event (U$_{co}$ = 0.354 m/s, Fr$_c$ = 0.195) compared to the winter storm event (U$_{co}$ = 0.523 m/s, Fr$_c$ = 0.249) (Fr$_c$ calculated using Equation 6.8). As Fr$_c$ increases the drag coefficient (C$_D$) decreases (Parola et al., 2000). For this

study, the drag coefficient was calculated at 1.8 for both summer and winter storm events which was determined using Table 6.4.

$$B_r = \frac{w_p}{w_p + w_u} \tag{6.7}$$

Equation 6.7 calculates flow blockage ratio (B_r) using wetted area unobstructed by the structure (w_u) and wetted area blocked by the structure (w_p) (Parola et al., 2000).

$$Fr_c = \frac{U_{co}}{\sqrt{g\overline{h_{fc}}}} \tag{6.8}$$

Equation 6.8 calculates contracted flow Froude number (Fr_c) using Contracted flow velocity (U_{co}), gravity (g) and average flow depth in the flow contraction ($\overline{h_{fc}}$) (Parola et al., 2000).

Table 6.4: C_D for debris on piers (Parola et al., 2000).

B_r - range	Fr_c - range	C_D
$B_r < 0.36$	$Fr_c < 0.4$	$C_D \approx 1.8$
$B_r < 0.36$	$0.4 < Fr_c < 0.8$	$C_D \approx 2.6 - 2\ Fr_c$
$0.36 < B_r < 0.77$	$Fr_c < 1$	$C_D \approx 3.1 - 3.6\ B_r$
$B_r > 0.77$	$Fr_c < 1$	$C_D \approx 1.4\ B_r$

The quantified component of average stream pressure on the debris due to the flow (P_D) was quantified as being higher during the winter storm event (P_D = 0.246) compared to the summer storm event (P_D = 0.113) (Equation 6.9). Increased P_D can account for debris to become unstable and to be washed downstream. The contracted flow velocity value was taken for the velocity reference (U_r) for both the summer and winter storm event as the blockage ratio exceeded 0.3 (Parola et al., 2000).

$$P_D = C_D\gamma\frac{(U_r)^2}{2g} \tag{6.9}$$

Equation 6.9 calculates average stream pressure on debris (P_D) using drag coefficient (C_D), specific weight of water (γ), velocity reference (U_r) and gravity (g) (Parola et al., 2000).

At low discharge when the flow is unable to surcharge the structure, the velocity decreases and seepage flow occurs through the structure. However, at the point of surcharge, dam porosity and the blockage ratio (Equation 6.7) begins to reduce. Dam porosity has greatest impact at low discharge, however, during high discharge, the soffit diameter or maximum height of structure above bed is seen as more important at reducing high discharge, as it takes longer for the structure to be surcharged and increases the time taken for seepage through the structure. To increase flow attenuation and the bankfull stage during high discharge, greater maximum height of the structure above the bed is required (Figure 6.21). To increase attenuation and the bankfull stage during low discharge, the WDD should have reduced porosity (Figure 6.21b).
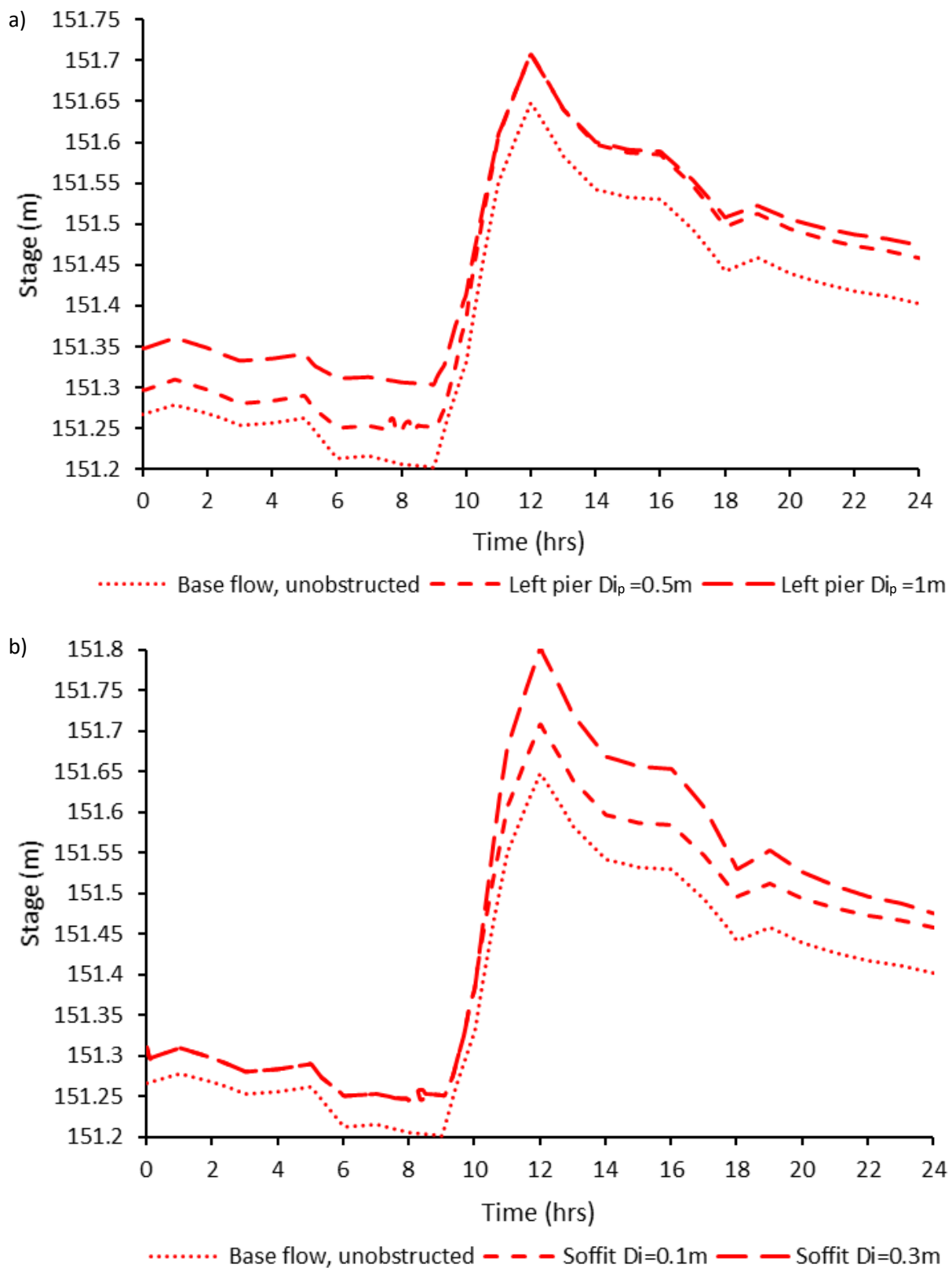
Figure 6.21: a) Line graph displaying summer storm event reduction in throughflow with increased left pier diameter (Di_p) from 0.5 m to 1 m. In low discharge, upstream flow depth increases caused by reduced throughflow. b) Line graph displaying increased stage with increased maximum height of the structure above the bed caused by soffit diameter widening from 0.1 m to 0.3 m (b). Low discharge is not affected as it does not reach the soffit base.

6.3.2.3. Stage-discharge relationship

To establish a relationship between the summer and winter storm events, two rating curves were constructed located at the NCDBDY (Figure 6.22a and b). Rating curves downstream of the WDD were required as changes to the WDD such as blockage can alter the stage-discharge relationship (Watson et al., 2016). Rating curves were constructed in EA format using Equation 6.10 (Ramsbottom and Whitlow, 2003). A stage-discharge rating quality assessment was conducted with an A1 grading achieved. An A1 quality rating curve demonstrates a rating in the modular range and within design limits and specifications with modelled flow depths calibrated by the pressure level sensors (Lamb et al., 2006b).

The summer rating curve (Figure 6.22a) showed the surcharge effect caused by the in-channel WDD. Methods of increasing rating curve accuracy from the determined ±20%, such as applying rating curve extension or the slope-area method were not applied as there was a transition from modular, to surcharge flow (Ramsbottom and Whitlow, 2003) though these effects were minimal. Figure 6.22a displays a surcharged structure with the flow regime split into two different sections. This change in the flow regime known as the modular limit is prominent at a bankfull stage (h_s) of 151.4 m and is created by the channel spanning horizontal key member which restricts the flow. Once this key member is surcharged the flow regime attempts to revert to modular flow rating conditions. This finding is supported by Ramsbottom and Whitlow (2003) who note the structure rating curve changes at the point of hydraulic restriction because of drowning at an in-channel obstacle causing the modular limit.

The winter rating curve (Figure 6.22b) displays higher discharge and flow depths compared to a summer storm event. The WDD has less effect with both the obstructed and unobstructed channel rating curves following a drowned flow pattern where supercritical flow over the structure does not occur with no modular flow present (Vasilyev, 2015).

$$Q = C(h_s + a)^\beta \qquad \text{where:} \, C = \frac{R^{\frac{1}{6}}}{n} \qquad (6.10)$$

Equation 6.10 calculates a Rating Curve shown with discharge (Q) using Chezy constant (C), Bankfull stage (h_s), Intercept in rating equation (a) and Power in rating equation (β) (Ramsbottom and Whitlow, 2003). The Chezy constant (C) can be calculated using the hydraulic radius (R) and Manning's n roughness coefficient (n) (Chow, 1959).
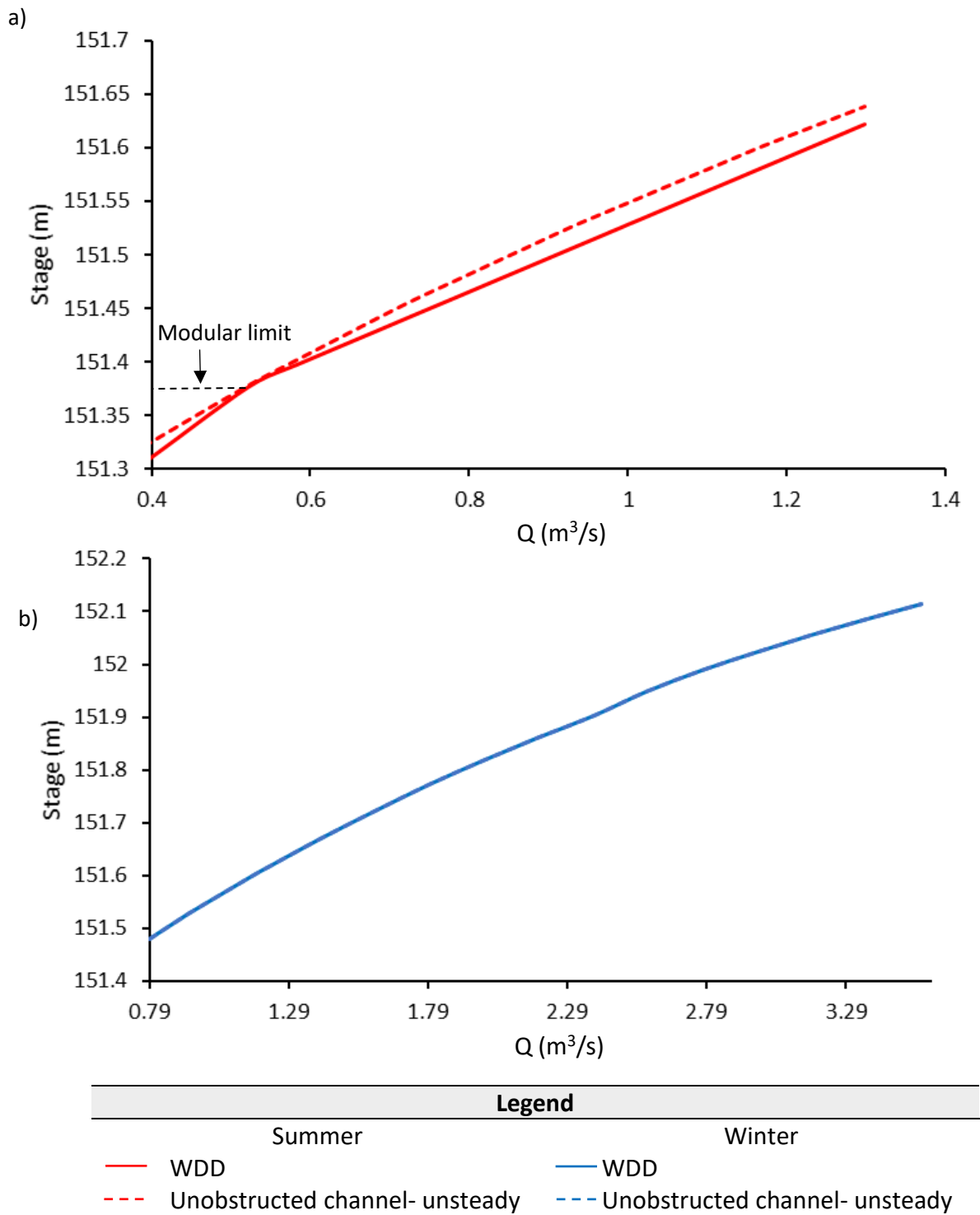
Figure 6.22: Rating curves displaying with and without WDDs. a) Summer rating curve and b) Winter rating curve.

6.3.2.4. Calibration

To verify summer and winter storm events, a comparison was made between the pressure level sensors and FM simulated stages. Two time-series graphs were constructed with accompanying statistics (Figure 6.23 and Figure 6.24). The summer upstream Pearson's correlation coefficient was calculated at 0.977 and downstream of the WDD was calculated at 0.972 therefore the statistical relationship between the pressure level sensors and the WDD representation within FM showed a very strong positive relationship (Equation 3.17 as shown in section 3.3.2.1.). During the winter storm event the Pearson's correlation statistical relationship was 0.88, upstream and 0.937, downstream of the WDD with a strong and very strong positive relationship given respectively.

A Chi-squared assessment was conducted for both the summer and winter storm events, between the observed readings (pressure level sensors) and the expected readings (FM) (Equation 6.11). P-values of 1 were quantified for both upstream and downstream of the WDD with a significance of 0. As the p-values equal 1 the null hypothesis that there was no relationship between the two variables was rejected. This statistical assessment supports that the structural representation produced in FM significantly represented WDD 23 located at Wilderhope Brook.

$$C_s = \sum \frac{(z_i - \hat{z}_i)^2}{\hat{z}_i}$$
(6.11)

Equation 6.11 determines the Chi-squared (C_s) statistical test using expected vertical values ($\hat{z}_i$) and observed vertical values (Z_i).

Statistical significance was further quantified using a t-test Paired Two Sample for Means method (Equation 3.18 as shown in section 3.3.2.1.). The summer storm event upstream absolute value of the t-statistic (-5.758) was lower than the Critical t value for both the FM representation (1.661) and pressure level sensor (1.985) datasets. Since the P-values for FM (5.1×10^{-8}) and the pressure level sensors (1.02×10^{-7}) were lower than the alpha (0.05) the null hypothesis was rejected and therefore the means of both datasets are not equal (Figure 6.23).

While, downstream of the WDD the null hypothesis was additionally rejected. The winter storm events showed an absolute value of the t-statistic (upstream: -1.93 and downstream: 10.106) with the upstream dataset being higher than the critical t value and downstream being lower than the critical t value. Since all P-values for the winter storm event were lower than the alpha (0.05) the means of the datasets were not equal (Figure 6.24).

The summer storm event, FM dataset more closely followed the observed pressure level sensor readings during low discharge, however, at 12 hrs during peak discharge, the projected FM variance was lower at 0.088 m compared to the observed pressure level sensors at 0.213 m, displaying a h_1-h_2 of 0.125 m. In comparison for the winter storm event, FM and pressure level sensor datasets followed a similar pattern with peaks and troughs. The pressure level sensors upstream and downstream of the WDD displayed slightly greater h_1-h_2 and attenuation compared to FM. This supports the work by Pinto et al. (2019) which also found that FM 1D simulations tend to underpredict stage upstream and overpredict stage downstream displaying a h_1-h_2 = 0.19 m. This h_1-h_2 deviation between FM and the pressure level sensors could be caused by the upstream pressure level sensor being located 3.8 m from the upstream face of the WDD and the upstream cross-section being located 15 m from the WDD or the h_1-h_2 deviation could be caused by vertical misalignment when converting the DSM into a DTM using manual editing to construct bed and banks.

	At / upstream		Downstream	
	FM	pressure level sensor	FM	pressure level sensor
Mean	151.458	151.49	151.379	151.335
Standard Error	0.008	0.0184	0.008	0.014
Standard deviation	0.137	0.182	0.132	0.139
Sample Variance	0.019	0.033	0.018	0.019
Kurtosis	-1.373	-1.351	-1.335	-1.22
Skewness	0.107	0.223	0.12	0.388
Range including outliers	0.454	0.552	0.438	0.424
Minimum	151.272	151.261	151.2	151.172
Maximum including outliers	151.726	151.813	151.638	151.596
Confidence Level (95.0%)	0.0159	0.037	0.015	0.028

t-Test: Paired Two Sample for Means		
	At / upstream	Downstream
Hypothesised mean difference	0	0
Degree of Freedom	96	96
t- statistic	-5.758	13.143
P (T ≤ t) one-tail (FM)	5.1Exp-8	1.75Exp-23
t Critical one-tail (FM)	1.661	1.661
P (T ≤ t) two-tail (pressure level sensor)	1.02Exp-7	3.5Exp-23
t Critical two-tail (pressure level sensors)	1.985	1.985

Figure 6.23: Time-series graph making comparison between summer unsteady state simulation and pressure level sensor stage. The FM cross-sections were taken 15 m upstream and 3 m downstream while the pressure level sensors were located 3.8 m upstream and 3.9 m downstream of the WDD face. Descriptive statistics are displayed in the confusion matrix.
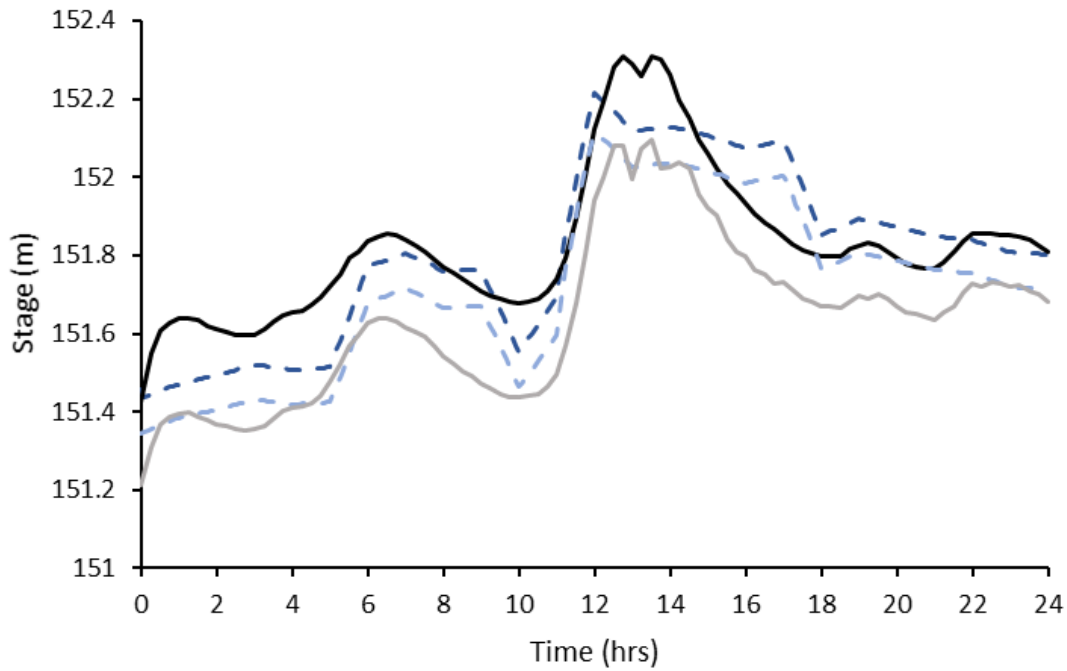
Legend			
FM		pressure level sensor	
---	15 m upstream	—	3.8 m upstream
---	3 m downstream	—	3.9 m downstream

	At / upstream		Downstream	
	FM	pressure level sensor	FM	pressure level sensor
Mean	151.806	151.825	151.716	151.635
Standard Error	0.013	0.019	0.013	0.021
Standard deviation	0.222	0.188	0.222	0.207
Sample Variance	0.049	0.035	0.049	0.043
Kurtosis	-1.078	0.923	-1.105	-0.367
Skewness	0.018	1.048	0.008	0.442
Range including outliers	0.776	0.884	0.769	0.883
Minimum	151.439	151.426	151.344	151.212
Maximum including outliers	152.214	152.31	152.113	152.095
Confidence Level (95.0%)	0.026	0.038	0.026	0.042

t-Test: Paired Two Sample for Means		
	At / upstream	Downstream
Hypothesised mean difference	0	0
Degree of Freedom	96	96
t- statistic	-1.93	10.106
P (T ≤ t) one-tail (FM)	0.028	4.41Exp-17
t Critical one-tail (FM)	1.661	1.661
P (T ≤ t) two-tail (pressure level sensor)	0.057	8.82Exp-17
t Critical two-tail (pressure level sensor)	1.985	1.985

Figure 6.24: Time-series graph making comparison between winter unsteady state simulation and pressure level sensor stage. The FM cross-section was taken at the WDD while the pressure level sensors were located 3.8 m upstream of the WDD face. Descriptive statistics are displayed in the confusion matrix.

6.3.3. Lower reach

6.3.3.1. Conveyance

A lower course conveyance graph (Appendix R) was constructed to improve model stability and enhance output accuracy by identifying and improving cross-sections with notable variance. Cross-sections displaying variance had panel markers added at relevant points. Wide extended cross-sections encompassing parts of the floodplain are displayed in Appendix R for instance cross-section 10, containing WDD 17 which has formed a 0.29 m deep pool.

6.3.3.2. Comparison between confined and unconfined channel

FEH catchment descriptors, determined total volume entering the channel as being 46,730.9 m^3 during the summer storm event and 160,910.4 m^3 during the winter storm event. At the B4368 bridge, for the summer storm event, the flow logger recorded a total volume of 36,620.48 m^3, showing a 21.64% decrease from the total volume that entered the channel throughout the catchment and a total volume of 32,133.79 m^3 using the Flood Estimation Handbook (FEH) catchment descriptors showing a 31.24% decrease. In comparison during the winter storm event, the flow logger measured a total volume of 119,452.47 m^3, showing a 25.76% decrease from the total volume that entered the channel throughout the catchment and a total volume of 102,155.16 m^3 using the FEH catchment descriptors showing a 36.51% decrease.

Unconfined channels are defined as channels that possess extensive flood plains across which over-bank flows spread, while channels with valley walls and lacking floodplains are confined channels (Montgomery and Buffington, 1998). Wilderhope Brook lower reach was simulated either being confined with glass walls or unconfined which enabled bank overtopping as represented through a reservoir unit. Different WDDs have different h_1-h_2 values in respect to discharge due to their design and location. During the winter storm event all WDDs in the confined channel displayed greater h_1-h_2 (Figure 6.25 and Figure 6.26) compared to the unconfined channel. During both summer and winter storm events in the confined channel,

WDD 14 displayed greatest h_1-h_2 (Figure 6.25e and Figure 6.26e), whereby both h_1-h_2 and discharge increased in respect to one another. WDD 14, took longer to be surcharged due to its modelled maximum height of the structure above the bed compared to the other WDDs. Once WDD 15 and 17 became surcharged, h_1-h_2 remained relatively constant at 0.035 m and 0.012 m (summer: 9 hrs and 10 hrs) (Figure 6.25d and b) and 0.027 m and 0.017 m (winter: 0 hrs and 5 hrs) (Figure 6.26d and b).

Results from the confined channel showed as discharge increased h_1-h_2 values also increased however, this did not happen in the unconfined channel. In the unconfined channel, once bank overtopping occurs, h_1-h_2 decreases and remained lower than in the confined channel. This is particularly noted at WDD 16 (Figure 6.25c and Figure 6.26c) and WDD 18 (Figure 6.25a and Figure 6.26a) where the unconfined channel h_1-h_2 follows the confined channel h_1-h_2 until bank overtopping. All modelled WDDs provided a step in the longitudinal profile. However, step size depends on WDD design, location and discharge.

Figure 6.25: Graphs displaying summer storm event h_1-h_2 over time for WDD: a) 18, b) 17, c) 16, d) 15, e) 14. Each graph compares the confined to the unconfined channel. Discharge is shown as bar graph (secondary axis) to provide a reference for time to peak discharge.
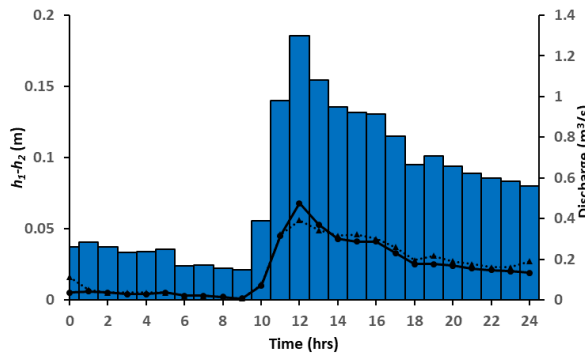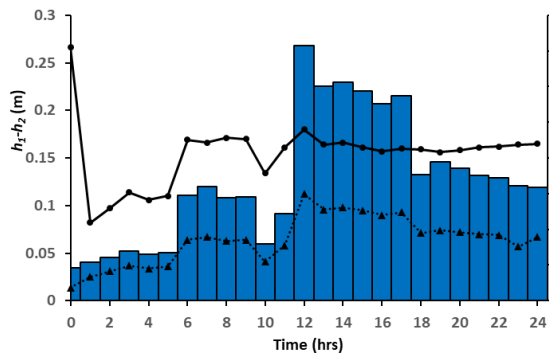
a) WDD 18
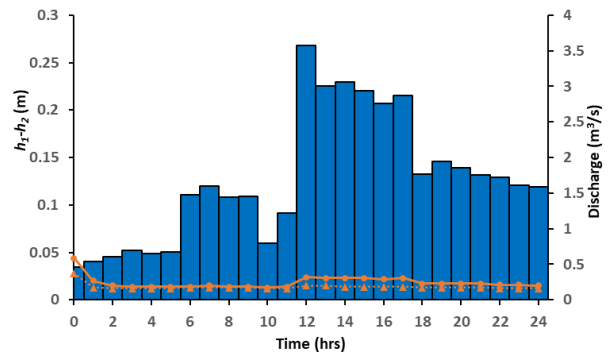
b) WDD 17
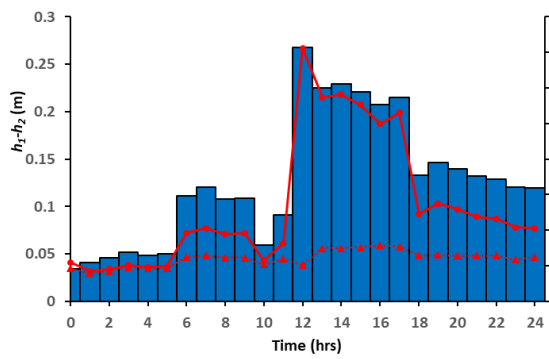
c) WDD 16
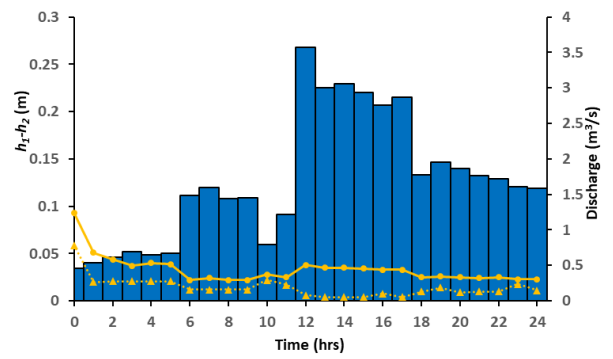
d) WDD 15
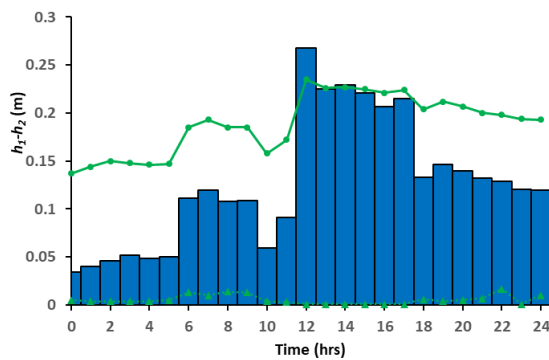
e) WDD 14
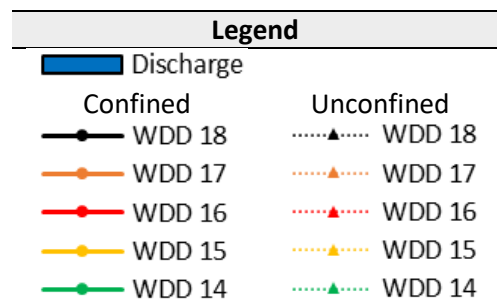
Figure 6.26: Graphs displaying winter storm event h_1-h_2 over time for WDD: a) 18, b) 17, c) 16, d) 15, e) 14. Each graph compares the confined to the unconfined channel. Discharge is shown as bar graph (secondary axis) to provide a reference for time to peak discharge.

At peak discharge (12 hrs), for both summer and winter storm events, the confined channel displayed greater h_1-h_2 and hence greater total in-channel attenuation (T_A) produced by the WDDs (Figure 6.27). Confined channel results show the larger the discharge, the larger the h_1-h_2. In comparison, for the unconfined channel, having obstructions or not, poses little T_A difference (Figure 6.28). Therefore, to show greatest contrast to T_A in the unobstructed channel, the channel should be confined with WDDs installed in deep entrenched channels. WDDs placed in an unconfined channel showed, as bank overtopping increased, h_1-h_2 decreased. This in turn reduces the effectiveness of WDDs in attenuating in-channel discharge as the flow is directed over the floodplain.
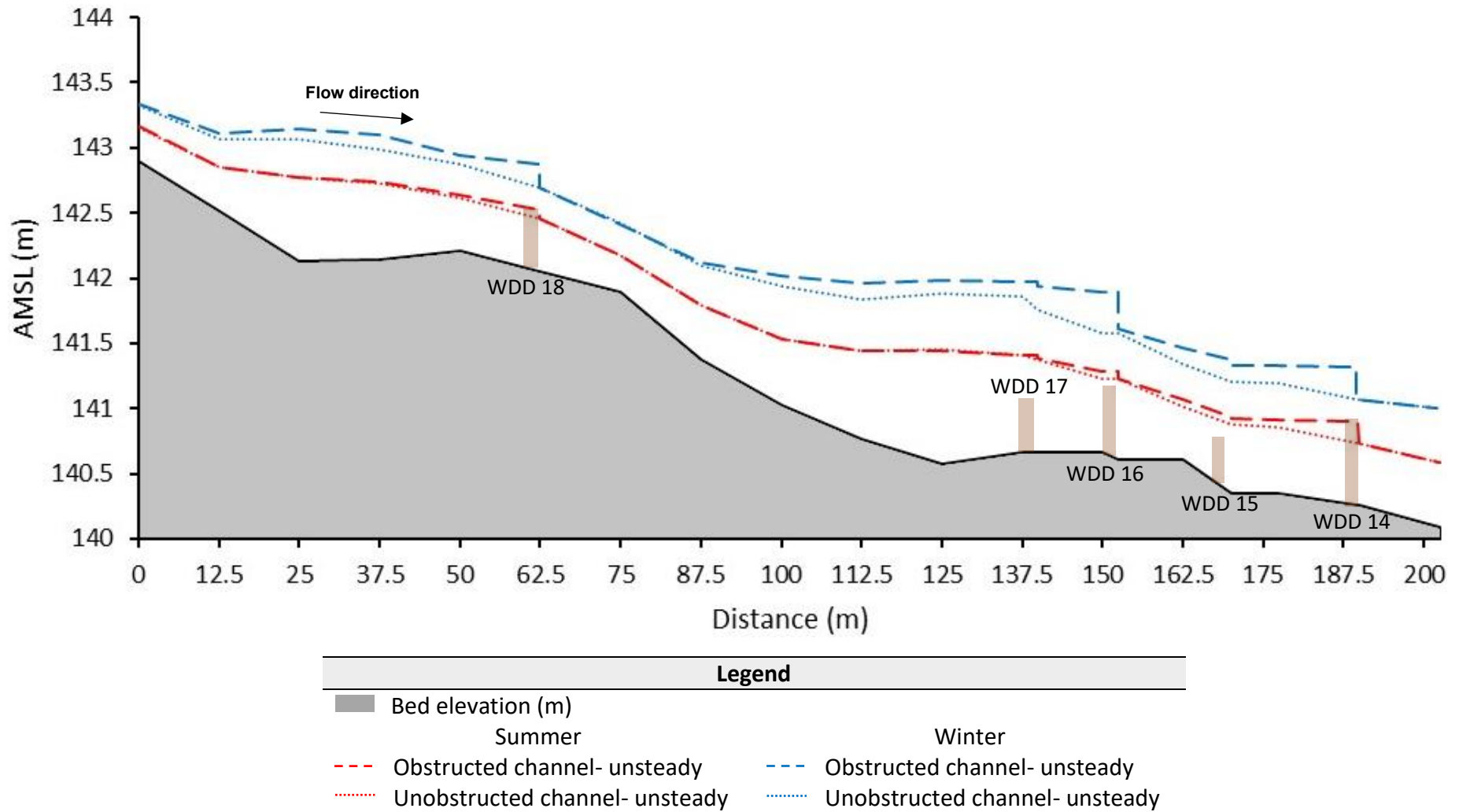
Figure 6.27: Longitudinal profile displaying h_1-h_2 for both summer and winter storm events. Glass walls have been applied (dflood = 10 m).
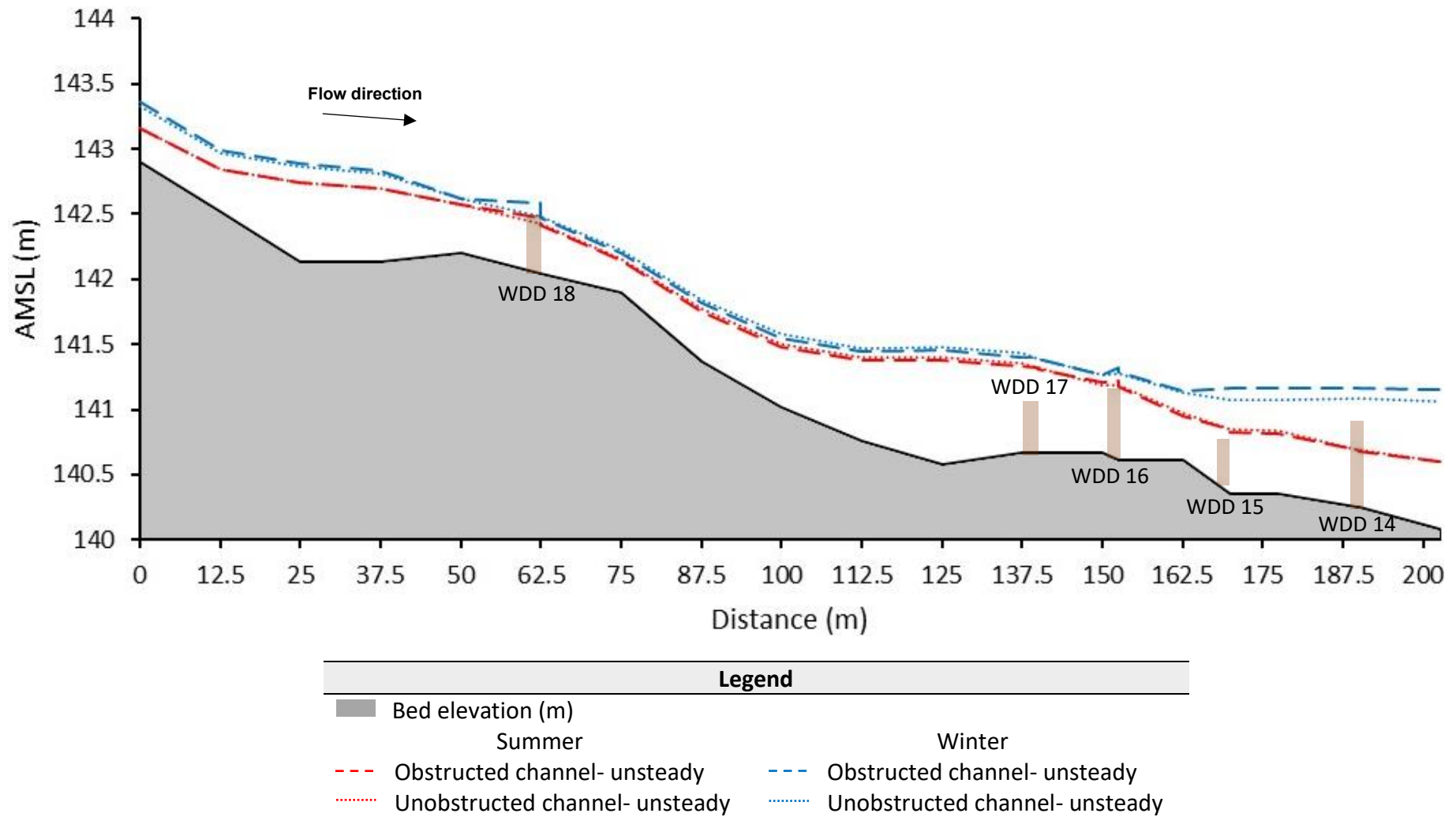
Figure 6.28: Longitudinal profile displaying h_1-h_2 for both summer and winter storm events. Floodplain has been applied and glass walls removed.

During the winter storm event towards the bottom of the lower reach, flow depth increases as it approaches the ford. In the unconfined channel with an upstream flow depth of 0.909 m, ponding at the ford submerges WDD 14-15 and hence reduces the WDDs effectiveness in attenuating peak discharge (Figure 6.28). In the unconfined channel WDD 14 provided the least in-channel attenuation at 0.001 m^3 (Table 6.5). WDD 14 is located on a narrow channel section which restricts the hydraulic radius value, however ponding at this location reduces the restricted hydraulic radius effects with slower localised velocity (0.059 m/s). In comparison, in the confined channel, localised velocities quickened by 1.042 m/s. In the confined channel, an upstream flow depth of 0.247 m meant WDD 14 provided the greatest in-channel attenuation at 5.417 m^3 (Table 6.5). This is because bank overflow was not feeding into the pond in the unconfined channel which lowered the depth of the pond. Due to greater h_1-h_2 and WDD location, channel morphological change is prone to occur. This finding supports Benn et al. (2004) who states if channel narrowing occurs, this increases the upstream flow depth and h_1-h_2 across the structure. This could potentially cause WDD 14 to become mobile during high discharge with the average stream pressure on the debris due to the flow was calculated at 0.599 (Equation 6.9). In the unconfined channel with ponding caused by bank overtopping this reduces the likelihood of WDD 14 becoming mobile during high discharge.

Table 6.5: Displaying WDD in-channel attenuation prior to bank overtopping at 11 hrs 25 mins (summer), 5 hrs 30 mins (winter). Attenuation calculated on the assumption cross-sectional area did not change upstream to the point where flow depth in the unobstructed channel equalled flow depth in the obstructed channel. T_A has been calculated.

	Confined channel		Unconfined channel	
WDD	Summer (m^3)	Winter (m^3)	Summer (m^3)	Winter (m^3)
18	1.327	3.938	0.996	2.095
17	0.039	1.16	0.115	0.145
16	0.252	4.677	0.151	0.193
15	0.675	1.463	0.516	1.328
14	5.417	12.041	0.001	0.003
T_A:	7.71	23.279	1.778	3.759

During the summer storm event at peak discharge, WDDs 14-18 had a T_A = 7.71 m^3 (confined channel) and a T_A = 1.77 m^3 (unconfined channel) (Table 6.5). WDDs 14-18, T_A was larger in

the winter compared to the summer and therefore as discharge increases greater attenuation occurs. In the confined channel a trend forms where attenuation increases further down the longitudinal profile. In comparison in the unconfined channel, the opposite occurs whereby greatest attenuation takes place in the upper course.

All 105 WDDs were extrapolated to obtain catchment in-channel total attenuation (T_A). This was produced from WDDs 14-18 and WDD 23 for the confined channel and WDD 14-18 for the unconfined channel T_A results at peak discharge for both summer and winter storm events. Extrapolation was based on stratified sampling whereby the WDDs were selected as being typical of the 105 WDDs within Wilderhope Brook catchment. Localised descriptors of the geomorphology and dam design spatially alter and therefore the extrapolation method provides an approximation to T_A within Wilderhope Brook catchment (Archer et al., 2016). For the summer storm event WDD induced T_A = 161.91 m^3 (confined channel) and T_A = 31.338 m^3 (unconfined channel) and for the Winter storm event T_A = 488.859 m^3 (confined channel) and T_A = 78.939 m^3 (unconfined channel). FEH catchment descriptors, determined total flow entering into the channel for both storm events as being 46,730.9 m^3 (Summer) and 160,910.4 m^3 (Winter). Therefore, for the obstructed channel, summer storm event discharge reduced by total in-channel attenuation as a percentage of total flow volume (B_A) of 0.356% (confined channel) and B_A = 0.067% (unconfined channel) compared to the winter storm event, B_A = 0.304% (confined channel) and B_A = 0.049% (unconfined channel).

6.3.3.3. Bank overtopping

Bank overtopping initiates 12.5 m downstream of the culvert positioned under the B4368 bridge for 62.5 m. Bank overtopping also initiates 137.5 m downstream of the B4368 bridge for 50 m. Overbank flow re-enters the channel at 187.5 m for 25 m at the ford used to access the northern field section. For overbank flow to re-enter the channel downstream it travels 145 m across the floodplain (Figure 6.29). The lower course floodplain consists primarily of improved grassland used for sheep and cattle grazing with the landcover having a Manning's n roughness coefficient of 0.03 s/m$^{\frac{1}{3}}$ compared to an earth channel clean with 0.022 s/m$^{\frac{1}{3}}$ (Chow, 1959). This meant that the overbank flow was subjected to increased friction which

slowed the flow. For instance, during the winter storm event in an obstructed channel, bank overtopping initiated at 0 hrs for cross-sections 13 and 14 before re-entering the main channel downstream at cross-section 15 and 16 at 30 mins.

In the unobstructed channel, cross-sections 13/14 showed more bank overtopping for a longer duration than the obstructed channel. For instance, at cross-section 13 during the winter storm event, bank overtopping initiated at 10 hrs 5 mins with peak discharge modelled at 0.718 m^3/s in the unobstructed channel and at 11 hrs with peak discharge modelled at 0.402 m^3/s in the obstructed channel (Appendix S). In comparison the opposite occurred with cross-sections located in the upper part of the study reach. Cross-section 4 containing WDD 18 had bank overtopping occurring at 10 hrs 35 mins with peak discharge modelled at 0.16 m^3/s and in the unobstructed channel, bank overtopping occurred at 10 hrs 55 mins with peak discharge modelled at 0.074 m^3/s (Appendix S). The channel containing WDDs had more bank overtopping occurring towards the upper part of the study reach while the unobstructed channel had greater bank overtopping occurring in the lower part of the study reach (Figure 6.30).

During the summer storm event, cross-section 12 was the only cross-section that overtopped with WDDs installed but did not overtop in the unobstructed channel (Figure 6.29a; Appendix S). WDD 15 located in cross-section 13 attenuated 0.675 m^3 (confined channel) and 0.516 m^3 (unconfined channel) which heightened the upstream flow depth and created 1.43 m^3 of cross-sectional bank overtopping in the unconfined channel (Table 6.6).
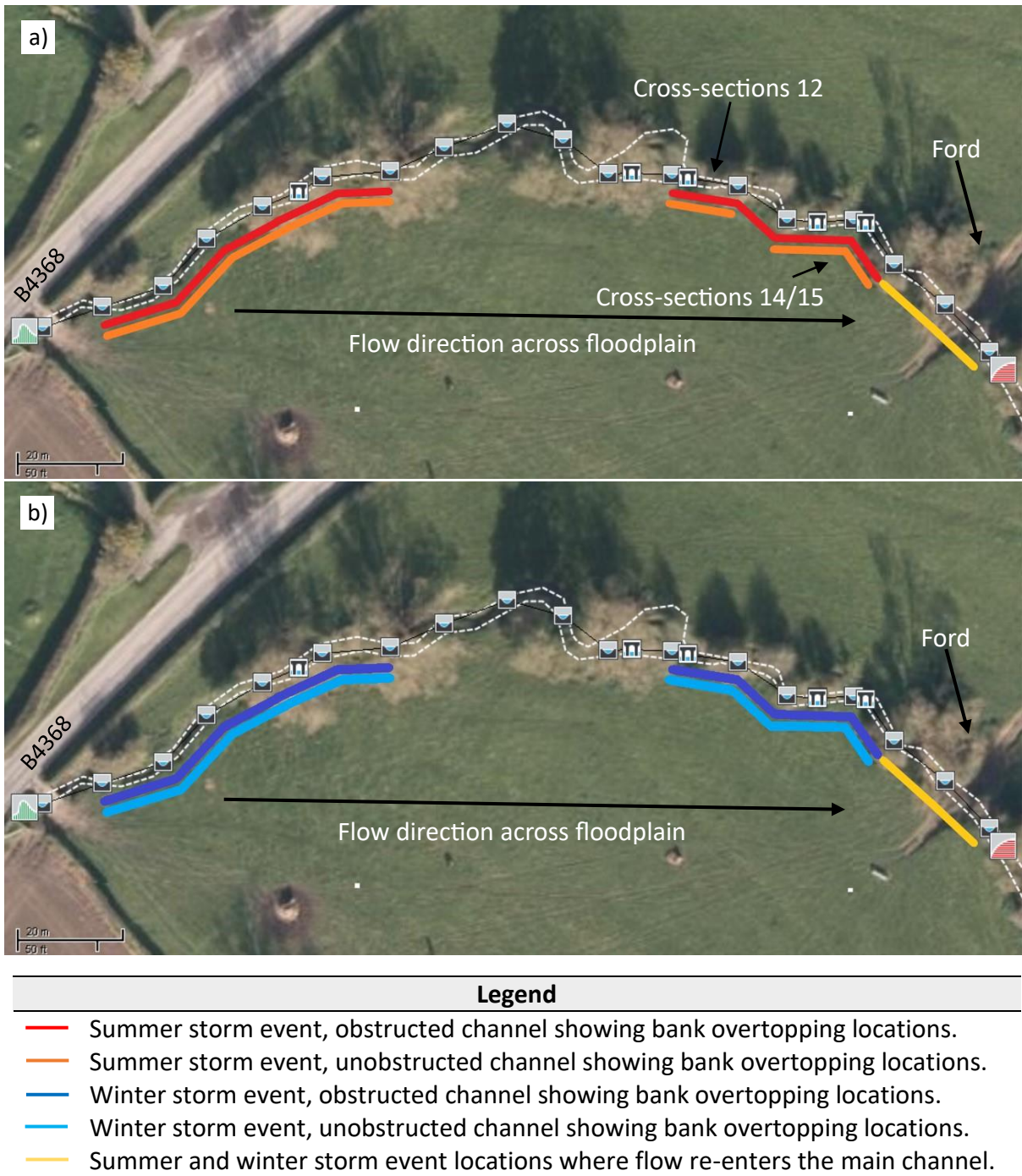
Figure 6.29: a) Summer storm event map displaying Wilderhope Brook lower reach where bank overtopping occurred with and without WDDs installed. b) Winter storm event map. White dotted line displays water course longitudinal profile with cross-sections set at 12.5 m distances, 5 WDD positions marked with pier-loss bridge unit symbol, QTBDY located at the B4368 bridge and NCDBDY located at the downstream ford.
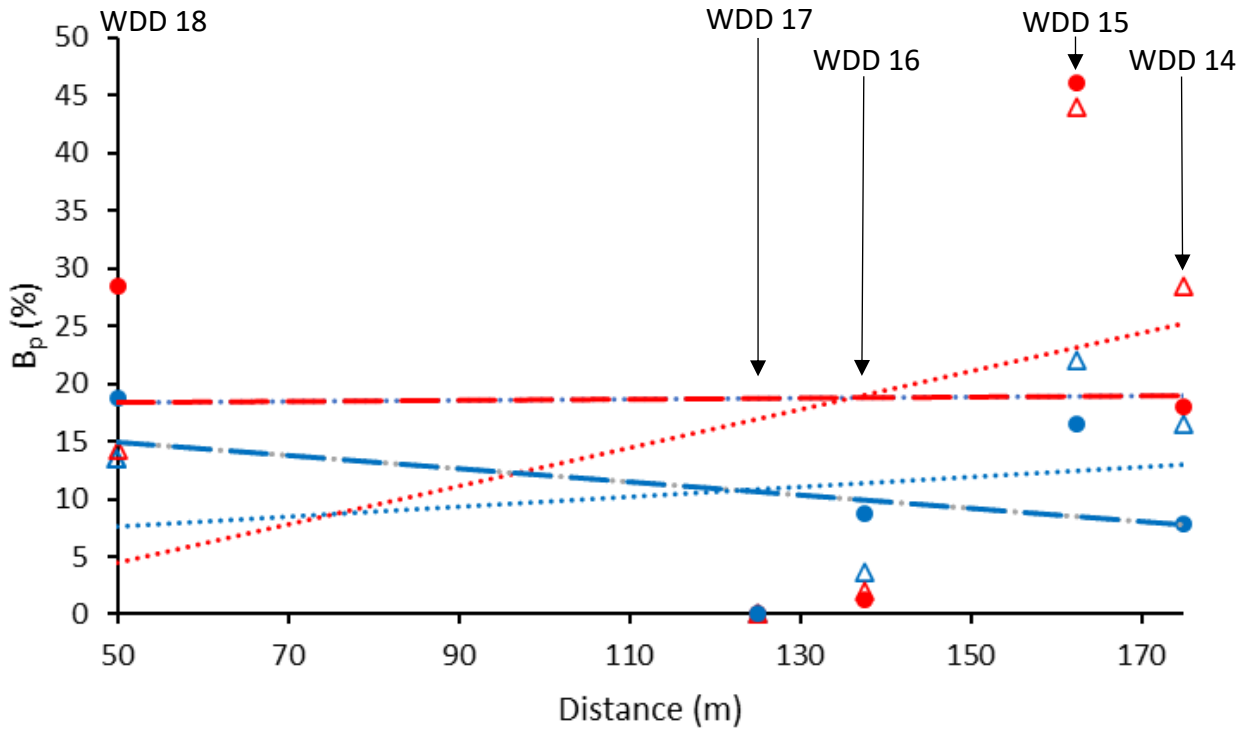
Summer	Trendline equations
O WDD % of total flow	-
Δ Unobstructed channel % of total flow	-
- - - WDD trendline	Distance = $0.0049B_p$ + 18.133
········ Unobstructed channel trendline	Distance = $0.1653B_p$ - 3.7176
Winter	
O WDD % of total flow	-
Δ Unobstructed channel % of total flow	-
- - - WDD trendline	Distance = $-0.0567B_p$ + 17.762
········ Unobstructed channel trendline	Distance = $0.0431B_p$ + 5.5082

Figure 6.30: Graph displaying when WDDs are installed they create more bank overtopping in the upper course compared to the unobstructed channel whereby bank overtopping in more prone to occur in the lower course with increased discharge created by the ReFH unit. Trendlines with equations are displayed whereby distance and total floodplain attenuation as a percentage of total flow volume (B_p) are displayed.

Table 6.6: Displaying bank overtopping volume for each cross-section. Table includes which cross-sections have WDDs, total floodplain attenuation (T_p), total re-entered channel and total remaining on the floodplain.

Cross-sections		Summer, obstructed (m³)	Summer, unobstructed (m³)	Winter, obstructed (m³)	Winter, unobstructed (m³)
1		321.87	314.24	23864.96	23864.96
2		2.61	2.17	6098.3	6098.3
3		8.12	13.1	8944.66	3506.41
4	WDD 18	1565.02	451.56	17511.07	10966.64
5		5.93	22.41	736.88	1484.61
6		0	0	0	0
7		0	0	0	0
8		0	0	0	0
9		0	0	0	0
10	WDD 17	0	0	0	0
11	WDD 16	70.46	64.71	8171.04	3042.1
12		1.43	0	5229.02	1429.77
13	WDD 15	2540.86	1387.87	15400.64	18027.97
14	WDD 14	992.44	897	7390.35	13473.9
T_p:		5508.74	3153.06	93346.92	81894.66
15		-2936.8	-1680.82	-47015.9	-40759.4
16		-2570.54	-1471.14	-45686	-41035.7
Total re-entered channel:		-5507.34	-3151.96	-92701.9	-81795.1
Total remaining on floodplain:		1.4	1.1	645.02	99.56

For the summer storm event, total floodplain attenuation (T_p) of 5,508.74 m³ (obstructed channel) and T_p = 3,151.06 m³ (unobstructed channel). At the B4368 bridge, the flow logger recorded a total flow volume of 36,620.48 m³ while the FEH projected a total flow volume of 32,133.79 m³ during the summer storm event. Therefore, as obtained from the flow logger, total floodplain attenuation as a percentage of total flow volume (B_p) downstream of the B4368 bridge was calculated at B_p = 15.04% (obstructed channel) and B_p = 8.6% (unobstructed channel). In comparison, the FEH catchment descriptors projected a B_p = 17.14% (obstructed channel) and B_p = 9.81% (unobstructed channel). Therefore, there was a strong correlation between the flow logger and the FEH.

During the winter storm event, bank overtopping accounted for a total floodplain attenuation (T_p) value of 93,346.42 m³ (obstructed channel) and 81,894.66 m³ (unobstructed channel). At

the B4368 bridge, the flow logger recorded a total flow volume of 119,452.47 m^3 while the FEH projected a total flow volume of 102,155.16 m^3 during the winter storm event. Therefore, as obtained from the flow logger, B_p = 78.15% (obstructed channel) and B_p = 68.56% (unobstructed channel). The FEH catchment descriptors projected B_p = 91.38% (obstructed channel) and B_p = 80.17% (unobstructed channel).

Floodplains and sacrificial land can act as extra water storage areas which slow the flow during periods of bank overtopping (Woltemade and Potter, 1994; McCartney and Naden, 1995). To acquire catchment attenuation (T_A+T_p) it is useful to understand the interaction between the main channel and the floodplain (O'Sullivan et al., 2012). If T_p is added to all 105 WDD induced T_A, T_A+T_p can significantly increase, particularly noted in small water courses with small carrying capacities. During the summer storm event, T_A = 31.388 m^3 while T_p = 5508.74 m^3 and therefore T_A+T_p = 5,540.128 m^3. This means when applying the FEH catchment descriptors determining total flow entering into the channel, catchment attenuation percentage (B_A+B_p) was calculated at 11.855%, a large increase from the amount than can be attenuated solely in-channel (confined channel: B_A = 0.356% and unconfined channel: B_A = 0.067%). This result shows WDDs positioned on floodplains can significantly cause more attenuation compared to just in-channel attenuation. For instance, once bank overtopping occurred, there was ≈ 33x more attenuation. In an unobstructed channel T_p = 3,153.06 m^3, causing B_A+B_p to reduce to 6.74%. Therefore, WDDs created ≈ 1.75x more T_A+T_p than without them. In comparison during the winter storm event, T_A = 78.939 m^3 while T_p = 93,346.92 m^3 with T_A+T_p = 93,425.859 m^3. Therefore, in an obstructed channel the B_A+B_p = 58.061% with this percentage increase caused by larger discharge. A B_A+B_p = 58.061% shows ≈ 191x more attenuation compared to just in-channel attenuation from B_A = 0.304% (confined channel) and B_A = 0.049% (unconfined channel). Once again this is because with a larger discharge, more bank overtopping can occur with excess flow attenuated on the floodplain. However, once flow re-enters into the channel the floodplain stops acting as a storage area. Typically, floodplain storage areas have been noted as being 200-1000 m^3 (Quinn et al., 2013b). A B_A+B_p = 58.061% could be regarded as an overestimate as T_A+T_p is site specific depending upon catchment descriptors such as floodplain geomorphology and landcover type (Metcalfe et al., 2017). In an unobstructed channel T_p = 81,894.66 m^3 meaning the percentage reduces to B_A+B_p = 50.894%. These results show WDDs are effective at enhancing floodplain connectivity. Modelling studies outlining WDD effects on

flood reduction are shown in Appendix S. Findings from studies (Appendix S) including the present study found WDD reduce downstream peak discharge. However, in an unconfined channel as discharge increases T_A reduces. When T_p is considered, during high discharge, attenuation increases with a larger percentage.

A larger total flow volume re-entered the obstructed channel compared to the unobstructed channel for both summer and winter storm events (Figure 6.4). For the summer storm event, the obstructed channel simulation projected 99.98% of total flow volume re-entered the channel leaving 1.4 m^3 on the floodplain and in the unobstructed channel this percentage decreased to 99.97%, leaving 1.1 m^3 on the floodplain. In comparison, during the winter storm event, the obstructed channel simulation projected 99.31% of total flow volume re-entered the channel leaving 645.02 m^3 on the floodplain. In the unobstructed channel this decreased to 99.56 m^3 with a larger percentage of total flow re-entering the channel (99.88%). Therefore, during high discharge a larger percentage of the total flow volume does not re-enter the channel unlike during lower discharge with a lower percentage remaining on the floodplain.

All cross-sections with WDDs exhibited bank overtopping apart from WDD 17 which is located on a meander in a pool whereby during high discharge the meander neck can submerge rather than spilling onto the floodplain. By increasing floodplain connectivity, the attenuation effect is enhanced (Ngai et al., 2017). The main channel width widens at cross-section 10 which enables a flood storage area particularly noted during high discharge (Appendix U, WDD 17).

6.3.3.4. Woody debris dam design

Summer simulations with lower discharge and structures being more porous with less detritus blocking spacings between key members, blockage ratio reduces compared to the winter. As the blockage ratio reduces, h_1-h_2 increases in respect to discharge in the confined channel. For instance, at low discharge, the h_1-h_2 value can be negligible, though proportionately, at low discharge the h_1-h_2 proportion can be greater than at high discharge (Figure 6.31). In an unconfined channel the relationship between discharge and h_1-h_2 reduces with bank overtopping causing discharge to by-pass the WDD through overflow.
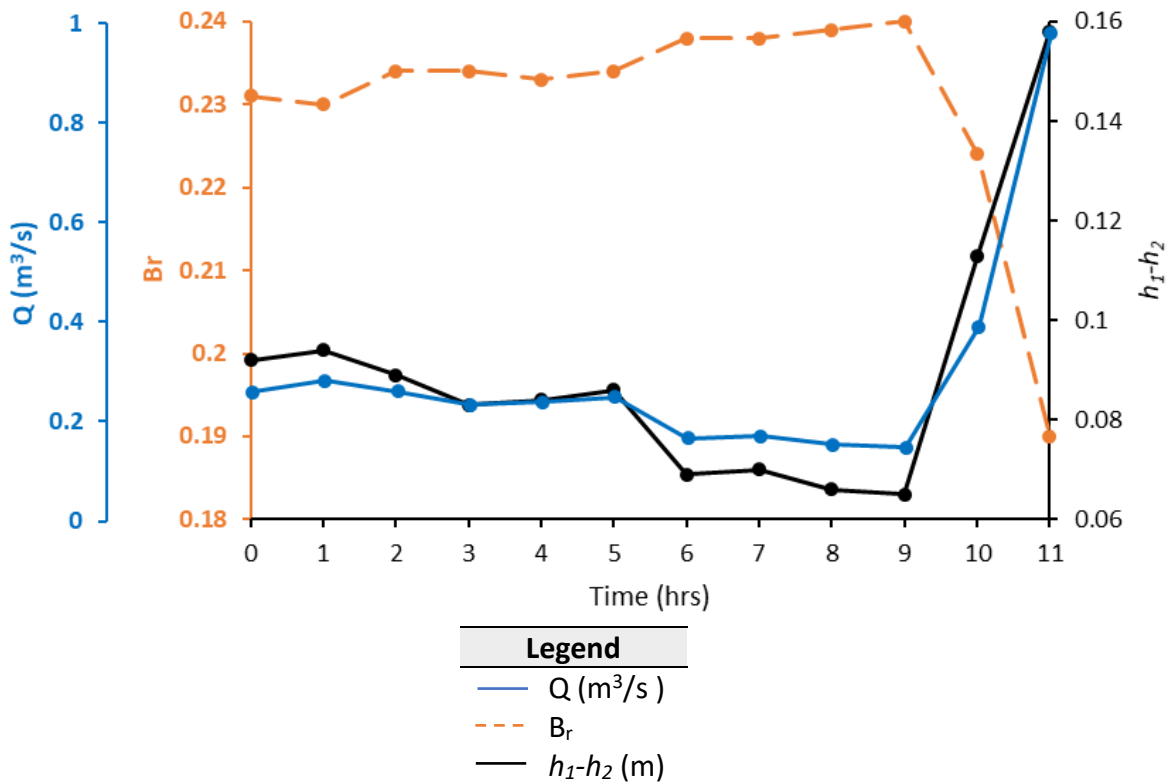
Figure 6.31: WDD 18, summer storm event graph making comparison between blockage ratio (B_r) and afflux (h_1-h_2) for WDD 18. The diagram displays blockage ratio as inversely proportional to the afflux. Maximum time set at 11 hrs (to the nearest hour before bank overtopping at 11 hrs 25 mins).

During the summer storm event, the network of 5 WDDs (14-18) showed travel time across the 0.2 km section within the channel from the B4368 bridge to the ford took 5 mins, with and without WDDs. However, peak discharge reduced from 1.292 m³/s to 1.291 m³/s.

Figure 6.32a shows the unobstructed channel had steeper rising and falling limbs, indicating when comparison is made between the unobstructed to the obstructed channel, the unobstructed channel is more prone to flash flood events. Flash flood events can alter the WDD hydraulic characteristics, such as porosity, and can lead to wash-out. At the 12 hrs 10 mins mark the obstructed channel displayed higher discharge (1.285 m³/s) than the unobstructed channel (1.284 m³/s). This shows the obstructed channel took longer to return to the normal flow depth and had a more gradually sloped falling limb.

During the winter storm event, the obstructed channel showed greater reduction in peak discharge (3.515 m³/s) in respect to the unobstructed channel discharge (3.532 m³/s), with a

difference of 0.017 m^3/s (Figure 6.32b). Similar to the summer storm event, the winter storm event travel time (from the B4368 bridge to the ford) at peak discharge in the unobstructed channel was shown to be 5 mins. However, with WDDs this extended to 10 mins which reveals that the WDDs attenuated peak discharge for longer (Figure 6.32b). The summer and winter storm events both showed the unobstructed channel was more prone to higher discharges during flash flood events with steeper rising and falling limbs. However, the obstructed channel had more gradually sloped rising and falling limbs, being flatter and spacing the high discharge over a longer period.
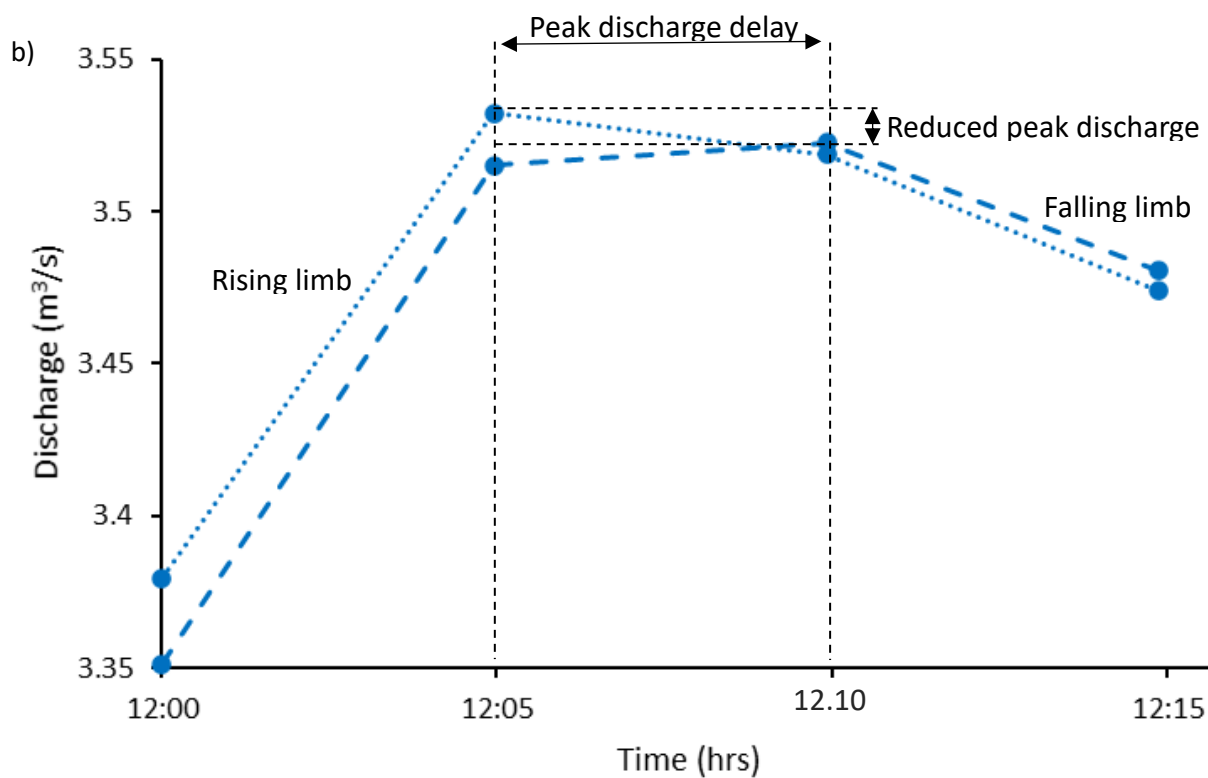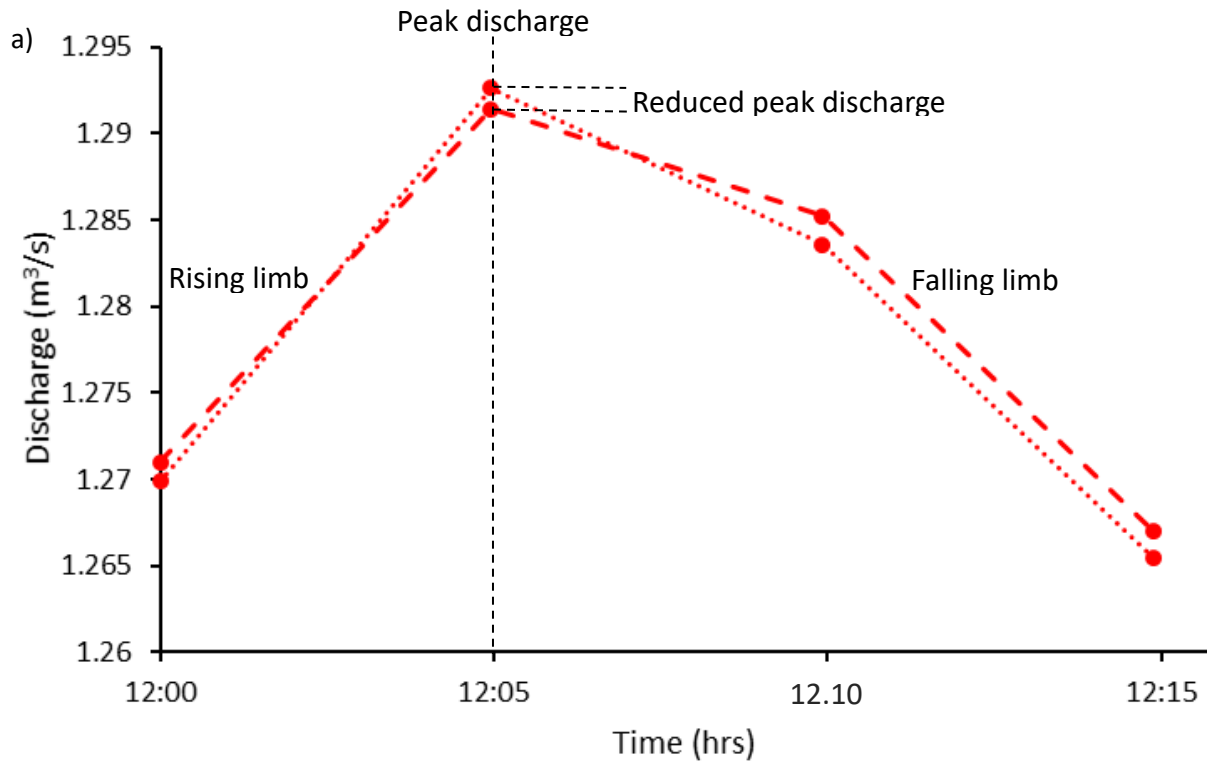
Figure 6.32: a) Summer, time-series / hydrograph displaying peak storm event. Time-series taken at the ford showing with and without WDDs 14-18. Results show lag time remained the same but peak discharge decreased by 0.001 m³/s within the 200 m section. Peak discharge occurred at the B4368 bridge at 12 hrs, taking 5 mins to reach the ford. b) Winter, time series / hydrograph displaying peak storm event. Results show lag time increased by 5 mins and peak discharge reduced by 0.017 m³/s.

6.4. Discussion

This study makes comparison between confined and unconfined channels. Findings show that in the confined channel, during the winter storm event there was an in-channel total attenuation of 23.279 m^3 and during the summer storm event this decreased to 7.71 m^3. There was ≈ 3x greater in-channel total attenuation during the winter storm event potentially due to the sub-surface layer being pre-saturated by Storm Ciara, which would have decreased infiltration, enhanced surface-runoff and increased flow depth. As discharge increased during Storm Dennis (winter event), in-channel attenuation increased until the WDD became surcharged and submerged.

In the unconfined channel, bank overtopping occurred with increased channel–floodplain connectivity from the summer to winter storm events, both including and excluding WDDs. WDDs displaced increased water onto the floodplain during the winter storm event (obstructed channel: 93,346.92 m^3, unobstructed channel: 81,894.66 m^3) compared to the summer storm event (obstructed channel: 5,508.74 m^3, unobstructed channel: 3,153.06 m^3). Simulations revealed that WDDs enhanced lateral flow onto the floodplain, supporting the premise that WDDs increase channel-floodplain connectivity (Thomas and Nesbit, 2012; Keys et al., 2018).

The results showed that the WDDs were highly effective in attenuating the flow in severe discharge events. Realistically, the effectiveness of the WDDs in modelling are dependent upon parameters inclusive of storage capacity to catchment area, whether drainage characteristics would allow recovery between high discharge events, the full capacity of the storage in the catchment with infiltration and residence times. Metcalfe et al. (2018) supports this view stating that it is inevitable that flood modellers have to make some assumptions. Metcalfe et al. (2018), who simulated enhanced hillslope storage using a 1 m high barrier at the downstream boundary of the lumped hydrological response unit, reflect upon storage and impact on runoff including capacity such as position on the hillslope, the distance from access tracks and the channel, the type of location and construction materials and whether storage would be on shallow hillslopes, narrow ephemeral channels or on wide floodplains. Pearson (2020) comments that it would be unlikely that a severe discharge event would sufficiently

attenuate the flow in a catchment with a relatively small storage capacity created with bunds. Furthermore, it is unlikely there would be sufficient attenuation at the peak of an event if some WDD backwaters were full prior to the peak.

This thesis has the advantage of automated field site data, including pressure level sensors, tipping bucket rain gauge and flow logger readings which verifies modelling predictions. Detailed hydrodynamic data for accurate modelling predictions, particularly for high discharge events can rarely be attained in the field to support modelling predictions (Metcalfe et al., 2018). McParland (2021) states that his research uses datasets on the hydrodynamics of large woody dams based on manual field measurements to acquire necessary data to calibrate and validate the model results.

WDDs should be installed in areas where there is a floodplain so when bank overtopping occurs high-valued areas are not exposed to flood risk. During bank overtopping, friction increases with the Manning's n roughness coefficient for an earth channel clean determined at 0.022 $s/m^{\frac{1}{3}}$ compared to improved grassland at 0.03 $s/m^{\frac{1}{3}}$ (Chow, 1959), slowing the flow. As a result, lag time increases which was evidenced during the summer storm event at cross-section 13 where discharge took 30 mins to begin to re-enter the channel at cross-section 15, while the discharge remaining in the channel took ≤5 mins to reach cross-section 15 located at the ford. As the farmer uses the ford as an access point to the northern field section, compacted ground intercepts surface flow creating flow pathways back into the channel. In the unconfined channel, WDDs are shown to be effective in raising flow depth to promote out of bank temporary storage on the floodplain. This supports the work of Thomas and Nisbet (2012) who found that once flow depth reached 100% Q_{bf}, the bank was overtopped and water spilled onto the floodplain, where it re-joined the channel further downstream. To increase lag time, landcover such as riparian buffer zones with higher Manning's n roughness coefficients could be grown on the floodplain. Riparian zones can control overflow to take a more sinuous route around vegetation, providing greater infiltration and evaporation time. Nicholson et al. (2015) suggest the use of overland flow barriers as an anthropogenic mechanism to retain high discharge for the duration of the storm event. Overland flow interception such as bunds constructed of soil, wood or stones are used at the Belford site

(Quinn et al., 2013b) to temporarily retain surface runoff on the floodplain and prevent fast surface runoff from quickly re-entering into the channel.

Catchment attenuation significantly increases when total floodplain attenuation is accounted for, as a small percentage increase is attenuated in-channel compared to on the floodplain. For instance, during the summer storm event, the confined channel: B_A = 0.356%, unconfined channel: B_A = 0.067% and unconfined channel including floodplain: B_A+B_p = 11.855%. During the winter storm event a similar pattern follows, confined channel: B_A = 0.304%, unconfined channel: B_A = 0.049% and unconfined channel including floodplain: B_A+B_p = 58.061%. During the winter storm event more flow overtopped the banks and was stored on the floodplain compared to the summer storm event. This meant with greater floodplain attenuation, there was more water to re-enter the channel. However, the amount of water that re-entered the channel was lower than the amount which overtopped the bank. The floodplain acted as a flood storage area where water over time could be removed from the flow regime through evaporation. The longer the water remained on the floodplain, the longer the water has to evaporate. Additionally, as high discharge recedes, the water table lowers providing more infiltration which slows the flow.

WDD 18 positioned closest to the B4368 bridge created a high level of bank overtopping (summer: 1,565.02 m^3, winter: 17,511.07 m^3). This finding corroborates Metcalfe et al. (2017) in that the first WDD reduced peak discharge either through creating bank overtopping or in-channel attenuation (summer in-channel attenuation: 0.996 m^3, winter in-channel attenuation: 2.095 m^3). In a confined channel, WDDs mimic the Swiss cheese model (Figure 6.33) whereby it is a closed system with discharge being unable to leave and re-enter into the system further downstream. Each WDD, reduces the discharge in respect to WDD design, location and channel geomorphology. However, in an unconfined channel, it is an open system whereby bank overtopping can enable discharge to re-enter into the channel further downstream, hence negating the Swiss cheese model. In this study overflow did not re-enter into the channel until cross-sections 15 and 16, located at the ford. Due to discharge removed from the channel, in-channel attenuation reduced at WDD 17.

Studies such as Muhawenimana et al. (2022) tried to examine the effectiveness of a network of WDDs by modelling eight different WDDs as one structure. As previously outlined, each

WDD is different with a different associated bathymetry. Comparison between studies cannot be made as eight WDDs condensed into one structure generalises structural blockage and inundation which creates inaccurate results. The present study models each individual WDD and examines them as a network.
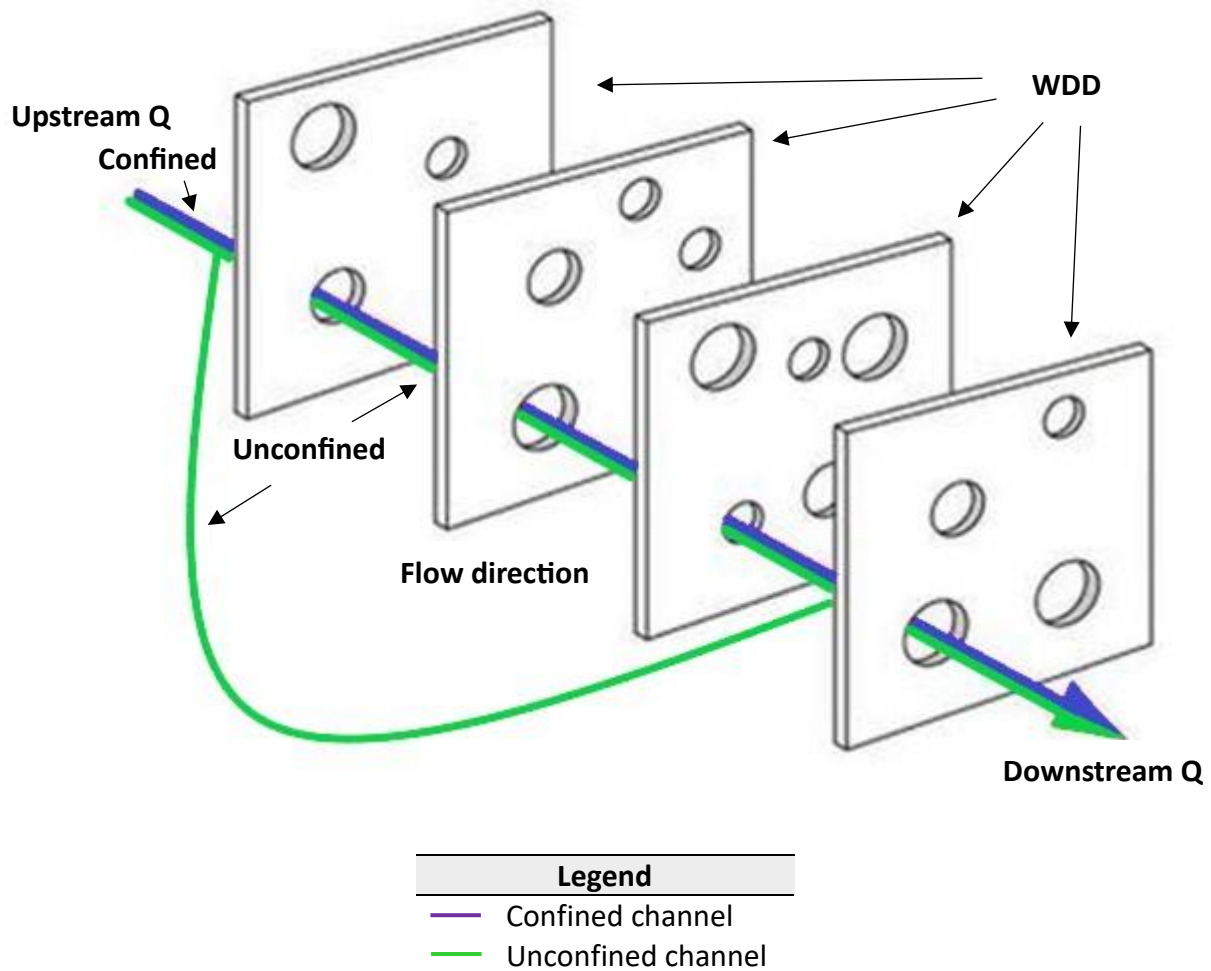
Figure 6.33: Diagrammatical representation of WDDs explained through the Swiss cheese model (adapted from Azadegan, 2022). In a confined channel, upstream discharge reduces through each barrier / WDD until discharge travels through the system. In an unconfined channel discharge can leave the system and re-enter further downstream.

At WDD 18 with increased bank overtopping, h_1-h_2 reduces because as upstream flow depth increases it can overtop the bank and travel over the floodplain rather than surcharging the WDD. To maximise the WDDs effectiveness in attenuating flow, WDD design should account for flow pathways. WDD design at a study site located in Pickering shows WDDs that span across the floodplain (Figure 6.34) slow the flow by intercepting surface flow pathways. In

comparison, WDDs installed at Wilderhope in the mid-upper reach are channel confined (Appendix U) with the effectiveness in slowing the flow dependent upon channel characteristics such as the hydraulic radius or WDD form to function. Findings support the work shown in chapter 3 whereby in the confined channel when the hydraulic radius is restricted, h_1-h_2 is greater than when the channel is unconfined or has an enlarged hydraulic radius. Upon equilibrium, h_1-h_2 decreases until the upstream flow depth equals the downstream flow depth. In this study, the hydraulic radius did not temporally alter as bed erosion did not occur and therefore the confined channel showed increased h_1-h_2. Until the point of bank overtopping, the confined and unconfined channels followed the same attenuation pattern. Upon bank overtopping, the hydraulic radius increases making h_1-h_2 decrease. WDDs change their role down the longitudinal profile. In the upper reach the channel is confined by steep valley slopes and hence WDDs cause increased in-channel attenuation. In the lower reach with a wide gently sloped floodplain, WDDs increase bank overtopping and floodplain connectivity. This is corroborated by Metcalfe et al. (2017) who found downstream WDDs attenuated greatest flow by diverting water onto the floodplain. Therefore, down the longitudinal profile the role of WDDs change from creating in-channel attenuation to increasing bank overtopping. This means the attenuation process changes from studying the hydraulic confinement posed by the WDD to analysing floodplain connectivity. During the summer storm event, WDDs increased floodplain connectivity by 74.71% whereas during the winter storm event floodplain connectivity was increased by 13.98% compared to the unobstructed channel. Though the proportion is higher in the summer storm event, the winter storm event diverted a larger quantity of water onto the floodplain (summer: 2,355.68 m^3, winter: 11,452.26 m^3).

Figure 6.34: Photograph displaying a WDD that spans the floodplain at Pickering (Peak Chief Executive, 2016).

Results showed that during high discharge, in a confined channel, tall WDDs increase in-channel attenuation. In the upper reach with a steep channel slope angle / gradient, WDDs should be tall for greatest in-channel attenuation (Figure 6.35). In the lower reach WDDs should be built to the bankfull stage as once bank overtopping occurs WDD in-channel attenuation reduces while floodplain connectivity increases. This supports the work by Marston (1982) who found tall WDDs take longer to be surcharged while raising the bankfull stage. WDDs with low porosity can impound peak flows, increasing the head and dissipating potential stream energy, however, once surcharged this effect reduces (Wilkinson et al., 2010).
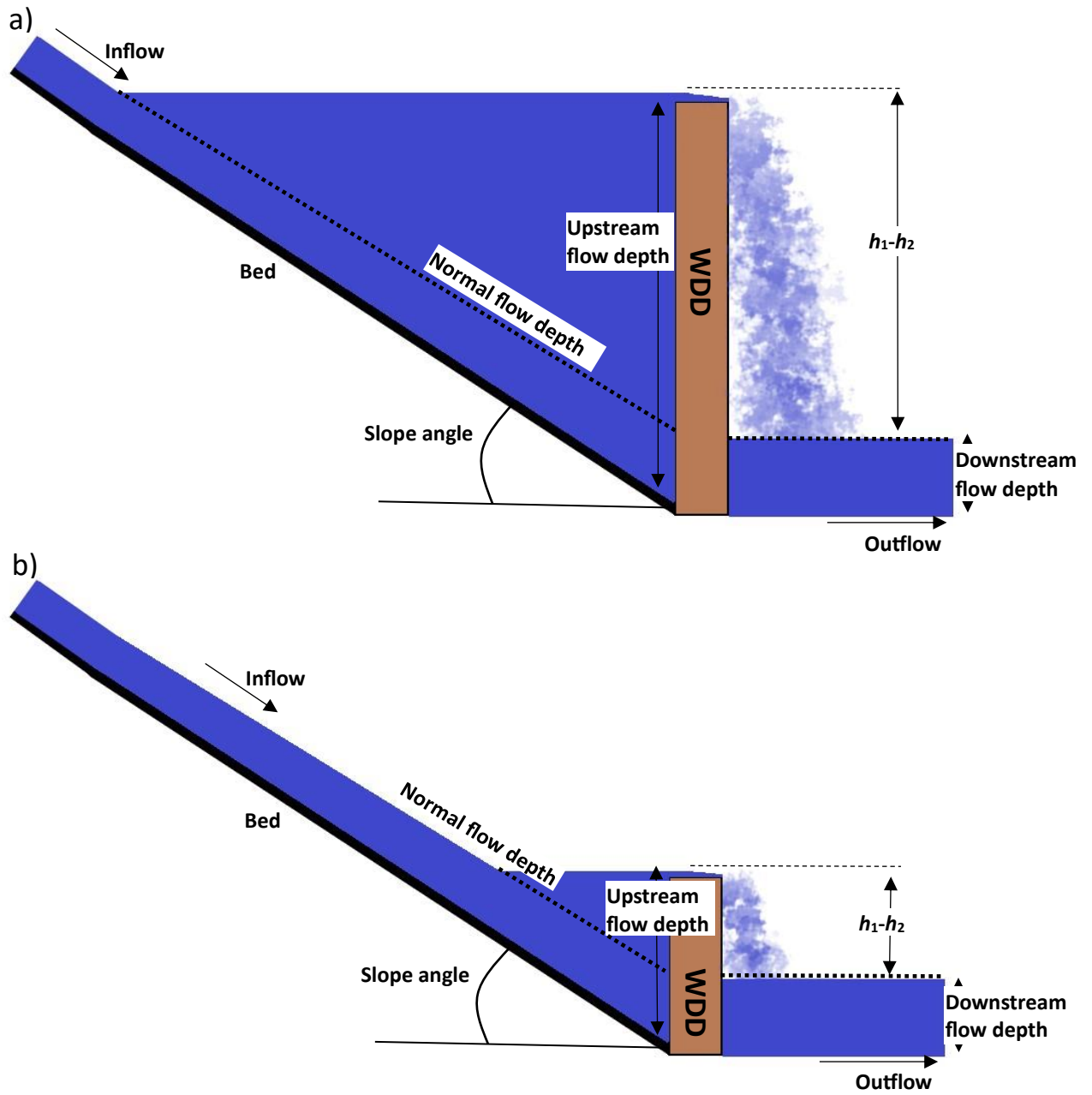
Figure 6.35: Comparison between two WDD heights placed in the upper reach with a steep channel slope angle. The tall WDD (a) has a greater h_1-h_2 compared to a short WDD (b). Normal flow depths are also displayed.

A meander formed between cross-sections 9 and 10 and during high discharge, as flow depth increases the meander neck submerges. On the longitudinal profile this is shown as a pool and downstream at the ford the hydraulic radius increases, whereby due to hydraulic radius changes, flow depth varies. As discharge increases the cross-sectional shape changes (Nelson, 2016). This indicates WDD design in respect to location is site specific (Keys et al., 2018). In respect to design and location, partial WDD 14 causes more in-channel attenuation than some active WDDs (16/17). This is because WDD 14 is located on a narrow channel section, but if this partial WDD was located in an area with a large hydraulic radius and blockage ratio then h_1-h_2 would reduce. WDD 17, which is located in an area of low-lying land, has a low blockage ratio and as flow approaches, upstream localised velocity slows which raises the upstream flow depth. These findings corroborate Benn et al. (2004) who state that the smaller the blockage ratio value the larger the h_1-h_2. However, as WDD 17 is located in a pool this increases downstream flow depth and reduces the value of h_1-h_2 compared to the case where no pool is present.

It has been suggested WDDs be installed at distances between 7–10 times the bankfull stage width (Linstead and Gurnell, 1999). WDD 15 has a bankfull stage width of 4.5 m and would need WDD 14 to be located at a minimum distance of 31.5 m. Therefore, the placement of the downstream WDD 14 was outside the threshold working distance to prevent backwater affecting the upstream WDD. Though the efficacy of WDD 15 was reduced due to its location, in an unconfined channel it nonetheless attenuated 0.516 m^3 (summer storm event) and 1.328 m^3 (winter storm event), which created bank overtopping at cross-section 12 which did not happen in an unobstructed channel. Though floodplain storage occurred the values were small.

For WDD 23, during both summer and winter storm events peak discharge, upstream specific energy (E_1) to downstream specific energy (E_2) decreased from E_1 = 0.907 J/Kg to E_2 = 0.874 J/Kg (summer storm event) and E_1 = 1.666 J/Kg to E_2 = 1.645 J/Kg (winter storm event) (Equation 6.12). As stated by Zimmerman et al. (1967) and Smith (1992) kinetic energy is dissipated by the WDD roughness which reduced downstream discharge of the structure. For the summer storm event during peak discharge, kinetic energy was calculated as being 398.83 J within 1 m upstream, and 602.92 J within 1 m downstream (Equation 6.13). Kinetic energy

(KE) is gained after a WDD with increased downstream localised velocity leading to bed erosion and downstream scour hole development (Heede, 1972; FISRWG, 1998).

$$E_1 = h_1 + \frac{Q^2}{2gh_1{}^2} \tag{6.12}$$

Specific energy Equation 6.12 compares upstream and downstream specific energy (E_1 upstream of the WDD) using upstream flow depth (h_1), discharge (Q) and gravity (g) (Hamill, 1995).

$$KE = \frac{1}{2}mU_1{}^2 \qquad\qquad \text{where: } m = \rho.\,V_{ol} \tag{6.13}$$

Equation 6.13 calculated Kinetic energy (KE) using mass of water (m) and mean velocity (U_0) where mass of water (m) is calculated using relative submerged specific density (ρ) and volume (V). Within the present study V was calculated at a 1 m distance (x-direction).

During high discharge, the velocity reference increases, which is likely to increase the average stream pressure on the debris due to the flow suggests WDD 23 could become unanchored and mobile. This finding corroborates SEPA (2015) as to why it is important to monitor WDDs particularly after a high discharge event, whereby it is stated physical features should be identified which may affect flood pathways and possible receptors for instance debris blockage culvert entrances. The Environment Agency (2013) note caution should be taken with WDDs so that they do not become detached and cause downstream blockage which can affect public safety.

6.4.1. Future research

Accuracy refers to how close a measurement or result is from a known or accepted value. Precision is defined as how reproducible measurements or results are (Ranstam, 2008). For this study a photogrammetric DSM supporting a resolution: 0.25 m, horizontal accuracy: ±1 m RMSE, vertical accuracy: ±1.5 m RMSE was acquired. To increase accuracy of the model these

variables could be further improved. When constructing cross-sections, the accuracy was dependent upon resolution. To increase model accuracy higher resolution would be required. Model precision and accuracy was improved by manually editing to remove trees, however, the reproducibility will alter between studies depending upon care taken in editing the base map. Cross-sectional placement will also vary between studies as repeating results would need the same cross-sections taken at the same place at the same time without variation. WDD design can be interpreted differently and therefore the blockage ratio may vary. This study applies a hydraulic structure representation and alters the Manning's n using pier-loss bridge units to establish a modelling unit that accounts for the physical properties of the WDD (Ngai et al., 2017; Gap: 2.4.8.4). Further research could involve use of other units to quantify WDD effects on flood attenuation and comparing to the bridge pier-loss method.

The site under study is relatively small and the impact of the WDDs is correspondently small. Further research would be to undertake similar measuring and modelling for a much larger site where the effects would be more impactful.

6.5. Conclusion

This study demonstrated that the installation of WDDs at Wilderhope Brook reduced peak discharge. Findings showed for the summer storm event a network of 5 WDDs reduced downstream discharge by 0.001 m^3/s but did not delay flood peak over a 0.2 km reach for a 1:100-year event. During the winter storm event, with a 1:50-year return rate, the network of 5 WDDs reduced downstream discharge by 0.017 m^3/s and delayed the peak discharge by 5 mins. These results, agree with previous findings, e.g. Thomas and Nisbet (2012), who found a network of 5 WDDs, reduced flow velocity by 2.1 m/s and delayed peak discharge by 15 mins over a 0.5 km reach section for a 1:100-year event. In the present study, extrapolated results over the entire catchment showed WDDs reduced peak discharge in the summer by B_A = 0.356% (confined channel), B_A = 0.067% (unconfined channel) or B_A+B_p = 11.855% (unconfined channel including floodplain attenuation) and during the winter by B_A = 0.304% (confined channel), B_A = 0.049% (unconfined channel) or B_A+B_p = 58.061% (unconfined channel including floodplain attenuation). In an unconfined channel, the larger the discharge the smaller the T_A

but in a confined channel the larger the discharge the larger the T_A. When the floodplain is accounted for, the larger the discharge, the larger the B_A+B_p. The 5 WDDs were effective in mitigating downstream flooding by collectively providing a T_A = 7.71 m³ (confined channel) and T_A = 1.778 m³ (unconfined channel) in the summer storm event and T_A = 23.279 m³ (confined channel) and T_A = 3.759 m³ (unconfined channel) in the winter storm event. WDDs also provided more bank overtopping (summer: T_p = 5,508.74 m³, winter: T_p = 93,346.92 m³) in comparison to an unobstructed channel (summer: T_p = 3,153.06 m³, winter: T_p = 81,894.66 m³). Therefore, as obstructed channels caused more bank overtopping, more attenuation occurred compared to an unobstructed channel.

Structural design with associated geomorphology is important in respect to attenuation rate. Down the longitudinal profile WDDs were found to change their role. In the upper reach the channel is confined by steep valley slopes and hence WDDs cause increased in-channel attenuation. In the lower reach with a wide gently sloped floodplain, WDDs increase bank overtopping, enhancing channel-floodplain connectivity. The height of a WDD is important when considering an appropriate structural design to attenuate peak discharge. Tall WDDs positioned in an area prone to bank overtopping means discharge will travel over the floodplain rather than surcharge the structure. By extending WDDs across the floodplain this could increase lag time, providing longer water storage and more time for infiltration. Additionally, low porosity WDDs increase attenuation during low discharge which creates backwater pools. However, during high discharge, these backwater pools act as additional water supply which can lead to WDDs being surcharged sooner.

This study shows that WDDs have the potential to work well with other NFM techniques spread across the catchment such as River corridor enhancement or floodplain storage to lengthen lag time. Heightened WDDs are effective in an unconfined channel where they attenuate in-channel flow and can enhance lateral flow onto the floodplain to create temporary storage.

7

Conclusions and Recommendations

7.1. Summary

Though there is increased interest in the hydro-morphological effects of WDDs for flood purposes and finding ways to realistically represent them in hydraulic modelling, there remains limited understanding of the complex effects of WDDs on hydrodynamics and how to harness their morphological changes to reduce flood risk. Without this understanding there can be little headway into finding a standardised method of designing an engineered WDD to function effectively. Past flume experimentation, on single horizontal key members and their hydraulic and morphological effects, led the way to some understanding of these processes but such experimentation reduces the complexity of the physical characteristics of WDDs which consist of multiple key members in varying arrangements and temporally change in porosity. Without a standard design, literature continues to use Gregory et al. (1985) classifications, which were intended to reflect the hydraulic impacts of WDDs however within the same classification, two active dams can vary widely in porosity and blockage area.

7.2. Overall findings

This thesis has focused on developing a modelling methodology which was then validated in Flood Modeller empirically, in assessing the effectiveness of WDDs in slowing peak storm flows. In the following sub-sections, the key findings of this study are reported as related to the four key objectives, outlined in the Literature Review, section 2.9. The first two objectives will be addressed as separate sub-sections, and the final two objectives will be addressed together.

7.2.1. Assessment of the impact of different WDDs on bathymetric evolution

Flume experimentation, shows by treating WDDs as multiple key members with measured gaps below the base key member and between key members, rather than single cylinders makes the model more realistic. This thesis provides a unique means to gain insight into the hydraulics and local scour depths for different designs. Results show discharge and structural arrangements of key members significantly impact upon scour extent whereby the e size impacts on the maximum scour depth. Structures on or close to the bed generate the deepest maximum scour depth which is influenced by G, whereby small G generates turbulence and downstream vortices to enhance the maximum scour depth. At 100 Q_{bf}, series 1A with e = 0 and G = 10 mm creates a maximum scour depth of 61 mm compared to series 4A with e = 15 mm and G = 20 mm creates a maximum scour depth of 47 mm. This finding on gap size is important as those engineered active WDDs with the lower key member on or close to the bed with small G have the least porosity and are the most effective at flow attenuation. This thesis found active WDDs were ≈ 44% less effective at attenuating the flow, after high discharge due to enhanced erosion underneath, changing them into complete WDDs. This is caused by the structure reducing the wetted area which increases the shear velocity, forming a pressure difference upstream and downstream of the structure. Gap size could be manipulated to predict and control the form to function required at the specific location.

7.2.2. Determine scale and location effectiveness of WDDs

The field study quantified site-specific catchment descriptors, which in turn was used in the hydro-environmental modelling for real-world applications. Results show WDD form influences morphological function, and this could have beneficial or adverse flood risk affect depending upon location. The most geomorphologically active WDDs with low porosity cause deeper pools and enhance bed heterogeneity with undulating forced pool-riffle sequencing which dissipates energy. However, WDDs placed at a meander can induce an adverse effect with chute formation which shortens the flow pathway and increases channel slope, speeding the flow to downstream communities. This finding highlights the importance of managing

WDDs particularly after a storm event to counter the local erosion that has taken place. Over time, WDDs can change in their design through decay and accumulation of detritus and so regular maintenance is essential to check they are functioning within the design parameters. There is no one size fits all designs for WDDs. They are influenced by the unique catchment characteristics, and their forms have to be tailored to suit the location they are placed in within that catchment.

7.2.3. An empirically derived hydraulic unit for NFM prediction and assessing the effectiveness of WDDs using the developed modelling approach

Within Flood Modeller, pressure level sensor data at one WDD was used to calibrate the model in order to examine the effectiveness of pier-loss bridge units in representing WDDs. Statistical significance showed pier-loss bridge units were effective in replicating WDDs at Wilderhope Brook. For the summer storm event, a very strong relationship between the pressure level sensors and Flood Modeller as calculated with a Pearson's correlation coefficient of 0.977 (upstream) and 0.972 (downstream) and for the winter storm event the relationship was weaker, though not statistically significant with a strong (0.88: upstream) and very strong (0.937: downstream) relationship. This suggests the higher the discharge, the weaker the relationship between the pressure level sensors and Flood Modeller though not altering significantly. Thesis findings address the knowledge gap in the need for a standardised tool to represent a WDD within the modelling domain by giving a new conceptualisation for a hydraulic representation of a WDD by using a blockage area in a 1D model.

Modelling showed that a network of 5 WDDs over a 0.2 km reach reduced downstream peak discharge by 0.001 m^3/s and did not delay peak discharge during the summer storm event (10-12th June 2019) whilst during the winter storm event (15-17th Feb. 2020), peak discharge was reduced by 0.017 m^3/s and delayed by 5 mins. These results show WDDs alone did not significantly impact upon attenuating peak discharge and therefore, should not be viewed as a single solution but rather as part of a wider solution in the broader context of NFM. Within NFM, WDDs which help to slow in-channel flows, should be regarded in combination with

other nature-based solutions, for instance using forestry in the upper catchment hills to intercept precipitation or using containment bunds on low-lying land to enhance floodplain storage, providing greater time for infiltration. Within the wider context of flood attenuation, nature-based solutions are complementary to traditional techniques. NFM techniques are used alongside traditional engineering methods to help reduce, for example, the required height of flood walls or embankments and to extend their life.

Bank overtopping can significantly increase floodplain attenuation where floodplain storage has more time for infiltration and evaporation. Computational modelling shows, at Wilderhope Brook, the percentage of flood water attenuated significantly increased when bank overtopping occurred, whereby during the summer storm event a catchment attenuation percentage of 11.855% was displayed and during the winter storm event this increased to 58.061%. Therefore, out of channel and floodplain storage significantly increased total in-channel attenuation and the larger the discharge, the larger the catchment attenuation percentage. For maximum WDD effectiveness in attenuating the flow, WDDs should be placed on floodplains where bank overtopping can occur. This thesis advocates that WDDs spanning across the floodplain enables greater attenuation whereby flow can still be attenuated after bank overtopping occurs. When the channel is confined as in the upper course, tall engineered WDDs should be installed to provide greater time before structural surcharge.

7.3. Future Research

Further research needs to assess the inclusion of hydrology, and sediment within the modelling of WDDs within flood prediction tools. This is in its infancy with literature beginning to discuss the importance of including morphological impact of WDDs to flood risk. This study found that adverse geomorphological effects of WDDs, depending upon their location and form, can generate cutoffs or can erode the channel beneath active WDDs which reduces their effectivity, impacting negatively upon flood risk.

Rather than installing different engineered WDD designs in various locations on a trial-and-error basis, simulations should test networks of WDDs in respect to design and location, which would enable assessment of their ability to attenuate flow prior to their installation.

Flood Modeller provides the means to examine WDD induced flow attenuation with a non-erodible bed, however, future research could use specialised hydro-environmental modelling software to examine WDD induced flow attenuation with bed evolution. This would show how the channel evolved over time. However, to precisely model a network of WDDs both the bathymetric and WDD evolution would need to be simulated which would require a high level of computational power and catchment detail.

WDDs are appropriate for use in helping to mitigate flooding when viewed as part of the holistic nature-based solutions within the uplands and can be considered a complementary measure to conventional flood defences. Though this study has indicated that networks of WDDs alone have negligible effect on reducing and delaying the flood peak, it was seen that they have potential to force bank overtopping onto the floodplain, increasing water storage which can impose a greater impact. There needs to be further quantitative research in modelling a combination of nature-based solutions as there are currently few empirical studies of their combined effects with research needed on WDDs to include reforestation, and planting on the flood plain which would have greater impact on catchment scale flood risk.

This thesis examines the impact of WDDs, which are appropriate to use for NFM purposes as they attenuate and slow the flow at the local scale and have the potential to divert water onto the floodplain for temporary storage. The local impact of WDDs on flood attenuation in the uplands may be small, particularly when compared to the collective range of NFM features including water storage ponds and bunds and reforestation, but downstream their impacts may have even less effect. This study does not include the reduction in the amount of water reaching rivers through infiltration rates, interception and evaporation by trees and vegetation, and so the flood peak discharge could be smaller downstream. Further research into nature-based solutions in the uplands, to include the effects upon flooding at the distant, downstream urban location, is therefore required.

References

Abbe, T. B., Montgomery, D. R. (1996) Large woody debris jams, channel hydraulics and habitat formation in large rivers. *Regulated Rivers: Research and Management*, 12(**2-3**): 201-221.

Abbe, T. B., Pess, G., Montgomery, D. R., Fetherston, K. L. (2003) *Integrating Engineered Logjam Technology into River Rehabilitation*, 17: 443-490. In: Montgomery, D. R., Bolton, S., Booth, D. B., Wall, L. (eds.) *Restoration of Puget Sound Rivers*. Seattle, Washington: University of Washington Press.

Abdullah, A. F. B. (2012) *A Methodology for Processing Raw Lidar Data. To support urban flood modelling framework*. UNESCO-IHE Institute for Water Education (Netherlands), University of Technology (Netherlands).

Addy, S., Wilkinson, M. E. (2019) Representing natural and artificial in-channel large wood in numerical hydraulic and hydrological models. *WIREs Water,* 6(**6**): e1389.

Alfieri, L., Feyen, L., Salamon, P., Burek, P., Thielen, J. (2016) Modelling the socio-economic impact of river floods in Europe. *Nat. Hazards Earth Syst. Sci.,* 2015-347.

Ali, A. M., Solomatine, D. P., Di Baldassarre, G. (2015) Assessing the impact of different sources of topographic data on 1-D hydraulic modelling of floods. *Hydrology and Earth System Sciences*, 19(**1**): 631-643.

Al-Naji, A., Gibson, K., Lee, S., Chahi, J. (2017) Real Time Apnoea Monitoring of Children Using the Microsoft Kinect Sensor: A Pilot Study. *Sensors*, 17(**2**): 286.

Alvarez, A. (2005) *Channel Planform Dynamics of an Alluvial Tropical River.* PhD, Geography. Texas A & M University.

Ambient Environmental Assessment (2022) *Detailed flood modelling to understand flood risk in virtually any environment throughout the UK*.

Ambiental (2019) *Detailed Hydraulic (Flood) Modelling*. https://www.ambiental.co.uk/services/detailed-hydraulic-flood-modelling/ (accessed: 20.09.23).

An, H., Cheng, L., Zhao, M., Tang, G, Draper, S. (2016) Detecting scour and liquefaction using OBS sensors. *8th International Conference on Scour and Erosion. Oxford, U.K. 12-15 September 2016*. London: CRC Press, 535-542.

Andersen, M. R., Jensen, T., Lisouski, P., Mortensen, A. K., Hansen, M. K., Gregersen, T., Ahrendt, P. (2012) *Kinect depth sensor evaluation for computer vision applications.* Department of Engineering, Aarhus University. Denmark. 1-35 - Technical report ECE-TR-6 https://tidsskrift.dk/ece/article/view/21221 (accessed: 26.09.23).

Andrews, S. (2010) *Xbox 360 Kinect Review*. Trusted Reviews. https://www.trustedreviews.com/reviews/xbox-360-kinect (accessed: 20.09.23).

Archer, D., Bathurst, J., Newson, M. (2016) Piecing together the flood management mosaic. *The Environment.* CIWEM publication. Brentford: Syon Publishing, (**21**): 37-39.

ArcMap (2021a) *What is a TIN surface*. https://desktop.arcgis.com/en/arcmap/latest/manage-data/tin/fundamentals-of-tin-surfaces.htm#:~:text=Triangular%20irregular%20networks%20(TIN)%20have,set%20of%20vertices%20(points). (accessed: 20.09.23).

ArcMap (2021b) Interpolate Irregular Data function. https://desktop.arcgis.com/en/arcmap/latest/manage-data/raster-and-images/interpolate-irregular-data.htm (accessed: 23.09.23).

Azadegan, A. (2022) *Layered Defense: Why Your Supply Chain Should Be Like Swiss Cheese.* Risk methods. https://www.riskmethods.net/resilient-enterprise/supply-chain-swiss-cheese (accessed: 24.09.23).

Babister, M., Barton, C. (eds.) (2012) *Australian Rainfall & Runoff Revision Project 15: Two dimensional Modelling in Urban and Rural Floodplains*. Stage 1 & 2 Report. *P15/S1/009*. November 2012. Engineers Australia Water Engineering.

Bair, R. T., Segura, C., Lorion, C. M. (2019) Quantifying restoration success of wood introductions to increase Coho Salmon winter habitat. *Earth Surface Dynamics,* 73(**3**): 841-857.

Barlow, J., Moore, F., Burgess-Gamble, L. (2014) *Delivering benefits through evidence: working with natural processes to reduce flood risk*. R&D framework: science report. Report – SC130004/R2. FCERM. Bristol. Environment Agency.

Barnsley, I., Spake, R., Sheffield, J., Leyland, J., Sikes, T., Sear, D. (2021) Exploring the Capability of Natural Flood Management Approaches in Groundwater-Dominated Chalk Streams. *Water*, 13(**2212**): 1-21.

Basso, F., Menegatti, E., Pretto, A. (2018) Robust Intrinsic and Extrinsic Calibration of RGB-D Cameras. *IEEE Transactions on Robotics,* 34(**5**): 1-18.

Beebe, J. T. (2000) Flume Studies of the Effect of Perpendicular Log Obstructions on Flow Patterns and Bed Topography. *JTB Environmental Systems Inc*., 9 - 27.

Beechie, T. J., Sear, D. A., Olden, J. D., Pess, G. R., Buffington, J. M., Moir, H., Roni, P., Pollock, M. M. (2010) Process-based principles for restoring river ecosystems. *Bioscience*, 60(**3**): 209-222.

Benfield, E. F. (1996) Leaf Breakdown in stream Ecosystems. In Hauer, F.R., Lamberti, G. A. (eds.) *Methods in Stream Ecology*. New York: Academic Press. 579-589.

Benn, J. R., Mantz, P., Lamb, R., Riddell, J., Nalluri, C. (2004) Afflux at bridges and culverts-Review of current knowledge and practice. *Defra/Environment Agency Flood and Coastal Defence. R&D Technical Report W5A-061/TR1*, 5-6: 25-54.

Benn, J., Hankin, B., Kitchen, A., Lamb, R., van Leeuwen, Z., Sayers, B. (2019) *Delivering Benefits through Evidence: Blockage management guide*. SC110005/R2. Bristol: Environment Agency.

Bennett, S. J., Ghaneeizad, S. M., Gallisdorfer, M. S., Cai, D., Atkinson, J. F., Simon, A., Langendoen, E. J. (2015) Flow, turbulence, and drag associated with engineered log jams in a fixed-bed experimental channel. *Geomorphology*, 248: 172–184.

Berenbrock, C., Trammer, A. W. (2008) *Simulation of Flow, Sediment Transport, and Sediment Mobility of the Lower Coeurd'Alene River, Idaho*. United States Geological Survey. USGS, Scientific Investigation Report, 2008-5093.

Beschta, R. L. (1979) Debris Removal and Its Effects on Sedimentation in an Oregon Coast Range Stream. *Northwest Science,* 53: 71-77.

Beschta, R. L. (1983) The effects of large organic debris upon channel morphology: a flume study. In *Proceedings of the D. B. Simons Symposium on Erosion and Sedimentation,* Fort. Collins Colorado. Simons, Li and Associates. 8-63 to 8-78.

Betsholtz, A., Nordlöf, B. (2017*) Potentials and limitations of 1D, 2D and coupled 1D-2D flood modelling in HEC-RAS. A case study on Höje river*. Masters thesis. TVVR 17/5003. Division of Water Resources Engineering, Department of Building & Environmental Technology, Lund University, Sweden.

Bevan, A. (1948) *Floods and forestry*. University of Washington Forest Club Quarterly US Forest Service. 22, no. 2.

Bilby, R. E., Likens, G. E. (1980) Importance of Organic Debris Dams in the structure and function of Stream Ecosystems. *Ecology,* 61(**5**): 1107- 1113.

Black, A., Peskett, L., MacDonald, A., Young, A., Spray, C., Ball, T., Thomas, H., Werritty, A. (2021) Natural flood management lag time and catchment scale: Results from an empirical nested catchment study. *Journal of Flood Risk Management*, 14(**3**): e12717.

BlueSky (2021) *Aerial Survey*. BlueSky. https://www.bluesky-world.com/aerial-survey-overview (accessed: 24.09.23).

Bokhove, O., Kelmanson, M. A., Kent, T. (2018) On using flood-excess volume to assess natural flood management, exemplified for extreme 2007 and 2015 floods in Yorkshire. EarthArXiv. *Proc. Roy. Soc. A*

Bradshaw, S. (2017) *Leaky Woody Dams—What Are the Differences and What Works Best*? http://slowtheflow.net/leaky-woody-dams-what-are-the-differences-and-what-works-best/ (accessed: 21.09.23).

Brice, J. C. (1984) Planform properties of Meandering Streams. In Elliot, C. M. (ed.) *River Meandering*, 1-15. New York: American Society of Civil Engineers.

Brierley, G. J., Fryirs, K. A. (2013) *Geomorphology and River Management: Applications of the River Styles Framework*. New Jersey: John Wiley & Sons.

British Geological Survey (2021) *Geology of Britain Viewer (classic)*. mapapps.bgs.ac.uk/geologyofbritain/home.html (accessed: 28.09.23).

Brown, D. (2002) Close-Range Camera Calibration. *Photogramm. Eng.,* 37(**8**): 855–866.

Brunner, G. W. (2016) *HEC-RAS River Analysis System: Hydraulic Reference Manual*, Davis, CA, USA: US Army Corps of Engineers, Institute for Water Resources, Hydrologic Engineering Center.

Brunner, G. W., Warner, J. C., Wolfe, B. C., Piper, S. S., Marston, L. (2021) *HEC-RAS, River Analysis System Applications Guide.* US Army Corps of Engineers Hydrologic Engineering Center (HEC). 1-517.

Buffington, J. M. (2003) Gravel-Bed Rivers V. *Advancing Earth and Space Sciences*, 84(**13**): 122.

Burgess-Gamble, L., Ngai, R., Wilkinson, M., Nisbet, T., Pontee, N., Harvey, R., Kipling, K., Addy, S., Rose, S., Maslen, S., Jay, H., Nicholson, A., Page, T., Jonczyk, J. Quinn, P. (2018) *Working with Natural Processes – Evidence Directory,* SC150005. Bristol: Environment Agency.

Burrus, N. (2011) Kinect RGB Demo. *Manctl Labs*. http://nicolas.burrus.name/index.php/Main/HomePage (accessed: 24.09.23).

Caamaño, D., Goodwin, P., Buffington, J. M. (2012) Flow structure through pool-riffle sequences and a conceptual model for their sustainability in gravel-bed rivers. *River Research and Application.*

Caamaño, D., Goodwin, P., Buffington, J. M., Liou, J. C. P., Daley-Laursen, S. (2009) Unifying Criterion for the Velocity Reversal Hypothesis in Gravel-Bed Rivers. *Journal of Hydraulic Engineering*, 135(**1**): 66-70.

Cheng, L., Yeow, K., Zang, Z., Li, F. (2014) 3D scour below pipelines under waves and combined waves and currents. *Coastal Engineering*, 83: 137-149.

Cherry, J., Beschta, R. L. (1989) Coarse woody debris and channel morphology: a flume study. *Water Resources Bulletin*, 25(**5**): 1031–36.

Chiew, Y. M. (1991) Prediction of maximum scour depth at submarine pipelines. *Hydraulic Engineering,* 117(**4**): 452– 466.

Chourasiya, S., Mohapatra, P. K., Tripathi, S. (2017) Non-intrusive underwater measurement of mobile bottom surface. *Advances in Water Resources*, 104: 76-88.

Chow, V. T. (1959) *Open-channel hydraulics.* New York, USA: McGraw-Hill.

Christidis, N., McCarthy, M., Cotterill, D., Stott, P. A. (2021) Record-breaking daily rainfall in the United Kingdom and the role of anthropogenic forcings. *Atmospheric Science Letters.* 22(**7**): 1-9.

Chu, J. (2017) *Kinect V1 Rgb and Depth Camera Calibration. Some Basic Terminology.* https://jasonchu1313.github.io/2017/10/01/kinect-calibration/ (accessed: 27.09.23).

Clarke, C. (1995) Sediment sources and their environmental controls. In: Foster, I., Gurnell, A., Webb, B. W. (eds.) *Sediment and water quality in river catchments.* Chichester: John Wiley and Sons Ltd.

Clifford, N. J. (1993) Formation of riffle—pool sequences: field evidence for an autogenetic process. Sedimentary Geology, 85(**1-4**): 39-51.

Clifford, N. J., Richards, K. S. (1992) The reversal hypothesis and the maintenance of riffle-pool sequences: a review and field appraisal. In: Carling, P. A., Petts, G. E. (eds.), *Lowland Floodplain Rivers: Geomorphological Perspectives*. Chichester, U. K: John Wiley and Sons Ltd. 43-70.

Collell, M. R., Flikweert, J., Wicks, J. (2019) *Delivering Benefits through Evidence: Asset performance tools: channel conveyance assessment guidance*. Environment Agency. SC140005/R2.

Collier, M., Webb, R. H., Schmidt, J. C. (1996) *Dams and rivers: A primer on the downstream effects of dams*. US. Geological Survey Circular vol. 1126 (June). Tucson, AZ: U.S. Geological Survey.

Collins, B. D., Montgomery, D. R., Fetherston, K. L., Abbe, T. B. (2012) The Floodplain Large-Wood Cycle Hypothesis: A Mechanism for the Physical and Biotic Structuring of Temperate Forested Alluvial Valleys in the North Pacific Coastal Ecoregion. *Geomorphology*, 139-140: 460-470

Committee on Climate Change (2018) *Managing the coast in a changing climate*. 1-70. https://www.theccc.org.uk/publication/managing-the-coast-in-a-changing-climate/ (accessed: 26.09.23).

Constantine, J. A., McLean, S. R., Dunne, T. (2010) A mechanism of chute cutoff along large meandering rivers with uniform floodplain topography. *Geological Society of America Bulletin*, 122(**5-6**): 855-869.

Cook B., Forrester J., Bracken L., Spray C., Oughton E. (2016) Competing paradigms of flood management in the Scottish/English borderlands. *Disaster Prev. Manag.,* 25(**3**): 314–328.

Cordone., A. J., Kelley, D. W. (1961) The influences of inorganic sediment on the aquatic life of streams. *Calif. Dep. Fish Game,* 47(**2**): 189-228.

Credit Valley Conservation (2015) *Fluvial Geomorphic Guidelines*. Fact Sheet: geomorphological hazards – confined and unconfined watercourses.

Critchley, W., Siegert, K., Chapman, K. (1991) *Water Harvesting. A Manual for the Design and Construction of Water Harvesting Schemes for Plant Production*. AGL Miscellaneous Paper No. 17. Food and agriculture organization of the United Nations, Rome – Scientific Publishers. (AGL/MISC/17/91).

Crowder, R. A. (2009) *7 Hydraulic analysis and design*. FDG2. 7: 1-44. https://consult.environment-agency.gov.uk/engagement/bostonbarriertwao/results/appendix-5---environment-agency--2010--hydraulic-analysis-and-design--practical-application-of-hydraulic-modelling.-in-r.j.-crowder--fluvial-design-guide.pdf (accessed: 26.09.23).

Crowder, R. A., Pepper, A. T., Whitlow, C., Sleigh, A., Wright, N., Tomlin, C. (2004) *Benchmarking of hydraulic river modelling software packages*. R&D Technical Report: W5-105/TR0, DEFRA. Bristol: Environment Agency, 1-14.

Curran, J. C., Tan, L. (2010) An investigation of bed armoring process and the formation of microclusters. *Proc., Joint Federal Interagency Conf. 2010: Hydrology and Sedimentation for a Changing Future: Existing and Emerging Issues,* JFIC, Las Vegas, 1–12.

Curran, J. H., Wohl, E. E. (2003) Large woody debris and flow resistance in step-pool channels, Cascade Range, Washington. *Geomorphology*, 51(**1–3**): 141–157.

Dadson, S. J., Hall, J. W., Murgatroyd, A., Acreman, M., Bates, P., Beven, K., Heathwaite, L., Holden, J., Holman, I. P., Lane, S. N., O'Connell, E., Penning-Rowsell, E., Reynard, N., David Sear, D., Thorne, C., Wilby, R. (2017) A restatement of the natural science evidence concerning catchment-based 'natural' flood management in the UK. *Proc. R. Soc. A* 473: 20160706.

Dangerfield, S. F. (2013) *The Effects of Sediment Loading on Morphology and Flood Risk in a Lowland River System*. PhD. University of Nottingham.

Dasallas, L., Kim, Y., An, H. (2019) Case study of Hec-Ras1D-2D Coupling Simulation: 2002 Baeksan Flood Event in Korea. *Water*, 11(**10**): 2048.

Davidson, S. (2016) *Modelling disturbance and channel evolution in mountain streams.* Doctor of Philosophy, The University of British Columbia (Vancouver).

De Musso, N. M., Capolongo, D., Caldara, M., Surian, N., Pennetta, L. (2020) Channel Changes and Controlling Factors over the Past 150 Years in the Basento River (Southern Italy). *Water*, 12(**1**): 307.

DEFRA (2009) *Fluvial Design Guide*. https://www.gov.uk/flood-and-coastal-erosion-risk-management-research-reports/fluvial-design-guide (accessed: 24.09.23).

DEFRA (2019) *A Green Future: Our 25 Year Plan to Improve the Environment*. London: Department for Environment, Food & Rural Affairs.

DEFRA (2019) *A Green Future: Our 25 Year Plan to Improve the Environment.* London: Department for Environment, Food & Rural Affairs.

https://www.gov.uk/government/publications/25-year-environment-plan (accessed: 21.09.23).

DEFRA (2020) *The Enablers and Barriers to the Delivery of Natural Flood Management Projects*. Final report FD2713. https://assets.publishing.service.gov.uk/media/6038c9e8d3bf7f039403e918/14754_FD2713_Final_Report__1_.pdf (accessed: 25.09.23).

Dey, S., Singh, N.P. (2008) Clear-water scour below underwater pipelines under steady flow. *Journal of Hydraulic Engineering,* 134: 588–600.

Diehl, R.M., Gourevitch, J.D., Drago, S., Wemple, B. C. (2021) Improving flood hazard datasets using a low-complexity, probabilistic floodplain mapping approach. *PLoS ONE,* 16(**3**): e0248683. https://journals.plos.org/plosone/article?id=10.1371/journal.pone.0248683

Dixon, S. J. (2013) *Investigating the effects of large wood and forest management on flood risk and flood hydrology*. PhD thesis., University of Southampton: Southampton, 1-406.

Dixon, S. J. (2015) A dimensionless statistical analysis of logjam form and process. *Ecohydrology*, DOI: 10.1002/eco.1710

Dixon, S. J., Sear, D. A., Odoni, N. A., Sykes, T., Lane, S. N. (2016) The effects of river restoration on catchment scale flood risk and flood hydrology. *Earth Surface Processes and Landforms,* 41(**7**): 997–1008.

Domino, S. P. (2023) *Chapter 7 - Unstructured finite volume approaches for turbulence*. 275-317. In: Moser, R. D. (eds.) *Numerical Methods in Turbulence, Numerical Methods in Turbulence Simulation*. Academic Press, Computational Thermal and Fluid Mechanics Department, Sandia National Laboratories, Albuquerque, NM, United States.

Dong, Y., Lei, T., Li, S., Yuan, C., Zhou, S., Yang, X. (2015) Effects of rye grass coverage on soil loss from loess slopes. *International Soil and Water Conservation Research*, 3(**3**): 170-182.

Du, H. M., Donat, M. G., Zong, S., Alexander, L. V., Manzanas, R., Kruger, A., Choi, G., Salinger, J., He, H. S., Li, M-H., Fujibe, F., Nandintsetseg, B., Rehman, S., Abbas, F., Rusticucci, M., Srivastava, A., Zhai, P., Lippmann, T., Yabi, I., Stambaugh, M. C., Wang, S., Batbold, A., Teles de Oliveira, P., Adrees, M., Hou, W., Santos e Silva, C, M., Lucio, P, S., Wu, Z. (2022) *Extreme Precipitation on Consecutive Days Occurs More Often in a Warming Climate.* Bulletin of the American Meteorological Society, 103(**4**): E1130–E1145.

Dyer, M. (2004) Performance of flood embankments in England and Wales. *Water Management*, 157(**4**): 177-186. https://www.icevirtuallibrary.com/doi/abs/10.1680/wama.2004.157.4.177

EDINA. (2021) *Digimap, Lidar*. https://digimap.edina.ac.uk/lidar (accessed: 22.09.23).

EEA (2015) *Exploring nature-based solutions. The role of green infrastructure in mitigating the impacts of weather- and climate change-related natural hazards.* Technical report No.12/2015, Luxembourg: European Environment Agency.

Eekhout, J. P. C., Hoitink, A. J. F. (2015) Chute cutoff as a morphological response to stream reconstruction: The possible role of backwater. *Water Resources Research*, 51(**5**): 3339 – 3352.

Ellis, N., Anderson, K., Brazier, R. (2021) Mainstreaming natural flood management: A proposed research framework derived from a critical evaluation of current knowledge. *Progress in Physical Geography,* 1-23.

Ellis-Sugai, B., Godwin, D. C. (2002) *Going with the flow. Understanding Effects of Land Management on Rivers, Floods, and Floodplains.* USA: Oregon State University. ORESU-T-01-003.

Elosegi, A., Diez, J. R., Ortiz, J. M., Flores, L. (2016) Pools, channel form, and sediment storage in wood-restored streams: Potential effects on downstream reservoirs. *Geomorphology*, 279.

EngineerExcel (2023) *Colebrook-White Equation.* https://engineerexcel.com/colebrook-white-equation/#How_to_Solve_Colebrook_Equation_for_f (accessed: 25.09.23)

Engineering Toolbox (2001) *Manning's Roughness Coefficient*. https://www.engineeringtoolbox.com/mannings-roughness-d_799.html (accessed: 23.09.23)

Engineers Edge (2023) *Moody Chart*. https://www.engineersedge.com/graphics/moodys-diagram.png (accessed: 20.09.23).

Environment Agency (2007) *Geomorphological Monitoring Guidelines for River Restoration Schemes*. Final Report. Job No. B0435600. Bristol: Environment Agency.

Environment Agency (2009) *Flooding in England: A National Assessment of Flood Risk*. Bristol: Environment Agency.

Environment Agency (2010) *Working with Natural Processes to Manage Flood and Coastal Erosion Risk*. Bristol: Environment Agency.

Environment Agency (2014) *Working with natural processes to reduce flood risk*. R&D framework science report. Report SC130004/R2. Bristol: Environment Agency.

Environment Agency (2016) *Delivering benefits through evidence: Design, operation and adaptation of reservoirs for flood storage*. SC120001/R.

Environment Agency (2017) *Appendix A Natural Flood Management Literature Review*. https://consult.environment-agency.gov.uk/yorkshire/slowing-the-flow-in-the-rivers-ouse-and-foss-a-lon/supporting_documents/York%20Slowing%20the%20Flow%20Appendix%20A%20%20NFM%20literature%20review.pdf (accessed: 23.09.23).

Environment Agency (2019) *Research and Analysis. Long-term investment scenarios (LTIS).* Bristol: Environment Agency.

Environment Agency (2021a) *Research and analysis. Using the power of nature to increase flood resilience.* https://www.gov.uk/government/publications/natural-flood-management-programme-initial-findings/using-the-power-of-nature-to-increase-flood-resilience (accessed: 23.09.23).

Environment agency (2021b) *Represent river channels, floodplains and pipe networks (pathway).* https://www.gov.uk/government/publications/river-modelling-technical-standards-and-assessment/represent-river-channels-floodplains-and-pipe-networks-pathway (accessed: 23.09.23).

Environment Agency (2021c) Guidance Hydraulic modelling: best practice (model approach). https://www.gov.uk/government/publications/river-modelling-technical-standards-and-assessment/hydraulic-modelling-best-practice-model-approach#:~:text=The%20advantages%20of%20a%201D,range%20of%20hydraulic%20structures%20options (accessed: 27.09.23).

Environment agency (2022a) *LIDAR Composite DTM 2017 – 2m.* Environment Agency. data.gov.uk https://ckan.publishing.service.gov.uk/dataset/lidar-composite-dtm-2017-2m (accessed: 28.09.23).

Environment Agency (2022b) *Research and Analysis. Natural Flood Management Programme: evaluation report.* https://www.gov.uk/government/publications/natural-flood-management-programme-evaluation-report/natural-flood-management-programme-evaluation-report (accessed: 23.09.23).

Ervine A., MacLeod A. B. (1999) Modelling a river channel with distant flood banks. *Proceedings of the ICE – Water Maritime and Energy,* 21–33.

ESRI (2021a) *Use a DSM to derive DTM values.* https://pro.arcgis.com/en/pro-app/latest/help/analysis/image-analyst/use-a-dsm-to-derive-dtm-values.htm#GUID-6F1CA2BB-BAAD-45D3-8C67-90AE5E7B3B99 (accessed: 28.09.23).

ESRI (2021b) *Pixel Editor in ArcGIS Pro.* https://pro.arcgis.com/en/pro-app/latest/help/analysis/image-analyst/pixel-editor-in-arcgis-pro.htm (accessed: 28.09.23).

Evans, E., Ashley, R., Hall, J., Penning-Rowsell, E., Saul, A., Sayers, P., Throne, C., Watkinson, A. (2004) *Foresight. Future Flooding. Scientific summary: Volumes 1 and 2.* London: Office of Science and Technology. https://www.gov.uk/government/publications/future-flooding

Everett, G., Lamond, J., Morzillo, A. T., Chan, F. K. S., Matsler, A. M. (2015) Sustainable drainage systems: Helping people live with water. *Proc. Inst. Civil Eng.* 169: 94–104.

Eyquem, J. (2007) Using fluvial geomorphology to inform integrated river basin management. *Water and Environment Journal*, 21(**1**): 54-60.

Falconer, R. A. (1986) *Mathematical modelling of flow and pollutant transport in rivers, lakes, estuaries and coastal waters*. Vol. II. University of Birmingham. 2nd – 4th September 1986.

Falconer, R. A. (no date) *Research equipment. Hyder Hydraulics Laboratory*. Cardiff University. https://www.cardiff.ac.uk/research-equipment/facilities/view/hyder-hydraulics-laboratory.

Faustini, J., Jones, J. A. (2003) Influence of Large Woody Debris on Channel Morphology and Dynamics in Steep, Boulder-Rich Mountain Streams, Western Cascades, Oregon. *Geomorphology*, 51(**1**): 187-205.

Federal Emergency Management Agency (2019) *Recipes for resilience, technical version: Using the Flood Depth Grids to Identify Risk.* https://www.fema.gov/sites/default/files/documents/fema_depth-grids-technical.pdf

Federal Interagency Stream Restoration Working Group (2001) *Stream corridor restoration: principles, processes and practices.* FISRWG, GPO Item No. 0120-A; SuDocs No. A 57.6/2: EN3/PT.653

Fenton, J. D. (2010) Calculating resistance to flow in open channels. *Alternative Hydraulics,* 2(**5**): 1-7.

Ferguson, C., Fenner, R. (2020) Evaluating the effectiveness of catchment-scale approaches in mitigating urban surface water flooding. *Philosophical Transactions A Math Phys. Eng. Sci.*,378(2168): 20190203. https://www.ncbi.nlm.nih.gov/pmc/articles/PMC7061965/

Fisher, G. B., Magilligan F. J., Kaste J. M., Nislow K. H. (2010) Constraining the timescales of sediment sequestration associated with large woody debris using cosmogenic [7]Be. *Journal of Geophysical Research*, 115(**F1**).

FISRWG (1998) *Stream Corridor Restoration: Principles, Processes, and Practices.* By the Federal Interagency Stream Restoration Working Group (FISRWG) (15 Federal agencies of the US gov't). GPO Item No. 0120-A; SuDocs No. A57.6/2: EN 3/PT.653. ISBN-0-934213-59-3. Revised: 2001.

Fleming, G. (2002) Learning to live with rivers - the ICE's report to government. *Civil Engineering,* 150: 15-21.

Forest Research (2021) *Phytophthora disease of alder (Phytophthora alni)* https://www.forestresearch.gov.uk/tools-and-resources/fthr/pest-and-disease-resources/phytophthora-disease-of-alder/#:~:text=Phytophthora%20disease%20of%20alder%20is,20th%20and%20early%2021st%20centuries (accessed: 29.09.23).

Fowler, H. J., Kilsby, C. J. (2003) Implications of changes in seasonal and annual extreme rainfall. *Geophysical Research Letters. Advance Earth and Space Sciences*, 30(**13**): 1720.

Fredsøe, J. (2016) Pipeline Seabed Interaction. *Journal of Waterway, Port, Coastal, and Ocean Engineering*, 1-65.

Friend, P., F., Sinha, R. (1993) Braiding and Meandering Parameters. *Geological society, London, Special Publications*, 75(**1**): 105.

Frontline Solvers (2021) *T-Test: Paired Two Sample for Means*. https://www.solver.com/t-test-paired-two-sample-means (accessed: 28.09.23).

Fryirs, K.A. and Brierley, G. J. (2013) *Geomorphic Analysis of River Systems: An Approach to Reading the Landscape.* Hoboken: Wiley-Blackwell.

Fuller, I. C., Macklin, M. G., Toonen, W. H., Turner, J., Norton, K. (2019) A 2000 year record of palaeo floods in a volcanically-reset catchment: Whanganui River, New Zealand. *Global and Planetary Change*, 181: 1-12.

Future Climate Info. (2022) *Re-wilding Streams: Letting Nature Control Flooding.* https://futureclimateinfo.com/re-wilding-streams-letting-nature-control-flooding/ (accessed: 26.09.23).

Gao, F. P., Yang, B., Wu, Y. X., Yan, S. M. (2006) Steady current induced seabed scour around a vibrating pipeline. *Applied Ocean Research,* 28: 291–298.

Garcia-Navarro, P., Fras A., Villanueva I. (1999) Dam-break flow simulation: some results for one-dimensional models of real cases. *Journal of Hydrology*, 216: 227–247.

Gilbert, G. K. (1914) Transportation of debris by running water. *U.S. Geol. Surv. Prof. Pap.* 86-221.

Gippel, C. J. (1995) Environmental Hydraulics of Large Woody Debris in Streams and Rivers. *Journal of Environmental Engineering*, 121(**5**): 388-395.

Gippel, C. J., O'Neill I. C., Finlayson B. L. (1992) The Hydraulic Basis of Snag Management. *Centre for Environmental Applied Hydrology,* Melbourne: University of Melbourne.

Gordon, N. D., McMahon, T. A., Finlayson, B. L., Gippel, C. J., Nathan, R. J. (2005) *Stream Hydrology: an Introduction for Ecologists* (2nd ed.) Chichester, West Sussex: John Wiley and Sons.

Grabowski, R. C., Gurnell, A. M., Burgess-Gamble, L., England, J., Holland, D., Klaar, M. J., Morrissey, I., Uttley, C., Wharton, G. (2019) The current state of the use of large wood in river restoration and management. *Water and Environment Journal*, 33 (**3**): 366-377.

Grass, A. J. (1970) Initial instability of fine bed sand: American Society of Civil Engineers, Proceedings, *Journal of the Hydraulics Division,* 96: 619 - 632.

Gregory, J. M., McEnery, J. A. (2017) Process-Based Friction Factor for Pipe Flow. *Open Journal of Fluid Mechanics,* 07(**2**): 219-230.

Gregory, K. J., Gurnell, A. M., Hill, C. T. (1985) The permanence of debris dams related to river channel processes. *Hydrological Sciences Journal*, 30(**3**): 371-381.

Gregory, S. V., Meleason, M. A., Sobota, D. J. (2003) Modeling the dynamics of wood in streams and rivers. In: Gregory, S., Boyer, K., Gurnell, A. M. (eds.), *The Ecology and Management of Wood in World Rivers*. American Fisheries Society, Symposium 37, Bethesda, Maryland, 315-335.

Grenfell, M. C., Aalto, R., Nicolas, A. (2012) Chute channel dynamics in large, sand-bed meandering rivers. *Earth Surface Processes and Landforms*, 37(**3**):315 - 331

Grygoruk, M., Nowak, M. (2014) Spatial and Temporal Variability of Channel Retention in a Lowland Temperate Forest Stream Settled by European Beaver (Castor fiber). *Forests*. 5: 2276-2288.

Gurnell, A. M., Grabowski, R. C. (2016) Vegetation-hydrogeomorphology interactions in a low-energy, human-impacted river. *River Research and Applications*, 32(**2**): 202-215.

Gurnell, A. M., Gregory, K. J., Petts, G. E. (1995) The role of course woody debris in forest aquatic habitats: implications for management. *Aquatic conservation*, 5: 143-166.

Gurnell, A. M., Piegay, H., Swanson, F. J., Gregory, S. V. (2002) Large wood and fluvial processes. *freshwater biology*, 47: 601-619.

Gurnell, A. M., Sweet, R. (1998) The distribution of large woody debris accumulations and pools in relation to woodland stream management in a small, low-gradient stream. *Earth Surface Processes and Landforms*, 23(**12**): 1101-1121.

Guy, H. P. (1964) *An Analysis of some storm-period variables affecting stream sediment transport. Sediment transport in alluvial channels.* Geological survey professional paper 462-E. United States Government Printing Office, Washington. United States Department of the Interior. Geological Survey.

Habibi, M. (1994) *Sediment Transport Estimation Methods for River Systems*. Doctor of Philosophy, University of Wollongong.

Hall, J. E., Holzer, D. M. Beechie, T. J. (2007) Predicting river floodplain and lateral channel migration for salmon habitat conservation. *Journal of the American Water Resources Association*, 43: 786-797.

Hall, J., Evans, E. P., Penning-Rowsell, E. C., Sayers, P., Thorne, C. R., Saul, A. J. (2003) Quantified scenarios analysis of drivers and impacts of changing flood risk in England and Wales: 2030-2100. *Environmental Hazards*, 4(**3**):51-65.

Hamill, L. (1995) *Understanding Hydraulics. A guide to the basic principles of hydraulics with an explanation of the essential theory.* Hampshire and London: Macmillan Press Ltd.

Han, Y., Feng, G., Ouyang, Y. (2018) Effects of Soil and Water Conservation Practices on Runoff, Sediment and Nutrient Losses. *Water,* 10(**1333**): 1-13.

Hankin, B., Arnott, S., Whiteman, M., Burgess-Gamble, L., Rose, S. (2017) *Working with Natural Processes - Using flood risk evidence to make the case for NFM*. Bristol. Environment Agency. SC150005.

Hankin, B., Hewitt, I., Sander, G., Federico Danieli, F., Giuseppe Formetta, G., Kamilova, A., Kretzschmar, A., Kiradjiev, K., Wong, C., Pegler, S., Lamb, R. (2020) A risk-based, network analysis of distributed in-stream leaky barriers for flood risk management. *Natural Hazards and Earth System Sciences*, 20(**10**): 2567-2584.

Hartman, G., Scrivener, J. C., Holtby, L. B., Powell, L. (1987) Some effects of different streamside treatments on physical conditions and fish population processes in Carnation Creek, a coastal rain forest stream in British Columbia. In *Streamside management: forestry and fishery interactions.* Salo E. O., Cundy, T. W. (eds.), Inst. of Forest Resources, Seattle, USA: University of Washington, 330-372.

Hassan, M. A., Church, M., Lisle, T. E., Brardinoni, F., Benda, L., Grant, G. E. (2005) Sediment Transport and Channel Morphology of Small, Forested Streams. *Journal of the American Water Resources Association (JAWRA)*, 41(**4**): 853-876.

Haunton, B. (2023) email, Furnues, D. August.

Heathwaite, A. L., Burt, T. P., Trudgill, S. T. (1989) Runoff, sediment, and solute delivery in agricultural drainage basins - a scale dependent approach. *International Association of Hydrological Sciences Publication,* 182: 175-191.

Heathwaite, A. L., Burt, T. P., Trudgill, S. T. (1990) Land use controls on sediment delivery in lowland agricultural catchments, 69-87, In Boardman, J., Foster, I. D. L., Dearing, J. (eds.) *Soil Erosion on Agricultural Land.* Chichester: Wiley.

Heede, B. H. (1972) Influence of a forest on the hydraulic geometry of two mountain streams. *Water Resources Bulletin,* 8: 523-530.

Heede, B. H. (1981). Dynamics of selected mountain streams in the Western United States of America. *Zeitschrift fur Geomorphology*, 25: 17-32.

Henderson, L. F. (1974) On the Fluid Mechanics of Human Crowd Motion. *Transportation Research*, 8: 509-515. https://doi.org/10.1016/0041-1647(74)90027-6

Henshaw, A. J., Thorne, C. R., Clifford, N. J. (2013) Identifying causes and controls of river bank erosion in a British upland catchment. *Catena*, 100: 107-119.

Herrera, C. D., Kannala, J., Heikkilä, J. (2011) Accurate and practical calibration of a depth and color camera pair. *Proceedings of the 14th International Conference on Computer Analysis of Images and Patterns*; Seville, Spain. 29–31 August 2011, 437–445.

Hey, R. D., Thorne, C. R. (1986) Stable channels with mobile gravel beds. *Journal of Hydraulic Engineering*, 112(**8**): 671-689.

Hill, B., Liang, Q., Bosher, L., Chen, H., Nicholson, A. (2023) A systematic review of natural flood management modelling: Approaches, limitations, and potential solutions. *Journal of Flood Risk Management*. 16(**3**): e12899.

Hilldale, R. C., Mooney, D. M. (2007) Identifying stream habitat features with a two-dimensional hydraulic model. *Reclamation*; *Managing Water in the West*. Technical Series No. TS-YSS-12. U.S. Department of the Interior, Bureau of Reclamation, Denver CO: Technical Service Center.

Hollis, J. (2021) *What we've learnt from the £15m NFM Programme*. Environment Agency. https://research.reading.ac.uk/nerc-nfm/wp-content/uploads/sites/81/2021/03/NERC-Conference_Jon-Hollis.pdf

Horacio, J. (2014) *River Sinuosity Index: geomorphological characterisation.* Technical Note 2. CIREF and Wetlands International*, 1-6.

Hosseiny, H., Nazari, F., Smith, V., Nataraj, C. (2020) A Framework for Modelling Flood Depth Using a Hybrid of Hydraulics and Machine Learning. *Scientific Reports*, 10: 8222.

Huang, R., Zeng, Y., Zha, W., Yang, F. (2022) Investigation of flow characteristics in open channel with leaky barriers. *Journal of Hydrology,* 613, part A: 128328.

Hubble, T. C. T., Docker, B. B., Rutherford, I. D. (2010) The role of riparian trees in maintaining river bank stability: a review of Australian Experience and Practice. *Ecological Engineering*, 36(**3**): 292-304.

Hughes, F. M. R. (ed.) (2003) *The Flooded Forest: Guidance for policy makers and river managers in Europe on the restoration of floodplain forests*. FLOBAR2, Department of Geography, University of Cambridge, UK. 1-96.

I-Hsien Porter, R. A. (2011) *An Evaluation of a Hydrological Model Used to Predict the Impact of Flow Attenuation on Downstream Flood Flows.* MSc. Durham theses, Durham University.

ImageMeter (2021) https://imagemeter.com/ (accessed: 28.09.23)

Imran, J., Kassem, A., Khan, S. M. (2004) Three-dimensional modelling of density current. I. Flow in straight confined and unconfined channels. *Journal of Hydraulic Research***, 42(**6**): 578-590.

Institute of Hydrology (1999) *The Flood Estimation Handbook*, 5 volumes and associated software. Wallingford, UK: Institute of Hydrology.

IPCC (2013) *Climate Change 2013: The Physical Science Basis. Contribution of Working Group I to the Fifth Assessment Report of the Intergovernmental Panel on Climate Change* [Stocker, T.F., D. Qin, G.-K. Plattner, M. Tignor, S.K. Allen, J. Boschung, A. Nauels, Y. Xia, V. Bex and P.M. Midgley (eds.)]. Cambridge, United Kingdom and New York, NY, US: Cambridge University Press, 1-1535.

IPCC (2014) *Climate Change 2014: Impacts, Adaptation and Vulnerability. Part A: Global and Sectoral Aspects. Contribution of Working Group II to the Fifth Assessment Report of the*

Intergovernmental Panel on Climate Change [Field, C. B., Barros, V. R., Dokken, D. J., Mach, K. J., Mastrandrea, M. D., Bilir, T. E., Chatterjee, M., Ebi, K. L., Estrada, Y. O., Genova, R. C., Girma, B., Kissel, E. S., Levy, A. N., MacCracken, S., Mastrandrea, P. R., White, L. L. (eds.)]. Cambridge, United Kingdom and New York, NY, USA: Cambridge University Press, 1-1132.

IPCC (2021) Summary for Policymakers. In: *Climate Change 2021: The Physical Science Basis. Contribution of Working Group I to the Sixth Assessment Report of the Intergovernmental Panel on Climate Change* [Masson-Delmotte, V., Zhai, P., Pirani, A., Connors, S. L., Péan, C., Berger, S.,Caud, N.,Chen, Y., Goldfarb, L., Gomis, M. I., Huang, M., Leitzell, K., Lonnoy, E., Matthews, J. B. R., Maycock, T. K., Waterfield, T., Yelekçi, O., Yu, R., Zhou, B. (eds.)]. Cambridge University Press.

Iwasaki, T., Shimizu, Y., Kimura, I. (2016) Numerical simulation of bar and bank erosion in a vegetated floodplain: A case study in the Otofuke River. *Adv. Water Resource*, 93: 118–134.

Jackson, J. R., Pasternack, G. B., Wheaton, J. M. (2015) Virtual manipulation of topography to test potential pool-riffle maintenance mechanisms. *Geomorphology*, 228: 617-627.

Jacobs Flood Modeller (2023a) *Simplifying your flood modelling.* https://www.jacobs.com/technology/flood-modeller#:~:text=It%20enables%20you%20to%20confidently,the%20impacts%20of%20climate%20change.&text=Flood%20Modeller%20allows%20you%20to,and%20the%20latest%20hydrological%20methods.(accessed: 22.09.23).

Jacobs Flood Modeller (2023b) *Boundaries.* https://www.floodmodeller.com/boundaries#:~:text=Flow%20boundaries%20define%20the%20variation,water%20leaves%20the%20model%20network. (accessed: 23.09.23),

Jacobs Flood Modeller (2023c) *2D Solvers*. https://www.floodmodeller.com/2dsolvers

Jacobs Flood Modeller: Online Manual (2021a) *Pier-loss Bridge*. http://help.floodmodeller.com/floodmodeller/Technical_Reference/1D_Nodes_Reference/Bridges/Pier_Loss_Bridge.htm (accessed: 20.09.23).

Jacobs Flood Modeller: Online Manual. (2021b) *Steady Flows.* http://help.floodmodeller.com/floodmodeller/Technical_Reference/1D_Modelling_Theory/Steady_Flows/Steady_Flows.htm (accessed: 25.09.23).

Jacobs Flood Modeller: Online Manual. (2021c) *Pseudo-Timestepping Method.* http://help.floodmodeller.com/floodmodeller/Technical_Reference/1D_Modelling_Theory/Steady_Flows/Pseudo-Timestepping_Method.htm (accessed: 25.09.23).

Jacobs Flood Modeller: Online Manual. (2021d) *1D River Solvers.* https://www.floodmodeller.com/1driversolvers (accessed: 25.09.23).

Jacobs Flood Modeller: Online Manual. (2021e) *Flow Time Boundary.* http://help.floodmodeller.com/floodmodeller/Technical_Reference/1D_Nodes_Reference/Boundaries/Flow_Time_Boundary.htm (accessed: 25.09.23)

Jacobs Flood Modeller: Online Manual. (2021f) *Conveyance and Cross-section Property Display.*
https://help.floodmodeller.com/floodmodeller/Technical_Reference/1D_Nodes_Reference/Rivers/Conveyance_and_Cross-Section_Property_Display.htm

Jacobs Flood Modeller: Online Manual. (2021g) *US BPR Bridge*.
https://help.floodmodeller.com/floodmodeller/Technical_Reference/1D_Nodes_Reference/Bridges/US_BPR_Bridge.htm (accessed: 25.09.23).

Jacobs Flood Modeller: Online Manual. (2021h) *1D Model Health Checker*.
https://help.floodmodeller.com/floodmodeller/Introduction_1D_Model_Health_Checker.htm (accessed: 25.09.23).

Jacobs Flood Modeller: Online Manual. (2022a) *1D diagnostics messages.*
https://help.floodmodeller.com/docs/diagnostics-messages (accessed: 25.09.23).

Jacobs Flood Modeller: Online Manual. (2022b) *River Section.*
https://help.floodmodeller.com/docs/river-section-overview (accessed: 25.09.23).

Jacobs Flood Modeller: Online Manual. (2022c) *Hydrodynamic Channel Flows*.
https://help.floodmodeller.com/docs/hydrodynamic-channel-flows (accessed: 25.09.23).

Jacobs Flood Modeller: Online Manual. (2022d) *Why use 2D modelling*?
https://help.floodmodeller.com/v1/docs/why-use-2d-modelling (accessed: 25.09.23).

Jacobs Flood Modeller: Online Manual. (2022e) *Boundaries*.
https://help.floodmodeller.com/docs/2d-components-boundaries (accessed: 25.09.23).

Jacobs Flood Modeller: Online Manual. (2022f) *The 2D ADI solver*.
https://help.floodmodeller.com/docs/the-2d-adi-solver (accessed: 25.09.23).

Jacobs Flood Modeller: Online Manual. (2022g) *Supercritical Flows.*
Help.floodmodeller.com/docs/supercritical-flows (accessed: 25.09.23).

James, L. A., Hodgson, M. E., Ghoshal, S., Megison Latiolais, M. (2012) Geomorphic change detection using historic maps and DEM differencing: The temporal dimension of geospatial analysis. *Geomorphology*, 137: 181-198.

Jarrett, R. D. (1985) *Determination of Roughness Coefficients for streams in Colorado,* U.S. Geological Survey, Water Resources Investigations Report. Lakewood, Colorado: US Department of the Interior, 85–4004.

Jongman, B., Ward, P. J., Aerts, J. C. J. H. (2012) Global exposure to river and coastal flooding-long term trends and changes. *Global Environmental Change*, 22, 823-835.

Jowett, I. G. (1993) A method for objectively identifying pool, run, and riffle habitats from physical measurements. *New Zealand Journal of Marine and Freshwater Research*, 27: 241-248.

Joyce, H. M., Warburton, J., Hardy, R. J. (2020) A catchment scale assessment of patterns and controls of historic 2D river planform adjustment. *Geomorphology*, 354: 1-19.

Julien, P. Y. (1998) *Erosion and Sedimentation.* Edinburgh Building, Cambridge: Cambridge University Press.

Kail, J., Hering, D., Muhar, S., Gerhard, M., Preis, S. (2007) The use of large wood in stream restoration: Experiences from 50 projects in Germany and Austria. *Journal of Applied Ecology*, 44: 1145-1155.

Kasvi, E., Laamanen, L., Lotsari, E., Alho, P. (2017) Flow Patterns and Morphological Changes in a Sandy Meander Bend during a Flood—Spatially and Temporally Intensive ADCP Measurement Approach. *Water*, 9(**2**): 106.

Keller, E. A. (1971) Areal sorting of bed-load material: The hypothesis of velocity reversal. *Geological Society America Bulletin,* 82: 753-756.

Keller, E. A., Florsheim, J. L. (1993) Velocity-reversal hypothesis: A model approach. *Earth Surface Processes Landforms,* 18: 733-740.

Keller, E. A., MacDonald, A., Tally, T., Merritt, N. J. (1995) Effects of large organic debris on channel morphology and sediment storage in selected tributaries of Redwood Creek, Northwestern California. US Geological Survey Professional Paper 1454. *Geological Sciences, University of California*, 1-29

Keller, E. A., Swanson F. J. (1979) Effects of large organic material on channel form and fluvial processes. *Earth Surface Processes Landforms,* 4: 361–380.

Keller, E. A., Tally, T. (1979) Effects of large organic debris on channel form and fluvial processes in the coastal redwood environment. In Rhodes, D. D., Williams, G. P. (eds.) *Adjustments of the fluvial system, 169-197. Proceedings, Tenth Annual Geomorphology Symposium,* State University of New York, Binghamton. Dubuque, Iowa: Kendall/Hunt Publishing Company, 169-197.

Keys, T. A., Govener, H., Jones, C. N., Hession, W. C., Hester, E. T., Scott, D. T. (2018) Effects of large wood on floodplain connectivity in a headwater mid-Atlantic stream. *Ecological Engineering*, 118: 134-142.

Khoshelham, K., Elberink, S. O. (2012) Accuracy and Resolution of Kinect Depth Data for Indoor Mapping Applications. *Sensors*, 12: 1437-1454.

Kibbler, A. (2021) Memories of the Flood 2020 Still Linger for Some in Ludlow. Ludlow and Tenbury Wells, *Advertiser* (16 February).

Kironoto, B. A., Graf, W. H. (1994) Turbulence characteristics in rough uniform open-channel flow. *Proc. Inst. Civ. Engrs Wat., Marit. And Energy*, 106: 333-344.

Kitts, D. (2010) *The Hydraulic and Hydrological Performance of Large Wood Accumulation in a Low-Order Forest Stream.* Doctor of Philosophy, University of Southampton, Southampton, UK.

Knighton, D. (1998*) Fluvial forms and processes: A new perspective*. London: Hodder Arnold.

Kocaman, S., Hasan Güzel, H., Evangelista, S., Ozmen-, H., Viccione, G. (2020) Experimental and Numerical Analysis of a Dam-Break Flow through Different Contraction Geometries of the Channel. *Water*, 12: 1124.

Kondolf, G., M. (1997) Hungry Water: Effects of Dams and Gravel Mining on River Channels. *Environment Management*, 21(**4**): 533-551.

Krzeminskaa, D., Kerkhofb, T., Skaalsveena, K., Stolte, J. (2019) Effect of riparian vegetation on stream bank stability in small agricultural catchments. *Catena*, 172: 87-96.

Kvocka, D. (2017) *Modelling elevations, inundation extent and hazard risk for extreme flood events*. PhD. Cardiff University.

La Torre Torres, I. B., Amatya, D. M., Sun, G., Callahan, T. J. (2011) Seasonal rainfall–runoff relationships in a lowland forested watershed in the south eastern USA. *USDA Forest Service / UNL Faculty Publications, Paper 139. Hydrological Processes,* 25(**13**): 2032-2045.

Lachat, E., Macher, H., Landes, T., Grussenmeyer, P. (2015) Assessment and Calibration of a RGB-D Camera (Kinect v2 Sensor) Towards a Potential Use for Close-Range 3D Modeling. *Remote sensing,* 7: 13070-13097.

Lamb, R., Mantz, P., Atabay, S., Benn, J., Pepper, A. (2006a) *Recent advances in modelling flood water levels at bridges and culverts.* JBA Consulting Engineers & Scientists. http://www.river-conveyance.net/aes/documents/phase1/12_Lamb_RecentAdvancesInFloodWaterLevelsBridges_Defra200603A-1.pdf

Lamb, R., Zaidman, M. D., Archer, D. R., Marsh, T. J., Lees, M. L. (2006b) *River Gauging Station Data Quality Classification (GSDQ).* R&D Technical Report W6-058/TR. Bristol. Environment Agency, 136.

Landau, M. J., Choo, B. Y., Beling, P. A. (2016) Simulating Kinect Infrared and Depth Images. *IEEE Transactions on Cybernetics*, 46(**12**): 3018-3031.

Lane, E. W. (1954) *The importance of fluvial morphology in hydraulic engineering*. Hydraulic Laboratory Report No. 372. United States Department of the Interior Bureau of Reclamation. Engineering Laboratories Division Hydraulic Laboratory Branch. Commissioner's Office: Denver, Colorado. 81 (**745**): 1-17.

Lane, E. W. (1955) The importance of fluvial morphology in hydraulic engineering. *American Society of Civil Engineers Proceedings Separate*, 81(**745**): 1-17.

Lane, S. N., Chandler, J. H., Richards, K. S. (1994) Developments in Monitoring and Modelling Small-scale River Bed Topography. *Earth Surface Processes and Landforms*, 19: 349 368.

Langran, G. (1992) *Time in Geographic Information Systems.* London: Taylor and Francis.

Lavers, T., Charlesworth, S. M., Lashford, C., Warwick, F., Fried, J. (2022) The Performance of Natural Flood Management at the Large Catchment-Scale: A Case Study in the Warwickshire Stour Valley. *Water*, 14(**23**): 3836.

Lawler, D. M., Thorne, C. R., Hooke J. M. (1997) Bank erosion and instability In Thorne, C. R., Hey, R. D., Newson, M. D. (eds.) *Applied Fluvial Geomorphology for River Engineering and Management*, Chichester: John Wiley and Sons Ltd., 137-172

Leakey, S., Hewett, C. J. M., Glenis, V., Quinn, P. F. (2020) Modelling the Impact of Leaky Barriers with a 1D Godunov-Type Scheme for the Shallow Water Equations. *Water*, 12(**2**): 371.

Lee, J. Y., Forrest, A. L., Hardjanto, F. A., Chai, S., Cossu, R., Leong, Z. Q. (2018) Development of current-induced scour beneath elevated subsea pipelines. *Journal of Ocean Engineering and Science*, 265 – 281.

Leopold, L. B., Wolman, M. G. (1957) River Channel Patterns: Braided, Meandering, and Straight. *United States Geological Survey Professional Paper*. no. 282B, US Government Printing Office: Washington, DC., 47BP.

Leopold, L. B., Wolman, M. G. Miller, J. P. (1964) *Fluvial Processes in Geomorphology*. San Francisco, California: W. H. Freeman and Company. 522.

Li, X. (2018) *Feature Based Calibration of a Network of Kinect Sensors.* MSc. thesis. The University of Western Ontario.

Lindroth, E. M., Rhoads, B. L., Castillo, C. R., Czuba, J. A., Güneralp, İ., Edmonds, D. (2020). Spatial variability in bankfull stage and bank elevations of lowland meandering rivers: Relation to rating curves and channel planform characteristics. *Water Resources Research,* 56: 1-24.

Linstead, C., Gurnell, A. M. (1999) *Large woody debris in British Headwater rivers: physical habitat and management guidelines.* R&D Technical Report W185, School of Geography and Environmental Sciences, University of Birmingham. Bristol: Environment Agency.

Lisle, T. E. (1986) Stabilization of a gravel channel by large streamside obstructions and bedrock bends, Jacoby Creek, northwestern California. *Geological Society of America Bulletin*, 97: 999-1011.

Liu, Y., Gebremeskel, S., De Smedt, F., Hoffmann, L., Pfister, L. (2004) Simulation of flood reduction by natural river rehabilitation using a distributed hydrological model. *Hydrology and Earth System Sciences Discussions*, 8: 1129-1140.

Liu, Z., Merwade, V. (2018) *Accounting for model structure parameter and input forcing uncertainty in flood inundation modelling using Bayesian model averaging*. Purdue University, U.S. Elsevier.

Lo, H. W., Smith, M., Klaar, M., Woulds, C. (2021) Potential secondary effects of in-stream wood structures installed for natural flood management: A conceptual model. *WIREs water,* 8(**e1546**): 1-22.

Lull, H., Reinhart, K. (1972) *Forests and floods in the eastern United States.* Res. Pap. NE-226. Upper Darby, PA: U.S. Department of Agriculture, Forest Service, Northeastern Forest Experiment Station. 1-94

Mackay, C., Suter, S., Albert, N., Morton, S., Yamagata, K. (2015) Large scale flexible mesh 2D modelling of the Lower Namoi Valley. *Floodplain Management Australia National Conference,* Brisbane, Australia*.* https://www.floodplainconference.com/papers2015/Craig%20Mackay.pdf

MacWilliams, M. L., Wheaton, J. M., Pasternack, G. B., Street, R. L. (2006) Flow convergence routing hypothesis for pool-riffle maintenance in alluvial rivers. *Water Resources Research*, 42(**10**): 1-21.

Madej, M. A. (1999) Temporal and spatial variability in thalweg profiles of a gravel-bed river. *Earth Surface Profiles and Landforms,* 24(**12**): 1153-1169.

Magliulo, P., Bozzi, F., Pignone, M. (2016) Assessing the planform changes of the Tammaro River (southern Italy) from 1870 to 1955 using a GIS-aided historical map analysis. *Environ. Earth Science*, 75:355.

Mallick, T., Das, P., P., Majumdar, A., K. (2014) Characterizations of Noise in Kinect Depth Images: A Review. *IEEE Sensors Journal,* 14(**6**): 1731-1740.

Mankoff, K. D. (2020) email, Furnues, D. May.

Mankoff, K. D., Russo, T.A. (2013) The Kinect: a low-cost, high-resolution, short-range 3D camera. *Earth Surf. Process. Landforms*, 38: 926–936.

Manners, R. B. (2006) *The structure and hydraulics of natural woody debris jams.* Master of Arts thesis. Department of Geography, University of North Carolina, Chapel Hill, 1-119.

Manners, R. B., Doyle, M. W. (2008) A mechanistic model of woody debris jam evolution and its application to wood-based restoration and management. *River Research and Applications*, 24(**8**): 1104–1123.

Manners, R. B., Doyle, M. W., Small, M. J. (2007) Structure and hydraulics of natural woody debris jams. *Water resources Research,* 43(**6**): 2-17.

Mant, J. M., Soar, P. J. (2009) Understanding River Restoration. [PowerPoint presentation] *Training Events. The River Restoration Centre Workshops, Module 1.* https://www.therrc.co.uk/sites/default/files/files/Training/events_archive/RRC_Workshops/Module_1_2009/presentation_feb_2009_complete.pdf (accessed: 24.09.23).

Marston R. A. (1982) The geomorphic significance of log steps in forest streams**.** *Annals of the American Association of Geographers*, 72: 99-108.

Martin, M. (2017) *Pool-Riffle Maintenance, youtube image.* https://www.youtube.com/watch?v=RGM1X6rcWEE (Accessed: 12.12.18).

Matlab (2020a) What Is Camera Calibration? *MathWorks, Help Center.* https://ch.mathworks.com/help/vision/ug/camera-calibration.html#:~:text=Radial%20distortion%20occurs%20when%20light,xdistorted%2C%20ydistorted)%3A (accessed: 28.09.23).

Matlab (2020b) Evaluating the Accuracy of Single Camera Calibration. *MathWorks, Help Center.* https://ch.mathworks.com/help/vision/examples/evaluating-the-accuracy-of-single-camera-calibration.html (accessed: 28.09.23).

Maxwell, A. R., Papanicolaou, A. N. (2001) Step-pool morphology in high-gradient streams. *International Journal of Sediment Research,* 16(**3**): 280-290.

McCartney, M. P., Naden, P. S. (1995) A Semi-Empirical investigation of the influence of floodPlain Storage on Flood Flow. *Journal of the Institution of Water and Environment Management*, 9(**3**): 236-246.

McIntyre, N., C. Thorne, C. (eds.) (2013) *Land use management effects on flood flows and sediments – guidance on prediction.* London: CIRIA.

McParland, M. (2019) Modelling the effects of large woody dams on sedimentary processes. *River Restoration Centre. 20th Annual Network Conference.* University of Liverpool. Liverpool. Britannia Adelphi Hotel.

McParland, M. (2021) *Modelling the Hydraulic and Sediment Dynamics of Leaky Barriers in Relation to Natural Flood Management*. Doctor of Philosophy. University of Liverpool.

McParland, M., Cudden, J., Crowder, R. (2023) email, Furnues, D. February.

Met Office (2019) *Wet weather June 2019*. https://www.metoffice.gov.uk/binaries/content/assets/metofficegovuk/pdf/weather/learn-about/uk-past-events/interesting/2019/2019_006_rainfall_lincolnshire.pdf

Met Office (2020) *Storm Dennis*. https://www.metoffice.gov.uk/binaries/content/assets/metofficegovuk/pdf/weather/learn-about/uk-past-events/interesting/2020/2020_03_storm_dennis.pdf

Met Office (2023) *Historic station data*. https://www.metoffice.gov.uk/research/climate/maps-and-data/historic-station-data

Metcalfe, P., Beven, K., Hankin, B., Lamb, R. (2017) A modelling framework for evaluation of the hydrological impacts of nature-based approaches to flood risk management, with application to in-channel interventions across a 29km² scale catchment in the United Kingdom. *Hydrological Processes,* 31(**9**): 1734-1748.

Metcalfe, P., Beven, K., Hankin, B., Lamb, R. (2018) A new method, with application, for analysis for the impacts on flood risk of widely distributed enhanced hillslope storage. *Hydrology and Earth System Sciences*, 22(**4**): 2589-2605.

Milan, D. J., Heritage, G. L., Large, A. R. G. (2002) Tracer pebble entrainment and deposition loci: influence of flow character and implications for riffle-pool maintenance. *Geological Society of London,* 191: 133-148.

Minnesota Department of Transportation (2000) Drainage Manual. *Office of Bridges and Structures*. 4: 89-120.

Montgomery, D. R., Abbe, T. B. (2006) Influence of logjam-formed hard points on the formation of valley-bottom landforms in an old-growth forest valley, Queets River, Washington, USA. *Quaternary Research*, 65(**1**): 147-155.

Montgomery, D. R., Buffington, J. M. (1993) *Channel classification, prediction of channel response, and assessment of channel condition.* Olympia, Washington: State Department of Natural Resources Report, TFW-SH10-93-002, U.S.A. 84.

Montgomery, D. R., Buffington, J. M. (1997) Channel-reach morphology in mountain drainage basins. *Geological Sciences of America Bulletin*, 109(**5**): 596-611.

Montgomery, D. R., Buffington, J. M. (1998) Channel Processes, Classification, and Response. In Naiman, R. J., Bilby, R. E. (eds.) *River Ecology and Management*. New York: Springer-Verlag. 13–42.

Montgomery, D. R., Buffington, J. M., Smith, R. D., Schmidt, K. M., Pess, G. (1995) Pool spacing in forest channels. *Water Resources Research*, 31(**4**): 1097-1105.

Montgomery, D. R., Buffington, J. R., Smith, R. D., Schmidt, K. M., Pess, G. (1995) Pool Spacing in Forest Channels. *Water Resources Research,* 31(**4**): 1097-1105.

Montgomery, D. R., Collins, B. D., Buffington, J. M., Abbe, T. B. (2003) Geomorphic effects of wood in rivers. *American Fisheries Society Symposium,* 37: 21-47.

Moore, R. J., Cole, S. J., Dunn, S., Ghimire, S., Golding, B. W., Pierce, C. E., Roberts, N. M., Speight, L. (2015) *Surface water flood forecasting for urban communities*, CREW report CRW2012_03.

Mousa, Y. A., Bulatov, D., Abed, F. M., Helmholz, P. (2021*)* DTM Extraction and building detection in DSMs having large holes. *Proceedings SPIE 11864, Remote Sensing Technologies and Applications in Urban Environments VI,* 118640H.

Muhawenimana V., Tucker R., Rowley S. J., Follett E., Pan S., Wilson C. A. M. E. (June 2022) In-Channel Natural Flood Management Approach to Flood Risk Management: Modelling Applications on a Small Catchment in the UK. *Proceedings of the 39th IAHR World Congress From Snow to Sea*. Grenada, Spain: IAHR.

Muhawenimana, V., Wilson, C., Nefjodova, J., Cable, J. (2021) Flood attenuation hydraulics of channel-spanning leaky barriers. *Journal of Hydrology*. 596(**121731**): 1-9.

Müller, S., Wilson, C. A. M. E., Ouro, P., Cable, J. (2021) Experimental investigation of physical leaky barrier design implications on juvenile rainbow trout (Oncorhynchus mykiss) movement. *Water Resources Research*, 57(**8**): [e2021WR030111].

Nagel, D. E., Buffington, J. M., Parkes, S. L., Wenger, S., Goode, J. R. (2014) *A Landscape Scale Valley Confinement Algorithm: Delineating Unconfined Valley Bottoms for Geomorphic, Aquatic, and Riparian Applications*. Gen. Tech. Rep. RMRS-GTR-321. Fort Collins, CO: US Department of Agriculture, Forest Service, Rocky Mountain Research Station. 42

National Geographic. (2019) *Flooding*. https://www.nationalgeographic.org/encyclopedia/flood-plain/ (accessed: 3. 2023).

National Infrastructure Commission (2022) *Reducing the Risk of Surface Water flooding*. London: HMSO.

Neden, G. (21.12.18) *photograph of Wilderhope Brook dam (29)*. Diddlebury Parish Flood Action Group. https://www.diddleburyparish.co.uk/flood-action-group. (accessed: 12.09.23)

Néelz, S., Pender, G. (2009) *Desktop review of 2D hydraulic modelling packages.* Science Report: SC080035. Bristol: DEFRA: Environment Agency.

Nelson, S. A. (2016) *River Systems & Causes of Flooding.* Tulane University. https://www2.tulane.edu/~sanelson/Natural_Disasters/riversystems.htm (accessed:22.09.23).

Newcastle University, Environment Agency (2011) *Runoff Attenuation Features A guide for all those working in catchment Management*. Belford Catchment Solutions Project – a partnership project between the Environment Agency, Newcastle University and Local Landowners.

Nezu, I., Nakagawa, H. (1993) *Turbulence in Open Channel Flows*. Balkema, Rotterdam: IAHR Monograph.

Ngai, R., Wilkinson, M., Nisbet, T., Harvey, R., Addy S., Burgess-Gamble, L., Rose, S., Maslen, S., Nicholson, A., Page, T., Jonczyk, J., Quinn, P. (2017) *Working with Natural Processes – Appendix 2: Literature review*, SC150005, Bristol: Environment Agency.

Nicholson, A. R., Quinn, P. F., Wilkinson, M. E. (2015) *Case study 16*. Belford Natural Flood Management Scheme, Northumberland. https://ewn.erdc.dren.mil/wp-/uploads/2021/04/case_study_16_belford.pdf (accessed: 28.09.23).

Nicholson, A. R., Wilkinson, M. E., O'Donnell, G. M., Quinn, P. F. (2012) Runoff attenuation features: a sustainable flood mitigation strategy in the Belford catchment, UK. *Area*, 44(**4**): 463-469.

Nietch, C. T., Borst, M., Schubauer-Berigan, J. P. (2005) Risk management of sediment stress: A framework for sediment risk management research. *Environmental Management*, 36(**2**): 175-194.

Nikolopoulos, E. I., Borga, M., Zoccatelli, D., Anagnostou, E. N. (2014) Catchment-scale storm velocity: quantification, scale dependence and effect on flood response. *Hydrological Sciences Journal*, 59(**7**): 1363-1376.

Nikuradse, J. (1933) *Strömungsgesetze in rauhen,* Rohren Forschung auf dem Gebeite des Ingenieur-wesens, Ausgabe B Band 4. (English Translation: *Laws of flow in rough pipes,* tech. Memo. 1292, Natl. Adv. Comm. For Aeron, Washington D. C., 1950.

Nisbet, T., Thomas, H., Roe, P. (2017) *Case Study 12. Slowing the Flow at Pickering*. 1-11.

Nkwunonwo, U. C., Whitworth, M., Baily, B. (2020) A review of the current status of flood modelling for urban flood risk management in the developing countries. *Scientific African*, 7: e00269.

Norbury, M., Phillips, H., Macdonald N., Brown, D., Boothroyd, R., Wilson, C., Quinn, P., Shaw, D. (2021) Quantifying the hydrological implications of pre- and post-installation willowed engineered log jams in the Pennine Uplands, NW England. *Journal of Hydrology*. 603: 1-45.

Norbury, M., Shaw, D., Jones, P. (2018) Combining Hydraulic Modelling with Partnership Working: Towards a Practical Natural Flood Management Approach. *Ice Publishing*, 1-43.

O'Brien, G. R., Wheaton, J. M., Fryirs, K., Macfarlane, W. M., Brierley, G., Whitehead, K., Gilbert, J., Volk, C. (2019) Mapping valley bottom confinement at the network scale. *Earth Surface Processes and Landforms*, 44(**9**): 1828-1845.

O'Connell, P. E., Ewen, J., O'Donnell, G., Quinn, P. (2007) Is there a link between agricultural land-use management and flooding? *Hydrology and Earth Systems Sciences*, 11(**1**): 96-107.

Odoni, N. A., Lane, S. N. (2010a) *Assessment of the impact of upstream land management measures on flood flows in Pickering using OVERFLOW.* Contract report to Forest Research for the Slowing the Flow at Pickering project. Durham: Durham University.

Odoni, N. A., Lane, S. N. (2010b) Knowledge-theoretic models in hydrology. *Progress in Physical Geography: Earth and Environment,* 34: 151-171.

Oliver, C. D., Hinckley, T. M. (1987) Species, stand structures and silvicultural manipulation patterns for the streamside zone. In *Streamside management: forestry and fishery interactions*, Salo E. O., Cundy, T. W. (eds.) pp. 259-276. University of Washington, Seattle, Washington, USA: Institute of Forest Resources.

Oliveto, G., Hager, W. H. (2005) Further results to time- dependent local scour at bridge elements. *ASCE Journal of Hydraulic Engineering,* 131(**2**): 97-105.

Oniemayin, I. B., Tenebe. I. T., Emenike, P. C., Busari, A. B., Gideon, D. K. (2016) Spectral Responses and Classification of Earth's Features on Satellite Imagery. 3rd *International Conference on African Development Issues*, Department of Civil Engineering, Nigeria: Covenant University.

Osei, N. A., Gurnell, A. M., Harvey, G. L. (2015) The role of large wood in retaining fine sediment, organic matter and plant propagules in a small, single-thread forest river. *Geomorphology,* 235: 77-87.

O'Sullivan, J. J., Ahilan, S., Bruen, M. (2012) Indexing floodplain effects for flood estimation. In: *IAHR World Congress 2011: Balance and Uncertainty: Water in a Changing World.* 34th IAHR World Congress: 33rd Hydrology and Water Resources Symposium. 10th Conference on Hydraulics in Water Engineering, 26 Jun - 01 Jul 2011, Brisbane, Australia. International Assn for Hydro-Environment Engineering and Research, 3984 - 3991.

Ouma, Y. O. (2019) On the Use of Low-Cost RGB-D Sensors for Autonomous Pothole Detection with Spatial Fuzzy'*c*-Means Segmentation. *Geographic Information Systems in Geospatial Intelligence, IntechOpen,* 1-30*.*

Owens, P. N., Petticrew, E. L., van der Perk, M. (2010) Sediment response to catchment disturbances. *Journal of Soils and Sediment,* 10:591-596.

Ozturk, D., Sesli, F. A. (2015) Determination of Temporal Changes in the Sinuosity and Braiding Characteristics of the Kizilirmak River, Turkey. *Political Journal of Environmental Studies,* 24(**5**): 2095-2112.

Pagliari, D., Pinto, L. (2015) Calibration of Kinect for Xbox One and Comparison between the Two Generations of Microsoft Sensors. *Sensors*, 15(**11**): 27569-27589.

Paiva, R. C. D., Collischonn, W., Tucci, C. E. M. (2011) Large scale hydrologic and hydrodynamic modelling using limited data and a GIS based approach. *Journal of Hydrology*, 406: 170-181.

Palmer, M. (2012) *Agricultural fine sediment: Sources, pathways and mitigation.* PhD. University of Newcastle upon Tyne.

Papanicolaou, A. N., Bressan, F., Fox, J., Kramer, C. K. and Kjos, L. (2018a) Role of Structure Submergence on Scour Evolution in Gravel Bed Rivers: Application to Slope-Crested Structures. *Journal of Hydraulic Engineering*, 144(**2**).

Papanicolaou, A. N., Wyssmann, M. A., Merook, A., Mohammadi, S. (2018b) *Investigation of Flow and Local Scour Characteristics around Permeable Washington State Department of Transportation (WSDOT) Dolotimber Engineered Logjams (ELJ)* WSDOT Research Report: Office of Research & Library Services.

Parker, C., Henshaw, A. J., Harvey, G. L., Sayer, C. D. (2017) Reintroduced large wood modifies fine sediment transport and storage in a lowland river channel. *Earth Surface Processes and Landforms,* 42(**11**), 1693–1703.

Parkyn, S. (2004) *Review of Riparian Buffer Zone Effectiveness*. MAF Technical Paper. No: 2004/05. MAF Information Bureau. Wellington, New Zealand: Ministry of Agriculture and Forestry.

Parola, A. C., Apeldt, C. J., Jempson, M. A. (2000) *Debris Forces on Highway Bridges. National Cooperative Highway Research Program (NCHRP) Report No. 445*, Transportation Research Board, Washington, D. C: National Academy Press.

Pattison, I., Lane, S. N. (2012) The link between land-use management and fluvial flood risk: A chaotic conception? *Progress in Physical Geography: Earth and Environment,* 36(**1**): 72-92.

Pattison, I., Lane, S. N., Hardy, R. J. Reaney, S. M. (2014) The role of tributary relative timing and sequencing in controlling large floods. *Water Resources Research,* 50(**7**): 5444-5458.

Peak Chief Executive (2016) *Simple, effective woody debris dams.* (29 June). https://twitter.com/PeakChief/status/748110638912765952/photo/2 (accessed: 03.03.23).

Pearson, E. G. (2020) *Modelling the interactions between geomorphological processes and Natural Flood Management*. Doctor of Philosophy, University of Leeds: Leeds. 251 pp.

Pender, G., Néelz, S. (2011) Flood inundation modeling to support flood risk management. Flood Risk Science and Management. In Pender, G., Faulkner, H. (eds) *Flood Risk Science and Management*, Oxford: Blackwell. 234–257.

Penna, N., Coscarella, F., Gaudio, R. (2020a) Flow, turbulence, and drag associated with engineered log jams in a fixed-bed experimental channel. *Water,* 12(**143**): 1-18.

Penna, N., Coscarella, F., Gaudio, R. (2020b) Turbulent Flow Field around Horizontal Cylinders with Scour Hole. w*ater*, 12(**143**): 1 -18.

Philips, J. D. (2010) The job of the river. *Earth Surface Processes and Landforms*, 35(**3**): 305-313.

Pinter, N., Miller, K., Wlosinski, J. H., van der Ploeg, R. R. (2004) Recurrent shoaling and channel dredging, Middle and Upper Mississippi River, USA. *Journal of Hydrology*, 290: 275-296.

Pinter, N., van der Ploeg, R. R., Schweigert, P., Hoefer, G. (2006) Flood magnification on the River Rhine. *Hydrological Processes,* 20(**1**): 147-164.

Pinto, C., Ing, R., Browning, B., Delboni, V., Wilson, H., Martyn, D., Harvey, G. L. (2019) Hydromorphological, hydraulic and ecological effects of restored wood: Findings and reflections from an academic partnership approach. *Water and Environment Journal*, 33: 353-365.

Pitt, M. (2008). *The Pitt Review: Learning lessons from the 2007 floods.* London: Cabinet Office.

Pohlmann, S. T. L., Harkness, E. F., Astley, S. M. (2016) Evaluation of Kinect 3D sensor for Healthcare Imagining. *Journal of Medical and Biological Engineering,* 36: 857-870.

Poindexter, C. M., Rusello, P. J., Variano, E. A. (2011) Acoustic Doppler velocimeter-induced acoustic streaming and its implications for measurement. *Experiments in Fluids*, 50: 1429–1442.

Postel, S. (1999) *Pillar of Sand: Can the Irrigation Miracle Last?* New York: WW Norton.

Quinn, P. F., Hewett, C. J. M., Jonczyk, J., Glenis, V. (2007) *The PROACTIVE approach to Farm Integrated Runoff Management (FIRM) Plans. Flood storage on farms*. Newcastle: Newcastle University.

Quinn, P. F., Hewett, C. J. M., Wilkinson, M. E., Adams, R. (2022) The Role of Runoff Attenuation Features (RAFs) in Natural Flood Management. *Water*, 14(**23**): 3807.

Quinn, P., O'Donnell, G., Nicholson, A., Wilkinson, M., Owen, G., Jonczyk, J., Barber, N., Hardwick M., Davies, G. (2013a) *Potential Use of Runoff Attenuation Features in Small Rural Catchments for Flood Mitigation.* NFM RAF Report, 1-34.

Quinn, P., O'Donnell, G., Nicholson, A., Wilkinson, M., Owen, G., Jonczyk, J., Barber, N., Hardwick, M., Davies, G. (June, 2013b) *National Flood Management Runoff Attenuation Features report: potential use of runoff attenuation features in small rural catchments for flood mitigation.* Newcastle University.

Rahman, M. A., Ennos, A. R. (2016) *What we know and don't know about the surface runoff reduction potential of urban trees*. Environmental Sciences, University of Hull: Kingston-upon, Hull, UK, 1-14.

Rajneesh, K., Anil, B. (2015) Probability analysis of return period of daily maximum rainfall in annual data set of Ludhiana, Punjab. *Indian Journal of Agricultural Research,* 49(**2**): 160.

Ramsbottom, D. M., Whitlow, C. D. (2003) *Extension of Rating Curves at Gauging Stations Best Practice Guidance Manual*. R&D Manual W6-061/M. Bristol: Environment Agency. 1-254.

Randall, N. P., Donnison, L. M., Lewis, P. J., James, K. L. (2015) How effective are on-farm mitigation measures for delivering an improved water environment? A systematic map. *Environmental Evidence*, 4(**18**).

Ranstam J. (2008) Methodological Note: Accuracy, precision, and validity. *Acta Radiologica*, 49(**1**): 105-106.

Rasche, D., Reinhardt-Imjela, C., Schulte, A., Wenzel, R. (2019) Hydrodynamic simulation of the effects of in-channel large woody debris on the flood hydrographs of a low mountain range creek, Ore Mountains, Germany. *Hydrology and Earth System Sciences Discussions*, 1–24.

Refsgaard, J. C., Henriksen, H. J. (2004) Modelling guidelines – Terminology and guiding principles. *Advances in Water Resources*, 27(**1**): 71-82.

Rehbock, T. H. (1929) *Wassermessung mit scharfkantigen Ueberfallwehren*, Z. VDI. 73(**27**): 817-823.

Richards, K. S. (1978) Simulation of flow geometry in a riffle-pool stream. *Earth Surface Processes and Landforms,* 3: 345-354.

Robinson, R. A., Sutherland, W. J. (2002) Post war changes in arable farming and biodiversity in Great Britain. *Journal of Applied Ecology,* 39(**1**): 157-176.

Robinwood and Forestry Commission Wales (2008) *Evaluation of large woody debris in watercourses*. Robinwood Robinflood report for the Interreg IIIC project, Robinwood.

Robison, E., Beschta, R. (1990) Coarse woody debris and channel morphology interactions for undisturbed streams in southeast Alaska, USA. *Earth Surface Processes and Landforms*, 15: 149–56.

Rodriguez-Iturbe, I., Valdes, J. B. (1979) The Geomorphologic Structure of Hydrologic Response. *Water Resources Research,* 15(**6**):1409-1420.

Roland, C. S., Balzter, H. (2007) Data Fusion for Reconstruction of a DTM, Under a Woodland Canopy, From Airborne L-band InSAR. *IEEE Transactions on Geoscience and Remote Sensing*, 45(**5**): 1154-1163.

Rolauffs, P. (1999) Untersuchungen zur Besiedlung von Biber-dämmen durch Insekten unter besonderer Berticksichtigung der Emergenz. Staatsexamensarbeit, Essen, 1-160

Roni, P., Beechie, T., Pess, G., Hansen, K. (2014) Wood placement in river restoration: fact, fiction, and future direction. *Canadian Journal of Fisheries and Aquatic Sciences*, 7(**3**).

Rosgen, D. E. (1994) A classification of natural rivers. *Catena*, 22(**3**): 169-199.

Rosgen, D. L. (1996) *Applied River Morphology.* Pagosa Springs, Colorado: Wildland Hydrology Books.

Rowntree, K. M., Dollar, E. S. J. (1999) Vegetation Controls on Channel Stability in the Bell River, Eastern Cape, South Africa. *Earth Surface Processes and Landforms*, 24(**2**): 127-134.

Rural Payments Agency (2020) *Countryside Stewardship: Higher Tier Manual*. Department for Environment Food and Rural Affairs. https://assets.publishing.service.gov.uk/government/uploads/system/uploads/attachment_data/file/920470/CS_Higher_Tier_v2.0.pdf (accessed: 24,09.23).

Rural Payments Agency, Natural England (2020) *RP33: Large leaky woody dams*. https://www.gov.uk/countryside-stewardship-grants/rp33-large-leaky-woody-dams (accessed: 24.09.23).

Salazar, S., Francés F., Komma, J., Blume, T., Francke, T., Bronstert, A., Blöschl, G. (2012) A comparative analysis of the effectiveness of flood management measures based on the concept of "retaining water in the landscape" in different European hydro-climatic regions. *Natural Hazards and Earth Systems Sciences,* 12(**11**): 3287-3306.

Samuels, P. G. (1990) Cross-section Locations in 1-D Models. *Proceedings of International Conference on River Flood Hydraulics.* 17-20 September, Presented at Hydraulics Research Wallington, UK. Chichester: John Wiley, 339-350.

Sarbolandi, H., Lefloch, D., Kolb, A. (2015) Kinect Range Sensing: Structured-Light versus Time-of-Flight Kinect. Institute for Vision and Graphics, University of Siegen, Germany. *Journal of Computer Vision and Image Understanding*, 139: 1-20.

Sato, M., Kobayashi, T. (2012) A fundamental study of the flow past a circular cylinder using Abaqus/CFD. *SIMULIA Community Conference*, 1-15.

Schlichting, H. (1979) *Boundary-Layer Theory*. 7.ed. New York: McGraw-Hill.

Schumm, S. A. (1963) Sinuosity of alluvial rivers on the Great Plains. *Geological Society of America Bulletin*, 74: 1089-1100.

Sear, D. A., Millington, C. E., Kitts, D. R., Jeffries, R. (2010) Logjam controls on channel: floodplain interactions in wooded catchments and their role in the formation of multi-channel patterns. *Geomorphology*, 116: 305–319.

Sear, D. A., Newson, M. D., Thorne, C. R. (2004) *Guidebook of applied fluvial* geomorphology*: Defra / Environment Agency Flood and Coastal Defence R&D Programme* (Technical Report, FD1914). London: Defra Flood Management Division. 256.

Seddon, J. A. (1900) River hydraulics. *Trans. Am. Soc. Civ. Eng.,* 43: 1-183.

Senior, J. G., Trigg, M. A., Willis, T. (2022) Physical representation of hillslope leaky barriers in 2D hydraulic models: A case study from the Calder Valley. *Journal of Flood Risk Management*, CIWEM, 15(**3**): e12821.

SEPA (2015) *Natural Flood Management Handbook.* Stirling: Scottish Environment Protection Agency (SEPA).

SEPA (2016) *Flood modelling guidance for responsible authorities*. Stirling: Scottish Environment Protection Agency.

SEPA (2020) *Flood Modelling Guidance for Responsible Authorities*. Version 1.1. www.sepa.org.uk/media/219653/flood_model_guidance_v2.pdf (accessed: 25.09.23).

SEPA and Forestry Commission Scotland (2012) *Flood Risk Management (Scotland) Act 2009: methods to screen and quantify natural flood management effects*. Stirling: Scottish Environment Protection Agency.

Shields, F. D., Gippel, C. J. (1995) Prediction of effects of woody debris removal on flow resistance. *Journal of Hydraulic Engineering*, 121(**4**): 341–354.

Shields, F. D., Knight, S. S., Cooper, C. M. (1994) Effects of channel incision on base flow stream habitats and fishes. *Environmental Management,* 18: 43-57.

Shields, F. F., Alonso, C. V. (2012) Assessment of flow forces on large wood in rivers. *Water Resources Research*, 48(**4**): 1-16.

Sholtes, J., Doyle, M. W. (2011) Effect of Channel Restoration on Flood Wave Attenuation. *Journal of Hydraulic Engineering,* 137(**2**): 196-208.

Simoes, F. (2014) Shear velocity criterion for incipient motion of sediment. *Water Science and Engineering*, 7(**2**): 183-193.

Simon, A., Castro, J. (2003) Measurement and Analysis of Alluvial Channel Form. In Kondolf, G. M., Piegay, G. M. (eds.) *Tools in Fluvial Geomorphology.* Chichester: Wiley. 289-322.

Singh, R. Y. (2005) Sustainable Management of Headwater resources: Interface drainage analysis of a water divide. In Jansky, L., Haigh, M. J., Prasad, H. (eds.) *Sustainable Management of Headwater Resources: Research from Africa and India.* New York: United Nations University Press. 87-105.

Slater, L. J. (2016) To what extent have changes in channel capacity contributed to flood hazard trends in England and Wales? *Earth Surface Processes and Landforms*, 41(**8**): 1115-1128.

Slater, L. J., Singer, M. B., Kirchner, J. W. (2015) Hydrologic versus geomorphic drivers of trends in flood hazard. *Geophysical Research Letters*, 42(**2**): 370-376.

Smisek, J. (2020) email, Furnues, D., May.

Smisek, J., Jancosek, M., Pajdla, T. (2011) 3D with Kinect. *IEEE International Conference on Computer Vision Workshops*, Barcelona, 2011, 1154-1160.

Smith, R. (2019) Shropshire Weather: Thunderstorms hit parts of the county. *Shropshire Star News*. (25 June).

Smith, R. D. (1992) Geomorphic effects of large woody debris in streams. In Neary, D., Ross, K. C., Coleman, S. S. (eds.) *National hydrology workshop proceedings. General Technical Report RM-GTR-279.* United States Department of Agriculture Forest Service. 113-127.

Smith, R. D., Sidle, R. C., Porter, P. E., Noel, J. R. (1993). Effects of experimental removal of woody debris on the channel morphology of a forest, gravel-bed stream. *J. Hydrol*., 152(**1-4**): 153-178.

Smith, S. (8 December 2020) *2020 floods*. Communities Overview Committee. Shropshire Council, UK. https://shropshire.gov.uk/committee-services/documents/s26101/Flooding%20Communities%20Overview%20December%202020.pdf

Smock, L. A., Metzler, G. M., Gladden, J. E. (1989) Role of Debris Dams in the Structure and Functioning of Low-Gradient Headwater Streams. *Ecology,* 70(**3**): 764-775.

Southard, J. (2006) 12.090 *Introduction to Fluid Motions, Sediment Transport, and Current-Generated Sedimentary Structures.* Massachusetts Institute of Technology: MIT OpenCourseWare. https://ocw.mit.edu. License: Creative Commons BY-NC-SA. (accessed: 28.09.23).

Spreitzer, G., Tunnicliffe, J., Friedrich, H. (2021) Effects of large wood (LW) blockage on bedload connectivity in the presence of a hydraulic structure. *Ecological Engineering*, 161: 106156.

Spring, K. R., Flynn, B. O., Long, J. C., Davidson, M. W. (2020) *Spatial Resolution in Digital* Imaging. *The Source for Microscopy Education*.

https://www.microscopyu.com/tutorials/spatial-resolution-in-digital-imaging (accessed: 26.09.23).

Stall, J. B., Yang, C. T. (1972) *Hydraulic Geometry and Low Streamflow regimen*. WRC Research Report No 54. Project No B-051-ILL. University of Illinois: Water Resources Center. 1-34.

Stantec (2018) *Entrenchment Ratio.* Iowa Department of Natural Resources, Iowa River Restoration Toolbox. 3325 South Timberline Road, Suite 150 Fort Collins, Colorado 80525-2903.

Stommel, M., Beetz, M., Xu, W. L. (2013) Inpainting of missing values in the Kinect sensor's depth maps based on background estimates. *Sensors IEEE,* 1-10.

Sumer, B. M., Fredsøe, J. (2006) *Hydrodynamics Around Cylindrical Structures*. Vol 26. London: World Scientific Publishing Co. Pte. Ltd.

Svoboda, C. D., Russell, K. (2011) Flume Analysis of Engineered Large Wood Structures for Scour Development and Habitat. *World Environmental and Water Resources Congress*, 2572-2581.

Szasz, T., Katal-Urban, G., Petrovanster, B., Pereanez, M. (2011) *Hardware*. V-Pollock. https://Inf.u-szeged.hu/projectdirs/ssip2011/teamA/hardware.html (accessed: 23.04.22).

Tammela, S., Marttila, H., Dey, S; Kløve, B. (2010) Effect and design of an underminer structure. *Journal of Hydraulic Research,* 48(**2**): 188-196.

Tanner, P. W. G. (1978) Desiccation structures (mud cracks, etc.). In: Middleton, G. V., Church, M. J., Coniglio, M., Hardie, L. A., Longstaffe, F. J. (eds.) *Encyclopedia of Sediments and Sedimentary Rocks*. Encyclopedia of Earth Sciences Series. Dordrecht: Springer.

Tanoue, M., Hirabayashi, Y., Ikeuchi, H. (2016) Global-scale river flood vulnerability in the last fifty years. *Scientific Reports*, 6: 36021.

Tape store. (2020) thetapestore.co.uk/tapes-rules/tape-measures/tape-accuracy/class-1-tape-measues.

Taylor, M., Clarke, L. (2021) *Monitoring the Impact of Leaky Barriers used for Natural Flood Management on Three River Reaches in the Stroud Frome and Twyver Catchments*, Gloucestershire: UK. Report.

Teng. J., Jakeman, A. J., Vaze, J., Croke, B. F. W., Dutta, D., Kim, S. (2017) Flood inundation modelling: A review of methods, recent advances and uncertainty analysis. *Environmental Modelling & Software,* 90: 201- 216.

Tetzlaff, D., Seibert, J., McGuire, K. J., Laudon, H., Burns, D. A., Dunn, S. M., Soulsby, C. (2009) How does landscape structure influence catchment transit time across different geomorphic provinces? *Hydrological Processes*, 23(**6**), 945–953.

Thames21 (2021) *Natural Flood Management – Leaky Woody Barrier Installation Guide.* https://www.thames21.org.uk/wp-content/uploads/2021/03/Leaky-Woody-Dams-Updated-04.02.21.docx (accessed: 24.09.23).

Thomas, H., Nisbet, T. (2012) Modelling the hydraulic impact of reintroducing large woody debris into watercourses. *Journal of Flood Risk Management,* 5(**2**): 164-174.

Thomas, H., Nisbet, T. R. (2017) Slowing the flow in Pickering: Quantifying the effect of catchment woodland planting on flooding using the soil conservation service Curve Number method. *International Journal of Safety and Security Engineering*, 6(**3**): 466–474.

Thompson, A. (1986) Secondary flows and the pool-riffle unit: a case study of the processes of meander development. *Earth Surface Processes and Landforms*, 11: 631-641.

Thompson, D. M. (1995) The effect of large organic debris on sediment processes and stream morphology in Vermont. *Geomorphology*, 11: 235-244.

Thompson, D. M. (2010) The velocity-reversal hypothesis revisited. *Progress in Physical Geography,* 35(**1**): 123-132.

Thompson, D. M. (2012) The challenge of modelling pool-riffle morphologies in channels with different densities of large woody debris and boulders. *Earth Surface Processes and Landforms*, 37(**2**): 223–239.

Thompson, D. M. (2013) Pool-riffle. In: Shroder, J. (Ed. in Chief), Wohl, E. (Ed.)*. Treatise on Geomorphology*. *Fluvial Geomorphology.* San Diego, CA: Academic Press., 8: 364-378.

Thompson, D. M., McCarrick, C. R. (2010) A flume experiment on the effect of constriction shape on the formation of forced pools. *Hydrology and Earth System Sciences,* 14: 1321–1330.

Thompson, D. M., Nelson, J. M., Wohl, E. E. (1998) Interactions between pool geometry and hydraulics. *Water Resources Research*, 34: 3673–3681.

Thompson, D. M., Wohl, E. E. (2009) The linkage between velocity patterns and sediment entrainment in a pool-riffle unit. *Earth Surface Processes and Landforms,* 34: 177– 192.

Thompson, D. M., Wohl, E. E., Jarret, R. D. (1999) Velocity reversals and sediment sorting in pools and riffles controlled by channel constrictions. *Geomorphology*, 27: 229–241.

Thompson, D. M., Wohl, E. E., Jarrett, R. D. (1996) A revised velocity-reversal and sediment-sorting model for a high-gradient, pool-riffle stream. *Physical Geography*, 17: 142–156.

Thompson, M. S. A. Brooks, S. J., Sayer, C. D., Woodward, G., Axmacher, J. C., Perkins, D. M., Gray, C. (2017) Large woody debris "rewilding" rapidly restores biodiversity in riverine food webs. *Journal of applied ecology*, 55(**2**): 895-904.

Thorne, C. (2011) Challenges to integrated sediment management. *Proceedings of the Advances in River Science 2011 Conference- Accounting for sediment, habitat and morphology in integrated river and flood risk management.* Swansea University, April, 2011.

Todd-Burley, N., Halwyn, A., Wem, C., Ing, R., Hemsworth, M. (2021) *Delivering benefits through evidence. Understanding river channel sensitivity to geomorphological changes. Literature review and understanding factors that influence river channel change*. FRS17183/R1. Flood and Coastal Erosion Risk Management Research and Development Programme. Bristol: Environment Agency.

Toledo, M. A., Ahumada, A. L., Palacios, G. P. I. (2020) Alterations in the course of the Seco River and loss of agricultural land, Tucumán province, Argentina. *Bol. Soc. Geo. Mex*. 72(**2**): 1405-3322.

Tomsett, C. (2021) *Assessing Eco-Geomorphic Interactions Across Scales Using Novel UAV Based Remote Sensing Techniques and Modelling*. Doctor of Philosophy. University of Southampton.

Trigg, M. (2016) *3.4 Fluvial flood modelling*. Caribbean Disaster Emergency Management Agency (CDEMA). https://www.cdema.org/virtuallibrary/index.php/charim-hbook/methodology/3-flood-hazards/3-4-fluvial-flood-modelling (accessed: 24.09.23).

UK Centre for Ecology and Hydrology (2022) *Flood Estimation Handbook Web Service*. Wallingford HydroSolutions, UK. https://fehweb.ceh.ac.uk/GB/map (accessed: 27.09.23).

UK Government (2021a) *LIDAR Composite* DTM 2017 - 2m. https://data.gov.uk/dataset/002d24f0-0056-4176-b55e-171ba7f0e0d5/lidar-composite-dtm-2017-2m (accessed: 28.09.23).

UK Government (2021b) *Hydraulic modelling: best practice (model approach): Guidance*. https://www.gov.uk/government/publications/river-modelling-technical-standards-and-assessment/hydraulic-modelling-best-practice-model-approach (accessed: 28.09.23).

UK Government (2021c) *Estimate flood flow from rainfall and river flow data (source): Guidance*. https://www.gov.uk/government/publications/river-modelling-technical-standards-and-assessment/estimate-flood-flow-from-rainfall-and-river-flow-data-source (accessed: 28.09.23).

Umholtz, T. (2020) *Soil Infiltration. Soil Quality Kit- Guide for Educators*. Natural Resources Conservation Service United States Department of Agriculture. https://web.archive.org/web/20200208195848/https://www.nrcs.usda.gov/Internet/FSE_DOCUMENTS/nrcs142p2_053268.pdf (accessed: 24.09.23).

Van Dijk, W. M., Schuurman, F., Van de Lageweg, W. I., Kleinhans, M. G. (2014) Bifurcation instability and chute cutoff development in meandering gravel-bed rivers. *Geomorphology*, 213: 277-291.

Van Dijk, W. M., Van De Lageweg, W. I., Kleinhans, M. G. (2012) Experimental meandering river with chute cutoffs. *Journal of Geophysical Research: Earth Surfaces*, 117: 1-18.

Vasilyev, K. (2015) *Flood Modeller in River Modelling A Practical Perspective*. CH2M HILL. https://data.aquacloud.net/public/2019/we-watereurope/LIBRARY/Lectures/isis/FM%20HydroEurope%202015.pdf (accessed: 24.09.23).

Vojinovic, Z., Tutulic, D. (2009) On the use of 1D and coupled 1D-2D modelling approaches for assessment of flood damage in urban areas. *Urban Water Journal*, 6: 183-199.

von Lany, P. H., Palmer, J., Thorne, C. R., Evans, E. P., Penning-Rowsell, E. C. (2015) *Future Coastal flooding and coastal erosion risks.* ICE Virtual Publishing. Queen's Printer and Controller of HMSO. https://www.icevirtuallibrary.com/doi/abs/10.1680/ffacer.34495.0022?src=recsys&mobileUi=0 (accessed: 21.09.23).

Wallerstein, N. P., Thorne, C. R. (1995) *Impact of In-channel Organic Debris on Channel Geomorphology and In-Channel Structures. First Quarterly Report to the US Army Corps of Engineers,* 1-6-95(**ADA297046**): 1-7.

Wallerstein, N. P., Thorne, C. R. (1997) *Impacts of woody debris on fluvial processes and channel morphology in stable and unstable streams.* Department of Geography, University of Nottingham, Final Report, June 1997 Prepared for *US Army Research Development and Standardization Group UK, London*. Contract number N68171-96-C-9041. R&D 7897-EN-09.

Wallerstein, N. P., Thorne, C. R. (2004) Influence of large woody debris on morphological evolution of incised sand-bed channels. *Geomorphology*, 57(**1-2**): 53-73.

Wang, H., Leng, X., Chanson, H. (2017) Hydraulic jumps and breaking bores: modelling and analysis. *Engineering and Computational Mechanics*, 170(**EM1**): 25-42.

Wang, S., Hassan, M. A., Xie, X. (2006) Relationship between suspended sediment load, channel geometry and land area increment in the Yellow River Delta. *Catena*, 65: 302 – 314.

Wang, Z., Zhang, K. (2012) Principle of equivalency of bed structures and bed load motion. *International Journal of Sediment Research*, 27: 288-305.

Wasenmüller O., Stricker, D. (2017) Comparison of Kinect V1 and V2 Depth Images in Terms of Accuracy and Precision. In: Chen C. S., Lu, J., Ma, K. K. (eds.) *Computer Vision – ACCV 2016 Workshops. ACCV 2016.* Lecture Notes in Computer Science, 10117: 34-35.

Water Friendly Farming (2020). *Optimising leaky Barriers to prevent collapse and improve performance*. Water Friendly Farming Case Study. https://www.gwct.org.uk/media/1162619/fht-leaky-dams-final.pdf (accessed: 21.09.23).

Watson, M., Horrell, G., Doyle, M. (2016) *National Environmental Monitoring Standards (NEMS). Rating Curves. Construction of stage–discharge and velocity-index ratings.* Version 1.0. February. Tasman District Council. New Zealand.

Waylen, K. A., Holstead, K. L., Colley, K., Hopkins, J. (2017) Challenges to enabling and implementing Natural Flood Management in Scotland. *Journal of Flood Risk Management, CIWEM,* 11(**S2**): S1078 – S1089.

Webber, J., Gibbs, J., Hendry, S. (2004) *Phytophthora Disease of Alder*. Information Note. Edinburgh: Forestry Commission.

Welling, R. (2019) *Influence of large wood on sediment routing in a mixed bedrock-alluvial stream.* MSc. Geosciences. University of Montana, Minneapolis.

Welton, P., Quinn, P. (2011) *Runoff Attenuation Features. A guide for all those working in catchment management*. Environment Agency and Newcastle University. https://research.ncl.ac.uk/proactive/belford/papers/Runoff_Attenuation_Features_Handbook_final.pdf (accessed: 26.09.23).

Werner M. G. F. (2001) Impact of grid size in GIS based flood extent mapping using a 1D flow model. *Physic Chem Earth, Part B: Hydrology, Oceans and Atmosphere,* 26: 517–522.

Werritty, A. (2006) Sustainable Flood Management: oxymoron or new paradigm? *Royal Geographical Society*, 38(**1**): 16-23.

Wesselink, A., Warner J., Abu Syed M., Chan F., Duc Tran D., Haq H., Huthoff F., Le Thuy N., Pinter N., Van Staveren M. (2015) Trends in flood risk management in deltas around the world: are we going 'soft'. *Int. J. Water Gov.*, 3: 25– 46.

Wheater, H., Reynolds, B., Mcintyre, N., Marshall, M., Jackson, B., Solloway, I., Frogbrook, Z., Francis, O., Chell, J. (2008) *Impacts of upland land management on flood risk: Multi-scale modelling methodology and results from the Pontbren experiment*. Flood Risk Management Research Consortium (FRMRC) Research Report UR 16 (Issue December 2008), Manchester. http://nora.nerc.ac.uk/id/eprint/5890/1/ur16_impacts_upland_land_management_wp2_2_v1_0.pdf (accessed: 24.09.23).

Wheater, H.S. (2006) Flood hazard and management: a UK perspective. *Philosophical Transactions of the Royal Society A: Mathematical, Physical and Engineering Sciences*, 364(**1845**): 2135–2145.

Wilby, R. L., Beven, K. J., Reynard, N. S. (2008) Climate change and fluvial flood risk in the UK: more of the same? *Hydrological Processes,* 22: 2511-2523.

Wildman L. A., MacBroom J. G. (2005) The evolution of gravel bed channels after dam removal: Case study of the Anaconda and Union City Dam removals. *Geomorphology*, 71(**1-2**): 245-262.

Wilkinson, M. E., Addy, S., Quinn, P. F. Stutter, M. (2019) Natural flood management: small-scale progress and larger-scale challenges. *Scottish Geographical Journal*, 135(**1-2**): 23-32.

Wilkinson, M. E., Quinn, P. F., Welton, P. (2010) Runoff management during the September 2008 floods in the Belford catchment, Northumberland. *Journal of Flood Risk Management,* 3: 285–295.

Wingfield, T., Macdonald, N., Peters, K., Spees, J., Potter, K. (2019) Natural Flood Management: Beyond the evidence debate. *Area*, 1-9.

Winsemius, H. C., Aerts, J. C. J. H., Van Beek, L. P. H., Bierkens, M. F. P., Bouwman, A., Jongman, B., Kwadijk, J. C. J., Ligtvoet, W., Lucas, P. L., Van Vuuren, D. P., Ward, P. J. (2016) Global drivers of future river flood risk. *Nature Climate Change*, 6: 381-385.

Winterbottom, S. J. (1995) *An analysis of channel change on the Rivers Tay and Tummel, Scotland, using GIS and remote sensing techniques*. PhD Thesis. Department of Environmental Science, University of Stirling.

Wohl, E. (2007) Channel-Unit Hydraulics on a Pool-Riffle Channel. *Physical Geography*, 28(**3**): 233-248.

Wohl, E. (2011) Threshold-Induced Complex Behavior of Wood in Mountain Streams. *Geology,* 39: 587-590.

Wohl, E. (2014) A legacy of absence: Wood removal in US rivers. *Progress in Physical Geography: Earth and Environment,* 38(**5**).

Wohl, E. (2015) Legacy effects on sediments on river corridors. *Earth-Science Reviews*. 147: 30-53.

Wohl, E., Bledsoe, B. P., Fausch, K. D., Kramer, N., Bestgen, K. R., Gooseff, M. N. (2016) Management of Large Wood in Streams: An Overview and Proposed Framework for Hazard Evaluation. *Journal of the American Water Resources Association (JAWRA)* 52(**2**): 315-335.

Wohl, E., Scott, D. N. (2017) Wood and sediment storage and dynamics in river corridors*. Earth Surface Processes and Landforms*, 42(**1**): 5-23.

Woltemade, C. J., Potter, K. W. (1994) A watershed modelling analysis of fluvial geomorphologic influences on flood peak attenuation. *Water Resour. Res*., 30(**6**): 1933-1942.

Woolcock, M. (2012) Environment Agency, *Borehole record.* BGS ID: 18963004 http://scans.bgs.ac.uk/sobi_scans/boreholes/18963004/images/18962972.html (accessed: 02.03.23).

Wuang. R., Zeng, Y, Zha, W., Yang, F. (2022) Investigation of flow characteristics in open channel with leaky barriers. *Journal of Hydrology,* 613: A 128328.

Xing, Y., Zhao, D. L., Ma, D. G., Gan, W. D. (2018) *IOP Conf. Ser. Earth and Environ. Sci.,* Vol. **191** 012077. Three-dimensional modeling of flow characteristics and the influence of non-hydrostatic pressure in a 193° sharp open channel bend. *The 4th International Conference on Water Resource.* 17-21 July 2018. Kaohsiung City, Taiwan.

Xu, Y., Liu, X. (2017) Effects of Different In-Stream Structure Representations in Computational Fluid Dynamics Models – Taking Engineered Log Jams (ELJ) as an Example. *Water*, 9(**2**): 110.

Yang, C. T. (1971) Potential Energy and Stream Morphology. *Water Resources Research*, 7(**2**): 311-322.

Yang, C. T., Song, C. C. S., Michael, D., Woldenberg, J. (1981) Hydraulic geometry and minimum rate of energy dissipation. *Water Resources Research,* 17(**4**): 1014-1018.

Yang, L., Zhang, L., Dong, H., Alelaiwi, A., Saddick, E. (2015) Evaluating and Improving the Depth Accuracy of Kinect for Windows v2. *IEEE sensor Journal*, 15: 4275-4285.

Yang, S., Shi, B., Guo, Y. (2019) Investigation on scour scale of piggyback pipeline under wave conditions. *Ocean Engineering,* 182: 196-202.

Yao, Z., Xiao, J., Ta, W., Jia, X. (2013) Planform channel dynamics along the Ningxia–Inner Mongolia reaches of the Yellow River from 1958 to 2008: analysis using Landsat images and topographic maps. *Environmental Earth Science*, 70: 97–106.

Yarnell, D. L. (1934) *Bridge piers as channel obstructions.* Technical Bulletin164465, United States Department of Agriculture, Economic Research Service.

Zayed, Y. Loft, P. (2019) *Agriculture: historical statistics.* Briefing paper 3339 (House of Commons Library) 25 June. https://commonslibrary.parliament.uk/research-briefings/sn03339/ (accessed: 28.09.23)

Zhang, C., Zhang, Z. (2011) Calibration between depth and color sensors for commodity depth cameras. In *Proceedings of the 2011 IEEE International Conference on Multimedia and Expo, ICME 2011, 11-15 July 2011,* Barcelona: IEEE, 1-6.

Zhao, E., Shi, B., Qu, K., Dong, W., Zhang, J. (2018) Experimental and Numerical Investigation of Local Scour Around Submarine Piggyback Pipeline Under Steady Current. *Journal of Ocean University of China (Oceanic and Coastal Sea Research),* 17(**2**): 244-256.

Zimmerman, R. C., Goodlet, J. E., Comer, G. H. (1967) The influence of vegetation on channel form of small streams. *International Association of Scientific Hydrology,* 75: 255-275.

Zinger, J. A., Rhoads, B. L., Best, J. L. (2011) Extreme sediment pulses generated by bend cutoffs along a large meandering river. *Nature Geoscience*, 4(**10**): 675-678.

Appendix A: Table displaying flume experimentation, structure, descriptions, characteristics and results.

Structure designs	Description	Series	Runs	t (hrs)	Q (l/s)	Q (m³/s)	B (y-dir.) (mm)	Di_c (z-dir.) (mm)	$3Di_c$ (z-dir.) (mm)	Number of key	Rows x columns arrangement	h_t (mm)	G (mm)	Undisturbed channel W	Ap	Br	h (m)	U_0 (m/s)	R (m)	Re*	Average Fr	Max. exit dune height, centre line	Max. scour depth along centre line
1	Single-column vertical stack WDD design with G = 10 mm or G = $0.4Di_c$ and e = 0.	Series A 100% Q_{bf}	1	48	22	0.022	600	25	75	3	3 x 1	0, 35, 70	10	0.09	0.045	0.5	0.15	0.244	0.1	31.32	0.202	47..1	51.7
			2	84																		52.6	58
			3	96																		55.1	61
		Series B 80% Q_{bf}	1	96	18	0.018								0.078		0.58	0.13	0.222	0.09	29.83	0.204	49.8	22.4
			2	96																		49.7	37.3
			3	96																		41.9	40.1
2	Single-column vertical stack WDD design with G = 10 mm or G = $0.4Di_c$ and e = 35 mm or e = $1.4Di_c$.	Series A 100% Q_{bf}	1	96	22	0.022						50, 85, 120		0.09		0.5	0.15	0.244	0.1	31.32	0.202	49.8	47.2
			2	96																		52.5	54.2
		Series B 80% Q_{bf}	1	96	18	0.018								0.078		0.58	0.13	0.222	0.09	29.83	0.204	51.7	42.2
			2	96																		57.6	38.2
3	Single-column vertical stack WDD design with G = 20 mm or G = $0.8Di_c$ and e = 0.	Series A 100% Q_{bf}	1	96	22	0.022						0, 45, 90	20	0.09		0.5	0.15	0.244	0.1	31.32	0.202	42.8	49.1
																						34	47.1
		Series B 80% Q_{bf}	1	96	18	0.018								0.078		0.58	0.13	0.222	0.09	29.83	0.204	50.8	46
																						50.6	48.2
4	Single-column vertical stack WDD design with G = 20 mm or G = $0.8Di_c$ and e=15 mm or e = $0.6Di_c$.	Series A 100% Q_{bf}	1	96	22	0.022						15, 60, 105		0.09		0.5	0.15	0.244	0.1	31.32	0.202	47.7	47.1
		Series B 80% Q_{bf}	1	96	18	0.018								0.078		0.58	0.13	0.222	0.09	29.83	0.204	43.8	35.2

Appendix B: Hydraulic parameters from published literature compared to present flume experimentation.

Study / Date	Di_c (mm)	d_r (mm)	h (mm)	U_0 (m/s)	t_e (hrs)	B_r	Maximum scour depth (mm)	Horizontal or Vertical
Cherry and Beschta (1989)	12.7	40	-	0.110 – 0.280	7.5	-	-	Horizontal
Chiew (1991)	32 ÷ 63	33 ÷ 1.70	50 ÷ 180	-	> 24	-	98	Horizontal
Beebe (2000)	63	0.44 0.44 0.44	126 90 65	0.278 0.234 0.199	2.5	0.50 0.70 0.97	59 57 57	Horizontal
Gao et al. (2006)	32	0.38	400	0.255	4	0.16	18	Horizontal
Dey and Singh (2008)	40	1.86	200	0.497	12	0.2	56	Horizontal
Lee et al. (2018)	48	0.52	288	20 results	-	0.16	20 results	Horizontal
Penna et al. (2020b)	30	1.53	74	0.280	24	0.41	46 57 42	Horizontal
Present flume experimentation	75	1	150 130	0.244 0.222	80.5 71.5	0.50 0.56	16 results	Horizontal

Appendix C: Kinect resolution as the step size between one DN and the next when converted to mm (adapted from Mankoff and Russo, 2013). Flume experimentation Kinect distances displayed in red. The lower the Z_{bs} to the object the more Kinect resolution increases. There is a quadratic relationship between Z_{bs} and step size. Kinect has a minimum working distance of 0.8 m.
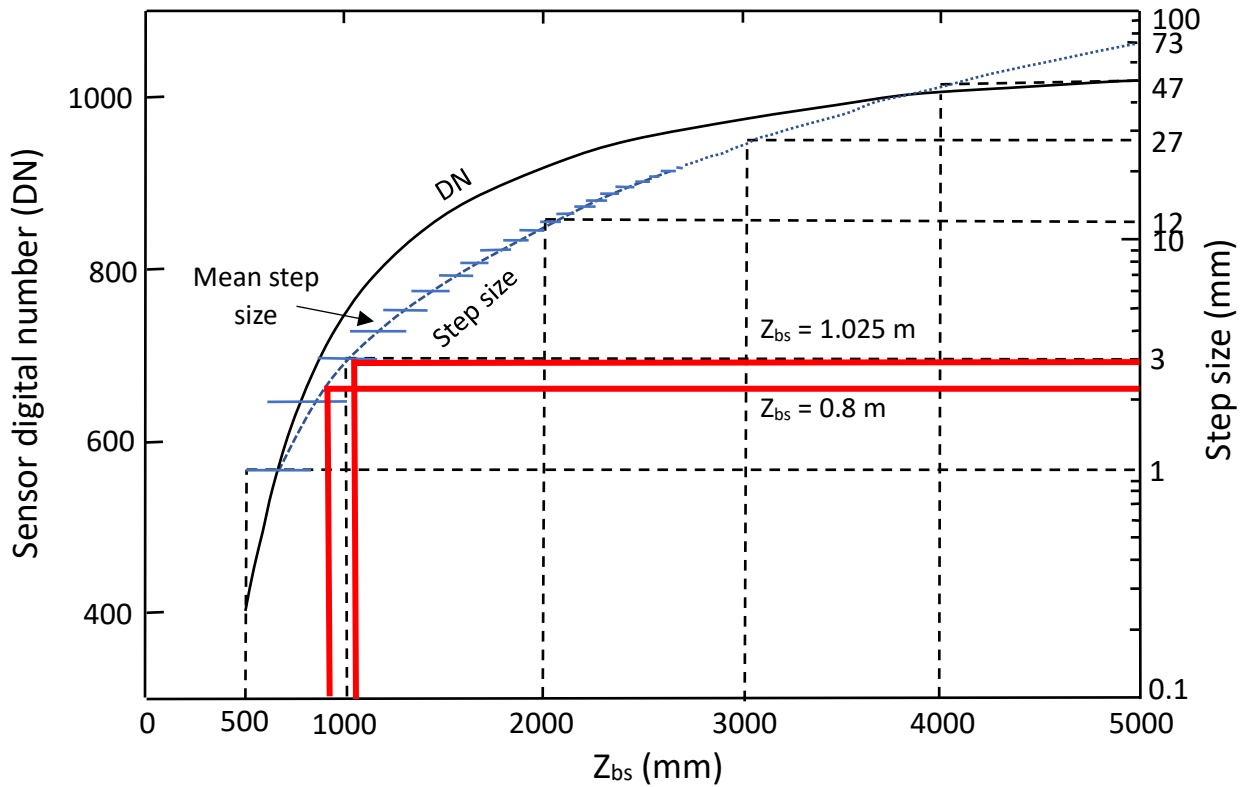
Appendix D: Kinect IR camera information including camera intrinsic parameters used in the present study. The larger the focal length, the narrower the view angle and the higher the magnification, increasing accuracy. Distortion coefficient is a means of quantifying radial and tangential distortions. All studies showed similar radial and tangential distortion values compared to the present study and therefore the redefined parameters were considered sufficiently accurate.

Present study: Imaging sensor	Camera name	Kinect v1.0 IR camera
	Type:	Aptina MT9M001 CMOS
	Model:	1414
	Resolution (Px)	640x480
	Pixel size (µm)	5.2
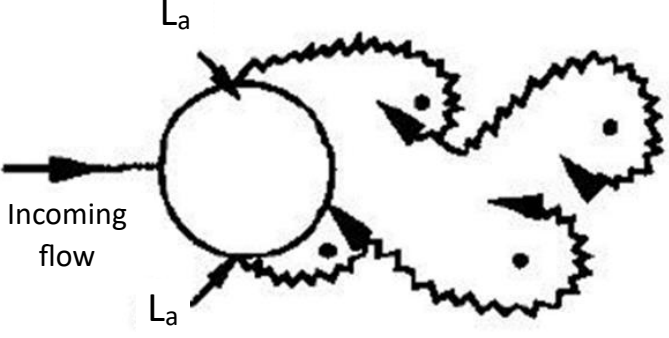
Studies:			Present study	Chu (2017)	Burrus (2011)	Herrera (2011)
			Value	Value	Value	Value
Interior parameters	Focal length	f_x (px)	587.78	589.32	595.99	586.80
		f_y (px)	585.73	589.85	592.44	577.70
	Principal point	c_x (px)	319.50	321.14	314.43	318.92
		c_y (px)	257.61	235.56	227.05	231.46
	Radial lens distortion coefficients	k_1	0.1314	0.1090	−0.1567	0
		k_2	-0.2389	-0.2398	0.6467	0
	Tangential lens distortion coefficients	p_1	0	-0.0020	0.0012	0
		p_2	0	-0.0029	0.0004	0

Appendix E: The Moody Diagram is widely used to determine the friction factor for fluid flow (adapted from Engineers Edge, 2023). The diagram combines the effects of Re_h and ε to determine the f. The relationship is non-linear and displays a complex interaction between viscous and boundary roughness effects. The Moody Diagram is based on the Colebrook-White Equation 3.15 (Gregory and McEnergy, 2017). Series A and series B points have been displayed on the diagram.
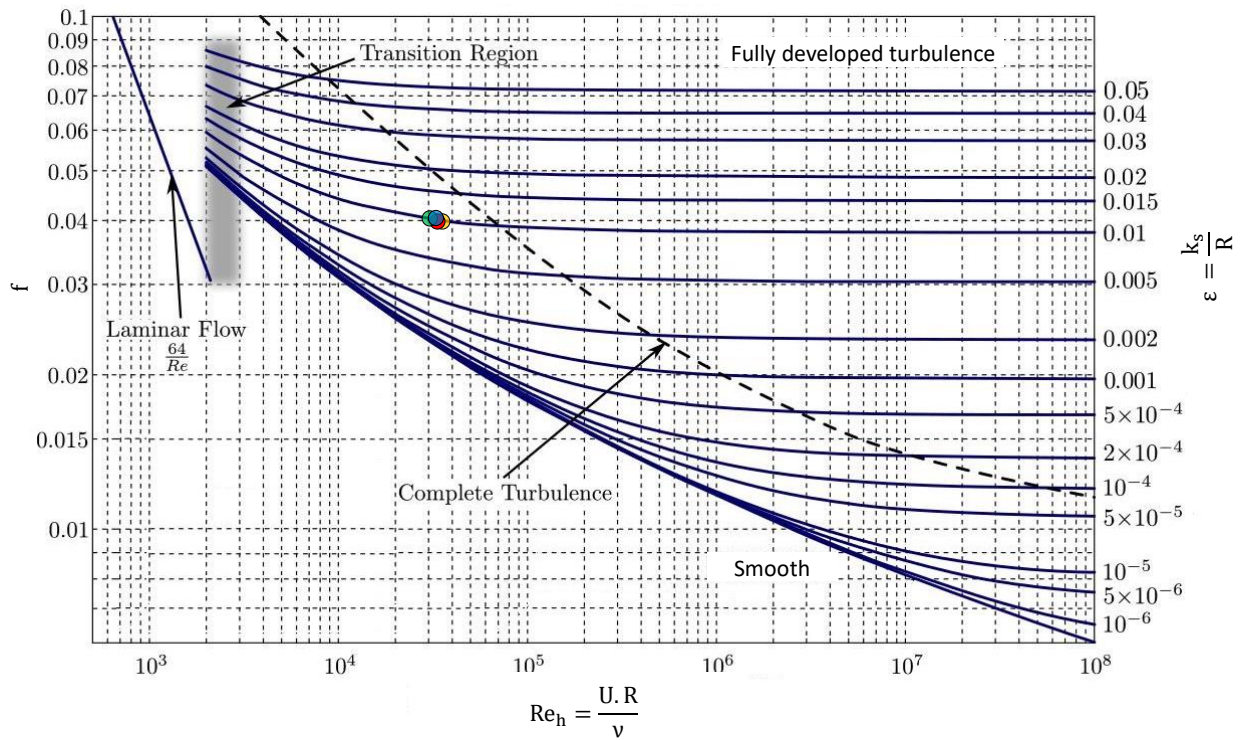
Legend		
	Series A	Series B
0.5 m upstream of the structure	🔴	🟢
0.5 m downstream of the structure	🟡	🔵

Appendix F: The schema shows streamlines depicting formation of vortices downstream of a horizontal key member at the relevant Re_c, with the boundary layer separation zone (L_a) displayed (adapted from Schlichting, 1979 and Sumer and Fredsøe, 2006). Information on series A and B flow regime and characteristics are given indicating vortex street instabilities.

Reynolds Number regime: Flow regime Flow form	Series A: $Re_c = 18300$ Series B: $Re_c = 16650$ Subcritical regime.
	Adapted from Sumer and Fredsøe (2006).
Flow characteristics Strouhal number Separation angle (θ_s)	Laminar with vortex street instabilities. $St = 0.21$ $\theta_s \approx 80°$
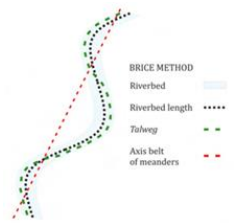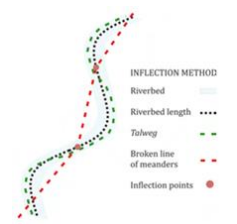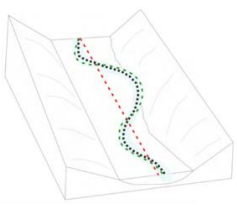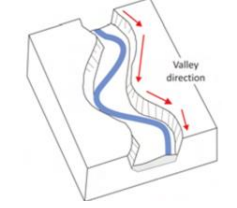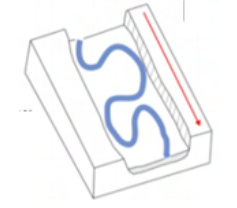
Appendix G: Literature synopsis giving details of similar investigations.

Author	Study description	Method	Findings
Lane, S. N., Chandler, J. H., Richards, K. S. (1994) Developments in Monitoring and Modelling Small-scale River Bed Topography. *Earth Surface Processes and Landforms,* 19: 349 368.	This study used a fluvial geomorphology technique combining analytical photogrammetry with rapid ground surveying for river channel topography, flow hydraulics and sediment transport.	Location: actively braiding proglacial stream approx. 300 m from the snout of the Haut Glacier d'Arolla, in the Pennine Alps, Valais, Switzerland. • Analytical photogrammetry: Measured the image coordinates on two photographs with known camera orientations and positions. Manipulated using terrain modelling packages. • Data acquisition from underwater zones: record of patterns of erosion and deposition made. A bed survey was undertaken when there was a problem with the photogrammetric approach taking under water views. • DTM using Intergraph InSitesInRoads developed for roadway modelling. This allowed for visualising and quantifying spatial distribution of erosion and deposition.	• Over 2 days the section of river channel started to shift towards the right bank resulting in trimming of the downstream end of a bar attached to the right bank. • A small amount of fill was also recorded along the left of the river channel within this time. • The lower overnight flow was also associated with the deposition of a new mid-channel bar.
Yao, Z., Xiao, J., Ta, W., Jia, X. (2013). Planform channel dynamics along the Ningxia–Inner Mongolia reaches of the Yellow River from 1958 to 2008: analysis using Landsat images and topographic maps.	Channel planform dynamics were analysed to determine changes in width, sinuosity, and shoreline migration rates between 1958 and 2008, based on topographic maps (1958 and 1967), derived from aerial photographs, a field survey	Location: Yellow River, China. • Two topographic maps, based on a field survey and combined with the interpretation of aerial photographs (1958 and 1967) were used to plot the channel planform. Maps were scanned and georeferencing in ArcGIS. • In ArcGIS, continuous polygons were created to represent the stream channel in	• Topographic maps and Landsat imagery showed the Ningxia–Inner Mongolia reaches of the Yellow River underwent changes in channel geometry between 1958 and 2008. • The channel length increased and deceased during various periods which led to changes in sinuosity.

Environ. Earth Science, 70 :97–106.	and satellite imagery (1977, 1990, 2000, and 2008).	• each year to create a georeferenced polygon coverage of the active channel. • Riverbank locations in each of the 6 years were compared using ArcGIS polygons, an erosion or accretion attribute was assigned to change in positions of the shorelines along the river banks over 2 years.	• The channel area expanded and contracted but showed a general shift towards the south.
Magliulo, P., Bozzi, F., Pignone, M. (2016) Assessing the planform changes of the Tammaro River (southern Italy) from 1870 to 1955 using a GIS-aided historical map analysis. *Environ. Earth Science,* 75:355.	Planform changes of the Tammaro River (1870 – 1955) by an ArcGIS analysis of historical maps.	• Historical topographic map sheets were scanned at a resolution of 800 dpi, saved as TIFF file and imported into the ArcGIS 9.3. • A mean error of ≈ ±5 m and ≈ ±8 m was calculated on 1:25,000 and 1:50,000 historical maps. • The length of the centrelines of 1870, 1909 and 1955 were calculated using ArcGIS and subdivided into 14 reaches. For each reach, the length was calculated using ArcGIS. • The Sinuosity Index (S_i) (Schumm 1963) was obtained by dividing the length of the channel by the length of the correspondent valley axis segment. The total length of the valley axis was calculated by adding the length of each segment. By calculating the ratio between the centreline length and the valley axis length, the sinuosity index of the whole hydraulic radius. Tammaro was obtained. Mean width was calculated following the method proposed by Surian et al. (2008) by dividing the active channel area by the centreline length (L_{cmax}). • Rainfall and discharge data was obtained. • A geomorphological field-survey was carried out to check, the validity of the data collected from the topographic map analysis.	• Between 1870 and 1955, a widening of the active channel occurred, which affected 9 of the 14 study reaches and the whole river, whose mean width increased. • Between 1870 and 1909, the whole river underwent a slight shortening but lengthened between 1909 and 1955. • Lengthening (1909 - 1955), only occurred in 8 reaches. • Variations in channel length were associated to variations in sinuosity. • Between 1909 and 1955, a marked increase in number of all types of fluvial bars occurred. • Subdivided reaches highlighted the morpho-evolutionary trend of the river was hetrogenous throughout the whole watercourse.

Appendix H: A matrix displaying sinuosity index methods with their advantages and disadvantages with schematics from Horacio (2014).

Method:	Description:	Advantage:	Disadvantage:	Schematic:
Total sinuosity method	This is a coefficient-based method to find the total channel sinuosity from beginning to end of the chosen channel section using a straight-line approach.	-	-	-
Brice method	The Brice method is defined as the ratio between the length of the riverbed and the length of the axis of meanders. This method is sometimes referred to as 'length of the central axis of meanders method'.	This method is the most universally accepted and can easily be adjusted between medium and small scales	-	
Inflection sinuosity method	This is method is similar to the Brice method except it is obtained by linking the inflection points on a series of meanders and is used as the denominator of Equation 5.7.	The Inflection point technique establishes the sinuosity of each individual meander.	As a catchment wide approach the inflection technique lacks precision as it tends to produce a lower result than the Brice method.	
Leopold and Wolman method	This method divides the thalweg length by the valley length.	This is a compensatory approach between the Brice method and the Inflection sinuosity method, in an attempt to enhance precision.	The Leopold and Wolman method gives the additional problem of determining the Thalweg.	
Hydraulic sinuosity (Muller) method	Formulated by dividing the length of the riverbed by the average length of the valley.	This method takes morphometric valley and meander direction change into account.	Hydraulic sinuosity method tends to give values higher than that of reality.	
Topographical sinuosity method	This is defined as the relation between the average length of the valley and the shortest distance between the beginning and end of the channel.	This method encapsulates meanders in enclosed valleys.	As meanders extend the value of the ratio loses reliability because the average valley length is the same as the straight line of the beginning and end of the riverbed.	

Appendix I: Displaying soil information regarding Wilderhope Brook catchment, data obtained from Cranfield Soil and Agrifood Institute: Soilscape (LandIS).

Soils:	Fertility:	Drainage:	Water profile:
Fine silty soil over shale: Fine silty soils with slowly permeable subsoils and slight seasonal waterlogging, associated with well drained fine loamy calcareous soils over limestone and well drained fine silty soils over siltstone.	Moderate to high	Slightly impeded drainage	Farmed land is drained and therefore vulnerable to pollution runoff and rapid through-flow to streams; surface capping can trigger erosion of fine sediment
Reddish fine and coarse loamy soil: Slowly permeable seasonally waterlogged reddish fine and coarse loamy soils and similar soils with slight seasonal waterlogging. Some deep coarse loamy soils seasonally affected by groundwater.	Moderate	Impeded drainage	Main risks are associated with overland flow from compacted or poached fields. Organic slurry, dirty water, fertiliser, pathogens and fine sediment can all move in suspension or solution with overland flow or drain water
Stoneless fine silty to clayey soil over shale: Slowly permeable seasonally waterlogged often stoneless fine silty or fine silty over clayey soils on rock. Some silty soils, with slowly permeable subsoil and slight seasonal waterlogging.	Low	"	"
Fine silty and loamy soil: Well drained coarse silty soils over limestone. Occasional similar but fine silty and coarse loamy soils.	"	Freely draining	Groundwater contamination with nitrate; siltation and nutrient enrichment of streams from soil erosion on certain of these soils
Coarse silty loam soil: Deep stoneless permeable reddish fine silty soils. Similar coarse silty soils locally. Associated with fine silty soils variably affected by groundwater.	Moderate to high	"	Groundwater tables are shallow and therefore vulnerable to leached pollutants such as nitrate and pesticides. Flooding of cultivated fields can scour topsoil and increased silt in the river

Appendix J: Comparing RAB, OTT HydroMet and Hydro International proposals.

RAB	OTT	Hydro International
No map given	Map displaying locations of equipment monitoring sites.	Map displaying locations of equipment monitoring sites.
Proposals: • Monitoring to support the upstream and downstream stream depth monitoring at three WDD sites. • Discharge monitoring in the lower course. • Rainfall monitoring at the catchment boundary. • Real-time monitoring of flow depth at a selected number of gauge locations providing support for stakeholder and community/landowner engagement • Use of RiverTrack devices which are easily installed, adaptable and can be moved if the monitoring strategy changes – no civils work required • Lasting legacy with the community by providing community flood alerting and community ownership of long-term stream monitoring at several locations	Proposals: • Pressure level sensors were installed to monitor flow depth upstream and downstream of 3 chosen WDDs in the upper, middle and lower catchments. • Lambrecht 4cm^3 tipping bucket rain gauge to be installed at Stanway Farm. • A Hach FL900 logger and AV9000 velocity flow sensor to be set up at a chosen location. OTT technicians to download data manually and results sent to funders.	Proposals: • Monitoring of Wilderhope Brook for velocity and water depth at the outflow. • h will be measured in upper, middle and lower course of Wilderhope brook. • Option of monitoring Wilderhope's river continuity in the upper course, by placing depth sensors before and after a WDD.

Equipment:
• Rivertrack velocity sensor deployed on Wilderhope Brook lower course.
• Two stream level monitors in lower course of Wilderhope, placed either side of the WDD.
• Two stream level monitors in middle course of Wilderhope, placed either side of the WDD.
• Two stream level monitors in upper course of Wilderhope, placed either side of the WDD.
	Equipment:
	• 2x Orpheus Mini pressure level sensors with a working depth of 0-4 m. Readings were taken every 15 mins. Pressure level sensors installed in an MDPE stilling tube positioned upstream and downstream of 3 WDDs. This included:
	  • Two stream level monitors in lower course of Wilderhope, placed either side of the WDD.
	  • Two stream level monitors in middle course of Wilderhope,
		Equipment:
		• Nivus PCM4 velocity sensor deployed on Wilderhope on lower course.
		• 3 options of deploying a data logger in lower course of Wilderhope, either side of the WDD.
		• 3 options of deploying a data logger in middle course of Wilderhope, either side of the WDD.
		• 2 options of deploying a data logger in upper course of Wilderhope, down of the WDD.

• 5" storage rain gauge placed at Stanway Farm.	placed either side of the WDD. • Two stream level monitors in upper course of Wilderhope, placed either side of the WDD. • Hach FL900 Flow Logger supporting an AV9000 Area Velocity Sensor.	• 1 option of deploying a data logger in upper course of Wilderhope, either side of the WDD. • 2 options of deploying a data logger in upper course of Wilderhope, up of the WDD.
Equipment analysis / differences: • The Rivertrack systems equipment is used for velocity and stream depth; weather proof ultra-sonic flow sensor (accuracy: ±2 mm), offering a continual display of flow depth using WiFi, allowing live level data to be uploaded remotely via the RiverTrack Communities web portal. • Casella rain gauge can be used as part of an automated system with the necessary interface. RAB also propose a 5" manual storage rain gauge to be used as a quality assurance to check the Casella rain gauge.	Equipment analysis / differences: • Lambrecht 4cm^3 tipping bucket rain gauge supporting a Hobo pendant event logger (precision: 0.2 mm; measuring range: 0-16 mm/min).	Equipment analysis / differences: • Nivus PCM4 velocity sensor (accuracy: ±2 mm) temporarily measure flow velocity from depths as low as 3cm up to several meters. The Nivus PCM4 is a combi-sensor which will simultaneously detect flow velocity and depth. This velocity sensor has a pre-configured rechargeable lead gel battery, so no need to replace batteries. Device is read using its USB interface for connecting to PC, HSLI will regularly travel to site to download data when required. • The ME77X are piezoresistive ceramic sensors used for measuring flow pressure (accuracy: ± 1% FS), though accuracy is not as high as the Orpheus mini water level logger provided by OTT. • SDI-12, submersible transmitter works with depths > 0.5 m. The transmitter (accuracy: 0.1% FS) may not be appropriate for measuring shallow depths.
Equipment maintained by contractors	Equipment maintained by contractors	Equipment maintained by contractors

Appendix K: Photographs displaying woody debris dam maintenance and anthropogenically induced valley / channel bank change.

Appendix L: Lambrecht 4cm^3 tipping bucket rain gauge supporting a Hobo pendant event logger installed at Stanway Farm to the Northwest of Wilderhope Brook catchment.

Appendix M: A sample woody debris dam recording form, with woody debris dam 23 displayed. These recording forms were used to categorise all 105 woody debris dams along Wilderhope Brook longitudinal profile.

Lg. Wood (d≥20cm) ✓   Med. Wood (10≥d>20cm) ✓   Sm. Wood (d<10 cm) ✓

No. stems present   1   4   100

Principal species used? *circle* (Alder) Hazel   Hawthorn   Blackthorn   Ash   Oak   Other

Vertical gap below WDB, LHS: ___0cm___   Vertical gap below on WDB, RHS: __40cm__
Note: LHS and RHS denote side of channel when looking downstream
     30cm deep pool upstream, possible scour underneath.
Maximum vertical gap below WDB: ___40cm___

Maximum WDB height above channel bed: ___1.3m___

Approximate avg. solid volume fraction (SVF) of downstream terminus cross-section: _____
                                        medium dense brush

Approx. SVF of upstream terminus: _____   Approx. SVF of plan view: _____

Approx. maximum cross-sectional avg. SVF: _____   Location within jam: _____

Approx. top channel width: __3.8m__   Approx. bottom channel width: __2.75m__

Approx. maximum longitudinal length of WDB: __1.5m__

Distance to nearest upstream jam: _____   To nearest downstream jam: __6m__

Does backwater reach end of previous upstream WDB? *circle*   Y   (N)
Does next WDB backwater reach end of this WDB?   Y   (N)
Berm / bank barrier created to reduce overflow erosion?   Y   (N)
     If yes *circle type*   brash   large timber

Principle timbers pinned? (Y)   N   Stakes and wire at bank (Y)   N
Backfilled with brash?   (Y)   N

Describe anchoring method of key members:
     Steaked on LHS.
     Pinned to tree growing in river.

Describe type of key member/prinicipal construction method (ex. Large tree, crissy-crossy, flat boards):
     medium wood backfilled, natural accumulation.

Note: complete WDB spans channel but no apparent sediment effects; active WDB affects sediment transport
WDB classification: partial   complete   (active)

Is an upstream backwater present? (Y)   N   Is a downstream plunge pool present? (Y)   N
     If yes: Diagram/dimensions of backwater and depth of fine particle deposits:
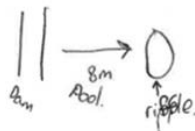
Diagram/dimensions of plunge pool/gravel deposition and comment on sediment transport:
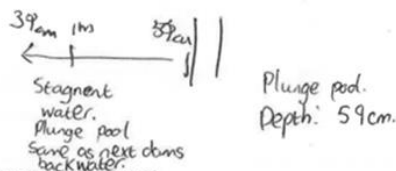
Comment on apparent land use surrounding channel:
     Grassy, Grazing land.

Comment on channel characteristics:
     Incised valley, with grass on inside bank.

Appendix N: Literature synopsis giving details of similar investigations.

Journal:	Model type and state:	Approach used to predict WDD hydraulic and hydrological models.	Model validation / calibration.	Aim and findings.
Bair, R. T., Segura, C., Lorion, C. M. (2019) Quantifying restoration success of wood introductions to increase Coho Salmon winter habitat. Earth Surface Dynamics. 73(**3**): 841-857.	Nays2DH Unsteady simulations Simulates: 3 alluvial stream reaches in Mill Creek, a tributary of the Siletz River in the Oregon Coast Range. Site 1 is in the main stem of Mill Creek, Site 2 is located in Cerine Creek, Site 3 is located in South Fork. Details of Large Wood (LW): Channel spanning. Engineered dams. Catchment area: 5 km^2 Blockage: unknown Width: 10 m Length:123 m	Geometry adjustment.	Validation: None given. Calibration: field calibrated.	Aim: To model the hydraulic effects of the introduction of LW on components of fish habitat in three gravel-bed streams. Findings: To quantify how the addition of LW potentially changes stream hydraulics to provide a net benefit to juvenile salmonid habitat. Post-LW distributions of shear stress and velocity indicated increased hydraulic and habitat heterogeneity associated with habitat suitability for salmonids. Model predictions: reach average Q_{bf} values of shear stress before the LW additions Site 1: 23.41 Nm^{-2}, Site 2: 12.24 Nm^{-2}, Site 3: 22.27 Nm^{-2} [18%-49% reductions in shear stress after LW].

Metcalfe, P., Beven, K., Hankin, B., Lamb, R. (2017) A modelling framework for evaluation of the hydrological impacts of nature-based approaches to flood risk management, with application to in-channel interventions across a 29-km² scale catchment in the United Kingdom. *Hydrological Processes*, 31(**9**): 1734–1748.	Dynamic TOPMODEL Simulates: The Brompton catchment in the Swale, Ure Nidd and Upper Ouse WFD management catchment, N. Yorkshire, U.K., part of the River Humber Basin District. Details of WDD: varied. Blockage: unknown. Catchment area: 29.3 km². Width: 2 m. Length: 35 reaches identified with a median length of 674 m.	Hydraulic Structure Representation.	Calibration: Rainfall data from the Leeming AWS used showing similar times and quantities. $\approx$ 5000 realisations with parameters selected at random from the ranges given in the double peaked storm, applying a performance metric.	Aim: To evaluate the impact on storm runoff response of a small, intensively cultivated catchment to emplacement of various configurations of in-channel features. 2 storms: 1st storm, peak Q: 19.2 m³/s and 2nd storm 2 months later. Findings: Much of the attenuation due to the lower barriers, mainly through their effect of reconnecting the floodplain with the channel +diverting overbanked flow through the rougher riparian area. Double-peaked storm event – aggregated storage can be retained but storage is unused or overloaded. Storage can become saturated in intermediate events and unable to recover quickly enough for later storms.
Pinto, C., Ing, R., Browning, B., Delboni, V., Wilson, H., Martyn, D., Harvey, G. L. (2019) Hydromorphological, hydraulic and ecological effects of restored wood: Findings and reflections from an academic partnership approach. *Water and*	Flood Modeller Steady simulations Details of WDD: partial engineered dams. Catchment: Located in S.E. England. 4 sites in the River Loddon catchment: 3 sites on River Blackwater and 1 site on the River Whitewater.	Roughness adjustment + Hydraulic structure representation. (manipulates Manning's n at cross-sections with large wood and blockage ratios using length of large	Calibration: Manual adjustment of roughness values and comparison of predicted and measured water values. Cross-sections given Manning's n of: without wood: 0.05-0.2 $s/m^{\frac{1}{3}}$, bare logs: 0.04 $s/m^{\frac{1}{3}}$, thick foliage: 0.15 $s/m^{\frac{1}{3}}$.	Aim: 1) Characterise the physical structure of restored LW. 2) Quantify the effects of LWs on hydromorphology and mesohabitats. 3) Assess benthic invertebrate diversity. 4) Assess extent to which the method used to represent LWs influences 1D hydrodynamic modelling. Results:

Environment Journal, 33: 353–365.	Blockage: 37.7 – 74.1% of channel blocked. Width: ≈ 8 m. Length: 700 m.	wood relative to channel width).		1) Complex dams most effective at providing channel and habitat recovery. 2) More emergent and submerged macrophytes in restored wood reaches than natural wood reaches. 3) Lack of consistency between habitat heterogeneity and biodiversity in restored systems and naturally occurring LWs. 4) Blockage ratio / Manning's n roughness approaches to represent LW features generated similar stage profiles. However, both displayed issues predicting spatial stage values.
Rasche, D., Reinhardt-Imjela, C., Schulte, A., Wenzel, R. (2019) Hydrodynamic simulation of the effects of in-channel large woody debris on the flood hydrographs of a low mountain range creek, Ore Mountains, Germany. *Hydrology and Earth System Sciences Discussions*, 1–24.	HYDRO_AS-2D Unsteady simulations Simulates: long reach of the Ullersdorfer Teichbächel, a creek in the Ore Mountains (S.E. Germany), a small first order headwater creek. Details of LW: Channel-spanning. Engineered WDDs. Catchment area: 1.8 km^2. Blockage: unknown. Width: 0.8-0.3 m.	Roughness adjustment	Validation: Discharge time series comparison from field experiments of the model outputs with field observations with and without stable Large Wood. Good fit between the observed flood hydrographs of field small flood events and the model results without and with stable in-channel LW. Nash–Sutcliffe efficiency (NSE): 0.9, ratio of the RMSE to the standard deviation of observed values (RSR): 0.32, Percent bias (PBIAS): −7.7%.	Aim: to simulate the physical effects of stable in-channel LW elements on flood hydrographs in a creek reach in low mountain ranges using a 2D hydrodynamic model and previously conducted field experiments. Results: The two-dimensional hydrodynamic model closely mimics the flow conditions of the field experiments without LW (variant RV), especially the rising limb and the flood peak are accurately represented, and minor deviations can be observed along the hydrograph's falling limb only due to the broader shape of the simulated hydrograph.

	Length: 282 m.		Calibration: A good model calibration was achieved for baseline, no LW conditions: NSE: 0.99, RSR: 0.11, PBIAS: −3.5%	The LW affects flow upstream and downstream in an area that is larger than the wood piece. The effect of stable in-channel LW was simulated using roughness coefficients.
Xu, Y., Liu, X. (2017) Effects of different in-stream structure representations in computational fluid dynamics models— Taking engineered log jams (ELJ) as an example. *Water,* 9(**2**): 110.	OpenFOAM Mesh generation tool snappyHexMesh in OpenFOAM was used to generate the body-fitted mesh for Engineered WDD. Steady flow Blockage: unknown. Details of WDD: bank attached (partial jam). Engineered WDD. Fully resolved WDD in 3D. Catchment area: unknown. Width: 40.5 m. Length: unknown.	Explicit 3D representation + Porosity model.	The computational model was validated with experimental data in a flume where a scaled model of E. WDD was placed. Velocity and turbulent kinetic energy predictions visually matched experimental observations conducted in a flume (Bennett et al., 2015). Observations for calibration or validation: *Visual comparison of velocity and turbulent KE.* Calibration: None given.	Evaluated the effects of geometric simplification of an example in-stream structure, an Engineered Log Jam (ELJ), in computational models. 3 different representations: full resolution, porous media model and solid barrier model. The 3 models were compared and analysed on various aspects related to the stability and functionalities of the structures. The porous media model and solid barrier model, which are computationally economic, can describe the flow dynamics only to some extent. Results also show the flow passing through the porous in-stream structure has a significant impact on mean velocity, turbulence, KE, carrying capacity and integral wake length.

Appendix O: Map displaying United Kingdom spatial rainfall intensities from 10-12 June 2019. Wilderhope catchment received a total rainfall of ≈ 75-100 mm of rainfall over the 3 days (Met Office, 2019).
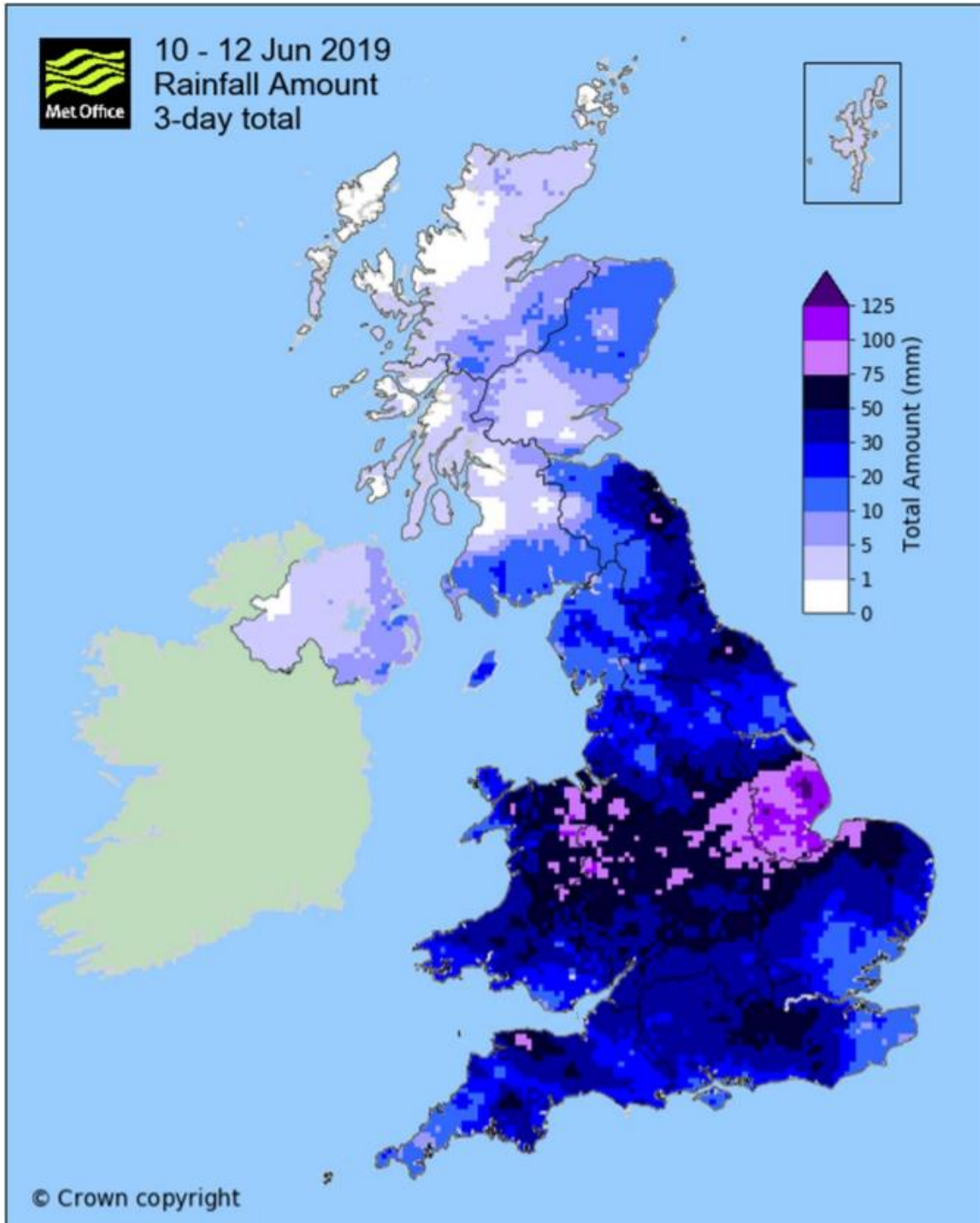
Appendix P: Map displaying United Kingdom spatial rainfall intensities from 15-16 Feb 2020. Wilderhope catchment received a total rainfall of ≈ 50-75 mm of rainfall over the 3 days (Met Office, 2019).
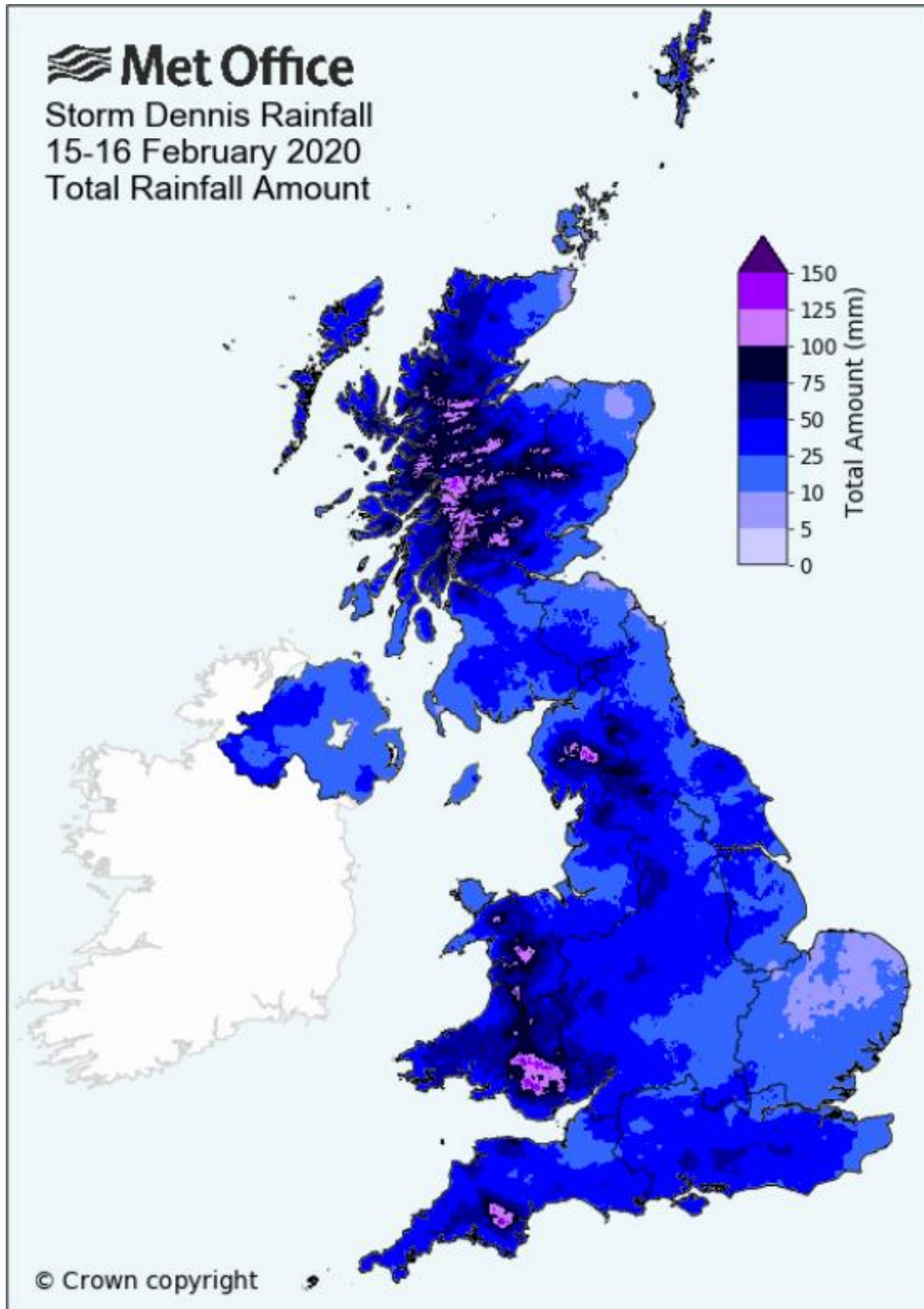
Appendix Q: Upstream and downstream cross-sectional conveyance.
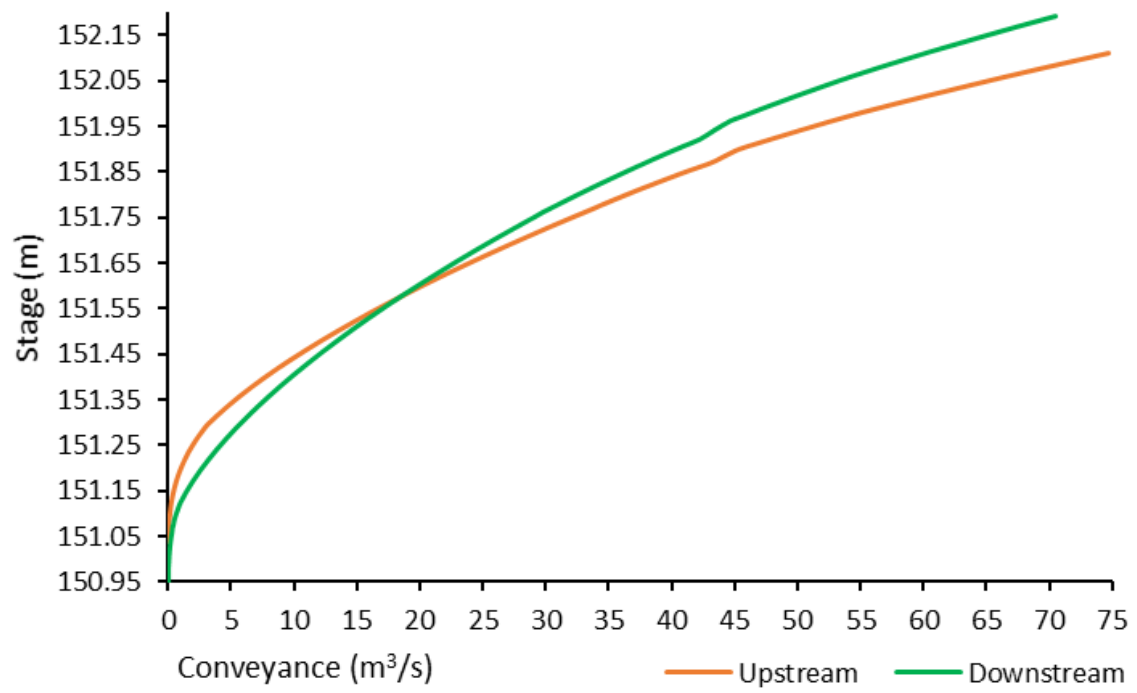
Appendix R: Lower reach, cross-sectional conveyance with 'Wilderhope_1' located at the B4368 bridge and 'Wilderhope_17' located at the Wilderhope Brook lower reach ford. Cross-sections are spaced at regular 12.5 m distances.
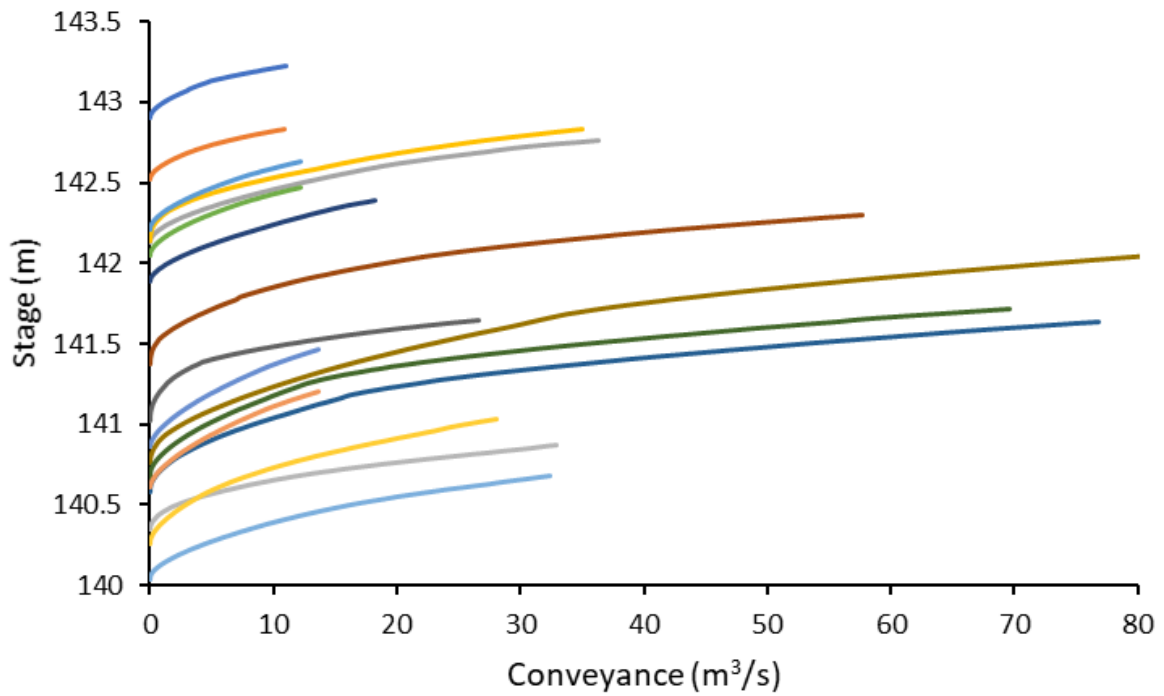
Appendix S: A comparison between flood reduction (%) at different United Kingdom sites.

Studies	Catchment	WDD number (W_n)	Return period (years)	Percentage of reduced flow
Present study	Shropshire, Wilderhope Brook	105	100	Excluding floodplain attenuation. Confined: B_A = 0.356%, Unconfined: B_A = 0.067% (summer storm event) and Confined: B_A = 0.304%, Unconfined B_A = 0.049% (winter storm event). Including floodplain attenuation. Unconfined: $B_A + B_p$ = 11.855% (summer storm event) and Unconfined: $B_A + B_p$ = 58.061% (winter storm event).
Nisbet et al. (2017)	North Yorkshire, Pickering Beck	167 + 187 heather bale dams	-	15-20% with around half of the reduction associated with upstream land management interventions and half associated with flood storage bund.
Nicholson et al. (2015)	Northumberland, Belford Burn	14	15	> 30%, this includes use of network of attenuation features (35 RAFs including storage ponds).
Odoni and Lane (2010b)	North Yorkshire, Pickering Beck	100	100	7.5%

Appendix T: Long term time-lapse photography documenting woody debris dam evolution and dam change. Two photograph datasets taken in both August (2019) and February (2020). Woody debris dam categorisation displays dam design using Gregory et al. (1985) definitions along with vertical spacing between two key members or aperture size.

Partial WDD 14
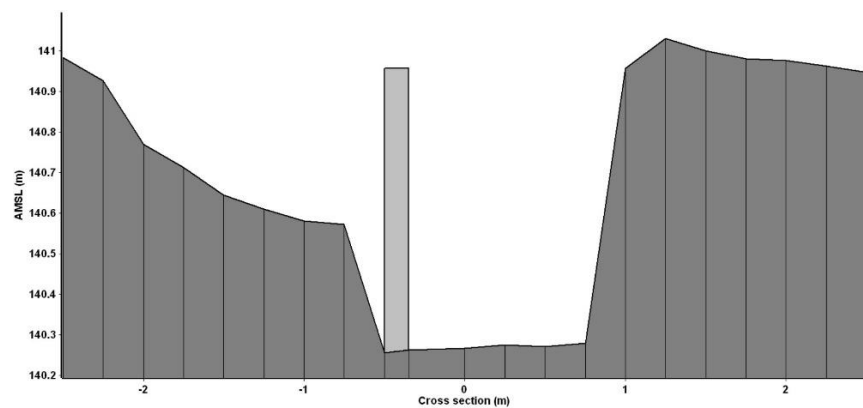
Summer (August 2019)   Winter (February 2020)
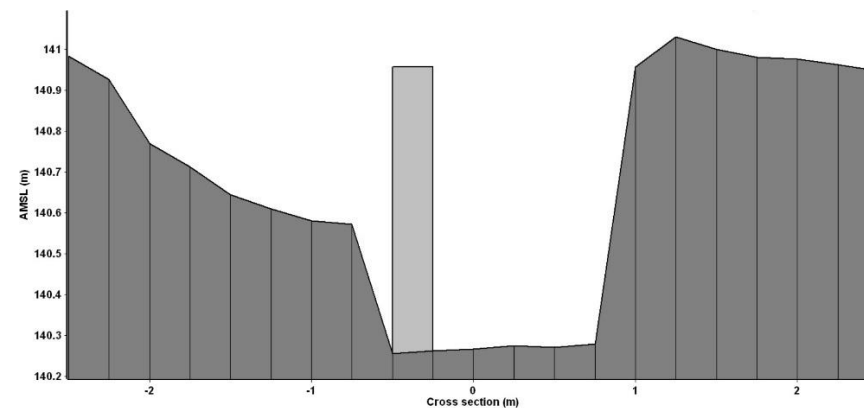
Active WDD 15

Summer (August 2019)   Winter (February 2020)
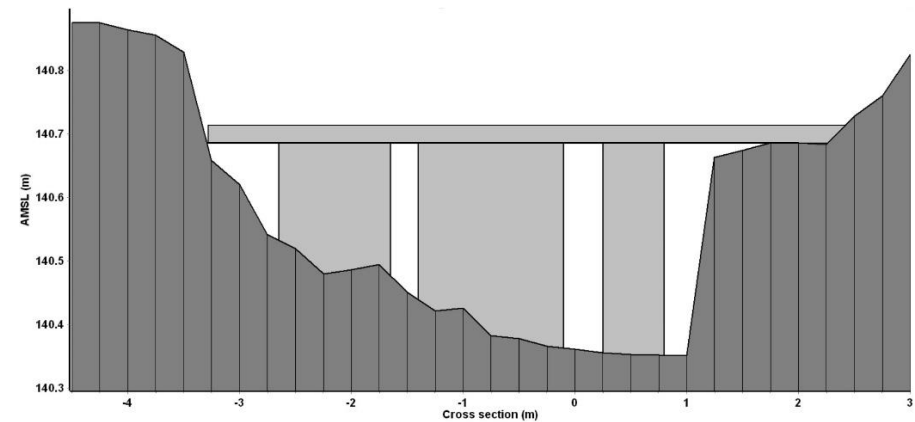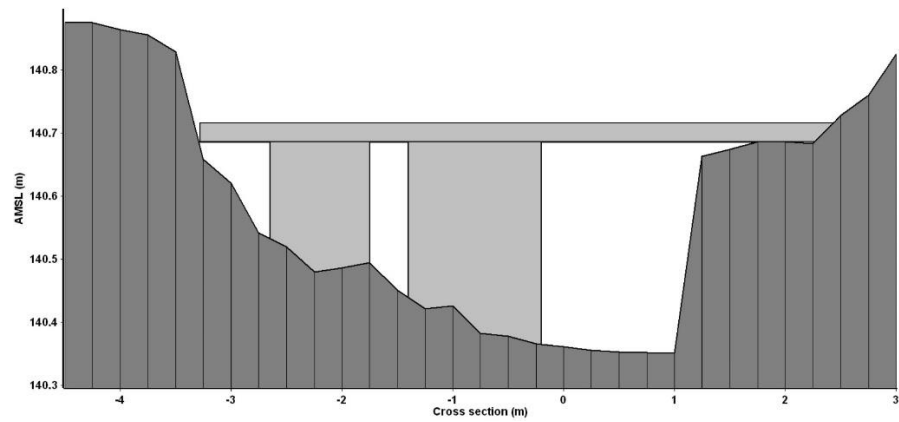
Active WDD 16
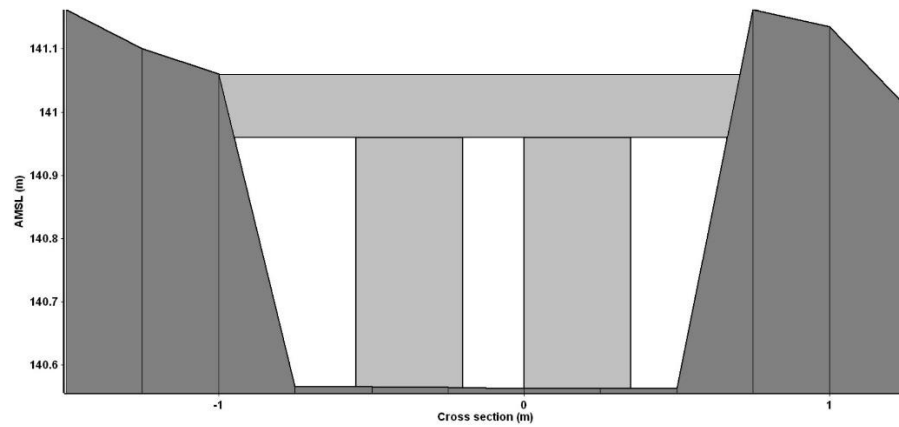
Summer (August 2019)   Winter (February 2020)

Active WDD 17

Summer (August 2019)   Winter (February 2020)
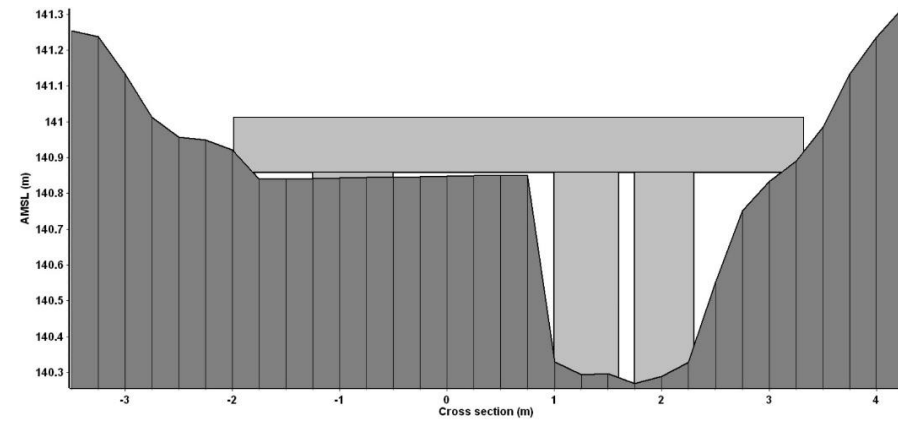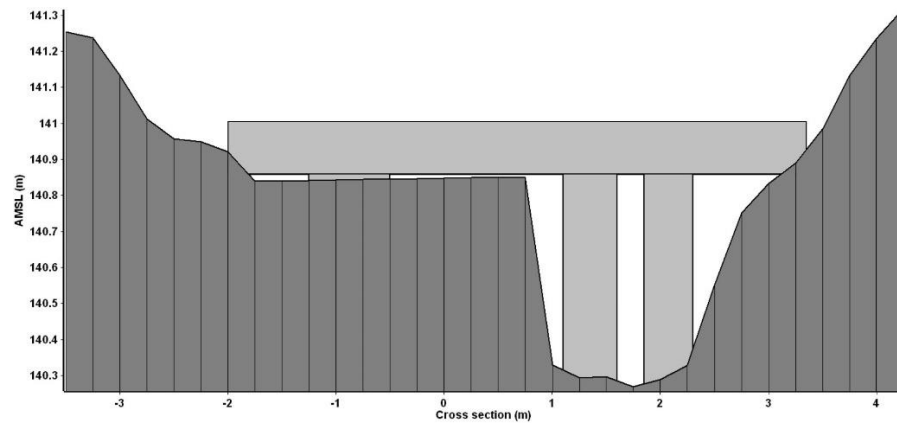
Partial WDD 18

Summer (August 2019)   Winter (February 2020)
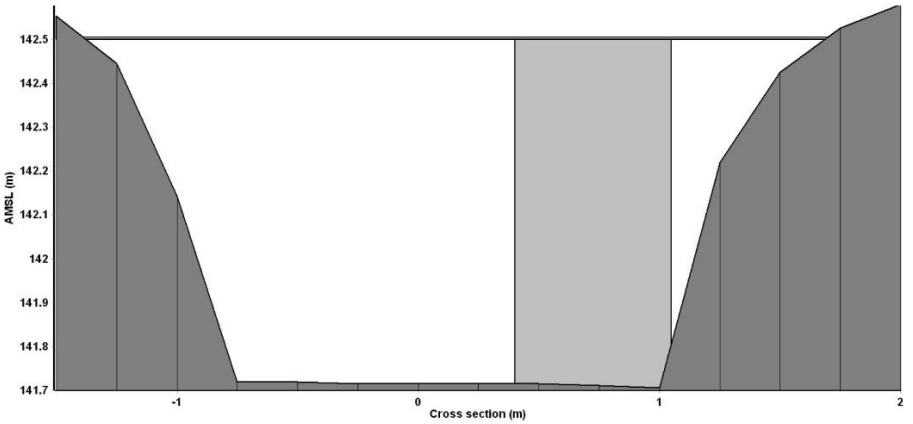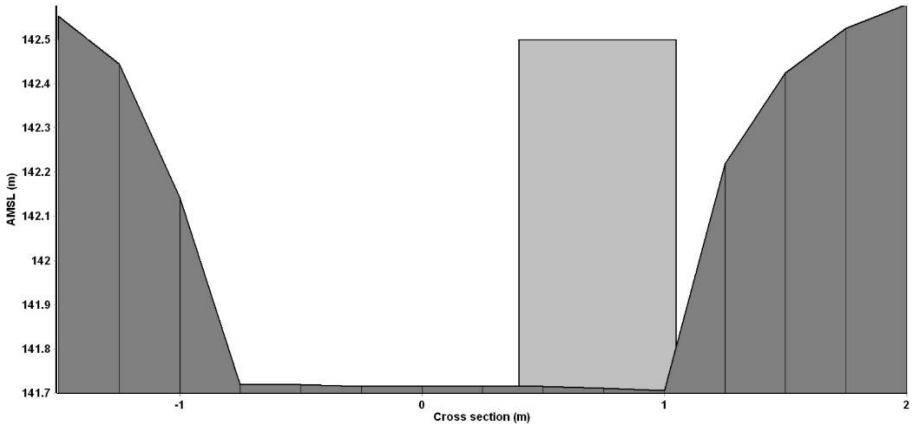
Same blockage area applied to both summer and winter storm events due to single key member blocking right side of the channel.
Diagram facing down stream narrow 0.001 m bridge soffit to deck applied to winter to create little surcharge resistance but not to the summer.

Appendix U: Cross-section, bank overtopping displaying both summer and winter storm events.

Constructed cross-sections have same axis scale so comparison can be made. Discharge above 0 m³/s displays bank overtopping while discharge below 0 m³/s displays flow re-entering into the channel.

Cross-section 1: Located at the B4368 bridge.
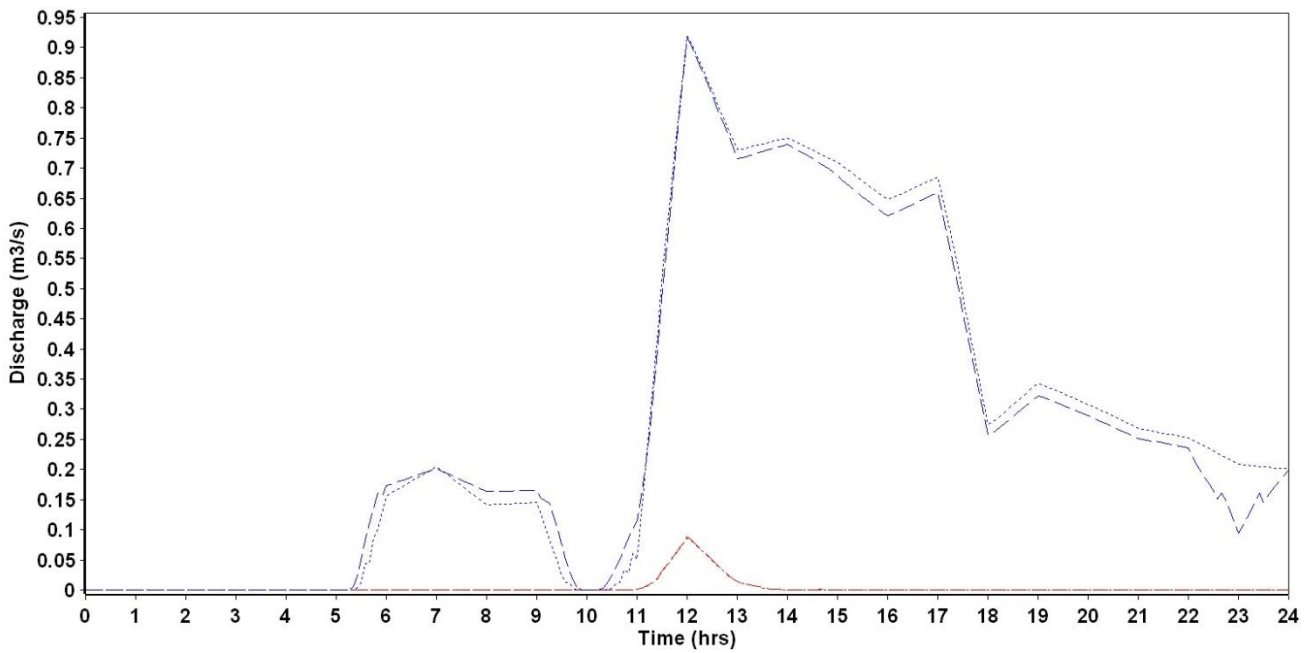
Cross-section 2:
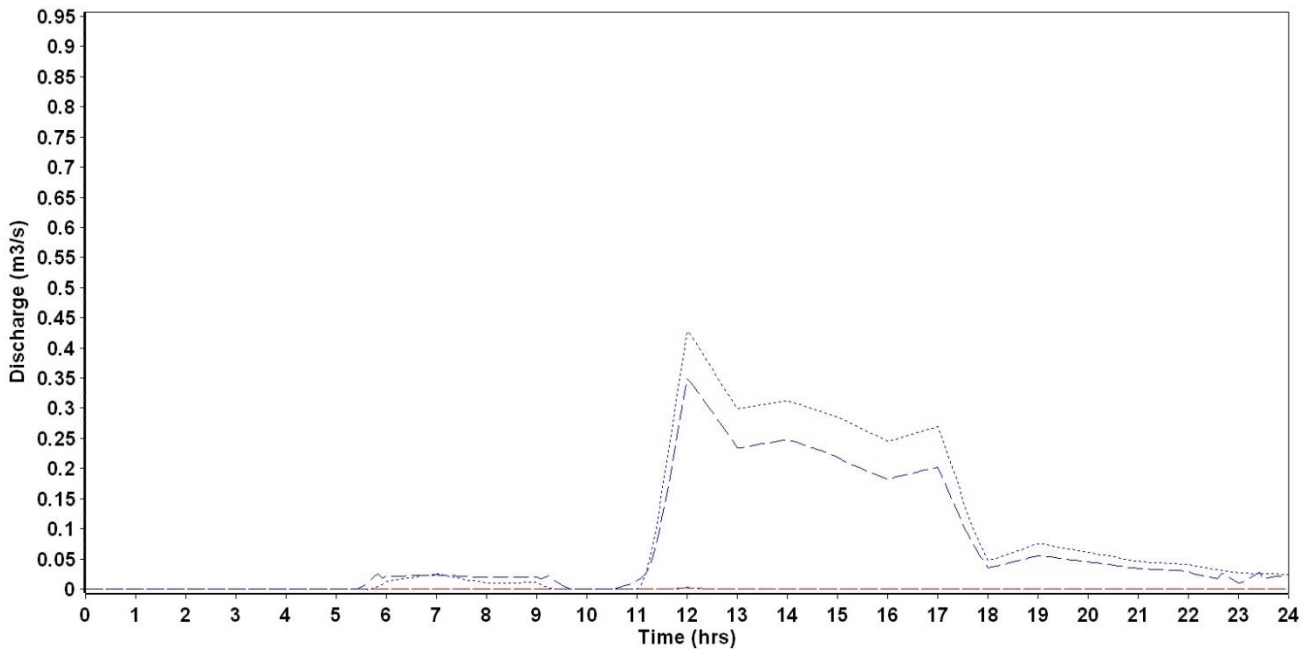
Summer	Winter
Obstructed channel	Obstructed channel
Unobstructed channel	Unobstructed channel

Cross-section 3:
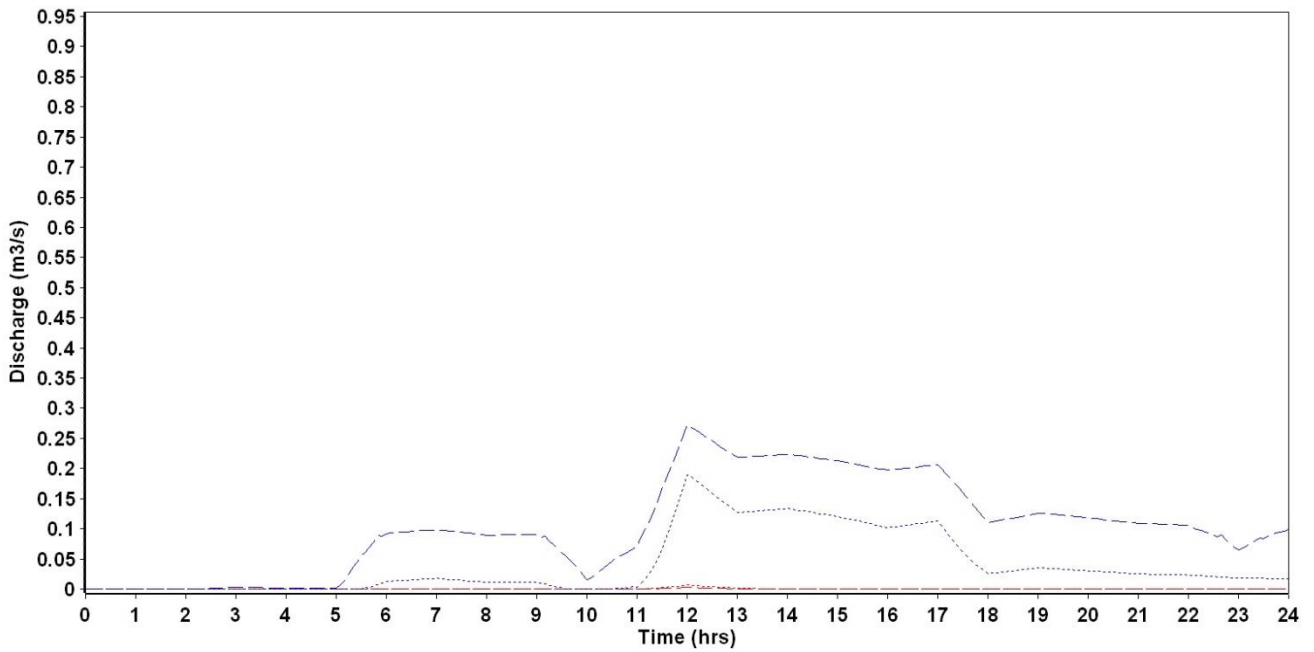
Cross-section 4: WDD 18 located at this cross-section.
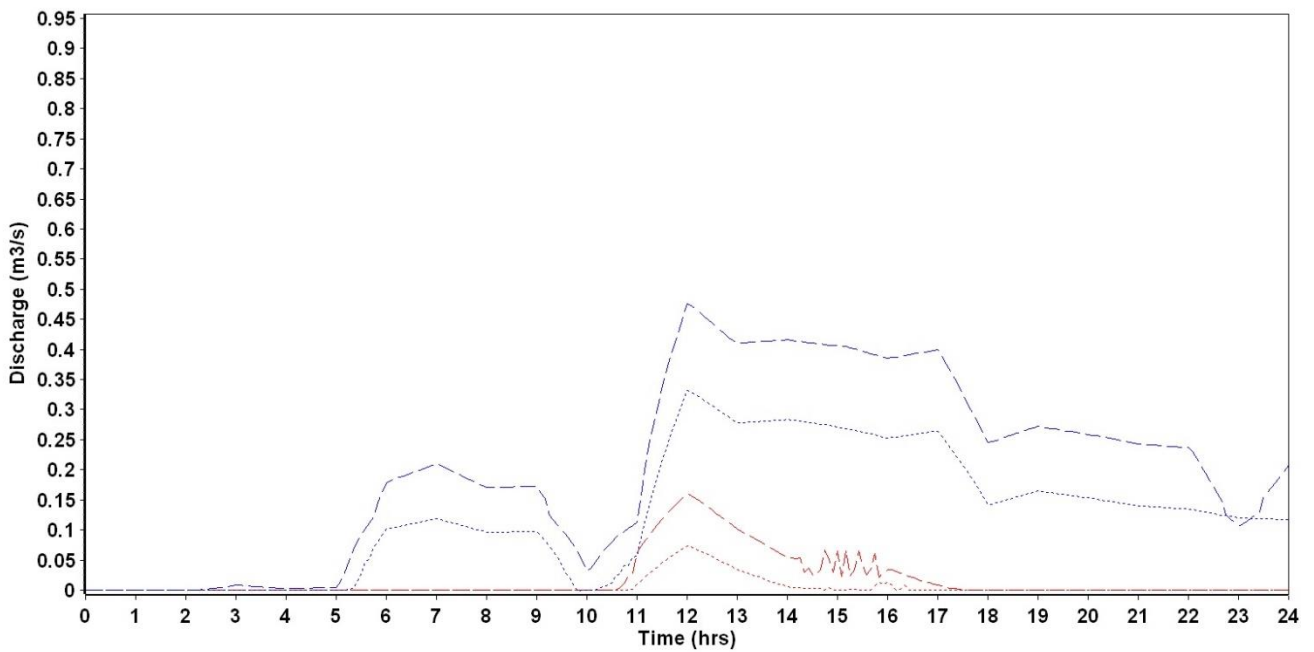
Summer		Winter	
- - - Obstructed channel		- - - Obstructed channel	
·········· Unobstructed channel		·········· Unobstructed channel	

Cross-section 5:
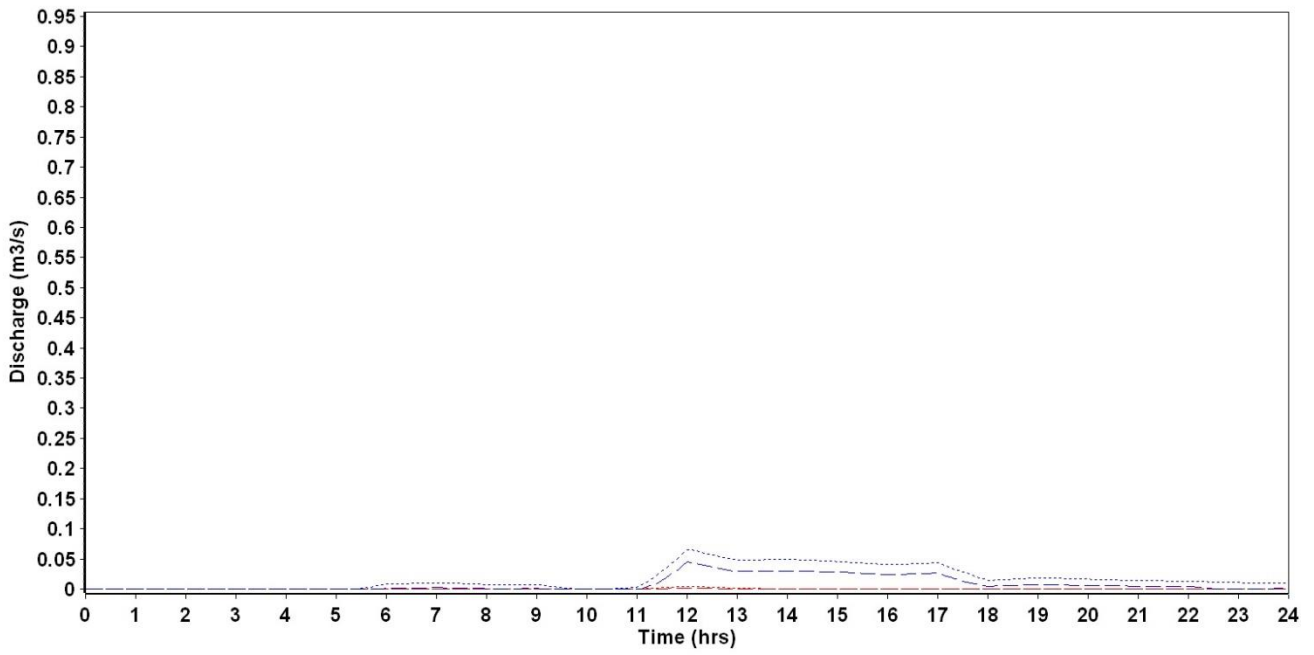
Cross-section 6: No bank overtopping occurred at both summer and winter storm event.
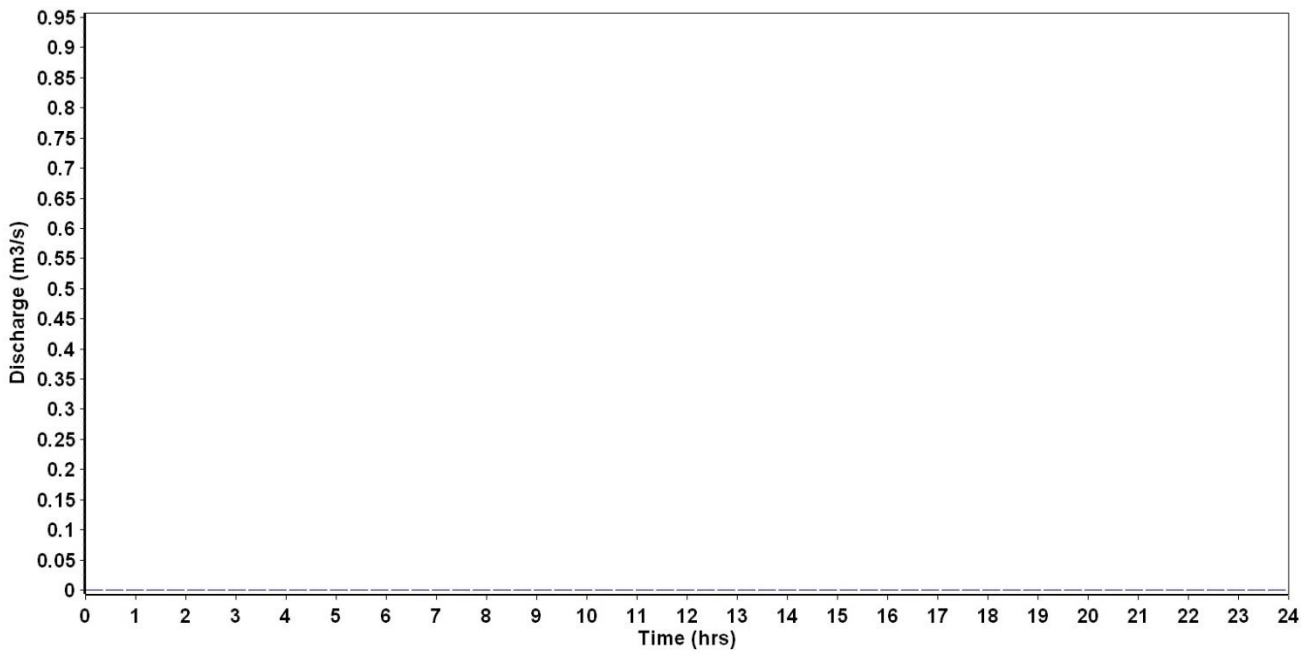
	Summer		Winter
---	Obstructed channel	---	Obstructed channel
....	Unobstructed channel	....	Unobstructed channel

Cross-section 7: No bank overtopping occurred at both summer and winter storm event.
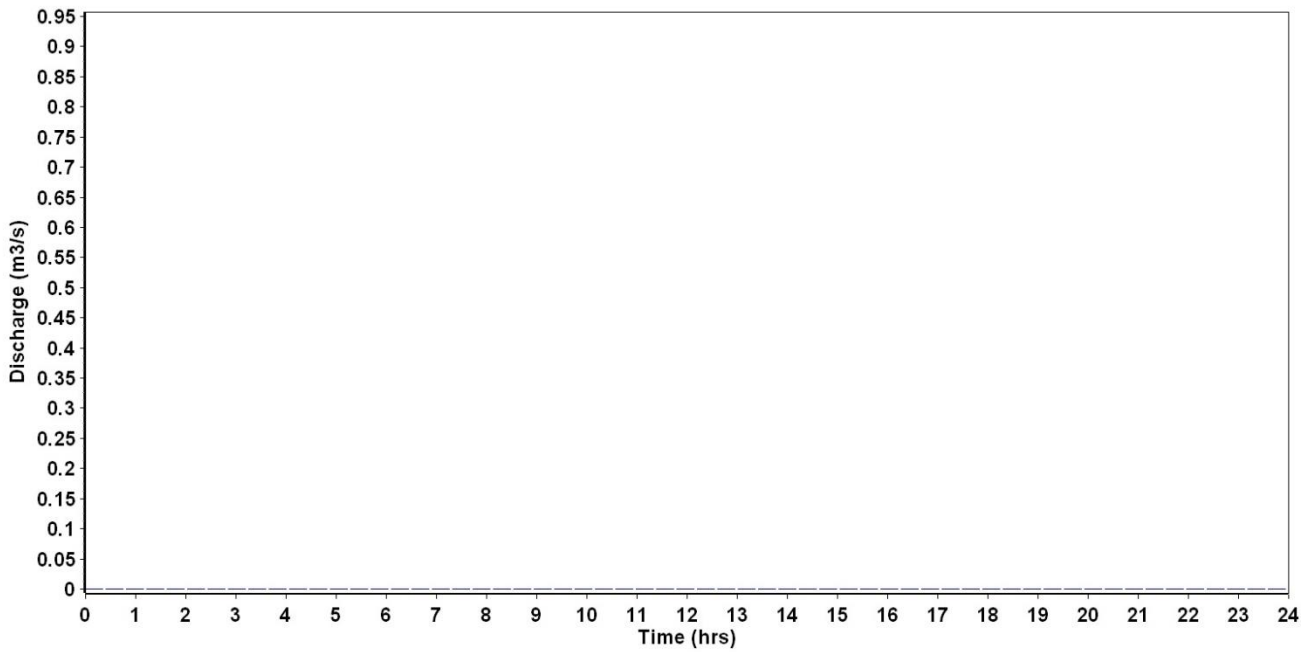
Cross-section 8: No bank overtopping occurred at both summer and winter storm event.
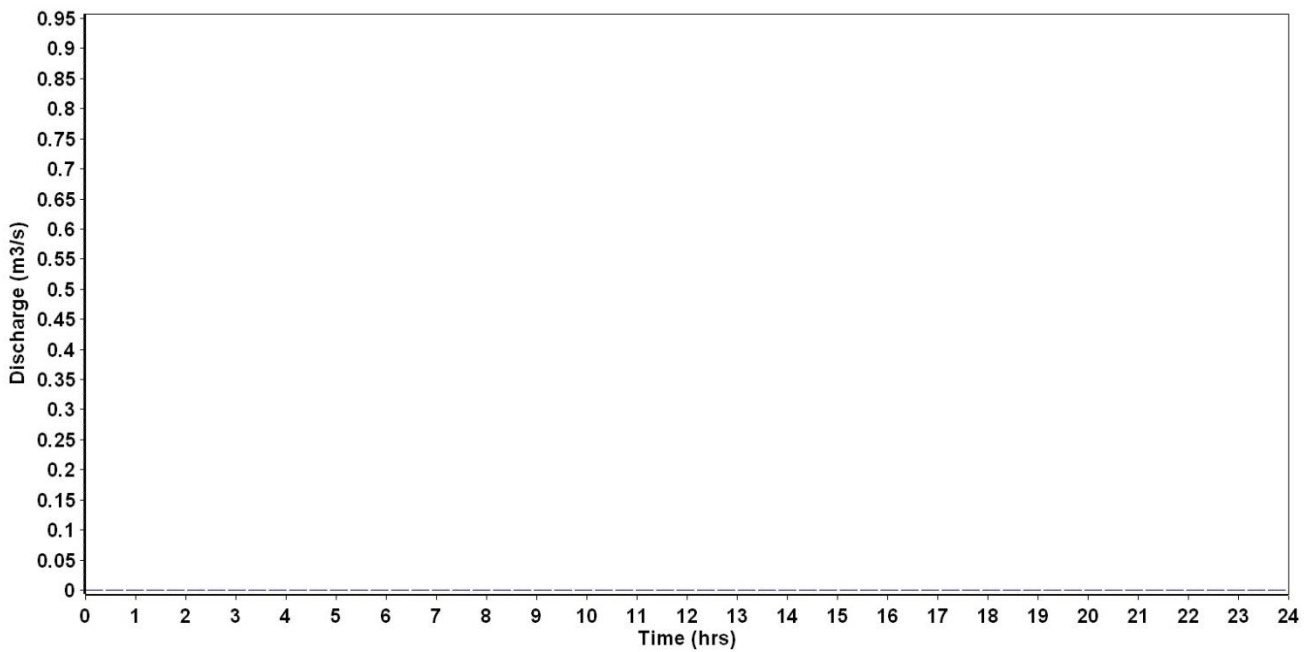
Summer	Winter
– – – Obstructed channel	– – – Obstructed channel
·········· Unobstructed channel	·········· Unobstructed channel

Cross-section 9: No bank overtopping occurred at both summer and winter storm event.
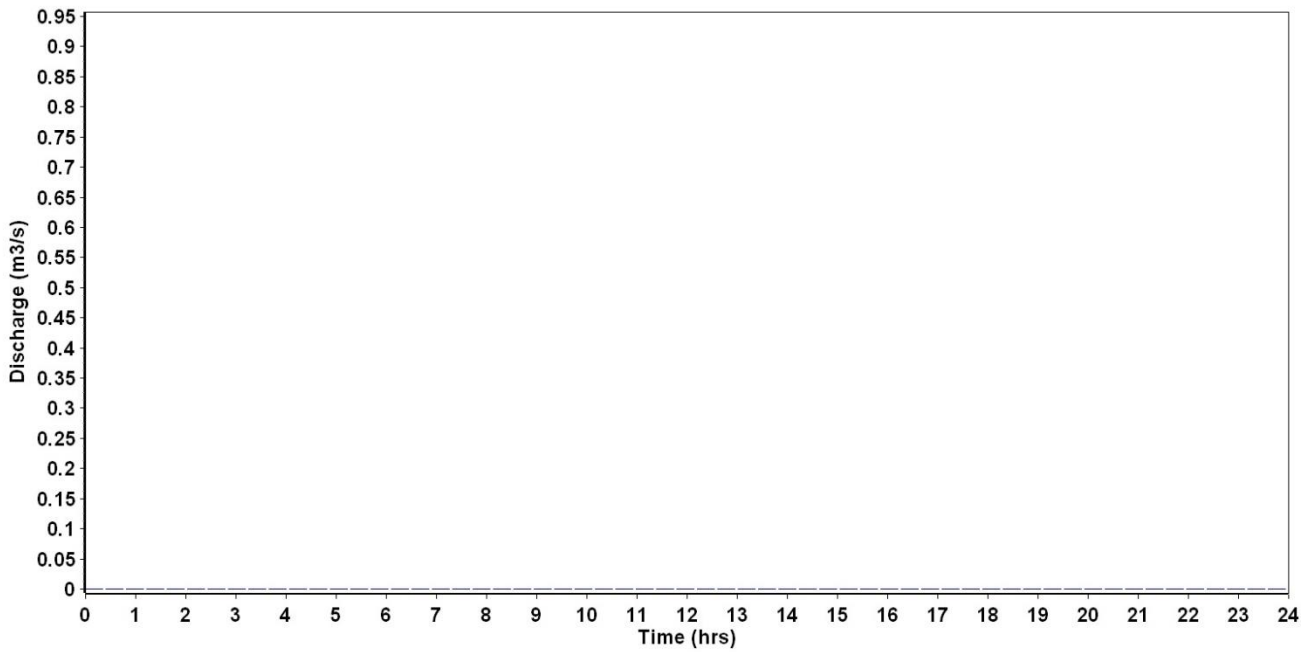
Cross-section 10: No bank overtopping occurred at both summer and winter storm event. WDD 17 located at this cross-section.
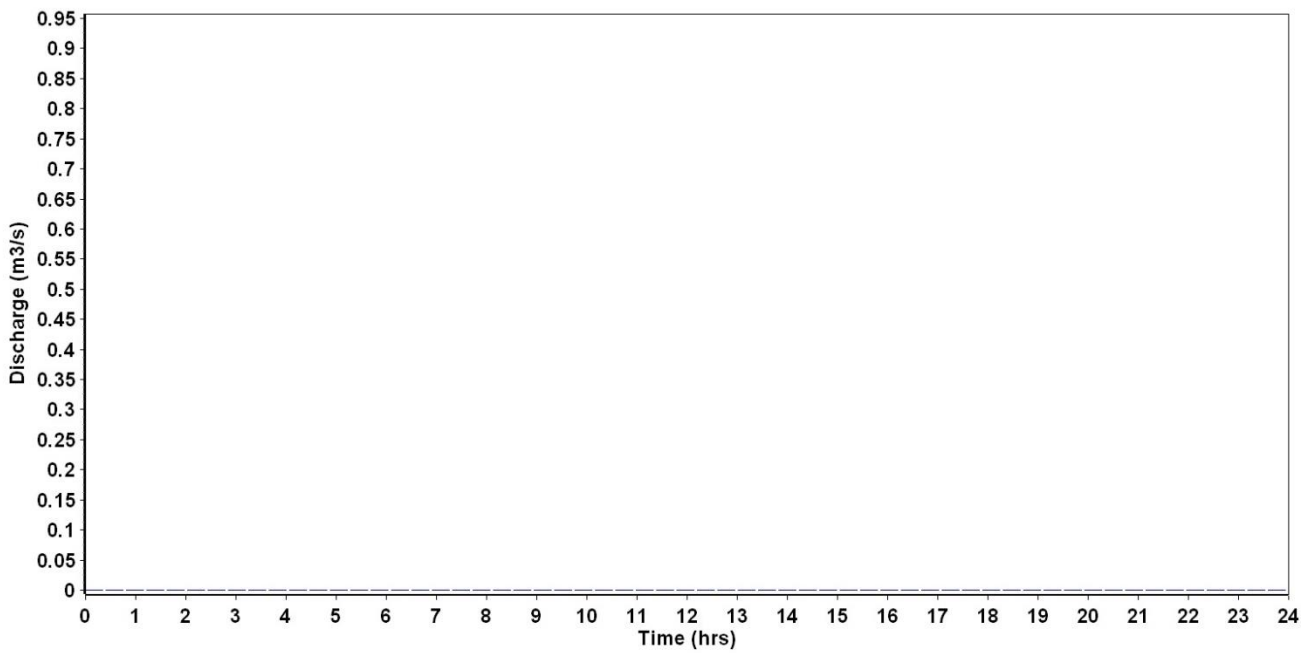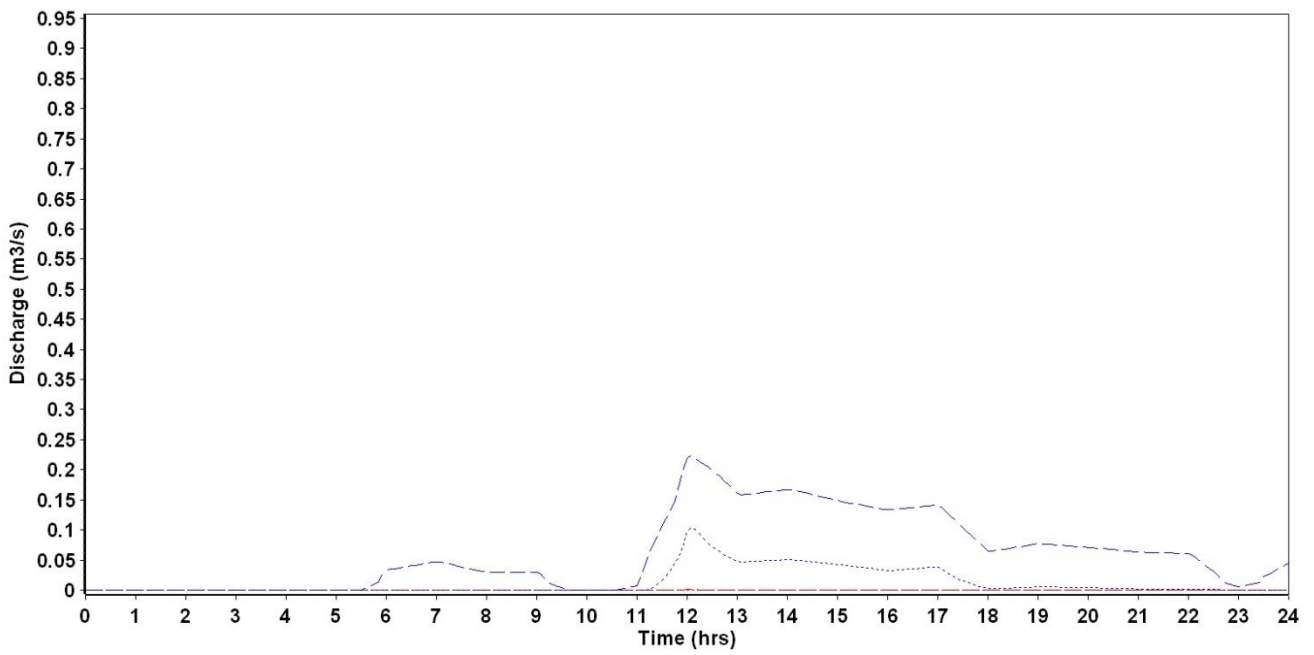

	Summer		Winter
- - -	Obstructed channel	- - -	Obstructed channel
········	Unobstructed channel	········	Unobstructed channel

Cross-section 11: WDD 16 located at this cross-section.
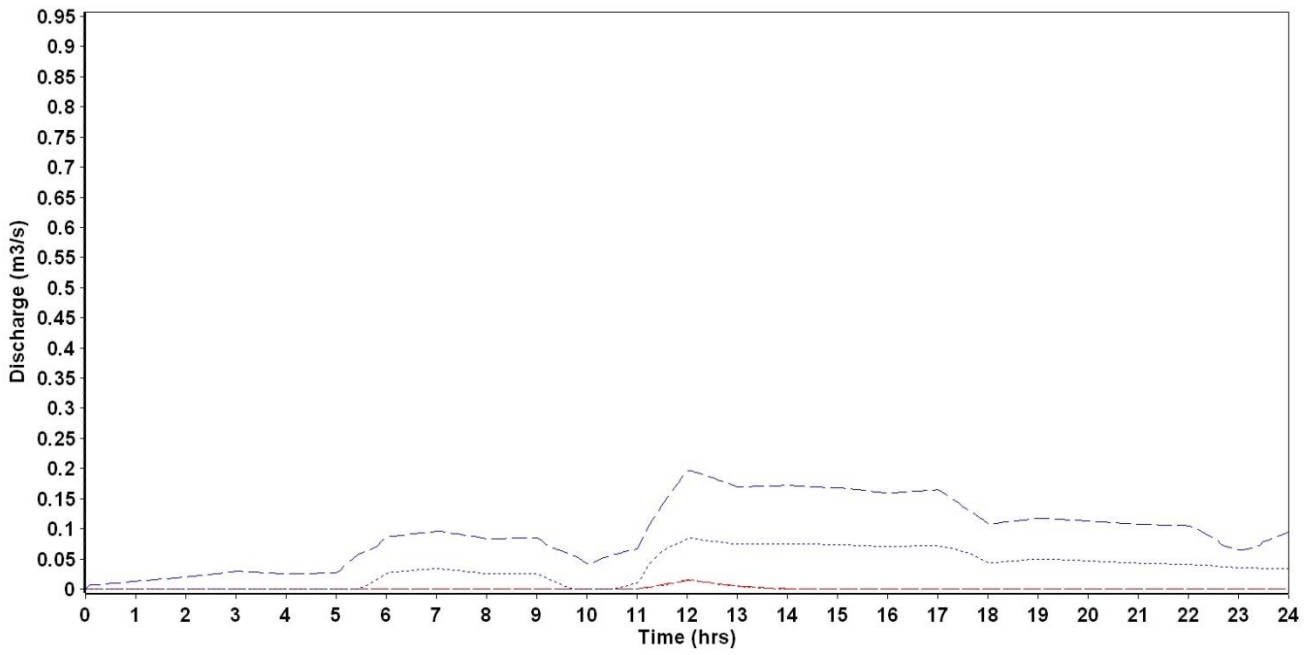
Cross-section 12:

Summer	Winter
– – – Obstructed channel	– – – Obstructed channel
·········· Unobstructed channel	·········· Unobstructed channel

Cross-section 13: WDD 15 located at this cross-section.
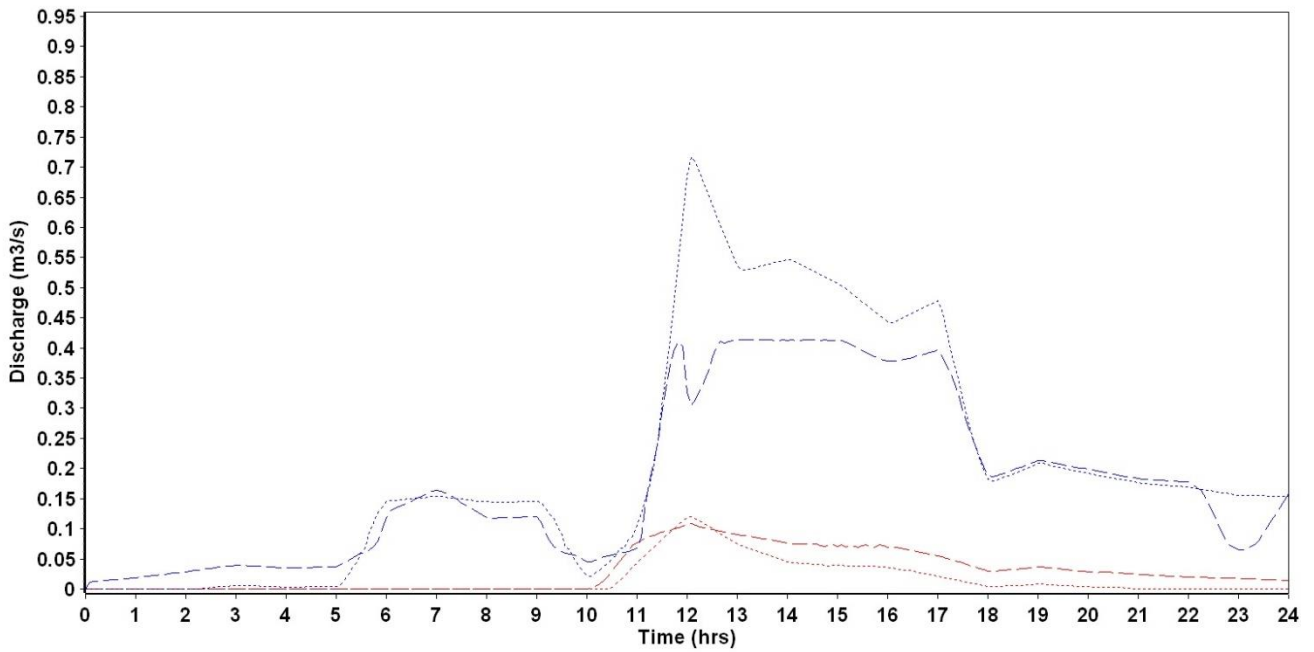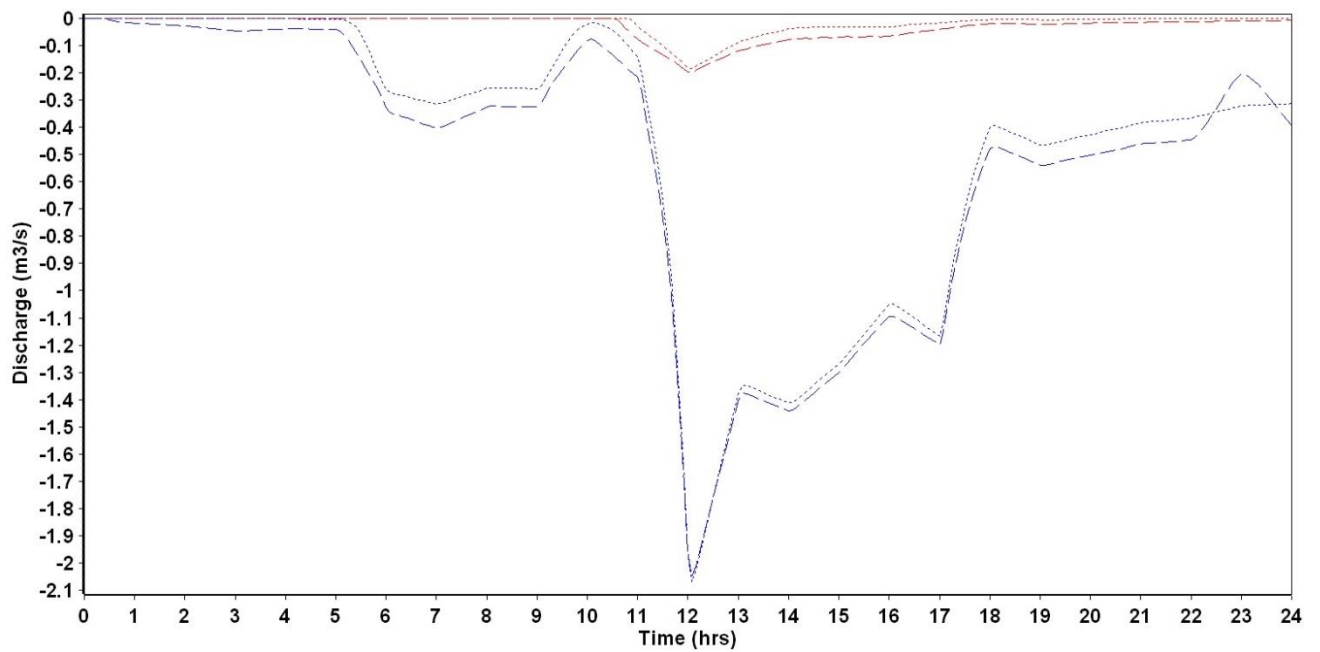

Cross-section 14: WDD 14 located at this cross-section.
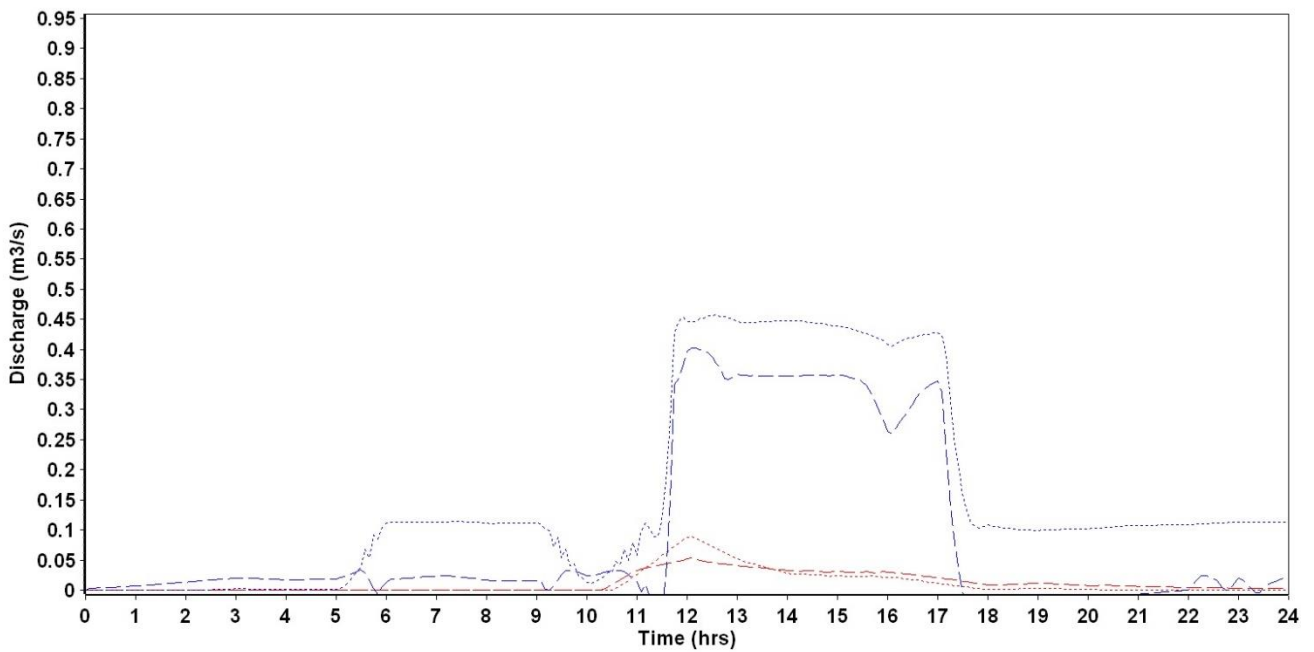
Summer		Winter	
- - - Obstructed channel		- - - Obstructed channel	
········· Unobstructed channel		········· Unobstructed channel	

Cross-section 15: Flow re-entering the channel.
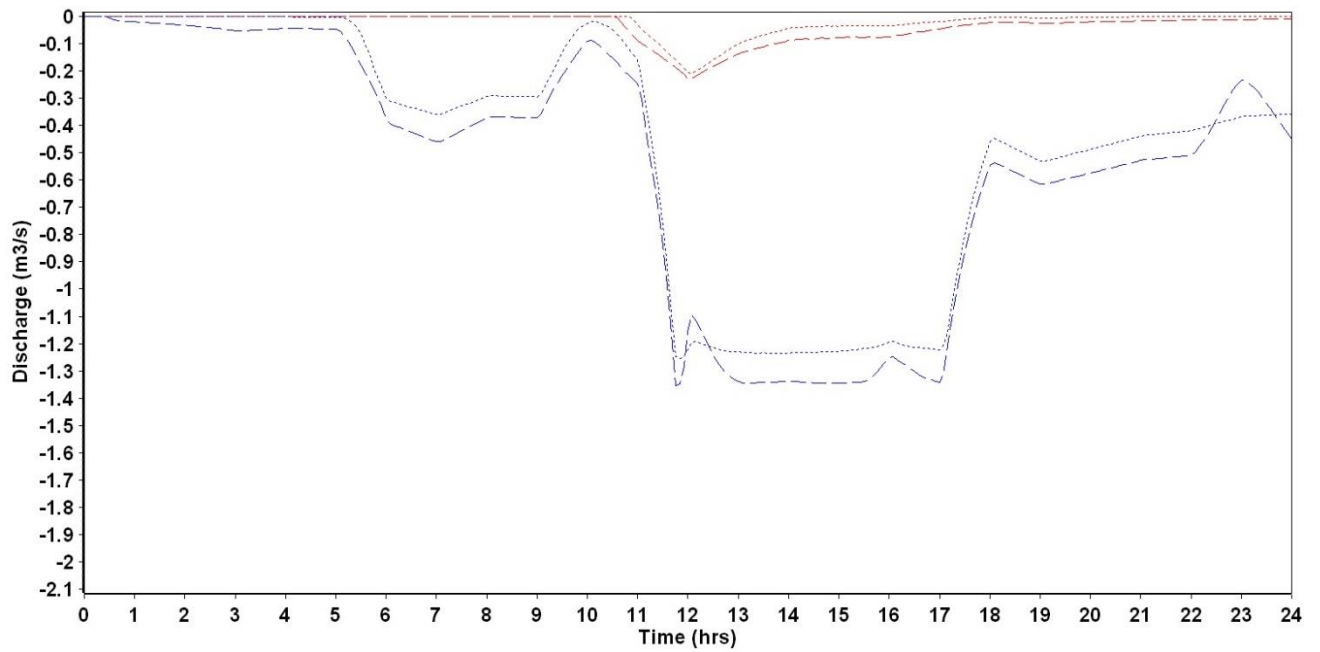
Cross-section 16: Flow re-entering the channel.

Summer	Winter
--- Obstructed channel	--- Obstructed channel
········ Unobstructed channel	········ Unobstructed channel